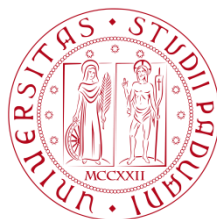


Atti della XX Riunione Nazionale di Elettromagnetismo



Padova, 15-18 settembre 2014



**UNIVERSITÀ
DEGLI STUDI
DI PADOVA**



The XX RiNEm was organized by SIEm, Società Italiana di Elettromagnetismo, and by the Photonics and Electromagnetics Group, University of Padova.

CONFERENCE CHAIR

A. Galtarossa, University of Padova

CONFERENCE STEERING COMMITTEE

P. Bassi, University of Bologna

A. Galtarossa, University of Padova

T. Isernia, University of Reggio Calabria

G. Manara, University of Pisa

A. Massa, University of Trento

L. Perregrini, University of Pavia

G. Schettini, University of Roma Tre

LOCAL ORGANIZATION

E. Autizi, University of Padova

A.-D. Capobianco, University of Padova

L. Palmieri, University of Padova

M. Santagiustina, University of Padova

Cover picture: Piazza della Frutta (from <http://padovacultura.padovanet.it>)

ISBN 978-88-907599-4-9

THE XX RiNEM WAS PROMOTED BY



AND ORGANIZED BY



UNIVERSITÀ
DEGLI STUDI
DI PADOVA



UNDER THE AUSPICES OF



Society AEIT per la Tecnologia
dell'Informazione e delle Comunicazioni

Gruppo Tematico
"Fotonica ed Elettro-ottica"



consorzio nazionale
interuniversitario
per le telecomunicazioni



Comune di Padova



PATROCINIO
REGIONE DEL VENETO

AND WAS SPONSORED BY



The XX Italian Meeting on Electromagnetics takes place in Padova on 15–18 September 2014. This edition has been organized by the Photonics and Electromagnetics Group of the University of Padova. The event represents an unique occasion for researchers working in the field and coming from different universities, research centers, and company/industries to meet and exchange their latest experiences and results.

The contributions submitted for presentation to this edition of the meeting have been grouped in 12 oral and 1 poster sessions. The scientific program foresees also an URSI special session, a session “InSIEm - giovani verso l’impresa” with the aim of encouraging encounters between the research world and the industrial one, and an initial plenary session, where eminent invited experts coming from international universities will present their research achievements in different fields in electromagnetics from microwaves to optics.

This meeting represents also a great opportunity for students to be exposed to the country-wide state of the art in electromagnetics. To stimulate an active participation of young researchers and PhD students three different prizes (Barzilai Prize, Latmiral Prize, and Sannino Prize) will be also awarded and announced at the closing session.

*Paolo Lampariello
President of SIEm*

The XX “*Riunione Nazionale di Elettromagnetismo*” took place in Padova, hosted by the University of Padova, from Monday 15th to Thursday 18th, September 2014. The XX RiNEM was promoted by the Italian Electromagnetics Society (SIEM), and organized by the Photonics and Electromagnetics Group of the Department of Information Engineering of the University of Padova, with the sponsorship of the IEEE Italian Chapter, EuMA, URSI, MECSA, AICT, AEIT, CNIT, the Veneto Region, the Padova Province, the Padova Municipality and the University of Padova.

The XX RiNEM started in the morning of September 15th with the URSI meeting in Archivio Antico of the Palazzo Bo.

The Opening Ceremony, on September 15th, was hosted in the historical Aula Magna of the Palazzo Bo, with three plenary talks: Anders Overgaard Bjarklev, President the Technical University of Denmark, “*Microwave and Photonic Metamaterials - The DTU Perspective*”; Max Lemme, University of Siegen, Germany, “*Graphene and related Two-Dimensional Materials: a Toolkit for Future Electronics Applications?*”; Giulio Peruzzi, University of Padova and Accademia Galileiana di Scienze Lettere e Arti, “*Tops, vortices, and fields. Maxwell and the use of analogies and metaphors in science*”.



All technical sessions and the technical exhibition were hosted from September 16th to September 18th at Centro Congressi “A. Luciani”.



On Tuesday 17th afternoon, in cooperation with CNIT and sponsored by EuMA the first edition of the event “*InSIEM-giovani verso l’impresa*” was opened

by Paolo Lampariello, SIEm President, and by Gianni Vernazza, CNIT Director. In the first part there were seven invited talks of a Board of Experts, all affiliated to Science Parks and Innovation Incubators. In the second part there was a poster session where junior researchers from SIEm and CNIT presented innovative projects dedicated to the technological transfer and the industrial development. Four prizes for the best ideas were assigned to young inventors: Daniele Melati, Cecilia Occhiuzzi, Alessandro Polo and Luca Schenato. The four prizes were awarded during the Gala Dinner in the Sala Rossini of the historical Caffè Pedrocchi.



There were twelve oral sessions (scheduled to run in parallel pairs) with 77 oral presentations and one poster session with 49 posters.

The 2014 Barzilai Prize for young authors was awarded *ex-æquo* to “Exploiting compressive sensing in MNP enhanced MWI for breast cancer imaging”, authored by Martina Bevacqua and Rosa Scapatucci, and “Leaky wave interactions with a planar interface between dissipative media”, authored by Nicola Tedeschi.

The 2014 Latmiral Prize for the best poster presented by a young author was awarded to “A statistical model for the propagation through wave-chaotic systems”, authored by Gabriele Gradoni.

The 2014 Sannino Prize for the best paper presented by a young author on microwave and millimeter waves in circuits and devices was awarded to Fabrizio Chiarello with the paper “Fast tunable fiber optical frequency comb based on cascaded four-wave mixing”.

The success of the XX RiNEm was the result of the concurrent efforts and dedication of many people. Special thanks to the Members of the Steering Committee for the organization of the technical sessions: Paolo Bassi, Tommaso Isernia, Giuliano Manara, Andrea Massa, Luca Perregrini and Giuseppe Schettini. The Local Organizing Committee, composed by Elena Autizi, Antonio Daniele Capobianco, Luca Palmieri and Marco Santagiustina, gave a great contribution in organizing the XX RiNEm and in preparing the website and the proceedings.

I would express on behalf of all participants my sincere appreciation and gratitude to all of them and to the sponsors. Thanks to their commitment and talent the XX RiNEm was a pleasant and rewarding experience for all of us.

Andrea Galtarossa
Conference Chair of the XX RiNEm

RiNEm: Previous Editions

- I. L'Aquila, 24–25 June 1976
Chair: Prof. Fernando Bardati
- II. Pavia, 2–4 October 1978
Chair: Prof. Giuseppe Conciauro
- III. Bari, 25–27 June, 1980
Chair: Prof. Roberto De Leo
- IV. Firenze, 4–6 October, 1982
Chair: Prof.ssa Annamaria Scheggi
- V. Saint Vincent, 9–12 October 1984
Chair: Prof. Mario Orefice
- VI. Trieste, 22–24 October 1986
Chair: Prof. Edoardo Carli
- VII. Frascati, 5–8 September 1988
Chair: Prof. Fernando Bardati
- VIII. Capri, 9–12 October 1990
Chair: Prof. Giorgio Franceschetti
- IX. La Cittadella, 5–8 October 1992
Chair: Prof. Roberto Sorrentino
- X. Cesena, 21–23 September 1994
Chair: Prof. Gabriele Falciasecca
- XI. Firenze, 1–4 October 1996
Chair: Prof.ssa Laura Ronchi Abbozzo
- XII. Cetraro, 28 September – 1 October 1998
Chair: Prof. Giuseppe Di Massa
- XIII. Como, 25–28 September 2000
Chair: Prof. Carlo Capsoni
- XIV. Ancona, 16–19 September 2002
Chair: Prof. Tullio Rozzi
- XV. Cagliari, 13–16 September 2004
Chair: Prof. Giuseppe Mazzeola
- XVI. Genova, 18–21 September 2006
Chair: Prof. Matteo Pastorino
- XVII. Lecce, 15–19 September 2008
Chair: Prof. Luciano Tarricone
- XVIII. Benevento, 6–10 September 2010
Chair: Prof. Innocenzo Pinto
- XIX. Roma, 10–14 September 2012
Chairs: Prof. Giuseppe Schettini and Prof. Lucio Vegni

Program at a glance

	Monday	Tuesday	Wednesday		Thursday	
08:30–09:00		Registration	Registration		Registration	
09:00–09:30						
09:30–10:00		SIEm meeting (Auditorium)	Session 1 EMF for energy and environment applications (Sala A)	Session 2 Optical fibers (Sala B)	Session 7 Metamaterials (Sala A)	Session 8 Numerical methods (Sala B)
10:00–10:30						
10:30–11:00			Poster		Coffee break	
11:00–11:30						
11:30–12:00	URSI meeting (Archivio Antico)	Lunch		Session 9 Nanomaterials (Sala A)	Session 10 Remote sensing (Sala B)	
12:00–12:30						
12:30–13:00	Lunch	Lunch		Lunch		
13:00–13:30						
13:30–14:00						
14:00–14:30	Plenary Session (Aula Magna)	InSIEm (Auditorium)	Session 3 Microwaves and RFID (Sala A)	Session 4 Integrated and nonlinear optics (Sala B)	Session 11 Bio-EM and biomedical applications (Sala A)	Session 12 Inverse scattering problems (Sala B)
14:30–15:00						
15:00–15:30		Coffee break	Coffee break		Prizes and conclusion (Sala A)	
15:30–16:00						
16:00–16:30	Plenary Session (Aula Magna)	Poster – InSIEm (Auditorium)	Session 5 Antennas (Sala A)	Session 6 EMF propagation (Sala B)		
16:30–17:00						
17:00–17:30						
17:30–18:00						
18:00–18:30						
18:30–19:00						
19:00–19:30						
19:30–20:00						
20:00–23:00	Social dinner (Caffè Pedrocchi)					
	Palazzo Bo	Centro Congressi "A. Luciani"				

Plenary Session

Monday, September 15th, 14:30 – 18:15
Aula Magna, Palazzo Bo

Chair: Paolo Lampariello, University of Roma La Sapienza

- PL.1** *Microwave and photonic metamaterials – The DTU perspective,*
Anders Overgaard Bjarklev, President the Technical University of
Denmark 26
- PL.2** *Graphene and related two-dimensional materials: a toolkit for future
electronics applications?,* Max Lemme, University of Siegen,
Germany 27
- PL.3** *Tops, vortices and fields. Maxwell and the use of analogies and
metaphors in science,* Giulio Peruzzi, University of Padova and
Accademia Galileiana di Scienze Lettere e Arti 28

Session 1: EMF for energy and environment applications

Wednesday, September 17th, 9:30 – 11:00
Sala A, Centro Congressi “A. Luciani”

Chair: Alessandro Toscano, University of Roma Tre

- S1.1 *Power waves and conjugate image impedance matching for wireless power transfer links*, Dionigi M., Mongiardo M. 29
- S1.2 *Electromagnetic field level control in built-up areas*, Franceschetti G., Iodice A., Riccio D., Ruello G. 33
- S1.3 *Hierarchical in silico validation procedure for biomass estimation techniques based on dielectric spectroscopy*, Muzi M., Mangini F., Stoja E. 37
- S1.4 *Circularly polarized robust antennas for wireless monitoring of concrete structures*, Castorina G., Mauro G.S., Morabito A.F., Di Donato L., Sorbello G. 41
- S1.5 *Surface and air heat island of Milan: spatial and temporal analysis from MODIS*, Anniballe R., Bonafoni S., Pierdicca N. 45
- S1.6 *SIEm meets COMSOL*

Session 2: Optical fibers

Wednesday, September 17th, 9:30 – 11:00
Sala B, Centro Congressi “A. Luciani”

Chair: Stefano Selleri, University of Parma

S2.1	<i>Photonic crystal fibers with reduced symmetry for high power lasers,</i> Coscelli E., Molardi C., Poli F., Cucinotta A., Selleri S.	49
S2.2	<i>Confinement loss scaling law analysis in tube lattice fibers,</i> Masruri M., Vincetti L., Cucinotta A., Selleri S.	53
S2.3	<i>Modal analysis of holey fiber mode-selective couplers,</i> Parini A., Riesen N., Argyros A., Lwin R., Leon-Saval S.G., Love J.D., Bellanca G., Bassi P.	57
S2.4	<i>DNA biosensors implemented on functionalized microstructured optical fibers Bragg gratings,</i> Candiani A., Cucinotta A., Selleri S.	61
S2.5	<i>High power fiber lasers for additive manufacturing applications,</i> Braglia A., Liu Y., Perrone G.	65
S2.6	<i>Coupling mechanism in multimode fibers,</i> Palmieri L., Santagiustina M., Galtarossa A.	69

Session 3: Microwaves and RFID

Wednesday, September 17th, 14:30 – 16:30
Sala A, Centro Congressi “A. Luciani”

Chair: Riccardo Tascone, CNR-IEIIT, Torino

S3.1	<i>A novel antenna for UHF RFID, Casula G.A.</i>	73
S3.2	<i>Design of a W band correlation unit, Addamo G., Peverini O.A., Virone G., Tascone R., Lumia M., Orta R.</i>	77
S3.3	<i>Wearable auto-tuning antenna for COSPAS-SARSAT rescue applications, Baroni A., Nepa P.</i>	81
S3.4	<i>Manufacture and test of an innovative configuration of printed UWB antenna, Mazzocchi S., Galli A., Sassaroli D., Zucca M.</i>	85
S3.5	<i>Near-field modular antenna for UHF RFID desktop reader applications, Caso R., Michel A., Buffi A.</i>	89
S3.6	<i>Analysis of lossy waveguide components by the BI-RME method combined with a perturbation technique, Giannini A., Bozzi M., Bressan M., Pasian M., Perregrini L.</i>	93
S3.7	<i>Wearable textile microwave components in substrate integrated waveguide technology, Moro R., Agneessens S., Rogier H., Bozzi M.</i>	97
S3.8	<i>SIEm meets ANRITSU</i>	

Session 4: Integrated and nonlinear optics

Wednesday, September 17th, 14:30 – 16:30
Sala B, Centro Congressi “A. Luciani”

Chair: Paolo Bassi, University of Bologna

- S4.1** *Extreme waves in nonlinear optics and oceanography*, Baronio F., Conforti M., Degasperis A., Onorato M., Wabnitz S. 101
- S4.2** *Non-invasive light detection on a silicon photonic chip*, Morichetti F., Grillanda S., Carminati M., Ferrari G., Sampietro M., Melloni A. . 105
- S4.3** *Backward second-harmonic generation of near infrared picosecond pulses*, Busacca A.C., Stivala S., Cino A.C., Curcio L., Tomasino A., Assanto G. 109
- S4.4** *The outcomes of SAPPHIRE, a generic foundry platform for silicon photonics*, Morichetti F., Annoni A., Grillanda S., Orlandi P., Malaguti S., Parini A., Strain M.J., Sorel M., Bellanca G., Bassi P., Melloni A. 113
- S4.5** *Collision enhanced dispersive wave generation*, Tonello A., Modotto D., Krupa K., Labruyère A., Shalaby B.M., Couderc V., Barthélémy A., Minoni U., Wabnitz S., Aceves A.B. 117
- S4.6** *Mesoscopic photonic crystals based stable planar cavities*, Magno G., Monmayrant A., Grande M., Lozes-Dupuy F., Gauthier-Lafaye O., Calò G., Petruzzelli V. 121
- S4.7** *Exploitation of whispering gallery mode resonances for characterization of rare-earth doped glass devices*, Palma G., De Palma L., Yano T., Nazabal V., Kishi T., Moréac A., Ferrari M., Prudenzano F. 125
- S4.8** *Radiating shock waves in passive optical resonators*, Malaguti S., Conforti M., Bellanca G., Trillo S. 129

Session 5: Antennas

Wednesday, September 17th, 17:00 – 19:00
Sala A, Centro Congressi “A. Luciani”

Chair: Giuseppe Mazzarella, University of Cagliari

S5.1	<i>Laboratory tests assessing a nonredundant NF-FF transformation technique with plane-polar scanning</i> , D’Agostino F., Ferrara F., Gennarelli C., Guerriero R., Migliozzi M.	133
S5.2	<i>Fabry-Perot antenna with improved bandwidth</i> , Di Massa G., Moreno H.O., Costanzo S.	137
S5.3	<i>Compressed sensing/sparse recovery approach for array diagnosis using undersampled near-field data</i> , Costanzo S., Migliore M. D., Borgia A., Pinchera D., Di Massa G.	141
S5.4	<i>Design of a planar sub-array for smart antenna applications</i> , Di Filippo M., Lucci L., Pelosi G., Selleri S.	145
S5.5	<i>Reconfigurable concentric circular arrays: a novel hybrid synthesis method</i> , Bucci O.M., Perna S., Pinchera D.	149
S5.6	<i>New tools for analysis and synthesis of real antenna devices</i> , Rocca P.	153
S5.7	<i>Strategies for scattering reduction of antenna arrays</i> , Genovesi S., Costa F., Monorchio A., Manara G.	157
S5.8	<i>Substrate Integrated Waveguide (SIW) cavity-backed patch antenna</i> , Losito O., Castellano T., Chiapperino M., Bozzetti M., Venanzoni G., Angeloni G., Renghini C., Carta P., Mencarelli D., Farina M., Morini A., Prudenzeno F.	161

Session 6: EMF propagation

Wednesday, September 17th, 17:00 – 19:00
Sala B, Centro Congressi “A. Luciani”

Chair: Piero Tognolatti, University of L’Aquila

- S6.1 *Wigner function approach for the radiation of complex electromagnetic sources*, Gradoni G. 165
- S6.2 *Study of the multipath distribution in urban environment for 5G mobile radio*, Barbiroli M., Degli-Esposti V., Falciasecca G., Fuschini F., Tian L., Vitucci E.M. 169
- S6.3 *On the scattering by a cylindrical target below a rough Gaussian surface*, Ponti C. 173
- S6.4 *Electromagnetic scattering by a dielectric sphere embedded in a circular cylinder*, Mangini F., Tedeschi N. 177
- S6.5 *Plane-wave scattering by a perfectly conducting elliptic cylinder near a plane surface*, Santini C., Mangini F., Tedeschi N. 181
- S6.6 *A novel Bessel beam launcher based on higher-order leaky modes*, Fuscaldo W., Valerio G., Galli A., Sauleau R., Ettorre M. 185
- S6.7 *Radiofrequency power coupled to high-density plasmas for driving current in thermonuclear reactors*, Amicucci L., Cardinali A., Castaldo C., Cesario R., Galli A., Napoli F., Schettini G., Tuccillo A.A. 189
- S6.8 *Electromagnetic backscattering models for a couple of buildings*, Ciotola A., Di Martino G., Iodice A., Riccio D., Ruello G. 193

Session 7: Metamaterials
In memory of prof. Giorgio Gerosa

Thursday, September 18th, 9:00 – 11:00
Sala A, Centro Congressi “A. Luciani”

Chair: Paolo Lampariello, University of Roma La Sapienza

S7.1	<i>Epsilon-near-zero based antennas, La Spada L., Vegni L.</i>	197
S7.2	<i>Metamaterial-based electromagnetic wave absorber, La Spada L., Vegni L.</i>	201
S7.3	<i>Radiation from vertical dipoles in the presence of homogenized omnidirectional metasurfaces, Di Ruscio D., Burghignoli P., Baccarelli P., Galli A.</i>	205
S7.4	<i>On the applications of a particular electric-magnetic uniaxial lossy medium, Khalid M.</i>	209
S7.5	<i>A hybrid algorithm for overcoming the branch ambiguity problem in the retrieval of the equivalent parameters of a double negative metamaterial, Sgrò A., De Carlo D., Angiulli G.</i>	213
S7.6	<i>Use of metamaterials to improve electrical and radiating performances of horn antennas, Barbuto M., Bilotti F., Monti A., Ramaccia D., Toscano A.</i>	217
S7.7	<i>Chipless RFID with metasurfaces, Costa F., Genovesi S., Monorchio A., Manara G.</i>	221

Session 8: Numerical methods

Thursday, September 18th, 9:00 – 11:00
Sala B, Centro Congressi “A. Luciani”

Chair: Luca Perregrini, University of Pavia

- S8.1** *A mortar-element method for the analysis of cylindrical guiding structures*, Tibaldi A., Addamo G. 225
- S8.2** *Source stirring analysis for reverberation chambers*, Cerri G., De Leo A., Mariani Primiani V., Russo P. 229
- S8.3** *Modeling the electromagnetic field in anisotropic inhomogeneous magnetized plasma of ECR ion sources*, Torrisi G., Mascali D., Neri L., Sorbello G., Celona L., Castro G., Di Donato L., Isernia T., Gammino S. 233
- S8.4** *Assessment of the performances of GMRES(r) using a domain decomposition approach as a preconditioner*, Ntibarikure L., Pelosi G., Selleri S. 237
- S8.5** *A new approach the analysis of sectorial elliptic waveguides*, Fanti A., Mazzearella G. 241
- S8.6** *Beam coupling impedance simulation and RF measurements of a passive extraction septum for particle absorbing in the CERN proton synchrotron*, Persichelli S., Migliorati M. 245
- S8.7** *SIEm meets ANSYS*

Session 9: Nanomaterials

Thursday, September 18th, 11:30 – 13:00
Sala A, Centro Congressi “A. Luciani”

Chair: Costantino De Angelis, University of Brescia

- S9.1** *Novel FD-BPM formulation for the analysis of graphene-assisted optical devices*, Capobianco A.D., Locatelli A., De Angelis C., Boscolo S., Midrio M. 249
- S9.2** *Graphene-based one-dimensional grating for enhanced absorbers*, Grande M., Vincenti M.A., Stomeo T., Bianco G.V., De Ceglia D., Magno G., Petruzzelli V., Bruno G., De Vittorio M., Scalora M., D’Orazio A. 253
- S9.3** *Material-by-design for advanced electromagnetic devices*, Oliveri G. 257
- S9.4** *Characterization of nanocomposites based on MWCNTs for radar absorbing applications*, Miscuglio M., Hajj Yahya M., Savi P., Giorcelli M., Tagliaferro A. 261
- S9.5** *Graphene-assisted amplitude and phase modulation in silicon photonics*, Midrio M., Galli P., Romagnoli M., Kimerling L.C., Michel J. 265

Session 10: Remote sensing

Thursday, September 18th, 11:30 – 13:00
Sala B, Centro Congressi “A. Luciani”

Chair: Daniele Riccio, University of Napoli Federico II

- S10.1** *Remote retuning of X-band mini weather radar using ground clutter echoes*, Bertoldo S., Lucianaz C., Rorato O., Allegretti M., Perona G. 269
- S10.2** *Electromagnetic-based approach for RGB representation of SAR multitemporal data*, Amitrano D., Di Martino G., Iodice A., Riccio D., Ruello G. 273
- S10.3** *Electromagnetic model for SAR shape from shading*, Di Martino G., Di Simone A., Iodice A., Riccio D., Ruello G. 277
- S10.4** *TELAER: an italian interferometric airborne SAR system*, Perna S., Berardino P., Esposito C., Fornaro G., Gifuni A., Jackson G., Pauciuolo A., Lanari R. 281
- S10.5** *GNSS-R signal strength sensitivity to soil moisture*, Notarpietro R., Pei Y., Savi P. 285
- S10.6** *Modeling the polarimetric response to atmospheric precipitation on synthetic aperture radar imagery over ocean*, Polverari F., Mori S., Pulvirenti L., Pierdicca N., Marzano F.S. 289

Session 11: Bioelectromagnetism and biomedical applications

Thursday, September 18th, 14:30 – 16:00
Sala A, Centro Congressi “A. Luciani”

Chair: Guglielmo D’Inzeo, University of Roma La Sapienza

- S11.1** *Monitoring of tissue shrinkage during a microwave thermal ablation procedure*, Farina L., Weiss N., Nissenbaum Y., Cavagnaro M., Lopresto V., Pinto R., Tosoratti N., Amabile C., Cassarino S., Goldberg S.N. 293
- S11.2** *Nanoscale imaging through optical fiber extrinsic micro-cavity scanning microscopy*, Di Donato A., Pietrangelo T., Mencarelli D., Farina M. 297
- S11.3** *A mm-wave 2D ultra-wideband radar for breast tumour imaging*, Moscato S., Matrone G., Pasian M., Mazzanti A., Bozzi M., Perregrini L., Svelto F., Magenes G., Arcioni P., Summers P. 301
- S11.4** *A comparison of simple models to evaluate dielectric properties of human tissues at 2.45 GHz from water content*, Cavagnaro M., Frezza F., Laurita R., Tannino M. 305
- S11.5** *Contrast aided blind focusing of the electromagnetic field for microwave hyperthermia*, Bellizzi G., Bucci O.M. 309
- S11.6** *Exploiting compressive sensing in MNP enhanced MWI for breast cancer imaging*, Bevacqua M., Scapaticci R. 313

Session 12: Inverse scattering problems

Thursday, September 18th, 14:30 – 16:00
Sala B, Centro Congressi “A. Luciani”

Chair: Tommaso Isernia, Mediterranean University of Reggio Calabria

- S12.1** *Observing scattered fields in view and frequency diversities,*
Maisto M.A., Solimene R., Pierri R. 317
- S12.2** *A numerical microwave tomographic algorithm to improve reconstruction
of buried objects,* Comite D., Galli A., Catapano I., Soldovieri F. .. 321
- S12.3** *Innovative passive techniques for crowd opportunistic wireless
localization,* Viani F. 325
- S12.4** *Direct and inverse scattering of axially moving multilayer elliptic
cylinders,* Pastorino M., Raffetto M., Randazzo A. 329
- S12.5** *Synthetic experiments and field conditioning as an effective approach to
inverse scattering,* Bevacqua M., Di Donato L., Crocco L.,
Isernia T. 333

Poster Session

Wednesday, September 17th, 11:00 – 13:00
Centro Congressi “A. Luciani”

Chair: Antonio-D. Capobianco, Marco Santagiustina, Luca Palmieri,
University of Padova

- P.01** *A printed LPDA fed by a coplanar waveguide for wideband applications*, Casula G.A., Montisci G., Mazzarella G., Maxia P. 337
- P.02** *A numerical method to account for digitally-modulated carriers in time-modulated antenna arrays*, Masotti D., Francia P., Mastri F., Costanzo A., Rizzoli V. 341
- P.03** *A microwave displacement sensor system exploiting electromagnetic interferometry*, Costanzo A., Fantuzzi M., Masotti D., Rizzoli V. 345
- P.04** *Positioning errors compensation in a nonredundant spherical NF-FF transformation: experimental evidences*, D’Agostino F., Ferrara F., Gennarelli C., Guerriero R., Migliozzi M. 349
- P.05** *A simple and effective algorithm for the power synthesis of reconfigurable arrays with near-field nulls*, Buttazzoni G., Vescovo R. 353
- P.06** *UAV-based antenna verification system: extracted AUT pattern*, Paonessa F., Virone G., Peverini O.A., Addamo G., Orta R., Tascone R., Bolli P. 357
- P.07** *Research activities on UHF RFID systems at the University of Pisa - Research Unit*, Buffi A., Michel A., Caso R., D’Alessandro A., Baroni A., Nepa P. 361
- P.08** *Energy harvesting from electromagnetic emissions compact fluorescent lamps*, Monti G., Congedo F., Arcuti P., Tarricone L. 365
- P.09** *Wireless sensor network planning with electromagnetics*, Di Martino G., Iodice A., Riccio D., Ruello G. 369
- P.10** *Miniaturized fractal-shaped reflect arrays for wide-angle fixed-beam applications*, Costanzo S., Venneri F. 373
- P.11** *Data model for the exchange of augmented geometrical information: design and implementation*, Rossi F., Sabbadini M., Mioc F. 377
- P.12** *EBG-based spatial filters for directive antennas: a comparison between two different mechanisms*, Ceccuzzi S., Pajewski L., Ponti C., Schettini G. 381
- P.13** *Innovative wireless solutions for smart cities*, Giarola E., Marchesi S., Polo A., Robol F., Viani F., Zappini L., Zorer A., Massa A. 385

P.14	<i>Entropy based clutter mitigation in TWI</i> , Cuccaro A., Solimene R., Pierri R.	389
P.15	<i>Nanoparticle studies for biomedical applications</i> , Iovine R., Tarparelli R., Vegni L.	393
P.16	<i>Experimental generation and measurement of orbital angular momentum radio waves</i> , Spinello F., Mari E., Parisi G., Tamburini F., Romanato F., Somedà C.G.	397
P.17	<i>Homework Open-source Platform (HOP) to test the students' knowledge in electromagnetics</i> , Zappelli L.	401
P.18	<i>Wideband THz time domain spectroscopy set-up based on ultrafast pulsed laser: model and experiments</i> , Tomasino A., Stivala S., Busacca A.C., Cino A.C., Peccianti M., Morandotti R.	405
P.19	<i>A statistical model for the propagation through wave chaotic systems</i> , Gradoni G.	409
P.20	<i>Electromagnetic technology for visually impaired people</i> , Di Mattia V.	413
P.21	<i>The Italian contribution to the low frequency aperture array of the square kilometer array</i> , Bolli P., Bianchi G., Lingua A., Monari J., Murgia M., Perini F., Pupillo G., Schillirò F., Tartarini G., Virone G.	417
P.22	<i>Bit error rate evaluation of a silicon-on-insulator optical-network-on-chip router</i> , Parini A., Annoni A., Morichetti F., Melloni A., Bellanca G. ..	421
P.23	<i>Electromagnetic interaction with an alignment of spheres within a host sphere</i> , Mangini F.	425
P.24	<i>A convergence study between the models of a multilayer sphere and a radial uniaxial sphere</i> , Mangini F., Tedeschi N.	429
P.25	<i>REweighted, STandardized, Recursively Iterated Cerebral Tomography Algorithm (RESTRICTA).</i> , Muzi M.	433
P.26	<i>Cylindrical-wave reflection by plane interfaces as a solution of the inhomogeneous Bessel equation</i> , Tedeschi N.	437
P.27	<i>Leaky wave interactions with a planar interface between dissipative media</i> , Tedeschi N.	441
P.28	<i>Fast tunable fiber optical frequency comb based on cascaded four-wave mixing</i> , Chiarello F.	445
P.29	<i>Phaseless microwave imaging of dielectric targets: a combined two-probes/inexact-Newton method</i> , Costanzo S., Borgia A., Di Massa G., Pastorino M., Randazzo A.	449

P.30	<i>Radar activity at University of Calabria</i> , Costanzo S., Di Massa G., Spadafora F., Raffo A., Borgia A., Costanzo A., Morrone L.	453
P.31	<i>Measurement and simulation of stirring effects of field probes in a reverberation chamber</i> , Bastianelli L., Mariani Primiani V., Moglie F.	457
P.32	<i>SiGe BiCMOS technology for Ka-band SatCom on the move user terminals</i> , Boccia L., Shamsafar A., Arnieri E., Sandhu A.I., Amendola G., Purtova T., Tarabani F., Valenta V., Schumacher H., Meniconi E., Kaynak M., Tillack B., Luo Q., Gao S., Ziegler V.	461
P.33	<i>Design of magnetic-resonant wireless power transfer links realized with class E amplifiers</i> , Dionigi M., Leuzzi G., Lombardi F.M., Mongiardo M., Stornelli V.	465
P.34	<i>Neural network approaches to polarimetric SAR data processing</i> , Avezzano R.G., Del Frate F., Schiavon G.	469
P.35	<i>Grating lobes in synthetic arrays: effects and compensation</i> , Di Martino G., Iodice A., Riccio D., Ruello G.	473
P.36	<i>Analytical optimization methods to design coils for magnetic field gradients</i> , Tannino M., Mangini F.	477
P.37	<i>Hydrometeor extinction modeling for free-space optical channel characterization: rain and snow effects</i> , Mori S., Marzano F.S., Tosi Beleffi G.M., Di Bartolo S.	481
P.38	<i>All-solid photonic bandgap fibers with microstructured cladding</i> , Coscelli E., Poli F., Cucinotta A., Selleri S.	485
P.39	<i>Arc curvature effect on confinement loss in hypocycloid hollow core Kagome fibers</i> , Masruri M., Vincetti L., Debord B., Alharbi M., Bradley T., Fourcade-Dutin C., Wang Y.Y., G�r�me F., Benabid F. ..	489
P.40	<i>Processing of thin film materials by means of ns and ps laser radiation</i> , Sozzi M., Lutey A., Selleri S., Cucinotta A.	493
P.41	<i>Synthetic aperture interferometric radiometer: design, trade-off and technology</i> , Pompili S., Marzano F.S., Varchetta S.	497
P.42	<i>Imaging and inverse scattering @ ELEDIA research center</i> , Donelli M., Anselmi N., Oliveri G., Poli L., Rocca P., Tenuti L., Salucci M., Massa A.	501
P.43	<i>Electromagnetic interaction with the stained glass windows of the Magdalene chapel in the basilica in Assisi</i> , Rivaroli L., Stoja E., Mangini F.	505

P.44	<i>Antenna synthesis and analysis @ ELEDIA research center</i> , Donelli M., Anselmi N., Bekele E., Carlin M., Manica L., Oliveri G., Poli L., Rocca P., Salucci M., Tenuti L., Zambiasi L., Massa A.	509
P.45	<i>Statistical prediction of received frames along earth-satellite Ka-band links in deep space missions</i> , Biscarini M., Marzano F.S., Montopoli M., De Sanctis K., Iess L., Gregnanin M., Parisi M., Montagna M., Lanucara M.	513
P.46	<i>Radiation losses in substrate integrated waveguides: a formula for a quantitative determination</i> , Pasian M., Bozzi M., Perregrini L.	517
P.47	<i>Some recent advancements in optimal constrained power focusing for microwave hyperthermia</i> , Crocco L., Di Donato L., Iero D.A.M., Isernia T., Scapatucci R.	521
P.48	<i>A procedure for estimation on the electromagnetic field exposure levels</i> , Strappini M., Angelucci M., Vecchiocattivi M., Gianola P., Scotti R., Villani V., Migagheli D.	525
P.49	<i>In soil distributed temperature measurements for small scale physical models</i> , Bersan S., Schenato L., Rajendran A., Palmieri L., Cola S., Pasuto A., Galtarossa A., Simonini P.	529

MICROWAVE AND PHOTONIC METAMATERIALS – THE DTU PERSPECTIVE

Prof. Anders Overgaard Bjarklev

President the Technical University of Denmark

ABSTRACT

The Technical University of Denmark (DTU) was founded in 1829 by the discoverer of the coupling between electricity and magnetism, Hans Christian Ørsted, and today electromagnetics constitutes a major research area encompassing antennas, microwave circuits, optical communication, photonics, remote sensing and most recently the fascinating field of metamaterials.

This plenary talk will overview major DTU contributions to microwave and photonic metamaterial science and propose visions for the future of metamaterials. The talk will touch upon several topics, e.g. the homogenization of periodically structured metamaterials and the retrieval of physically meaningful material parameters constitute a central topic in metamaterial science and one that continuously attract significant research interests. Single and double negative metamaterials facilitate resonances in sub-wavelength structures and the nature of these resonances has been demonstrated for several canonical geometries such as composite cylinders and spheres with ideal or real material models and illuminated by plane waves or point sources. Also, if light propagating in a material can be slowed down, its interaction with the material can be enhanced. Using photonic crystal defect waveguides, it was recently shown that this effect can be used to enhance the gain of an active material, e.g. quantum wells or quantum dots, opening the possibility of realizing ultra-compact slow-light enhanced optical amplifiers for photonic integrated circuits.

Another topic will be structural colors: These offer an attractive approach to reduce the number of needed materials in a given product and it provides new perspectives for recycling and sustainability. Also, the role of optical metamaterials has evolved from pure exotic negative index cases and three-dimensional cloaking devices to more realistic examples, which have a strong potential for further development and photonic implementations. Among such examples so called epsilon-near-zero materials, hyperbolic (indefinite) metamaterials, optical topological insulators (non-magnetic optical diodes) and metamaterials with enhanced quantum functions, e.g. exhibiting giant photogalvanic effect.

The plenary speech will be based on the significant work and contributions of Lars-Ulrik Aaen Andersen, Samel Arslanagic, Olav Breinbjerg, Andrei Lavrinenko, Niels Asger Mortensen Jesper Mørk, Leif Katsuo Oxenlwe, and Anders O. Bjarklev, Technical University of Denmark.

GRAPHENE AND RELATED TWO-DIMENSIONAL MATERIALS: A TOOLKIT FOR FUTURE ELECTRONICS APPLICATIONS?

Prof. Max Lemme

University of Siegen, Germany

ABSTRACT

After an introduction of the state-of-the art in graphene and 2D materials and technology, this talk will discuss potential More-than-Moore applications for these materials. First, graphene field effect transistors (FETs) will be assessed for logic and radio frequency applications, followed by 2D FETs with semiconducting transition metal dichalcogenide (TMD) channels. Next, hot electron transistors with graphene components will be introduced that are projected to allow THz operation. Graphene is a broadband optoelectronic material that can operate from ultra-violet to THz radiation. TMDs are more limited in their spectral response, but show very high photon absorption. I will present examples for discrete photodetectors and modulators co-integrated with silicon photonics. Finally, the low mass of 2D materials makes them interesting for nanoelectromechanical systems. This will be discussed using the example of graphene membrane based piezoresistive pressure sensors.

TOPS, VORTICES, AND FIELDS. MAXWELL AND THE USE OF ANALOGIES AND METAPHORS IN SCIENCE

Prof. Giulio Peruzzi

University of Padova and Accademia Galileiana di Scienze Lettere e Arti

ABSTRACT

The use of analogies and metaphors goes along the whole historical path of modern science, which was born out of the Scientific Revolution. But a full awareness of the fundamental role of analogies and metaphors in the construction of science is acquired only in the nineteenth century, the century in which specialisation becomes more and more crucial to the growing of scientific knowledge. Actually, in phases of increasing specialisation, analogies and metaphors become important tools to reveal unexpected relations among different research areas and to disclose new research perspectives. Many scientists during the nineteenth century use these tools, but probably James Clerk Maxwell is the one who explores and exploits their power with the greatest epistemological awareness and skill. The overwhelming majority of the results of his researches, achieved in less than thirty years in physics, geophysics, physiology, metrology, engineering, are the prerequisites for important research areas up till now. One of the main reasons of the width and depth of his scientific production is actually the use of analogies and metaphors, which gives him the opportunity to connect different research areas by interpreting the results already obtained in a research area as a useful element to make progress in different and less known areas.

In this perspective, we will retrace some of Maxwell's most important scientific contributions, underlining the fertility of his approach for the subsequent development of science and technology.

POWER WAVES AND CONJUGATE IMAGE IMPEDANCE MATCHING FOR WIRELESS POWER TRANSFER LINKS

Marco Dionigi, Mauro Mongiardo

Department of Engineering
University of Perugia
Perugia, Italy
marco.dionigi@unipg.it; mauro.mongiardo@unipg.it

Abstract

The concept of power waves (PW) provides the correct framework to relate incident and reflected power in wireless power transfer (WPT) applications. For WPT problems it is customary to deal with complex impedances, either for the load, source, or reference, and it is therefore appropriate to use power waves and not the usual traveling waves.

In addition, for WPT networks, it is also necessary to use reference impedances, which satisfy the conjugate matched condition, i.e. the so-called conjugate image impedances. It is shown that the scattering matrix provides a meaningful description of a WPT link only when the appropriate reference impedances and scattering parameters definition are used.

Index Terms – Wireless power transmission, transmission efficiency, conjugate matching, maximum power transfer.

I. INTRODUCTION

Resonant Wireless Power Transfer (WPT) has received renewed interest after the experiment reported in [1]. Several investigations have been presented in the literature, see, e.g., [2] – [8] to cite just a few.

However, as noted in [9] – [14], when dealing with power transmission problems, the conventional definition of scattering parameters in terms of traveling waves proves not adequate. It is necessary to introduce power waves, a properly defined reflection coefficient, and appropriate reference impedances.

In this work, we introduce an analysis procedure based on the choice of conjugate image impedances as reference impedances for two-port networks [9].

II CONJUGATE IMAGE IMPEDANCES: DEFINITION AND COMPUTATION

For a two-port network the conjugate image impedances are defined such that when port two is closed with Z_{c2} we see, at port one, an impedance of value Z_{c1}^* ; similarly, when port one is closed with Z_{c1} we see—at port two—an impedance Z_{c2}^* . The values of the conjugate image

impedances Z_c and Z_{c2} can be computed as described in [9]. The impedance matrix of a two-port network is:

$$\begin{bmatrix} Z_{11} & Z_{12} \\ Z_{21} & Z_{22} \end{bmatrix}, \quad (1)$$

with $z_{ik}=r_{ik}+jx_{ik}$ ($i, k = 1, 2$). The conjugate image impedances for such network can be calculated using the elegant procedure of [9]; for a reciprocal network we can introduce:

$$\theta_r = \sqrt{\left(1 - \frac{r_{12}^2}{r_{11}r_{22}}\right) \left(1 + \frac{x_{12}^2}{r_{11}r_{22}}\right)} \quad (2)$$

$$\theta_x = \frac{r_{12}x_{12}}{r_{11}r_{22}} \quad (3)$$

The conjugate image impedances Z_{ci} can be obtained as:

$$Z_{c1} = r_{11}(\theta_r + j\theta_x) - jx_{11} \quad (4)$$

$$Z_{c2} = r_{22}(\theta_r + j\theta_x) - jx_{22} \quad (5)$$

III APPLICATION TO WPT SYSTEMS

Let us consider the structure shown in the left side of Fig. 1, where the first and last coils (input/output ports) are inductively coupled with the second and third coils. The second and the third coils are resonant at the operating frequency, while the first and the fourth coils may be chosen either configuration (resonant or not). This structure is similar to the one used in [1] and provides a viable example of a WPT system.

The structure of Fig. 1 (left side) can be characterized by taking measurements with a vector network analyzer (VNA) operating on 50-Ohms reference impedances (right side). It is advantageous to convert the scattering parameters into the impedance matrix and, from the latter, to compute the relative conjugate image parameters as described in the previous section. As an example, the conjugate image parameters for the measurements of Fig. 1 are reported in Fig. 2. It is apparent that, because of the negative sign of the conjugate impedance imaginary part, both ports of the circuit needs a series compensation capacitor in order to achieve the maximum transmission between the two ports. As an example, we have considered two different operating frequencies; at each frequency we have calculated the capacitance values from the reactance of the image parameters obtaining the values of 58.8 pF at 69.5 MHz and the value of 26 pF when an operating frequency of 68 MHz is used. The corresponding real parts of the image parameters are $R1=36.3\text{Ohm}$, $R2=56.5\text{Ohm}$ at 69.5 MHz and $R1=47.5\text{ Ohm}$, $R2=38.1\text{ Ohm}$ at 68 MHz. The correctly normalized scattering parameters are shown in Fig. 3. By comparing the latter figure with Fig. 1(right side) it becomes evident the importance of selecting as reference impedances the conjugate image impedances.

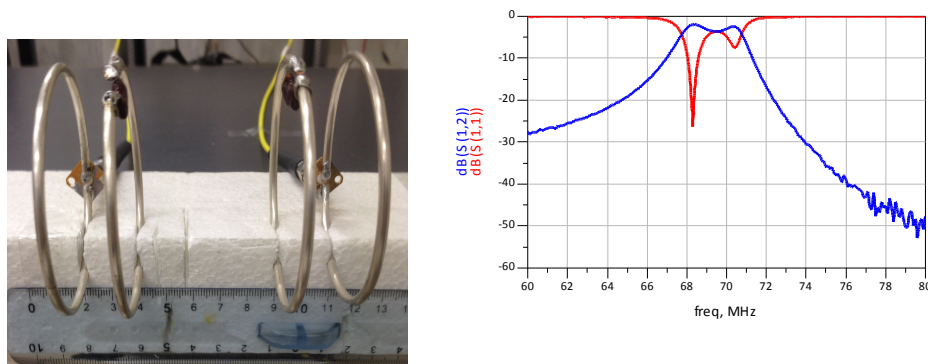


FIG. 1 – Experimental realization of a WPT system composed by a four-coil structure (left side). Measurements of the WPT system by using a vector network analyzer (VNA) operating on 50-Ohms reference impedances (right side).

IV CONCLUSIONS

Wireless power transfer is becoming increasingly important in a variety of applications. Equivalent network theory and the method of conjugate image impedances can provide a rigorous theoretical framework for achieving high efficiency links.

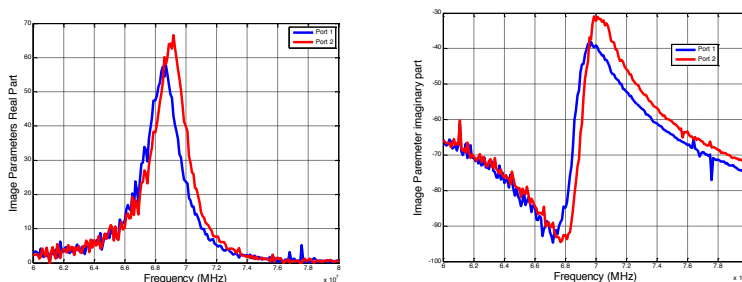


FIG. 2 – Conjugate Image Impedances of the WPT system.

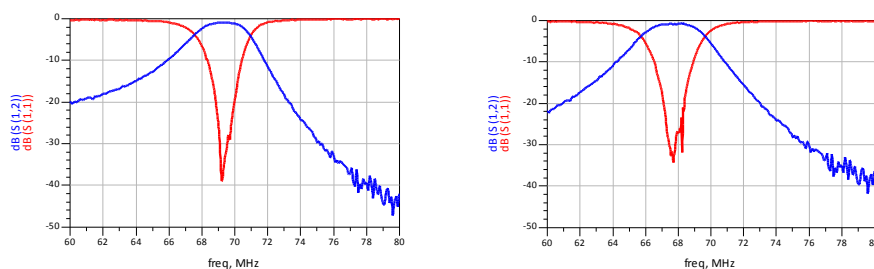


FIG. 3 – Scattering parameters as obtained by using as reference impedances the conjugate image impedances of the two-port network. The selected component values are: A) at 69.5MHz, C=58.5pF, R1=36.3Ohm, R2=56.5Ohm; B) at 68 MHz, C=26pF, R1=47.5 Ohm, R2=38.1. It is apparent that, by using as reference impedances the conjugate image impedances, we can achieve the highest efficiency.

REFERENCES

- [1] A. Kurs, A. Karalis, R. Moffatt, J. D. Joannopoulos, P. Fisher, and M. Soljacic, "Wireless power transfer via strongly coupled magnetic resonances," *Science*, vol. 317, no. 5834, pp. 83–86, 2007.
- [2] Z. N. Low, R. A. Chinga, R. Tseng, and J. Lin, "Design and Test of a High-Power High-Efficiency Loosely Coupled Planar Wireless Power Transfer System," *Industrial Electronics, IEEE Transactions on*, vol. 56, no. 5, pp. 1801–1812, Oct. 2009.
- [3] B. L. Cannon, J. F. Hoburg, D. D. Stancil, and S. C. Goldstein, "Magnetic Resonant Coupling As a Potential Means for Wireless Power Transfer to Multiple Small Receivers," *IEEE Transactions on Power Electronics*, vol. 24, no. 7, pp. 1819–1825, Oct. 2009.
- [4] A. P. Sample, D. A. Meyer, and J. R. Smith, "Analysis, Experimental Results, and Range Adaptation of Magnetically Coupled Resonators for Wireless Power Transfer," *Industrial Electronics, IEEE Transactions on*, vol. 58, no. 2, Oct. 2011.
- [5] M. Dionigi, A. Costanzo, F. Matri, and M. Mongiardo, "Magnetic Resonant Wireless Power Transfer," Chapter of the book "Wireless Power Transfer", p. 159, 2012.
- [6] M. Dionigi and M. Mongiardo, "CAD of wireless resonant energy links (WREL) realized by coils," in *IEEE MTT-S International Microwave Symposium digest*, IEEE. IEEE, 2010, pp. 1760–1763.
- [7] —, "CAD of efficient wireless power transmission systems," *Microwave Symposium Digest (MTT)*, 2011 IEEE MTT-S International, pp. 1–4, 2011.
- [8] M. Dionigi, S. Koziel, and M. Mongiardo, "Full-Wave Computer-Aided Optimization of Wireless Power Transfer Systems," accepted at *IEEE MTT-S International Microwave Symposium digest*, IEEE. IEEE, 2014.
- [9] S. Roberts, "Conjugate-Image Impedances," in *Proceedings of the IRE*, 1946, pp. 198–204.
- [10] K. Kurokawa, "Power Waves and the Scattering Matrix," *IEEE Transactions on Microwave Theory and Techniques*, vol. 13, no. 2, pp. 194–202, 1965.
- [11] P. Penfield, "Noise in Negative-Resistance Amplifiers," *Circuit Theory, IRE Transactions on*, vol. 7, no. 2, pp. 166–170, 1960.
- [12] J. Rahola, "Power Waves and Conjugate Matching," *IEEE Trans. Circuits Syst. II*, vol. 55, no. 1, pp. 92–96, 2008.
- [13] N. Inagaki, "Theory of Image Impedance Matching for Inductively Coupled Power Transfer Systems," to appear on *Microwave Theory and Techniques, IEEE Transactions on*, no. 99, pp. 1–8, 2014.
- [14] D. A. Frickey, "Conversions between S, Z, Y, H, ABCD, and T parameters which are valid for complex source and load impedances," *Microwave Theory and Techniques, IEEE Transactions on*, vol. 42, no. 2, pp. 205–211, 1994.

ELECTROMAGNETIC FIELD LEVEL CONTROL IN BUILT-UP AREAS

Giorgio Franceschetti, Antonio Iodice, Daniele Riccio, Giuseppe Ruello

Department of Electric Engineering and Information Technology,
Università degli Studi di Napoli Federico II, Naples, Italy
{gfrance; iodice; daniele.riccio; ruello}@unina.it

Abstract

A simple and cheap method for the evaluation of the electromagnetic (EM) field intensity at street level in a city area is here presented. The method is based on the measurement of the field level over a limited number of points in the city, and on the use of a numerical software code that allows computation of the EM field in a built-up area, when the three-dimensional (3-D) topography of the city is prescribed, as well as the radiating EM sources. By properly combining measurements and simulations, the field values all over the city are numerically computed in real time.

Index Terms – Electromagnetic wave propagation, field measurements, ray tracing, simulation.

I. INTRODUCTION

In this paper, we present a simple and cheap evaluation of the electromagnetic (EM) exposure level, for citizens in the city environment. To the best of our knowledge, no attempt to systematically and continuously measure the EM field level in built-up areas has been experimented. It is very likely that this absence is motivated by the spatially very fast varying feature of the EM field, in the built-up environment. Accordingly, a very large number of measuring sensors should be disseminated within the city area, with the consequence of an unreasonable overall cost of instruments' acquisition, and operational expenses. To overcome this problem, we propose a method based on the intelligent use of a numerical software code [1-3] that allows computation of the EM field in a built-up area, when the three-dimensional (3-D) topography of the city is prescribed, as well as the radiating EM sources (location, individual input power and antenna radiation diagram). Imagine that we distribute a limited number of EM level measuring sensors in the area of the city under control, and continuously transmit, real-time, these measured values to an Operational Control Centre (OCC). On the other side, we evaluate, at the OCC, the EM field level, all over the city, that would be generated by applying a one Watt power at the input terminal of each operating antenna. It is obvious that computed and measured values of the EM field would not coincide at the measuring points' sites: however, the coincidence could be enforced by proper adjustment of the input powers at the antenna terminals in the software tool, as explained in Sect. II. This procedure, implemented continuously in time, allows evaluation

not only of the EM field at any point over the city, but also of the values of the input power at each antenna site.

II. RATIONALE

Consider a built up area, for which a digital description of the buildings and of the terrain is available. Let us assume that in this area M transmitting antennas are present, the locations of which are known, as well as their radiation pattern. Conversely, their input powers x_j , with $j=1, \dots, M$, are unknown. In addition, let us assume that in this area we distribute N sensors, with $N > M$, able to measure the overall electric field intensities y_i at their locations, with $i=1, \dots, N$. Proper time averaging is performed to reduce fast fading effects.

Let us define $A_{i,j}$ the field intensity (i.e., the square modulus of the electric field) produced by the j -th antenna at the location of the i -th sensor, when the input powers of all antennas are unitary. Reasonably assuming that fields radiated by different antennas are uncorrelated, the actual field intensity y_i at the i -th sensor location is the sum of the field intensities radiated by each unit-power antenna, $A_{i,j}$, each one multiplied by the correspondent actual (unknown) antenna input power, x_j . Accordingly, we can write

$$\underline{\underline{A}} \cdot \underline{x} = \underline{y} \quad , \quad (1)$$

where $\underline{\underline{A}}$ is the N -row, M -column matrix whose elements are $A_{i,j}$, \underline{x} is the M -element column vector whose elements are x_j , and \underline{y} is the N -element column vector whose elements are y_i , i.e. the actual field intensity values at the sensors' sites.

By using a 3-D ray-tracing software code, it is possible to compute the field radiated by each of the M antennas in the whole area (including, of course, the sensors' locations), by assuming a unit input power at each antenna. In the present work we employ the software code described and validated in [1-3]. Let us call $\hat{A}_{i,j}$ the estimates of $A_{i,j}$ computed by the software code, and \hat{y}_i the field measured by the i -th sensor. Due to software code inaccuracies, $\hat{A}_{i,j}$ will (hopefully slightly) differ from $A_{i,j}$, as well as, due to measurement errors, \hat{y}_i will slightly differ from y_i . Accordingly, antennas' input powers estimates \hat{x}_j can be obtained by minimising

$$\left\| \underline{\underline{\hat{A}}} \cdot \underline{\hat{x}} - \underline{\hat{y}} \right\| \quad , \quad (2)$$

where $\|\cdot\|$ stands for the quadratic norm in \mathfrak{R}^N .

Once input powers are computed, the field intensity at any point of the scene can be computed as the sum of the computed field intensities of the antennas, each one multiplied by the correspondent input power. Accordingly, a complete map of the field level is obtained.

Note that, for a large scene with many buildings and many antennas (for instance, an entire city), the time needed by the ray-tracing software

tool to compute the field radiated by each of the M antennas in the whole area maybe very large. However, this computation must be performed only once, in a preliminary phase, whereas computation of antennas input powers and subsequent evaluation of the field level map require a very short time. Accordingly, the field level map can be updated in real time, just following the sensor measurements change.

III. RESULTS

Full validation of the proposed technique requires a comparison of obtained field level map with results of a measurement campaign. This is currently being performed. However, as a first test of the method, we have generated the sensors' "measured" field values by using the ray-tracing software itself, considering different values of the input powers for the antennas; effects of measurement errors have been roughly simulated by adding normally distributed random errors to sensor "measured" values predicted by the ray-tracing tool; and software model inaccuracies have been simulated by considering different materials of the city buildings (a parameter that is accounted for in the ray-tracing software) for simulations of "measured" values and simulations for input power retrieval. Input powers retrieved by the proposed technique based on the simulated measurements have been then compared to those imposed at the beginning.

In the following, we report the results of one of the simulated experiments. In particular, we consider an about 1700 m x 1700 m area in the city of Naples, see Fig.1. Three transmitting dipole antennas have been considered, and five sensors have been supposed to be distributed in the area, as depicted in the map of Fig.1a. Actual and retrieved antenna input powers are compared in Table I, and the final obtained field level map is shown in Fig.1b.

Power values reported in Table I are obtained by averaging over 20 experiments obtained by using 20 different realisations of the random "measurement" error vector. Mean errors and standard deviations of the power retrieved values have turned out to be smaller than 0.1 W in all cases, except that for measurement error standard deviation σ equal to 0.1 V/m. For this high value of the error standard deviation, comparable to the error-free field values, retrieved antenna input powers are not in agreement with actual one, as expected. However, for lower values of the measurement error standard deviation, retrieved values are in good agreement with actual ones.

IV. CONCLUSION

In this paper, we have presented a simple and cheap evaluation of the EM exposure level, for citizens in the city environment. The method is able to assess the field intensity all over the considered urban area in real time. A measurement campaign for the full validation of the method is currently ongoing.

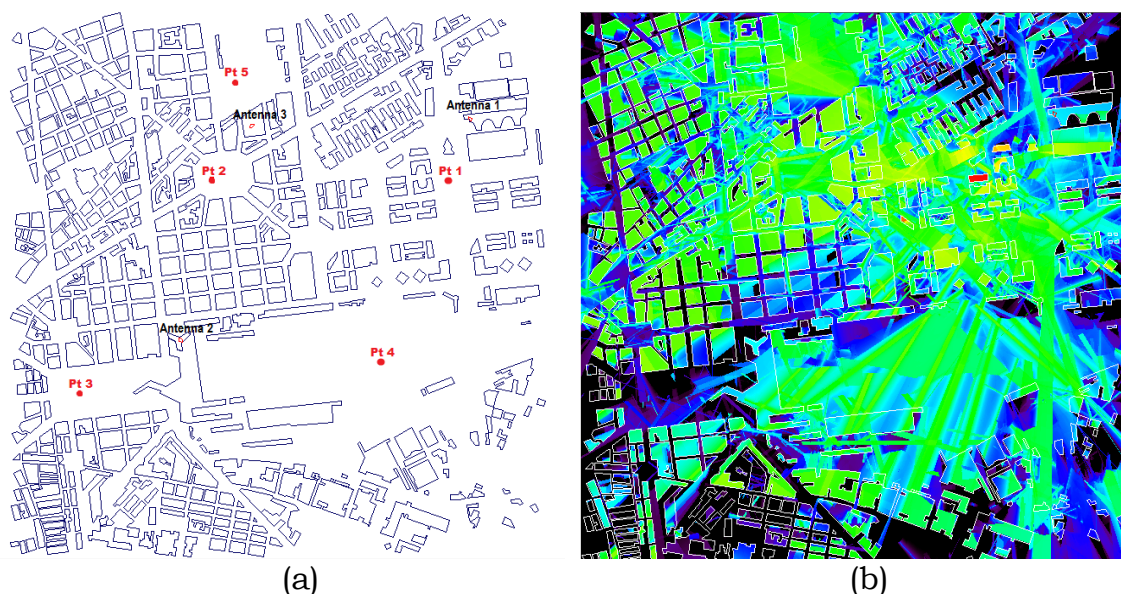


FIG. 1 – Area of Naples Central Station: antennas' and sensors' locations (a), and final field level map (b).

Table I - Actual and retrieved antenna input powers.

Error-free measured electric field amplitude values at the five sensors are: 0.322 V/m, 0.245 V/m, 0.0255 V/m, 0.134 V/m, 0.991 V/m; σ is the sensors' measurement error standard deviation

Antenna	Actual input powers	Retrieved input power for $\sigma = 0.001$ V/m	Retrieved input power for $\sigma = 0.01$ V/m	Retrieved input power for $\sigma = 0.1$ V/m
1	5.0 W	5.0 W	5.0 W	9.2 W
2	2.0 W	1.9 W	2.1 W	28.1 W
3	10.0 W	10.0 W	10.0 W	11.7 W

REFERENCES

- [1] G. Franceschetti, A. Iodice, D. Riccio, G. Ruello, "A Tool for Planning Electromagnetic Field Levels in Urban Areas", *Proceedings of the Antennas and Propagation Society International Symposium*, Monterey (USA), 2004, pp. 2211-2214.
- [2] G. Franceschetti, R. Guida, A. Iodice, D. Riccio, G. Ruello, "Verifica di un software per la previsione della radiocopertura", *Atti della XVI Riunione Nazionale di Elettromagnetismo*, Genova (Italy), 2006, pp.170-173.
- [3] G. Franceschetti, P. Imperatore, A. Iodice, D. Riccio, "Radio-Coverage Parallel Computation on Multi-Processor Platforms", *Proceedings of the 39th European Microwave Conference*, Rome (Italy), 2009, pp. 1575-1578.

Hierarchical in silico validation procedure for biomass estimation techniques based on dielectric spectroscopy

M. Muzi⁽¹⁾, F. Mangini⁽¹⁾, E. Stoja⁽²⁾

⁽¹⁾ Dept. of Information Engineering, Electronics and Telecommunications, "La Sapienza" University of Rome, Via Eudossiana 18, 00184 Roma, Italy

⁽²⁾ Engineering Department, Lancaster University, Bailrigg, Lancaster LA1 4YR, United Kingdom; marco.muzi@uniroma1.it

Abstract

In order to obtain an accurate estimation of the biomass as a function of the permittivity of the suspension, a simple in silico hierarchical procedure is proposed. The procedure is designed to perform the homogenization from the micro-scale to the macro-scale exploiting very simple analytical models and simulation setups under the hypothesis of diluted suspension (biomass less than 0.2). Results obtained show that it is possible to overcome some difficulties concerning the analytical treatment of the cellular shape by considering a sphere with the same dielectric behavior in the quantitative analysis of the biomass. The entire study is based on simulations performed in order to verify the correctness of the procedure. Obtained data are used in a biomass estimation scenario to show the efficacy of the procedure.

Index Terms – Dielectric Spectroscopy, Biomass, Homogenization Techniques.

I. INTRODUCTION

Taking advantage of the beta-dispersion phenomenon [1-3], it is possible to estimate the cellular culture biomass using dielectric spectroscopy as suggested in [4]. Since then the potentialities of the technique were studied, especially in the case of the monoculture suspensions [5-8].

Despite the technique's potentialities, the theoretical study of the phenomenon, especially in presence of particulate of irregular geometry, is often difficult to manage both in analysis and in simulation. To overcome this kind of issues, an in silico hierarchical validation procedure for dielectric-behavior models is proposed.

II. METHODS

The procedure is structured in 4 steps.

In this work the notation reported in Table 1 is adopted.

TABLE I – DEFINITION AND VALUES OF EM AND GEOMETRICAL PARAMETERS

Physical quantity	Symbol
Complex permittivity of the medium	ε_a^*
Permittivity of the membrane	ε_m^*
Permittivity of the cell core	ε_i^*
Cell radius	r
Membrane thickness	d
Volume fraction / Biomass	ϕ

The first step consists in the replacement of the original cell shape with a full sphere with same equivalent complex permittivity and volume. This provides a simplification in the geometry of the problem, avoiding considering the cellular shell in the case of presence of more objects in the simulation domain.

The homogenized complex permittivity $\hat{\varepsilon}_p^*$ to be assigned to the equivalent sphere is given by the following:

$$\hat{\varepsilon}_p^* = \varepsilon_a^* \frac{2(1-\phi)\varepsilon_a^* - (2+\phi)\varepsilon_i^*}{(1-\phi)\varepsilon_i^* - (1+2\phi)\varepsilon_a^*} \quad (1)$$

The second step consists in the homogenization of the whole suspension using Eq. (1), substituting the original shape of the suspended medium with full spheres with values of permittivity ε_p^* obtained in the previous step.

The simulation setup is the same used in the previous step. The only difference is the presence of more objects in the simulation domain. The number of those objects is such to obtain the desired value of the volume fraction. In all cases the geometrical dimensions of the domain remain the same.

The final step consists in the estimation of the biomass from the data acquired in the third step.

It is possible to obtain, under the hypothesis of shape uniformity of the suspended cells, an explicit relation for the biomass, as described by the following:

$$\hat{\phi} = \frac{(\hat{\varepsilon}_p^* + 2\varepsilon_a^*)(\varepsilon_a^* + \varepsilon_i^*)}{(\varepsilon_i^* - 2\varepsilon_a^*)(\hat{\varepsilon}_p^* - \varepsilon_a^*)} \quad (2)$$

where $\hat{\phi}$ is the estimated value of the biomass. Then it is possible to obtain an estimation of the biomass from knowable physical quantities.

By means of the above data, an estimation of biomass is performed using directly Eq. (2) or a brute-force search in order to confirm the validity of the estimation. Results are shown in Fig. 1.

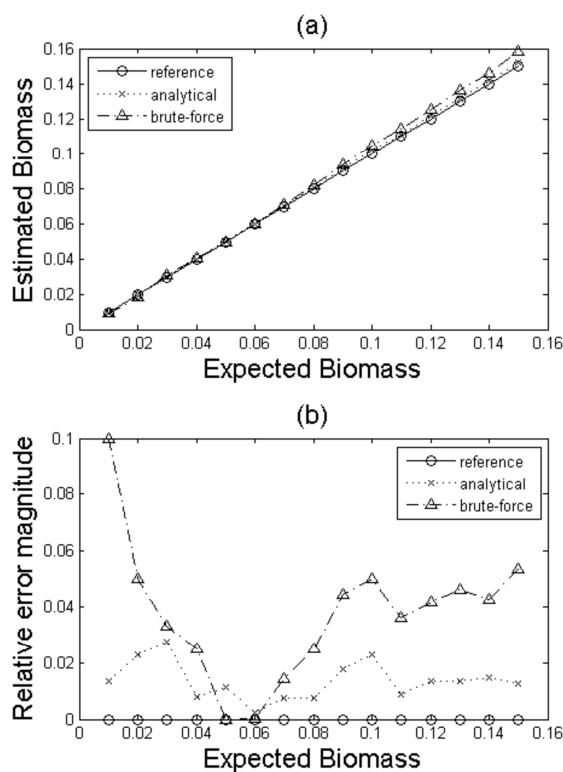


FIG. 1 (a) Biomass estimation values obtained from simulation performed at 100 kHz with equivalent permittivity values of the suspension; (b) estimation error.

The brute-force method consists in solving Maxwell Wagner manca il sostantivo in the interval $[0;1]$ with step of 0:001 searching $\hat{\phi}$ as the value that best fits the data.

Both methods used for the computation show a good accordance with the expected, though a better accuracy seems to be achieved by the use of Eq. (2) instead of the brute-force method.

III. DISCUSSION

As shown, the procedure produces a good agreement between the expected and the obtained data. The relative error is always less than 3%, while in the case of the brute-force method, the error reaches 10% and in general is greater along the permittivity range. Then the first is the best choice for this kind of problems.

IV. CONCLUSION

The hierarchical in silico validation procedure for biomass estimation techniques based on dielectric spectroscopy described above

seems to be a good tool for overcoming the actual technical limitations of the dielectric spectroscopy used as biomass estimation tool. This is possible thanks to the accuracy demonstrated by the procedure in the description of the phenomenon, as reported in the discussion, taking full advantage from this particular measurement technique.

Future work shall be centered on suspensions with the cells with anisotropic dielectric behavior or in general with a certain variability on geometric dimensions or dielectric properties of the core.

ACKNOWLEDGEMENT

This work is part of the research project: "Assessment techniques of three-dimensional (3D) cell growth and morphology in microgravity using electromagnetic diffraction", realized through the Italian Space Agency (ASI) co-financing.

REFERENCES

- [1] R. Hoerber, "Eine Methode die elektrische Leitfaehigkeit im Innern von Zellen zu messen," *Arch. Ges. Physiol.*, 133 (4-6), 237-253, 1910.
- [2] R. Hoerber, "Ein zweites Verfahren die Leitfaehigkeit im Innern von Zellen zu messen," *Arch. Ges. Physiol.*, 148 (4-5), 189-221, 1912.
- [3] R. Hoerber, "Messungen der inneren Leitfaehigkeit von Zellen III," *Arch. Ges. Physiol.*, 150 (1-2), 15-45, 1913.
- [4] C. M. Harris, R. W. Todd, S. J. Bungard, R. W. Lovitt, J. G. Morris, and D. B. Keli, "Dielectric permittivity of microbial suspensions at radio frequencies: a novel method for the real-time estimation of microbial biomass," *Enzyme Microb. Technol.*, 9, 181-186, 1987.
- [5] T. Noll and M. Biselli, "Dielectric spectroscopy in the cultivation of suspended and immobilized hybridoma cells," *J. Biotechnol.*, 63 (3), 187-198, 1998.
- [6] P. Ducommun, A. Kadouri, U. von Stockar, and I.W. Marison, "On-line determination of animal cell concentration in two industrial high-density culture processes by dielectric spectroscopy," *Biotechnol. Bioeng.*, 77 (3), 316-323, 2002.
- [7] C. Cannizzaro, R. Gugerli, I. Marison, and U. von Stockar, "On-line biomass monitoring of CHO perfusion culture with scanning dielectric spectroscopy," *Biotechnol. Bioeng.*, 84 (4), 597-610, 2003.
- [8] S. Ansorge, G. Esteban, C. Ghommidh, and G. Schmid, "Monitoring nutrient limitations by online capacitance measurements in batch and fed-batch CHO fermentations," Smith R. (Ed) Conference Proceedings to the 19th ESACT Meeting: Cell Technology for Cell Products. Springer, Dordrecht/NL, 3, 723-726, 2007.

CIRCULARLY POLARIZED ROBUST ANTENNAS FOR WIRELESS MONITORING OF CONCRETE STRUCTURES

G. Castorina^(1,3), G. S. Mauro^(1,3), A. F. Morabito⁽²⁾, L. Di Donato⁽¹⁾
G. Sorbello⁽¹⁾

- (1) Dept. of Electrical, Electronics and Informatics Engineering
University of Catania. Viale Andrea Doria, 6, 95125, Catania.
giovanni.castorina@dieei.unict.it
- (2) Dept. of Information Infrastructure and Sustainable Energy
Engineering, Mediterranean University of Reggio Calabria,
Via Graziella, Loc. Feo di Vito, 89122 Reggio Calabria (RC).
- (3) NTT New Tera Technology s.r.l. – Strada XIV, (Zona Industriale),
95100, Catania.

Abstract

We develop an embedded UHF circularly polarized patch antenna for possible application of health monitoring in concrete structures. The antenna is optimized for an optimal microwave power transmission to battery-less sensors and for wireless communications. The proposed design is very robust as the resulting $|S_{11}|$ is lower than -15 dB for different concrete types having permittivity in the range 4-9 and $\tan\delta$ in the range 0-0.3. Notably, the gain pattern is affected by the shape of concrete-air interface and this aspect is investigated. The experimental measurements in actual working condition will also be presented at the conference.

Index Terms – Concrete Structure Monitoring, Embedded Sensors, Patch Antennas, Circular Polarization.

I. INTRODUCTION

Interest in applications for health monitoring of concrete structures with embedded sensors keeps on increasing [1]-[2]. One of the key aspects concerning their implementation consists in the fact that sensors buried into the concrete are necessarily wireless and battery-less, therefore an efficient link budget between reader and sensor network is mandatory. In particular, whatever the type and the aging of concrete, the exploited antenna needs to be matched to its load (i.e., the sensor or the sensors) irrespective of the concrete type or aging [1]-[3]. In this work, we present a simple solution that addresses this requirement in an effective way. In particular, Sections II and III are devoted to describe and discuss the overall design scenario and the achieved numerical results, respectively. Conclusions follow

II. ANTENNA LAYOUT AND OPERATING ENVIRONMENT

The antenna is designed to operate in concrete structures and it is conceived to be positioned at about 3 cm far from a flat concrete-air interface.

As there are several types of concrete, the goal is to obtain an antenna which is minimally affected by the dielectric permittivity of the surrounding environment. A patch antenna can accomplish this goal because the EM field in its structure is, almost completely, confined between ground and patch [4]. Moreover, to increase robustness, a dielectric housing was added with a fixed dielectric constant $\epsilon_r = 6$ close to the typical concrete's dielectric permittivity [3].

The layout of the proposed antenna is shown in Fig. 1. It consists of a metallic patch with a ground plane printed on a dielectric substrate with $\epsilon_r = 9.8$. The radiating patch dimension (L_x and L_y) has been chosen according to an operation frequency of 900 MHz. Also, a 50 Ω coaxial cable is used to feed the antenna at coordinates (x,y) with respect to the center of the patch, see Fig 1 and Table I. Sheets of dielectric material are stacked over the patch and under the ground plane to form a thin plastic housing which encloses the antenna and protects the metallization from the concrete. The dielectric materials used for the antenna are laminates from Rogers Corporation: TMM[®] 10i for substrate and TMM[®] 6 for the protective layers. The above housing method, compared to the air box adopted in [1], allows a smoother permittivity transition, and respect to the enclosing solution chosen in [2], is simpler and less expensive, without compromising the performance of the antenna itself.

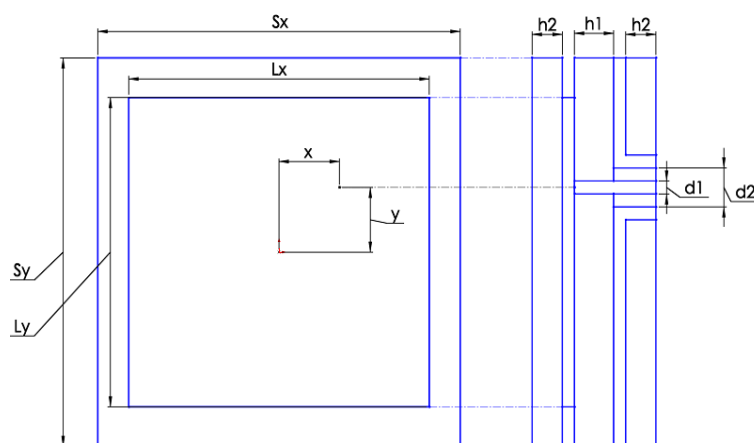


TABLE I – PARAMETERS

Par.	Value[mm]
Sx	60
Sy	60
Lx	49.6
Ly	47.6
x	10
y	10
h1	3.175
h2	2.54
d1	0.9
d2	2.98

FIG. 1 – Antenna layout, frontal and lateral view (not in scale).

III. NUMERICAL SIMULATIONS AND RESULTS

The above described structure was simulated by FEM method with ANSYS[®] HFSS considering different concrete background.

In order to operate with circular polarization, the proposed antenna supports two close orthogonally resonances. It is worth nothing that this circumstance leads two main advantages: 1) a good polarization

match with the reader antenna is guaranteed without alignment and 2) the double resonance allows a larger impedance bandwidth (Fig. 2). A large bandwidth is synonymous of robustness also versus permittivity variation: an antenna with a large impedance bandwidth will be matched even if a frequency shift may arise due to permittivity's changes in the concrete. This behavior can be clearly seen in Fig. 2. The $|S_{11}|$ of the proposed antenna is always below -15 dB at 900 MHz, even considering a dielectric loss tangent of 0.3, see Figs. 2-3a and Table II where also Axial Ratio and cross-polar discrimination are reported for different kind of concrete.

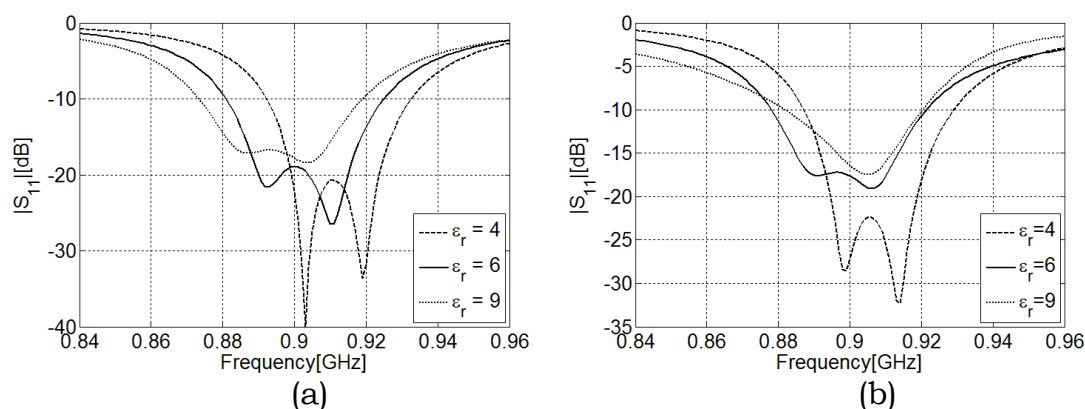


FIG. 2 – $|S_{11}|$ for different permittivity values of surrounding environment, $\epsilon_r=4,6$ and 9: (a) uniform indefinite background of concrete with $\tan\delta = 0$; (b) antenna inside a $15 \times 15 \times 15$ [cm³] concrete block with $\tan\delta = 0.03$.

Table II – Return Loss, Axial Ratio and XPD at 900 MHz in [dB]

Medium Permittivity	Indefinite Background			Concrete Block $15 \times 15 \times 15$ cm ³		
	$ S_{11} $	AR	XPD	$ S_{11} $	AR	XPD
4	-22.2	6.1	9.4	-27.2	2.3	17.5
6	-18.9	0.5	30.8	-17.6	3.2	14.8
9	-17.8	3.7	13.5	-16.2	2.1	18.3

In Fig. 3b the Left Hand Circular Polarization (LHCP) Gain pattern is shown for the cut $\varphi = 0^\circ$ (x-z plane) and for the antenna placed in a concrete cubic box with increasing volume. In broadside direction ($\theta = 0^\circ$) the LHCP gain is -1.78, -2.54 and -5.56 dB for a box with edge of 15, 30 and 45 cm respectively. We verified that the worst case is around -7.5 dB for other configurations not shown here. The concrete-air interface and block dimensions are variable and hence the radiation pattern is altered accordingly, however the worst case can be considered and tolerated in the link budget since the reader and the buried antenna are expected to be quite close.

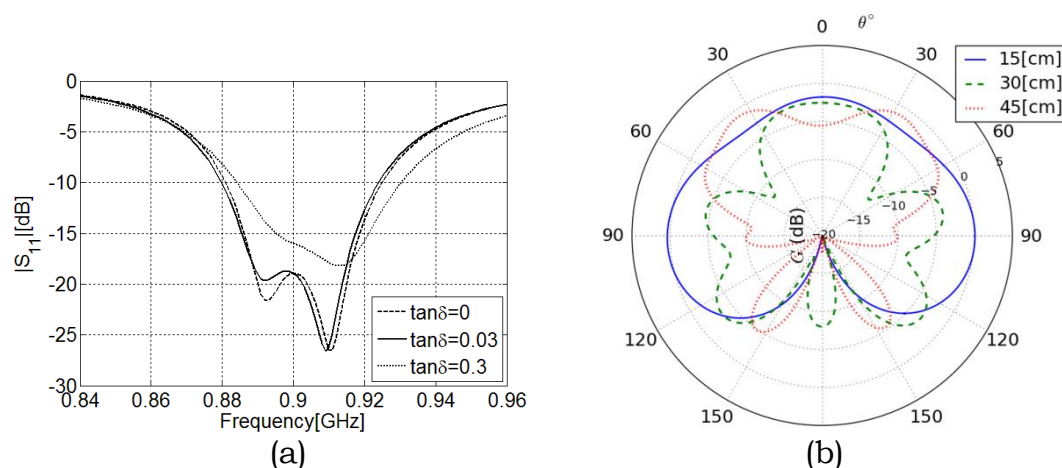


FIG. 3 – Antenna performance: (a) $|S_{11}|$ with different dielectric loss tangent with $\epsilon_r=6$; (b) LHCP gain pattern for different concrete block size.

IV. CONCLUSION

A circularly polarized antenna has been designed to be robust with respect to the environment permittivity changes. It has been found that the antenna remains well matched, within $|S_{11}| < -15$ dB, for a wide range of permittivity and loss tangent values. The use of circularly polarized antennas allows a good polarization matching as the worst estimated axial ratio is 6.1 dB. Although the gain pattern varies, depending on the shape and dimensions of the concrete-air interface, the on-axis (negative) gain remains reasonable in all configurations. The results achieved in this study suggest that the proposed antenna allows an efficient electromagnetic power transfer to battery-less embedded sensors for health monitoring of concrete infrastructures.

Acknowledgement: This work is developed under the project number G13F12000020004 funded by the POR FESR Sicilia 2007-2013 program.

REFERENCES

- [1] Xiaohua Jin and Mohammad Ali, “Reflection and Transmission Properties of Embedded Dipoles and PIFAs inside Concrete at 915 MHz” *Antennas and Propagation Society International Symposium, 2009. APSURSI '09. IEEE*
- [2] Seung-Hwan Jeong and Hae-Won Son, “UHF RFID Tag Antenna for Embedded Use in a Concrete Floor” *Antennas and Wireless Propagation Letters, IEEE (Volume:10) RFID Virtual Journal, IEEE, pp. 1158 – 1161, 2011.*
- [3] C. Thajudeen, A. Hoorfar, F. Ahmad and T. Dogaru, “Measured complex permittivity of walls with different hydration levels and the effect on power estimation of TWRI target returns”, *Progress In Electromagnetics Research B, Vol. 30, 177-199, 2011*
- [4] Constantine A. Balanis, “Antenna Theory Analysis and Design”, 3rd ed., *John Wiley & Sons, Inc., 2005 Chapter: 14, Paragraph: 2.*

Surface and air heat island of Milan: spatial and temporal analysis from MODIS

R. Anniballe⁽¹⁾, S. Bonafoni⁽²⁾, N. Pierdicca⁽¹⁾,

⁽¹⁾*Department of Information Engineering, Electronics and Telecommunications, Sapienza University of Rome, via Eudossiana 18, 00184 Roma, Italy, roberta.anniballe@gmail.com*

⁽²⁾*Department of Engineering, University of Perugia, via G. Duranti 93, 06125 Perugia, Italy*

Abstract

In this work the urban heat island (UHI) maps were produced over Milan using data provided by the Moderate-resolution Imaging Spectroradiometer (MODIS). Two types of UHI were analyzed simultaneously: the canopy layer heat island (CLHI) and the surface urban heat island (SUHI). The SUHI and CLHI maps allow to monitor the spatial and temporal evolution of surface and air heating and also to point out and quantify the different features (e.g. magnitude, spatial extent, orientation and UHI centre location) using a Gaussian surface fitting. This results indicate that the SUHI effect is a noticeable phenomenon throughout the whole diurnal cycle: it has a stronger intensity in the daytime with peaks around 9-10 K while in the nighttime it decreases by a factor of 2. In contrast, the CLHI during the daytime is absent and after sunset shows features similar to the nighttime SUHI.

Index Terms – MODIS sensor, Gaussian fit, surface and air temperature, urban heat island.

I. INTRODUCTION

The extreme urban heating during summer months may constitute a public health threat, especially for old people living in cities with respect to those living in rural areas. Urban areas can cause an increase of the local air and surface temperatures compared to those of the surrounding rural areas: this effect is quantified by the urban heat island (UHI) intensity, describing the difference in temperature between the urban locations and the surrounding rural background. The UHI effects may influence human health, the quality of life of urban residents, energy consumption, and other adverse climate effects, such as air pollution.

Satellite remote sensing is an excellent tool for examining the UHI effects: unlike in situ measurements, which provide sparsely distributed data, spaceborne sensors allow to monitor the urban heating with a global spatial coverage, ensuring a better analysis of the intra-urban UHI spatial variability.

In this work, using MODERate-resolution Imaging Spectroradiometer (MODIS) observations, we face simultaneously with two types of UHI [1]: the canopy layer heat island (CLHI) and the surface

urban heat island (SUHI). The SUHI describes the changes in temperature at the surface, whereas the CLHI refers to a warming of the urban air, in the portion between the ground and the top of buildings and city trees. SUHI and CLHI maps were realized over Milan in order to monitor the spatial and temporal evolution of the surface and air heating process, highlighting also the clear different patterns.

II. DATA ANALYSIS

We selected an area around the city centre of 39 km², comprising the outskirts of Milan, neighboring municipal districts, industrial estates, rural areas. Datasets acquired by MODIS instruments on the Terra and Aqua satellites were employed, selecting several categories of MODIS products from June to September between the years 2007 and 2010.

The analysis was carried out processing the land surface temperature (LST) and the 2-meter air temperature (T_{air}) and then obtaining the SUHI and CLHI patterns using a method described by Streutker [2-3]. In this method a Gaussian surface is used to fit the spatially distributed UHI maps as follows:

$$T(x, y) = T_0 + a_1 x + a_2 y + UHI(x, y)$$

$$UHI(x, y) = a_0 \times \exp \left[-\frac{((x-x_0)\cos\phi + (y-y_0)\sin\phi)^2}{0.5a_x^2} - \frac{((y-y_0)\cos\phi - (x-x_0)\sin\phi)^2}{0.5a_y^2} \right] \quad (1)$$

where (x, y) represents the location of a pixel, $T(x, y)$ is the LST or the T_{air} of a pixel at (x, y) , T_0 is the rural surface/air temperature mean value, a_1 and a_2 are the coefficients describing the spatial gradient of the rural temperature, and $UHI(x, y)$ is the pixel-based heat island intensity. Such a least-square fit provides an estimate of the magnitude (a_0) of the UHI maximum intensity for the selected area, of the spatial extent (a_x and a_y), orientation (ϕ), and central location (x_0 and y_0) of the heat island. In order to perform the fit, first cloud pixels were masked out for each image. The rural temperature surface is then subtracted from the $T(x, y)$ image, obtaining the UHI pattern. Finally, the $UHI(x, y)$ image is then fit to a Gaussian surface, determining the parameters describing the magnitude, the spatial extents, the orientation and central location of the UHI [2].

III. RESULTS

The above methodology was applied to LST and T_{air} MODIS derived data, and the results for instantaneous and monthly averaged images will be summarizes in the following.

For each image, the descriptive parameters for the Gaussian fit of the $UHI(x, y)$ pattern were inferred as reported in Fig.1 for SUHI maps on 15th July 2007, where (x, y) corresponds to the longitude-latitude. In this figure the four daily passes of MODIS sensor are shown.

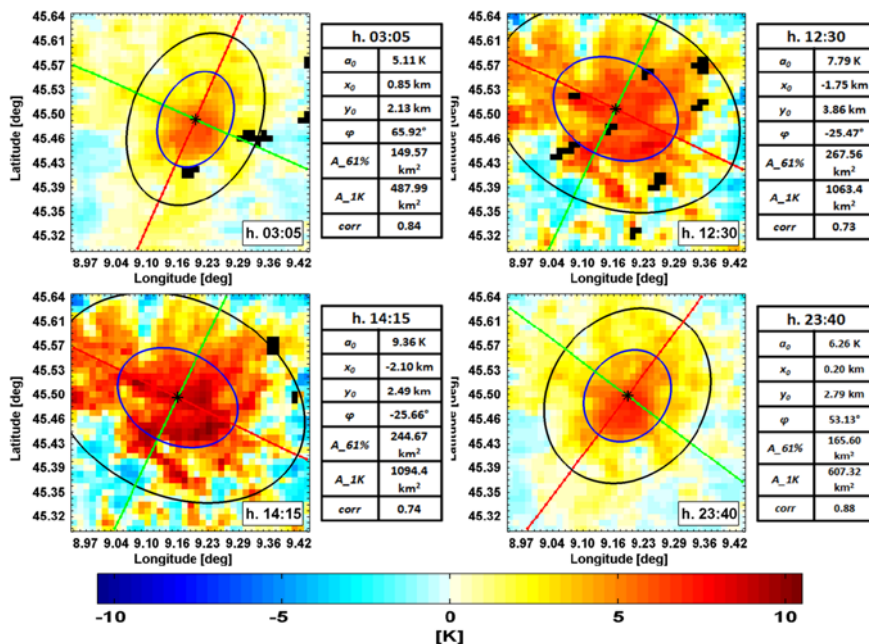


Fig. 1. Daily cycle of SUHI maps [K] above Milan area on 15th July 2007. Gaussian fit parameters: a_0 is the SUHI magnitude, ϕ is the orientation, x_0 and y_0 are the central location of UHI. $A_{61\%}$ is the area at which the temperature falls to the 61% of its maximum value (inner ellipse) and A_{1K} is the area for which the SUHI temperature is greater than 1 K (outer ellipse). $corr$ is the correlation coefficient between the Gaussian model and the *UHI* image. Hours are in CEST date format (CEST=UTC+2). Black pixels are cloudy pixels

Also, the monthly averages of UHI parameters from June to September 2007-2010 were carried out, in order to analyze the main characteristics of the diurnal cycle of the UHI as a long-term trend.

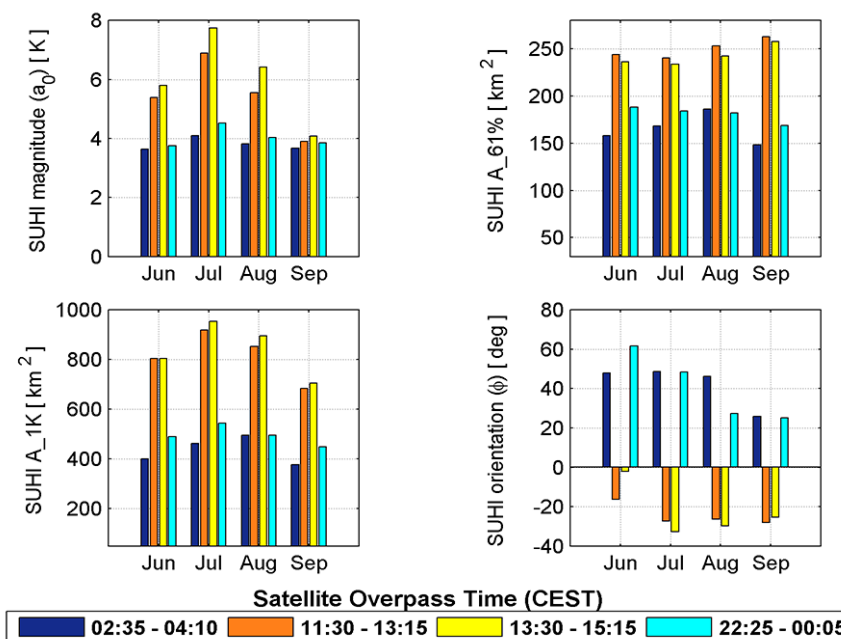


Fig. 2. Daily cycle of SUHI parameters above Milan area: SUHI magnitude (a_0), $A_{61\%}$, A_{1K} , orientation ϕ . Average for summer months 2007-2010.

Figure 2 shows a peak of the average SUHI magnitude in the early afternoon and in July (around 8 K), with a noticeable difference between the daytime and nighttime except for September. The CLHI emerges only after sunset with an average intensity around 3–4 K (not shown in figure), with SUHI and CLHI showing similar features in the nighttime. The SUHI extent grows during the daytime, with a uniform A_{61%} all through the months. Both nighttime SUHI's A_{61%} and A_{1K} are greater than the correspondent for CLHI.

The parameter ϕ suggests an orientation along the North-West and South-East (NW-SE) quarters in the daytime and a reversal during the night (NE-SW quarters). The daytime SUHI orientation can be mainly ascribed to the heating in the North-West built-up area.

Concerning also the central location of the SUHI pattern, the average shift in latitude (y_0) with respect to the city centre is around 2 km in the nighttime and around 3-4 km in the daytime in the north direction, confirming the effect of the urban pixels in the north part of the Milan area. The average shift in longitude (x_0) is negligible during the night, while it ranges around 2-4 km in the daytime in the west direction. The trend of the night CLHI central location is similar to the correspondent for SUHI.

IV. CONCLUSION

This study points out that the SUHI persists throughout the diurnal cycle with a greater intensity in the daytime, with peaks around 9-10 K, when the CLHI is basically absent. The CLHI emerges only after sunset, with SUHI and CLHI showing similar features in the nighttime. The analysis of other Gaussian parameters reveals interesting behaviors of the UHI patterns, such as the SUHI orientation reversal during the daily cycle that can be mainly ascribed to the heating in the North-West built-up area. Therefore this fitting technique can be adopted as a support tool providing quantitative information useful to investigate the behavior of SUHI and CLHI and if their changes are related to each other.

REFERENCES

- [1] Voogt, J. A. (2004). Urban Heat Island: Hotter Cities. *ActionBioscience.org* (available online: <http://www.actionbioscience.org/environment/voogt.html>).
- [2] Streutker, D. R. (2002). A remote sensing study of the urban heat island of Houston, Texas. *International Journal of Remote Sensing*, 23, 2595–2608.
- [3] Streutker, D. R. (2003). Satellite-measured growth of the urban heat island of Houston, Texas. *Remote Sensing of Environment*, 85(3), 282–289.

PHOTONIC CRYSTAL FIBERS WITH REDUCED SYMMETRY FOR HIGH POWER LASERS

E. Coscelli⁽¹⁾, C. Molardi⁽¹⁾, F. Poli⁽¹⁾, A. Cucinotta⁽¹⁾, S. Selleri⁽¹⁾

⁽¹⁾ Information Engineering Department, University of Parma
Parco Area delle Scienze 181/a, 43124 Parma, Italy
enrico.coscelli@unipr.it

Abstract

Innovative Photonic Crystal Fibers with optimized air-hole matrix, designed to break the C_{6v} symmetry of the inner cladding while preserving their feasibility through the stack-and-draw technique, are presented. The possibility to provide stable SM guiding at 2 μm with core diameter up to 80 μm and a coupled pump power exceeding 300 W is demonstrated by means of a full-vector modal solver based on the finite element method with embedded thermal model, to account for the effects of heating on the mode confinement. Effective suppression of the high-order modes under a heat load of 340 W/m, while keeping an effective area exceeding 2500 μm^2 , has been proved.

Index Terms – Fiber lasers, photonic crystal fibers, thermo-optic effect.

I. INTRODUCTION

Soft-tissue medicine, remote sensing, communication, industrial processing and LIDAR are only a few examples of applications that are currently pushing the research of high power sources in the 2 μm - 3 μm range, which is also attractive for the possibility to lower the safety requirements thank to of the eye-safe nature of the scattered light at these wavelengths [1]. Thulium-doped fiber lasers are of particular interest for these applications, being able to combine the good properties of the fiber medium, including high brightness, premium beam quality and compactness, together with the possibility to obtain emission on a relatively wide band around 2 μm , when pumped with widely-available diodes emitting at 790 nm.

One of the main issues regarding the development of Tm-doped fiber laser systems is the thermal management. Indeed, the large quantum defect causes significant heat generation in the fiber core which, through thermo-optic effect, yields to a refractive index gradient along the cross-section. As a consequence, one or more High-Order Modes (HOMs) may become guided, jeopardizing the output beam quality [2].

Double-Cladding Photonic Crystal Fibers (DC-PCFs) have been one of the key elements to the rushing growth of fiber laser output power and pulse energy, thanks to their superior capabilities in terms of achievable effective area in the Single-Mode (SM) regime [3],[4]. A few Tm-doped PCFs have been proposed, mostly based on the same design principles of well-established Yb-doped PCFs [5],[6]. Nevertheless, several issues arise with these fibers due to the quantum defect, and their

performances are still limited. Recently, PCF designs with air-hole arrangement specifically designed to break the typical C_{6v} symmetry have been shown to provide enhanced delocalization of the HOMs [7]. In this paper two designs of TM-doped DC-PCFs with Symmetry-Free cladding (SF-PCFs) and core diameter of $80 \mu\text{m}$ are presented, and their guiding properties are analyzed and compared by means of a full-vector modal solver based on the finite-element method with embedded thermal model to investigate the effects of thermally-induced refractive index change [8].

II. RESULTS AND DISCUSSION

The cross-sections of the two considered SF-PCFs are shown in Fig. 1. Both of them have been designed by selectively choosing air-holes from an underlying triangular cladding lattice with pitch $\Lambda = 14.4 \mu\text{m}$, to allow fabrication with the stack-and-draw process normally used for PCFs. The inner cladding of the first one, named SF-PCFa and shown in Fig. 1(a), is obtained removing air-holes to form two hexagonal layers, rotated with respect to each other. Three more air-holes have been kept to further weaken symmetry of the cross-section. The air-holes have normalized diameter $d/\Lambda = 0.24$. The 19 innermost unit cells have been Tm-doped. The fiber core has a corner-to-corner distance of about $80 \mu\text{m}$ and the edge of resulting doped hexagonal region is $36 \mu\text{m}$. An air-cladding with inner radius of $260 \mu\text{m}$ surrounds the cross-section, to provide pump guiding. The second fiber, named SF-PCFb and shown in Fig. 1(b), has again a 19-cell doped core, with the same size of the one of SF-PCFa. Only six air-holes have been kept in the first cladding ring, and they have been chosen not to be aligned with the corners of the doped hexagonal area. Three arms, made each of three air-holes, extend into the cladding providing a clockwise “spin” to the cross-section. Three further air-holes are added in order to avoid excessive leakage of the FM. The air-holes have normalized diameter $d/\Lambda = 0.4$. Both SF-PCFs are rod-type fibers, with outer diameter 1.7 mm . The Fundamental Mode (FM) and the most detrimental HOM, that is the one with the largest overlap integral Γ with the doped core [8], have been calculated for different heating conditions, assuming the fiber to be 1 m

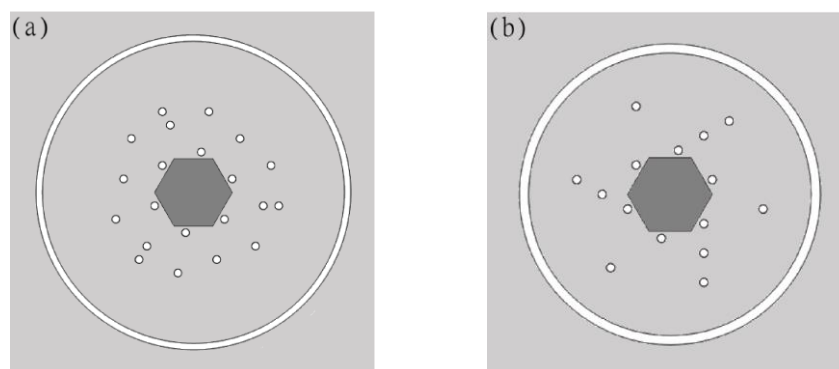


Fig. 1 – Cross-section of (a) SF-PCFa and (b) SF-PCFb.

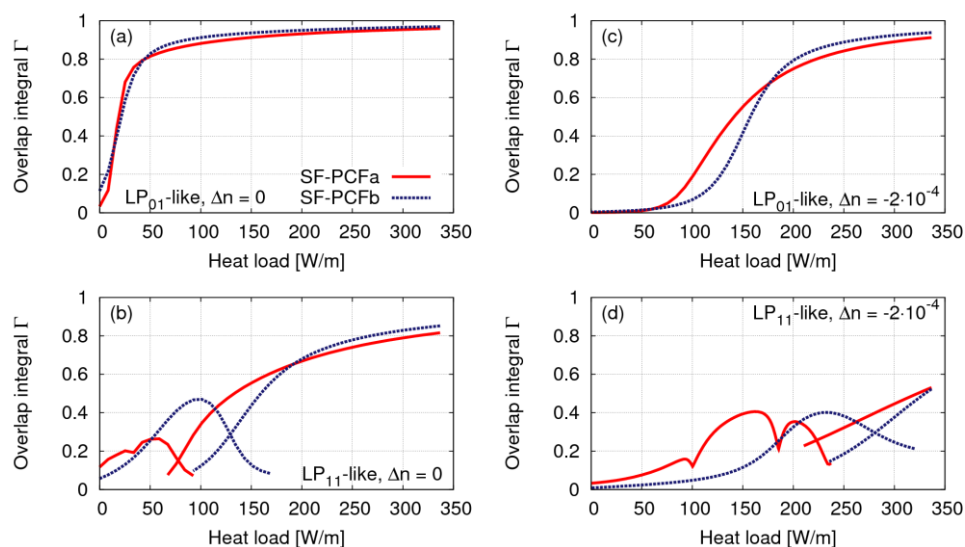


Fig. 2 – Overlap integral of the (a) FM and (b) most detrimental HOM of the two SF-PCFs without down doping. The same results are reported in (c) and (d) for the two SF-PCFs with core down doping $-2 \cdot 10^{-4}$.

long and cooled with water forced convection at the temperature $T = 14^\circ\text{C}$, with heat transfer coefficient $h = 2000 \text{ W}/(\text{m}^2 \text{ K})$. Coupled pump power between 0 W and 300 W has been considered, leading to a heat load q between 0 W/m and 340 W/m in the last 10 cm of the PCFs closer to the pumping end.

Fig. 2(a)-(b) show the overlap integral of the LP_{01} -like FM and of the most detrimental HOM, the LP_{11} -like, as a function of the heat load q , calculated for the two considered SF-PCFs at $\lambda = 2000 \text{ nm}$. In this case the core refractive index is matched with the pure silica one. Notice that when the pump is turned off, that is with no heat load applied, the overlap of the FM of both fibers is very low and the mode field is mostly spread outside from the core. As soon as a moderate heat load is applied, the FM Γ value quickly raises, reaching values above 0.8 with $q = 40 \text{ W}/\text{m}$. On the contrary, pump power has to be increased to reach at least $q = 150 \text{ W}/\text{m}$ to obtain significant confinement of the HOMs. Modal discrimination $\Delta\Gamma$, that is the difference between FM and HOM overlap, larger than 0.3 is found in the heat load range $20 \text{ W}/\text{m} < q < 200 \text{ W}/\text{m}$ for both fibers and it corresponds to effectively SM regime. At $q = 200 \text{ W}/\text{m}$ an effective area of $2500 \mu\text{m}^2$ is obtained. One possible way to allow SM propagation under a heavier heat load is to apply core down-doping, which pre-compensates for the refractive index increase due to thermo-optic effect. Fig. 2(c)-(d) show the overlap integral of the FM and HOM of the two considered SF-PCFs with a down-doping of the core by $-2 \cdot 10^{-4}$. The lower core refractive index hinders the confinement of the FM of both fibers, particularly at low heat load values. As a consequence, $q > 160 \text{ W}/\text{m}$ is required to obtain $\Gamma > 0.6$, preventing from efficient amplification at lower power levels. Tight FM confinement is reached at the highest heat load values, with overlap larger than 0.9.

Strong HOM delocalization is obtained in the whole considered heat load range, with maximum Γ value slightly above 0.5 when $q = 340$ W/m is generated. As a consequence, both SF-PCFs are effectively SM when the heat load exceeds 160 W/m. With a heat load of 250 W/m an effective area of $3200 \mu\text{m}^2$ is obtained, which decreases to about $2800 \mu\text{m}^2$ at the highest considered heat load of 340 W/m.

III. CONCLUSION

Two innovative designs of Tm-doped rod-type PCFs with reduced cladding symmetry have been analyzed by means of a full-vector modal solver based on the finite-element method. The effects of severe heating, due to the large quantum defect of Tm ions, have been included by means of a simple thermal model, to investigate the modal properties in a plausible operating scenario. The results have shown that SF-PCFs can provide effective delocalization of the high-order modes at $\lambda = 2 \mu\text{m}$ even at high power levels, provided that suitable down-doping of the core refractive index is applied. Furthermore, an effective area of more than $2500 \mu\text{m}^2$ in single-mode regime under a heat load of 340 W/m has been demonstrated.

REFERENCES

- [1] S.D. Jackson, "Towards high-power mid-infrared emission from a fiber laser," *Nature Photonics*, vol. 6, pp. 423-431, Jul. 2012.
- [2] D.C. Brown, H.J. Hoffman, "Thermal, stress, and thermo-optic effects in high average power double-clad silica fiber lasers," *IEEE Journal of Quantum Electronics*, vol. 37, pp. 207-217, Feb. 2001.
- [3] A. Tünnermann, T. Schreiber, J. Limpert, "Fiber lasers and amplifiers: an ultrafast performance evolution," *Applied Optics*, vol. 49, pp. F71-F78, Sept. 2010.
- [4] D. J. Richardson, J. Nilsson, W. A. Clarkson, "High power fiber lasers: current status and future perspectives," *J. Optical Soc. Am. B*, vol. 27, pp. B63-B92, Nov. 2010.
- [5] N. Madsch, P. Kadwani, R.A. Sims, L. Leick, J. Broeng, L. Shah, M. Richardson, "Lasing in thulium-doped polarizing photonic crystal fiber," *Optics Letters*, vol. 36, pp. 3873-3875, Oct. 2011.
- [6] F. Jansen, F. Stutzki, C. Jauregui, J. Limpert, A. Tünnermann, "High-power very large mode-area Thulium-doped fiber laser," *Optics Letters*, vol. 37, pp. 4546-4548, 2012.
- [7] R. Dauliat, D. Gaponov, A. Benoit, F. Salin, K. Schuster, R. Jamier, P. Roy, "Inner cladding microstructuring based on symmetry reduction for improvement of single mode robustness in VLMA fiber," *Optics Express*, vol. 21, pp. 18927-18936, Aug. 2013.
- [8] E. Coscelli, A. Cucinotta, "Modeling thermo-optic effect in large mode area double cladding photonic crystal fibers," *Int. J. Modern Physics B*, online, Feb. 2014.

CONFINEMENT LOSS SCALING LAW ANALYSIS IN TUBE LATTICE FIBERS

M. Masruri⁽¹⁾, L. Vincetti⁽²⁾, A. Cucinotta⁽¹⁾, S. Selleri⁽¹⁾

⁽¹⁾ Department of Information Engineering, University of Parma
Via Usberti 6/b, 43124 Parma, Italy
stefano.selleri@unipr.it

⁽²⁾ Department of Engineering “Enzo Ferrari”, University of Modena
and Reggio Emilia
Via Vignolese 905b, 41100 Parma, Italy
luca.vincetti@unimore.it

Abstract

Low loss and flexible circular tube lattice fibers (CTLFs) have been recently proposed and experimentally demonstrated. To reduce propagation loss, they require very large hollow core size leading to big and hardly flexible fibers. Scaling law analysis plays an important role in determining the best trade-off between low loss and small fiber diameter. In this work, the dependence of the confinement on wavelength and core radius is numerically investigated. Results show that confinement loss scales with the 4.5 power of core size and working wavelength, stronger than other hollow core fibers such as Kagome, Bragg, and Tube fibers.

Index Terms – Hollow core fibers, Inhibited coupling fibers, Propagation loss.

I. INTRODUCTION

Hollow core fiber (HCF) consists of an optical guiding central air-core surrounded by an arrangement of dielectric tubes running along its length. HCFs provides a new platform for light-gas interaction study [1] and applications where material properties are a limiting factor such as high power laser pulse delivery [2], mid, far infrared and THz transmission [3],[4]. Recently circular tube lattice fibers (CTLF) have been experimentally demonstrated and match many of these conditions [3,4,5]. CTLFs have shown a significant lower propagation loss with respect to the bulk material one over a wide spectral range. To reach this goal, a core size much bigger than the wavelength is required. This leads to big and hardly flexible fibers in mid infrared and THz applications. An optimized design of CTLFs thus requires a trade-off between low loss and small fiber diameter. In this work the relationship between confinement loss, working wavelength and core size in the CTLFs is numerically analyzed.

The paper is organized as follow. In section 2 the CTLFs waveguiding mechanism will be briefly introduced. In section 3 numerical results will be shown. Conclusion follows.

II. WAVEGUIDING MECHANISM IN CTLF

In CTLFs the hollow core is obtained by arranging N dielectric tubes in a circular pattern. Fig. 1(a) shows the cross section of CTLFs and structure parameters. The tubes have dielectric refractive index n_H , thickness t , and outer radius r_{ext} . The background material is air.

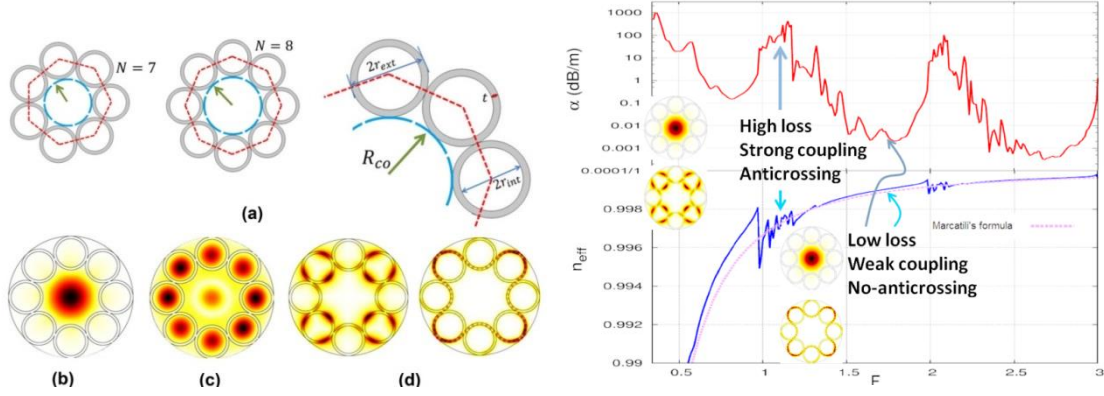


FIG. 1 Left – (a) Circular tube lattice fiber geometries, (b) Core Mode, (c) Cladding hole mode, and (d) dielectric modes with low (left) and high azimuthal dependence (right). Right - Confinement loss (top) and effective index (bottom) of the HE_{11} FM of CTLF with $N = 8$, $t = 0.131 \text{ mm}$, $r_{ext} = 0.873 \text{ mm}$. Approximate n_{eff} of the FM, obtained with Marcatili's formula [7], is also shown.

The core size depends on the number and size of the tubes:

$$R_{co}(N, r_{ext}) = r_{ext} \left[\frac{1}{\sin\left(\frac{\pi}{N}\right)} - 1 \right]. \quad (1)$$

CTLFs support three different kinds of modes shown in Figure 1(b)-(d): core modes, cladding hole modes, and cladding dielectric modes [6]. Conversely to Photonic Band Gap Fibers, in CTLF cladding supports modes at any given wavelength. The waveguiding is guaranteed by the inhibited coupling (IC) between core modes and cladding modes. High coupling and thus high loss can only occur with cladding dielectric modes having low azimuthal dependence (Figure 1(d) left) [6]. Fig. 1(right) shows the confinement loss (top) and dispersion curve (bottom) of the fundamental mode (FM) HE_{11} of a CTLF designed for THz applications, with $N = 8$, $r_{ext} = 0.873 \text{ mm}$, and $t = 0.131 \text{ mm}$, $n_H = 1.5207$ (Zeonex at 1 THz). High loss regions and anticrossing in the dispersion curve fall at integer values of the normalized frequency F :

$$F = \frac{2t}{\lambda} \sqrt{n_H^2 - 1} \quad (2)$$

corresponding to resonances between FM and low azimuthal dependence cladding dielectric modes [6]. Inside the low loss transmission windows (TWs), FM resonates with high azimuthal dependent cladding modes and the coupling is significantly weaker.

III. NUMERICAL RESULTS

The analysis of the dependence of the FM confinement loss on the fiber core size and working wavelength is essential for the fiber design optimization. Confinement loss scales with $R_{co}^{-3}\lambda^2$ for an air hole surrounded by an infinite dielectric medium, being R_{co} the core radius and λ the wavelength [7]. In a single tube fiber confinement loss scales with $R_{co}^{-4}\lambda^3$ [8], whereas it scales with $R_{co}^{-3}\lambda^3$ in case of Kagome fibers [9]. It is thus reasonable to assume that also in CTLFs the confinement might be expressed as:

$$CL = K \frac{\lambda^q}{R_{co}^p}, \quad p, q \in N^+ \quad (3)$$

where both p and q are generic coefficients that must be determined and K an arbitrary constant.

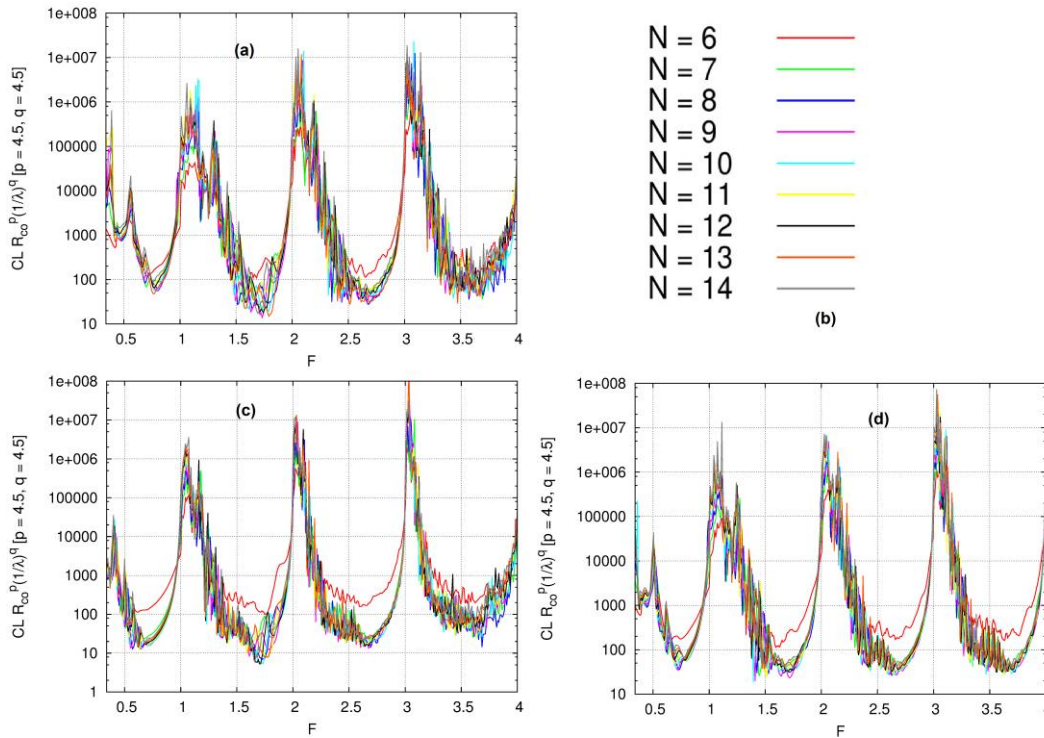


FIG. 2 – Normalized Confinement loss versus F for three different geometrical parameters of CTLFs (number of tubes, tube radius and tube thickness). (a) $t = 0.131 \text{ mm}$, $r_{ext} = 0.873 \text{ mm}$. (c) $t = 0.131 \text{ mm}$, $r_{ext} = 1.747 \text{ mm}$. (d) $t = 0.1048 \text{ mm}$, $r_{ext} = 0.873 \text{ mm}$.

In Fig. 2, the normalized confinement loss versus F of the CTLF analyzed in the previous section, for different geometrical parameters t and r_{ext} as well as number of tubes N is reported. The CTLFs here considered have different high loss frequencies and core size according to eq. (1) and (2). Despite that, the numerical results show that by using the value $p = 4.5$ and $q = 4.5$, the curves are almost overlapped over the first four TWs. An exception is the case of $N = 6$ which is due to the extra coupling between the fundamental core mode HE_{11} and the

cladding hole modes [10]. In fact, for $N = 6$ the core size is similar to the hole size of the tubes and FM resonates with dielectric hole modes. All results here reported show that CL varies according to eq. (3) with $p = 4.5$ and $q = 4.5$ irrespective on geometrical parameters, working wavelength and core size.

IV. CONCLUSION

Scaling laws of the CL of CTLFs have been numerically investigated to obtain design guidelines for small and flexible low loss fibers. Results have shown CL exhibits a stronger dependence of core size and wavelength with respect to other kind of hollow core fibers such as Tube, Bragg, and Kagome fibers since it scale as the 4.5 power of both core radius and wavelength.

REFERENCES

- [1] F. Benabid, et al, "Stimulated Raman Scattering in Hydrogen-Filled Hollow-Core Photonic Crystal Fiber," *Science* 298 (5592), 399–402 (2002).
- [2] J. D. Shephard, et al, "High energy nanosecond laser pulses delivered single-mode through hollow-core PBG fibers," *Opt. Express* 12 (4), 717–723 (2004).
- [3] Andrey D. Pryamikov, et al, "Demonstration of a waveguide regime for a silica hollow - core microstructured optical fiber with a negative curvature of the core boundary in the spectral region $> 3.5 \mu\text{m}$," *Opt. Express* 19, 1441–1448 (2011)
- [4] L. Vincetti, "Numerical analysis of plastic hollow core microstructured fiber for Terahertz applications," *Optical Fiber Technol.* 15 (4), 398–401 (2009)
- [5] V. Setti, L. Vincetti, and A. Argyros, "Flexible tube lattice fibers for terahertz applications," *Opt. Express* 21, 3388–3399 (2013)
- [6] L. Vincetti, and V. Setti, "Waveguiding mechanism in tube lattice fibers," *Opt. Express* 18, 23133–23146 (2010).
- [7] E. A. J. Marcatili, and R. A. Schmeltzer, "Hollow metallic and dielectric waveguides for long distance optical transmission and lasers," *Bell Syst. Tech. J.* 43, 1783–1809 (1964).
- [8] A. B. Manenkov, "Quasi optics of waveguides with selective reflecting dielectric walls," *Proc. of the Fifth Colloquim on Microwave Communications, Budapest, Hungary, June 1974.*
- [9] D. S. Wu, A. Argyros, and S. G. Leon-Saval, "Reducing the size of hollow terahertz waveguides," *J. Lightwave Technol.* 29, 97–103 (2011).
- [10] M. Masruri, et al. " Confinement loss scaling law analysis in tube lattice fibers for terahertz applications ", *Proc. SPIE 8985, Terahertz, RF, Millimeter, and Submillimeter-Wave Technology and Applications VII, 89850F* (2014).

MODAL ANALYSIS OF HOLEY FIBER MODE-SELECTIVE COUPLERS

A. Parini⁽¹⁾, N. Riesen⁽²⁾, A. Argyros⁽³⁾, R. Lwin⁽³⁾, S. G. Leon-Saval⁽³⁾,
J. D. Love⁽²⁾, G. Bellanca⁽¹⁾, P. Bassi⁽⁴⁾

⁽¹⁾ Department of Engineering, University of Ferrara, Italy.

⁽²⁾ RSPE, The Australian National University, Canberra,
ACT 0200, Australia.

⁽³⁾ IPOS, University of Sydney, NSW 2006, Australia.

⁽⁴⁾ Department of Electrical, Electronic and Information Engineering,
University of Bologna, Italy.

paolo.bassi@unibo.it

Abstract

Mode Division Multiplexing is currently investigated as a possible way to increase fiber system capacity. With this approach, different modes of the same fiber carry distinct information. One of the problems to be solved in these systems concerns coupling/decoupling of the various modes to/from the same fiber. In this presentation, the mode features of a mode mux/demux based on holey fibers are investigated, with particular emphasis on optimal device design. Some preliminary experimental results will also be presented.

Index Terms – Mode Division Multiplexing, Holey Fibers, Modeling.

I. INTRODUCTION

The need to increase the capacity of optical transmission systems has pushed research to investigate new solutions. After trying to increase the system capacity using WDM, Polarization Division Multiplexing, Orthogonal Frequency Division Multiplexing (OFDM) and Multilevel Modulation, the Non Linear Shannon Capacity Limit [1] is soon to be reached. To overcome this problem, and to raise the available bandwidth, Spatial Multiplexing Techniques (namely Mode Division Multiplexing in few mode optical fibers and multicore optical fibers) are currently being investigated [2]. The former approach considers different modes propagating in a single fiber core, each mode carrying distinct information. The latter, on the contrary, uses many single mode cores within the same cladding. Both solutions allow space saving, which is crucial in data centers or other environments where space is a constraint. Both of them, however, present a serious problem: coupling among modes in the same fiber, or between adjacent cores, which creates channel interference effects. Such a problem can be overcome by using classical MIMO techniques [3] in the former case, or careful core topological choices [4] in the latter one. The separation of the closely spaced fiber cores or the different modes propagating in the same fiber core is a further challenging task.

This work concentrates on the design of mode coupling/decoupling devices to/from a few-mode fiber. Some solutions have been proposed

so far. Selective mode decoupling can be done, for example, by looking for synchronous conditions between the multimode waveguide and a single mode one. This can be met in longitudinally varying devices, where synchronicity is obtained by varying the angle between the coupled waveguides [5], or in suitably designed cylindrical structures with different transversal size, so that two different modes have the same longitudinal propagation constant [6].

In this work, theoretical and preliminary experimental results of mode selective coupling in Holey Fiber couplers will be reported.

II. SELECTIVE MODE COUPLER STRUCTURE

The cross-sections of the two separate fiber cores as well as of the overall coupler are shown in Fig. 1. The structures have been chosen after a numerical study that considered many possible geometries via both a Finite Difference package and a commercial FEM code [7]. Two rings of holes for each fiber core resulted in an optimal trade-off between high coupling strength and low overall device radiation loss.

The two separate fiber cores have been designed to be synchronous for two different modes: the LP_{11} mode of the large-core and the LP_{01} mode of the small-core. To put the two cores close enough to guarantee coupling, a slight change in the fiber structure had to be made, as shown in Fig. 1c, where the radius of the hole in the coupling region has also been suitably tailored.

The LP_{11} mode has two orthogonal linear degenerate polarizations, generally denoted as LP_{11a} (two intensity lobes with vertical zero line) and LP_{11b} (two intensity lobes with horizontal zero line). In the coupler, supermodes exist. Two of them, whose components are shown in Fig. 2, exhibit symmetry compatible with a Perfect Magnetic Conductor, PMC, placed along the horizontal axis. The remaining two, whose components are shown in Fig. 3, exhibit symmetry compatible with a Perfect Electric Conductor, PEC, placed along the horizontal axis. The small complex part of the calculated propagation constant of the supermodes implies the existence of some losses in the coupler.

III. SELECTIVE MODE COUPLER BEHAVIOUR

When the large fiber core gets closer to the smaller one, coupling between LP_{11a} and LP_{11b} and the supermodes occurs. However, the field shapes allow only the LP_{11a} large components to couple efficiently with the large components of the supermodes. The LP_{11b} large components couple in fact with the small ones of the supermodes, so coupling does not practically occur in this case.

The overall behavior of the coupler was numerically tested using a Finite Difference BPM full vectorial code [8]. A prototype of the device has been realized by drilling and drawing of a solid PMMA preform rod [9]. The excellent agreement between the calculated and measured field intensities in the 3 dB coupling section is shown in Fig. 4.

The power evolution calculated along the propagation distance confirms that the radiation losses are very small.

The calculated coupling efficiency spectral behavior of the proposed coupler is shown in Fig. 5. As one can see, coupling is not very sensitive to wavelength. This is a further feature that can be exploited in the device design, for example for applications at different wavelengths.

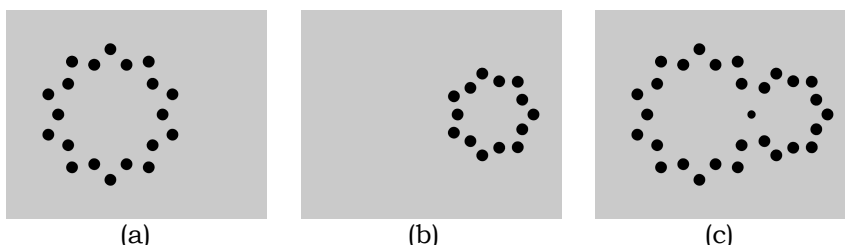


FIG. 1 – (a) Large-core fiber guiding LP₁₁ mode, (b) Small-core fiber guiding LP₀₁ mode, (c) Coupler. All the figures show a 50×40 μm area.

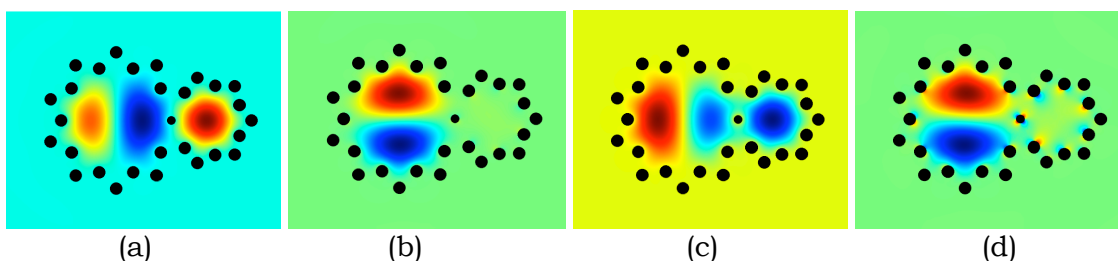


FIG. 2 – Supermodes with symmetry with respect to a horizontal PMC plane: (a,b) E_x (larger) and E_y components of the first one; (c,d) E_x (larger) and E_y fields of the second one.

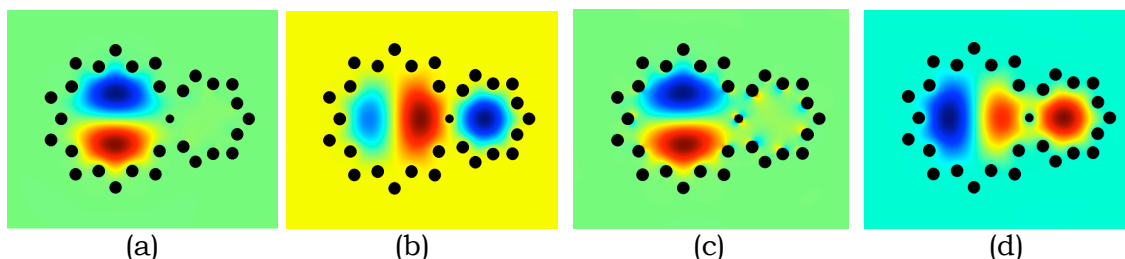


FIG. 3 – Supermodes with symmetry with respect to a horizontal PEC plane: (a,b) E_x and E_y (larger) components of the first one; (c,d) E_x and E_y (larger) fields of the second one.

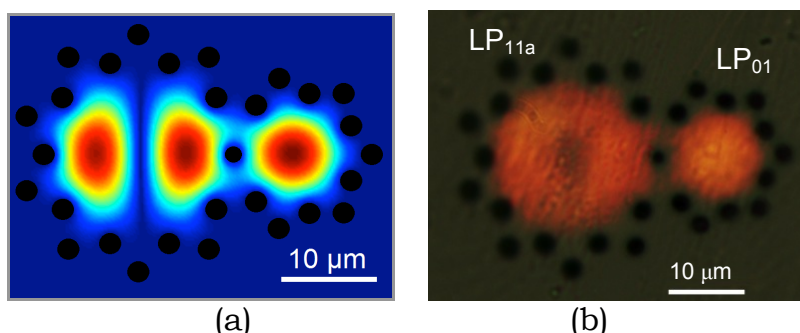


FIG. 4 – Intensity distribution at the 3 dB coupling section: (a) BPM simulation, (b) Experimental result (broadband excitation).

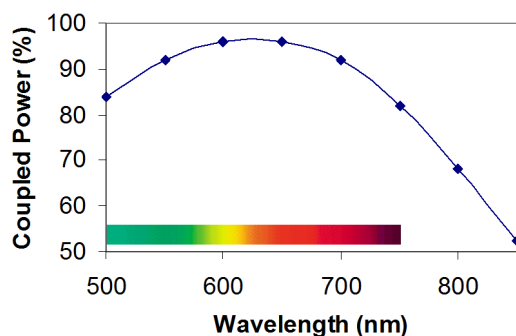


FIG. 5 – Spectral response of the proposed coupler.

IV. CONCLUSION

A selective mode coupler realized using Holey Fibers has been investigated. Experimental results are in excellent agreement with theoretical predictions. The device is suited for mux/demux operations in mode multiplexed systems for high transmission bandwidth. Its features (high coupling efficiency, low loss, low wavelength sensitivity) make it a promising solution worthy of further analysis.

REFERENCES

- [1] R. Essiambre, G. Kramer, P. J. Winzer, G. J. Foschini, B. Goebel, "Capacity limits of optical fiber networks," *IEEE J. Lightw. Technol.*, vol. 28 (4), pp. 662–701, Feb. 15, 2010.
- [2] S. Randel, "Space-Division Multiplexed Transmission," Proc. of OFC/NFOEC 2013, March 17-21, 2013, paper OW4F.1, Anaheim, California.
- [3] T. Sakamoto, T. Mori, T. Yamamoto, N. Hanzawa, S. Tomita, F. Yamamoto, K. Saitoh, M. Koshiba, "Mode-Division Multiplexing Transmission System With DMD-Independent Low Complexity MIMO Processing," *IEEE J. Lightw. Technol.*, vol. 31 (13), pp. 2192-2199, July 2013.
- [4] T. Hayashi, T. Taru, O. Shimakawa, T. Sasaki, E. Sasaoka, "Design and fabrication of ultra-low crosstalk and low-loss multi-core fiber," *Opt. Express*, vol. 19 (17), 16576-92.
- [5] P. Bassi, G. Falciasecca, M. Zoboli, "Experimental results on coupling Between optical fibers operating in low multimode regime," Proc. of 5th RiNEmA, St. Vincent (Aosta), 9-12 October 1984, pp. 329-332.
- [6] J. D. Love, N. Riesen, "Mode-selective couplers for few-mode optical fiber networks," *Opt. Lett.*, vol. 37 (19), pp.3990-3992, 2012.
- [7] Comsol multiphysics, <http://www.comsol.com>.
- [8] F. Fogli, L. Saccomandi, P. Bassi, G. Bellanca, S. Trillo, "Full vectorial BPM modeling of Index-Guiding Photonic Crystal Fibers and Couplers," *Optics Express*, vol. 10 (1), pp. 54-59, January 14, 2002.
- [9] N. Riesen, A. Argyros, A. Parini, R. Lwin, S. G. Leon-Saval, G. Bellanca, P. Bassi, J. D. Love, "Holey Fibre Mode-Selective Couplers," Proc. of the Australian and New Zealand Conference on Optics and Photonics (ANZCOP) 2013, paper P34, December 8-11, 2013, Fremantle, Perth, Western Australia.

DNA BIOSENSORS IMPLEMENTED ON FUNCTIONALIZED MICROSTRUCTURED OPTICAL FIBERS BRAGG GRATINGS

A. Candiani, A. Cucinotta, S. Selleri

Department of Information Engineering, Parma University
Area Parco delle Scienze 181/A, 43124, Parma, Italy
stefano.selleri@unipr.it

Abstract

A novel DNA sensing platform based on a Peptide Nucleic Acid - functionalized Microstructured Optical Fibers gratings has been demonstrated. The inner surface of different MOFs has been functionalized using PNA probes for specific DNA target sequences detection, and oligonucleotide-functionalized gold nanoparticles used to form a sandwich-like system for signal amplification. Spectral measurements of the reflected signal reveal a clear wavelength shift of the reflected modes when the infiltrated complementary DNA matches with the PNA probes placed on the inner fiber surface. Measurements have also been made using the mismatched DNA solution, containing a single nucleotide polymorphism, showing no significant changes in the reflected spectrum.

Index Terms – Biosensors, DNA detection, Microstructured Optical Fibers (MOFs), Fiber Bragg Gratings (FBGs), Peptide Nucleic Acid (PNA), Gold Nanoparticles (AuNPs).

I. INTRODUCTION

Biophotonics represents a very attractive and promising field of interest for biosensing applications [1]. Hybrid optical fibers bearing specific probes for DNA detection are advanced tools in which the sensing element can be integrated in a microfluidic device for the generation of optical signals [2, 3]. In particular, Microstructured Optical Fibers (MOFs) have the unique feature of presenting a cross-section defined by air-hole arrays, allowing to perform internal functionalization [4, 5]. In this work, the feasibility of a novel specific DNA sensing platform, based on the use of MOFs bearing a Bragg grating, is described, together with a strategy for enhancement of the optical signal based on the use of gold NanoParticles (Au NPs). Very specific Peptide Nucleic Acid (PNA) probes, OligoNucleotide (ON) mimics that are well suited for specific DNA target sequences detection, have been used due to their highly favourable properties in DNA hybridization and chemical and biological stability.

II. EXPERIMENTAL SETUP AND RESULTS

Two different MOFs, where a Bragg grating (BG) was previously inscribed, were tested for optical DNA detection: a grape-fruit geometry MOF (see Fig. 1a) and a single mode LMA-10 fiber (see fig.1b).

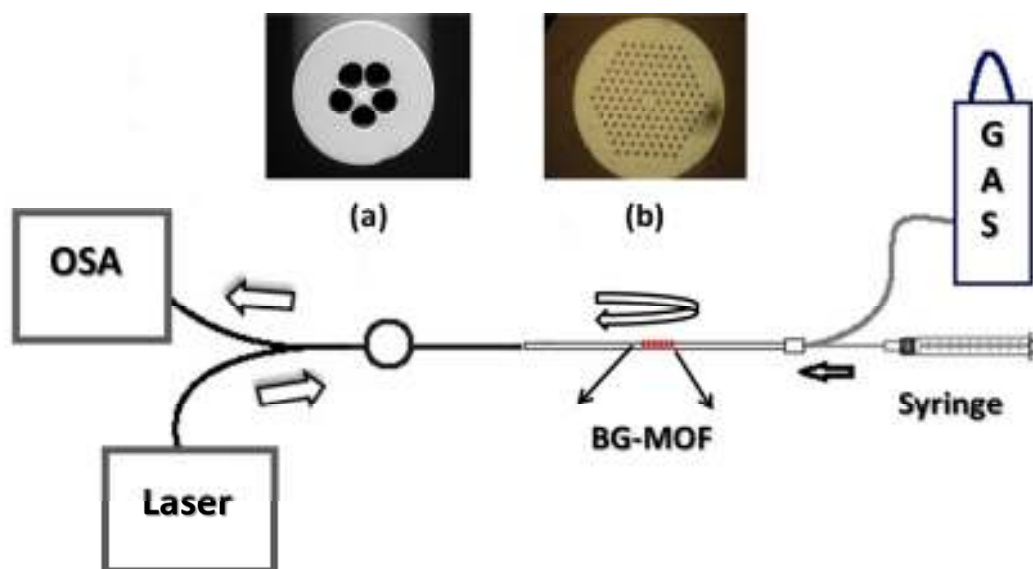


Fig. 1- Experimental setup. Optical image of the a) grape-fruit geometry and of the b) LMA-10 fiber.

The most stable modification for an optical fiber silica surface can be obtained by tethering of biomolecules or other probes through a silanization procedure, as described in a previous work [6]. The functionalization procedure is the same for both MOFs, except for the PNA probes: the first fiber was functionalized using PNA complementary to the Cystic Fibrosis (CF) gene mutation DNA, while the second fiber was prepared using PNA complementary to the genomic DNA from Genetic Modified Organism (GMO) soy flour. Internal derivatization was obtained by applying a nitrogen pressure of 2 atm to an in-house built apparatus comprised by a PTFE tubing reservoir containing the solutions, connected to the end of the fiber through a HPLC PEEK ferrule junction. After each treatment, the fibers were washed with the corresponding solvent, and the liquid was completely removed by a nitrogen flux.

An Amplified Stimulated Emission (ASE) source (ASE 1600, NTT Electronics), used as a broadband light source, was connected to a fiber optic circulator 1x2 (1530-1570nm bandwidth), as shown in Fig. 1, and the reflected signal was analyzed using an Optical Spectrum Analyzer (OSA) (Ando AQ-6315A). DNA infiltration process were performed by infiltrating the MOFs using a syringe pump (KD Scientific 100 series). The system was connected to a high pressure micro-filtered nitrogen line, to empty and dry the fibers after infiltration. In order to make the

setup even more reliable, a high precision dynamometer was also used to keep the fibers always with the same tension. The measurements were made in a clean room environment with a temperature control system. Spectral measurements of the reflected signals have been recorded at the beginning and at the end of every hybridization phase. In Fig. 1 the experimental setup is shown.

For the grape fruit fiber, the DNA solution was infiltrated through the fiber capillaries for 1 hour, and then the fiber was emptied using nitrogen. Subsequently, the oligonucleotide-functionalized gold nanoparticles (ON-AuNPs) solution was infiltrated for another hour, and then the fiber was washed with PBS and emptied again. The golden NPs bind to the DNA target, increasing the refractive index contrast between the silica surface of the capillaries and the analyte. The maximum shift observed for the more sensitive reflected high order band was around 0.27 nm towards the red (see Fig. 2a), whereas no significant changes were observed in the fundamental mode. Several measurements were carried out by using the same functionalized fiber in order to evaluate the repeatability of the device. We used the DNA solution to verify the reproducibility of a single measurement. The recovery of the fiber was done by washing the fiber capillaries with PBS for approximately 24 hours with a pressure of 10atm. Three more re-hybridization processes were implemented using the same conditions described earlier, showing very similar results.

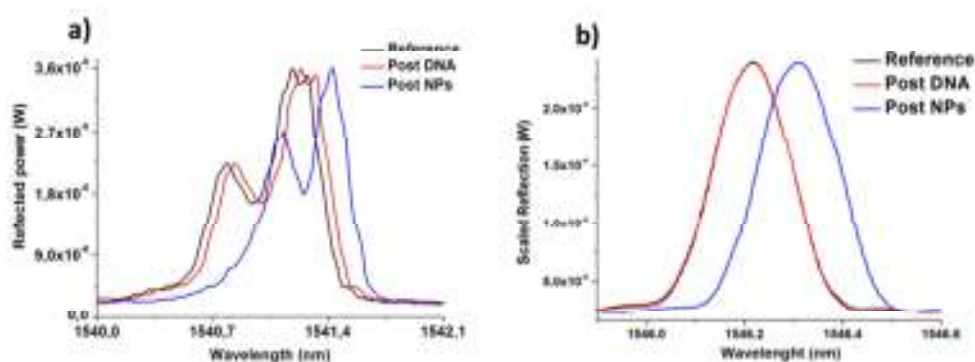


Fig. 2: a) Wavelength shift of the high order reflection mode obtained for the “grapefruit” geometry PCF after cystic fibrosis DNA sequence and ON-AuNPs infiltrations in the full-match DNA target experiment. b) The same graph for the “LMA10” fiber after genomic DNA from soy flour and ON-AuNPs infiltrations.

The LMA-10 was prepared following the same functionalization procedure, but using PNA complementary to the genomic DNA from GMO soy flour. Such measurements were carried out infiltrating different concentrations of the DNA target in solutions of genomic DNA not genetically modified: the experiments were conducted by initially

flowing the target solution through the fiber for 50 minutes, then the fiber was washed using PBS solution and dried with a nitrogen flux. Subsequently, ON-AuNPs were infiltrated, using the same condition of the previous experiment. Once data have been collected, the fiber was dried again and finally washed with PBS pH = 7. Preliminary results show that when the genomic DNA genetically modified is in a percentage equal to or less than 1% over the total genomic DNA in the solution, no significant changes are observed in the reflected spectral Bragg band. On the contrary, when the percentage of DNA is equal to 10% of the total DNA present in the infiltrated solution, a clear spectral shift of ~0.08 nm of the reflected fundamental mode is observed, as reported in Fig. 2b. More experiments were realized on the same fiber, and the measurements confirmed the same trends.

In this work, a novel DNA biosensing platform based on Bragg grating inscribed in a MOFs previously functionalized using PNA probes has been presented. The optical devices has shown a significant shift of the reflected high order Bragg mode when DNA molecules complementary to the PNA probes before, and then functionalized golden nanoparticles were infiltrated into the MOFs. This approach demonstrates the feasibility of realizing sensors for biological measurements observing the signal reflected by a Bragg grating, utilizing different fibers as probes.

REFERENCES

- [1] X. Fan, IM. White, "Optofluidic Microsystems for Chemical and Biological Analysis," *Nat. Photonics* 2011, 5, 591-597.
- [2] A. Candiani, M. Sozzi, A. Cucinotta, S. Selleri, R. Veneziano, R. Corradini, R. Marchelli, P. Childs, and S. Pissadakis, "Optical fiber ring cavity sensor for label-free DNA detection", *IEEE Journal of Selected Topics in Quantum Electronics*, "IEEE Journal of Selected Topics in Quantum Electronics", vol. 18, no. 3, pp. 1176-1183, 2012.
- [3] R. Corradini, S. Selleri, "Photonic Crystal Fiber for Physical, Chemical and Biological Sensing" Chapter 11 in "Photonic Crystal Fibers for Physical, Chemical and Biological Sensing" e-book, M. Prisco, A. Cutolo and A. Cusano editors, pp. 189-202, Bentham Science Publisher, 2012.
- [4] E. Coscelli, M. Sozzi, F. Poli, D. Passaro, A. Cucinotta, S. Selleri, R. Corradini, and R. Marchelli "Toward A Highly Specific DNA Biosensor: PNA-Modified Suspended-Core Photonic Crystal Fibers", *IEEE Journal of Selected Topic in Quantum Electronic*, Vol. 16, pp. 967-972, (2010).
- [5] R. D'Agata, R. Corradini, G. Grasso, R. Marchelli, G. Spoto, "Ultrasensitive Detection of DNA by PNA and Nanoparticle-Enhanced Surface Plasmon Resonance Imaging," *ChemBiochem* 2008, 9, 2067 – 2070.
- [6] A. Candiani, A. Bertucci, S. Giannetti, M. Konstantaki, A. Manicardi, S. Pissadakis, A. Cucinotta, R. Corradini, S. Selleri, "Label-free DNA biosensor based on a peptide nucleic acid-functionalized microstructured optical fiber-Bragg grating," *Journal of Biomedical Optics* 18(5), 57004 (2013).

HIGH POWER FIBER LASERS FOR ADDITIVE MANUFACTURING APPLICATIONS

A. Braglia⁽¹⁾, Y. Liu⁽¹⁾, G. Perrone⁽¹⁾

⁽¹⁾ Department of Electronics and Telecommunications,
Politecnico di Torino

C.so Duca degli Abruzzi 24, 10129 Torino, Italy

andrea.braglia@polito.it yu.liu@polito.it guido.perrone@polito.it

Abstract

The advent of novel laser-based additive manufacturing machines will require new types of lasers that combine kilowatt range output power with excellent beam quality. The paper describes the fabrication of a prototype of such lasers in which key component is a pump combiner specifically designed to take advantage of multi-emitter pump diodes. Preliminary results, limited to the available pump, have demonstrated the possibility to obtain over 0.6 kW of emitted power for almost 1 kW of pump power, with a beam parameter product lower than 0.5 mm·mrad.

Index Terms – Fiber lasers, Laser-based additive manufacturing, High-power pump combiners.

I. INTRODUCTION

Additive Manufacturing (AM, also known as “3D printing”) is a revolutionary technique for the realization of complex three-dimensional objects by aggregation of successive layers of metallic or polymeric powders. This fabrication technique is attracting great attention in industrial manufacturing not only because it allows producing components with complex geometries directly from CAD models, but also for the capability to densify new alloys that are not obtainable with more traditional procedures, and for the more efficient use of raw materials that leads to more sustainable production.

Focusing on metals, one of the most effective powder aggregation methods is that based on the selective action of a laser beam, typically generated by a high power fiber laser. Today, these AM machines are mainly using the so-called “powder-bed” approach, in which a layer of powders is spread across all the working area, and a laser beam selectively melts them along its path; then, the process is repeated until the desired thickness is achieved [1,2]. These machines use relative low power lasers (typically few hundreds of watt), are intrinsically slow, and can manufacture just small parts, so they find principal applications in higher added value manufacturing areas, such as aerospace and biomedics, only. In order to overcome these limitations, a new generation of machines based on “sprayed power” approach is currently

being proposed [2]. As the name implies, these machines spray and immediately densify the metal powders using a special nozzle in which a laser beam is coaxial with the powder stream. This method has the key advantage of depositing the powders only where needed, but it requires lasers that are simultaneously very powerful (to increase the processing speed) and with high beam quality (to allow focusing on a smaller area and thus improving the resolution). In turn, these requirements call for the development of a new class of fiber laser sources with output power in the kilowatt range, while maintaining an almost diffraction limited beam quality. The paper presents the realization of a continuous wave, high beam quality, fiber laser capable of emitting more than 0.6 kW of CW power, limited to the currently available pump power. This is the first step toward a 1 kW nearly single mode fiber laser module, which is based on new pump combiners specifically designed to take advantage of the latest high power multi-emitter pump laser diodes.

II. HIGH POWER LASER ARCHITECTURE

New additive manufacturing machines are equipped with fiber lasers because of their several advantages over more traditional gas and solid-state lasers, such as superior mode control and beam quality, larger heat dissipation capacity, higher efficiency and simplified beam delivery given the intrinsic guiding nature of the fiber. In early designs, fiber lasers were making use of discrete bulk optics for in- and out-coupling with the active fiber [3-4], whereas today all-fiber solutions are the standard for industrial applications due to their compactness, robustness, and most importantly, alignment free. One of the key aspects for power scaling of these lasers is thus the development of efficient all-fiber pump combiners able to work with the high power multi-emitter diodes recently made available on the market. The high power fiber laser presented in this paper uses a 19/1 fused-fiber pump combiner, which has been designed and manufactured by the authors specifically to couple up to 18 fiber-pigtailed multi-emitter pump diodes with the active fiber (Fig.1). For this use the central input port of the combiner is left intentionally free to avoid back reflection problems. The combiner has been tested with 18 pump diode modules, each able to emit about 60 W at about 915 nm, for a total of nearly 1 kW of pump power. The laser cavity in Fig.1 is constituted by a couple of fiber Bragg gratings (FBGs) and a large-mode-area (LMA) ytterbium-doped double-clad fiber; then the output goes through a cladding mode stripper (not shown in Fig.1) where cladding light, including leaky signal and residual pump, is filtered.

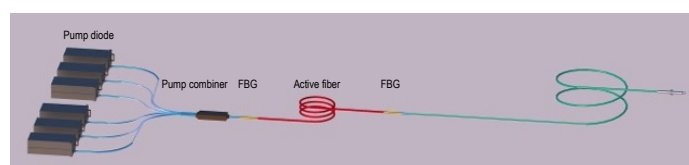


FIG. 1 – Schematic layout of the high power laser module in all-fiber format.

Before being realized, the laser cavity has been properly designed in order to optimize its performance: for this, a model that solves pump and signal propagation equations simultaneously with the rate equations for the ytterbium relevant energy levels has been developed [5]. The correct estimation of the actual active fiber parameters is crucial to run meaningful design simulations; for this reason in the presented case these parameters have been estimated by fitting some measurements taken from a laser built using a short spare span of fiber with simulations. The most important parameter for very high power lasers is the optical conversion efficiency, since higher efficiency not only means larger output power and less wasted power, but also implies less heat generated and thus lower probability of catastrophic failure. Fig.2 reports an example of the active fiber length optimization for a given level of input pump power.

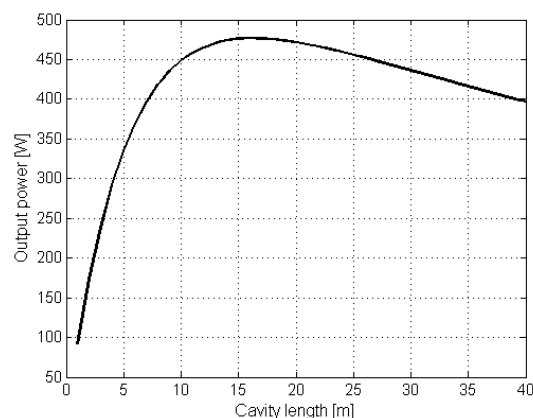


FIG. 2 – Calculated output power versus the length of active fiber assuming 700 W of launched pump power.

III. EXPERIMENTAL RESULTS

After the design optimization, a fiber cavity has been realized following the architecture described in the previous section. Given the use of a large mode area double cladding fiber to lower the power density in the core, special care has been paid in laying the fiber and controlled curvatures have been introduced to suppress oscillation of higher order modes.

The input-output characteristic curve of the obtained laser is shown in Fig.3: over 63% of efficiency has been obtained, with about 0.6 kW of signal power for about 0.95 kW of pump power. The maximum output was only limited by the available pump power and showed no evidence of roll-over; therefore, it is envisioned that, 1 kW laser output can be achieved by improving pump power to the order of 1.6 kW. The achieved beam parameter product is about 0.5 mm·mrad, which is in line with the requirements for the target applications. The curve in Fig.3 shows also that measurements and simulations are in excellent agreement,

demonstrating that the active fiber parameters used in the simulator are well representative of the actual fiber behavior. This adds further confidence in the design of the laser from which a power in excess of 1 kW is expected once a suitable pump power will be available.

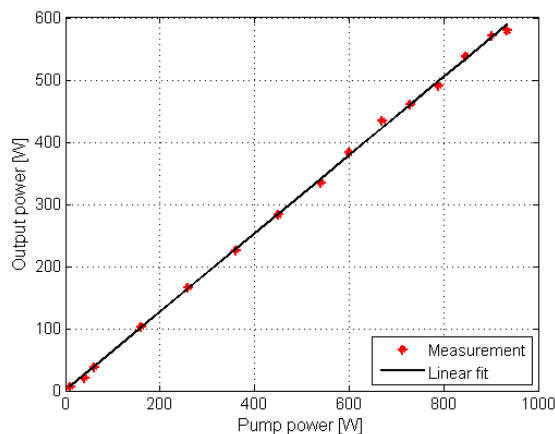


FIG. 3 – Characteristics of the developed fiber laser.

IV. CONCLUSION

A prototype of a fiber laser with output power and beam quality suitable for being used in the next generation of laser-based additive manufacturing machines has been presented. The laser architecture exploits an ad hoc pump combiner specifically suited for being used with high power multi-emitter pump diodes. The currently obtained power is limited by the available pump power to about 0.6 kW, but both theoretical simulations and preliminary experimental results allows predicting that scaling to over 1 kW CW power could be achieved without sensible degradation of the emitted beam quality.

REFERENCES

- [1] I. Gibson, D.W. Rosen, B. Stucker, “Additive manufacturing technologies: rapid prototyping to direct digital manufacturing, *Springer*, 2010.
- [2] Wohlers Associates, “Additive Manufacturing and 3D Printing - State of the Industry”, 2013.
- [3] Y. Jeong, J.K. Sahu, D.N. Payne, J. Nilsson, “Ytterbium-doped large-core fiber laser with 1.36 kW continuous-wave output power,” *Opt. Express* **12**(25), 6088-6092 (2004).
- [4] Y. Jeong, A.J. Boyland, J.K. Sahu, S. Chung, J. Nilsson and D.N. Payne, “Multi-kilowatt single-mode ytterbium-doped large-core fiber laser,” *J. Opt. Soc. Korea* **13**(4), 416-422 (2009).
- [5] A. Braglia, A. Califano, Y. Liu and G. Perrone, “Architectures and components for high power CW fiber lasers,” *Int. J. Mod. Phys. B*, DOI: 10.1142/S0217979214420016 (2014).

COUPLING MECHANISMS IN MULTIMODE FIBERS

Luca Palmieri, Marco Santagiustina, Andrea Galtarossa

Department of Information Engineering, University of Padova, Italy
luca.palmieri@dei.unipd.it

Abstract

Ultra-large bandwidth applications in optical fiber communication systems have revived the interest about multimode optical fibers because of spatial division multiplexing. In this framework, understanding the mechanisms that originate mode coupling is very useful to develop more accurate propagation models and optimized fiber designs. The paper analyzes common sources of mode coupling and their effects.

Index Terms – Fiber optic, few-mode fibers, mode coupling.

I. INTRODUCTION

Spurred by the foreseen “capacity crunch” of worldwide communications, research activity has focused on multimode optical fibers and spatial division multiplexing as a mean to increase system capacity [1, 2].

In an ideal fiber, where no mode coupling occurs, each mode of propagation can be considered as an independent communication channel. In real fibers, however, mode coupling (MD) occurs, severely limiting the actual capacity of a multimode fiber. Mode coupling is caused by asymmetries in the fiber cross-section that break its ideal cylindrical symmetry. When these perturbations are relatively weak and/or groups of degenerate modes are well separated, coupling among different mode manifolds is negligible even if coupling within each manifold still holds, and a dispersion similar to polarization mode dispersion (PMD) takes place. On the opposite side, when perturbations are relatively strong and/or groups of degenerate modes are not much separated, mode coupling occurs also among different manifolds, leading to propagation in the so called strong mode-coupling regime.

The theoretical models adopted so far accounts for coupling in a statistical way, assuming that coupling is “statistically isotropic” [3]. This choice however is not supported by physical evidence, but made only for mathematical convenience. A deeper understanding of coupling mechanisms is therefore important for a better description of multimode propagation. In this perspective, we describe the most common sources of perturbation and their effects on mode coupling.

II. ANALYSIS OF COUPLING MECHANISMS

Let $\vec{c}(z)$ be the N -dimensional vector with the complex amplitudes of each of the N modes propagating in the fiber. The dependence of \vec{c} on z is just a consequence of mode coupling and is governed by the equation $d\vec{c}/dz = -j(\vec{\beta} + \mathbf{K})\vec{c}$, where $\vec{\beta} = \text{diag}(\beta_1, \dots, \beta_N)$ is a diagonal matrix with the propagation constants β_i of the ideal modes, and the $N \times N$ matrix

K represents the coupling per unit length (or equivalently the coupling rate) [4]. Its elements can be evaluated by the integrals [4]

$$K_{\mu,\nu} = \frac{\omega}{j^4} \int_0^\infty \int_0^{2\pi} r \mathbf{E}_\mu^* \tilde{\epsilon} \mathbf{E}_\nu d\phi dr = K_{\nu,\mu}^*, \quad (1)$$

where r and ϕ are the transverse coordinates of the cylindrical reference frame (the third component z being the fiber axis), $\tilde{\epsilon}$ is the 3×3 matrix representing the perturbation term that must be added to the dielectric tensor of the ideal fiber to obtain the perturbed one, and the 3-dimensional vectors \mathbf{E}_μ and \mathbf{E}_ν are the complete electric fields (i.e. both transverse and longitudinal components) of modes μ and ν , properly normalized. We assume the ideal fiber as an isotropic and symmetrical step-index fiber.

We recall that the transverse electric field of the $LP_{n,p}$ mode reads $\mathbf{E}_{n,p}^{(t)} = f_{n,p}(r)g_n(\phi)\mathbf{e}$, where $n = 0, 1, \dots$ is the azimuthal order of the mode, $f_{n,p}(r)$ is a proper Bessel function, $g_n(\phi)$ can be set equal to either $\cos n\phi$ or $\sin n\phi$, and the unit vector \mathbf{e} represents the mode polarization, either \mathbf{x} or \mathbf{y} . Conversely, the longitudinal component can be evaluated as $E_{n,p}^{(z)} = -(j/\beta_{n,p})\nabla \cdot \mathbf{E}_{n,p}^{(t)}$ and it can be represented in general as $E_{n,p}^{(z)} = u_{n,p}(r)v_n(\phi)$, where $u_{n,p}(r)$ is a linear combination of Bessel functions and v_n is a linear combination of terms like $\cos(n \pm 1)\phi$ or $\sin(n \pm 1)\phi$ [5].

The evaluation of the integrals (1) for different modes and different kinds of perturbation is quite cumbersome, however looking at symmetries it is possible to draw some general conclusions. The crucial point is that also the perturbation $\tilde{\epsilon}$ can be expressed as a sum of terms that depends on ϕ through harmonic functions $\sin k\phi$ and $\cos k\phi$, for some integer value(s) of k . Therefore, consider two LP modes of azimuthal order n and m (which are by definition non-negative) and a perturbation of azimuthal order k , then the integral (1) (evaluated with respect to ϕ) is necessarily zero if none of the following relations holds:

$$n \pm k \pm m = 0, \quad (2)$$

$$n \pm k \pm (m \pm 1) = 0, \quad (3)$$

$$(n \pm 1) \pm k \pm (m \pm 1) = 0, \quad (4)$$

where conditions (2), (3) and (4) correspond, respectively, to coupling among transverse-transverse, transverse-longitudinal, longitudinal-longitudinal components of the modes. Notice that these conditions are necessary but not sufficient, because (1) can still be zero in few cases because of orthogonality conditions.

Several specific cases are considered in the following. Before that, however, note that the longitudinal components of the modes are negligible compared with the transverse one; therefore, transverse-transverse coupling is in general the stronger one. We remark also that while the matrix K describes the rate at which coupling occurs, the actual coupling is a cumulative effect that depends also on $\vec{\beta}$; due to this term, coupling among non-degenerate modes is in general weak, basically because of their phase mismatch.

	LP _{0,1}	LP _{1,1}	LP _{2,1}	LP _{0,2}	LP _{3,1}
LP _{0,1}	●				
LP _{1,1}		●			
LP _{2,1}			●		
LP _{0,2}				●	
LP _{3,1}					●

(a)

	LP _{0,1}	LP _{1,1}	LP _{2,1}	LP _{0,2}	LP _{3,1}
LP _{0,1}	○		●	○	
LP _{1,1}		●			●
LP _{2,1}	●		○	●	
LP _{0,2}	○		●	○	
LP _{3,1}		●			○

(b)

FIG. 1 – Schematic representation of coupling among the first few LP modes due to (a) birefringence and (b) core ellipticity. Full circles indicate coupling occurring among transverse components of the field, while empty circles correspond to coupling among longitudinal components.

II.1 Birefringence

One of the most popular case is linear birefringent fiber, i.e. it is made of anisotropic dielectric. Assuming for simplicity that the birefringence axes are aligned to the reference frame, the tensor of perturbation is diagonal and reads $\tilde{\epsilon} = (\delta\epsilon/2) \text{diag}(1, -1, 0)$. Consequently, the azimuthal order is $k = 0$, and since all elements in the third row and third column are zero, only transverse-transverse couplings of modes with the same azimuthal order can occur. More detailed analysis would however reveal that if the modes are different (despite the same azimuthal order) (1) vanishes after integration with respect to r , because of orthogonality relations. As a result, birefringence can cause only coupling within each manifold of degenerate modes, as sketched in fig. 1(a).

II.2 Core ellipticity

A slightly elliptical core can be represented by the scalar perturbation $\tilde{\epsilon} \simeq \sigma \epsilon_0 (n_{co}^2 - n_{cl}^2) \delta(r - a) \cos 2\phi$, where σ is a form factor, a is the average core radius and n_{co} and n_{cl} are the refractive indices of core and cladding, respectively [6]. Being a scalar perturbation, only transverse-transverse or longitudinal-longitudinal coupling can exist, whereas transverse-longitudinal does not occur. The azimuthal order of perturbation is $k = 2$, hence condition (2) yields $n = m = 1$ and $|n - m| = 2$, while (4) yields $n = m$, $n + m = 4$ and $|n - m| = 4$. Results are summarized in fig. 1(b).

II.3 Twist

When a fiber is mechanically twisted the shear stresses exerted on the silica and the corresponding elasto-optical effect induce a perturbation of the permittivity tensor whose non-zero components read $\epsilon_{1,3} = \epsilon_{3,1} = -(g\tau\epsilon_0 n_{av})r \sin\phi$ and $\epsilon_{2,3} = \epsilon_{3,2} = (g\tau\epsilon_0 n_{av})r \cos\phi$, where $\epsilon_{i,j}$ is the (i, j) element of $\tilde{\epsilon}$, τ is the twist applied per unit length, $g \simeq 0.15$ is an elasto-optic coefficient, and n_{av} is the mean refractive index [6]. The azimuthal order is $k = 1$ and, owing to the matrix structure, only transverse-longitudinal coupling can occur. Condition (3) then imply that coupling can occur only between modes with the same order, $n = m$, or with orders differing by 2, $|n - m| = 2$, as sketched in fig. 2.

	LP _{0,1}	LP _{1,1}	LP _{2,1}	LP _{0,2}	LP _{3,1}
LP _{0,1}	●		●	●	
LP _{1,1}		●			●
LP _{2,1}	●		●	●	
LP _{0,2}	●		●	●	
LP _{3,1}		●			●

FIG. 2 – Schematic representation of coupling among the first few LP modes due to twist; half-full circles indicate coupling occurring between transverse and longitudinal components, which are expected to have medium strength.

II.4 Magnetic field

When an optical fiber is exposed to a magnetic field oriented parallel to the fiber axis, Faraday rotation of polarization occurs [5–7]. The magnetic field perturbs the dielectric permittivity in such a way that the only non-zero elements are $\epsilon_{1,2} = -\epsilon_{2,1} = j(\lambda n_{av}/\pi)B_f V$, where λ is the wavelength, B_f is the magnetic field component along the fiber axis, and V is the Verdet constant (about 0.6 rad/T/m at 1550 nm for silica). The situation is analogous to that of birefringence shown in fig. 1(a): coupling occurs only between transverse-transverse components within degenerate manifolds (non-degenerate modes with the same azimuthal order do not couple because of orthogonality relations).

ACKNOWLEDGMENTS

This work has been partially supported by the Italian Ministry of University and Research through ROAD-NGN project (PRIN2010-2011), and it has been made within the agreement with ISCTI, Rome. AG is also with IIUSE, Southeast University, Nanjing, China in the framework of "High-end foreign expert" project.

REFERENCES

- [1] Chralyvy, A., "The coming capacity crunch," in [35th European Conference on Optical Communication, 2009. ECOC '09], Plenary paper (2009).
- [2] Morioka, T., Awaji, Y., Ryf, R., Winzer, P., Richardson, D., and Poletti, F., "Enhancing optical communications with brand new fibers," *IEEE Communications Magazine* **50**(2), s31–s42 (2012).
- [3] Antonelli, C., Mecozzi, A., Shtaf, M., and Winzer, P. J., "Random coupling between groups of degenerate fiber modes in mode multiplexed transmission," *Optics Express* **21**(8), 9484–9490 (2013).
- [4] Marcuse, D., "Coupled-mode theory for anisotropic optical waveguides," *Bell System Technol. J.* **54**, 985–995 (1975). Journal Article.
- [5] Someda, C. G., [Electromagnetic waves], CRC/Taylor & Francis, Boca Raton, FL (2006).
- [6] Ulrich, R. and Simon, A., "Polarization optics of twisted single-mode fibers," *Appl. Opt.* **18**, 2241–2251 (1979). Journal Article.
- [7] Palmieri, L. and Galtarossa, A., "Distributed polarization-sensitive reflectometry in nonreciprocal single-mode optical fibers," *J. Lightwave Technol.* **29**(21), 3178–3184 (2011).

A NOVEL ANTENNA FOR UHF RFID

Giovanni Andrea Casula⁽¹⁾

⁽¹⁾ Dipartimento di Ingegneria Elettrica ed Elettronica of the
University of Cagliari, Italy
a.casula@diee.unica.it

Abstract

A new printed antenna is proposed as a passive tag for UHF Radio Frequency Identification (RFID). The proposed antenna has a size significantly smaller than a printed dipole antenna working in the same UHF frequency band. Nevertheless, its operating bandwidth is quite large, since it encompasses all worldwide UHF RFID bands, and extends well beyond at both edges. The antenna has been designed using a general purpose 3D CAD, CST Microwave Studio, and measured results are in very good agreement with simulations. The proposed passive RFID tag meets both the objectives of low-cost and size reduction.

Index Terms – Passive RFID, UHF, Wideband Tag Antenna.

I. INTRODUCTION

In recent years, automatic identification procedures have become very popular in many areas, such as retail and distribution logistics. Automatic identification procedures exist to provide information about people, animals, and goods in transit. Among them, Radio Frequency Identification (RFID) is a rapidly developing technology, which uses RF signals for automatic identification of objects. The object to be recognized carries a transponder, which can be uniquely identified with a code stored in its microchip. The transponder, or tag, can take any desired shape, either exposed to particular external conditions, or covered with suitable materials, according with the use of the object on which the tag is applied. A tag can also store a large amount of information, read and written in real time at distances up to several meters. Nowadays, several standards have been defined for RFID systems, such as ISO, Class 0, Class 1, and Gen 2, and each country has its own frequency allocation for RFIDs. RFID systems operating in a range greater than a meter (where “range” indicates the maximum distance between reader and transponder), are classified as long-haul systems [1]. Devices that belong to this class operate using electromagnetic waves at UHF frequencies (866–869 MHz in Europe, 902–928 MHz in America, and 950–956 MHz in Japan), or at microwave frequencies, which generally can be identified in the range from 2.5 GHz to 5.4 GHz; these devices must therefore operate in the far field region. In the past literature, a number of RFID antennas have been proposed, both for passive and active tags, including circular patch antennas [2], covered slot antennas [3], folded dipole antennas [4],

meander antennas [5], and so on. In this work we present a printed antenna designed as a tag antenna, working in the whole UHF frequency band used for RFID (from 860MHz to 960MHz). The designed antenna is versatile and can be easily tuned both to feed different chips and to be mounted on boxes with different size and/or content. The antenna has been designed using a general purpose 3D CAD, CST Microwave Studio, and then manufactured. The measured results are in very good agreement with the simulations.

II. ANTENNA DESIGN

A tag antenna must fulfil some peculiar specifications. The tag should be easily tunable to any frequency within UHF RFID band (namely, 860–960 MHz) for various contents in the final assembly, for example when the tag is inserted into a label and placed on a cardboard box. The tag should have a size as small as possible to fit into standard cards or labels. The far field pattern should be omnidirectional, in order to maximize the read range performances. Because of the size and tunability requirements, the best geometry considered so far for such antennas is a meandered dipole, since meandering allows the antenna to be as compact as possible, furthermore providing an omnidirectional far field pattern in the plane perpendicular to the axis of the meander. Besides, a meander antenna can be easily tuned by varying the lengths of meander lines, in order to obtain optimum reactance and resistance matching. As a matter of fact, an RFID tag must be a low-cost device, and this imposes restrictions both on the antenna structure and on the choice of the proper materials for its construction, including the microchip used. Typical conductors used in tags are copper, aluminum, and silver ink, while typical dielectric layers are low-cost flexible and rigid PCB substrates, like FR4. Furthermore, an RFID tag must be a reliable device, able to sustain variations due to temperature, humidity, stress, and to survive to processes such as label insertion, printing and lamination. In order to fulfil the specifications of a typical tag (namely, minimize the production cost, ensure the reliability, and so on), the proposed antenna is printed on one side of a FR-4 substrate, a robust and cheap material, quite suitable for RFID structures. The antenna has been designed requiring an input match of 50 Ohm at the feeding port (Fig. 1a), and the structure has been optimized to achieve an operating frequency band covering the entire range required by UHF RFID devices. In order to use the antenna as a tag of RFID UHF, the feeding port must be replaced with a commercial chip, and the antenna has to be modified in order to be conjugate-matched to the input impedance of the chip. The width of the feeding port has been chosen to allow the insertion of almost each available commercial chip. The geometry of the proposed antenna, shown in Fig.1a, has a very simple, and symmetrical, structure, and only one dielectric layer, and consists of a long meandered dipole, used to minimize the size of the tag. These

are very important features, since tag form and size must allow an easy embedding or attaching to the required objects (cardboard boxes, airline baggage strips, identification cards, and so on), or fitting inside a printed label. The geometrical dimensions of the proposed antenna are: $W = 4.30$ mm; $L_1 = 11.70$ mm; $L_2 = 34.30$ mm; $L_3 = 13.00$ mm; $L_4 = 12.15$ mm; $L_5 = 8.70$ mm; $L_6 = 14.30$ mm; $L_0 = 86.60$ mm; $L_V = 59.40$ mm; Gap = 9.40 mm. This compact and planar structure can be used in many applications, such as RFID tags printed in smart cards, and other wireless handheld devices.

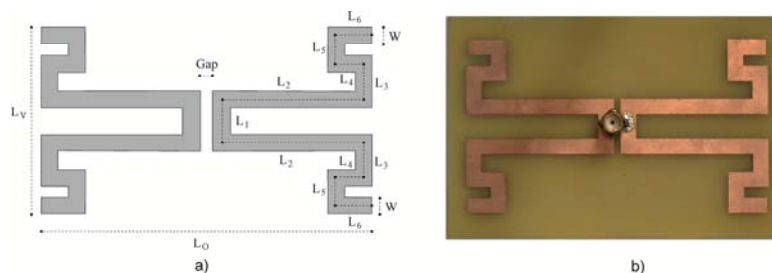


FIG. 1 – a) Layout of the designed TAG antenna. b) Photo of the designed TAG antenna.

III. RESULTS

The antenna shown in Fig.1a has been analysed with CST Microwave Studio, a commercial software for the simulation of 3D electromagnetic structures. The antenna substrate is the FR-4, with a dielectric constant of 4.3, a thickness of 1.535 mm and a loss tangent of 0.02. The metallization is made by copper, with a thickness of 0.035 mm. Fig.1b shows a photo of the manufactured RFID tag antenna. The simulated and measured reflection coefficient for the tag antenna in Fig.1 is shown in Fig.2a, and a very good agreement is found between experimental results and simulations. The -10 dB bandwidth is equal to 125 MHz (from 850 MHz to 975 MHz), covering the whole frequency band of the worldwide UHF RFID systems. The E-Plane and H-Plane radiation patterns, simulated and measured at 900 MHz, are shown in Fig.2b, and are broadside and bidirectional in the H-Plane, and omnidirectional in the E-plane, with a peak antenna gain equal to 1.8 dB. The far-field pattern is almost constant in the whole working bandwidth (850-975 MHz), with a negligible maximum variation of 0.1 dB of the peak gain. The cross-polar component is not shown because it is 40 dB below the co-polar radiated field. It is worth noting that, due to the symmetrical structure, the main radiation direction of the presented antenna tends to be perpendicular to the antenna surface, and this facilitates the identification of the target objects for the RFID tag antenna. In Fig.2c, the simulated gain in the broadside direction is reported in a wide frequency band, namely from 750 to 1050 MHz, and, as apparent, it keeps almost constant even in this large frequency range. Also the simulated radiation efficiency is very high in a large

frequency band, as shown in Fig.2c. The simulated total efficiency, which takes into account also the input mismatching, is coherent with the reflection coefficient shown in Fig.2a, and is greater than 80% in the frequency band from 825 to 1025 MHz, with a percentage bandwidth of 22%.

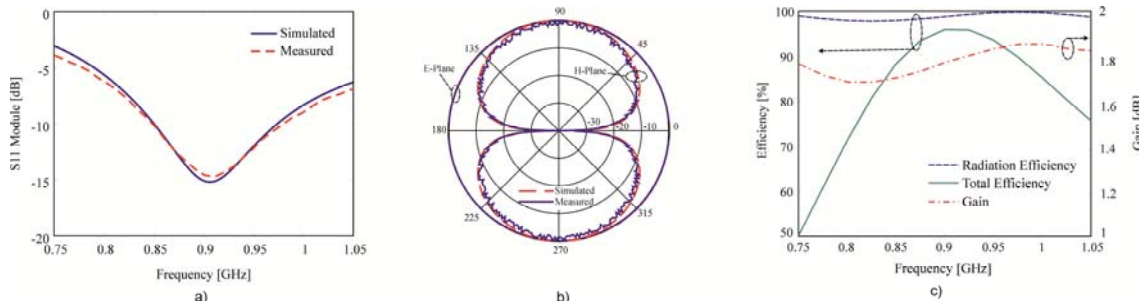


FIG. 2 – a) Reflection coefficient; b) Normalized Far-Field Pattern (dB) at 900 MHz; c) Gain in the broadside direction and efficiency of the designed TAG antenna shown in Fig.1.

IV. CONCLUSION

A printed antenna is proposed as a passive tag for UHF RF-ID. The antenna, designed with CST Microwave Studio, commercial software for the simulation of 3D electromagnetic structures, has a bandwidth of 160 MHz and a gain of 1.7 dB, and measured results are in very good agreement with the simulations. In particular, the proposed antennas have a length shorter about 50% with respect to a normal printed dipole working in the same frequency band, and compared to the existing antennas with the same structures, a significantly greater operational bandwidth is achieved. Furthermore, the proposed antennas has a size which perfectly fits with the dimensions of typical smart cards, have also a high mechanical strength, are highly feasible, can be easily adapted to other areas of wireless applications, and are able to operate both at the UHF frequency of 868 MHz (in Europe), at the frequency of 915MHz (USA), and at the frequency of 955MHz (Asia), helping to the circulation and practical applications of the RFID merchandise in the world.

REFERENCES

- [1] K. Finkenzeller, *RFID Handbook: Radio-Frequency Identification Fundamentals and Applications*, 2nd ed: Wiley, 2004.
- [2] S. K. Padhi, N. C. Karmakar, C. L. Law, and S. Aditya, "A dual polarized aperture coupled circular patch antenna using a C-shaped coupling slot," *IEEE Trans. Antennas Propag.*, vol. 51, no. 12, pp. 3295–3298, Dec. 2003.
- [3] S.-Y. Chen and P. Hsu, "CPW-fed folded-slot antenna for 5.8 GHz RFID tags," *Electron. Lett.*, vol. 24, pp. 1516–1517, Nov. 2004.
- [4] Q. Xianming and Y. Ning, "A folded dipole antenna for RFID," in *Proc. IEEE Antennas and Propagation Soc. Int. Symp.*, vol. 1, Jun. 2004, pp.97–100.
- [5] G. Marrocco, "Gain-optimized self-resonant meander line antennas for RFID applications," *Antennas Wireless Propag. Lett.*, vol. 2, no. 21, pp. 302–305, 2003.

DESIGN OF A W BAND CORRELATION UNIT

G. Addamo⁽¹⁾, O. A. Peverini⁽¹⁾, G. Virone⁽¹⁾, R. Tascone⁽¹⁾, M. Lumia⁽¹⁾
and R. Orta⁽¹⁾

⁽¹⁾ Consiglio Nazionale delle Ricerche, Istituto di Elettronica e di Ingegneria dell'Informazione e delle Telecomunicazioni (CNR-IEIIT) c/o Politecnico di Torino, Corso Duca degli Abruzzi 24, 10129, Torino, Italy.

⁽¹⁾ giuseppe.addamo@ieiit.cnr.it

Abstract

In this work the design of W-band correlation unit operating in the frequency band [85,104]GHz is presented. The main components of the device are four H-plane -3dB direction couplers and a 90deg phase shifter. Both have been synthesized exploiting a design technique based on a distributed-parameter-circuit model. The relation between received and measured Stokes parameters is described by a matrix equation whose undesired terms have been minimized.

Index Terms – Correlation Unit, H-plane Directional Coupler, Phase Shifter.

I. INTRODUCTION

Astrophysical researchers are, nowadays, particularly interested on the investigation of the polarization state of the Cosmic Background Microwave (CMB) radiation [1]. The measurement of CMB is, indeed, one of the key objectives for a deep knowledge of the cosmological reionization history. One of the critical point of these measurements is represented by the fact that the CMB polarized component is quite weak with respect to the unpolarized background. Hence, in order to detect this signal, measurement instruments should present very high sensitivity and the systematic errors have to be minimized. This goal can be achieved by exploiting clusters of high performances polarimeters. Figure 1 shows a general scheme of correlation polarimeter. The radiation under test, which is represented by (Q, U, I, V) Stokes parameters, is collected by the antenna. The polarizer then converts the circular polarizations into two linear ones. Finally the orthomode transducer (OMT) routes them into two different rectangular waveguides. From the A and B OMT outputs the measured Stokes parameters Q_m and U_m are obtained as the real and imaginary part of the correlation product $\langle A \bar{B} \rangle$.

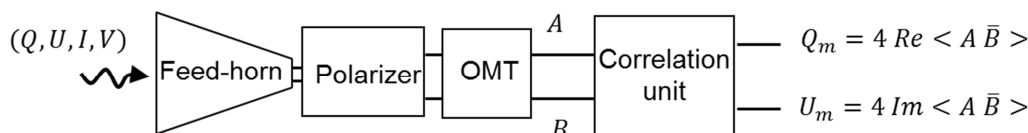


Figure 1 Scheme of a correlation unit.

This product is generally performed by the correlation unit. The typical problem of the heterodyne receivers where the quantity $\langle A \bar{B} \rangle$ is

computed after down-conversion stage can be avoided by an analogical conversion. On the other hand, micro-strip solution is usually neglected due to the leakage problem which can affect significantly the performances of the chain, in particular when high frequency bands are considered. In these cases a waveguide correlation unit represents a good compromise between performances and costs. In this work we present the design of a 20% band waveguide correlation unit operating in the frequency range [85,104] GHz. The device has been obtained exploiting the architecture described in [2] for the case of a 10% Ka-band correlation unit for the Sky Polarization Observatory project (SPOrt) and the Baloon-borne radiometers for the Sky Polarization Observations projects (Bar-SPOrt) [3].

II. CORRELATION UNIT

The scheme of the correlation unit is shown in Fig. 2. It is composed by four H-plane -3dB directional couplers and a 90deg phase shifter. The input signals A and B are split into two branches and subsequently combined in order to produce two couples of outputs signals $C_1; C_2$ and $C_3; C_4$ which are proportional, in the ideal case, to $A \mp B$ and $A \mp iB$, respectively. The detection of the outputs is performed by a square law diodes connected to the output ports and then the converted signals are sent to two differential instrumentation amplifiers (both not shown in the figure) in order to obtain the measured Q_m and U_m Stokes parameters:

$$\begin{aligned} Q_m &= \langle |C_2|^2 - |C_1|^2 \rangle = \langle |A+B|^2 - |A-B|^2 \rangle = 4\text{Re} \langle A\bar{B} \rangle = Q \\ U_m &= \langle |C_4|^2 - |C_3|^2 \rangle = \langle |A+iB|^2 - |A-iB|^2 \rangle = 4\text{Im} \langle A\bar{B} \rangle = U \end{aligned}$$

From the previous equations it should be noted that the signals Q_m and U_m do not depend on the quantities $|A|^2$ and $|B|^2$ because they are eliminated by cancellation. This is no longer true in the real case where a perfect cancellation does not occur owing to the non-ideal behavior of the various components. It can be shown that, in the real scenario, Q_m and U_m are related to the input Stokes parameters by the following matrix relation:

$$\begin{bmatrix} Q_m \\ U_m \end{bmatrix} = \begin{bmatrix} H_{QQ} & H_{QU} \\ H_{UQ} & H_{UU} \end{bmatrix} \begin{bmatrix} Q \\ U \end{bmatrix} + \begin{bmatrix} K_{QI} & K_{QV} \\ K_{UI} & K_{UV} \end{bmatrix} \begin{bmatrix} I \\ V \end{bmatrix} = \mathbf{H} \begin{bmatrix} Q \\ U \end{bmatrix} + \mathbf{K} \begin{bmatrix} I \\ V \end{bmatrix}$$

where the matrices \mathbf{H} and \mathbf{K} are related to the scattering matrix \mathbf{S} of the correlation unit and $I = \langle |A|^2 + |B|^2 \rangle$ and $V = \langle |A|^2 - |B|^2 \rangle$. Since I and V are several orders of magnitude higher than Q and U , the minimization of the elements of the matrix \mathbf{K} is necessary to increase the sensitivity of the polarimeters. Similarly the minimization of the off-diagonal terms of \mathbf{H} is useful to guarantee the polarization purity. To this end the H-plane directional couplers have been synthesized exploiting a generalized version of the design technique presented in [3].

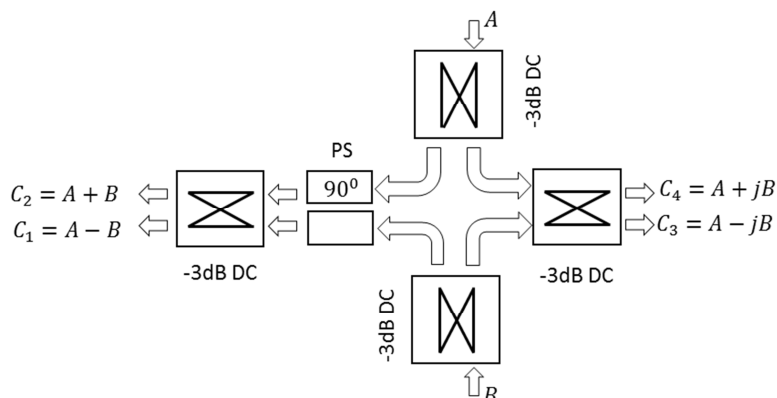


Figure 2 Scheme of the waveguide correlation unit. It is composed by four -3dB directional coupler and one 90deg phase shifter (PS). The input signals are A and B, the output ones are C_i with $i=1,4$.

In particular the device is described in terms of the sum and difference mode basis. For these modes a distributed-parameter-circuit model is introduced and the coupling slots dimensions and their reciprocal distance have been obtained directly using a proper identification technique which takes into account a simultaneous control of the differential phase shift between the transmission coefficients of these two modes and their reflection coefficients.

Since the optimum condition for an H-plane coupler consists on coupling slots with very small heights, the matching for the difference mode is automatically satisfied and this simplifies the coupler design.

A similar design technique has been applied for the design of the 90 degree phase shifter. According to a platelet technology and spark erosion technique in the design two mechanical constrains have been considered. Firstly the heights of the phase shifter stubs and coupling slots are constant and realized through a fixed 0.1 mm thickness plate. Secondly the widths are limited to a minimum value of 0.5 mm in order to simplify and reduce the costs of the possible manufacture process.

III. NUMERICAL RESULTS

The directional couplers consist on eleven apertures and the phase shifter is composed by twelve stubs. Exploiting the five-level scheme shown in [2], the longitudinal length of overall structure is 90mm, its transversal dimension is 5mm x 18mm. The correlation unit performances are reported in Figures 3-5 in terms of reflection coefficients at the input ports and the magnitude of the elements of the matrices \mathbf{H} and \mathbf{K} . In the band H_{QU} and H_{UQ} are better than -18dB and -25dB, respectively. Note that the improvement of these levels would require more complex and longer directional couplers. The spectral distribution of the elements of \mathbf{K} , which quantifies the rejection of the I and V Stokes parameters, shows that K_{QV} and K_{UV} are almost -15dB and K_{QI} and K_{UI} are better than -24dB and -38dB, respectively.

IV. CONCLUSIONS

In this work the performances of a W-band correlation unit has been presented. The device has good performances and its optimum with respect to the architecture considered and the classical mechanical constraints. In order to improve the performances more complex solutions are under investigation.

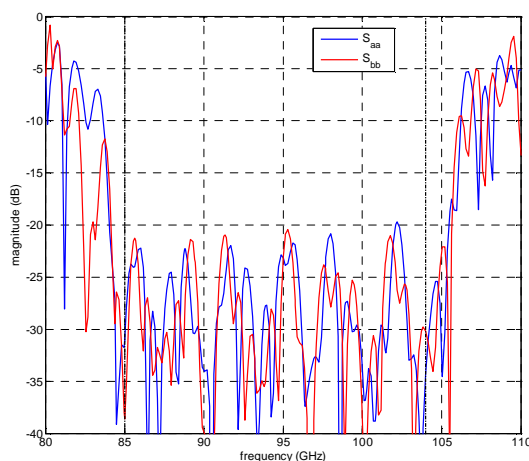


Fig. 3 Magnitude of the reflection coefficients at the input ports A and B of the correlation unit.

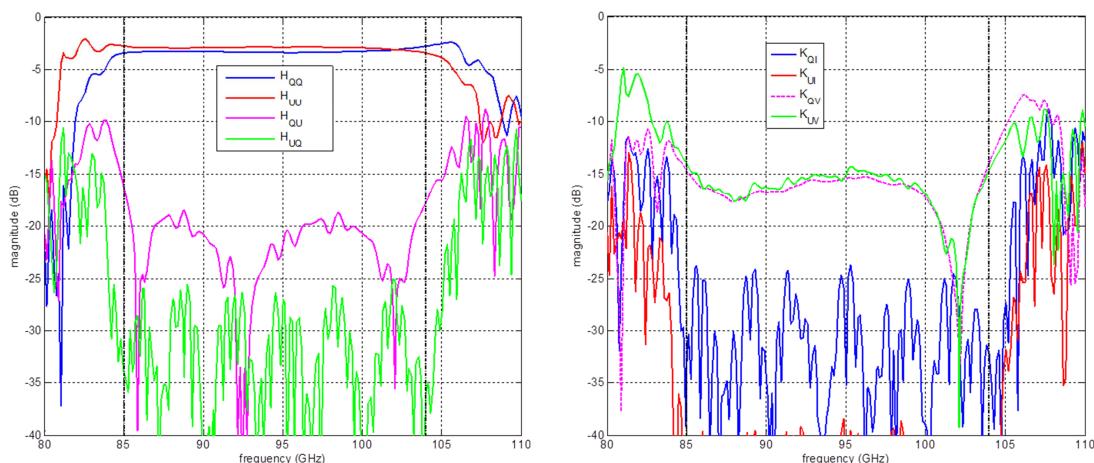


Fig. 4 Direct and off-diagonal terms of the matrix \mathbf{H} (left) and elements of the matrix \mathbf{K} (right). The vertical lines refers to the operative frequency band [85,104] GHz.

REFERENCES

- [1] M. Bersanelli, et al., “A coherent polarimeter Array for the Large Scale Polarization Explorer (LSPE) balloon experiment”, in Proc. of the SPIE Conference, The Netherlands, July 2012.
- [2] G. Virone et al, “Five-Level Waveguide Correlation Unit for Astrophysical Polarimetric Measurements” *IEEE Trans. Microw. Theory and Tech.* vol. 55, no. 2, February 2007.
- [3] S. Cortiglioni, et al., “The Sky Polarization Observatory”, *New Astronomy*, vol. 9, no. 4, pp. 297-327, May 2004.
- [4] R. Tascone et al, “Scattering matrix approach for the design of microwave filters”, *IEEE Trans. Microw. Theory and Tech.*, vol. 48, no. 3, pp. 423-430, Mar. 2000.

WEARABLE AUTO-TUNING ANTENNA FOR COSPAS-SARSAT RESCUE APPLICATIONS

A. Baroni, P. Nepa

Department of Information Engineering, University of Pisa, Italy

Via Caruso 16, 56122 Pisa, Italy

a.baroni@for.unipi.it , p.nepa@iet.unipi.it

Abstract

In this paper the feasibility study of a closed-loop reconfigurable wearable antenna is investigated. The presented system is developed for being equipped on a commercial life-jacket used on board of vessels as a safety item. The antenna should be compliant with the Cospas-Sarsat - Search and Rescue system being able to transmit a distress beacon at a frequency of 406MHz (UHF-band) in an emergency situation.

Index Terms – Cospas-Sarsat System, Auto-Tuning Network, Wearable Antenna.

I. INTRODUCTION

An open issue for safety in the maritime scenario is the localization of a castaway after a shipwreck or after being fallen over board. A life-jacket could assure a primary security system avoiding drowning, but a transmitting system directly mounted on it could improve the survivor's localization.

In this case, several precautions should be taken in order to assure signal transmission in adverse condition. Indeed the person that is fallen into the water could wet the antenna, or could change its position because of movement induced by the sea waves or because of a panic attack. Moreover the electromagnetic coupling between the transmitting antenna and the human body could affect several antenna parameters such as the input impedance, the radiating pattern or his polarization characteristics. In particular the antenna impedance mismatch could reduce the radiating efficiency of the antenna, leading the transmitter to increase the transmitting power, and causing a significantly reduction of the battery lifetime. Therefore, a dynamically reconfigurable transmitting antenna could significantly increase the effectiveness and the reliability of a Search and Rescue system.

Several studies have been conducted in this field and many solutions have been proposed. In [1], a review of reconfigurable systems that could use mechanical system, RF switches or a tunable material is presented.

In [2], a system in which the impedance is controlled using a combination of a quarter-wavelength ($\lambda/4$) transmission line with several capacitors and inductors is shown. In [3], a solution in which the antenna is directly loaded with MEMS switches is presented but it

does not represent a low cost solution (the latter requirements should be a must for antennas integrated onto a life-jacket).

In this paper, preliminary results of a feasibility study regarding a closed-loop reconfigurable wearable antenna integrated onto a life-jacket are presented. This preliminary study is oriented to the realization of a tuning circuit and of a tuning algorithm for an antenna that has to operate at the frequency of the Cospas – Sarsat system (406MHz) [4]. The automatic tuning should mitigate the variations induced on the antenna impedance matching by both the proximity of the human body and sea surface, as well as the natural movements of the wearer [5].

II. SYSTEM CONCEPT OVERVIEW

The block diagram of the auto-tuning antenna is depicted in Fig. 1. A closed-loop control circuit (auto tuning network) has been inserted between the two main blocks (signal generator and wearable antenna), in order to assure the maximum radiated power for the transmission of a distress beacon.

The auto-tuning network has to change a set of parameters of the impedance matching network, starting from an estimation of the reflection coefficient (S_{11}) and according to a dedicated tuning algorithm. A microcontroller is responsible for both the estimation of the reflection coefficient and for changes into the impedance network.

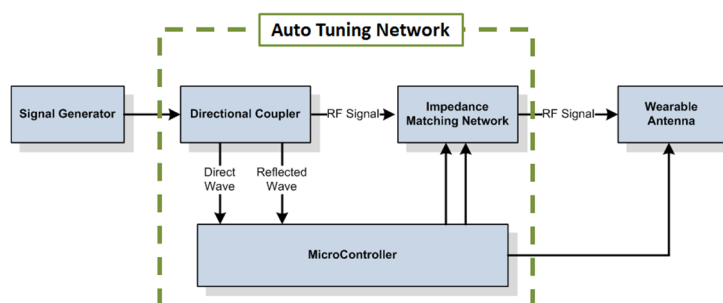


FIG. 1 – Block scheme of the auto-tuning antenna.

The microcontroller mounted on board of the system could also act directly on the antenna electrical configuration.

The antenna that has been chosen for realizing a prototype is a meandered folded dipole [6], which has been proposed for being integrated onto the floating parts of a commercial life-jacket. Several measurements have been performed in order to better understand the behavior of the antenna input impedance when it is close to the human body, in terms of the S_{11} parameter. Measured data for the input impedance of the body worn antenna have been collected in several conditions, according to a set of possible positions that a body could assume (man standing, man crouched, man seated, man with a hand in front of the antenna).

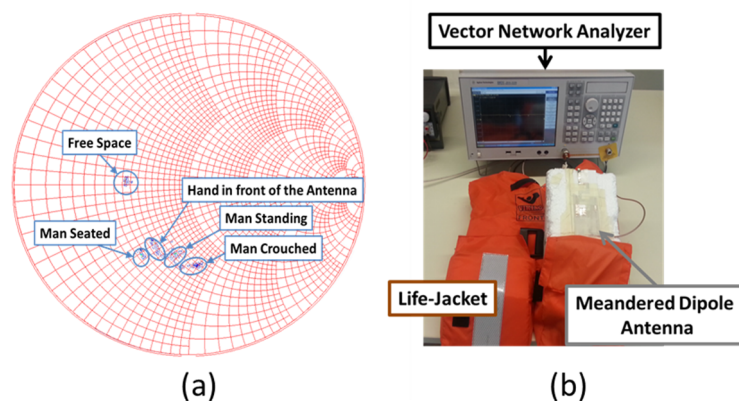


FIG. 2 – (a) Measured reflection coefficient on the Smith Chart for several positions of the antenna's wearer (the measured value for the free-standing antenna is also shown, as a reference).
 (b) Measurement setup. The reflection coefficient of the meandered dipole antenna integrated on a life-jacket has been measured through a vector network analyzer.

As a first approximation, it could be stated that the human body acts as a series capacitor for the selected antenna (see Fig. 2). Therefore the impedance matching network should operate as a simple series inductance for compensating the effect of the body. However this situation would not represent the best solution because the inductance should have a variable behavior with respect to the time and it could be difficult to achieve an electronically controlled variable inductance. In order to guarantee a better tuning of the antenna an appropriate double-L impedance matching network has been identified, with every of the two stages that included a variable capacitor. These two variable capacitors could provide the two degrees of freedom necessary for perfectly tuning the reflection coefficient of the antenna in terms of magnitude and phase.

Another key point is represented by the algorithm that has to control the reconfigurable impedance network. The microcontroller should execute the minimum amount of mathematical operations in order to minimize circuit response delay time. The requirement of "fast adaptation" must be compatible with the typical speed of human body movements.

III. PRELIMINARY RESULTS

The antenna in [6] has been worn by a volunteer; the reflection coefficient data have been collected for 3 minutes while the person was performing random movements.

In order to evaluate the improvement in terms of S_{11} the behavior of the auto-tuning network (impedance matching network and auto-tuning algorithm) has been simulated through numerical simulations. In particular the impedance matching network has been simulated as a

double L-network, with every stage made up of a series inductor and a shunt variable capacitor. It has been assumed that the capacitors were able to modify their capacity with a step of 1pF. The implemented algorithm is an iterative algorithm that continuously changes the values of the two capacitors while searching the best "adaptation point" for each samples of the reflection coefficient received in input.

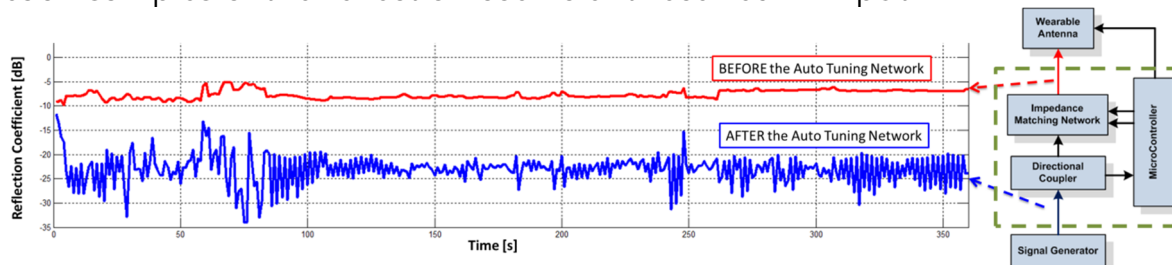


FIG. 3 – Reflection coefficient (in dB) as a function of time (sec).

The results are shown in Fig. 3. It is possible to see how the use of an auto-tuning circuit can improve the value of the S_{11} . Indeed the reflection coefficient passes from a mean value of -7.6dB (before the auto-tuning network) to a mean value of -23 dB (after the auto tuning network), with a measured mean improvement in S_{11} of 15.4dB.

IV. CONCLUSIONS

In this paper the feasibility of closed-loop reconfigurable wearable UHF-band antenna has been shown. In this framework, the algorithm and the impedance matching network have been verified through numerical simulations using the reflection coefficient data collected when a meandered folded dipole antenna was worn by a volunteer.

Work is in progress to implement a circuit prototype so that a system demonstrator can be tested in a realistic scenario.

REFERENCES

- [1] R. L. Haupt and M. Lanagan "Reconfigurable Antennas" *IEEE Antennas and Propagation Magazine*, vol. 55(1), pp. 49-61, February 2013
- [2] K. Brito and R. Nunes de Lima "Tunable Impedance Matching Network" *2007 SBMO/IEEE MTT-S International Microwave & Optoelectronics Conference*
- [3] N. Haider, D. Caratelli, and A. G. Yarovoy "Recent Developments in Reconfigurable and Multiband Antenna Technology" *International Journal of Antennas and Propagation Volume 2013*
- [4] [Online]. Available: <http://www.cospas-sarsat.org>
- [5] P. Nepa, G. Manara, "On the stochastic characterization of wearable antennas," *PIERS 2013 (Progress in Electromagnetics Research Symposium)*, p. 1, Stockholm, Sweden, August 12-15, 2013.
- [6] Serra, A., P. Nepa, and G. Manara, "A wearable two-antenna system on a life jacket for Cospas-Sarsat Personal Locator Beacons," *IEEE Trans. Antennas and Propagation*, Vol. 60(2), pp. 1035-1042, February 2012.

MANUFACTURE AND TEST OF AN INNOVATIVE CONFIGURATION OF PRINTED UWB ANTENNA

S. Mazzocchi⁽¹⁾⁽²⁾, A. Galli⁽²⁾, D. Sassaroli⁽¹⁾, M. Zucca⁽³⁾

⁽¹⁾ Hardware Development Department, D.&P. Electronic Systems srl
Viale Balilla 9-11, 00044 Frascati (RM), Italy
s.mazzocchi@depelsys.it , d.sassaroli@depelsys.it

⁽²⁾ Information Engineering, Electronics and Telecommunications
Department, "Sapienza" University of Rome
Via Eudossiana 18, 00184 Rome, Italy
simona.mazzocchi@gmail.com , galli@diet.uniroma1.it

⁽³⁾ Chief Technology Office, Selex Electronic System
Via Tiburtina km 12,400, 00131 Rome, Italy
marco.zucca@selex-es.com

Abstract

Starting from an innovative low-cost and compact topology of planar radiating element, based on printed dipoles in rhombic configuration on stacked layers for dual-pol Ultra-Wide-Band (UWB) applications, this work describes the evolution of the antenna from the designed layout to prototyping and testing. The analysis is first focused on the optimization processes involving the construction parameters that affect the antenna matching impedance in the operative bandwidth (ranging from S to Ka band). Consequently, the experimental tests on a manufactured antenna prototype show the agreement between simulations and measurements, in terms of return/insertion losses and radiation patterns, thus confirming various attractive features of the proposed topology for multifunctional applications.

Index Terms – Ultra Wide Band (UWB), Printed antennas, Prototypal realization, Microwave measurements.

I. INTRODUCTION

Modern ultra-wide-band (UWB) systems for multifunctional radar, communications, and sensing applications need suitable radiating elements able to guarantee advanced performance in very extended bandwidths [1],[2].

A complete analysis, from the design and optimization processes to prototypal manufacturing and testing, is carried out here on a recently-proposed topology of UWB planar antenna, constituted by elements with printed strips in suitable rhombic configuration on a multilayer configuration for dual polarization [3]. The chosen structure (whose layout is sketched in Fig. 1) presents several attractive features, such as simplicity of geometry, low cost of materials and of realization process, flexibility in feeding, versatility of performance in terms of very wide band, polarization, and radiation patterns.

After recalling the basic properties of the proposed topology (Sec. II), optimization and compared tests from simulations and measurements are presented on the UWB radiative features of the antenna (Sec. III), and conclusive remarks and perspectives are outlined (Sec. IV).

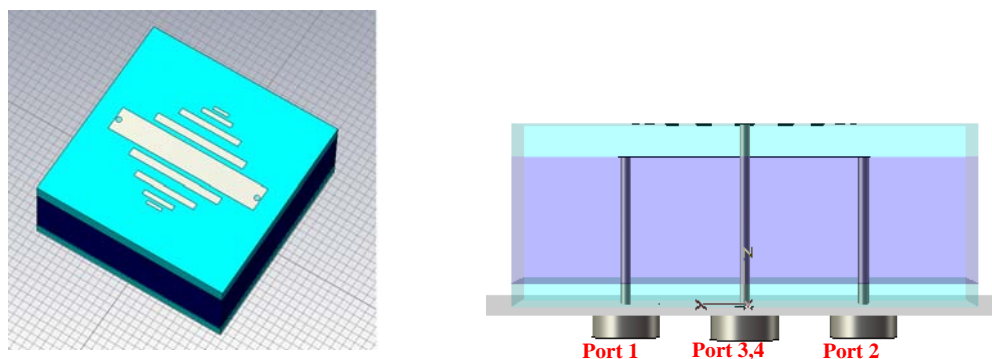


FIG. 1 - UWB radiating element designed, realized, and tested in this work: (a) top view; (b) lateral view of a multilayer configuration: metal strips placed orthogonally on two different interfaces ('inner' and 'top') for dual-pol applications, with proper pairs of coaxial-probe feeding.

II. THE UWB ANTENNA TOPOLOGY

The basic antenna element considered here is constituted by a planar dielectric stacked structure with a number of printed dipoles of different size suitably arranged in a rhombic shape [3], as sketched in Fig. 1(a) (top view).

The working principle exploits resonance effects of properly scaled printed dipoles, enabling for a multiple extension of the operational band. Further band enlargement derives from a multilayer arrangement of different dielectrics. In this topology, the central dipole is differentially fed on opposite sides through a pair of coaxial cables, the other close dipoles being dummy (just passively coupled). Another printed set of dipoles, rotated by 90° with respect to the first one, is placed and fed on a different dielectric interface of the multilayered structure. This double printed configuration allows for a circular polarization, with the excitement of both the central dipoles through a balanced feeding system. The dual-pol element is therefore particularly compact and easy to fabricate. The basic antenna structure considered in the following is specifically composed by a three-layer grounded dielectric stack. A detail of the multilayered configuration is shown in Fig. 1(b) (lateral view).

The topology of the antenna allows for action on a wide number of physical and geometrical parameters to reach the expected UWB behavior. This makes the design process particularly complex and delicate. Based on a CAD tool, CST Microwave Studio, some different structures have been identified in previous work [3], and further optimized and implemented in this context.

III. THE UWB ANTENNA IMPLEMENTATION AND MEASUREMENTS

Starting from simulations of a reference 'ideal' UWB antenna configuration (i.e., which has no specific constraints linked to the manufacturing process), our geometrical layout has properly been adjusted in order to accurately model most of the construction parameters that affect the performance of a 'real' antenna element (available height and electrical features of laminates, micro-coaxial cables and via-holes for insertion, lossy features of dielectrics and metalization, etc.). Thus, a modified 'realistic' antenna structure is delineated with respect to the ideal one. These construction parameters modify the performance from what expected from the first analysis and have been taken into account in an optimization process which brings to the final layout.

A comparison between the matching impedance of the ideal and of the realistic layout is first required to define the effective operative bandwidth of the prototype. As shown in Fig. 1(b), the antenna has four different ports, feeding the central dipoles on the two layers. The analysis of the following scattering parameters, as a function of frequency, is therefore significant (with a proper port numbering): $|S_{11}|$ and $|S_{33}|$, i.e., the return loss (RL), which defines the reflection at ports 1 and 3 for the lower and upper dipole set, respectively; $|S_{43}|$, i.e., the insertion loss (IL), which quantifies loss effects on the central (upper) dipoles; $|S_{13}|$, i.e., the mutual coupling (MC), which accounts for the interaction between upper- and lower-dipole configuration.

Compared results for the simulated scattering parameters of our ideal and realistic antenna layouts are presented in Fig. 2. In Fig. 2(a), the frequency behavior of RL is shown, which determines the operative bandwidth of the UWB antenna: in the ideal layout (blue line), the matching impedance (less than -10 dB threshold) is guaranteed from 2 GHz up to about 27 GHz, instead in the realistic layout (black line), some amount of increasing for RL is noted, particularly in the lower frequency range. In Fig. 2(b), concerning the behaviour of MC, a good isolation is found between the upper and lower dipoles (less than -10 dB for both ideal and realistic antennas). It is thus confirmed that the two dipole sets having orthogonal configurations could work almost independently and simultaneously, allowing us to obtain either linear or dual polarizations.

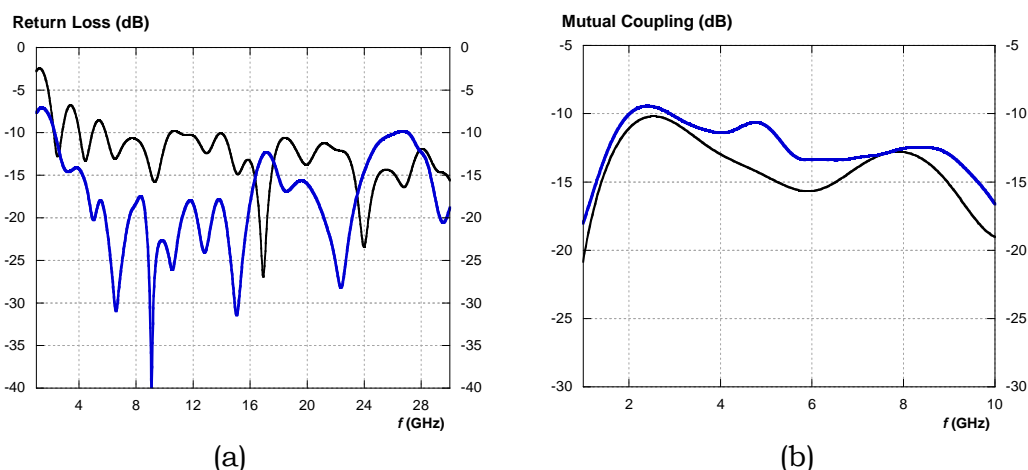


FIG. 2 – Frequency-selective features of the simulated ‘ideal’ (blue lines) and ‘realistic’ (black lines) UWB elements: (a) Return Loss $|S_{11}|$ (dB) vs. f ; (b) Mutual Coupling $|S_{13}|$ (dB) vs. f .

After properly considering the influence of the parameterization for our layout, a prototypal UWB antenna has been optimized, and then manufactured and tested. The measurements of impedance matching have provided a first evaluation on the effective operative bandwidth of the element. The direct comparison between simulations and measurements appears to be consistent in this case, because the measurement setup and the suitable boundary conditions considered in the simulations present close similarities.

In Fig. 3(a), the measurement setup for the matching features is shown, with the antenna prototype under test, a broadband free-space absorber around the element, the interconnection cables, terminations, and a network analyzer (Agilent Technologies). Full experimental tests on radiation patterns have also been performed by means of a StarLab equipment by Satimo.

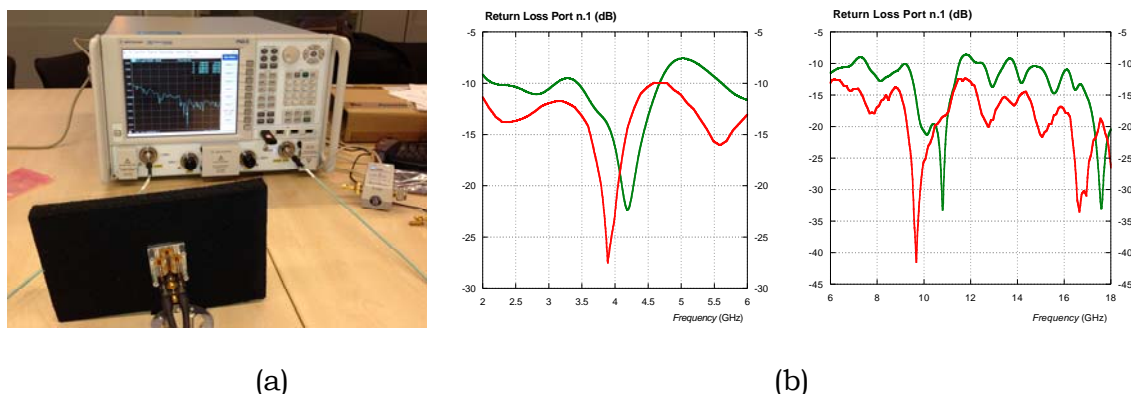


FIG. 3 – (a) Measurement set-up for the evaluation of S-parameters of the device under test, with the antenna bottom view; (b) Example of antenna Return Loss vs f : comparisons between measurements (red lines) and simulations (green lines) for the ‘inner’ (port 1) radiating structure, in 2-6 GHz (left) and in 6-18 GHz bands.

In the S-parameter evaluation, for each measurement only two ports are connected, the others having 50-Ohm terminations (up to 40 GHz). An example of compared results are given in Fig. 3(b), which shows both simulated and measured behaviors of the Return Loss vs. frequency (2-6 GHz, left, and 6-18 GHz, right) for the ‘inner’ radiating element (port 1 of Fig. 1), the behaviors of the ‘top’ element being quite similar.

As a general comment from the overall measurement tests, it is emphasized that a good agreement between theory and experiments is achieved. In the analysis of the behaviors of the scattering parameters, certain reductions of the magnitude and slight amounts of shift in frequency can be noted. These are mainly due to the fact that the measurement setup has some fixtures (cables, adapters, connectors, etc.), which affect the impedance matching but cannot be easily modeled in the simulation process. It is worth mentioning that the measured operative bandwidth for this prototypal antenna comes out even wider than the simulated one, ranging from about 2 GHz up to 38 GHz.

IV. CONCLUSION

A recently-proposed topology of microwave UWB dual-pol planar antenna, based on a suitable arrangement of printed dipoles in rhombic shapes, has shown interesting features thanks to its inexpensive and easy realization, compactness, and versatility of feeding. After realization and testing of a UWB prototype, the measured operative bandwidth has resulted even wider than what expected by simulations. Results on the radiation patterns and further extensions to scanning array configurations confirm the promising features.

REFERENCES

- [1] L. B. Allen, M. Dohle, E. Okon, W. Malik, A. Brown, and D. Edwards, Eds., *Ultra Wideband Antennas and Propagation for Communications, Radar and Imaging*. Wiley, 2006.
- [2] W. Wiesbeck, G. Adamiuk, and C. Sturm, “Principles of UWB antennas basic properties and design,” *Proc. IEEE*, vol. 97, no. 2, pp. 372-385, 2009.
- [3] G. Valerio, S. Mazzocchi, A. Galli, M. Ciattaglia, and M. Zucca, “New configurations of low-cost dual-polarized printed antennas for UWB arrays,” *Int. J. Antennas Propag.*, ID 786791, 10 pp., 2012.

NEAR-FIELD MODULAR ANTENNA FOR UHF RFID DESKTOP READER APPLICATIONS

R. Caso, A. Michel, A. Buffi

Department of Information Engineering, University of Pisa, Italy

Via Caruso 16, 56122 Pisa, Italy

r.caso, a.michel, a.buffi@iet.unipi.it

Abstract

A scalable modular antenna configuration consisting of a spiral Travelling Wave Antenna (TWA) which series-feeds an embedded resonating ring slot antenna is proposed in this paper for NF UHF RFID desktop reader applications. The spiral TWA geometry allows for exciting an almost homogeneous field on the antenna surface, making the tag detection on the reader antenna (near-field reactive region) almost independent on tag location and orientation. The circular polarized ring slot antenna, which is embedded in the TWA, is used to extend the read range up to the radiative near-field region.

Index Terms – UHF RFID, near field, desktop reader, modular antenna.

I. INTRODUCTION

The antenna near-field (NF) features have been applied to specific short-range radio systems (Near Field Communications [1], microwave wireless power transfer [2], Radio Frequency Identification (RFID) systems [3]-[4]). In such framework, NF UHF RFID systems have been developed to exploit the electromagnetic coupling that occurs in the near-field region with the advantages of the high reading and data rates that are typical of the UHF systems. Thus, it is important to maximize the field in a limited volume close to the reader antenna surface and to minimize the field radiated in the far-field region to prevent false-positive readings. Moreover, an as homogeneous as possible field distribution is required to avoid failed detections when the tag is arbitrarily located on the antenna surface. Depending on the specific application, different antenna technologies can be employed, as for example, near-field focused arrays [5], segmented loop antennas [6] or travelling wave antennas [7]-[10]. In the framework of UHF RFID desktop reader applications, it is worth noting that the tags readability is affected by both the item material the tag is attached to and the mutual coupling among tags in a stacked configuration. To face with above-mentioned issues, the authors proposed a modular antenna scheme [11] consisting of a Travelling Wave Antenna (TWA) which series-feeds an embedded resonating antenna. Thanks to such a modular configuration, the confined and uniform field distribution generated by the TWA is extended up to a few decimeters from the antenna surface by exploiting the radiation of a low-gain resonating antenna. In this paper, a specific modular antenna design is proposed,

by employing a spiral-shaped TWA that series-feeds a circular ring slot antenna.

II. ANTENNA LAYOUT AND NUMERICAL RESULTS

The geometry of the proposed NF modular antenna for UHF RFID desktop readers is shown in Fig. 1. The antenna is printed on a grounded 1.6mm-thick FR4 ($\epsilon_r=4.4$, $\text{tg}\delta=0.025$) dielectric substrate. A 50-ohm coaxial cable feeds a spiral shape TWA at the surface center, which in turn feeds a W-wide circular ring slot antenna etched in the antenna ground plane.

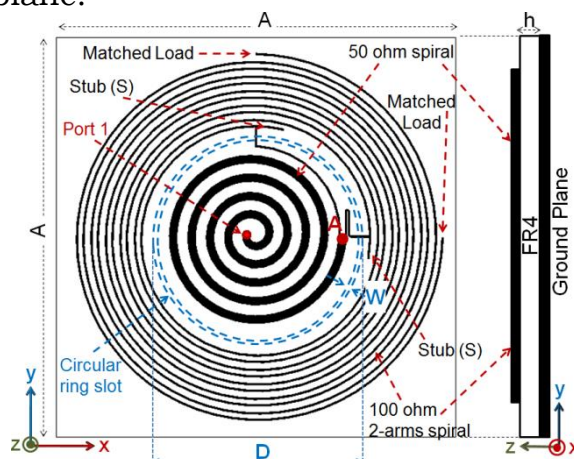


FIG. 1 – Top and lateral view of the proposed near-field modular antenna for UHF RFID desktop reader applications. The main geometrical parameters are: $A=150\text{mm}$, $D=40\text{mm}$, $h=1.53\text{mm}$, $S=24\text{mm}$, $W=1.4\text{mm}$.

The TWA radiation features [7]-[10] allows to obtain strong and uniform fields within a confined volume above the antenna surface (NF reactive region) for the whole area covered by the spiral. Moreover, this spiral geometry makes the tag detection almost independent on tag location and orientation, when tag lies on the antenna surface up to a distance of a few centimeters.

As already said, the spiral shape TWA feeds in turn the slot antenna. Thus, since the input power is partially lost in the substrate and radiated by the spiral transmission line, the circular ring slot antenna results fed by a reduced power level, so guaranteeing a low radiation into the far-field region. In details, the 50-ohm spiral-TWA is divided into two 100-ohm microstrip lines (point A in Fig. 1), that excite the circular slot through two signals with equal amplitude and a 90° phase shift. Such a configuration ensures the generation of a circularly polarization. Two S-length stubs are also foreseen beyond the circular ring slot to improve the input impedance matching. After that, the two 100-ohm microstrip lines extend until covering the whole antenna surface with a spiral shape surrounding the circular slot. Thus, an almost homogeneous field in the region close to the antenna border is also guaranteed. Moreover they end on a matched load, avoiding the generation of reflected waves. Such line extension can be of arbitrary

length, thus a scalable antenna solution is obtained; as an example, the overall antenna sizes of the proposed antenna are 150mm x 150mm. The antenna has been designed by using the CST Microwave Studio software. Due to the presence of the TWA, the frequency range where the reflection coefficient is below -14dB is much larger than the UHF RFID European band (865-868 MHz), making the antenna more robust to the presence of tagged item materials. In order to demonstrate the benefit of the proposed modular configuration, the spiral TWA with the embedded circular slot has been compared with a spiral-shaped microstrip line with the same layout (without the circular slot). In Fig. 2 and Fig. 3 the simulated magnetic field distributions of both antenna configurations at the frequency of 865 MHz are shown, considering an XY-plane just above the antenna surface and a transversal XZ-plane, respectively. The field distributions are normalized to the maximum magnetic field value associated to one of the two antennas (for each of the two considered cutting planes). In both configurations, the magnetic field distribution generated above the antenna surface is almost uniform, as required by NF UHF RFID applications.

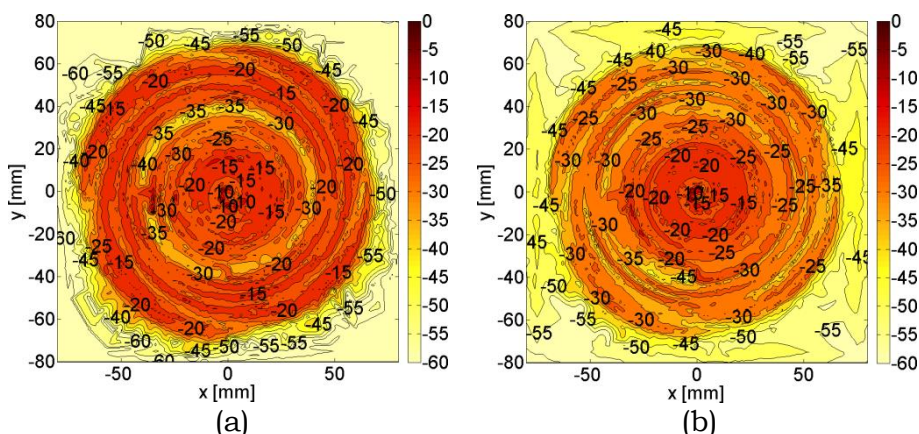


FIG. 2 – Normalized magnetic field (dB) distribution above the antenna surface (XY-plane) of (a) a spiral shaped microstrip line and (b) the proposed modular antenna (spiral shaped TWA with embedded circular slot).

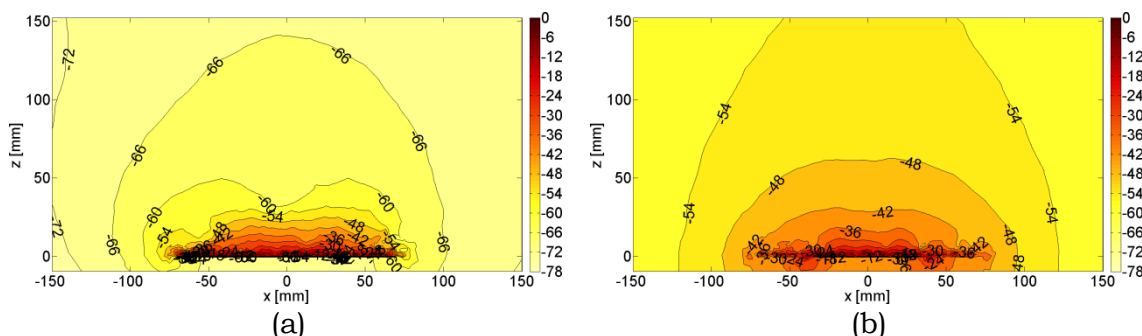


FIG. 3 – Normalized magnetic field (dB) distribution on a transverse plane (XZ-plane) of (a) a spiral shaped microstrip line and (b) the proposed modular antenna (spiral shaped TWA with embedded circular slot).

On the antenna surface, the spiral-shaped microstrip line is able to generate a magnetic field stronger than that one produced by the

modular antenna (Fig. 2), since in the latter the input power is partially radiated in the radiative NF region by the embedded slot antenna. However, thanks to the presence of the slot itself, the magnetic field generated at a longer distance by the modular antenna results significantly stronger than the field produced by the spiral-shaped microstrip line (Fig. 3) and this suggests the possibility to get an extended read range up to the radiative near-field region. Antenna prototyping is under progress and measurement results will be shown at the conference.

III. CONCLUSION

In this paper a modular antenna configuration, composed by a spiral shape TWA with an embedded resonating circular ring slot, has been presented for NF UHF RFID desktop reader applications. The two series connected antennas allow for an optimization of both the reactive and radiative near-field regions. Thanks to the presence of the TWA, the configuration can be easily scalable to fit into commercial desktop readers case of almost arbitrary sizes.

REFERENCES

- [1] R. Want, "Near field communication", *IEEE Pervasive Computing*, vol. 10, no. 3, pp. 4-7, 2011.
- [2] G. Franceschetti, G. Oliveri, P. Rocca, A. Massa, "Advances on remote wireless power transmission at the ELEDIA research center", *2013 IEEE Wireless Power Transfer (WPT)*, pp. 191-194, May 2013.
- [3] F. Fuschini, C. Piersanti, L. Sydanheimo, L. Ukkonen, G. Falciasecca, "Electromagnetic Analyses of Near Field UHF RFID Systems", *IEEE Trans. Antennas Propagation*, vol. 58, no. 5, pp. 1759-1770, May 2010.
- [4] A. Buffi, A. Michel, R. Caso, P. Nepa, "Near-field coupling in UHF-RFID systems", *URSI Int. Symp. on EM Theory (EMTS)*, pp. 408-411, May 2013.
- [5] A. Buffi, A. Serra, P. Nepa, H.-T. Chou, G. Manara, "A Focused Planar Microstrip Array for 2.4 GHz RFID Readers", *IEEE Trans. Antennas Propagation*, vol. 58, no. 5, pp. 1536-1544, May 2010.
- [6] X. Qing, C. K. Goh, Z. N. Chen, "Segmented loop antenna for UHF near-field RFID applications", *Electronics Letters*, vol. 45, no. 17, August 2009.
- [7] A. Michel, R. Caso, A. Buffi, P. Nepa, G. Isola, H.-T. Chou, "Design and Performance Analysis of a Planar Antenna for Near-Field UHF RFID Desktop Readers", *Asia-Pacific Microwave Conference (APMC)*, 2012.
- [8] A. Michel, R. Caso, A. Buffi, P. Nepa, G. Isola, "Meandered TWAS array for near-field UHF RFID applications", *Electronics Letters*, vol. 50, no. 1, pp.17-18, January 2014.
- [9] A. C. R. Medeiros, J. R. Costa, C. A. Fernandes, "RFID Reader Antennas for tag detection in self-confined volumes at UHF", *IEEE Antennas and Propagation Magazine*, vol. 53, no. 2, April 2011.
- [10] A. Ren, C. Wu, Y. Gao, Y. Yuan, "A Robust UHF Near-field RFID Reader Antenna", *IEEE Trans. Antennas Propagation*, vol. 60, no. 4, April 2012.
- [11] A. Michel, R. Caso, A. Buffi, P. Nepa, G. Isola, "Modular antenna for reactive and radiative near-field regions of UHF-RFID desktop readers", *URSI-GASS*, Beijing, China, August 2014.

ANALYSIS OF LOSSY WAVEGUIDE COMPONENTS BY THE BI-RME METHOD COMBINED WITH A PERTURBATION TECHNIQUE

A. Giannini, M. Bozzi, M. Bressan, M. Pasian, L. Perregrini

University of Pavia, Dept. of Electrical, Computer & Biomedical
Engineering
Via Adolfo Ferrata, 5, 27100 Pavia, Italy
luca.perregrini@unipv.it

Abstract

This paper presents a technique based on the combination of the Boundary Integral-Resonant Mode Expansion (BI-RME) method and of a perturbation approach for the modeling of waveguide components comprising lossy dielectric materials. The BI-RME method yields the frequency response in terms of a pole-expansion of the generalized admittance matrix. The perturbation technique is used to calculate the modified poles and residues of the admittance matrix due to the presence of losses. By adopting the segmentation technique, the proposed technique can be applied to waveguide components filled with a piece-wise homogeneous dielectric medium. The accuracy and robustness of the proposed method is validated through an example.

Index Terms – BI-RME method, lossy dielectric medium, perturbation technique, waveguide component.

I. INTRODUCTION

In the recent years, there is a growing interest in the modeling and design of waveguide components for a number of industrial power applications, including heating of dielectric materials, acceleration of chemical reactions, and melting purposes [1]. Many different numerical techniques has been proposed for the analysis of waveguide component and circuits including lossy media. Among them, the most flexible techniques are based on general purpose numerical methods, such as the Finite-Element Method (FEM) [2] and Finite Difference-Time Domain (FDTD) method [3]. Although these methods can easily handle with inhomogeneous and lossy materials, the use of more specialized techniques applied to particular classes of components may lead to more efficient and accurate simulation tools. Integral equation methods [4] usually lead to efficient electromagnetic solvers, but in most cases they are subject to severe limitations (e.g., particular geometries, homogeneous dielectric medium).

A particular implementation of the integral equation technique has been proposed under the name of the Boundary Integral-Resonant Mode Expansion (BI-RME) method, which applies to arbitrary waveguide components and yields their wideband frequency response in one single full-wave analysis, thus avoiding repeated frequency-by-frequency calculations [5]. This method has been applied to different classes of homogeneously-filled and lossless waveguide components, namely H-plane [6,7], E-plane [8,9], and fully three dimensional waveguide components [10].

This paper presents the extension of the BI-RME method to the modeling of waveguide components partially or totally filled with a lossy dielectric medium, by combining the BI-RME method with a perturbation approach. Moreover, the robustness of the method in the modeling of waveguide components filled with medium to highly lossy dielectric materials is assessed.

II. THEORETICAL FORMULATION

The BI-RME method is based on an original rapidly-convergent pole-expansion of the generalized admittance matrix (GAM) in the frequency domain and on the fast calculation of the resonant modes of the cavity obtained by short-circuiting the input ports [5]. The wideband expression of the GAM of an arbitrary waveguide component filled with a homogeneous and lossless dielectric medium with dielectric permittivity $\varepsilon = \varepsilon_0 \varepsilon_r$ and magnetic permeability $\mu = \mu_0$, is given by [5]

$$Y_{ij}(k_0) = \frac{A_{ij}}{j\eta_0 k_0} + \frac{jk_0 \varepsilon_r}{\eta_0} B_{ij} + \frac{jk_0^3 \varepsilon_r^2}{\eta_0} \sum_{p=1}^P \frac{C_{pi} C_{pi}}{k_p^2 (k_p^2 - k_0^2 \varepsilon_r)} \quad (1)$$

where Y_{ij} is the ij -element of the GAM, relating modal currents and voltages of the waveguide modes at the ports of the component, $k_0 = \omega/c$ is the wave-number in vacuum at the operation frequency, ω is the angular frequency, c is the speed of light, $\eta_0 = (\mu_0/\varepsilon_0)^{1/2}$. The frequency independent terms A_{ij} and B_{ij} represent the low-frequency behavior of the GAM, k_1, k_2, \dots, k_P are the wavenumbers of the first resonant modes of the cavity obtained by short-circuiting the ports, and C_{pi} is related to the coupling between the fields of the p -th cavity resonant mode and of the i -th port mode. The accuracy of (1) increases with P and it can be considered reasonably acceptable if the maximum resonant wavenumber k_P is two or three times larger than the wavenumber at the maximum operating frequency.

In order to account for losses in the dielectric medium, (1) is modified by means of a perturbation approach. The permittivity of the lossy dielectric material is defined as $\varepsilon = \varepsilon_0 \varepsilon_r + \sigma_d/j\omega$, where σ_d is the conductivity of the dielectric material. By introducing the quality factor $Q_p = \omega_p \varepsilon_0 \varepsilon_r / \sigma_d$, after some manipulations, the expression of the GAM results

$$Y_{ij}(k_0) = \frac{A_{ij}}{j\eta_0 k_0} + \sigma_d B_{ij} + \frac{jk_0 \varepsilon_r}{\eta_0} B_{ij} + \frac{k_0^2 \varepsilon_r^{3/2}}{\eta_0} \sum_{p=1}^P \frac{C_{pi} C_{pi}}{k_p (Q_p k_p^2 + jk_0 k_p \varepsilon_r^{1/2} - Q_p k_0^2 \varepsilon_r)} + \frac{jk_0^3 \varepsilon_r^2}{\eta_0} \sum_{p=1}^P \frac{C_{pi} C_{pi}}{k_p^2 (k_p^2 + jk_0 k_p \varepsilon_r^{1/2} / Q_p - k_0^2 \varepsilon_r)} \quad (2)$$

It is interesting to observe that expression (2) of the GAM preserves all advantages of (1), namely the matrices appearing in the expression are frequency independent and a single full-wave calculation allows for the wideband modeling of the waveguide component.

The application of the proposed method to arbitrary components filled with a lossy piece-wise homogeneous dielectric medium is based on the segmentation techniques: the inhomogeneous waveguide component (Fig. 1a) is divided into two homogeneous sub-circuits, one filled with air (Fig. 1b) and the other filled with dielectric (Fig. 1c). Each sub-circuit is analyzed separately, and characterized by its GAM, which are then combined to calculate the GAM of the overall component. In particular, when calculating the GAM of the air-filled sub-circuit, additional "connected ports" are defined at the boundary between air and dielectric, besides the external ports (corresponding to the modes of the terminal waveguides). Similarly, when considering the GAM of the dielectric-filled sub-circuit, the same connected ports are considered.

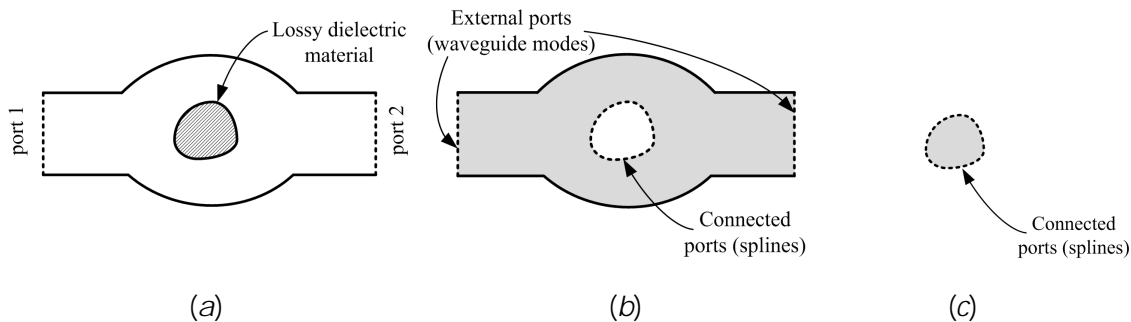


FIG. 1 – Segmentation of a waveguide component filled with a piece-wise homogeneous dielectric medium: (a) geometry of the whole component; (b) air-filled sub-circuit; (c) dielectric-filled sub-circuit.

III. VALIDATION EXAMPLE

As a validation example we consider a hollow rectangular waveguide comprising a centered dielectric cylinder, with dielectric permittivity $\epsilon_r=4$ and conductivity $\sigma_d=0.1$ S/m, corresponding to a loss tangent $\tan\delta=0.045$ at 10 GHz (Fig. 2a). The analysis by the BI-RME method has been performed by segmenting the structure in two sub-circuits, namely the air-filled rectangular waveguide with a cylindrical hole and the dielectric cylinder. The convergence of the method has been achieved considering four rectangular waveguide modes on each waveguide port, and sixteen connected ports (splines) on the boundary of the cylinder. In addition, $P=17$ unperturbed cavity modes have been adopted in the air-filled sub-circuit, and $P=10$ unperturbed cavity modes in the dielectric-filled sub-circuit. Fig. 2b shows the frequency response of the circuit: the result of the BI-RME method is compared with data from the commercial software HFSS.

Finally, to test the robustness of the method, the portion of power dissipated by dielectric loss versus conductivity has been calculated, at the frequency of 10 GHz (Fig. 2c). It appears from Fig. 2c that the BI-RME method provides accurate values of dissipated power even when dielectric losses are particularly high (up to a conductivity $\sigma_d=1$ S/m, corresponding to $\tan\delta=0.5$).

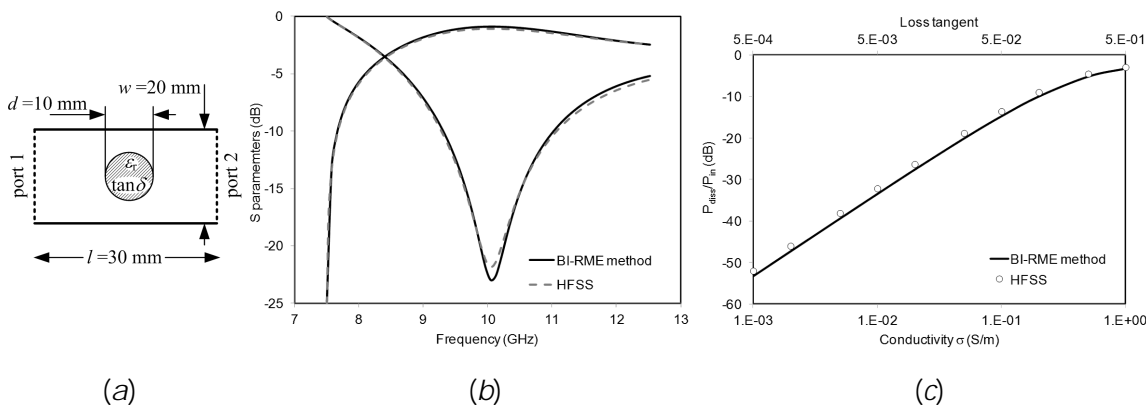


FIG. 2 – Rectangular waveguide embedding a high-loss dielectric cylinder: (a) geometry of the component (top view); (b) frequency response of the component; (c) portion of power dissipated by dielectric loss (in dB) versus conductivity (and loss tangent).

IV. CONCLUSION

This paper presented the combination of the BI-RME method with a perturbation approach for the analysis of arbitrary waveguide components filled with high loss dielectric material. The accuracy and robustness of the method have been shown through an example, involving dielectric materials with medium to high losses.

This simulation tool is particularly useful for applications in the field of industrial applications (including applicators for microwave heating) and devices for the electrical characterization of dielectric materials.

REFERENCES

- [1] A.C. Metaxas and R.J. Meredith, *Industrial Microwave Heating*, Peter Peregrinus Ltd., London, UK, 1993.
- [2] J. Jin, *The finite element method in electromagnetics*, J.Wiley & Sons, 1993.
- [3] A. Taflov and S.C. Hagness, *Computational Electrodynamics: The Finite-Difference Time-Domain Method*, 3rd Ed., Artech House, 2005.
- [4] J.L. Volakis and K. Sertel, *Integral Equation Methods for Electromagnetics*, SciTech Publishing, Inc., 2012.
- [5] G. Conciauro, M. Guglielmi, and R. Sorrentino, *Advanced Modal Analysis*, Wiley, New York, 2000.
- [6] P. Arcioni, M. Bressan, G. Conciauro, L. Perregrini, "Wideband Modeling of Arbitrarily Shaped E-Plane Waveguide Junctions by the 'Boundary Integral-Resonant Mode Expansion' Method," *IEEE Trans. on Microwave Theory and Techniques*, vol. 44, n. 11, p. 2083-2092, Nov. 1996.
- [7] P. Arcioni, M. Bressan, G. Conciauro, "Generalized admittance matrix of arbitrary E-plane waveguide junctions by the BI-RME method," *IEEE MTT-S Int. Microwave Symp.*, 1999.
- [8] G. Conciauro, P. Arcioni, M. Bressan, and L. Perregrini, "Wideband Modeling of Arbitrarily Shaped H-Plane Waveguide Components by the 'Boundary Integral-Resonant Mode Expansion' Method," *IEEE Trans. on Microwave Theory and Techniques*, Vol. 44, No. 7, pp. 1057-1066, July 1996.
- [9] P. Arcioni, M. Bressan, G. Conciauro, and L. Perregrini, "Generalized Y-Matrix of Arbitrary H-Plane Waveguide Junctions by the BI-RME Method," *IEEE MTT-S Int. Microwave Symp.*, 1997.
- [10] P. Arcioni, M. Bozzi, M. Bressan, and L. Perregrini, "A Novel CAD Tool for the Wideband Modeling of 3D Waveguide Components," *International Journal of RF and Microwave Computer-Aided Engineering*, Vol. 10, No. 3, pp. 183-189, May 2000.
- [11] K. Kurokawa, *An Introduction to the Theory of Microwave Circuits*, Academic Press, 1969.

WEARABLE TEXTILE MICROWAVE COMPONENTS IN SUBSTRATE INTEGRATED WAVEGUIDE TECHNOLOGY

R. Moro⁽¹⁾, S. Agneessens⁽²⁾, Hendrik Rogier⁽²⁾, M. Bozzi⁽¹⁾

- (1) Department of Electrical, Computer and Biomedical Engineering,
University of Pavia, Pavia, Italy
riccardo.moro@unipv.it, maurizio.bozzi@unipv.it
- (2) Department of Information Technology-IMEC, University of Ghent,
Ghent, Belgium
sam.agneessens@intec.ugent.be, hendrik.rogier@ugent.be

Abstract

This paper describes the design, manufacturing, and testing of a new class of textile microwave components for wearable applications, implemented in substrate integrated waveguide (SIW) technology. Two different configurations of textile SIW interconnects are compared, showing that the folded wearable SIW structure is considerably smaller than its standard counterpart and provides comparable performance. A folded textile SIW filter operating at 2.45 GHz is designed and tested. The filter combines excellent performance in the pass-band and good out-of-band rejection. Finally, a folded SIW cavity-backed patch antenna at 2.45 GHz is fabricated and experimentally verified.

Index Terms – Cavity-backed antenna, folded waveguide, substrate integrated waveguide, textile material, wearable systems.

I. INTRODUCTION

The development of a new class of applications exploiting the potential of intelligent clothing and smart textiles is attracting more and more interest [1]. Specifically, the design of wireless communication systems for wearable applications is an attractive field of research. A textile integrated system, in fact, exploits its potential to conform with the body shape, without disturbing the movements of the user, and result in more comfortable on-body solutions. This new class of wearable electronic systems addresses specific requirements related to several innovative fields, such as healthcare, military applications, and public safety. For these applications, different antenna typologies fabricated on textile materials have been proposed, in order to achieve not only good electromagnetic performance, but also robust and comfortable systems [2]. In particular it was demonstrated that SIW textile antennas are suitable for body-worn systems [3]. SIW technology enables the integration of different components into a single substrate, including passive and active devices, antennas, etc., with a low-cost fabrication process. Therefore, by adopting SIW technology, a loss reduction is achieved, thus increasing the efficiency of the system [4]. Furthermore, the physical dimensions of the complete system can be minimized thanks to the potential of this technology to easily realize multilayer structures.

In this paper, the implementation of a novel class of textile passive components (such as interconnects and filters) and antennas, realized in substrate integrated waveguide technology, is presented.

II. SIW TEXTILE INTERCONNECTS

In this work, a closed cell expanded rubber, usually adopted as a protective foam against impact in fire-fighters suits, was chosen as a substrate for the fabrication of the SIW components. For the conductive layers, instead of copper sheets, a commercially available electro-textile (name Taffeta), which exhibits a surface resistivity $R_s=0.18 \Omega/\text{sq}$ at 2.45 GHz, was selected. The 3.94 mm-thick textile substrate is not produced for microwave applications and, therefore, an accurate characterization of the material over the frequency band of interest (2.45 GHz ISM band) is mandatory. For this reason, two different methods were adopted to evaluate the electrical parameters of the foam: a broadband technique based on two microstrip lines with different length [5] and a dedicated material characterization technique, which consists of analyzing the resonance frequencies and the quality factors of the modes of a square SIW cavity. From these analyses it results that the dielectric permittivity and loss tangent of the foam are $\epsilon_r=1.45$ and $\tan \delta=0.017$. After evaluating the electrical characteristics of the substrate, a standard SIW structure and a folded SIW (SIFW) interconnect on textile were designed. The layouts and the simulated and measured scattering parameters of the two typologies of SIW interconnects are shown in Fig. 1. In both cases, $|S_{11}|$ and $|S_{21}|$ exhibit a good agreement between simulated and measured data. Thanks to the multilayer structure, the SIFW presents a size reduction of 47.8% with respect to the standard SIW interconnect.

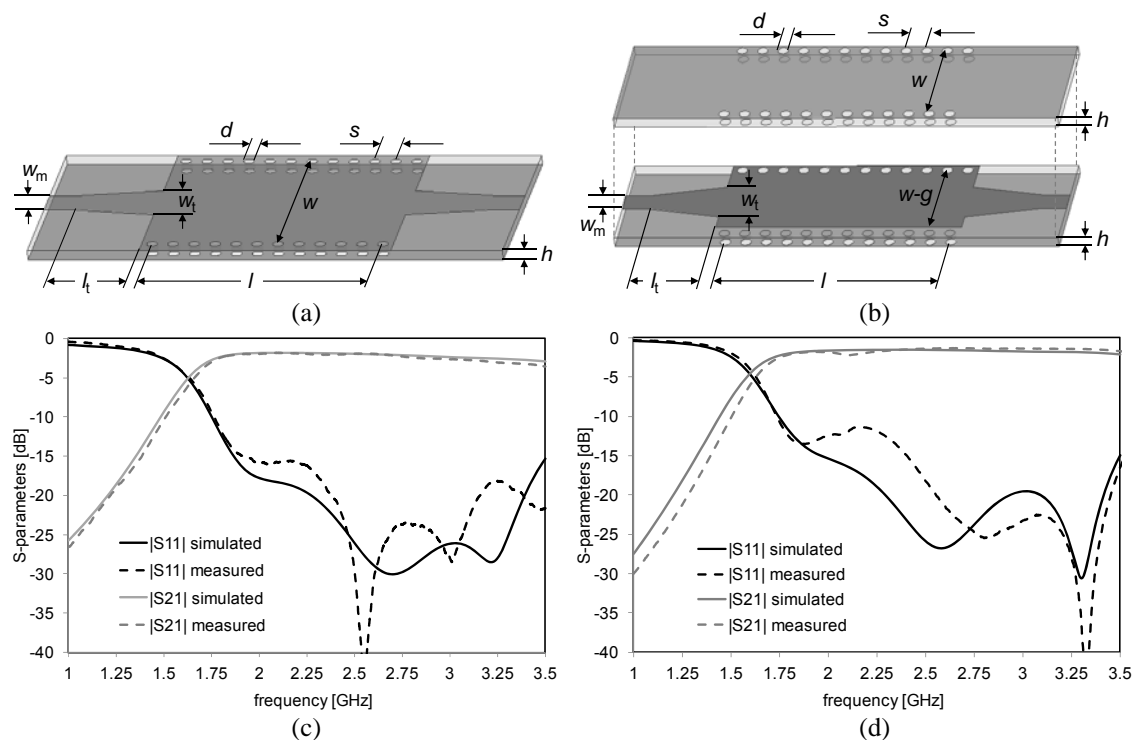


FIG. 1 – Textile SIW interconnects: (a) standard SIW structure (dimensions in mm: $l_t=32.7$, $w_t=23$, $w_m=13$, $h=3.94$, $s=8$, $d=4$, $w=79$, $l=96$); (b) SIFW structure (dimensions in mm: $l_t=28.7$, $w_t=19.6$, $w_m=8.5$, $h=3.94$, $s=8$, $d=4$, $g=4$, $w=41.2$, $l=96$); (c) simulated and measured scattering parameters of the standard SIW interconnect; (d) simulated and measured scattering parameters of the SIFW interconnect.

III. FOLDED SIW TEXTILE FILTERS AND ANTENNAS

A two-pole SIFW band-pass filter, based on the topology presented in [6], was designed to operate in the frequency band centered at 2.45 GHz. The structure is similar to the SIFW proposed in Sec. II, with three slots cut out in the central conductive sheet; two metalized posts at the two ends of the filter were added as shown in Fig. 2a. The filter was fabricated by using two textile layers with thickness of 3.94 mm and a central conductive sheet glued in between. It was experimentally verified and the measured results are in good agreement with simulation data (Fig. 2b).

The 3 dB bandwidth of the filter is 725 MHz and the insertion loss is 2.3 dB at 2.45 GHz. The frequency response in terms of $|S_{11}|$ exhibits two poles in the pass-band; three transmission zeros above the transmission band permit to obtain a very good filter selectivity and to improve the out-of-band rejection. Moreover, with this configuration, the length of the filter is significantly reduced with respect to standard in-line filter topologies.

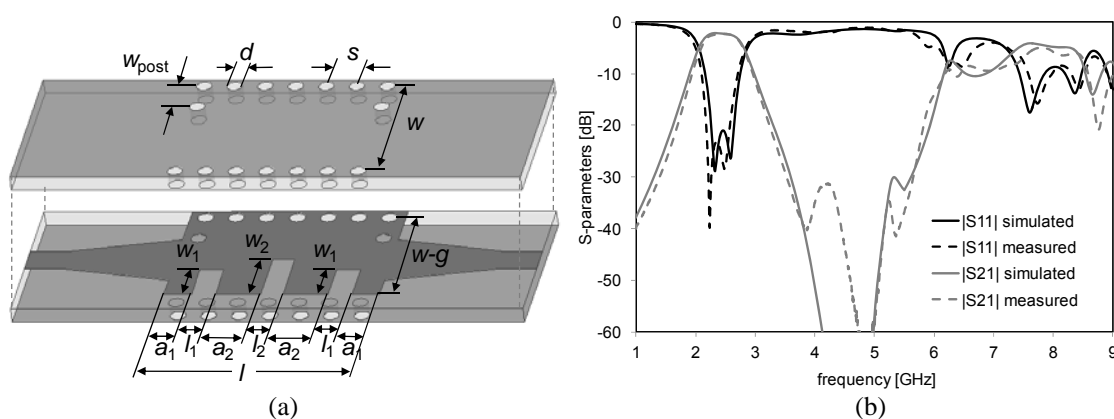


FIG. 2 – Textile SIFW filter: (a) structure (dimensions in mm: $w=41.2$, $g=4$, $d=4$, $s=8$, $l=56.3$, $w_{post}=9.9$, $l_1=6.3$, $l_2=5.9$, $w_1=12$, $w_2=17$, $a_1=7.2$, $a_2=11.7$), (b) simulated and measured scattering parameters.

Besides passive components such as interconnects and filters, a folded SIW cavity-backed patch antenna was designed and implemented on textile. The proposed antenna topology consists of a folded SIW cavity with a square ring aperture cut out in the top metal layer, thus forming a radiating patch with side L_2 (Fig. 3a). In order to obtain the folded SIW cavity, two textile layers with the same thickness of 3.94 mm were stacked and an inner metal patch with side L_1 was glued in between. A metal via, implemented by a rivet, was placed in the centre of the cavity to connect the bottom ground plane and the lower metal patch. All the dimensions of the antenna were optimized to both minimize the size of the antenna and maximize its radiation efficiency. The antenna is fed from the back side by a coaxial probe. A prototype of the antenna was fabricated and a picture is shown in Fig.3b. The antenna was measured in stand-alone condition to evaluate its electromagnetic performance (Fig.3c,d). The return loss is larger than 10 dB over a frequency band of 130 MHz around 2.45 GHz, with a maximum input matching at the frequency of 2.43 GHz. The antenna exhibits an overall efficiency of 74%, with a maximum gain of 5.93 dBi at boresight direction. The front-to-back ratio of the antenna is approximately 18 dB.

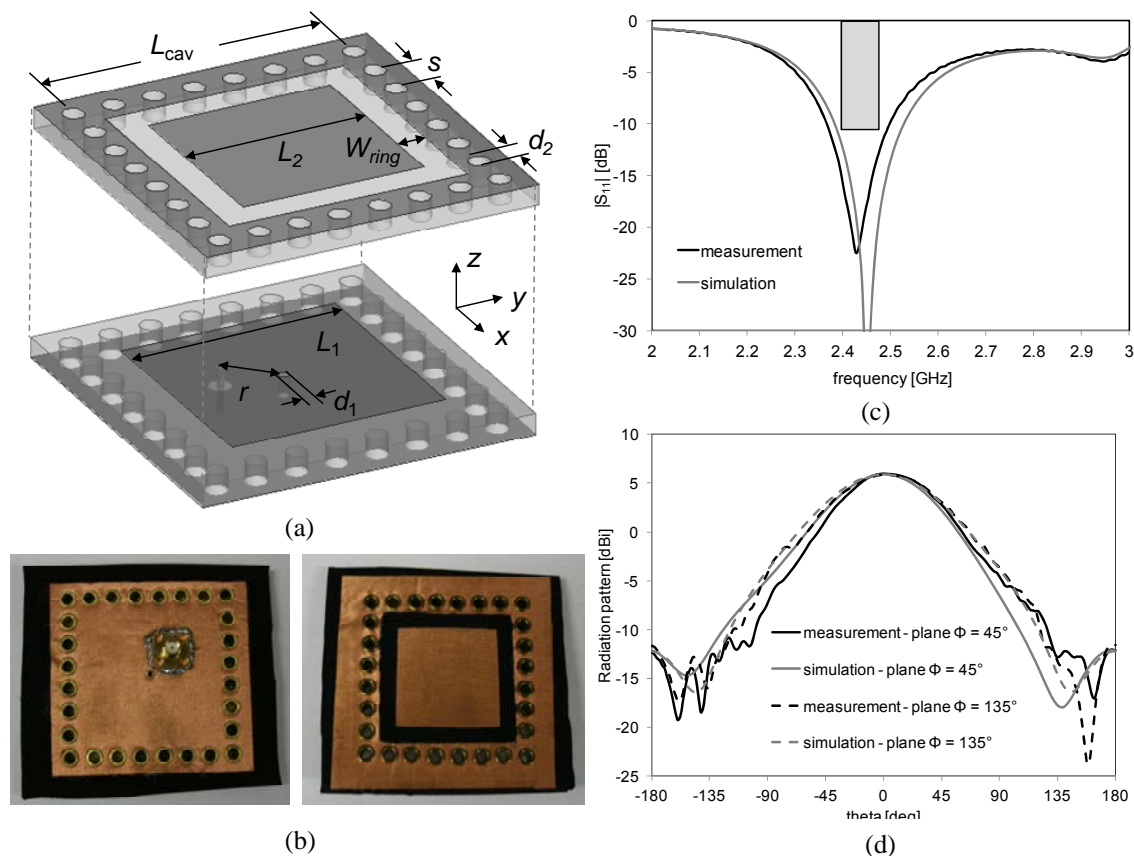


FIG. 3 – Folded SIW cavity-backed patch antenna: (a) structure (dimensions in mm: $L_{cav}=54.1$, $L_2=35$, $W_{ring}=5.5$, $L_1=41.2$, $d_1=2$, $d_2=4$, $s=8$, $r=11.3$); (b) photographs of the feed and radiating sides; (c) simulated and measured input matching; (d) simulated and measured radiation patterns.

IV. CONCLUSION

The design of several SIW components and antennas realized entirely in textile materials, including interconnects, a band-pass filter, and a cavity-backed antenna, has been presented. The prototypes are light, flexible, and very compact, and exhibit good electromagnetic performance. These properties make the components suitable for a complete system integration in smart textiles.

REFERENCES

- [1] J. Lilja *et al.*, "Body-Worn Antennas Making a Splash: Lifejacket-Integrated Antennas for Global Search and Rescue Satellite System," *IEEE Antennas and Propagation Magazine*, vol. 55, no. 2, pp. 324-341, 2013.
- [2] C. Hertleer *et al.*, "A Textile Antenna for Off-Body Communication Integrated Into Protective Clothing for Firefighters," *IEEE Transactions on Antennas and Propagation*, Vol. 57, No. 4, pp. 919-925, April 2009.
- [3] R. Moro, S. Agneessens, H. Rogier, and M. Bozzi, "Wearable Textile Antenna in Substrate Integrated Waveguide Technology," *IET Electronics Letters*, Vol. 48, No. 16, pp. 985-987, August 2, 2012.
- [4] R. Garg, I. Bahl, M. Bozzi, *Microstrip Lines and Slotlines*, 3rd ed. Artech House, 2013.
- [5] F. Declercq *et al.*, "Environmental High Frequency Characterization of Fabrics based on a Novel Surrogate Modelling Antenna Technique", *IEEE Transactions on Antennas and Propagation*, Vol. 61, No. 10, pp. 5200-5213, Oct. 2013.
- [6] Z. Wang *et al.*, "Partial H-plane bandpass filters based on substrate integrated folded waveguide (SIFW)," *Proc. of Asia Pacific Microwave Conference*, Dec. 2009.

EXTREME WAVES IN NONLINEAR OPTICS AND OCEANOGRAPHY

F. Baronio⁽¹⁾, M. Conforti⁽²⁾, A. Degasperis⁽¹⁾, M. Onorato⁽³⁾, S. Wabnitz⁽¹⁾

⁽¹⁾ Department of Information Engineering, University of Brescia
Via Branze 38, 25123 Brescia, Italy

⁽²⁾ PhLAM/IRCICA UMR 8523/USR 3380, CNRS-Université Lille 1,
F-59655 Villeneuve d'Ascq, France

⁽³⁾ Department of Physics, University of Torino, via P. Giuria, 10125
Torino, Italy
fabio.baronio@unibs.it

Abstract

We report and discuss analytical solutions of the vector nonlinear Schrodinger equation that describe rogue waves in the defocusing regime. This family of solutions includes bright-dark and dark-dark rogue waves. The existence of vector rogue waves in the defocusing regime is expected to be a crucial progress in explaining extreme waves in a variety of physical scenarios described by multi-component systems, from oceanography to optics and plasma physics.

Index Terms – Extreme Waves, Nonlinear Optics, Oceanography.

I. INTRODUCTION

Rogue waves are extremely violent phenomena in the ocean: an encounter with such a wave can be disastrous even to big ocean liners. These waves can be also very dangerous for various hydrotechnic constructions. This makes the study of rogue waves a very important problem. Hence, it is not surprising that the phenomenon of rogue waves has attracted ample attention of oceanographers in the last decade [1]. However, although the existence of rogue waves has now been confirmed by multiple observations, uncertainty remains on their fundamental origins. This hampers systematic approaches to study their characteristics, including the predictability of their appearance. The research on rogue waves in oceans has attracted recently the attention of researchers in many other fields in physics. Rogue waves have been observed in nonlinear optics and lasers, atmosphere, plasma physics, and matter waves. The possibility to reach a general understanding of rogue-wave formation is still an open question. Nonetheless, the ongoing debate stimulates the comparison of predictions and observations between distinct topical areas, in particular hydrodynamics and nonlinear optics [2], in situations where analogous dynamical behaviors can be identified through the use of common mathematical models.

So far, the focusing nonlinear Schrodinger equation (NLSE) has played a pivotal role as a universal model for rogue wave solutions. The Peregrine soliton, predicted 30 years ago, is the simplest rogue-wave

solution associated with the focusing NLSE, and it has been recently experimentally observed in optical fibers, water-wave tanks, and plasmas.

While rogue wave investigations are flourishing in several fields of science, moving beyond the standard focusing NLSE description in order to model more general and important classes of physical systems is both relevant and necessary. In this direction, recent developments consist in i) including dissipative terms, since a substantial supply of energy (f.i., wind in oceanography) is generally required to drive rogue wave formation [3], or in ii) including higher-order perturbation terms such as in the Hirota equation and in the Sasa-Satsuma equation, because of the high amplitude or great steepness of a rogue wave, or in iii) considering wave propagation in 2+1 dimensions as for the Davey-Stewartson equation. Additional important progress has been recently obtained by extending the search for rogue wave solutions to coupled-wave systems, since numerous physical phenomena require modeling waves with two or more components in order to account for different modes, frequencies, or polarizations. When compared to scalar dynamical systems, vector systems may allow for energy transfer between their additional degrees of freedom, which potentially yields rich and significant new families of vector rogue-wave solutions. Indeed, rogue-wave families have been recently found as solutions of the focusing vector NLSE (VNLSE) [4], the Three Wave Resonant Interaction equations [5], the coupled Hirota equations, and the Long-Wave-Short-Wave resonance.

It is a well established fact that, for the scalar NLSE, the focusing nonlinear regime is a prerequisite for the emergence of regular or random rogue waves. To the contrary, in the scalar case the defocusing nonlinear regime does not allow for rogue wave solutions, even of dark nature. In coupled-wave systems, is the focusing regime still a prerequisite for the existence of rogue wave solutions? Or it possible to find examples of rogue waves in defocusing regimes?

Here, we show the existence of rogue wave solutions of the VNLSE in the defocusing regime.

II. ROGUE WAVES IN DEFOCUSING REGIMES

We consider the VNLSE which we write in the following dimensionless form:

$$\begin{aligned} iE^{(1)}_t + E^{(1)}_{xx} - 2(|E^{(1)}|^2 + |E^{(2)}|^2)E^{(1)} &= 0 \\ iE^{(2)}_t + E^{(2)}_{xx} - 2(|E^{(1)}|^2 + |E^{(2)}|^2)E^{(2)} &= 0 \end{aligned} \quad (1)$$

where $E^{(1)}$, $E^{(2)}$ represent the wave envelopes and x , t are the transverse and longitudinal coordinates, respectively. Each subscripted variable in Eqs. (1) stands for partial differentiation. Like the scalar NLSE, also the

focusing VNLSE possesses rogue wave solitons [4]. Unlike the scalar case, and far from being obvious, we find that rational solutions of the defocusing VNLSE do indeed exist, with the property of representing amplitude peaks which are localized in both spatio-temporal coordinates. These solutions are constructed by means of the standard Darboux dressing method, and they can be expressed as:

$$E^{(j)} = E^{(j)_0} \left[\frac{p^2 x^2 + p^4 t^2 + px(\eta_j + \beta\theta_j) - i\eta_j p^2 t + \beta\theta_j}{p^2 x^2 + p^4 t^2 + \beta(px + 1)} \right], \quad (2)$$

where

$$E^{(j)_0} = \alpha_j e^{i(q_j x - v_j t)}, \quad v_j = q_j^2 + 2(\alpha_1^2 + \alpha_2^2), \quad j = 1, 2; \quad (3)$$

represent the backgrounds of expression (2),

$$\eta_j = 4p^2 / (p^2 + 4q_j^2), \quad \theta_j = (2q_j + ip) / (2q_j - ip), \quad j = 1, 2;$$

$$\beta = p^3 / \chi(p^2 + 4q_1 q_2), \quad p = 2 \operatorname{Im}(\lambda + k),$$

$$q_1 + q_2 = 2 \operatorname{Re}(\lambda + k), \quad q_1 - q_2 = 2q, \quad \chi = \operatorname{Im}(k)$$

As for the computation of the complex value of k and λ , k is one of the complex solutions of a fourth order polynomial, and λ is the double solution of a third order polynomial which depends on α_1 , α_2 , q (see [6] for details). The expressions reported above depend on three real parameters which originate from naked solutions, namely from the backgrounds: the amplitudes α_1 , α_2 and the "frequency" difference of the waves $2q$. Figure 1 shows a typical dark-bright solution.

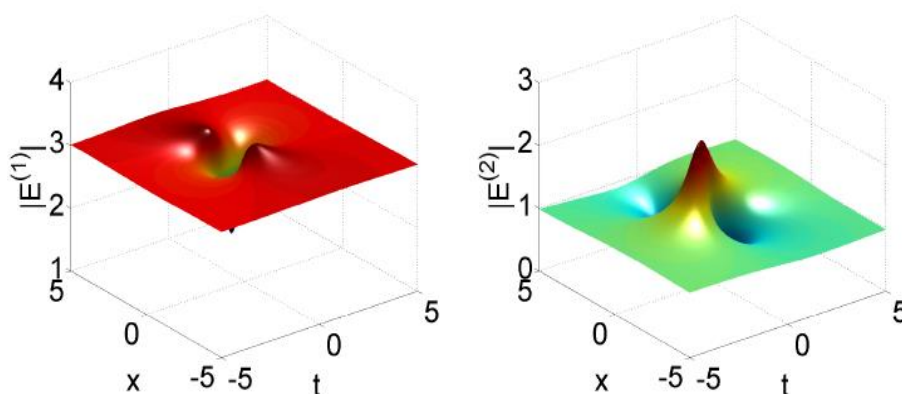


FIG. 1 – Typical Dark-Bright Rogue wave distribution $|E^{(1)}|$ and $|E^{(2)}|$ of the VNLSE system. Here, $\alpha_1=3$, $\alpha_2=1$, $q=1$. $k=2.36+1.1i$ and $\lambda=-1.69-1.79i$.

The family of solutions found in the defocusing regime, possesses a novel feature with respect to families of solutions previously reported in focusing regimes. In fact, in the defocusing regime, threshold conditions exist for rogue waves existence, which depend on the amplitudes, and the "frequency" difference of the waves. We found the following rogue wave existence condition:

$$(\alpha_1^2 + \alpha_2^2)^3 - 12(\alpha_1^4 - 7\alpha_1^2\alpha_2^2 + \alpha_2^4)q^2 + 48(\alpha_1^2 + \alpha_2^2)q^4 - 64q^6 > 0$$

III. CONCLUSIONS

We presented and analyzed exact, explicit rogue-wave solutions of the defocusing VNLSE. This family of solutions includes both bright and dark components. The existence of rogue wave solutions in the defocusing regime is expected to be crucial in explaining extreme waves in a variety of practical multi-component defocusing systems, from oceanography to optics and plasma physics.

ACKNOWLEDGEMENT

The present research was supported by the Italian Ministry of University and Research (MIUR, Project Nb.2009P3K72Z, Project Nb. 2012BFNWZ2), and by ONR (Grant Nb. 214 N000141010991).

REFERENCES

- [1] N. Akhmediev and E. Pelinovsky, "Editorial-Rogue Waves-Towards a Unifying Concept?: Discussions and Debates," *Eur. Phys. J. Special Topics* 185, p.1, 2010.
- [2] M. Onorato, S. Residori, U. Bortolozzo, A. Montina, and F.T. Arecchi, "Rogue waves and their generating mechanisms in different physical contexts," *Physics Reports* 528, p.47, 2013.
- [3] C. Lecaplain, Ph. Grelu, J.M. Soto-Crespo, and N. Akhmediev, "Super rogue waves: observation of a higher-order breather in water waves," *Phys. Rev. E* 108, p. 233901, 2012.
- [4] F. Baronio, A. Degasperis, M. Conforti, and S. Wabnitz, "Solutions of the vector nonlinear Schrödinger equations: evidence for deterministic rogue waves," *Phys. Rev. Lett.* 109, p. 044102, 2012.
- [5] F. Baronio, M. Conforti, A. Degasperis, and S. Lombardo, "Rogue Waves Emerging from the resonant Interaction of three waves," *Phys. Rev. Lett.* 111, p. 114101, 2013.
- [6] F. Baronio, M. Conforti, A. Degasperis, S. Lombardo, M. Onorato, and S. Wabnitz "Vector Rogue waves and Baseband Modulation Instability in Defocusing Regimes," *ArXiv:1403.3802*, 2014.

NON-INVASIVE LIGHT DETECTION ON A SILICON PHOTONIC CHIP

F. Morichetti, S. Grillanda, M. Carminati, G. Ferrari, M. Sampietro,
A. Melloni

Dipartimento di Elettronica, Informazione e Bioingegneria,
Politecnico di Milano

Via Ponzio 34/5, 20133 Milano, Italy

francesco.morichetti@polimi.it

Abstract

One of the main barriers to the development of complex system-on-chip photonic architectures is the lack of non-invasive tools to monitor the light inside optical waveguides. In this work, we present a transparent light detector integrated on a silicon photonic platform, that neither introduces appreciable perturbations of the optical field nor requires photon tapping from the waveguide. The proposed ContactLess Photonic Integrated Probe (CLIPP) exploits a capacitive access to the waveguide to measure the light dependent change of the waveguide electric conductance due to surface state absorption at the core-cladding interface. Light monitoring with a sensitivity down to -30 dBm, a dynamic range of 40 dB, and a μ s-scale time response is achieved in silicon waveguides and microring resonators, enabling real time monitoring and tuning of photonic integrated circuits.

Index Terms – Integrated optics, optical waveguides, photonic integrated circuits, silicon photonics.

I. INTRODUCTION

Although photonic technologies have reached extreme performances in the miniaturization of integrated optical devices [1], a number of open issues still prevent from the realization of complex functional systems-on-chip. A major challenge is the concept of transparent detectors, that are light probes capable to monitor the status of a photonic integrated circuit (PIC) without perturbing its operation. On-chip light monitoring is currently achieved by tapping a fraction of the light from the waveguide, but this approach is not scalable to circuits with tens or hundreds of monitoring points. Transparent detectors are envisioned as one of the key enabling technologies in integrated optics, paving the way to a new era of complex, self-configuring [2], feedback-controlled [3], adaptive, integrated photonics.

In this contribution, we demonstrate non-invasive light detection on a silicon photonic chip through a ContactLess Integrated Photonics Probe (CLIPP) [4], that neither introduces appreciable light perturbations nor requires additional photon tapping operations. By measuring the variation of the waveguide electric conductivity associated with intrinsic surface states absorption (SSA), light intensity is monitored with very high sensitivity (-30 dBm), a dynamic range larger than 40 dB, and in a time scale of few tens of microseconds.

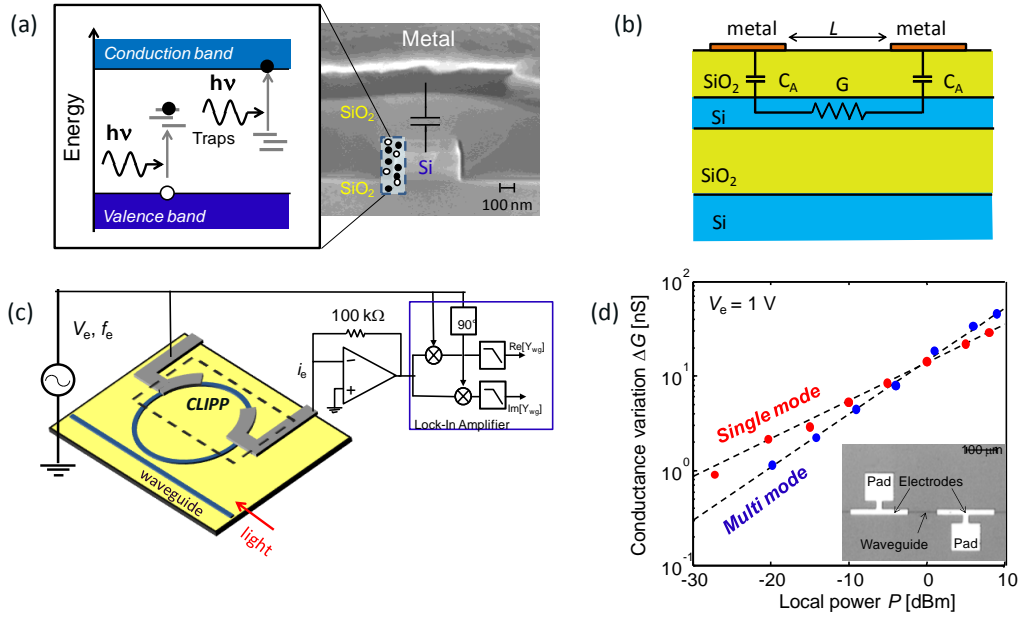


FIG. 1 – (a) SEM photograph of a Si waveguide and schematic of the SSA mechanisms generating free carriers at the core-cladding interface. (b) Equivalent electric circuit of the CLIPP along the longitudinal waveguide section. (c) Experimental setup for the electric impedance read-out of the CLIPP. (d) Measured conductance variation ΔG of a 100 μm long CLIPP versus waveguide optical power P , for a single mode and a multimode waveguide; the inset shows a top view photograph of the CLIPP.

II. THE CLIPP CONCEPT

The CLIPP concept was demonstrated by using conventional Si channel waveguides fabricated on a 220 nm SOI platform. As shown in Fig. 1(a), the Si core has a rectangular shape and is buried in a SiO₂ cladding. The longitudinal cross-section of the waveguide, along with its equivalent electric circuit, is shown in Fig. 1(b). Two electrodes are deposited above the upper cladding at a distance L and at a sufficient spacing ($> 1 \mu\text{m}$) from the core to avoid additional losses. The SiO₂ layer provides the access capacitance C_A from the electrodes to the core, the latter acting essentially as a resistor, with a conductance G of about 8 nS for a 100 μm -long waveguide section (10^{15} cm^{-3} p-doping of the SOI wafers).

When light propagates in the waveguide, free carriers generated at the core-cladding interface by SSA mechanisms modify the electric properties of the waveguide. As shown in Fig. 1(c), the light-dependent conductance variation ΔG is measured by exciting one electrode of the CLIPP with a voltage V_e at a suitable frequency f_e (in order to bypass C_A), and by reading the electric signal at the other electrode with a lock-in detection scheme. Figure 1(d) shows light monitoring, at a wavelength of 1550 nm, in a single mode (480 nm width, red circles) and a multimode (1 μm width, blue circles) waveguide with $L = 100 \mu\text{m}$ ($V_e = 1 \text{ V}$, $f_e = 1 \text{ MHz}$). Light monitoring with -30 dBm sensitivity, 40 dB dynamic range,

and μs scale time response was achieved, thanks to a sensitivity in the conductance measurement better than 1 nS [5].

The driving signal applied to the CLIPP introduces a phase perturbation of about 0.4 mrad/V, which is induced by a small electro-optic effect of the silicon waveguide [4]. At $V_e = 1$ V, this corresponds to less than 0.2 ppm change of the waveguide effective index, which is comparable to the perturbation induced by a temperature change smaller than 3 mK, thus confirming the minimally invasive nature of the CLIPP.

III. MONITORING AND TUNING OF MICRORING RESONATORS

Compactness, light transparency, and ease of fabrication enable the integration of the CLIPP inside generic PICs without constraining the design and technology of the waveguide underneath. For instance, Fig. 2(a) shows a Si microring resonator with a CLIPP and a thermal actuator integrated inside. The ring has a round trip length of 516 μm , a free-spectral-range of 138 GHz, and a linewidth of 87 pm (10.8 GHz). The CLIPP can be used to directly observe the light intensity inside the ring, this information being not accessible with conventional photodetectors without introducing a perturbation of the quality factor. Fig. 2(b) shows the CLIPP measurement of the normalized intra-cavity light intensity when the resonant wavelength of the ring is thermally red-shifted by driving the heater from 0 to 4 V. When the CLIPP and the heater are switched on, neither a change in the quality factor (about 18000) is observed, nor a significant thermal or electric crosstalk between the heater and the CLIPP.

CLIPP-assisted light monitoring can be exploited for tuning the transfer function of more complex devices, such as the filter of Fig. 3(a), consisting of two directly coupled ring resonators. Thermal actuators are placed in each ring and CLIPPs are positioned on the Through port and inside each resonator. Fig. 3(b) shows a very good agreement between the Through port transmission measured with an external optical spectrum analyzer (OSA) (blue dashed lines) and with the

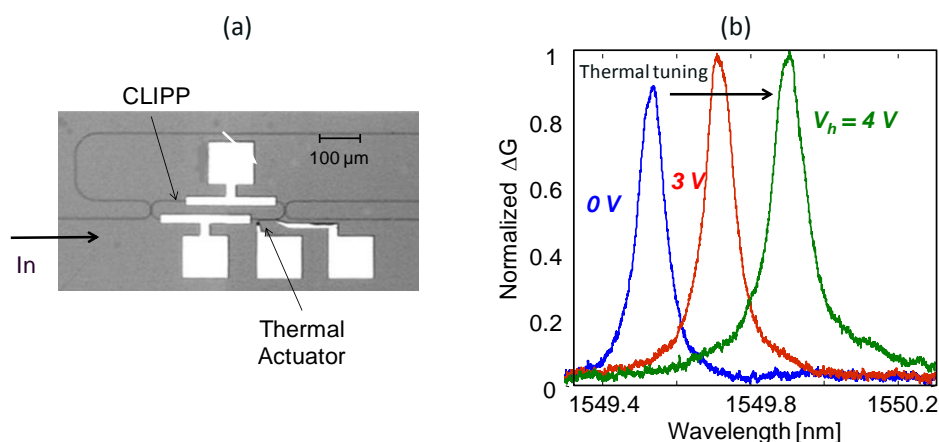


FIG. 2 – (a) Photograph of a microring resonator with a CLIPP and a thermal actuator integrated inside. (b) Normalized light intensity measured by the CLIPP inside the resonator for different heater voltage.

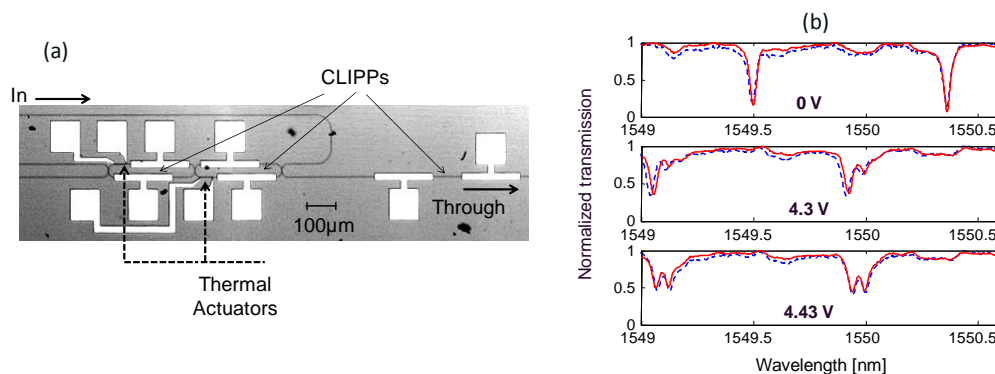


FIG. 3 – (a) Photograph of a two-ring filter with integrated CLIPPS and thermal actuators. (b) Normalized optical transmission measured at the Through port by an OSA (dashed blue lines) and by the CLIPP at the Through port (red solid lines) for different heater voltage.

integrated CLIPP (red solid lines) when the voltage driving the heater is increased from 0 V to 4.43 V to compensate the resonance mismatch of the two rings.

IV. CONCLUSION

Non-invasive light detection was demonstrated on a silicon photonic chip by measuring the light-dependent change of the electrical conductivity of the optical waveguides. The CLIPP introduces a perturbation as low as 0.2 ppm/V in the waveguide effective index, which is negligible compared to the residual temperature fluctuations of any thermally stabilized chip. The CLIPP technology is simple, inherently CMOS compatible, and scalable to many probing points per chip, enabling tuning and feedback control of generic photonic architectures.

ACKNOWLEDGEMENT

This work was supported by the Italian PRIN 2009 project Shared Access Platform to Photonic Integrated Resources (SAPPHIRE) and by the European Project BBOI of the 7th EU Framework Program. The authors gratefully acknowledge M. Sorel, M. J. Strain and the staff of JWNC at Glasgow University for the fabrication of the photonic devices.

REFERENCES

- [1] J. Sun *et al.*, "Large-scale nanophotonic phased array," *Nature*, vol. 493, no. 7431, pp. 195–199, Jan. 2013.
- [2] D. A. B. Miller, "Designing linear optical components," *Opt. & Phot. News*, vol. 24, no. 12, p. 38, Dec. 2013.
- [3] F. Morichetti *et al.*, "Toward feedback-controlled integrated photonics," *IEEE Photonics Journal*, Apr. 2014. doi:10.1109/JPHOT.2014.2310203
- [4] F. Morichetti *et al.*, "Non-Invasive On-Chip Light Observation by Contactless Waveguide Conductivity Monitoring," *IEEE J. Selected Topics in Quantum Electronics*, vol. 20, no.4, pp.1,10, July-Aug. 2014.
- [5] M. Carminati *et al.*, "ZeptoFarad capacitance detection with a miniaturized CMOS current front-end for nanoscale sensors," *Sens. Actuators A, Phys.*, vol. 172, no. 1, pp. 117– 123, Dec. 2011.

BACKWARD SECOND-HARMONIC GENERATION OF NEAR INFRARED PICOSECOND PULSES

A. C. Busacca⁽¹⁾, S. Stivala⁽¹⁾, A. C. Cino⁽¹⁾, L. Curcio⁽¹⁾, A. Tomasino⁽¹⁾,
and G. Assanto⁽²⁾

⁽¹⁾ DEIM, University of Palermo, Viale delle Scienze Bldg. 9, 90128,
Palermo, Italy

⁽²⁾ Nonlinear Optics and OptoElectronics Lab (NooEL), University of
Rome “Roma Tre”, 00146 Rome, Italy
salvatore.stivala@unipa.it

Abstract

We report on backward second-harmonic generation using picosecond laser pulses in congruent lithium niobate with 3.2 μm periodic poling. By tuning both the pump wavelength and the sample temperature, we observed three resonant peaks in the range 1530-1730 nm, corresponding to 16th, 17th and 18th quasi-phase-matching orders, respectively. A maximum conversion efficiency of 0.475 % was achieved at the 16th order with a 10 kW peak pump power. The latter is the highest conversion reported in bulk to date, for the backward configuration, with an improvement greater than 50% with respect to those previously achieved with nanosecond pulses for the same order of resonance.

Index Terms – Nonlinear Optics, Parametric Processes, Harmonic Generation and Mixing, Picosecond Phenomena.

I. INTRODUCTION

Periodic domain inversion by electric field poling of nonlinear ferroelectric crystals is a well-known technique to achieve efficient second-harmonic generation (SHG) via quasi-phase matching (QPM) [1]. If the poling period is short enough, QPM SHG can occur between fundamental frequency (FF) and SH waves traveling in opposite directions, yielding backward-SHG (BSHG) [2]. Until now, counter-propagating geometries have been analyzed and, in a few cases, demonstrated towards various second order nonlinear optical effects, including gap solitons, mirrorless parametric oscillators, pulse shaping and phase conjugation. BSHG experiments were reported with continuous waves (cw) [3] and either ns or fs pulses [4, 5].

Herein, we present what we believe are the first results on picosecond BSHG of near infrared laser pulses in a 3.2 μm periodically poled lithium niobate (PPLN) crystal, 3 mm in length. Three resonant peaks were measured between 1530 and 1730 nm, corresponding to 16th, 17th and 18th QPM orders in the backward configuration, with a conversion efficiency of 4.75×10^{-5} %/W for the 16th order.

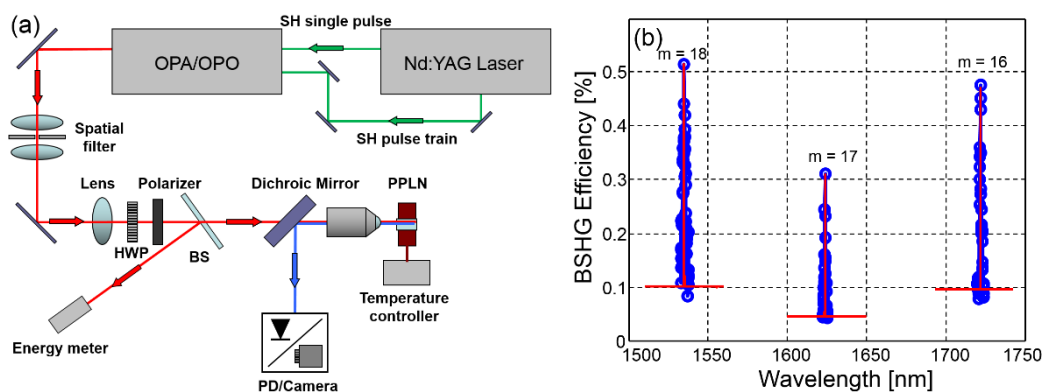


FIG. 1 – (a) Experimental setup for BSHG measurements. HWP: half-wave-plate; BS: beam splitter; PD: photodetector. (b) FF wavelength scan showing three QPM peaks in BSHG conversion efficiency: the solid lines from the model are in good agreement with the experimental data (circles). FF peak power were 10 kW, 8 kW and 15 kW for 16th, 17th and 18th orders, respectively

II. SAMPLE FABRICATION

The PPLN sample was prepared starting from a 500 μm -thick optical-grade wafer of congruent Lithium Niobate (LN). By standard photolithography, a grating of period $\Lambda = 3.2 \mu\text{m}$ was defined over a length $L = 3\text{mm}$ on a 2 μm -thick film of positive photoresist spin-coated on the $-Z$ facet. After development, the pattern was soft-baked overnight at 90°C and hard-baked for 3 hours at 130°C, in order to provide a better adhesion between the photoresist and the substrate while improving insulation. For the poling process, the sample was contacted with gel-electrolyte layers and, in order to exceed the LN coercive field and obtain a charge-controlled domain inversion, single 1.3kV pulses were applied over a 10 kV offset for appropriate time intervals. Finally, the end-facets of the chip were polished.

III. NONLINEAR CHARACTERIZATION AND DATA ANALYSIS

For the nonlinear characterization, we employed the set-up sketched in Fig. 1(a). The source was an optical parametric amplifier/oscillator (OPA/OPO) pumped by a frequency-doubled picosecond Nd:YAG pump at 1.064 μm . The OPA/OPO provides 25 ps pulses at 10 Hz rep-rate, tunable in the range 0.72-2.1 μm . After spatial filtering to yield a TEM₀₀ mode, the laser beam was gently focused by a 10x microscope objective at the input of the periodically poled region to a waist of about 20 μm . A Peltier cell and a temperature controller were employed to either keep the crystal at a constant temperature during wavelength tuning or perform temperature tuning during measurements at fixed wavelengths.

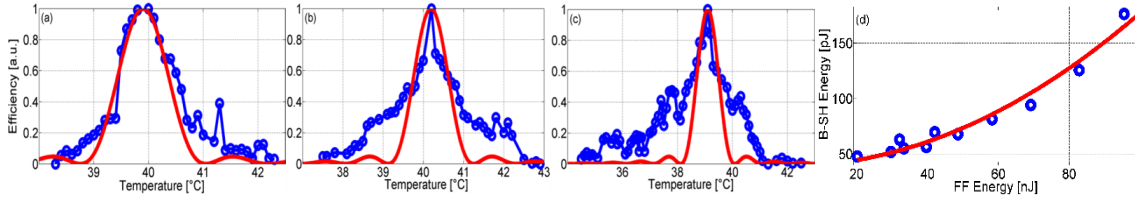


FIG. 2 - Measured (circles) and calculated (solid line) BSHG conversion efficiency for the (a) 16th, (b) 17th and (c) 18th QPM order versus temperature. FF wavelength and peak power were 1722.0nm and 10 kW in (a); 1623.9nm and 8 kW in (b); 1535.1nm and 12 kW in (c). (d) BSHG energy vs input FF energy for the 16th resonant order.

A dichroic mirror helped separating the back-reflected FF pump from the generated backward-propagating SH. The energy of BSHG pulses was measured with a Si photodiode and a boxcar averager. Figure 1(b) graphs the measured BSHG conversion efficiency versus FF wavelength (λ_{FF}): three resonant peaks are visible at 1535.1, 1623.9 and 1722.0 nm, corresponding to the 18th, 17th and 16th QPM BSHG orders. The generation of frequency-doubled light for both odd and even resonant QPM orders stems from the unbalanced duty-cycle D of the nonlinear grating. The BSHG resonance for m^{th} -order QPM is given by:

$$\Delta k_{QPM} = \frac{4\pi}{\lambda_{FF}}(n_{FF} + n_{SH}) - \frac{2m\pi}{\Lambda} = 0, \quad (1)$$

where Δk_{QPM} is the wavevector mismatch, n_{FF} and n_{SH} are the extraordinary refractive indices at FF and SH, respectively; the latter can be evaluated using the temperature-dependent Sellmeier equations. Equation (1) is satisfied for $m = 16, 17, 18$ at the experimentally observed resonant wavelengths when the QPM grating has periods $\Lambda_{16} = 3.20053$, $\Lambda_{17} = 3.20128$ and $\Lambda_{18} = 3.19851$ μm , respectively. These values are remarkably close to the nominal poling period.

Figures 2(a)-2(c) show BSHG efficiency results versus temperature at fixed FF wavelengths, corresponding to the three BSHG resonances. For each resonant order, the BSHG signal exhibited a quadratic dependence on the FF pump: Fig. 2(d) details the most efficient case ($m = 16$).

We compared measured and predicted BSHG conversion efficiency. It is worth noting that we could not use the simplified expressions for quasi-cw or fs excitations [2]. For Gaussian FF pulses of duration τ , the SH pulses generated in a sample of length L have the form $H(t) = [P(\sqrt{2}M_b - \sqrt{2}T) + P(\sqrt{2}T) - 1]^2$ with $P(x)$ the integration of the normalized Gaussian probability function, $M_b = L(n_{SH} + n_{FF})/(\tau c)$ with c the speed of light in vacuum and $T = t/\tau$ a normalized time coordinate. By defining J_H as the integral of H , i.e., $J_H = \int_{-\infty}^{+\infty} H(T) dT$, the SH conversion efficiency can be expressed in terms of energy density per pulse as:

$$\eta = \frac{\int_{-\infty}^{+\infty} I_{SH} dt}{I_{FF} \tau} = \frac{\eta_0 d_{33}^2 I_{FF}^2 \tau^2 c^2 J_H}{2 n_{SH} n_{FF}^2 (n_{SH} + n_{FF})^4 \Lambda^2} \text{sinc}^2\left(\frac{\Delta k_{QPM} L}{2}\right) \quad (2)$$

with d_{33} the largest diagonal element of the second-order nonlinear susceptibility tensor, η_0 the vacuum impedance, I_{FF} and I_{SH} the peak intensities at FF and SH, respectively. We computed the conversion efficiency η from Eq. (2) using the material Sellmeier equations for the refractive indices and the actual values for sample length, pulse duration, FF peak intensity; d_{33} was the only fit parameter. The best fits of our data are shown as solid lines in Fig. 1(b) and in Fig. 2. The nonlinear coefficient d_{33} resulted equal to 29.03, 27.32, 25.13 pm/V, for $m = 16, 17, 18$, respectively. These d_{33} values are in close agreement with those provided by the crystal supplier. This confirms that the crystal nonlinearity was unaffected by the poling process, with an effectively optimized BSHG at the three resonant orders.

IV. CONCLUSION

We have observed - for the first time in the picosecond regime - BSHG in PPLN at three near-infrared wavelengths corresponding to 16th, 17th and 18th QPM resonances, with a conversion efficiency as high as 0.475% for the lowest order. Our experimental data are in agreement with a simple model for ps pulsed BSHG.

REFERENCES

- [1] M. M. Fejer, G. A. Magel, D. H. Jundt, and R. L. Byer, "Quasi-phase-matched second harmonic generation: tuning and tolerances," *IEEE J. Quantum Electron.* Vol. 28(11), pp. 2631–2654, Nov. 1992.
- [2] Y. J. Ding, J. U. Kang, and J. B. Khurgin, "Theory of backward second-harmonic generation using laser pulses in quasi-phase-matched second-order nonlinear media," *IEEE J. Quantum Electron.* vol. 34(6), pp. 966-974, June 1998.
- [3] S. Stivala, A. C. Busacca, L. Curcio, R. L. Oliveri, S. Riva-Sanseverino, and G. Assanto, "Continuous-wave backward frequency doubling in periodically poled lithium niobate," *Appl. Phys. Lett.* vol. 96(11), pp. 111110-1 – 111110-3, Mar. 2010.
- [4] J. U. Kang, Y. J. Ding, W. K. Burns, and J. S. Melinger, "Backward second-harmonic generation in periodically poled bulk LiNbO₃," *Opt. Lett.* vol. 22(12), pp. 862–864, June 1997.
- [5] X. Gu, R. Y. Korotkov, Y. J. Ding, J. U. Kang, and J. B. Khurgin, "Backward second-harmonic generation in periodically poled lithium niobate," *J. Opt. Soc. Am. B* vol. 15(5), pp. 1561-1566, May 1998.

THE OUTCOMES OF SAPPHIRE, A GENERIC FOUNDRY PLATFORM FOR SILICON PHOTONICS

F. Morichetti⁽¹⁾, A. Annoni⁽¹⁾, S. Grillanda⁽¹⁾, P. Orlandi⁽²⁾,
S. Malaguti⁽³⁾, A. Parini⁽³⁾, M. J. Strain⁽⁴⁾, M. Sorel⁽⁵⁾,
G. Bellanca⁽³⁾, P. Bassi⁽²⁾, A. Melloni⁽¹⁾

⁽¹⁾ Dipartimento di Elettronica, Informazione e Bioingegneria,
Politecnico di Milano, Via Ponzio 34/5, Milano 20133, Italy,
morichetti@elet.polimi.it

⁽²⁾ Dipartimento di Ingegneria dell'Energia Elettrica e Informazione,
Università di Bologna, Viale Risorgimento 2, Bologna 40136, Italy

⁽³⁾ Dipartimento di Ingegneria, Università degli Studi di Ferrara,
Via Saragat 1, Ferrara 44100, Italy

⁽⁴⁾ Institute of Photonics, University of Strathclyde, United Kingdom

⁽⁵⁾ School of Engineering, University of Glasgow, United Kingdom

Abstract

The PRIN 2009 Project SAPPHIRE has created the first national infrastructure for a shared access to a silicon photonic foundry. The goal has been accomplished developing dedicated design kits of silicon photonic building blocks together with software tools for high-level circuit design of Photonic Integrated Circuits (PICs). Here, we present successful examples of silicon photonic PICs fabricated in multi project wafers in the framework of the SAPPHIRE platform, demonstrating the flexibility and the viability of the generic foundry model for silicon photonics.

Index Terms – Circuit Design, Photonic Generic Foundry, Photonic Integrated Circuit, Silicon Photonics.

I. INTRODUCTION

In photonics, the generic foundry model is replacing the conventional paradigm of application-oriented methodology for the production of PICs. In this evolving scenario, the challenge of the PRIN 2009 Project SAPPHIRE (Shared Access Platform to PHotonic Integrated REsources) was to create the first national infrastructure enabling a shared access of different users to silicon photonic technologies [1]. Various specific services were created by SAPPHIRE for different kind of users: dedicated Design Kits (DKs) were developed for a silicon photonics foundry, the James Watt Nanofabrication Centre (JWNC) at the University of Glasgow; advanced software tools were created enabling high-level circuit design and statistical analysis of arbitrarily complex PICs [2]; support services were offered to the users for PIC design and generation of mask layouts compliant with foundry standards; designs from different users were collected and assembled in a multi project wafer layout; fabrication runs were qualified and chips sent to Users. This work presents a selection of projects carried out in the SAPPHIRE framework, demonstrating the success of the generic foundry model for photonics in the national contest.

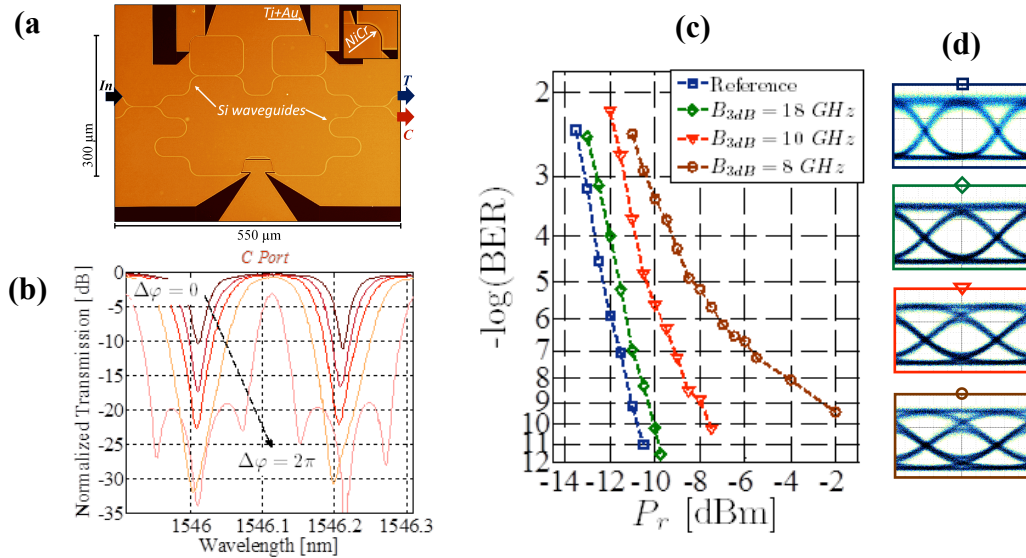


Fig. 1. (a) Picture of a tunable bandwidth filter. (b) Cross port C transmission from maximum ($\Delta\varphi = 0$) to minimum ($\Delta\varphi = 2\pi$) bandwidth for a 25 GHz FSR filter with $K_r = 0.79$. (c) BER measurements of a 10 Gbit/s NRZ OOK signal filtered by the 25 GHz FSR filter with 3dB bandwidths of 18 GHz (green diamonds), 10 GHz (red triangles), and 8 GHz (brown circles). Blue squares show the BER measured after propagation through a 5-mm long waveguide. (d) Eye diagrams for the different conditions. The optical signal-to-noise ratio, evaluated over 0.2 nm at the chip input, is 23 dB.

II. OUTCOMES OF THE SAPPHIRE PROJECT

As a first example of the SAPPHIRE outcomes [3], we present a compact ($< 0.6 \text{ mm}^2$ footprint) tunable bandwidth filter architecture, consisting of an unbalanced Mach-Zehnder Interferometer (MZI) loaded with two ring resonators (RRs) [see Fig. 1(a)]. Bandwidth tunability is achieved by controlling the absolute value of the phase shift φ_r antisymmetrically applied to the two RRs. The two 3 dB couplers allow equal performance at the output ports. The RRs power coupling coefficient K_r was optimized to obtain the maximum bandwidth tunability range, keeping acceptable minimum off-band rejection for practical applications.

The device behavior at the C port of a filter with FSR=25 GHz is shown in Fig. 1(b) for varying differential phase shift $\Delta\varphi=2\varphi_r$ between the two RRs. Maximum bandwidth condition occurs when $\Delta\varphi=0$. Heating up one of the ring resonators and cooling down the other in a push-pull configuration tunes the device bandwidth until $\Delta\varphi=2\pi$ is reached. Devices with different FSRs (200, 100, 25 GHz) were realized, exhibiting a tunability range spanning from at least 85% to less than 15% of the FSR, while preserving > 10 dB off-band rejection. Power consumption for bandwidth tuning is about 25 mW almost independently of the device FSR filter, while wavelength tuning of the filter central wavelength across the entire FSR requires 60 mW.

To evaluate the impact of the proposed device on the transmission of an optical signal, we measured the Bit Error Rate (BER) of a 10 Gbit/s nonreturn-to-zero (NRZ) on-off keying (OOK) data stream after transmission through the 25 GHz FSR filter C port.

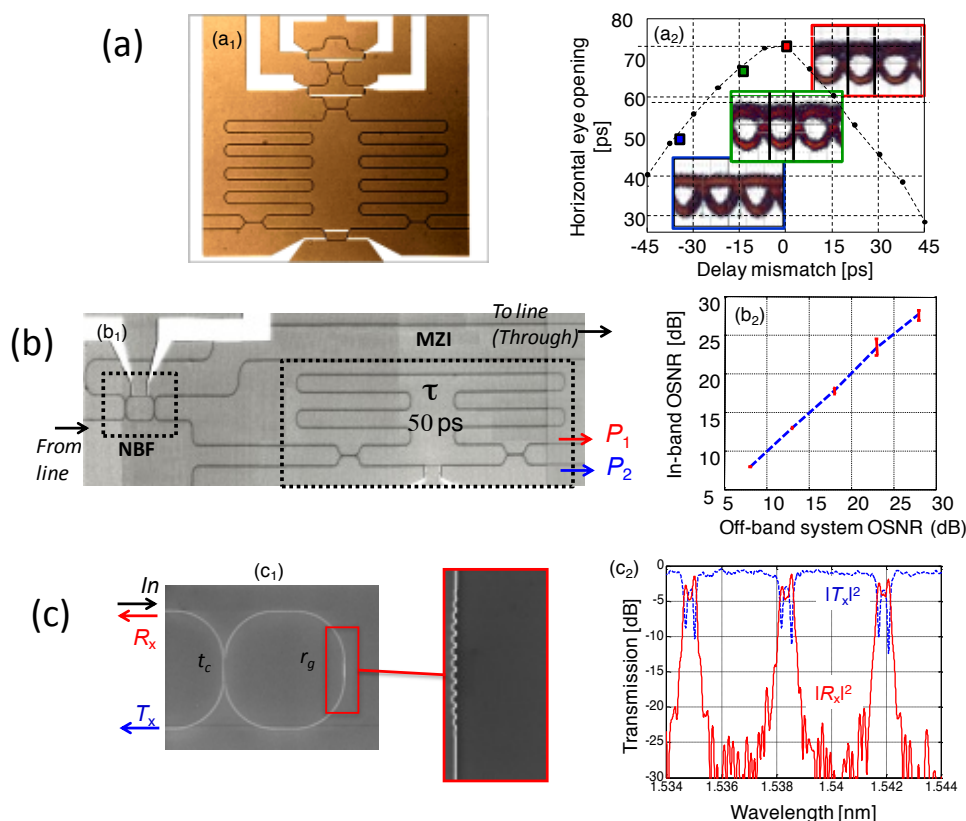


Fig. 2. A selection of silicon photonics PICs realized in the framework of the SAPPHIRE project: (a) Variable delay receiver for DQPSK signals: (a₁) photograph and (a₂) delay optimization for the detection of a 10 Gsym/s DPSK signal; (b) Integrated OSNR monitor: (b₁) photograph and (b₂) in-band OSNR measurement for a 10 Gb/s OOK NRZ signal; (c) Coupled-resonator dual-mode optical filters: (c₁) photograph and (c₂) measured spectral response of a second-order filter.

Fig. 1(c) shows the measured BER versus the received power (P_r) for different filter bandwidths. Fig 1(d) shows relative eye diagrams. Reducing the bandwidth to 10 GHz causes no appreciable quality loss. Simulations confirmed that signal degradation is mainly due to sideband filtering rather than to phase distortion.

Other examples of PICs successfully realized in the framework of the SAPPHIRE platform includes:

(a) *Variable delay receiver for DQPSK signals* [4]: the device, shown in Fig. 2(a₁), consists of a MZI loaded with a tunable delay line, realized by using a thermally tunable coupled-resonator optical waveguide providing a continuous delay from 66 ps to 102 ps. Delay tunability allows the optimization of the receiver performance for the detection of DPSK signals at any symbol rates between 9.8 and 15 Gsym/s. Fig. 2(a₂) shows delay optimization for a 10 Gsym/s DPSK signal;

(b) *High-sensitivity integrated OSNR monitor* [5]: the circuit, shown in Fig. 2(b₁), combines a thermally tunable microring resonator with an unbalanced MZI. This circuit was employed to perform OSNR monitoring of a 10 Gb/s OOK NRZ signal, with an accuracy of 0.4 dB

over a wide OSNR range, from 8 dB to 28 dB [see Fig. 2(b₂)]. Distortion introduced on the optical signal is extremely small, making this approach suitable for in-line monitoring of signal quality.

(c) *Coupled-resonator dual-mode optical filters* [6]: this filter concept, shown in Fig. 2(c₁), consists of a chain of directly coupled microring resonators with a partial reflector embedded in the last resonator. The reflector induces a contradirectional coupling in the rings, doubling the effective order of the filter with respect to the number of coupled resonators. Second-order [see Fig. 2(c₂)] and fourth-order filters were demonstrated on the SAPPHIRE platform.

(d) *Wavelength Division multiplexing (WDM) on-chip passive router* [7]: a passive WDM router suitable for optical networking at chip level was realized and its performance, in terms of BER, where evaluated for three 10 Gb/s channels in WDM configuration.

III. CONCLUSION

The PRIN 2009 Project SAPPHIRE has created the first national platform for the shared access to a silicon photonic foundry. SAPPHIRE demonstrated a scientific and coordination success well above the expectations, involving also groups from other countries (Brazil and Spain). SAPPHIRE will continue to operate also after the termination of the project, assisting both novice and experienced users in their strategic and technical decisions and extending the platform even towards other technologies.

ACKNOWLEDGEMENT

The Authors thank the Italian PRIN 2009 project SAPPHIRE (<http://sapphire.dei.polimi.it/>) for funding this research activity and the support from the technical staffs of JWNC at Glasgow University.

REFERENCES

- [1] F. Morichetti *et al.*, "SAPPHIRE: A generic foundry platform for silicon photonics," *Atti della XIX Riunione Nazionale di Elettromagnetismo (RINEM 2012)*, pp. 410-413, Rome, 10-14 September 2012.
- [2] Web sites: Filarete srl, Italy, <http://www.aspicdesign.com>; Phoenix BV, The Netherlands, <http://www.phoenixbv.com>.
- [3] P. Orlandi *et al.*, "Photonic integrated filter with widely tunable bandwidth," *J. Lightwave Technol.*, vol. 32, no. 5, pp. 897-907, Mar. 2014.
- [4] M. Mattarei *et al.*, "Variable symbol-rate DPSK receiver based on a silicon photonics coupled-resonator delay line," submitted to *Optics Express*.
- [5] F. Morichetti *et al.*, "High-sensitivity in-band OSNR monitoring system integrated on a silicon photonics chip," *IEEE Phot. Techn. Lett.*, vol. 25, no. 19, pp. 1939-1942, Oct. 2013.
- [6] C. Alonso-Ramos *et al.*, "Dual-mode coupled-resonator integrated optical Filters," *IEEE Phot. Techn. Lett.* (in press).
- [7] A. Parini *et al.*, "BER Evaluation of a Passive SOI WDM Router," *IEEE Phot. Techn. Lett.*, vol. 25, no. 23, pp. 2285-2288, Dec. 2013.

COLLISION ENHANCED DISPERSIVE WAVE GENERATION

A. Tonello⁽¹⁾, D. Modotto⁽²⁾, K. Krupa⁽¹⁾, A. Labruyère⁽¹⁾,
B. M. Shalaby⁽¹⁾⁽³⁾, V. Couderc⁽¹⁾, A. Barthélémy⁽¹⁾, U. Minoni⁽²⁾,
S. Wabnitz⁽²⁾, A. B. Aceves⁽⁴⁾

⁽¹⁾ Université de Limoges, XLIM, UMR CNRS 7252,
123 Av. A. Thomas, 87060 Limoges, France

⁽²⁾ Dipartimento di Ingegneria dell'Informazione,
Università di Brescia, via Branze 38, 25123 Brescia, Italy

⁽³⁾ Physics Department, Faculty of Science,
Tanta University, Tanta, Egypt

⁽⁴⁾ Department of Mathematics,
Southern Methodist University, Dallas, USA

daniele.modotto@unibs.it

Abstract

Solitons propagating along a fiber when perturbed by higher-order dispersion terms transfer energy into linear dispersive waves. We consider the situation when solitons traveling at different speeds collide and analytically explain the dramatic enhancement of the dispersive wave power due to this soliton-soliton interaction; numerical simulations confirm the predictions of our theory.

Index Terms – Dispersive wave, nonlinear optics, soliton collision.

I. INTRODUCTION

Dispersive wave emission by intense optical pulses that propagate in optical fibers has been observed and studied since quite a long time [1]. An intense pulse can shed part of its energy on a linear wave only if the pulse and the wave share the same phase velocity: this condition can be easily fulfilled with the design of appropriate microstructured fibers (MFs). It has already been recognized that collisions among solitons, and interplay between solitons and linear waves, can further enhance the emitted DW energy and can also affect the spectral density distribution [2]. In this work we want to identify the different sources of DW emission which are activated during the finite life-time of the highly inelastic two-soliton collisions. Our analytical estimate proves that these transient sources are crucial in boosting the DW energy.

II. ANALYTICAL MODEL

Pulse propagation in a MF is conveniently described by a perturbed version of the Nonlinear Schrödinger Equation (NLSE) where a linear operator P , applied to the pulse envelope $A(z,t)$, describes higher-order

dispersion terms [1]. We assume that the input field is given by a pair of solitons with different carrier angular frequencies: U_0 (at frequency ω_0) and U_1 (at frequency $\omega_0 + \Omega$). By linearization of the NLSE, the spectrum of a relatively weak DW $F_k(\omega, z)$ in the presence of an intense soliton pulse $U_k(z, t)$ (with $k=0, 1$), can be obtained by solving

$$i \frac{\partial F_k}{\partial z} + \beta(\omega) F_k = S_k(\omega, z) \quad (1)$$

where the forcing terms $S_k(\omega, z)$ correspond to the product of the soliton Fourier transform by the linear operator P in the frequency domain. The solutions for F_k can be readily obtained and they confirm that resonances appear only if a well-known phase matching condition is satisfied ($\Delta\beta=0$) [1]. It is worth to underline that the sources S_0 and S_1 remain active for the entire length of the fiber, since they are associated with the propagation of the two solitons. On the other hand, whenever the two solitons collide in-phase they can merge into a single and brighter pulse: this “flash pulse” may have up to four times higher peak power and halved temporal duration with respect to the input pulses [2]. We model this flash U_F , which is localized both in time and space, as an hyperbolic secant in the time-domain multiplied by a Gaussian profile in the spatial domain. In spite of the short collision length L_W between the two solitons, U_F acts as an efficient source for DWs. Since the temporal duration of the flash is reduced with respect to that of the solitons, the amplitude of the spectral tails of the pumping pulses is enhanced by orders of magnitude leading to a huge increase in the DW amplitude. It turns out that the DW amplitude $F_F(z, \omega)$ at coordinate z and angular frequency ω is proportional to the following staircase function:

$$F_F(z, \omega) \propto \text{Exp}[-\xi^2(\omega)] \text{Erfi} \left\{ \left[\xi(\omega) + i \frac{z - z_0}{L_W} \right] - \text{Erfi} \left[\xi(\omega) - i \frac{z_0}{L_W} \right] \right\} \quad (2)$$

where $\text{Erfi}(x) = \text{Erf}(ix)/i$ is the imaginary error function, $\xi = \Delta\beta_F(\omega) L_W/2$, $\Delta\beta_F(\omega)$ is the phase-matching function for the pump flash pulse, L_W is the collision length and z_0 is the collision point.

III. DWs IN A DUAL CONCENTRIC CORE MICROSTRUCTURED FIBER

To test the validity of our theory we studied the solitons propagation along a dual concentric core MF [3]; Fig. 1(a) shows the difference between the reciprocal of the group velocity β_1 and its value $\beta_{1,0}$ at 1064 nm, and the group velocity dispersion β_2 . We consider the propagation and collision of two solitons U_0 (at 1064 nm) and U_1 (at 1081.7 nm) having a full-width at half maximum of 35 fs. Due to the different group velocities, these solitons collide at about $z=1.6$ m, as it is shown in Fig.1(b) where the time-domain and spectral density evolutions are reported as obtained by numerically solving the NLSE. As expected by

the phase-matching condition, two DWs grow around 900 nm and 1587 nm, but around the collision there is a clear staircase growth of both the DWs.

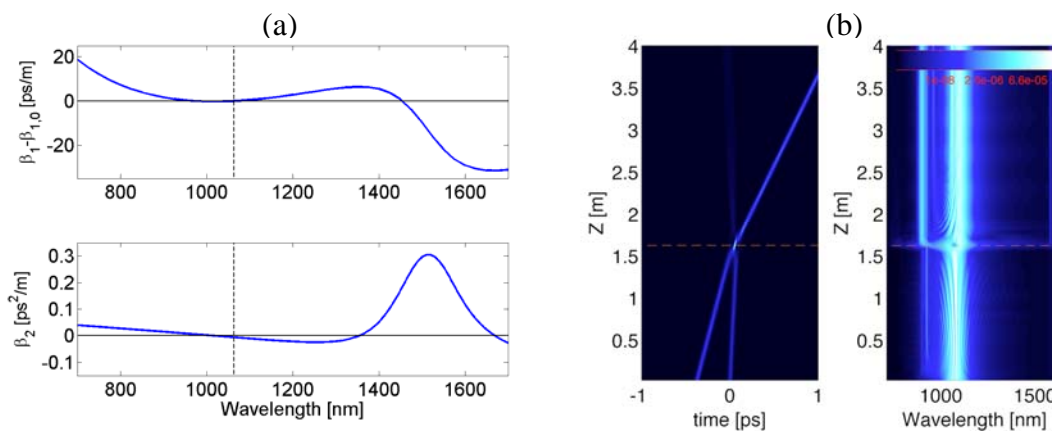


FIG. 1 – (a) Reciprocal of the group velocity (top) and group velocity dispersion (bottom) of the dual concentric core microstructured fiber; (b) collision between two solitons: temporal (left) and spectral evolutions (right).

The spectrogram of Fig. 2(a) shows how the spectral broadening due to the flash pulse fosters the DWs. By integrating the energy of each DW over a 8 THz bandwidth, the predicted staircase growth is more clearly observed, as it is displayed in Fig. 2(b).

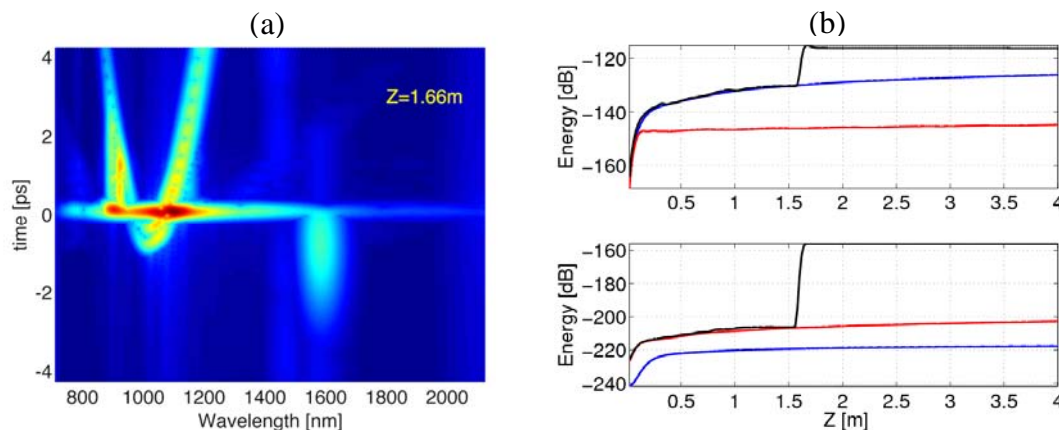


FIG. 2 – (a) Spectrogram after the collision (at $z=1.66$ m); (b) energies of the DWs around 900 nm (top panel) and 1587 nm (bottom panel).

Figure 3(a) compares the numerically calculated spectrum at the output of a 4 m long piece of MF as resulting after a two-soliton collision (black curve), to the spectra obtained when the two solitons independently propagate (blue and red curves): the collision brings about a largely broadened DW spectrum around 900 nm, as well as more than 25 dB of power enhancement of the narrow spectral peak around 1587 nm. In our model we used a flash pulse having a peak power four times higher than that of a single soliton with a half-time duration; Fig. 3(b) shows

the spectra predicted for F_0 , F_1 and F_F by solving Eq. (1) and using the analytical result for F_F : these theoretical spectra reproduce most of the features which are observed in the numerical solutions of Fig. 3(a) and confirm the validity of our approach.

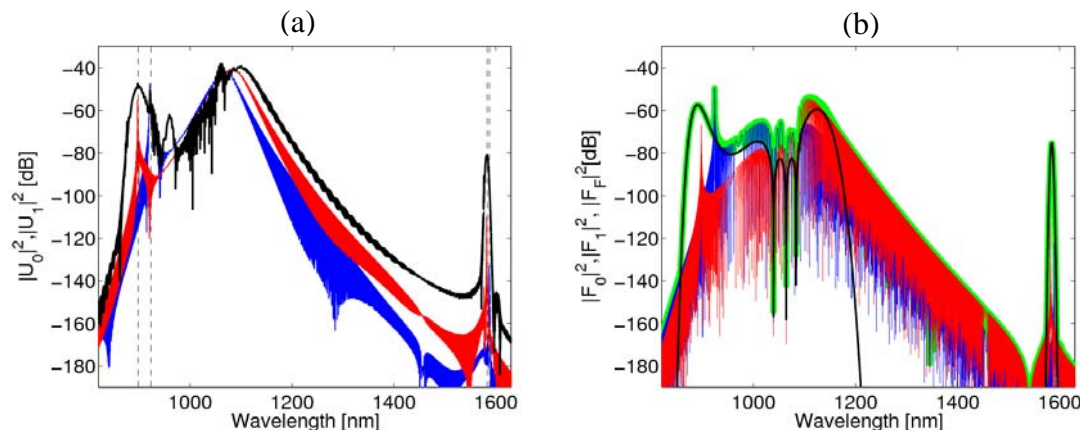


FIG. 3 – (a) NLSE numerical solutions after 4 m of MF: from individual solitons U_0 (blue) and U_1 (red) and from two-soliton collision (black); (b) analytical solutions for F_0 (blue), F_1 (red) and for the collision flash F_F (black); the green line combines the analytical solutions for F_0 , F_1 , F_F .

IV. CONCLUSION

We have shown that soliton-soliton collisions have a crucial role in shaping and enhancing DWs. Our study provides useful tools to interpret the spectra observable whenever interactions among pulses are present during the propagation in a microstructured fiber.

ACKNOWLEDGEMENT

We acknowledge the support of the project Dat@Diag financed by OSEO France and by Horiba Medical, and of the Italian Ministry of University and Research (grant no. 2012BFNWZ2).

REFERENCES

- [1] N. Akhmediev and M. Karlsson, “Cherenkov radiation emitted by solitons in optical fibers,” *Physical Review A*, vol. 51, pp. 2602-2607, 1995.
- [2] M. Erkintalo, G. Genty, and J. M. Dudley, “Giant dispersive wave generation through soliton collision,” *Optics Letters*, vol. 35, pp. 658-660, 2010.
- [3] G. Manili, A. Tonello, D. Modotto, M. Andreana, V. Couderc, U. Minoni, and S. Wabnitz, “Gigantic dispersive wave emission from dual concentric core microstructured fiber,” *Optics Letters*, vol. 37, pp. 4101-4103, 2012.

MESOSCOPIC PHOTONIC CRYSTALS BASED STABLE PLANAR CAVITIES

G. Magno^(1,2), A. Monmayrant^(2,3), M. Grande⁽¹⁾, F. Lozes-Dupuy^(2,3),
O. Gauthier-Lafaye^(2,3), G. Calò⁽¹⁾ and V. Petruzzelli⁽¹⁾

⁽¹⁾ Dipartimento di Ingegneria Elettrica e dell'Informazione (DEI),
Via Re David 200, Politecnico di Bari, 70125 Bari.

⁽²⁾ CNRS, LAAS, 7 avenue du colonel Roche, F-31400 Toulouse, France.

⁽³⁾ Univ. de Toulouse, LAAS, F-31400 Toulouse, France.

giovanni.magno@poliba.it

Abstract

Mesoscopic self-collimation is exploited to outwit instabilities in planar cavities allowing the conception of a novel class of stable microcavities. These show high Q factor and a peculiar 1D translational invariance along the defect, which is particularly attractive for biosensing, isolated object detection and lasing in active media.

Index Terms – Mesoscopic self-collimation, Photonic crystals, Microcavities.

I. INTRODUCTION

Self-collimating and controlled lateral dispersion based structures have captivated large research efforts since their demonstration in photonic crystals (PhC) [1]. In fact, these structures allow light to remain confined or to be focused (defocused) in a controlled way.

Mesoscopic Photonic Crystals (MPCs)[2] further extend the control on the lateral dispersion of light, offering several new degrees of freedom and introducing new features to be exploited. These structures can be described practically as multilayer periodic systems obtained by alternating slabs which lateral dispersion - characterized by the index of curvature n_c [2] - mutually compensates after one mesoscopic period, resulting in the phenomenon of mesoscopic self-collimation (MSC). In particular, MPCs with controlled reflectivity allow to envision two basic building blocks –antireflection structures and mirrors – that can be combined to conceive more complex devices based on MSC [3].

In this paper, a pair of MSC-mirrors will be exploited to design a novel class of stable microcavities. These, showing high Q factor and a peculiar 1D translational invariance along the defect, will be inspected by means of a well-established 2D-FDTD code [4].

II. DESIGN OF STABLE PLANAR MICROCAVITIES

Fig. 1(a) shows a drawing of a MPC obtained by alternating slabs of length d_1 of a 45-degree-tilted PhC (lattice constant a , air hole radius $r = 0.28a$) and slabs of length d_2 of bulk material ($n_{bulk} = 2.9$). To conceive the planar microcavity we will consider a 5-mesoscopic-period-long

version of the MPC-mirror described in [3], depicted in Fig. 1(b). Starting from this solution, we can easily design a Fabry-Perot-like cavity by placing two mirrors at the sides of a bulk slab defect of length L_d . This mirror shows an improved reflectivity ($R > 98\%$) if compared to its distributed Bragg reflector (DBR) counterpart ($R < 45\%$), when considering a plane wave at normal incidence. DBR counterpart is obtained by substituting the PhC slabs with a bulk material having a refractive index equal to the phase index of the PhC (n_{eq}). Moreover, MPC-mirror efficiently reflects back even an omnidirectional point source, as shown on Fig. 1(c) where the normalised transmitted and reflected power spectra, integrated along the monitor planes, are plotted for both the MPC-mirror and its DBR equivalent when the structure is excited by means of a point source. The first configuration shows a reflectivity higher than 68% whereas the latter is completely ineffective ($R < 5\%$).

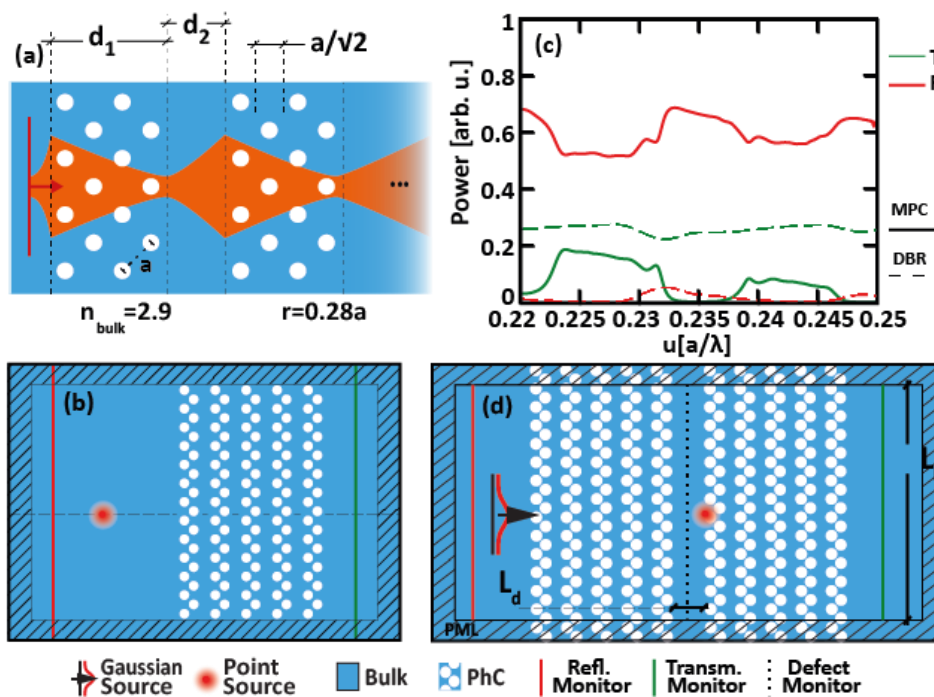


FIG. 1 – (a) Sketch of a MPC. (b) Sketch of the single MPC-mirror computational cell. (c) Normalised (green) transmittance and (red) reflectance, when (solid lines) a 5-period-long MPC mirror or (dashed lines) its DBR counterpart is considered, respectively. (d) Sketch of the whole cavity computational cell.

Subsequently, the planar cavity, depicted in Fig. 1(d), has been inspected and optimised by several simulations, as a function of L_d , when a pulsed point source is placed inside the defect. For a critical defect thickness $L_d = 5.336 [a]$ the highest obtained Q factor is ~ 12840 , which corresponds to a sharp resonance at $u_{cav} = 0.2351[a/\lambda]$ in the power spectrum calculated on a planar monitor located in the centre of the defect. Fig. 2(a) shows the Poynting vector for the scattered field

obtained by means of a continuous wave (CW) simulation performed at u_{cav} . On the left side of the input interface, the reflected beam is refocused, resembling the behaviour of a curved mirror. This behaviour allows the mode to remain steadily confined inside the defect. It is worth pointing out that, on the right of the input interface, a local maximum around $y = 0$ arises, which indicates the formation of the beam, unveiling the beamforming action in transmission of the MSC-mirror.

Thus, in order to inspect the excited mode, a CW simulation on the whole cavity is performed. Fig. 2(b) shows the energy density profile of the cavity after a normalised time of $t = 11.4 \cdot 10^4 [a]$. At this time, the stored energy in cavity reaches the 99% of its saturation level. Along the y -direction, the energy density remains confined thanks to the refocussing by the MPC-mirror, whereas along the x -direction, the energy confinement is due to a DBR-like mechanism. Moreover, if we excite the cavity by means of a source, with a Gaussian spatial profile, impinging on the cavity from the outside, with a waist along the y -direction of $17[a]$, the same energy distribution is achieved. Fig. 2(c) shows the transmitted and reflected power through the monitor shown in Fig. 1(d), normalised to the source power, as a function of the reduced time. When the cavity is fully charged the transmitted power is higher than 68%, the reflected power is almost 10% and the losses are almost 21%. Finally, Fig. 2(d) shows the x -component of the Poynting vector revealing that the transmitted power leaves the cavity as a Gaussian-like beam with the same waist as the source.

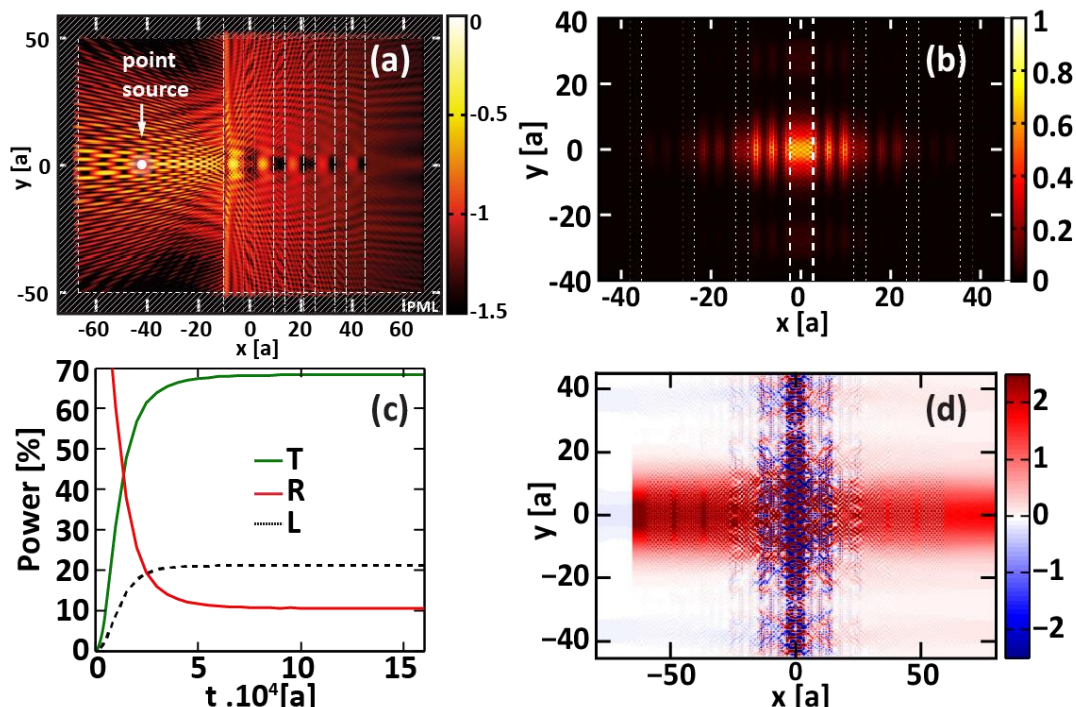


FIG. 2 – (a) Logarithm of the absolute value of the Poynting vector of the scattered fields when a single MPC-mirror at u_{cav} is considered. (b) Total energy density distribution. The superposed white dashed lines indicate the interfaces. (c) Transmittance (green curve), reflectance (red curve) and losses

(black dotted curve) as a function of the normalised time. (d) x -component of the Poynting vector at t equal to $11.4 \cdot 10^4 [a]$.

III. CONCLUSION

A novel stable MPC-mirror based planar microcavity has been designed. 2D-FDTD simulations show that, for a 5-mesoscopic-period-long-mirror cavity, a Q factor of 12840 is achieved. These results cannot be achieved by means of standard planar DBRs that lack for a lateral confinement mechanism provided here by the MPC-mirrors. Since the cavity mode properties depend neither on the vertical position nor on the vertical overall size of the cavity, a 2D confinement is achievable anywhere along the defect in an arbitrarily extended planar cavity. This greatly improves overlap chances between isolated objects and the confined mode for field enhancement, making this microcavity very attractive for optical biosensor applications. Moreover, thanks to the beamforming properties of the MPC-mirrors, this microcavity can be suitable for lasing in active media.

ACKNOWLEDGEMENT

The research has been conducted in the framework of the European Cooperation in Science and Technology ("COST") Action MP0805. G. Calò and V. Petruzzelli thank the Photonic Interconnect Technology for Chip Multiprocessing Architectures ("PHOTONICA") project under the Fondo per gli Investimenti della Ricerca di Base 2008 ("FIRB") program, funded by the Italian government and thanks to the facilities offered by the Apulia region laboratory project "Synthesis and characterization of new organic and nanostructured materials for electronics, photonics, and advanced technologies". M. G. thanks the U.S. Army International Technology Center Atlantic for financial support (W911NF-12-1-0292).

REFERENCES

- [1] H. Kosaka, T. Kawashima, A. Tomita, M. Notomi, T. Tamamura, T. Sato, and S. Kawakami, "Self-collimating phenomena in photonic crystals," *Appl. Phys. Lett.*, vol. 74 (9), pp. 1212–1214, 1999.
- [2] J. Arlandis, E. Centeno, R. Pollès, and A. Moreau, "Mesoscopic self-collimation and slow light in all-positive index layered photonic crystals," *Phys. Rev.*, pp. 1–4, 2012.
- [3] G. Magno, M. Grande, A. Monmayrant, F. Lozes-Dupuy, O. Gauthier-Lafaye, G. Calò, and V. Petruzzelli, "Controlled reflectivities in self-collimating mesoscopic photonic crystal," *J. Opt. Soc. Am. B*, vol. 31 (2), pp. 355–359, Jan. 2014.
- [4] A. F. Oskooi, D. Roundy, M. Ibanescu, P. Bermel, J. D. Joannopoulos, and S. G. Johnson, "MEEP: A flexible free-software package for electromagnetic simulations by the FDTD method," *Comput. Phys. Commun.*, vol. 181 (3), pp. 687–702, 2010.

Exploitation of Whispering Gallery Mode Resonances for Characterization of Rare-Earth Doped Glass Devices

G. Palma⁽¹⁾, L. De Palma⁽¹⁾, T. Yano⁽²⁾, V. Nazabal⁽³⁾, T. Kishi⁽²⁾, A. Moréac⁽⁴⁾, M. Ferrari⁽⁵⁾, F. Prudenzano⁽¹⁾

⁽¹⁾Politecnico di Bari, DEI - Dipartimento di Ingegneria Elettrica e dell'Informazione, Via E. Orabona 4, Bari, Italy, 70125

⁽²⁾Tokyo Institute of Technology, Department of Chemistry and Materials, 2-12-1 Ookayama, Meguro-ku Tokyo 152-8550, JAPAN,

⁽³⁾ISCR, UMR UR1-CNRS 6226, Université de RENNES 1, 35042 RENNES Cedex, FRANCE

⁽⁴⁾IPR, UMR CNRS 6626, Université Rennes 1, 35042 Rennes Cedex, FRANCE

⁽⁵⁾IFN-CNR CSMFO Lab., Via alla Cascata 56 c Povo, 38123 Trento, Italy
francesco.prudenzano@poliba.it

Abstract

The resonance of the whispering gallery modes is exploited to recover the ion-ion interaction parameters of an erbium Er^{3+} doped glass amplifier. The amplifier is constituted of a tapered chalcogenide fiber coupled to a Er^{3+} -doped chalcogenide microsphere. It has been modeled via a dedicated 3D numerical model, based on the coupled mode theory and solving the rate equations. The particle swarm optimization PSO approach has been employed to recover the spectroscopic parameters describing the ion-ion processes in Er^{3+} ions. The numerical results demonstrate the effectiveness of the proposed approach, they are interesting since the measurement of the energy transfer parameters needs a peculiar high-cost instrumentation.

Index Terms – Microresonator; lasers; optical fiber, chalcogenide glass, Whispering Gallery Mode propagation.

I. INTRODUCTION

Whispering gallery modes WGM resonances in dielectric microspheres have been extensively investigated and exploited for various applications [1]-[2]. Low threshold lasers with very narrow emission linewidth can be obtained by exciting WGMs in rare-earth doped microspheres. In a previous work [3] the particle swarm optimization (PSO) approach has been proposed by the authors to perform an efficient design of an amplifier constituted of a tapered chalcogenide fiber coupled to a Er^{3+} -doped chalcogenide microsphere. The PSO approach was preferred to the conventional design procedures, because in the latter ones the solution of the rate equation and power propagation equations is generally performed by optimizing, one by one,

each design parameter, with high time consumption. In fact, the nonlinearity of the equations, due to ion-ion interactions makes conventional algorithms computationally expensive. In this paper, the PSO approach is applied with the aim of solving the inverse problem, i.e. to recover the ion-ion interaction parameters of the rare earth, by supposing known (i.e. measured) the gain of an amplifying system operating close to 2.7 μm and based on Er^{3+} -doped chalcogenide microsphere coupled to a tapered fiber. The need to investigate chalcogenide microsphere is linked to the fabrication of intriguing preliminary microsphere prototypes of chalcogenide glass with the composition of $\text{Ga}_5\text{Ge}_{20}\text{Sb}_{10}\text{S}_{65}$ and doped with Erbium. Partly truncated spheres, called ‘supersphere’, working as a whispering gallery mode (WGM) resonator around its equatorial plane, have been lately fabricated via “surface-tension mold (StM) technique” [3-4]. The complete and accurate characterization of these prototypes is needed for microsphere design and refinement. The recovering of ion-ion interaction parameters plays a key role for the development of efficient fiber amplifiers or laser, since they can limit the gain/lasing efficiency.

II. THEORY

The amplifying system is constituted by a tapered optical fiber placed close to the equator of an Er^{3+} -doped chalcogenide microsphere. It is illustrated in Fig. 1 (a). An accurate 3D model for Er^{3+} -doped chalcogenide microspheres is employed for calculating the fitness function of the PSO procedure [5-6]. The developed numerical code includes the coupled mode theory and the rate equations model, the modal electromagnetic field distribution of the propagation modes in both tapered fiber and WGM in microsphere. The most relevant active phenomena in Er^{3+} -doped chalcogenide glass such as the absorption rates, at both pump and signal wavelengths, the stimulated emission rate at signal wavelength, the amplified spontaneous emission noise (ASE), the lifetime and branching ratios of the considered energy levels, the ion-ion energy transfers and the excited state absorption (ESA) have been considered. The optical and spectroscopic parameters employed in the model have been measured on chalcogenide glass [7]. The fitness function, to be minimized by the PSO, is the difference $F = |G_S - G_T|$; i) G_S is the amplifier gain G , simulated for the input pump power $P_p = 100$ mW, pump wavelength $\lambda_p = 980$ nm, signal wavelength $\lambda_s = 2.7 \mu\text{m}$, input signal power $P_s = -50$ dBm; thickness of the erbium-doped region $t = 3 \mu\text{m}$, erbium concentration $N_{\text{Er}} = 0.5$ w%; microsphere radius $R_o = 25 \mu\text{m}$; taper fiber radius $a = 700$ nm; taper angle $\delta = 0.03$ rad; microsphere-fiber gap $g = 560$ nm [3][5]; ii) G_T is the amplifier gain calculated for the up-dated PSO tentative solution. After a preliminary investigation, both social and cognitive PSO parameters have been chosen equal to $S = C = 1.494$, inertia weight has been linearly spaced from $I = 0.9$ to $I = 0.4$. The number

of particles is $M=24$. The moduli of E_x electric field component in the fiber and E_θ electric field component in the $\text{Ga}_5\text{Ge}_{20}\text{Sb}_{10}\text{S}_{65}$ microsphere without rare earth are illustrated in Fig. 1(b). The erbium ion-ion interaction parameters to be recovered via PSO are C_{33} , C_{22} and C_{41} , pertaining to the transitions illustrated in Fig. 2. Their values, employed for amplifier gain G_S calculation (target values) and recovered by PSO are reported in Table I. In all the cases, a deviation between them less than 10% is found.

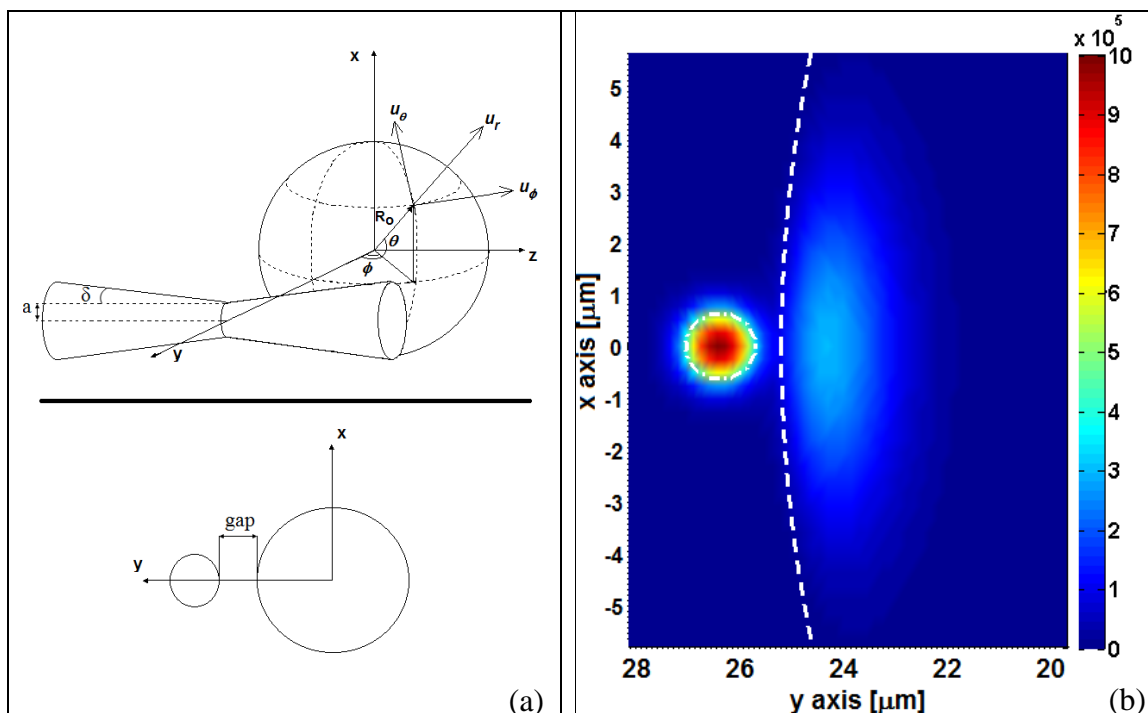


FIG. 1 – a) Geometry of the amplifying system made of fiber taper coupled to the microsphere; b) Moduli of E_x electric field component in the fiber and E_θ in the $\text{Ga}_5\text{Ge}_{20}\text{Sb}_{10}\text{S}_{65}$ microsphere without rare earth.

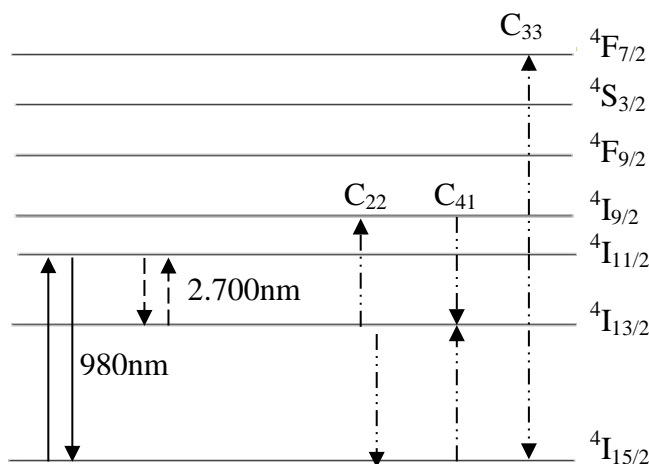


FIG. 2 – Erbium ion energy levels.

TABLE I – PSO RECOVERED PARAMETERS

Parameter	PSO recovered value	Target
C_{33} [m ³ /s]	1.97×10^{-23}	2×10^{-23}
C_{22} [m ³ /s]	2.7×10^{-23}	3×10^{-23}
C_{41} [m ³ /s]	4.7×10^{-24}	5×10^{-24}

III. CONCLUSION

The particle swarm optimization approach PSO has been employed to recover the parameters describing the Er³⁺ ion-ion interactions. The numerical results demonstrate the effectiveness of the proposed approach and are interesting since the measurement of the ion-ion parameters needs peculiar and high cost laboratory equipment.

ACKNOWLEDGEMENTS

This work has been partially supported within the MIUR plans: PON01 01224 “Sviluppo di tecnologie in guida d’onda integrata (SIW) per applicazioni ICT a microonde”; PONa3 00298 “Potenziamento delle strutture e delle dotazioni scientifiche e tecnologiche del polo scientifico e tecnologico Magna Grecia”; PON02_00576_3329762 Sistemi avanzati mini-invasivi di diagnosi e radioterapia” AMIDERHA.

REFERENCES

- [1] A. B. Matsko, and V. S. Ilchenko, “Optical Resonators With Whispering-Gallery Modes—Part I: Basics,” *IEEE Journal of Selected Topics in Quantum Electronics* 12(1), pp. 3-13, 2006.
- [2] Hai-Cang Ren, F. Vollmer, S. Arnold, A. Libchaber, “High-Q microsphere biosensor-analysis for adsorption of rodlike bacteria,” *Opt. Express* 15, pp. 17410-17423, 2007.
- [3] G. Palma, P. Bia, L. Mescia, T. Yano, V. Nazabal, J. Taguchi, A. Moreac, and F. Prudenzano, “Design of fiber coupled Er³⁺: chalcogenide microsphere amplifier via particle swarm optimization algorithm”, *Opt. Eng.* 53, p. 071805, November 2013.
- [4] T. Yano, S. Shibata, and T. Kishi, “Fabrication of micrometer-size glass solid immersion lens”, *J. Appl. Phys. B* 83, pp. 167–170, 2006.
- [5] L. Mescia, P. Bia, O. Losito, F. Prudenzano, “Design of Mid-IR Er³⁺-doped microsphere laser,” *IEEE Photonics Journal* 5, pp. 1501308, 2013.
- [6] L. Mescia, A. Giaquinto, G. Fornarelli, G. Acciani, M. De Sario, F. Prudenzano, “Particle swarm optimization for the design and characterization of silica-based photonic crystal fiber amplifiers,” *Journal of Non-Crystalline Solids* 357, pp 1851–1855, 2011.
- [7] V. Moizan, Nazabal, V., Troles, J., Houizot, P., Adam, J.-L., Smektala, F., Gadret, G., Pitois, S., Doualan, J.-L., Moncorgé, R., Canat, G., “Er³⁺-doped GeGaSbS glasses for mid-IR fibre laser application: Synthesis and rare earth spectroscopy”, *Optical Material*, 31 pp.39-46, 2008.

RADIATING SHOCK WAVES IN PASSIVE OPTICAL RESONATORS

S. Malaguti ⁽¹⁾, M. Conforti ⁽²⁾, G. Bellanca ⁽¹⁾, S. Trillo ⁽¹⁾

⁽¹⁾ Department of Engineering, University of Ferrara, Italy

⁽²⁾ PhLAM/IRCICA, CNRS-Université Lille 1, Villeneuve d'Ascq, France
stefano.trillo@unife.it

Abstract

We show that wave-breaking can occur in externally driven passive nonlinear resonators operating in the regime of weak normal dispersion. In this regime the cavity dynamics is ruled by shock waves of the mixed dissipative-dispersive type, and the output is characterized by strong spectral broadening with enhanced spectral peaks due to resonant radiation shed by the shock fronts.

Index Terms – Nonlinearity, Resonators, Shock-waves, Instabilities.

I. INTRODUCTION

Passive nonlinear cavities, both in fiber ring or micro-resonator configurations, are employed nowadays as switches, addressable optical buffers and frequency comb generators. Their dynamical behavior is extremely rich encompassing bistability, extended modulational and convective instabilities, symmetry breaking, self-pulsing, and soliton formation. These phenomena are well described in the framework of a mean-field approach where the external driving field and the damping are distributed along an unfolded resonator [1]. In the framework of this model, also known as Lugiato-Lefever equation [2], we show here that a novel regime is possible, when the cavity operates in the regime of weak normal group-velocity dispersion (GVD) [3]. In this case the intracavity field can undergo a gradient catastrophe forming dispersive shock waves (DSWs), i.e. expanding trains of fast oscillations that connect two quasi-continuous states of the cavity lying on different branches. When excited close to the zero-dispersion wavelength, the shock fronts radiate energy into linear waves at proper (phase-matching) frequencies, similarly to what recently reported for the cavity-less case [4-5].

II. THE MODEL FOR SHOCK WAVE FORMATION

Let us consider the following equation that rules the evolution of the normalized intracavity field u in dimensionless units

$$i\varepsilon \frac{\partial u}{\partial z} - \frac{\varepsilon^2 \beta_2}{2} \frac{\partial^2 u}{\partial t^2} - i \frac{\varepsilon^3 \beta_3}{6} \frac{\partial^3 u}{\partial t^3} + |u|^2 u = [\delta - i\alpha] u + i\sqrt{P}, \quad (1)$$

where δ is the detuning from cavity resonance, $P=P(t)$ is the external driving power, and α is the loss coefficient. In Eq. (1) we make use, without loss of generality, of a semiclassical scaling by introducing the

small scale parameter $\varepsilon=[L/L_d]^{1/2}$, whose powers weight the dispersive terms. Here L and $L_d=t_0^2/k''$ are the cavity length and dispersion length associated with duration t_0 of the input and physical GVD k'' . Furthermore $\beta_2=1$ ($\beta_2=-1$) for normal (anomalous) GVD, while β_3 weights third-order dispersion (TOD), while z is the unfolded distance along the resonators in units of length scale $[LL_d]^{1/2}$, (i.e., $z=\varepsilon$ corresponds to a single round-trip).

First, we consider the limit in which TOD is negligible. The steady state response $P_u=P_u(P)$, $P_u=|u|^2$ being the intracavity power, is bistable (i.e., three-folded, see Fig. 1a) whenever $\delta>3^{1/2}\alpha$ [1,2]. The bistable regime is envisaged to be the most favorable one for the developments of shock waves, provided that the GVD is normal ($\beta_2=1$), so that it does not counteract the nonlinear (Kerr) effect. Indeed, in this case, shock waves can develop between states belonging to the different branches (with positive slopes) of the bistable response. An example of this type is shown in Fig. 1 for the case of small losses α . The cavity is biased on the lower branch of the bistable response (blue dot in Fig. 1a) and an activation pulse (red curve in Fig. 1a) that exceeds the power of the first bistable knee (corresponding to power P_u^-), brings the central part of the intracavity field on the upper branch. This dynamics is accompanied by steepening of the pulse tails until symmetric virtually infinite gradients are formed (point of catastrophe). After this stage, the GVD becomes important and regularize the quasi-vertical fronts via the emission of fast wavetrains which expand within characteristic shock fans. This stage leads to so-called DSWs, shown in Fig. 1b,c.

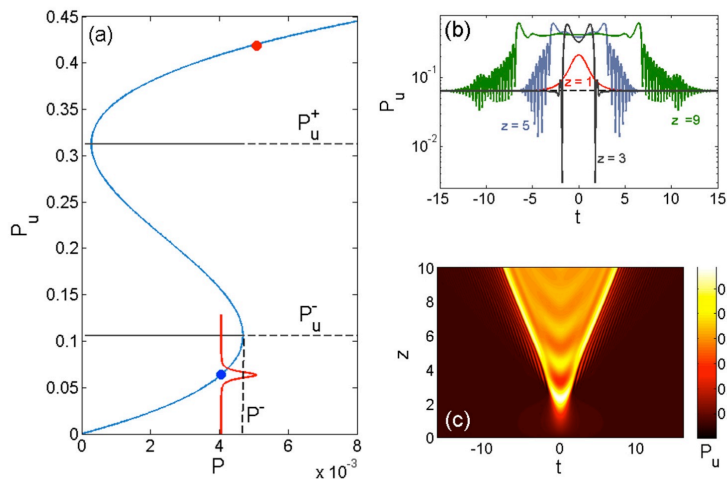


FIG. 1 – Generation of a DSW: (a) bistable response and activation pulse on top of the CW bias (red curve); (b) snapshots of the intracavity field at different number of circulation; (c) temporal dynamics. Here $\varepsilon=0.1$, $\alpha=0.03$, $\delta=\pi/10$.

Noteworthy, even if the activation pulse is arbitrarily weak, DSWs can form via a different mechanism which has no similarity for the case of free propagation (i.e., cavity-less case). In this case the upper branch is

reached via spontaneous modulation instability of the CW bias, which can occur due to the cavity boundary conditions (for free propagation in the normal GVD regime, no modulation instability is possible).

We also emphasize that, for higher loss coefficients, the shock waves acquire a mixed dissipative-dispersive structure, where the visibility of the oscillations is progressively reduced and the shock edges are smoothed out.

I. RADIATIVE EFFECTS FROM SOLITONS AND SHOCK WAVES

Whenever shock waves propagate in the presence of a nonvanishing TOD (i.e., when the cavity is pumped in the vicinity of a zero dispersion point), a resonance between the nonlinear fronts of the shock and linear waves can occur. Such resonance mechanism has been deeply investigated for solitons (i.e. in the anomalous GVD regime where Kerr effect and GVD mutually compensate) in the free-running case [6]. Here we extend the theory to passive resonators. A perturbative approach allows us to treat in a unified way the two cases of cavity solitons, namely localized solutions existing on a finite background in the anomalous GVD regime, and shock waves existing in the normal GVD regime. Such an approach yields the frequency of the resonant radiation $\omega = \omega_{RR}$ as a solution of the following algebraic phase-matching equation

$$\left[\beta_3 \frac{(\epsilon\omega)^3}{6} + \beta_2 \frac{(\epsilon\omega)^2}{2} - \frac{(\epsilon\omega)}{V} - \delta \right] + 2P_{uH} = 0 \quad (2)$$

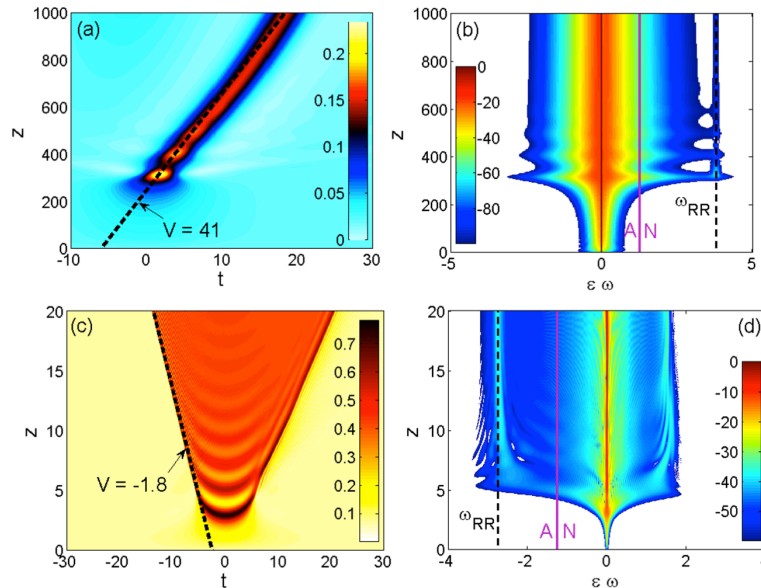


FIG. 2 – Resonant radiation from a cavity soliton (upper row) and a DSW (lower row): (a,c) Temporal evolutions (slope of dashed line gives velocity V) ; (b,d) Spectral evolutions (the vertical solid line separates the spectral domains characterized by anomalous (A) and normal (N) GVD, dashed black line correspond to ω_{RR} from Eq. (2)). Here $\epsilon=0.1$, $\alpha=0.03$, $\delta=\pi/10$, $\beta_3=0.5$.

In Eq. (2) P_{uH} is the power of the upper state and V stands for the velocity of the soliton or shock wave in the absolute frame used in Eq. (1). Physically $1/V$ represents the deviation from natural group-velocity expressed in terms of inverse velocities. While the term that contains V in Eq. (2) is crucial to determine the radiated frequency from shock waves that propagate with their own velocity, the same term becomes negligible for solitons. In both cases the radiated linear wave lies in the region of GVD of opposite sign with respect to the pump. As shown in Fig. 2, the frequencies of the radiated linear waves predicted from Eq. (2) are in excellent agreement with those found from numerical simulation of Eq. (1). Comparing Fig. 2a (soliton case) and Fig. 2c (shock wave), the different role of velocity in the two cases is clear.

II. CONCLUSION

In summary, we have analyzed in detail the wave-breaking mechanism in passive nonlinear resonators. We expect the shock fronts to radiate measurable linear waves. Similar effects are expected to occur in four-wave mixing with strong impact on the generation of frequency combs.

ACKNOWLEDGEMENT

The authors acknowledge funding by MIUR (grant PRIN 2012BFNWZ2).

REFERENCES

- [1] M. Haelterman, S. Trillo, and S. Wabnitz, "Additive-modulation-instability ring laser in the normal dispersion regime of a fiber", *Opt. Lett.* 17, 745 (1992).
- [2] L. A. Lugiato and R. Lefever, "Spatial dissipative structures in passive optical systems", *Phys. Rev. Lett.* 58, 2209 (1987).
- [3] S. Malaguti, G. Bellanca, S. Trillo, "Wave-breaking in coherently driven passive cavities", *Opt. Lett.* (2014), in press.
- [4] M. Conforti and S. Trillo, "Dispersive wave emission from wave breaking", *Opt. Lett.* 38, 3815 (2013); M. Conforti, F. Baronio, and S. Trillo, "Resonant radiation shed by dispersive shock waves", *Phys. Rev. A* 89, 013807 (2014).
- [5] K. E. Webb, Y. Q. Xu, M. Erkintalo, and S. G. Murdoch, "Generalized dispersive wave emission in nonlinear fiber optics", *Opt. Lett.* 38, 151 (2013).
- [6] N. Akhmediev and M. Karlsson, "Cherenkov radiation emitted by solitons in optical fibers", *Phys. Rev. A* 51, 2602 (1995).

LABORATORY TESTS ASSESSING A NONREDUNDANT NF-FF TRANSFORMATION TECHNIQUE WITH PLANE-POLAR SCANNING

F. D'Agostino, F. Ferrara, C. Gennarelli, R. Guerriero, M. Migliozi

D.I.In., Università di Salerno, via Giovanni Paolo II, 132 - 84084 Fisciano, Italy
{fdagostino, flferrara, cgennarelli, rguerriero, mmigliozi}@unisa.it

Abstract

The experimental validation of an effective near-field – far-field (NF-FF) transformation with plane-polar scanning, particularly suitable for quasi-planar antennas, is provided. Such a technique is based on the nonredundant sampling representations of the electromagnetic fields and uses an oblate ellipsoid to model the antenna. A two-dimensional optimal sampling expansion allows the efficient reconstruction of the voltage data needed by the classical plane-rectangular NF-FF transformation. It is so possible to remarkably lower the number of NF data to be acquired, thus reducing in a significant way the required measurement time. Some experimental results carried out at the UNISA Antenna Characterization Lab and assessing the effectiveness of the technique are shown.

Index Terms – antenna measurements, NF-FF transformations, plane-polar scanning, nonredundant representations of electromagnetic fields.

I. INTRODUCTION

Among the near-field–far-field (NF-FF) transformations, that using the plane-polar scanning (Fig. 1) has attracted considerable attention due to its peculiar characteristics [1]. The large computer time required in the earliest approach [1] to recover the antenna far field has been drastically reduced in [2] by reconstructing the plane-rectangular data from the plane-polar ones via the bivariate Lagrange interpolation, thus enabling the use of the FFT algorithm. By exploiting the spatial bandlimitation properties of radiated electromagnetic (EM) fields [3], an optimal sampling interpolation (OSI) algorithm of central type, which minimizes the truncation error, has been developed in [4] to accurately reconstruct the plane-rectangular NF data from the plane-polar ones. At variance of the previous approaches, the number of data for each ring stays bounded even if the ring radius goes toward infinity and, on increasing the measurement plane distance, the radial step can be remarkably larger than the previously adopted one. However, the overall number of samples is still unbounded when the radius of the scanning zone approaches infinity. At last, an efficient sampling representation over a plane from a nonredundant number of plane-polar samples, which stays finite also for an unbounded scanning plane, has been developed in [5], by applying the nonredundant sampling representations of the EM field [6] and assuming the antenna under test (AUT) as enclosed in an oblate ellipsoid, a source modelling particularly suitable for quasi-planar antennas. It has been so possible to obtain a remarkable reduction of the required NF data and, as a consequence, of the measurement time.

Aim of this work is just to provide the experimental validation of the NF-FF transformation with plane-polar scanning [5] based on the oblate ellipsoidal modelling of the AUT. Such a validation has been carried out at the antenna characterization laboratory of the University of Salerno.

II. NONREDUNDANT SAMPLING REPRESENTATION ON A PLANE

Let us consider a quasi-planar AUT enclosed in the smallest oblate ellipsoid Σ

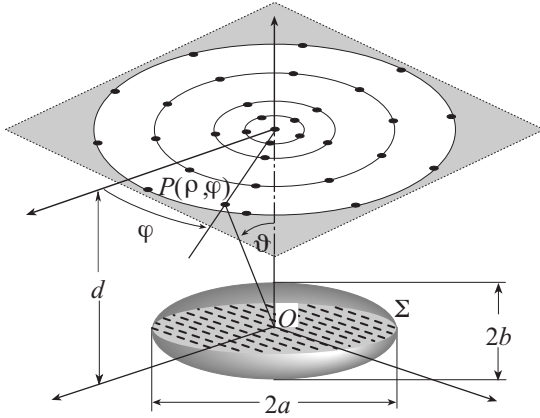


FIG. 1 – Plane-polar scanning.

$\gamma(\xi)$ is a proper phase function, and $\underline{r} = \underline{r}(\xi)$ is an optimal parameterization used to describe the observation curve (radial line or ring). The error, occurring when $\tilde{V}(\xi)$ is approximated by a bandlimited function, is negligible as the bandwidth exceeds a critical value W_ξ [6]. Therefore, it can be effectively controlled by choosing a bandwidth $\chi'W_\xi$, with $\chi' > 1$.

The bandwidth W_ξ and parameterization ξ relevant to a radial line, and the corresponding phase function γ are [5, 6]:

$$W_\xi = \beta \ell' / 2\pi ; \quad \xi = (\pi / 2) E(\sin^{-1}u | \varepsilon^2) / E(\pi / 2 | \varepsilon^2) \quad (1)$$

$$\gamma = \beta a \left[v \sqrt{(v^2 - 1) / (v^2 - \varepsilon^2)} - E(\cos^{-1} \sqrt{(1 - \varepsilon^2) / (v^2 - \varepsilon^2)} | \varepsilon^2) \right] \quad (2)$$

where $\ell' = 4a E(\pi / 2 | \varepsilon^2)$ is the length of the ellipse C' , intersection between Σ and the meridian plane through the observation point P , β is the wavenumber, $E(\cdot | \varepsilon^2)$ denotes the elliptic integral of second kind, and $u = (r_1 - r_2) / 2f$ and $v = (r_1 + r_2) / 2a$ are the elliptic coordinates, $r_{1,2}$ being the distances from P to the foci of C' . Moreover, $\varepsilon = f/a$ is the eccentricity of C' and $2f$ the focal distance. It is worthy to note that, in any meridian plane, the curves $\gamma = \text{const}$ and $\xi = \text{const}$ are ellipses and hyperbolas confocal to C' [5, 6].

On a ring, due to the symmetry, γ is constant and it is convenient to choose the angle φ as parameter. The related bandwidth [5, 6] is

$$W_\varphi(\xi) = \beta a \sin \vartheta_\infty(\xi) \quad (3)$$

$\vartheta_\infty = \sin^{-1}u$ being the ϑ angle of the asymptote to the hyperbola through P .

In light of the above results, the voltage at P can be evaluated [5, 6] via the following two-dimensional OSI expansion:

$$\tilde{V}(\xi(\vartheta), \varphi) = \sum_{n=n_0-q+1}^{n_0+q} \left\{ G(\xi, \xi_n, \bar{\xi}, N, N'') \sum_{m=m_0-p+1}^{m_0+p} \tilde{V}(\xi_n, \varphi_{m,n}) G(\varphi, \varphi_{m,n}, \bar{\varphi}, M_n, M_n'') \right\} \quad (4)$$

where $2q, 2p$ are the number of retained samples along ξ and φ , respectively, $n_0 = \text{Int}(\xi / \Delta\xi)$, $m_0 = \text{Int}(\varphi / \Delta\varphi_n)$, $\bar{\xi} = q\Delta\xi$, $\bar{\varphi} = p\Delta\varphi_n$,

$$\xi_n = n\Delta\xi = 2\pi n / (2N'' + 1) ; \quad N'' = \text{Int}(\chi N') + 1 ; \quad N' = \text{Int}(\chi' W_\xi) + 1 \quad (5)$$

$$\varphi_{m,n} = m\Delta\varphi_n = 2\pi m / (2M_n'' + 1) ; \quad M_n'' = \text{Int}(\chi M_n') + 1 ; \quad M_n' = \text{Int}[\chi^* W_\varphi(\xi_n)] + 1 \quad (6)$$

$$\chi^* = 1 + (\chi' - 1) \left[\sin \vartheta_\infty(\xi_n) \right]^{-2/3}; \quad N = N'' - N'; \quad M_n = M_n'' - M_n' \quad (7)$$

$\chi > 1$ is an oversampling factor needed to control the truncation error [6], $\text{Int}(x)$ denotes the integer part of x , and

$$G(\alpha, \alpha_k, \bar{\alpha}, L, L'') = \Omega_L[(\alpha - \alpha_k), \bar{\alpha}] D_{L'}(\alpha - \alpha_k) \quad (8)$$

Moreover,

$$D_{L'}(\alpha) = \frac{\sin[(2L'' + 1)\alpha/2]}{(2L'' + 1) \sin(\alpha/2)}; \quad \Omega_L(\alpha, \bar{\alpha}) = \frac{T_L[2\cos^2(\alpha/2)/\cos^2(\bar{\alpha}/2) - 1]}{T_L[2/\cos^2(\bar{\alpha}/2) - 1]} \quad (9)$$

are the Dirichlet and Tschebyscheff sampling functions, respectively, $T_L(\alpha)$ being the Tschebyscheff polynomial of degree L .

By using the expansion (4), it is possible to accurately evaluate V_φ and V_ρ at the points needed by the classical plane-rectangular NF-FF transformation [7]. It must be stressed that the probe corrected formulas in [7] are valid as long as the probe maintains its orientation with respect to the AUT and this requires its co-rotation with the AUT. This can be avoided by using a probe exhibiting only a first-order azimuthal dependence in its radiated far field. In such a case, the voltages V_V and V_H (measured by the probe and the rotated probe with co-rotation) can be evaluated from the knowledge of V_φ and V_ρ through the relations:

$$V_V = V_\varphi \cos \varphi - V_\rho \sin \varphi; \quad V_H = V_\varphi \sin \varphi + V_\rho \cos \varphi \quad (10)$$

III. EXPERIMENTAL RESULTS

The described NF-FF transformation has been experimentally assessed in the anechoic chamber of the Antenna Characterization Lab of the University of Salerno, equipped with a plane-polar NF facility system, besides the cylindrical and spherical ones. The considered antenna is a X-band flat plate slot array made by Rantec Microwave Systems Inc., having a diameter of about 46 cm, located on the plane $z = 0$ and operating at 9.3 GHz. This AUT has been modelled by an oblate ellipsoid with $a = 23.55$ cm and $b = 8.06$ cm, and the probe voltages have been collected on a circular zone of radius 110 cm on a plane at distance $d = 15.0$ cm from the AUT.

The amplitudes of the reconstructed voltages V_φ and V_ρ relevant to the radial lines at $\varphi = 30^\circ$ and $\varphi = 90^\circ$ are compared in Figs. 2 and 3 with those directly measured. As can be seen, the reconstructions are very accurate. At last, the FF patterns in the principal planes E and H reconstructed from the plane-polar NF data are compared in Figs. 4 and 5 with those recovered by employing the plane-rectangular scanning system available in an anechoic chamber of the antenna characterization laboratories of Selex ES. Although these reconstructions have been obtained with two different NF scanning techniques in two different anechoic chamber and, as a consequence, in quite different environmental conditions, a reasonably good agreement results.

It can be interesting to compare the number (2120) of used plane-polar samples, with that (21898) required by the previous NF-FF transformation [4] based on the spatial bandwidth properties of EM fields and with the one (29105) needed by applying the Rahmat-Samii's approaches [1, 2].

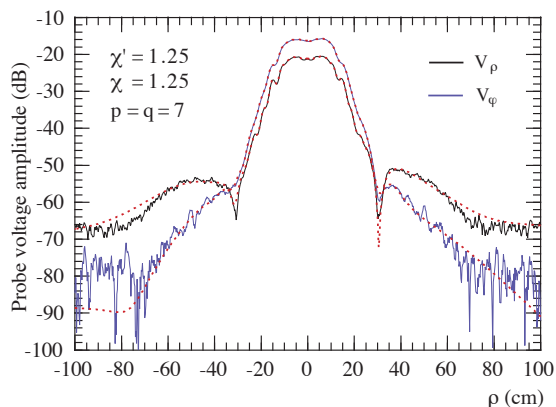


FIG. 2 – Amplitudes of V_φ , V_ρ on the radial line at $\varphi = 30^\circ$. Solid line: measured. Dashed line: recovered from plane-polar NF data.

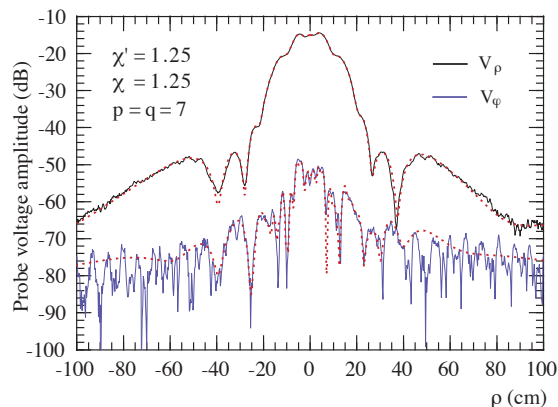


FIG. 3 – Amplitudes of V_φ , V_ρ on the radial line at $\varphi = 90^\circ$. Solid line: measured. Dashed line: recovered from plane-polar NF data.

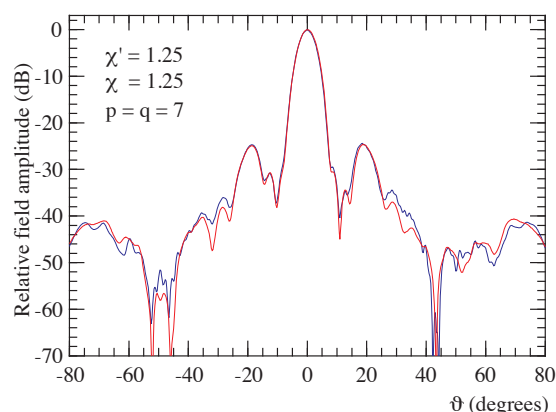


FIG. 4 – E-plane pattern. Blue line: recovered from plane-rectangular NF data. Red line: recovered from plane-polar NF data.

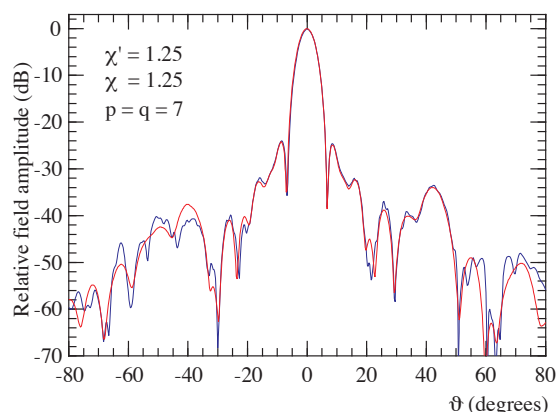


FIG. 5 – H-plane pattern. Blue line: recovered from plane-rectangular NF data. Red line: recovered from plane-polar NF data.

REFERENCES

- [1] Y. Rahmat-Samii, V. Galindo Israel, and R. Mittra, "A plane-polar approach for far-field construction from near-field measurements," *IEEE Trans. Antennas Prop.*, vol. AP-28, pp. 216-230, March 1980.
- [2] M.S. Gatti and Y. Rahmat-Samii, "FFT applications to plane-polar near-field antenna measurements," *IEEE Trans. Antennas Prop.*, vol. 36, pp. 781-791, June 1988.
- [3] O.M. Bucci and G. Franceschetti, "On the spatial bandwidth of scattered fields," *IEEE Trans. Antennas Prop.*, vol. AP-35, pp. 1445-1455, Dec. 1987.
- [4] O.M. Bucci, C. Gennarelli, and C. Savarese, "Fast and accurate near-field-far-field transformation by sampling interpolation of plane-polar measurements," *IEEE Trans. Antennas Prop.*, vol. 39, pp. 48-55, Jan. 1991.
- [5] O.M. Bucci, F. D'Agostino, C. Gennarelli, G. Riccio, and C. Savarese, "NF-FF transformation with plane-polar scanning: ellipsoidal modelling of the antenna," *Automatika*, vol. 41, pp. 159-164, 2000.
- [6] O.M. Bucci, C. Gennarelli, and C. Savarese, "Representation of electromagnetic fields over arbitrary surfaces by a finite and nonredundant number of samples," *IEEE Trans. Antennas Prop.*, vol. 46, pp. 351-359, March 1998.
- [7] E.B. Joy, W.M. Leach, G.P. Rodrigue, and D.T. Paris, "Applications of probe-compensated near-field measurements," *IEEE Trans. Antennas Prop.*, vol. AP-26, pp. 379-389, May 1978.

FABRY-PEROT ANTENNA WITH IMPROVED BANDWIDTH

G. Di Massa, H. O. Moreno, S. Costanzo
Dip. di Ing. Informatica, Modellistica, Elettronica e Sistemistica
Università della Calabria
dimassa@dimes.unical.it

Abstract

A new approach is proposed for the analysis and design of a planar Fabry-Perot antenna with improved bandwidth. The complete modal analysis of the field into the cavity leads to a simplified equivalent circuit, able to provide a reliable description of the coupling with the feeding waveguide, as well as to compute the equivalent currents on the radiating apertures, thus obtaining the radiated far-field. The proposed approach is preliminary validated on a metallic Fabry-Perot antenna structure. Then, a modified configuration based on a cavity partially-filled with a dielectric substrate is assumed to obtain a Fabry-Perot antenna with improved bandwidth features.

Index Terms – Fabry Perot Antenna, Modal analysis, Cavity Antennas.

I. INTRODUCTION

In this paper, a Fabry-Perot antenna composed by an open resonator with plane mirrors is considered. An equivalent circuit based on a modal analysis of the open resonator is adopted for the characterization of the proposed structure, in order to optimize the coupling between the feeding rectangular waveguide and the planar open cavity. Preliminary results on the metallic Fabry-Perot antenna are discussed as predicted by the adopted equivalent circuit. Then, a modified Fabry-Perot configuration based on the insertion of a dielectric substrate, is proposed to significantly improve the operation bandwidth of the original metallic Fabry-Perot structure. Experimental results on a K_u band partially-filled 8×8 elements array are successfully reported to demonstrate a radiation bandwidth improvement of about 48%.

II. METALLIC FABRY-PEROT ANTENNA

The antenna is a parallelepiped flat structure with a square flat metallic base that is coupled by a slot to a rectangular waveguide, and a radiating face composed by a metallic sheet where the radiating slots are cut (Fig. 1).

Following what developed in [1,2,3], the coupling between the field inside the cavity and the field into a rectangular metallic waveguide, assumed as cavity feed, is matched on the coupling aperture, thus allowing an equivalent circuit representation where only one cavity resonant mode is taken into account, while all TE_{n0} modes of the

exciting waveguide are considered. Under the above hypotheses, the equivalent circuit modeling both the cavity behavior and the cavity-to-waveguide coupling is derived.

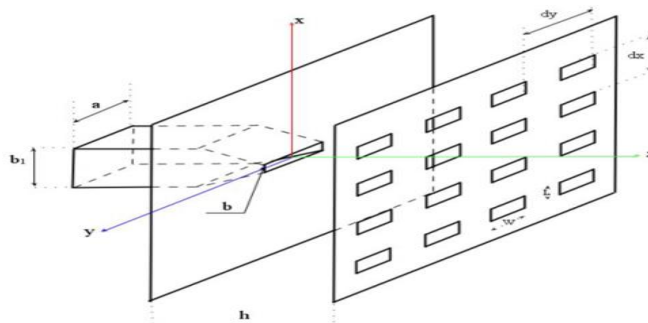


Fig. 1. Rectangular waveguide-to-cavity coupling.

When the second metallic sheet in Fig. 1 is replaced with a partially reflecting surface, an equivalent impedance is inserted into the circuit of Fig. 2.

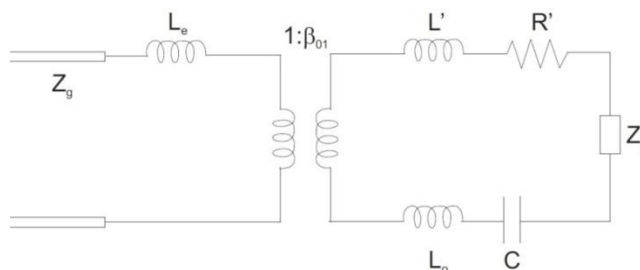


Fig. 2 Equivalent circuit of radiating cavity.

The reported circuit leads to optimize the transition between the waveguide and the cavity.

In order to compute the radiated field from the slots cut into one wall of the resonator, the electromagnetic field in the resonator is used to obtain the incident field on the slots and subsequently derive from it the equivalent magnetic current. Following the Bethe's original theory [4], the incident field is considered in the absence of the aperture.

Following the reasoning of previous paragraphs, the antenna configuration in Fig. 1 is considered.

An array of 16x16 elements is assumed, with dimensions $h=10$ mm, $d_x=10$ mm, $d_y=10$ mm, $W=7$ mm, $L=2$ mm. A feeding waveguide with dimensions $a=15.8$, $b_1=7.8$ mm is considered.

The analysis of the coupling between a rectangular cavity feeding waveguide and the planar open cavity is performed by taking into account the results of previous paragraphs. In particular, for the considered cavity of Fig. 1, the result reported in Fig. 3 is obtained. It is exploited to maximize the coupling between the waveguide and the cavity, thus terminating the feeding section into an aperture of size $a=15.8$, $b=1.1$ mm.

A first preliminary result of the radiation diagram using the simplified analysis of the proposed antenna is reported in Fig. 4 where, due to the tapering of the exciting field of the slots, a substantial reduction of the sidelobes can be observed.

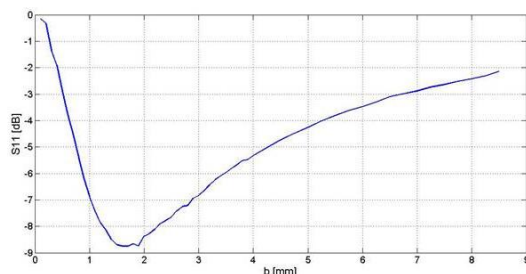


Fig. 3. Return loss vs. waveguide height.

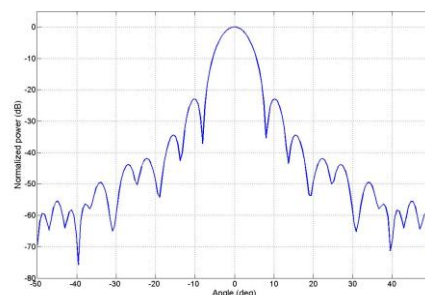


Fig. 4. Radiated field of metallic Fabry-Perot antenna.

III. Fabry-Perot antenna with improved bandwidth

In order to improve the operation bandwidth of the Fabry-Perot antenna configuration in Fig. 1, a modified structure partially-filled with a dielectric substrate is considered. In the following paragraphs, the expression of the electromagnetic field into the partially-filled cavity are derived, and experimental results on a Ku-band prototype are reported to show a significant bandwidth improvement with respect to the case of metallic Fabry-Perot structure.

In order to assess the analysis method outlined in the previous paragraphs, a partially-filled Fabry-Perot antenna composed by an array of 8x8 elements, with inter-element spacing $d_x=d_y=12.5$ mm and slot dimensions $W=6.35$ mm, $L=2$ mm, is realized and experimentally tested. A plane distance $l=h_1+h_2 = 9.662$ mm is considered, which is given by the sum of an empty space $h_1=8.9$ mm and a dielectric $\epsilon_r=2.33$ with thickness $h_2=0.762$ mm. The optimal coupling is obtained for a feeding waveguide with dimensions $a=18.8$ mm, $b=2$ mm, at a frequency $f=14.85$ GHz. The partially-filled Fabry-Perot antenna is realized and tested into the Microwave Laboratory at University of Calabria Fig. 5.

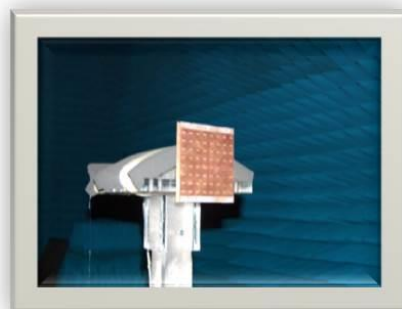


Fig. 5. Photograph of partially-filled Fabry-Perot antenna.

The enhanced bandwidth behavior of the partially-filled Fabry-Perot antenna can be easily observed from the boresight gain results illustrated in Fig. 6, where an improvement of about 48% is obtained with the insertion of the dielectric substrate, and a good agreement between simulations and measurements is demonstrated in the case of partially-filled antenna configuration.

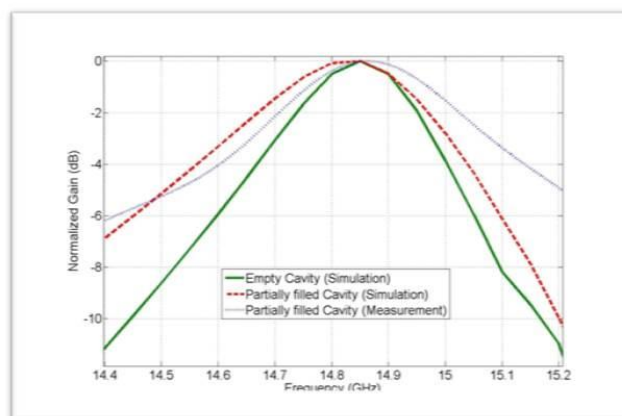


Fig. 6. Boresight gain vs. frequency: comparison between metallic and partially-filled Fabry-Perot antenna.

IV. CONCLUSION

An open planar cavity antenna has been presented in this work, by providing an equivalent simplified circuit and obtaining both input characteristics and radiation diagrams of the antenna. In particular, a modified configuration based on a cavity partially-filled with a dielectric substrate is proposed to significantly improve the antenna radiation bandwidth.

REFERENCES

- [1] O. Bucci, G. Di Massa, Open resonator powered by rectangular waveguide, IEE Proceedings-H, vol. 139, pp. 323-329, 1992.
- [2] G. Di Massa, S. Costanzo, O.H. Moreno, Open Resonator System for Reflectarray Elements Characterization, International Journal of Antennas and Propagation, 2012.
- [3] G. Di Massa, S. Costanzo, O.H. Moreno, Accurate circuit model of open resonator system for dielectric material characterization, Journal of Electromagnetic Waves and Applications, vol. 26, pp 783-794, 2012.
- [4] H.A Bethe, Theory of Diffraction from Small Holes, The Physical Review, vol. 66, pp 163-182. 1944.

COMPRESSED SENSING/SPARSE RECOVERY APPROACH FOR ARRAY DIAGNOSIS USING UNDERSAMPLED NEAR-FIELD DATA

S. Costanzo⁽¹⁾, M. D. Migliore⁽²⁾, A. Borgia⁽¹⁾, D. Pinchera⁽²⁾, G. Di Massa⁽¹⁾

⁽¹⁾ DIMES, Università della Calabria
Via P. Bucci, cubo 41D, 87036 Rende (CS), Italy
costanzo@deis.unical.it

⁽²⁾ DIEI, Università di Cassino e del Lazio Meridionale
Via Di Biasio 43, 03043 Cassino, Italy
mdmiglio@unicas.it

Abstract

A Compressed Sensing/Sparse Recovery approach is adopted in this work to accurately identify fault array elements by using undersampled near-field data. Experimental validations on a slotted-waveguide array are discussed to demonstrate the effectiveness of the proposed procedure, able to properly identify the failures positions from a set of measured data much smaller than the number of radiating elements.

Index Terms – Array antennas, array diagnosis, compressed sensing, near-field methods.

I. INTRODUCTION

The problem of failures identification in array antennas has received large attention in the academic as well as industrial contexts, with the aim to avoid performance degradations in terms of array gain and/or sidelobe levels. The most widely adopted approach is given by the back-propagation algorithm [1], which is based on the Fourier relationship between the fields on the array aperture and the measurement plane. In this approach, the sampling step is typically chosen equal to $\lambda/2$ to satisfy the Nyquist theory, thus requiring a large number of measurement points and a huge acquisition time. Alternative methods have been considered to reduce the data amount, by introducing a priori information [2] or a proper modeling [3] of the source. However, all these approaches generally require a set of measurements not smaller than the number of radiating elements. The most recent researches on Compressed Sensing/Sparse Recovery techniques suggest the possibility to obtain a number of data linearly increasing with the number of failures, but only logarithmically increasing with the number of array elements, thus allowing a significant reduction in the measured data amount.

In the present contribution, the compressed sensing approach outlined in [4] is applied to accurately identify fault array elements using undersampled near-field data. Experimental validations on a slotted-waveguide array are presented to show the effectiveness of the proposed array diagnosis technique.

II. FORMULATION

Let us consider an Array Under Test (AUT) consisting of N radiating elements located into known positions \mathbf{r}_n (Fig. 1). Let x_n and $\mathbf{f}_n(\theta, \varphi)$ be the excitation coefficient and the electric-field radiation pattern of the n -th radiating element, respectively. A probe having effective height $\mathbf{h}(\theta, \varphi)$ is placed into M spatial points \mathbf{r}_m , $m = 1, \dots, M$.

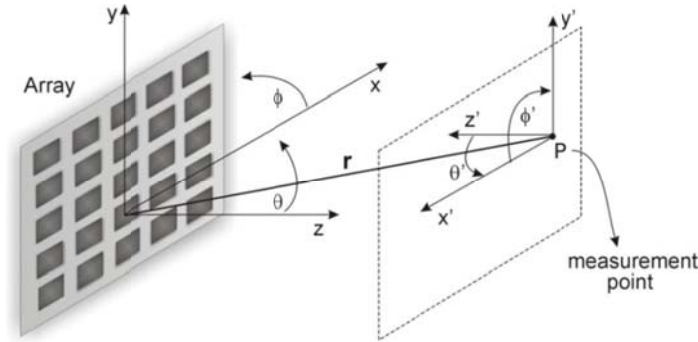


FIG. 1 – Problem geometry.

The voltage at the probe output can be expressed by a linear system of the kind:

$$\mathbf{A}\mathbf{x} = \mathbf{y} \quad (1)$$

wherein $\mathbf{y} = (\mathbf{y}_1, \mathbf{y}_2, \dots, \mathbf{y}_M)^T \in \mathbf{C}^M$, y_m being the probe voltage measured at point \mathbf{r}_m , $\mathbf{x} = (x_1, \dots, x_N)^T \in \mathbf{C}^N$, $\mathbf{A} \in \mathbf{C}^{M \times N}$ is a matrix whose (m, n) element is equal to $\exp(-j\beta r_{m,n}) / (4\pi r_{m,n}) \mathbf{f}(\theta_{m,n}, \varphi_{m,n}) \cdot \mathbf{h}(\theta'_{m,n}, \varphi'_{m,n})$, $r_{m,n} = |\mathbf{r}_m - \mathbf{r}_n|$, $\theta_{m,n}$ and $\varphi_{m,n}$ are the relative angles between the m -th measurement point and the n -th element position in a reference system centered on the n -th array radiating element.

In the present work, the problem of identification of fault elements into array antennas is considered. If assuming a number S of failures, this goal can be achieved by inverting the system (1), as proposed in [4], but requiring that $M \geq N$. Let us suppose $S \ll N$, as usually happens. As first step, we suppose to know (by measurements or available model/simulation) the field radiated by the failure-free array into M measurement points, thus obtaining a reference data vector \mathbf{y}_r . The relative excitations of the reference (failure-free) array are denoted by vector \mathbf{x}_r . In a successive step, we collect the field radiated by the array

with fault elements, thus obtaining a second vector y_d with associated excitations x_d . Now, let us consider the linear system (1), with:

$$x = x^r - x^d \quad (2)$$

$$y = y^r - y^d \quad (3)$$

x and y named as 'innovation' vectors. Since $S \ll N$, we have an equivalent problem involving a highly sparse array. Accordingly, the problem is *sparse*, i.e. the unknown vector has only a small number of not-null entries, and it can be solved by the following constraint minimization:

$$\min_x \|x\|_1 \quad (4)$$

subject to:

$$\|Ax - y\|_2 \leq \epsilon \quad (5)$$

wherein ϵ is related to the noise affecting the data.

III. EXPERIMENTAL RESULTS

A planar near-field setup is considered to validate the proposed array diagnosis approach using sparse data [5]. A X-band slotted-waveguide array with $N = 14$ radiating elements is assumed as AUT, while a standard rectangular waveguide is adopted as measuring probe (Fig. 2).

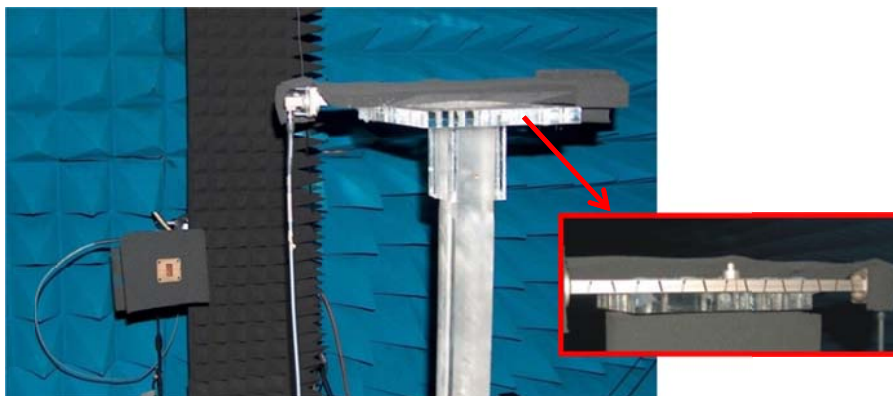


FIG. 2 – Measurement setup.

To apply the proposed diagnosis technique, near-field data are collected on a planar surface 40 cm away from the AUT, by assuming the presence of two failures (namely, with the 3rd and 11th slots covered by a conductive material), as illustrated in Fig. 3. The measured near-field amplitudes on the failure-free and two-fault arrays are reported in Fig. 3 (a) along the central line of the acquisition domain. A subset of $M = 11$ points from the original 41 points, $\lambda/2$ spaced, is considered, which is equivalent to a 2λ undersampling, and the procedure outlined in Section II is applied to obtain the result illustrated in Fig. 3 (b), where the difference between the excitation

coefficients of the failure-free and the two-faults array clearly identifies the failures at positions $n = 3$ and $n = 11$.

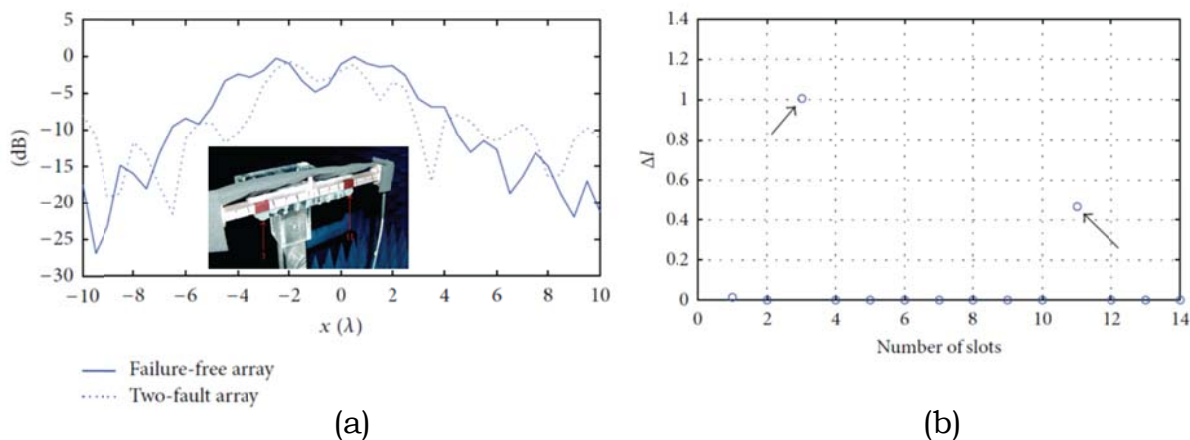


FIG. 3 – (a) Slotted-waveguide array with two failures and (b) measured near-field amplitude with and without failures.

IV. CONCLUSION

The problem of array diagnosis has been faced in this work by adopting an equivalent sparse formulation able to accurately identify fault elements by a set of undersampled data. Experimental validations have been discussed on a slotted-waveguide array, and future studies will be addressed to test the proposed approach on array of large dimensions.

REFERENCES

- [1] J. J. Lee, E. M. Ferrer, D. P. Woollen and K. M. Lee, "Near-field probe used as a diagnostic tool to locate defective elements in an array antenna," *IEEE Transactions on Antennas and Propagation*, vol. 36(3), pp. 884-889, 1988.
- [2] O. M. Bucci, C. Gennarelli and C. Savarese, "Representation of electromagnetic fields over arbitrary surfaces by a finite and non redundant number of samples," *IEEE Transactions on Antennas and Propagation*, vol. 46, pp. 361-369, 1998.
- [3] O. M. Bucci, M. D. Migliore, G. Panariello and G. Sgambato, "Accurate diagnosis of conformal array from near-field data using the matrix method," *IEEE Transactions on Antennas and Propagation*, vol. 53(3), pp. 1114-1120, 2005.
- [4] M. D. Migliore, "A compressed sensing approach for array diagnosis from a small set of near-field measurements," *IEEE Transactions on Antennas and Propagation*, vol. 59(6), pp. 2127-2133, 2011.
- [5] S. Costanzo, A. Borgia, G. Di Massa, D. Pinchera and M. D. Migliore, "Radar array diagnosis from undersampled data using a Compressed Sensing/Sparse Recovery technique," *Journal of Electrical and Computer Engineering*, vol.2013, Article ID 627410, 2013.

DESIGN OF A PLANAR SUB-ARRAY FOR SMART ANTENNA APPLICATIONS

M. di Filippo, L. Lucci, G. Pelosi, S. Selleri

Department of Information Engineering, University of Florence
Via di Santa Marta 3, 50139 Florence, Italy
[leonardo.lucci, giuseppe.pelosi, stefano.selleri]@unifi.it

Abstract

Paper presents a four element sub-array in planar technology for application in a smart antenna for mobile ad-hoc networks, where network reconfigurability is a requirement and hence a smart antenna able of self-configuring multiple beams a major advantage.

Index Terms – Smart antennas, mobile ad-hoc networks, planar antennas, finite elements.

I. INTRODUCTION

Mobile Ad-hoc NETWORKS (MANET) are opposed to infrastructured wireless networks, where each user directly communicates with an access point or base station, since they do not rely on a fixed infrastructure for its operation (Fig. 1) [1,2]. The MANET is a self-organizing temporary association of mobile nodes that communicate with each other over wireless links. Nodes that lie within each other's send range can communicate directly and are responsible for dynamically discovering each other. Furthermore, devices are free to join or leave the network and they may move randomly, possibly resulting in rapid and unpredictable topology changes.

In order to enable communication between nodes that are not directly within each other's send range, intermediate nodes act as routers that relay packets generated by other nodes to their destination. These nodes typically work on batteries, hence have energy limitations and exhibit great diversity in their range capabilities.

Despite these many issues, MANET offer numerous advantages. First of all, this type of network is highly suited for use in situations where a fixed infrastructure is not available, not trusted, too expensive or unreliable, like a crisis scenario (Earthquake, flood, fire) or when special events occur which require surveillance (Concerts, sport events, pilgrimages).

It is worth mentioning that devices forming the MANET need to be mobile, but are not necessarily portable or hand-held. Deployment of few larger mobile devices in key positions can ease the creation and maintaining of the MANET. These devices should be equipped with a smart antenna, with extended range, able to bring up most of the

network for its temporary duration, without substantial relocation, hence reducing the issues of changing network topology.

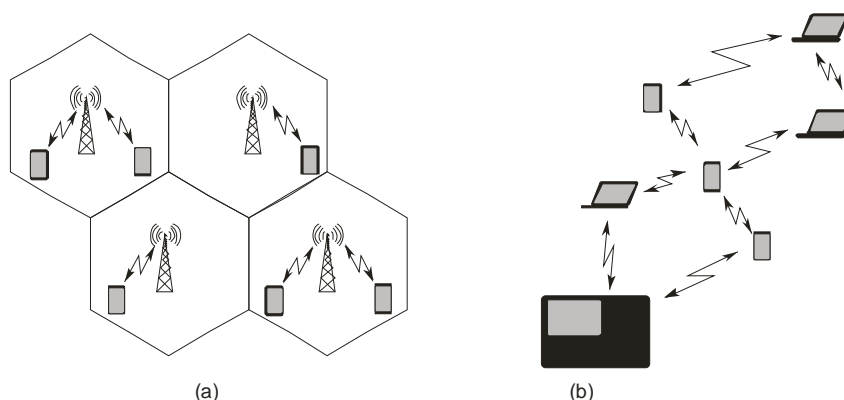


FIG. 1 – Conventional cellular network with fixed infrastructure (a); and mobile ad-hoc network (b).

Since the MANET main feature is anyway reconfigurability, the smart antenna should be able to project several independent beam, both for interconnection with other base stations and for connection with hand-held devices.

In this contribution the design of a cylindrical smart array antenna working at 5.4 GHz will be presented, focusing on the sub-array unit constituting the basic tile of the smart antenna. Section II will present the geometry of the antenna and of the tile, while section III will present numerical results. Finally section IV will draw some conclusions.

II. SMART ANTENNA CONFIGURATION

The basic geometry of the smart array is depicted in Fig. 2. It comprises 24 vertical sub-arrays, each with four linearly polarized rectangular patches. At sub-array level all patches are fed in phase, leading to a broadside diagram, phase control of the array is limited to the sub-array input line, allowing for beam steering in azimuth.

In principle, only 4 to 6 sub-arrays can effectively contribute to beam creation, in this project just 5 sub-arrays will be used at a time for each lobe, hence a smart feeding network will provide both the correct phases and the selection of the five sub-arrays needed for beam synthesis.

Indeed if 24 sub-arrays are used, then 24 partially overlapping sets of 5 contiguous sub-arrays can be defined, as the one marked in black and the one marked in orange in Fig. 2b. Each of these set need to scan electronically only $\pm 7.5^\circ$. To maintain mobility, the antenna is required to be compact, hence a diameter of less than 40 cm and an height less than 20 cm is sought for. By choosing sub-arrays of less than 5×20 cm the requirement is satisfied.

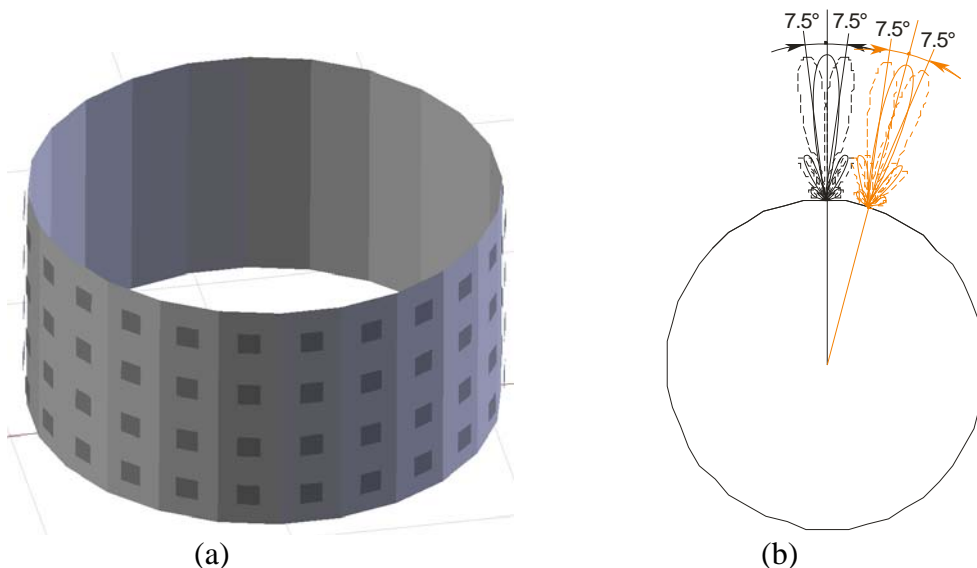


FIG. 2 – Cylindrical smart array antenna layout (a) and generation of beams in a 15° arc from a subset of 5 sub-arrays (b).

The single sub-array is a four patch printed array with non uniform element spacing and non-uniform feeding amplitudes. Relative amplitudes are 1 2 2 1, attained via the non-symmetrical dividers shown in Fig. 3, where all the sub-array dimensions are given in millimeters. Array is fed via a coaxial cable with a connector mounted beneath the antenna plane in the point shown in Fig. 3.

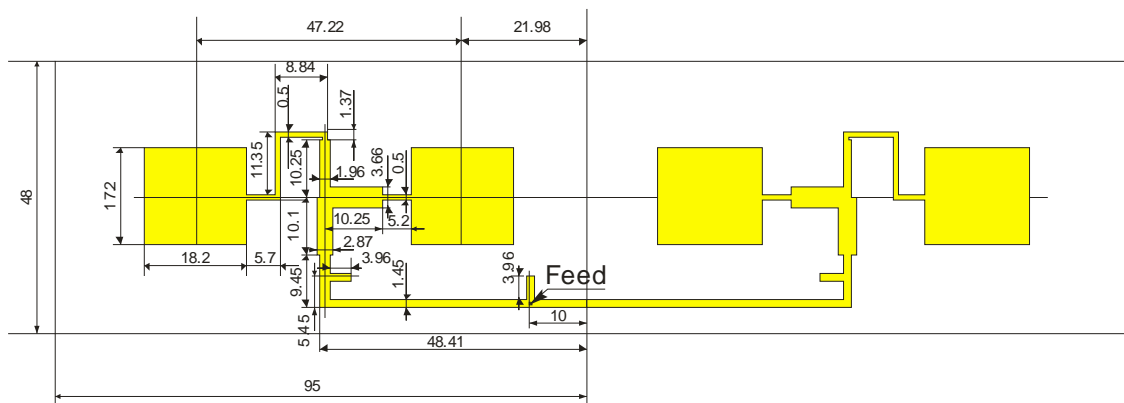


FIG. 3 – Sub-array layout and dimensions (mm).

III. NUMERICAL RESULTS

The structure presented was simulated via Finite Elements (FEM) [3] placing it in a computational box enclosed by perfectly matched layers (PML), so as to correctly take into account the finite ground plane. The obtained S_{11} at the coaxial feed port is reported in Fig. 4. Fig. 5 reports attained patterns for the single sub-array and for the group of five sub-arrays. Peak gain is 14.4 dB for the single sub-array and 20.1 dB for the group of five.

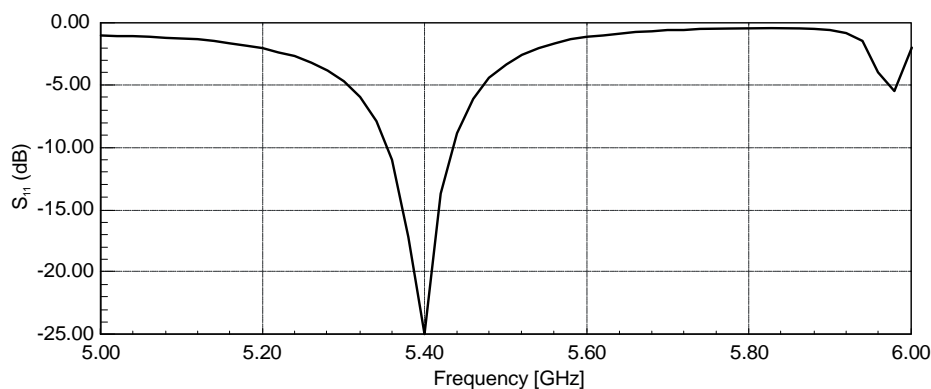


FIG. 4 – Simulated S11 at the sub-array coaxial feed port.

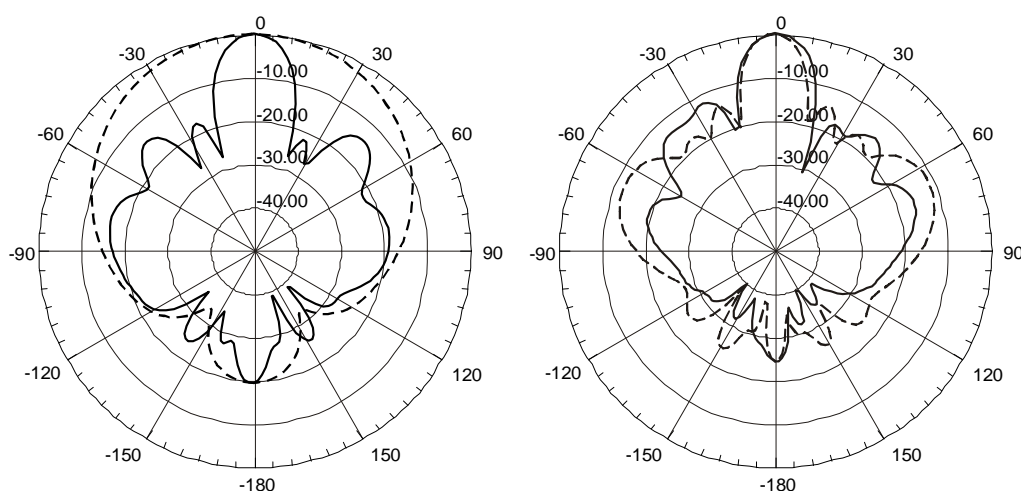


FIG. 5 – Simulated single sub-array pattern (left) and pattern generated by 5 contiguous sub-arrays on the cylindrical array (right). Solid line is elevation pattern (vertical), dashed line is azimuth pattern (horizontal).

IV. CONCLUSION

In this contribution a possible layout of smart antenna for MANET applications has been presented. Due to space limitations just the sub-array design has been discussed. Full array, including coupling, will be treated at the conference.

REFERENCES

- [1] J. Hoebeke, I. Moerman, B. Dhoedt, and P. Demeester, "An overview of mobile ad hoc networks: applications and challenges," *Proceedings of the 43rd European Telecommunications Congress, FITCE2004*, Ghent, Belgium, November 2004, pp. 60-66.
- [2] M. Frodigh, P. Johansson and P. Larsson, "Wireless Ad Hoc Networking: The Art of Networking without a Network," *Ericsson Review*, vol. 4, 2000.
- [3] G. Pelosi, R. Coccioli, S. Selleri, *Quick Finite Elements for Electromagnetic Waves*, Artech House, Boston, MA, 2nd Edition, 2009.

RECONFIGURABLE CONCENTRIC CIRCULAR ARRAYS: A NOVEL HYBRID SYNTHESIS METHOD

O.M Bucci⁽¹⁾, S. Perna⁽²⁾, D. Pinchera⁽³⁾

⁽¹⁾ DIETI, Università degli Studi di Napoli Federico II
Via Claudio 21, Napoli, Italy

bucci@unina.it

⁽²⁾ DI, Università degli Studi di Napoli "Parthenope"
Centro Direzionale Is.C4, Napoli, Italy

perna@uniparthenope.it

⁽³⁾ DIEI, Università degli Studi di Cassino e del Lazio Meridionale
Via G.Di Biasio 43, Cassino FR, Italy

pinchera@unicas.it

Abstract

In this contribution we focus on the synthesis of sparse circular arrays, i.e., non-periodic sparse arrays employing equi-amplitude radiators arranged in rings. In particular, we summarize some recent results obtained in the frame of the activities carried under a contract funded by the European Space Agency and focused on the development of an active multibeam sparse array demonstrator for satellite communications. More specifically, we address the synthesis of a reconfigurable sparse array tailored to the radiation of beams with two different beamwidths. The synthesis method is based on a hybrid approach, which exploits at best the partial convexity of the problem at hand. Numerical examples, showing the feasibility of the approach for satellite applications are included.

Index Terms – Antenna Array Synthesis, Sparse Arrays, Satellite Antennas.

I. INTRODUCTION

Recent advances in the synthesis of Direct Radiating Arrays (DRA) have shown that the use of isophoric sparse arrays, that is, non-periodic sparse DRA architectures employing equi-amplitude radiators, could be a viable and effective solution also for space applications [1]-[7].

In particular, in the frame of the activities carried under a contract funded by the European Space Agency (ESA) and relevant to the Invitation To Tender (ITT) in [2], it has recently been shown [7] that circular-concentric isophoric sparse arrays are capable to guarantee full Earth coverage from a geostationary orbit by means of steerable narrow (0.65°) beams with high gain (42.6dBi) and low sidelobes (lower than -20dB with respect to the level at the Edge of Coverage) with a number of elements as low as 368. This interesting result has been achieved by means of novel and effective synthesis techniques, originally proposed in [8], [10] and further developed in [9], [7], which allow an optimum tailoring of the sparse array geometry to the specific beam to be radiated.

In the satellite communication context could be however necessary that the antenna is capable to radiate patterns with two (or more) different beamwidths, as testified by the requirements listed in the aforementioned ESA ITT in [2]. Indeed, the next generation of satellite communication systems will involve the use of flexible antenna systems, capable to modify the radiation pattern in order to adapt the radiated beam to the different working conditions that would be required.

In this frame, it is important to observe that, if we consider a particular sparse array, synthesized for instance by means of the aforementioned techniques in [8]-[10], and we try to radiate (by means of a proper control on the phases of the radiating elements) a beam with a width different from that for which the array has been optimized, the resulting pattern would rather difficulty satisfy the requested specifications.

Accordingly, in order to radiate beams of different widths by means of the same sparse array, it is not appropriate to tailor its geometry to a single pattern. It is however necessary to tailor the geometry of the layout to a multiplicity of patterns. Roughly speaking, the array must be tailored to a particular “reconfigurability”.

To this aim, we have properly modified the approach proposed in [10]. In particular, in [10] the radii of the concentric ring arrays are computed by means of an evolutionary algorithm, whose cost function determines the optimal ring excitations (i.e. the number of feeds per ring) by means of the solution of a convex problem. In the new algorithm we have substituted the cost function with a more sophisticated one, which finds the optimum excitations of each ring in order to obtain the different required beamwidths, imposing that the two excitations share the same amplitude, in order to reconfigure the pattern by sole modification of the phase. Numerical examples showing the feasibility of the suggested approach for satellite applications are provided in the following section and are extracted from the work in [11].

II. RESULTS

According to the requirements listed in [2], the widths of the two different beams to be synthesized have been set equal to 0.65° and 3.25° , respectively. Moreover, the angles marking the edge of coverage of the nearest “iso-color” beam [1] have been set equal to 0.795° for the narrow beam and 3.975° for the wide beam. This means that in the considered multi-beam coverage scenario the zooming operation is thought to be enforced simultaneously for two adjacent iso-color beams.

As for the scanning capability, we have considered a very severe case, that is, we have supposed that both the radiated beams should be steered in such a way to guarantee full Earth coverage from GEO orbits. As shown in [7], this implies use of radiating feeds with size smaller than 3λ and, thus, a number of radiating elements that, in case we had to transmit only the narrower beam, would be on the order of 350-400, see [7]. Following the rationale shown in [7], in order to satisfy such

scanning requirements, we have to enforce the condition that for the broadside beam the SLL constraint should be satisfied up to an elevation angle approximately equal to 16° .

As for the array elements, we have considered optimal circular feeds of diameter equal 2.2λ , synthesized following the procedure described in [7].

Figure 1 reports a layout obtained by means of the approach discussed in the previous Section. It consists of 668 control points. For the boresight beam, phase control is necessary only to generate the wider beam. For both the (boresight) beams, it is reported the superposition of φ -cuts of the array directivity, along with a table containing main results. It can be seen that in the worst case a SLL less than -19.76 dB is obtained within the angular sector of interest, that is, for both the beams we are very close to the satisfaction of the -20 dB required level.

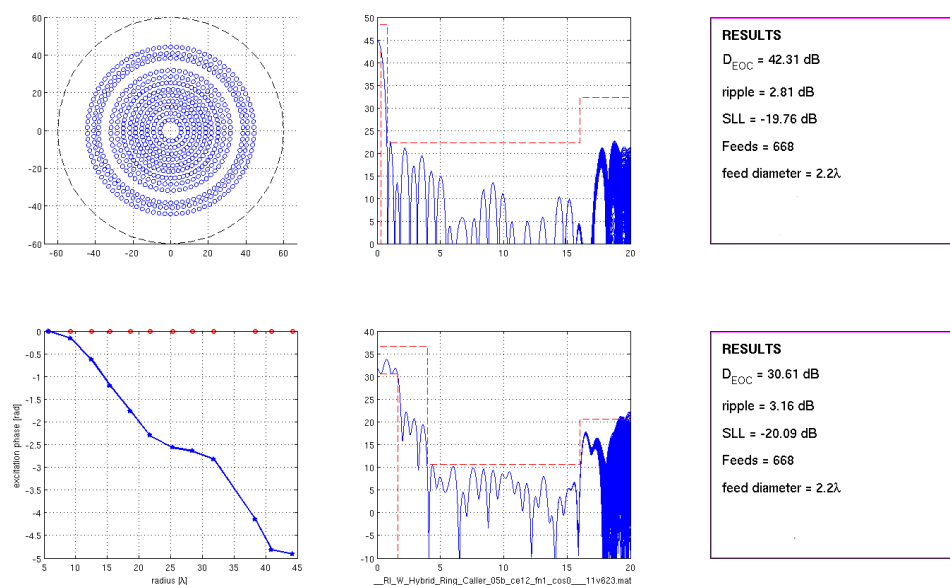


FIG. 1 – Top, from the left: 668 element layout employing 2.2λ diameter; superposition of the array directivity φ -cuts for the boresight narrower beam; corresponding results. Bottom: phase excitations of the layout ring arrays for the generation of the wider beam; superposition of the array directivity φ -cuts for the boresight wider beam; corresponding results.

III. CONCLUSION

The design of isophoric reconfigurable sparse arrays can not be achieved by applying phase-only synthesis techniques to a sparse array tailored for a specific beam: the position of the radiating elements of the array must be indeed tailored to the particular “reconfigurability” of the beam. The presented hybrid method has shown very good performances, which have allowed the satisfaction of the requirements of the contract related to the ITT in [2]. It has to be underlined that the

design method presented in this contribution for circular arrays could also be applied to other geometries, and this extension will be considered as a future development of this research.

ACKNOWLEDGEMENT

This work was supported in part by the European Space Agency under the ESA/ESTEC contract No. 4000102257 Active Multibeam Sparse Array Demonstrator.

REFERENCES

- [1] ESA/ESTEC Tender AO/1-5598/08/NL/ST, "Innovative Architectures For Reducing The Number Of Controls Of Multiple Beam Telecommunications Antennas". [Online]. Available: www.esa.int
- [2] ESA/ESTEC Tender AO/1-6338/09/NL/JD, "Active Multibeam Sparse Array Demonstrator". [Online]. Available: www.esa.int
- [3] G.Toso, C.Mangenot, and A.G.Roederer, "Sparse and thinned arrays for multiple beam satellite applications," *Proceedings of 29th ESA Antenna Workshop on Multiple Beams and Reconfigurable Antennas*, 2007.
- [4] M.C.Viganò, G.Toso, P.Angeletti, I.E.Lager, A.G. Yarovoy, D.Caratelli, "Sparse antenna array for Earth-coverage satellite applications," *Proc. of the 4th European Conf. on Antennas and Propagation*, (EUCAP 2010) Barcelona, Spain, 2010.
- [5] O.M.Bucci, T.Isernia, A.F.Morabito, S.Perna, D.Pinchera; "Aperiodic Arrays for Space Applications: an Effective Strategy for the Overall Design," *Proc. of the Third European Conf. on Antennas and Propagation* (EUCAP 2009), Berlin, Germany, 2009.
- [6] O.M.Bucci, T.Isernia, A.F.Morabito, S.Perna, D.Pinchera, "Density and Element-Size Tapering for the Design of Arrays with a Reduced Number of Control Points and High Efficiency," *4th European Conf. on Antennas and Propagation*, (EUCAP 2010) Barcelona, Spain, 2010.
- [7] O.M.Bucci, T.Isernia, S.Perna, D.Pinchera, "Isophoric Sparse Arrays Ensuring Global Coverage in Satellite Communications," *IEEE Transactions on Antennas and Propagation*, vol. 62, no. 4, April 2014
- [8] O. M. Bucci, S. Perna, "A deterministic two dimensional density taper approach for fast design of uniform amplitude pencil beams arrays," *IEEE Transactions on Antennas and Propagation*, vol. 59, n. 8, pp. 2952-2861, 2011.
- [9] O.M., Bucci, S. Perna, D. Pinchera, "Advances in the Deterministic Synthesis of Uniform Amplitude Pencil Beam Concentric Ring Arrays," *IEEE Transaction on Antennas and Propagation*, vol. 60, n. 7, pp. 3504-3509, 2012.
- [10] O. M. Bucci, D. Pinchera, "A Generalized Hybrid Approach for the Synthesis of Uniform Amplitude Pencil Beam Ring-Arrays," *IEEE Transactions on Antennas and Propagation*, Jan. 2012.
- [11] O.M., Bucci, S. Perna, D. Pinchera, "Isophoric Reconfigurable Sparse Arrays in Satellite Communications: an Hybrid Synthesis Approach", submitted to *IEEE Transactions on Antennas and Propagation*.

NEW TOOLS FOR ANALYSIS AND SYNTHESIS OF REAL ANTENNA DEVICES

P. Rocca

ELEDIA Research Center @ DISI, University of Trento
Via Sommarive 5, I-38123 Trento, Italy
paolo.rocca@disi.unitn.it

Abstract

The radiation characteristics of real antennas always deviate from the ideal ones defined through conventional synthesis methods since the inaccuracies and random errors that are unavoidable introduced throughout the manufacturing are not taken into account in the design process. In this work, a new mathematical tool based on the arithmetic of intervals and Interval Analysis (IA) is presented which allows the robust analysis as well as the robust design of antenna devices and systems. Assuming known the maximum tolerances on the antenna parameters or control-points, close-form expressions of the arising power pattern bounds are derived as a function of the input error tolerances. Two examples related to the robust analysis and design of phased antenna arrays and reflector antennas are discussed to show the versatility, efficiency and effectiveness of the proposed IA-based tools.

Index Terms – Pattern Tolerance Analysis, Robust Antenna Design, Antenna Arrays, Reflector Antennas, Excitation Errors, Surface Errors, Interval Analysis.

I. INTRODUCTION

The analysis of the tolerances on the power pattern generated by an array when manufacturing errors affect its control points (e.g., amplitude and/or phase coefficients) or by a reflector antenna when the reflector surface is characterized by inaccuracies (e.g., roughness) is a problem of great interest in the antenna community which has been studied for decades [1] and several different methods have been also recently proposed [2, 3]. On the one hand, the knowledge of the potential deviations from the nominal or average radiation performances is of interest to predict the antenna behavior when used in real operating conditions. On the other hand, the availability of fast analytic tools for evaluating the pattern tolerances enables the synthesis of robust and reliable antenna devices or systems avoiding and/or reducing the time, complexity, and costs of the calibration processes that, nowadays, are mandatory in many challenging applications. In the past, statistical approaches for pattern performance predictions have been proposed, based on either analytical [1, 2] or computational [3] strategies. By virtue of their intrinsic statistical nature and the fact that a-priori assumptions on the error distributions are required for the

analytical methods while Monte Carlo simulations are needed in case of computational techniques, the arising tolerance estimations turn out being only probabilistically verified.

Recently, an innovative mathematical tool for the analytic and exact computation of the power pattern bounds caused by tolerance errors on the array amplitude weights has been proposed [4]. Based on the use of Interval Analysis, without a-priori assumption on the error distributions and regardless the tolerance model for the amplifiers at disposal [5], the deviations of the actual power pattern from the nominal/ideal one have been expressed by exploiting the rules of interval arithmetic. Thanks to its generality, efficiency, and effectiveness, the IA-based tool has been then extended to deal with the tolerance analysis of reflector antennas with surface deformations on the parabolic disc [6].

In parallel, IA tools have been integrated with suitable global [7, 8] and local [9] optimization approaches for the design of robust beam-former weighting configurations. The methods can be used to allow the antenna designer to take into account the potential inaccuracies of the antenna realization from the beginning of the synthesis process.

A review of the proposed IA-based tools for the analysis and synthesis of real antennas is reported in this work, also envisaging further potential extension to other applications of practical interest.

II. INTERVAL ANALYSIS FOR ROBUST ANTENNA ANALYSIS

The field generated in far-field from linear antenna arrays or circularly-symmetric reflector antennas can be expressed by means of the following mathematical expression [4, 6]

$$E(\theta) = \sum_{n=1}^N E_n(\theta) \quad (1)$$

where $E_n(\theta)$ is the complex field contribution in the θ direction by the n -th array element (included the amplitude and phase weightings) or the n -th cell of the discretization of the antenna aperture, $n = 1, \dots, N$.

In case tolerances affect the array control points or deformations are present on the surface of the reflector, the radiated field (1) is unavoidably distorted. Since such errors are in general not a-priori known and it is unfeasible to perform an exhaustive evaluation of all error combinations, let us suppose such errors as included within intervals of values ($[A_n], [\xi]$) as shown in Fig. 1. These intervals are defined by means of upper and lower bounds, for example around the nominal value of the amplification weight a_n [Fig. 1(a)] or as a maximum deformation that can occur on the reflector surface with respect to the ideal surface [Fig. 1(b)].

Accordingly, the radiation pattern (1) can be expressed as a complex interval function

$$[E(\theta)] = \sum_{n=1}^N [E_n(\theta)] \quad (2)$$

where $[E_n(\theta)]$, $n = 1, \dots, N$ are complex intervals computed by using the rules of interval arithmetic [10]. The corresponding interval power pattern $[P(\theta)] = [E(\theta)][E(\theta)]^* = [P^{\text{inf}}(\theta); P^{\text{sup}}(\theta)]$ can be then obtained by applying the guidelines reported in [4, 6].

In Fig. 2(a), the upper $P^{\text{sup}}(\theta)$ and lower $P^{\text{inf}}(\theta)$ bounds of interval power patterns obtained when considering a reflector antenna with surface deformations having different maximum errors (expressed in terms of the working wavelength λ) are reported.

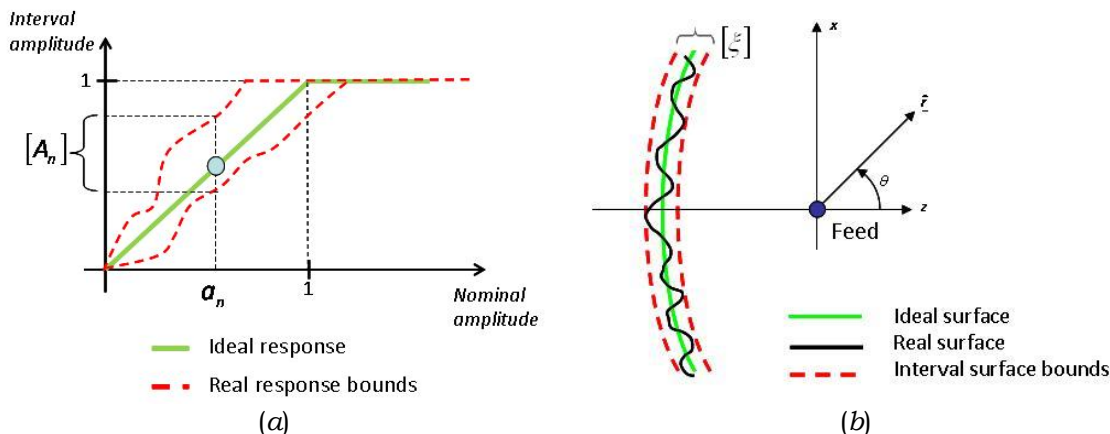


FIG. 1 – Examples of ideal and interval (a) amplifier model response and (b) reflector surface model.

III. INTERVAL ANALYSIS FOR ROBUST ANTENNA SYNTHESIS

Exploiting the IA-based analysis tool presented in the previous section, it is then possible to define robust synthesis methods for designing arrays or reflector antennas able to satisfy user-defined constraints [Fig. 2(b)] where tolerances on the control points or surface deformations are directly considered in the synthesis step. Towards this aim, suitable cost functions aimed at quantifying the violation of the mask constraints of the upper $P^{\text{sup}}(\theta)$ and lower $P^{\text{inf}}(\theta)$ bounds and effective IA-based design tools have been introduced [7, 9].

IV. CONCLUSION

Innovative tools based on Interval Analysis for the robust analysis and synthesis of the power patterns generated by realistic arrays and reflector antennas characterized by errors/inaccuracies on the antenna control points and/or surface structure have been presented. Starting from a realistic model of the tolerances, numerical bounds for the power patterns can be analyzed to give the array designer suitable indications on the arising performance thus avoiding time-expensive calibrations. As opposite, given user-defined mask power constraints to be satisfied, the values of the nominal control points or the maximum tolerance

errors guaranteeing the satisfaction of the requested constraints can be obtained by integrating the IA with suitable optimization strategies.

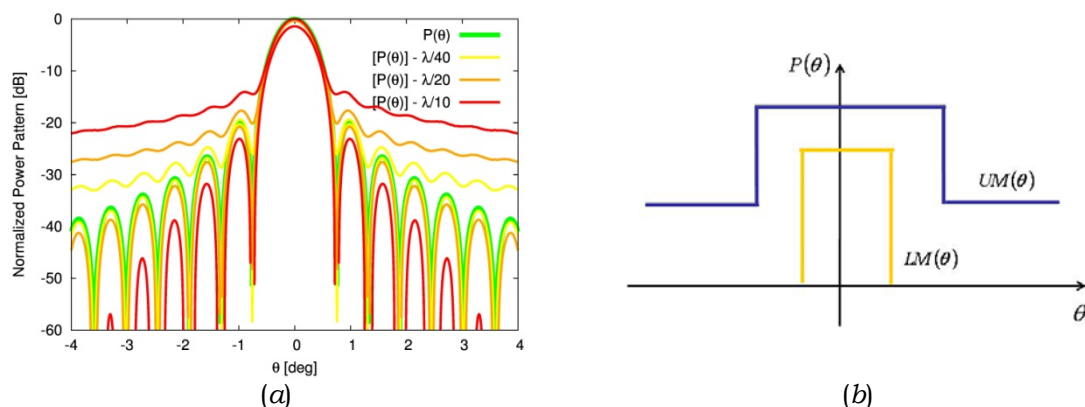


FIG. 2 – Plot of (a) the interval power pattern for different maximum surface errors and of (b) the user-defined mask for the robust antenna design.

REFERENCES

- [1] J. Ruze, "The effect of aperture errors on the antenna radiation pattern," *Nuovo Cimento*, vol. 9, no. 3, pp. 364-380, 1952.
- [2] S. Sinton and Y. Rahmat-Samii, "Random surface error effects on offset cylindrical reflector antennas," *IEEE Trans. Antennas Propag.*, vol. 51, no. 6, pp. 1331-1337, Jun. 2003.
- [3] J. Lee, Y. Lee, and H. Kim, "Decision on error tolerance in array element by the Monte Carlo method," *IEEE Trans. Antennas Propag.*, vol. 53, no. 4, pp. 1325-1331, Apr. 2005.
- [4] N. Anselmi, L. Manica, P. Rocca, and A. Massa, "Tolerance analysis of antenna arrays through interval arithmetic," *IEEE Trans. Antennas Propag.*, vol. 61, no. 11, pp. 5496-5507, Nov. 2013.
- [5] P. Rocca, L. Manica, N. Anselmi, and A. Massa, "Analysis of the pattern tolerances in linear arrays with arbitrary amplitude errors," *IEEE Antennas Wireless Propag. Lett.*, vol. 12, pp. 639-642, 2013.
- [6] P. Rocca, L. Manica, and A. Massa, "Interval arithmetic for pattern tolerance analysis of parabolic reflectors," *IEEE Trans. Antennas Propag.*, 2014, Submitted.
- [7] L. Manica, N. Anselmi, P. Rocca, and A. Massa, "Robust mask-constrained linear array synthesis through an interval-based Particle Swarm Optimization," *IET Microw. Antennas Propag.*, vol. 7, no. 12, pp. 976-984, 2013.
- [8] P. Rocca, M. Benedetti, M. Donelli, D. Franceschini, and A. Massa, "Evolutionary optimization as applied to inverse scattering problems," *Inverse Problems, Invited Topical Review Paper – 25th Year Special Issue of Inverse Problems*, vol. 24, pp. 1-41, 2009.
- [9] P. Rocca, L. Manica, N. Anselmi, and A. Massa, "Optimal synthesis of robust array configurations exploiting interval analysis and convex optimization," *IEEE Trans. Antennas Propag.*, 2014, Accepted for publication.
- [10] R. Boche, "Complex interval arithmetic with some applications," Tech. Report Lockheed Missiles & Space Company, California, pp. 1 - 33, Feb. 1966.

STRATEGIES FOR SCATTERING REDUCTION OF ANTENNA ARRAYS

S. Genovesi⁽¹⁾, F. Costa⁽¹⁾, A. Monorchio⁽¹⁾, G. Manara⁽¹⁾

⁽¹⁾ Dipartimento di Ingegneria dell'Informazione, Università di Pisa,
Via G. Caruso 16, 56122 Pisa, Italy
simone.genovesi@iet.unipi.it

Abstract

An overview of some of the most recent techniques proposed to reduce the Radar Cross Section of an array of antennas is addressed. In particular, the reduction of the electromagnetic echo is accomplished by resorting to structures exploiting the synergic design of Frequency Selective Surfaces and Resistive Periodic Surfaces. The properties and trade-offs of each solution are addressed as well as the performance offered by different strategies.

Index Terms – Low-RCS antennas, Radar Cross Section Reduction (RCSR), Electromagnetic Absorbers, Frequency Selective Surfaces (FSS), High Impedance Surfaces (HIS).

I. INTRODUCTION

The reduction of the electromagnetic field scattered by an object is a key issue in several applications and numerous efforts have been done to identify methods to achieve a Radar Cross Section Reduction (RCSR). Basically, most of the strategies adopted to accomplish this task rely either on the shaping of the target surfaces or on the use of Radar Absorbing Materials (RAMs). In the former case, the target shape or orientation is altered to redirect the scattered energy away from the detecting radar [1], whereas RAMs basically transform the radio frequency energy into heat [1]-[3].

Both solutions represent reliable countermeasures since the reflection from the metallic surfaces of an airplane or a vehicle can be decreased by covering them with radar absorbing materials or by modifying their original shape. However, if an antenna is installed on the platform the task becomes more challenging mainly for the following reasons:

- a) antennas significantly contribute to the overall RCS;
- b) antennas shape can be scarcely altered and an incorrect use of RAMs may degrade the overall radiation efficiency.

Moreover, shaping is not so efficient in the case of new bistatic radar systems [4],[5] since the scattering energy could be collected also by an opportunistic receiver. It is worth observing that the RCS of an array is determined by an antenna component and by a structural term [6]:

$$\sigma = \left| \sqrt{\sigma_s} - (1 - \Gamma_a) \sqrt{\sigma_a} e^{j\phi} \right|^2 \quad (1)$$

where σ is the total RCS of the target, σ_s is related to the field scattered by the short-circuited antenna, σ_a represents the field scattered by the antenna which involves the value of the port impedance, σ_a is the antenna reflection coefficient and σ is the relative phase between the two terms. Our investigation will be focused on the reduction of the structural term σ_s of an antenna array and it will be analyzed under the short circuit condition of the feeding port.

Since RCSR always imposes a trade-off among the decrease of radar signature, the increase in cost for maintenance of the system and the global performance, an optimized design has to balance advantages against disadvantages. Novel solutions have been recently proposed which are based on the exploitation of periodic surfaces [7]-[15]. Some of the most promising strategies that can be adopted to achieve a good level of RCSR will be addressed with particular emphasis on the use of properly designed hybrid metallic-resistive periodic surfaces. The proposed solutions will be tested on low-profile arrays of patch or slot antennas in order to quantitatively assess the performance. Particular attention will be devoted to the reduction of the radar signature for both normal and oblique plane wave incidence and to the effect on the antenna gain.

II. PERIODIC RESISTIVE SURFACE FOR RADAR CROSS SECTION REDUCTION OF A SLOT ANTENNA ARRAY

The considered test case is an array of slots printed on the top a dielectric layer of thickness t . A ground plane under the microstrip line feeding network is assumed at some distance d (Fig. 1(a)).

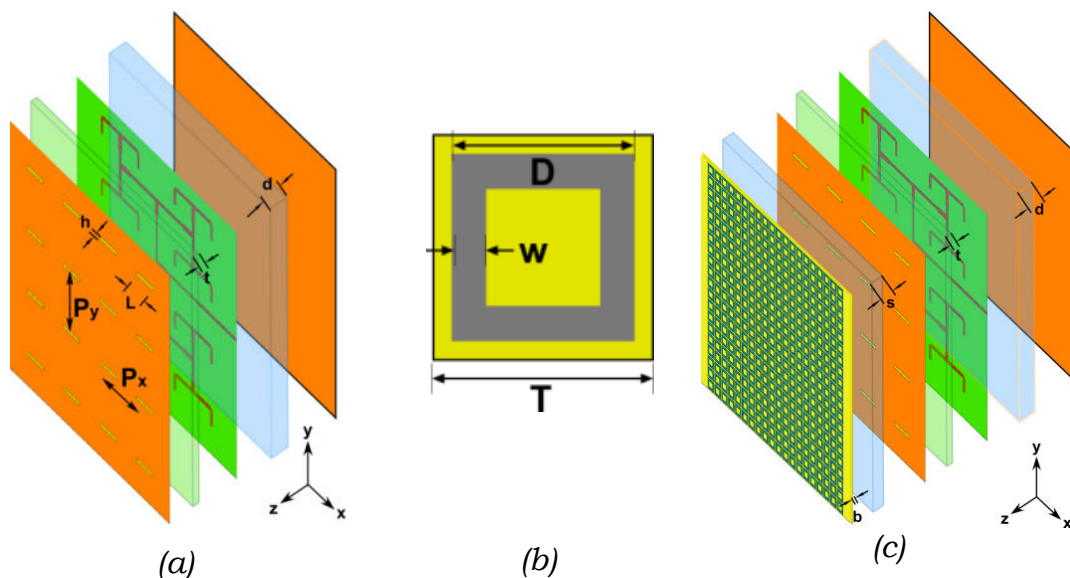


FIG. 1 – Exploded view of the antenna array placed on a metallic platform (a); unit cell of the proposed PRS (b); low RCS hybrid configuration (c).

The pursued task is to obtain a wideband RCSR of the array, possibly without decreasing the radiative properties of the system. A solution can be represented by the design of a radar absorbing material that has to be placed in front of the radiating aperture. To this aim, it is important to consider the working bandwidth of the array so to properly tailoring a periodic resistive surface that has to absorb the impinging wave. Since, the metallic slot-array plane behaves like a solid metallic ground plane for a normally impinging plane wave within the bandwidth 4.0 GHz-18.0 GHz, it is possible to exploit it for realizing an absorber by using a suitable Periodic Resistive Surface (PRS) placed at some proper distance s in front of it. The shape of the unit cell of the uniform PRS is illustrated in Fig. 1(b) whereas the tentative array design is shown in Fig.1(c). The PRS has been dimensioned to achieve the required bandwidth for normal incidence but the performance for obliquely incident plane waves has also been considered in order to estimate the reflection level for the bistatic case. The results of this analysis are reported in Fig. 2. As expected, the performance of the PRS deteriorates as the angle of incidence increases even if good level of low reflection is exhibited up to 30 degrees for both polarizations. Moreover, for greater angles the onset of grating lobes has to be taken into account.

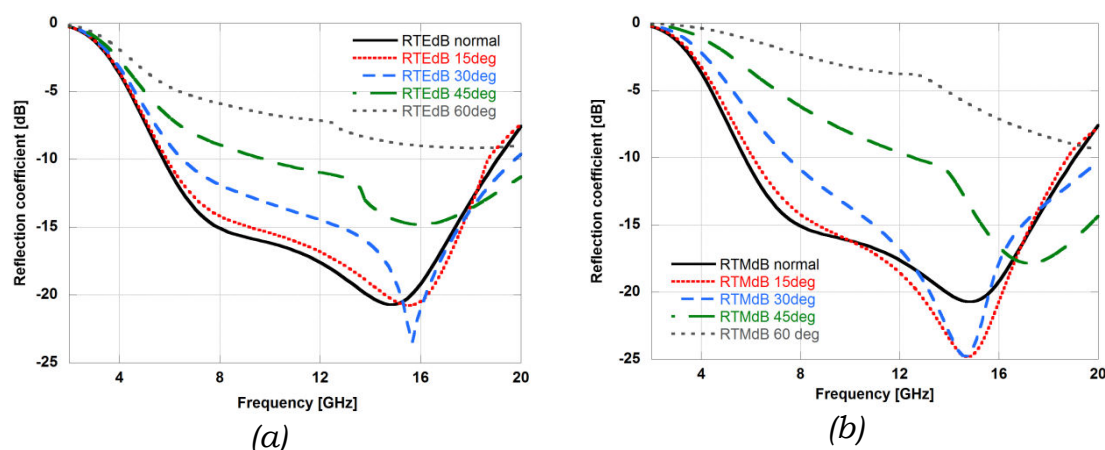


FIG. 2 – Reflection coefficient of the proposed PRS for different incidence angle of a plane wave with TE polarization (a) and TM polarization (b).

III. CONCLUSION

The reduction of the Radar Cross Section of an antenna array by resorting to suitably-designed periodic surfaces both resistive and metallic has been briefly presented. The performance of the proposed design both for monostatic and bistatic systems will be discussed at the conference.

REFERENCES

- [1] P. Y. Ufimtsev, "Comments on diffraction principles and limitations of RCS reduction techniques," *Proceedings of the IEEE*, vol. 84, no. 12, pp. 1830–1851, 1996.
- [2] T. Ishikawa, M. Shibuya, and T. Yamamura, "Electromagnetic wave absorbing material," US5094907 A10-Mar-1992.
- [3] K.-Y. Park, S.-E. Lee, C.-G. Kim, and J.-H. Han, "Fabrication and electromagnetic characteristics of electromagnetic wave absorbing sandwich structures," *Composites Science and Technology*, vol. 66, no. 3–4, pp. 576–584, Mar. 2006.
- [4] H. D. Griffiths, "From a different perspective: principles, practice and potential of bistatic radar," in *Radar Conference, 2003. Proceedings of the International*, 2003, pp. 1–7.
- [5] M. Cherniakov, *Bistatic Radars: Emerging Technology*. John Wiley & Sons, 2008.
- [6] R. B. Green, *The general theory of antenna scattering*, Ph.D. Dissertation, The Ohio State University, Columbus, December 1963.
- [7] F. Costa, S. Genovesi, and A. Monorchio, "A Frequency Selective Absorbing Ground Plane for Low-RCS Microstrip Antenna Arrays", *Progress in Electromagnetics Research*, vol. 126, pp. 317–332, 2012.
- [8] H. K. Jang, J. H. Shin, and C. G. Kim, "Low RCS patch array antenna with electromagnetic bandgap using a conducting polymer", *International Conference on Electromagnetics in Advanced Applications (ICEAA)*, pp.140-143, 20-24 Sept. 2010.
- [9] F. Costa, A. Monorchio, "A Frequency Selective Radome with Wideband Absorbing Properties" *IEEE Trans. Antennas Propag.*, vol. 60, no. 6, pp. 2740–2747, 2012.
- [10] J. P. Turpin, P. E. Sieber, and D. H. Werner, "Absorbing Ground Planes for Reducing Planar Antenna Radar Cross-Section Based on Frequency Selective Surfaces," *IEEE Antennas and Wireless Propagation Letters*, vol. 12, pp. 1456–1459, 2013.
- [11] S. Genovesi, F. Costa, and A. Monorchio, "Low-Profile Array With Reduced Radar Cross Section by Using Hybrid Frequency Selective Surfaces," *IEEE Transactions on Antennas and Propagation*, vol. 60, no. 5, pp. 2327–2335, May 2012.
- [12] T. Liu, X. Cao, J. Gao, Q. Zheng, W. Li, and H. Yang, "RCS Reduction of Waveguide Slot Antenna With Metamaterial Absorber," *IEEE Transactions on Antennas and Propagation*, vol. 61, no. 3, pp. 1479–1484, Mar. 2013.
- [13] S. Genovesi, F. Costa, and A. Monorchio, "Wideband Radar Cross Section Reduction of Slot Antennas Arrays," *IEEE Transactions on Antennas and Propagation*, vol. 62, no. 1, pp. 163–173, Jan. 2014.
- [14] W. Pan, C. Huang, P. Chen, X. Ma, C. Hu, and X. Luo, "A Low-RCS and High-Gain Partially Reflecting Surface Antenna," *IEEE Transactions on Antennas and Propagation*, vol. 62, no. 2, pp. 945–949, Feb. 2014.
- [15] J. C. Iriarte Galarregui, A. Tellechea Pereda, J. L. Martinez de Falcon, I. Ederra, R. Gonzalo, and P. de Maagt, "Broadband Radar Cross-Section Reduction Using AMC Technology," *IEEE Transactions on Antennas and Propagation*, vol. 61, no. 12, pp. 6136–6143, Dec. 2013.

SUBSTRATE INTEGRATED WAVEGUIDE (SIW) CAVITY-BACKED PATCH ANTENNA

O. Losito⁽¹⁾, T. Castellano⁽¹⁾, M. Chiapperino⁽¹⁾, M. Bozzetti⁽¹⁾, G. Venanzoni⁽¹⁾, G. Angeloni⁽²⁾, C. Renghini⁽²⁾, P. Carta⁽²⁾, D. Mencarelli⁽³⁾, M. Farina⁽³⁾, A. Morini⁽³⁾, F. Prudenzeno⁽¹⁾.

⁽¹⁾ Dipartimento di Ingegneria Elettrica e dell'Informazione, Politecnico di Bari, Via Orabona 4, 70125 Bari, Italy

⁽²⁾ R&D Department, Somacis Spa, Via Jesina 17, Castelfidardo 60022, Italy.

⁽³⁾ Dipartimento di Ingegneria dell'Informazione Università Politecnica delle Marche, Via delle Brece Bianche, 60131, Ancona, Italy.

francesco.prudenzeno@poliba.it

Abstract

A broadband cavity-backed patch antenna is designed and characterized. The substrate integrated waveguide (SIW) technology is employed to fabricate the cavity under the patch. The antenna, that operates in the frequency range 10.7-12.7 GHz exhibits a maximum gain $G=8.6$ dBi, it could be used in satellite communications systems as an array element.

Index Terms – SIW antenna; Cavity Backed antenna; Ku band antenna.

I. INTRODUCTION

Patch antenna performance can be improved via different techniques, e.g. employment of suspended substrates, multi-stack and metalized baking cavity [1]-[2]. Substrate Integrated Waveguide (SIW) technology allows low-cost implementation, fast prototyping, and precise manufacturing [3]-[8]. In this work, a broadband SIW cavity-backed microstrip patch antenna operating in Ku Band is proposed. The antenna geometry has been optimized with the aim of broadening the bandwidth and improving the gain.

II. ANTENNA DESIGN

The antenna is based on a stack of two substrates, the microstrip substrate and the cavity substrate. The patch is printed on the microstrip substrate. Metalized via holes are designed along a circular aperture in the cavity substrate as shown in Fig. 1, to obtain the lateral walls on which patch antenna is backed. Rogers Duroid 5880 with dielectric constant $\epsilon_{rs}=2.2$, has been chosen for both substrates.

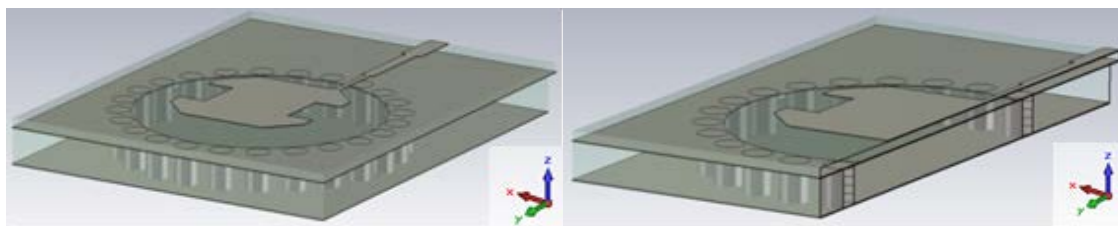


FIG. 1 – 3D Layout of the proposed SIW patch antenna, perspective and cross section view.

TABLE I - PARAMETERS OF THE OPTIMIZED ANTENNA

Parameter	Dimension
b	7.700 mm
w1	0.245 mm
w2	0.658 mm
w3	1.12 mm
l1	3.15 mm
l2	4.32 mm
l3	2.80 mm
n	1.443 mm
v	2.750 mm
m	7.523 mm
r	6.888 mm
α	15°
d	0.620 mm

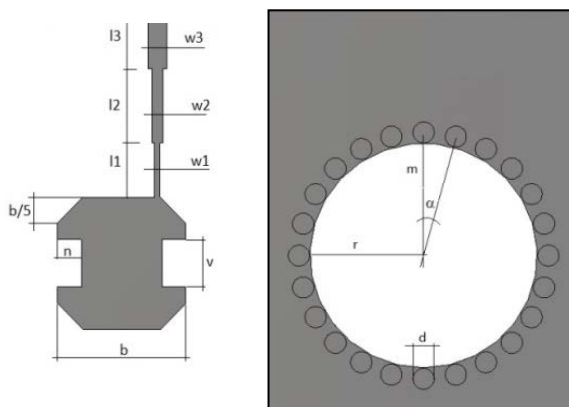


FIG. 2 – Layouts of the SIW cavity backed antenna

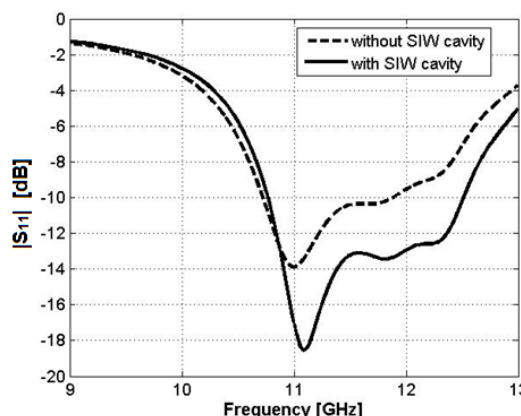


FIG. 3 – Simulated $|S_{11}|$ parameter versus frequency with and without SIW cavity.

The microstrip substrate thickness is $h_s=0.381$ mm while the cavity substrate thickness is $h_c=1.575$ mm. A number of simulations has been performed with the 3D commercial design software tool CST Microwave Studio®, in order to optimize the antenna performance. The optimized geometrical parameters of the antenna are indicated in Fig. 2 and listed in Table I. They allow a broad-band operation in the satellite communication frequency range 10.7 GHz-12.7 GHz. Lateral cuts in the patch layout improve the bandwidth, reducing the resonance frequency of the patch without increase of its surface. The performance improvement via SIW cavity is apparent in Fig. 3, illustrating $|S_{11}|$ versus frequency, simulated with and without SIW cavity.

III. RESULTS

The antenna prototype, fabricated by SOMACIS SPA, is shown in Fig. 4. The two layers are kept together through four screws. Fig. 5 illustrates a comparison between: a) simulated and measured $|S_{11}|$ versus frequency; b) simulated and measured gain. In both cases the agreement is good over the whole operation band. The maximum gain $G=8.6$ dBi value is obtained at frequency $f=11.7$ GHz.

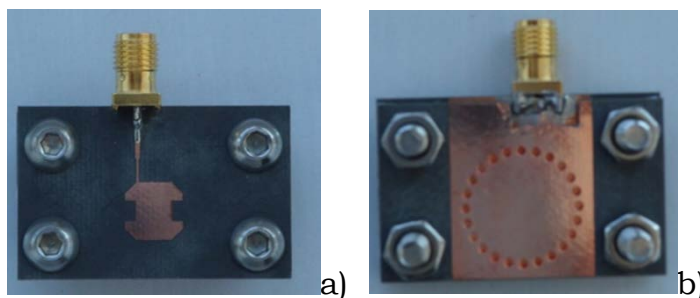


FIG. 4 – Prototype of manufactured dual layer antenna a) Top view b) bottom view.

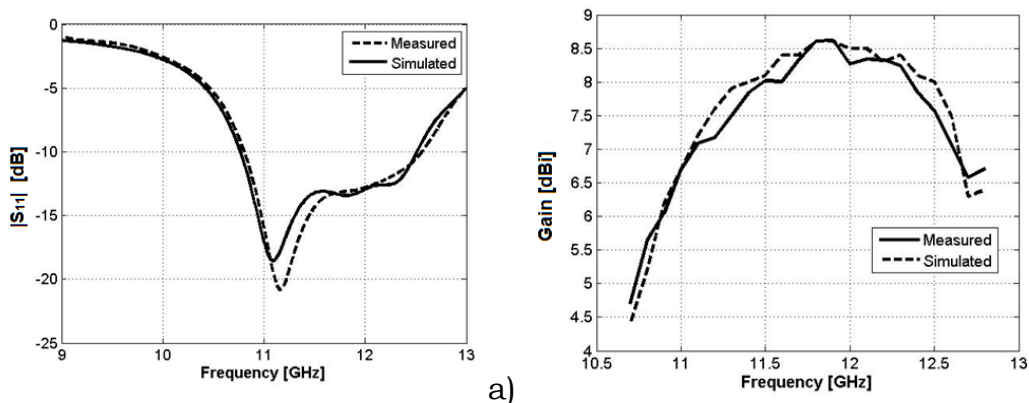


FIG. 5 – SIW Cavity baked antenna: a) simulated and measured $|S_{11}|$ and b) simulated and measured gain versus the frequency.

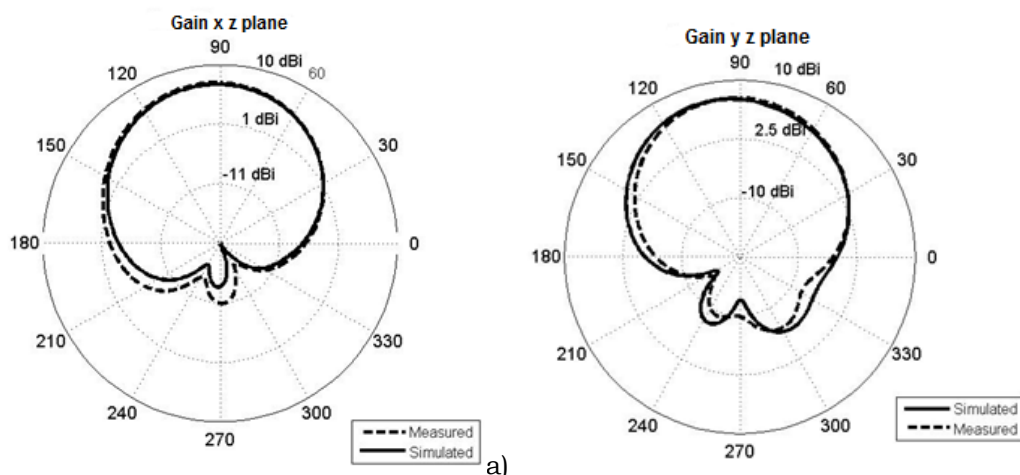


FIG. 6 – Simulated and measured antenna gain G at $f=11.7$ GHz in a) azimuth (x-z) and b) elevation (y-z).

Fig. 6 shows the simulated and measured antenna gain G , at the frequency $f=11.7$ GHz in a) azimuth (x - z plane) and b) elevation (y - z plane). The 3 dB beam width in azimuth is $w=85.5^\circ$. The obtained results encourage the fabrication of an antenna arrays, to be employed in satellite communications.

IV. CONCLUSION

A broadband SIW cavity-backed antenna has been manufactured. The gain is close to $G=8.6$ dBi at the frequency $f=11.7$ GHz. The antenna could be employed as single element for arrays operating in Ku-band.

ACKNOWLEDGEMENT

This work has been partially supported within the MIUR plans: PON01 01224 "Sviluppo di tecnologie in guida d'onda integrata (SIW) per applicazioni ICT a microonde"; PONa3 00298 "Potenziamento delle strutture e delle dotazioni scientifiche e tecnologiche del polo scientifico e tecnologico Magna Grecia"; PON02_00576_3329762 Sistemi avanzati mini-invasivi di diagnosi e radioterapia" AMIDERHA.

REFERENCES

- [1] S. Knyazev, "Microstrip antennas and arrays on the suspended substrate," ICECom 2003, *Proceeding of 17th International Conference on Applied Electromagnetics and Communications*, , pp. 168 – 171, 1-3 Oct. 2003, Dubrovnik, Croatia.
- [2] J.T. Aberle, "On the use of metallized cavities backing microstrip antennas," *Antennas and Propagation Society International Symposium*, Vol. 1, pp. 60 – 63, 1991.
- [3] D. Y. Kim, J. W. Lee, T. K. Lee, and C. Sik Cho, "Design of SIW Cavity-Backed Circular-Polarized Antennas Using Two Different Feeding Transitions," *IEEE Transaction on Antennas and Propagation*, 59, pp. 1398-1403, 2011.
- [4] Y. Cassivi, L. Perregri, P. Arcioni, M. Bressan, K. Wu, and G. Conciauro, "Dispersion characteristics of substrate integrated rectangular waveguide," *IEEE Microw. Wireless Compon. Lett.*, Vol. 12 (2), pp. 333-335, Feb. 2002.
- [5] M. Bozzi, F. Xu, D. Deslandes, and K. Wu, "Modeling and design considerations for substrate integrated waveguide circuits and components," TELSIS 2007, *8th International Conference on Telecommunications in Modern Satellite, Cable and Broadcasting Services*, pp. P-VII- P-XVI, Sep. 2007.
- [6] T. Castellano, O. Losito, L. Mescia, M. A. Chiapperino, G. Venanzoni, D. Mencarelli, G. Angeloni, C. Renghini, P. Carta, and F. Prudenzeno, "Feasibility Investigation of Low Cost Substrate Integrated Waveguide (SIW) Directional Couplers," *Progress In Electromagnetics Research B*, Vol. 59, pp. 31-44, 2014
- [7] O. Losito, L. Mescia, M. A. Chiapperino, T. Castellano, G. Venanzoni, D. Mencarelli, G. Angeloni, P. Carta, E. M. Starace, F. Prudenzeno "X-Band SIW Cavity-Backed Patch Antenna for Radar Applications" EuMW 2013 *European microwave Week*, pp. 6 - 11 October 2013 Nuremberg, Germany.
- [8] Mohamed H. Awida, Aly E. Fathy "Substrate-Integrated Waveguide Ku-Band Cavity-Backed 2x2 Microstrip Patch Array Antenna", *Antennas and Wireless Propagation Letters, IEEE*, vol8, pp. 1054-1056, Oct. 2009.

WIGNER FUNCTION APPROACH FOR THE RADIATION OF COMPLEX ELECTROMAGNETIC SOURCES

G. Gradoni⁽¹⁾

⁽¹⁾ School of Mathematical Sciences, University of Nottingham
University Park, NG7 2RD Nottingham, United Kingdom
gabriele.gradoni@nottingham.ac.uk

Abstract

The radiation of complex electromagnetic sources in either free-space or closed environments is studied through a statistical approach involving the field-field correlation function. A representation in dynamical phase-space, the Wigner distribution function, is used to unveil the wave mechanics of the source radiation. A transfer operator approach is used to transport source Wigner functions within the interior of complex cavities. The Perron-Frobenius approximation reduces the transport to a lower dimensional calculation, and therefore it can be computed efficiently. Achieved results are fundamental for understanding and predicting complex source radiation on a physical basis.

Index Terms – Cavity; phase space representation; statistical electromagnetics; Wigner distribution function

I. INTRODUCTION

Characterizing the radiation of electromagnetic (EM) sources reliably is a longstanding research issue in physics and engineering. In the context of electromagnetic compatibility (EMC), the radiation of electronic circuits is directly and indirectly responsible for the generation of EM pollution, which can reach dangerous but hard-to-predict levels due to interference and scattering effects. It is thus interesting to predict and control the radiation from EM sources in either free-space or closed environments. Any scenario involving complex sources and environments can in principle be characterized deterministically using numerically exact methods such as finite or boundary element methods. However, the geometrical structure or the boundary conditions are often too complicated or uncertain to be fully described within a mathematical model. Instead, a statistical perspective provides a more appropriate language to characterize complex sources. As often done in statistical mechanics, inferring that a complex system exhibits randomness, disorder, or chaotic behavior, yields an adequate starting point for describing its physical characteristics.

In this paper, we use the Wigner distribution function (WDF) formalism to propagate arbitrary field-field correlation functions. The WDF has the physical meaning of a distribution of waves in phase-space, i.e., the wave mechanical space, formed by the spatial position of the wave, and the momentum or direction of the associated wavevector.

II. CORRELATION OF VECTOR FIELDS

When the source is a made of complicated circuitry, there is a multitude of electronic components whose locations are uncertain, and whose excitation signals are intrinsically random, or highly sensitive to frequency. Then, the waves emitted from complex sources carry fluctuations, and can be conveniently treated as statistical random fields. We elect \hat{z} to be the principal axes of propagation. The source is located at $z=0$, and the detector is located at $z=D$. In order to uncover the kinetic properties of the source radiation, we need to represent fields in the momentum space $\underline{p}=[p_x, p_y]$, defined by the wavevector $\underline{k}=|\underline{k}|\underline{p}$ as

$$\begin{aligned} |\underline{p}| &= \sin \alpha, \\ T(\underline{p}) &= \sqrt{1-|\underline{p}|^2} = \cos \alpha, \end{aligned} \quad (1)$$

where α is the escape angle of the wave with respect to the normal vector to the source. It is worth noticing that (1) has the geometrical interpretation of direction cosines of the wavevector, with $T(\underline{p})$ kinematic operator. The field representation in \underline{p} -space can be achieved through a partial Fourier transformation $\underline{x}_\perp \xrightarrow{F} \underline{p}$ [1]. The idea is to propagate correlation functions rather than pure fields. The in-plane correlation tensor is defined as

$$\underline{\Gamma}_z(\underline{p}_1, \underline{p}_2) = \langle \underline{E}(\underline{p}, z) \otimes \underline{E}^H(\underline{p}, z) \rangle, \quad (2)$$

where H stands for the Hermitian conjugate, and $\langle \bullet \rangle$ represents the ensemble average over many statistically equivalent (subject to the same space-time fluctuations) source realizations. In the calculation of (2), we implicitly assume a statistical physics perspective of the EM system, where its evolution can be predicted through the asymptotic statistics of the ensemble to which sampled realizations belong. Therefore, evolving (2) along the ‘optical axes’ \hat{z} is more efficient than transporting probability distributions, while the transfer of energy out of the source can still be predicted accurately. Using the dyadic version of the Huygens principle, and upon application of the proper Dirichlet-to-Neumann mapping, yields

$$\underline{\Gamma}_z(\underline{p}_1, \underline{p}_2) = \underline{\rho}_1 \times \underline{I} \cdot \underline{\Gamma}_0(\underline{p}_1, \underline{p}_2) \cdot \underline{I} \times \underline{\rho}_2 \frac{e^{ikz[T(\underline{p}_1)-T(\underline{p}_2)]}}{T(\underline{p}_1)T(\underline{p}_2)}, \quad (3)$$

where $\underline{\Gamma}_0$ is the field-field correlation tensor at $z=0$, $\underline{\rho}_i = [\underline{p}_i, T(\underline{p}_i)\hat{z}]$, and \underline{I} is the unit dyad. In (3), the operator $T(\underline{p}_i)$ transports the in-plane

field distribution in phase-space according to the propagation of the field along z in configuration space. For scalar fields with in-plane polarization, we retrieve [2,3]

$$\Gamma_z^{(x,y)}(\underline{p}_1, \underline{p}_2) = \Gamma_0^{(x,y)} e^{ikz[T(\underline{p}_1) - T(\underline{p}_2)]}. \quad (4)$$

Complex sources radiating inside closed environments can be modeled through the transfer operator formalism [1]. Inherently, the field-field correlation tensor at the cavity boundary reads

$$\underline{\gamma}_{\underline{b}}(\underline{p}_1, \underline{p}_1) \simeq \left(\underline{\mathbb{I}} - \underline{\Upsilon} \otimes \underline{\Upsilon} \right)^{-1} \cdot \underline{\Gamma}_{\underline{b}}(\underline{p}_1, \underline{p}_1), \quad (5)$$

with transfer operator $\underline{\Upsilon}$, and physically meaning that the free-space correlation of the source radiation constitutes the cavity boundary illumination, which is perturbed by its reflections, transported through the cavity interior, and reaching the boundary again. The correlation (5) can be propagated to a cavity interior through the second Green identity.

III. WIGNER-WEYL TRANSFORMATION

The mechanical state of propagated waves is naturally defined in terms of position and direction of the wave-vector. Therefore, the position \underline{x}_\perp and the momentum \underline{p} form the wave-dynamical phase space. To achieve phase space densities of waves, i.e., the WDF, formally, the so-called Wigner-Weyl transform is applied to the correlation tensor, viz.,

$$W_z(\underline{x}_\perp, \underline{p}) = \frac{1}{(2\pi)^2} \iint e^{ik\underline{x}_\perp \cdot \underline{q}} \Gamma_z\left(\underline{p} + \frac{\underline{q}}{2}, \underline{p} - \frac{\underline{q}}{2}\right) d^2q. \quad (6)$$

Now, after plugging (4) into (6), and exploiting the inverse Wigner-Weyl transform to express the in-plane source correlation $\underline{\Gamma}_0$ in terms of a source WDF, we obtain

$$W_z^{(x,y)}(\underline{x}_\perp, \underline{p}) = \iiint \mathbb{K}_z^{(xx,yy)}(\underline{x}_\perp, \underline{x}'_\perp; \underline{p}, \underline{p}') W_0^{(x,y)}(\underline{x}'_\perp, \underline{p}') d^2x' d^2p', \quad (7)$$

where the kernel $\mathbb{K}_z^{(xx,yy)}$ is well approximated by a Dirac delta function. For near-homogeneous sources, often encountered in practice, the correlation becomes a slow function of \underline{x}_\perp , and correspondingly a localized function of its conjugate variable \underline{q} . It can be proved that this behavior leads to a Perron-Frobenius approximation [2,3], viz.,

$$W_z^{(x,y)}(\underline{x}_\perp, \underline{p}) \simeq W_0^{(x,y)}\left(\underline{x}_\perp - \frac{\underline{p}}{\sqrt{1 - |\underline{p}|^2}} z, \underline{p}\right), \quad (8)$$

meaning that the transport of wave densities is a Liouville equation, i.e., a flow in phase-space similar to a free-particle motion if evanescent

waves are excluded, i.e., $(\underline{x}, \underline{p}) \in \mathbb{R}^2 \times C^2$. The propagated correlation can be retrieved back taking the inverse Fourier transform of (7) or (8). The generalized Zernike theorem can be easily retrieved. When the source correlation is propagated through a closed cavity, we find that the transport of the WDF at the cavity boundary can be formally expressed by

$$\underline{\underline{w}}(\underline{p}, \underline{s}) = (\underline{\underline{I}} - \underline{\underline{\Psi}})^{-1} \cdot \underline{\underline{W}}_b(\underline{p}, \underline{s}), \quad (9)$$

where the operator

$$\underline{\underline{\Psi}}\{f\} = \iint \underline{\underline{\Upsilon}}\left(\underline{p} + \frac{\underline{q}}{2}\right) \otimes \underline{\underline{\Upsilon}}\left(\underline{p} - \frac{\underline{q}}{2}\right) \cdot e^{ik(b-b')\cdot\underline{q}} d\underline{q} \cdot f(\underline{p}', \underline{s}) d^2 p', \quad (10)$$

has kernel given by the correlation transport tensor. Numerical results are generated for Gaussian-Schell correlated sources propagating in free-space [2] and regular reflecting environments [3]. Wave chaotic cavities leads to a constant WDF (Berry's conjecture). This can be retrieved from (17) through an ergodic argument.

IV. CONCLUSION

We have developed a mathematical framework to investigate the radiation of complex electromagnetic sources in either free-space or closed environments. We found that the free-space radiation is well approximated by a flow in phase-space for which we calculated the dynamical map. The associated Liouville equation can be used to develop efficient computational solvers. This theory can be used and enriched to solve the radiation of sources in arbitrary cavities.

ACKNOWLEDGEMENT

Financial support from the UK Engineering and Physical Sciences Research Council (EPSRC).

REFERENCES

- [1] S. C. Creagh, H. B. Hamdin, and G. Tanner, "In-out decomposition of boundary integral equations," *Journal of Physics A*, vol. 46(43), pp. 435203, 2013.
- [2] G. Gradoni, S. C. Creagh, and G. Tanner, "Characterization of Electromagnetic Fields in Complex Systems Through Phase-Space Techniques," *Radio Science Meeting (USNC-URSI NRSM), 2013 US National Committee of URSI National*, January 8-11 2014, Boulder (CO), United States of America.
- [3] G. Gradoni, S. C. Creagh, and G. Tanner, "A Wigner Function Approach for Describing the Radiation of Complex Sources," *Electromagnetic Compatibility (EMC), 2014 IEEE International Symposium on*, August 3-7 2014, Raleigh (NC), United States of America.

STUDY OF THE MULTIPATH DISTRIBUTION IN URBAN ENVIRONMENT FOR 5G MOBILE RADIO

M. Barbiroli⁽¹⁾, V. Degli-Esposti⁽¹⁾, G. Falciasecca⁽¹⁾, F. Fuschini⁽¹⁾,
L. Tian⁽²⁾, E. M. Vitucci⁽³⁾

⁽¹⁾ Department of Electrical, Electronic and Information Engineering “G. Marconi”
University of Bologna

Viale Risorgimento 2, 40136 Bologna, Italy

⁽²⁾ Tongji University, Shanghai, China

⁽³⁾ CIRI-ICT - via Rasi e Spinelli, 176, 47521 - Cesena (FC), Italy
{marina.barbiroli, v.degliesposti, gabriele.falciasecca, franco.fuschini, li.tian,
enricomaria.vitucci}@unibo.it

Abstract

Advanced radio transmission and antenna techniques, such as MIMO, directive-antennas and beamforming have recently been proposed for high-speed communication systems. In this work we study the Power-Angular-Distribution for different receivers locations in urban scenario. The results show that directive-antennas and beamforming cannot rely simply on the position information of the radio terminals and the knowledge of the PAD can help implement optimal beamforming techniques for Mobile Back-Hauling systems and MIMO systems.

Index Terms – Mobile Radio Systems, LOS probability, Urban Propagation, Ray Tracing

I. INTRODUCTION

Fifth generation mobile radio system will have to cope with an exponential growth of mobile traffic in urban and indoor areas, as foreseen for the coming years. Therefore, small-cell overlay networks with radio access-points properly deployed within the urban structure and connected with the major concentration points or macro-cellular Base Station (BS) sites through high-capacity links will have to be designed [1]. Since small-cell sites will have to be placed in proper positions inside streets and major buildings to increase the off-load from the macro-cellular-layer, possibly without the constraints of wired connections, the use of Mobile Back-Hauling (MBH) at microwave or millimeter-wave bands appears very appropriate to the task [2].

Such MBH links however will often have to operate in Non Line Of Sight conditions and therefore will have to make use of MIMO beam-forming (or beam-switching) transmission techniques to properly exploit the space domain and achieve the required channel reliability and capacity. The present study is preliminary to the design of MBH systems in dense urban environments. First of all the NLOS probability in typical urban streets is derived through ray tracing simulation. Then the angular distribution of the signal at the radio terminal with respect to the radial direction between transmitter and receiver (“LOS direction”) is derived. Such characterization is of importance to design proper beamforming

strategy based on the knowledge of the positions of the terminals and/or of the multipath structure, and more generally to assess the feasibility of MBH for future generation systems.

II. THE LOS PROBABILITY AND PDA

The evaluation of LOS probability is a key aspect for future millimeter high capacity backhauling and for the design or deployment of high performance beamforming array. Moreover the angular information of received multipath components are crucial to assess the capacity potential of the MIMO channel and to implement proper Space-time coding strategies.

In this work the statistical Power-Angular-Distribution (PAD) at the receiver with respect to the radial direction is evaluated on the base of 3D ray-tracing simulations. Receiver (Rx) routes are considered instead of single Rx location, in order to account for the dynamic evolution of the channel in space/time. A full 3-D approach is adopted to properly account for possible multipath contributions originated by far, prominent buildings, which cannot be neglected for a reliable prediction of multipath propagation in urban environments, but would be discarded with two-dimensional approaches [3]. Both a geometrical and an electromagnetic description of each object (building, wall, terrain) must be input to the RT engine. Compound materials are treated adopting effective electromagnetic parameters, i.e., parameters representative of the overall behavior of the compound in terms of reflection, transmission and diffraction of an incoming wave. The following values of electrical permittivity and conductivity have been used here for building walls: $\epsilon_r=5$, $\sigma=1 \times 10^{-2}$ [S/m], which are recognized as the most appropriate in European cities [1]. Furthermore for the diffuse scattering the Effective Roughness (ER) approach is considered with a scattering coefficient $S=0.3$.

Simulations have been performed on the city area of Helsinki in a macro-cellular (BS1) scenario, along the routes GH and EF shown in Figure 1 .



Figure 1 The layout of the city of Helsinki, the positions of the BS and the receivers locations.

In the Rx route GH, the total number of measured receiver positions is equal to 166. And it is found that only one position is in LOS propagation conditions. So the LOS probability in route GH is equal to 1/166, which is approximately 0.6 percent. In order to find out the dominant radio path wherefrom the main contribution to the received power comes from, the PAD distribution of the signal has to be investigated.

For each receiver position along route GH, the PAD has been derived from RT simulation and then it has been rotated so to place the radial Tx-Rx direction on the reference x-axis direction. All single receiver's PAD have then been normalized and averaged into a single, overall Power-DoA-Distribution characteristic of the considered route/area (Figure 2 , Figure 3). The power is expressed in dBW, and the angles in degree. Besides, the resolution of the angle spread has been set to be 3 degrees.

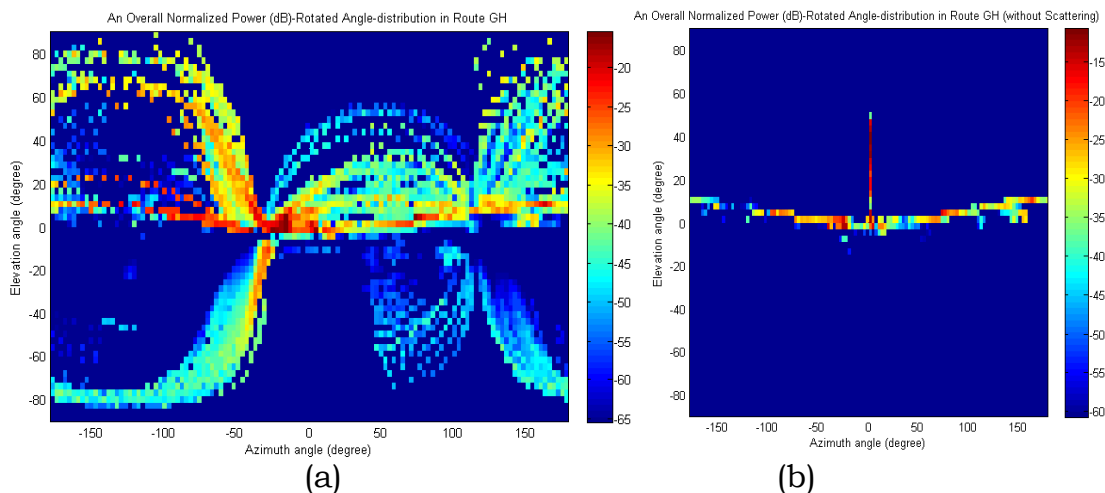


Figure 2 The overall Power-DoA-Distribution in route GH (a) ER scattering enabled, (b) scattering disabled.

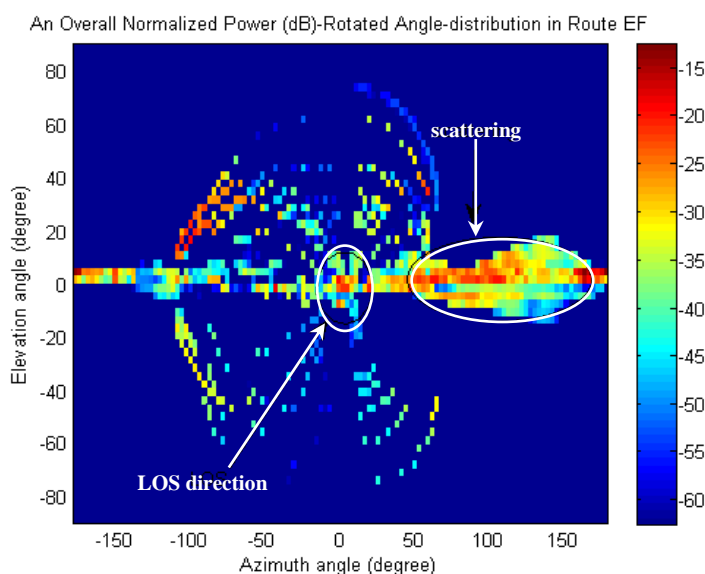


Figure 3 The overall Power-DoA-Distribution in route EF.

Figure 2 (a), and (b) show the overall PAD distribution in route GH considering in the total received power the effect of enabling ER scattering (Figure 2 (a)) or disabling it (Figure 2 (b)). As can be noted diffuse scattering is very important in a such a typical street canyon; is evident that the transmitter can illuminate almost all the buildings on the northern side of the street, and a considerable amount of the incident power is then scattered down directly to the receivers along the street. As shown in Figure 2 (a), there are many types of contribution to the overall Power-DoA-Distribution in Rx route GH. The point with elevation angle and azimuth angles equal to zero, is the “radial direction”. The dominant direction from where the power reach the receiver however appears to be the street direction from H to G, and also the opposite direction.

In the Rx route EF the LOS probability equals to 5/175, which is approximately 2.86 percent.

As can be seen in Figure 3 , the power contributions are mainly originated by the LOS direction, for the five location in LOS condition and by scatterings from the buildings located on the southern side of the bay, for most of the NLOS receiving locations.

III. CONCLUSION

Results of this preliminary study show the LOS probability is very small in dense urban macrocellular environment, thus directive-antenna and beamforming techniques cannot rely simply on the position information of the radio terminals to maximize the power-budget and guarantee reliable transmission. The analysis of the PAD distribution for different receivers locations show that diffuse scattering plays a key role in urban propagation. Moreover abrupt changes in the PAD and multipath structure are found, especially in the vicinity of street intersections. The results can help implement optimal beamforming techniques for MBH systems, and could help in planning the position of small-cell base stations in next generation mobile networks.

REFERENCES

- [1] S. Landström, H. Murai, A. Simonsson, “Deployment Aspects of LTE Pico Nodes”. IEEE International Conference on Communications Workshops (ICC 2011), vol.1, n. 5, pp. 5-9 Kyoto, Japan, June 5-9, 2011.
- [2] M. Coldrey, H. Koorapaty, J. E. Berg, Z. Ghebretensaé, J. Hansryd, A. Derneryd, S. Falahati, "Small-Cell Wireless Backhauling: A Non-Line-of-Sight Approach for Point-to-Point Microwave Links," Vehicular Technology Conference (VTC Fall), Quebec, Canada, Sept. 2012.
- [3] F. Fuschini, H. El-Sallabi, V. Degli-Esposti, L. Vuokko, D. Guiducci, and P. Vainikainen, “Analysis of multipath propagation in urban environment through multidimensional measurements and advanced ray tracing simulation,” IEEE Trans. Antennas Propag., vol. 56, no. 3, pp. 848–857, Mar. 2008.
- [4] L. M. Correia, Ed., Mobile broadband multimedia networks. New York: Academic Press, 2006.

ON THE SCATTERING BY A CYLINDRICAL TARGET BELOW A ROUGH GAUSSIAN SURFACE

C. Ponti

Department of Engineering, “Roma Tre” University
Via Vito Volterra 62, 00146, Roma, Italy
cristina.ponti@uniroma3.it

Abstract

Electromagnetic scattering of a two-dimensional beam by a cylinder buried below a slightly rough surface is solved, combining Cylindrical Wave Approach with Small Perturbation Method, in the first order approximation. Scattered fields are the superposition of zero-th order contributions, relevant to a flat surface, and first-order ones, dealing with surface deviations. A spectral representation is used for the cylindrical waves used as basis functions of the scattered field, as well as for the incident beam. The theory has been implemented for a surface with Gaussian roughness spectrum.

Index Terms – buried object detection, electromagnetic scattering, rough surfaces, spectral domain analysis.

I. INTRODUCTION

Solution of forward electromagnetic scattering by buried objects has important applications in the context of the ground penetrating radar (GPR) technique [1]. An advanced modeling may provide an improved understanding of GPR surveys under realistic conditions. Numerical results by the available scattering techniques may be also used as input data to test novel inversion algorithms. A scattering scenario with targets buried below rough surface may be used to model the typical unevenness of natural surface.

Models of random rough surface scattering are developed in the literature, following two main approaches: i.e., small perturbation method (SPM) [1] and Kirchhoff approximation [2].

In [3], the SPM method was combined to Cylindrical Wave Approach (CWA) to solve the scattering by a circular cross-section cylinder buried below an arbitrarily rough surface in an analytical way. Reflected and transmitted cylindrical functions were used as basis functions of the fields scattered by the cylinder, to define reflection and transmission of cylindrical waves through an interface. In the frame of SPM solution, they were decomposed in zero-th and first-order terms. In the numerical solution, a sinusoidal profile was used to implement the rough surface, and spectral integrals relevant to the cylindrical waves employed as basis functions of the scattered fields were evaluated in an accurate way. The technique presented in [3] is here solved for an arbitrary rough profile, i.e., for a surface with Gaussian rough spectrum on a periodic

interval. Fourier series expansion are used to deal with surface periodicity. Therefore, double spectral integrals relevant to the interaction of the scattered fields with the rough surface, in the first order approximation, are turned into single integrals. Numerical evaluation of spectral integrals is performed in an accurate way, leading to results both in near- and far-field regions.

II. THEORETICAL ANALYSIS

The geometry of the problem is sketched in Fig. 1(a). A two-dimensional beam impinges on a periodic rough surface given by a function $g(\zeta) = g(\zeta + L_n)$, being L_n the normalized surface length. Problem is solved through a scalar function $V(\xi, \zeta)$, standing for the electric (TM polarization) or magnetic (TE polarization) field. Such field is decomposed in further fields contribution, i.e., the source field V_i , modeled with a Gaussian beam, the reflected and transmitted beam V_r and V_t , respectively, and the scattered field contributions, V_s , V_{sr} , V_{st} . The scattered field V_s gives the field scattered by the buried cylinder in medium 2, whereas the fields V_{sr} and V_{st} are the scattered-reflected and scattered-transmitted field, respectively.

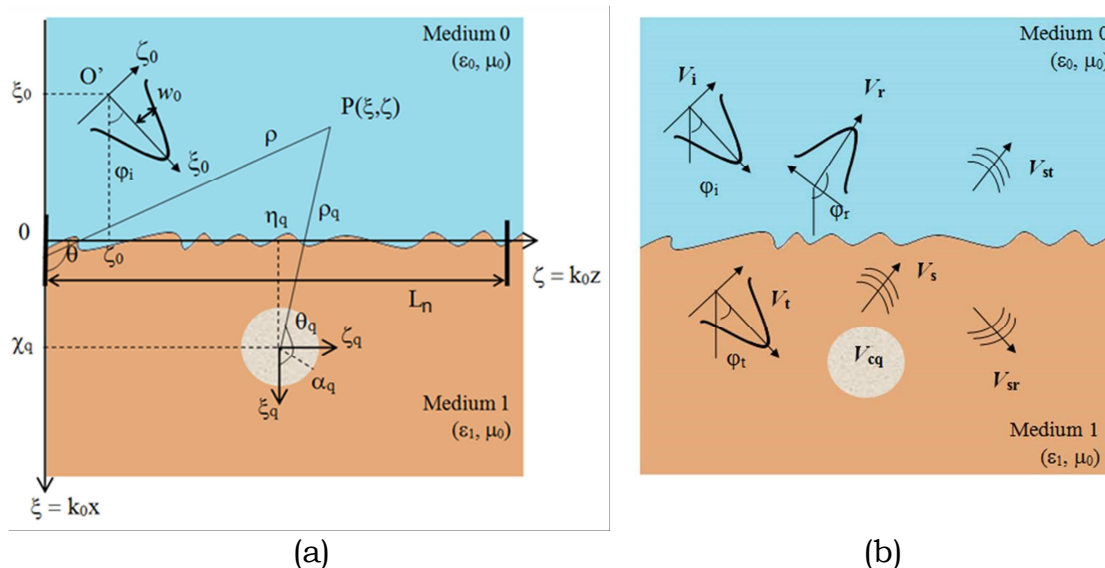


FIG. 1 – a) Geometry of the problem; b) Decomposition of the total field.

As to field contributions V_r , V_t , V_{sr} and V_{st} , dealing with the interaction with the rough surface in terms of reflection and transmission, they are defined in the frame of Small Perturbation Method, and result as the superposition of a zero-th order term and a first-order one. As to the scattered-reflected field, we have:

$$V_{sr}(\xi, \zeta) = V_0 \sum_{m=-\infty}^{+\infty} i^m c_{qm} \left\{ RW_m^{un} [n_1(-\xi_q - 2\chi_q), n_1\zeta_q] \right. \\ \left. + RW_{m,\ell}^{per} [n_1(-\xi_q - 2\chi_q), n_1\zeta_q, \chi_q] \right\} \quad (1)$$

where the perturbed term relevant to the interaction with a surface with Gaussian roughness spectrum is given by:

$$RW_{m,\ell}^{per}(-n_1\chi_q, 0, \chi_q) = \frac{1}{2\pi L_n} \sum_{u=-\infty}^{+\infty} \int_{-\infty}^{+\infty} \gamma_{10}(n_{\parallel}, u) F_m(-n_1\chi_q, n_{\parallel}) \\ \times e^{-i\sqrt{1-(n_{\parallel}+2\pi L_n)^2}\chi_q} e^{-i\ell \arctan\left[\frac{(n_{\parallel}+2\pi L_n)}{\sqrt{1-(n_{\parallel}+2\pi L_n)^2}}\right]} dn_{\parallel} \quad (2)$$

The same decomposition applies to the scattered-transmitted:

$$V_{st}(\xi, \zeta) = V_0 \sum_{m=-\infty}^{+\infty} i^m c_{qm} \left\{ TW_m^{un} [n_1(\xi + \chi_q), \zeta, \chi_q] \right. \\ \left. + TW_m^{per} [n_1(\xi + \chi_q), \zeta, \chi_q] \right\} \quad (3)$$

being in this case for the perturbed transmitted-cylindrical waves:

$$TW_m^{per}[-n_1(\xi + \chi_q), \zeta, \chi_q] = \frac{1}{2\pi L_n} \sum_{u=-\infty}^{+\infty} \int_{-\infty}^{+\infty} \tau_{10}(n_{\parallel}, u) F_m(-n_1\chi_q, n_{\parallel}) \\ \times e^{-i\sqrt{1-n_1(n_{\parallel}+2\pi L_n)^2}(\xi + \chi_q)} e^{in_1(n_{\parallel}+2\pi L_n)\zeta} dn_{\parallel} \quad (4)$$

III. NUMERICAL IMPLEMENTATION

In the numerical implementation, the samples of the Gaussian surface are generated applying Thorsos's theory [4], in the limits of SPM. The number of samples has been chosen according to the spectrum behavior, which in turns depends on the statistics of the Gaussian surface.

A numerical result of scattering by a PEC cylinder below a Gaussian rough surface is reported in Fig. 2, averaged over 10 surface realizations. The cylinder has normalized radius $\alpha = 0.32\pi$, and it is centered in $\chi_q = 5$. The lower medium has refraction index $n_1 = 2$. The statistics of the surface are: correlation length $\ell_n = 0.6\pi$, normalized height $h_n = 0.02\pi$; the normalized surface length is $L_n = 80\pi$. The incident field is a Gaussian beam in TM polarization with normalized beam waist $u_n = L_n/4$, and impinging in $\varphi = 0$.

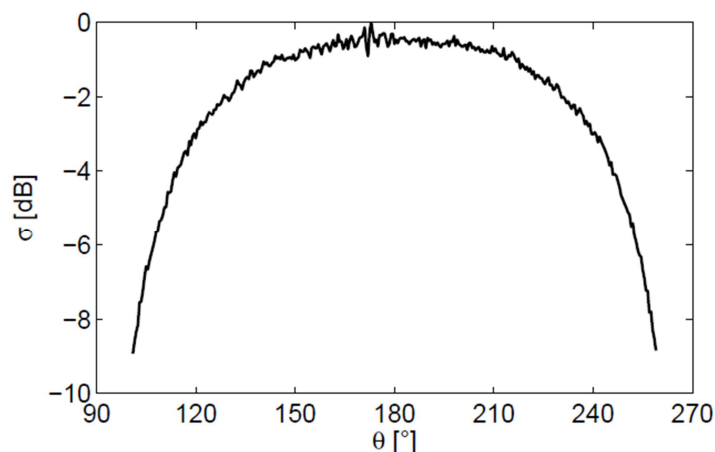


FIG. 2 – Scattered field by a buried PEC cylinder, averaged over 10 surface realizations.

IV. CONCLUSION

A semi-analytical technique to solve scattering by a cylinder below a rough surface has been presented. To cope with an infinite rough profile, a finite-width illumination field has been used, and a surface profile with Gaussian spectrum has been generated on a periodic interval. An interesting extension of the method would be the generalization to a finite set of buried cylinders, in order to simulate the scattering by multiple targets.

ACKNOWLEDGEMENT

This work is a contribution to COST Action TU1208 "Civil Engineering Applications of Ground Penetrating Radar."

REFERENCES

- [1] L. Tsang, J. A. Kong, and K.-H. Ding, *Scattering of Electromagnetic Waves: Theories and Applications*, Wiley, 2001.
- [2] F. G. Bass and I. M. Fuks, *Wave Scattering from Statistically Rough Surfaces*, Pergamon, 1979.
- [3] M. A. Fiaz, F. Frezza, L. Pajewski, C. Ponti, and G. Schettini, "Scattering by a circular cylinder buried under a slightly rough surface: the cylindrical-wave approach," *IEEE Trans. Antennas Propag.*, Vol. 60, pp. 2834–2842, June 2012.
- [4] E. I. Thorsos, "The validity of the Kirchhoff approximation for rough surface scattering using a Gaussian roughness spectrum," *J. Acoust. Soc. Am.*, Vol. 83, pp. 78–92, 1988.

ELECTROMAGNETIC SCATTERING BY A DIELECTRIC SPHERE EMBEDDED IN A CIRCULAR CYLINDER

F. Mangini⁽¹⁾ and N. Tedeschi⁽¹⁾

⁽¹⁾ Department of Information Engineering, Electronics and
Telecommunications, "La Sapienza" University of Rome,
Via Eudossiana 18, 00184 Roma, Italy
mangini@diet.uniroma1.it

Abstract

An analytical solution to the electromagnetic scattering of a plane wave by a sphere embedded in a circular, dielectric cylinder, is presented. The field components are expanded in series of cylindrical and spherical harmonics. Results obtained from simulations are presented.

Index Terms – Cylindrical harmonics, electromagnetic scattering, Mie theory, spherical harmonics.

I. INTRODUCTION

The scattering of electromagnetic plane waves by a cylinder or a sphere, is a classical topic in the literature [1,2]. However, the problem of the scattering by a sphere embedded in a circular, dielectric cylinder has not been investigated. The problem can be solved by representing the scattered and internal waves of the cylinder in cylindrical harmonics, and the scattered and internal waves of the sphere in spherical harmonics. Moreover, the scattered spherical wave must be represented as an integral of cylindrical harmonics and the internal cylindrical wave as a series of spherical waves. In this way, the boundary conditions can be applied and the unknown coefficients of the series can be computed.

II. THEORETICAL APPROACH

The geometry of the problem is depicted in Fig. 1. A cylinder of radius a containing a sphere of radius b is located at the center of a Cartesian coordinate system. The impinging radiation is a plane wave forming an angle ϑ_i with the z -axis, and its projection on the (x,y) plane forms an angle φ_i with the x -axis. Let ε_1 , μ_1 , k_1 , ε_2 , μ_2 , k_2 and ε_3 , μ_3 , k_3 be the relative permittivity, relative permeability and wavenumber of external medium, cylinder and sphere, respectively. A time dependence $e^{-i\omega t}$ is assumed and always omitted. The incident radiation is an elliptically-polarized plane wave with an electric field given by:

$$\underline{E}_i(\underline{r}) = \left(E_{\vartheta_i} \underline{g}_{0i} + E_{\varphi_i} \underline{\phi}_{0i} \right) e^{i\mathbf{k}_i \cdot \underline{r}} \quad (1)$$

where $\underline{\vartheta}_{0i}$, $\underline{\varphi}_{0i}$ and \underline{k}_{0i} are the unit vectors, see Fig. 1b.

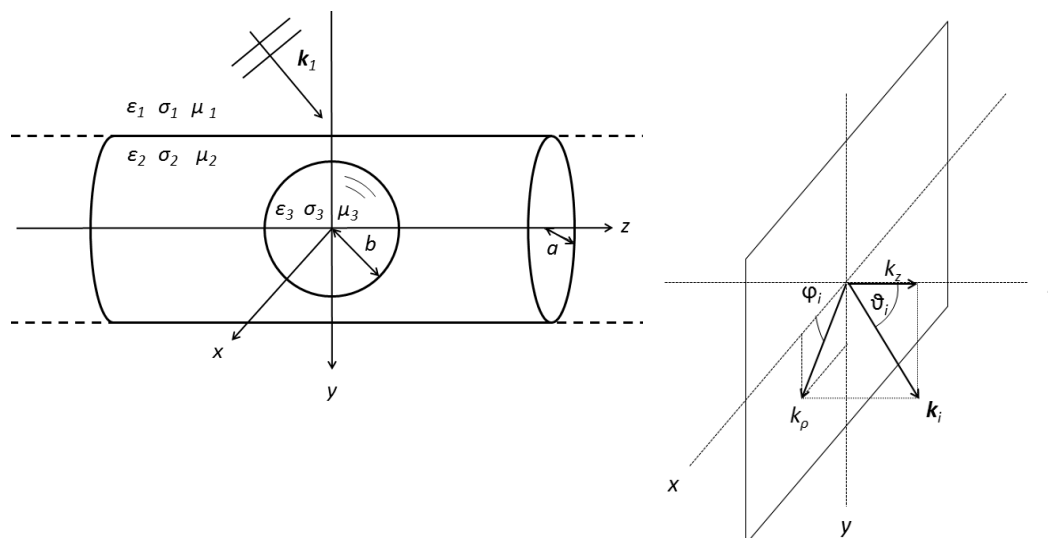


FIG. 1 – Statement of the problem.

The fields in all the domains are [3]:

$$\underline{E}_{sc}(\underline{r}) = \sum_{m=-\infty}^{+\infty} [c_m \underline{M}_m^{(3)}(k_1, \underline{r}) + d_m \underline{N}_m^{(3)}(k_1, \underline{r})] \quad (2)$$

$$\underline{E}_{ic}(\underline{r}) = \sum_{m=-\infty}^{+\infty} [e_m \underline{M}_m^{(1)}(k_2, \underline{r}) + f_m \underline{N}_m^{(1)}(k_2, \underline{r})] \quad (3)$$

$$\underline{E}_{ss}(\underline{r}) = \sum_{n=1}^{\infty} \sum_{m=-\infty}^{+\infty} [g_{mn} \underline{M}_{mn}^{(3)}(k_2, \underline{r}) + l_{mn} \underline{N}_{mn}^{(3)}(k_2, \underline{r})] \quad (4)$$

$$\underline{E}_{is}(\underline{r}) = \sum_{n=1}^{\infty} \sum_{m=-\infty}^{+\infty} [p_{mn} \underline{M}_{mn}^{(1)}(k_3, \underline{r}) + q_{mn} \underline{N}_{mn}^{(1)}(k_3, \underline{r})] \quad (5)$$

In order to apply the boundary conditions, the spherical waves can be written as integrals of cylindrical harmonics and the cylindrical waves can be expanded in series of spherical harmonics [4]. Therefore, the electric field inside the cylinder can be written as follows:

$$\underline{E}_{ic}(\underline{r}) = \sum_{m=-\infty}^{+\infty} k_i^{n-m+1} \frac{(2n+1)(n-m)!}{n(n+1)(n+m)!} \sin \mathcal{G}_i \left\{ e_m [\tau_{mn}(\cos \mathcal{G}_{ic}) \underline{M}_{mn}^{(1)}(\underline{r}) + i\pi_{mn}(\cos \mathcal{G}_{ic}) \underline{N}_{mn}^{(1)}(\underline{r})] + f_m [i\pi_{mn}(\cos \mathcal{G}_{ic}) \underline{M}_{mn}^{(1)}(\underline{r}) + \tau_{mn}(\cos \mathcal{G}_{ic}) \underline{N}_{mn}^{(1)}(\underline{r})] \right\}$$

and the scattered field from the sphere can be written as follows:

$$\underline{E}_{ss}(\underline{r}) = \sum_{n=1}^{\infty} \sum_{m=-\infty}^{+\infty} \frac{i^{m-n-1}}{2k} \left\{ g_{mn} \int_0^{\pi} [\tau_{mn}(\cos \alpha) \underline{M}_m^{(3)}(\underline{r}) + \pi_{mn}(\cos \alpha) \underline{N}_m^{(3)}(\underline{r})] d\alpha + l_{mn} \int_0^{\pi} [\pi_{mn}(\cos \alpha) \underline{M}_m^{(3)}(\underline{r}) + \tau_{mn}(\cos \alpha) \underline{N}_m^{(3)}(\underline{r})] d\alpha \right\}$$

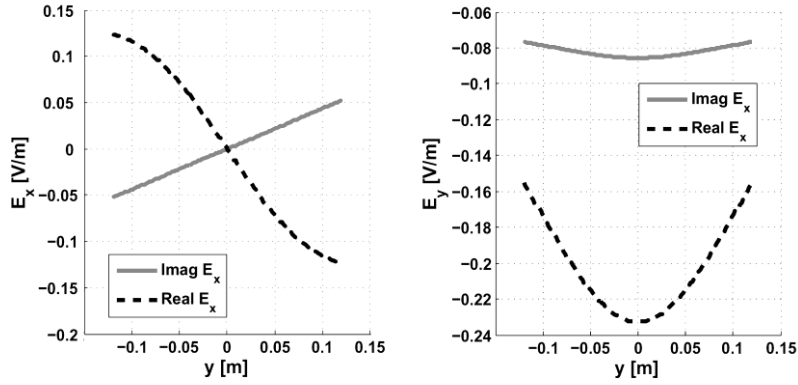


FIG. 2 – The real (dashed line) and imaginary (solid line) electric field components computed along a line of coordinate $(x; y) = (-2a; [-a; 0])$,

To solve the problem, we have to impose the boundary conditions on all the surfaces, i.e. on the cylindrical surface:

$$\rho_0 \times [\underline{E}_i(a_c, \varphi, z) + \underline{E}_{sc}(a_c, \varphi, z) - \underline{E}_{ic}(a_c, \varphi, z) - \underline{E}_{ss}(a_c, \varphi, z)] = 0$$

$$\rho_0 \times \left[\frac{1}{\mu_1} \nabla \times \underline{E}_i(a_c, \varphi, z) + \frac{1}{\mu_1} \nabla \times \underline{E}_{sc}(a_c, \varphi, z) - \frac{1}{\mu_2} \nabla \times \underline{E}_{ic}(a_c, \varphi, z) - \frac{1}{\mu_2} \nabla \times \underline{E}_{ss}(a_c, \varphi, z) \right] = 0$$

and on the spherical surface:

$$r_0 \times [\underline{E}_{ic}(a_s, \vartheta, \varphi) + \underline{E}_{ss}(a_s, \vartheta, \varphi) - \underline{E}_{is}(a_s, \vartheta, \varphi)] = 0$$

$$r_0 \times \left[\frac{1}{\mu_2} \nabla \times \underline{E}_{ic}(a_s, \vartheta, \varphi) + \frac{1}{\mu_2} \nabla \times \underline{E}_{ss}(a_s, \vartheta, \varphi) - \frac{1}{\mu_3} \nabla \times \underline{E}_{is}(a_s, \vartheta, \varphi) \right] = 0$$

Inserting the field expressions in the boundary conditions and applying the orthogonality properties of the Legendre and exponential functions the unknowns can be computed.

III. VALIDATIONS AND RESULTS

In this section, we present some numerical results obtained with a software based on Finite Element Methods (FEM): Comsol Multiphysics.

In Fig. 2, the electric field along a line of coordinates $(x; y) = ([-a, 0]; -2a)$ is shown, in the case of an internal sphere with radius $b = a/2$ and relative permittivity $\varepsilon_3 = 4$, placed at the center of the cylinder of radius $b = 0.12$ m and relative permittivity $\varepsilon_2 = 2.5$. The cylinder is immersed in air and the incident plane wave has unitary amplitude and has the electric field along y .

In Fig. 3, the electric field components are shown as function of frequency. In particular, the frequency range is from 30 MHz to 3 GHz. The geometrical and electromagnetic characteristics of the problem are the same of Fig. 2.

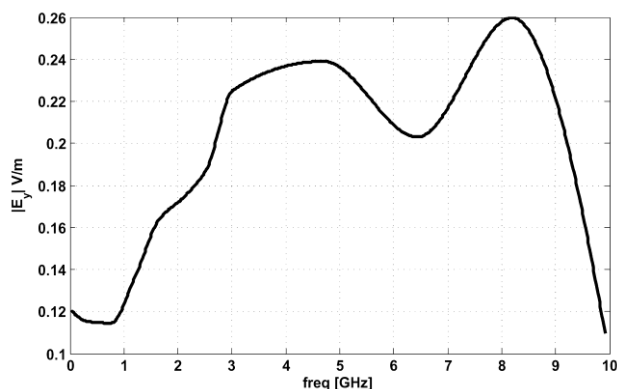


FIG. 3 – Magnitude of the electric field along y computed in the point of coordinate $(-2a; 0; 0)$, as function of the frequency.

IV. CONCLUSION

In this paper, a rigorous method to solve the electromagnetic scattering of an elliptical-polarized plane wave by a circular cylinder containing a dielectric sphere is presented. The solution has been achieved with an expansion of the fields in series of vectorial spherical and cylindrical harmonics. In order to apply the boundary conditions, the spherical waves have been written as integrals of cylindrical harmonics and the cylindrical waves have been written as series of spherical harmonics. Applying the orthogonality properties of the Legendre and exponential functions, a linear system has been obtained, and the unknowns have been computed. The scattered electric field, obtained through electromagnetic simulations, has been shown and a frequency study has been performed.

REFERENCES

- [1] M. Di Vico, F. Frezza, L. Pajewski, and G. Schettini, "Scattering by a finite set of perfectly conducting cylinders buried in a dielectric half space: spectral-domain solution," *IEEE Transactions on Antennas and Propagation*, vol. 53(2), pp. 719-727, Feb. 2005.
- [2] F. Frezza, F. Mangini, L. Pajewski, G. Schettini, and N. Tedeschi, "Spectral domain method for the electromagnetic scattering by a buried sphere," *Journal of the Optical Society of America A*, vol. 30(4), pp. 783-790, Apr. 2013.
- [3] J.A. Stratton, *Electromagnetic Theory*, McGraw-Hill, 1941.
- [4] G. Han, Y. Han, and H. Zhang, "Relations between cylindrical and spherical vector wavefunctions," *Journal of Optics A: Pure and Applied Optics*, vol. 10(1), (7 pp.), Jan. 2008.

PLANE-WAVE SCATTERING BY A PERFECTLY CONDUCTING ELLIPTIC CYLINDER NEAR A PLANE SURFACE

C. Santini ^(1*), F. Mangini ⁽¹⁾, and N. Tedeschi ⁽¹⁾

⁽¹⁾ Dept. of Information Engineering, Electronics and Telecommunications, "La Sapienza" University of Rome, Via Eudossiana 18, 00184 Rome, Italy, *carlo.santini@diet.uniroma1.it.

Abstract

In this paper we present a method for the analysis of the diffraction problem relevant to a homogeneous plane electromagnetic wave impinging on a perfectly conducting circular elliptical cylinder near a generally reflecting plane surface. The solution of the scattering problem is obtained by expanding the components of the electromagnetic field in terms of Elliptic Cylindrical Waves. The presence of the surface is taken into account by combining the plane-wave expansion of the Elliptic Cylindrical Waves with the complex reflection coefficient characterizing the surface. This method enables us to treat a wide variety of reflecting surfaces, and to find the solution of the scattering problem in both near and far regions for any polarization state of the incident field.

Index Terms – Electromagnetic scattering, elliptic cylinders, Mathieu functions, plane reflecting surface.

I. INTRODUCTION

The solution to the diffraction problem relevant to a plane wave impinging on a perfectly conducting elliptic cylinder in a homogeneous and isotropic medium may be found in many fundamental papers and electromagnetism texts [1], [2]. If the cylinder is placed near a perfectly conducting mirror, by using the image method, the problem may be reduced to that of two cylinders in a homogeneous medium [5]. In this paper we present a new method for the solution of the plane-wave scattering by a perfectly conducting elliptic cylinder placed near a plane surface. The proposed method is applicable to all cases in which the surface may be characterized by a reflection coefficient Γ . The solution of this problem may have several applications in the study of microwave components, radar detection of objects and diffractive optics. The theoretical analysis of the problem is presented in Section II, conclusions, including possible extensions of the present theory, are discussed in Section III.

II. THEORETICAL ANALYSIS

The geometric layout of the problem is shown in Fig. 1. We will refer to dimensionless Cartesian coordinates, thus $\xi = kx$, $\eta = ky$, $\zeta = kz$, where k is the wave number. The axis of the cylinder is parallel to the ζ axis and is placed at a distance $\eta_0 = k\delta$ from the interface. The wave vector of the incident field, \mathbf{k}^i , lies in the $\xi\eta$ plane. The angle between \mathbf{k}^i and the ξ axis is named φ . The component of the electromagnetic field parallel to the ζ axis will be identified by the symbol V , i.e. $V = E_z$ for TM polarization and $V = H_z$ for TE polarization.

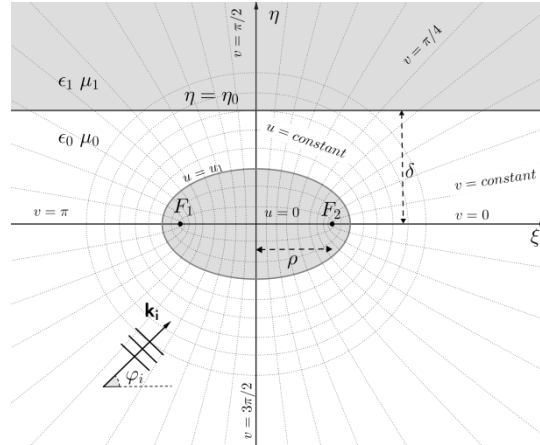


FIG. 1 – Geometry of the problem.

Symbols $k_{\parallel}^i, k_{\perp}^i$ denote the components of the incident field wave vector \mathbf{k}^i , thus $k_{\parallel}^i = k \sin \varphi$, $k_{\perp}^i = k \cos \varphi$. Symbols n_{\parallel} and n_{\perp} , denote the components of the unit vector $\mathbf{n} = \mathbf{k}/k$ parallel to \mathbf{k} . For applying continuity conditions on the elliptical boundary, it is preferable to introduce elliptical coordinates (u, v) , related to Cartesian coordinates by the relations $x = \rho \cosh u \cos v$ and $y = \rho \sinh u \sin v$, where ρ is the semi-focal distance of the reference ellipse. The boundary of the cylinder is identified by the elliptical coordinate value $u = u_1$. All fields will be expressed in terms of eigenfunctions of the Helmholtz equation in elliptical coordinates, i.e. Mathieu functions. We adopt a notation similar to the one used in [4], [5], denoting angular and radial Mathieu functions of type $j = 1, 2, 3, 4$ and index $n \in \mathbb{Z}$ by symbols $me_n(v)$ and $M_n^{(j)}(u)$, respectively, dropping, with no risk of ambiguity, the explicit dependence on the elliptical parameter $h^2 = \frac{1}{4}k^2\rho^2$. Following the method developed in [8], the total field V_{tot} may be expressed as the superposition of the incident field V_i , reflected field V_r , diffracted field V_d , diffracted-reflected field V_{dr} . By using the expansion of a plane wave in terms of Mathieu functions [4], the incident field V_i may be expressed as

$$V_i(\xi, \eta) = V_0 \sum_{m=-\infty}^{+\infty} i^m M_m^{(1)}(u) me_m(v) me_m(-\varphi). \quad (1)$$

The diffracted field V_d may be expressed as a series of Elliptic Cylindrical Waves (ECW),

$$V_d(\xi, \eta) = V_0 \sum_{m=-\infty}^{+\infty} i^m a_m me_m(-\varphi) ECW_m(\xi, \eta), \quad (2)$$

where a_m are unknown coefficients of the expansion and ECW functions are defined as $ECW_m(\xi, \eta) = M_m^{(3)}(u) me_m(v)$.

The reflected field V_r is expressed as

$$V_r(\xi, \eta) = V_0 \Gamma(n_{\parallel}^i) e^{i2\eta_0 n_{\perp}^i} \sum_{m=-\infty}^{+\infty} i^m M_m^{(1)}(u) me_m(v) me_m(-\varphi'), \quad (3)$$

where $\varphi' = -\varphi$ denotes the angle of propagation of the reflected wave.

The diffracted reflected field may be expressed as

$$V_{dr}(\xi, \eta) = V_d(\xi, 2\eta_0 - \eta) * \hat{\Gamma}(\xi) = V_0 \sum_{m=-\infty}^{+\infty} i^m a_m me_m(-\varphi) RECW_m(\xi, \eta), \quad (4)$$

where the asterisk denotes convolution with respect to the ξ variable, the symbol $\hat{\Gamma}(\xi)$ represents the inverse Fourier transform of the reflection coefficient and the Reflected Elliptic Cylindrical Wave functions, (RECW) have been introduced. The explicit expression of RECW functions may be given by means of the angular spectrum of the ECW with respect to the variable ξ . We denote such spectrum with the symbol $F_m(n_{\parallel}, \eta)$, thus expressing the ECW and RECW as

$$ECW_m(\xi, \eta) = \frac{1}{2\pi} \int_{-\infty}^{+\infty} F_m(n_{\parallel}, \eta) e^{i\xi n_{\parallel}} dn_{\parallel},$$

$$RECW_m(\xi, \eta) = \frac{1}{2\pi} \int_{-\infty}^{+\infty} \Gamma(n_{\parallel}) F_m(n_{\parallel}, \eta) e^{i\xi n_{\parallel}} dn_{\parallel}.$$

From integral representations of Mathieu functions [4], it is possible to derive the explicit expression of the angular spectrum of ECW, which can be written, for both homogeneous and evanescent waves:

$$F_m(n_{\parallel}, \eta) = \frac{2(-i)^m e^{i\eta n_{\perp}}}{n_{\perp}} me_m[\arccos(n_{\parallel})], \quad (5)$$

where $n_{\perp} = \sqrt{1 - n_{\parallel}^2}$. From Eq. (5) it is easy to notice that

$$F_m(n_{\parallel}, 2\eta_0 - \eta) = F_m(n_{\parallel}, 2\eta_0) e^{-i\eta n_{\perp}},$$

thus Eq. (4) may be rewritten as

$$V_{dr}(\xi, \eta) = V_0 \sum_{m=-\infty}^{+\infty} i^m a_m me_m(-\varphi) \frac{1}{2\pi} \int_{-\infty}^{+\infty} \Gamma(n_{\parallel}) F_m(n_{\parallel}, 2\eta_0) e^{-i\eta n_{\perp}} e^{i\xi n_{\parallel}} dn_{\parallel}. \quad (6)$$

The plane-wave factor in Eq. (6) may be expanded in terms of Mathieu functions, as in Eq. (3), obtaining

$$e^{-i\eta n_{\perp}} e^{i\xi n_{\parallel}} = \sum_{q=-\infty}^{+\infty} i^q M_q^{(1)}(u) me_q(v) me_q(-\psi'),$$

where $\psi' = -\psi$ and ψ specifies the propagation direction of a typical plane wave composing the angular spectrum: $\psi = \arccos(n_{\parallel})$. By using the explicit expression of $F_m(n_{\parallel}, 2\eta_0)$ from Eq. (5) and the Fourier series expansion of Angular Mathieu functions $me_n(\psi)$ [6]

$$me_m(\psi) = \sum_{l=-\infty}^{+\infty} c_{2l}^{m+2l} e^{i(m+2l)\psi}, \quad me_q(\psi) = \sum_{r=-\infty}^{+\infty} c_{2r}^{q+2r} e^{i(q+2r)\psi},$$

by posing $n = m + 2l$, $p = q + 2r$, introducing a factor $(-i)^{n+p} \cdot (+i)^{n+p} = 1$ and rearranging terms, Eq (6) becomes

$$V_{dr}(\xi, \eta) = V_0 \sum_{m=-\infty}^{+\infty} a_m me_m(-\varphi) \sum_{q=-\infty}^{+\infty} i^q M_q^{(1)}(u) me_q(v) \sum_{n=-\infty}^{+\infty} \sum_{p=-\infty}^{+\infty} c_{n-m}^m c_{p-q}^q i^{n+p} \cdot \frac{(-i)^{n+p}}{2\pi} \int_{-\infty}^{+\infty} \Gamma(n_{\parallel}) \frac{2e^{i2\eta_0 n_{\perp}}}{n_{\perp}} e^{i(n+p)\arccos(n_{\parallel})} dn_{\parallel},$$

where $n - m$ and $p - q$ assume only even values. As shown in [6], the integral term may be written in terms of a Reflected Cylindrical Waves

$$V_{dr}(\xi, \eta) = V_0 \sum_{m=-\infty}^{+\infty} a_m me_m(-\varphi) \cdot \sum_{q=-\infty}^{+\infty} i^q M_q^{(1)}(u) me_q(v) \sum_{n=-\infty}^{+\infty} \sum_{p=-\infty}^{+\infty} i^{n+p} c_{n-m}^m c_{p-q}^q RCW_{n+p}(0, 2\eta_0). \quad (7)$$

If Γ is constant with respect to n_{\parallel} , the field V_{dr} reduces to the field diffracted by an image cylinder placed in $\eta = 2\eta_0$, under the action of V_r

as incident field [5], [7]. By means of Eqs. (1-3, 7), it is possible to impose boundary conditions on the surface of the elliptic cylinder:

$$\begin{aligned} [V_i + V_r + V_d + V_{dr}]_{u=u_1} & \text{ for TM polarization} \\ [V_i + V_r + V_d + V_{dr}]'_{u=u_1} & \text{ for TE polarization} \end{aligned} \quad (8)$$

By using orthogonality relations of the angular Mathieu functions, from Eq. (8) is possible to obtain a linear system for the unknown coefficients a_m . Once the system has been solved, from the knowledge of the scalar function V , it is possible to obtain the total electromagnetic field for both polarization states.

III. CONCLUSIONS

A new analytical solution is presented for the diffraction of a homogeneous plane electromagnetic wave impinging on a perfectly conducting elliptical cylinder near a generally reflecting plane surface. This method extends previous results [3], [6] to the case of an elliptic cylinder and a non-perfectly reflecting mirror. The presented analytical solution is, in our opinion, suitable as for numerical applications and its computational complexity should not exceed those presented in [8], [9], whose results have proved to be extremely reliable. The proposed theoretical approach may be easily extended to the solution of the scattering of a plane wave by several single- or multi-layered dielectric elliptic cylinders buried in a dielectric half space relevant to a wide range of applications ranging from microwave to optic technology.

REFERENCES

- [1] P.M. Morse and P.L. Rubenstein, "The Diffraction of Waves By Ribbons and by Slits," *Phys. Rev.*, vol. 54, pp. 895–898, 1938.
- [2] J.A. Stratton, *Electromagnetic Theory*, McGraw-Hill, New York, 1941.
- [3] T. Masuda and Y. Miyazaki, "Analysis of Plane Wave Scattering by a Conducting Elliptic Cylinder Near a Ground Plane," *1999 International Symposium on Electromagnetic Compatibility*, pp. 292–295, 1999.
- [4] J. Meixner and F.W. Schäfke, *Mathieusche Funktionen und Sphäroidfunktionen*, Springer Verlag, Berlin, 1954.
- [5] K. Særmærk, "A Note on Addition Theorems for Mathieu Functions," *Z. angew. Math. Phys.*, vol. 10, pp. 426–428, 1959.
- [6] R. Borghi, F. Frezza, F. Gori, M. Santarsiero, and G. Schettini, "Plane-Wave Scattering by a Perfectly Conducting Circular Cylinder Near a Plane Surface: Cylindrical-Wave Approach," *J. Opt. Soc. Am. A*, vol. 13, pp. 483–493, 1996.
- [7] K. Særmærk, "Scattering of a Plane Monochromatic Wave by a System of Strips," *Appl. Sci. Res. Section B*, vol. 7, pp. 417–440, 1959.
- [8] R. Borghi, F. Frezza, M. Santarsiero, C. Santini, and G. Schettini, "Numerical Study of the Reflection of Cylindrical Waves by a Generally Reflecting Flat Surface," *J. Electromag. Waves Appl.*, vol. 13, pp. 27–50, 1999.
- [9] A. R. Sebak, "Transverse Magnetic Scattering by Parallel Conducting Elliptic Cylinders," *Can. J. Phys.*, vol. 89, pp. 1233–1241, 1991.

A NOVEL BESSEL BEAM LAUNCHER BASED ON HIGHER-ORDER LEAKY MODES

W. Fuscaldo⁽¹⁾⁽²⁾, G. Valerio⁽²⁾, A. Galli⁽¹⁾, R. Sauleau⁽²⁾, M. Ettorre⁽²⁾

(1) Department of Information Engineering, Electronics and Telecommunications (DIET), "Sapienza" University of Rome, 00184 Rome, Italy

fuscaldo@diet.uniroma1.it, galli@diet.uniroma1.it

(2) Institut d'Electronique et de Télécommunications de Rennes, IETR - UMR CNRS 6164, Université de Rennes 1, 35042 Rennes, France

Abstract

A novel leaky-wave radiator generating non-diffractive Bessel beams for millimeter waves is presented, based on a reference configuration recently investigated by one of the Authors for microwave applications. For increasing frequency ranges, a suitable higher-order leaky-wave mode is used here in order to overcome fabrication issues and reduce ohmic losses. As a useful design tool, closed-form equations are analytically derived for the considered structure. Full-wave simulation results validate the design equations and the overall proposed approach, thus allowing manufacture and test of a launcher prototype operating at 40 GHz.

Index Terms – Artificial surfaces, Bessel beams, High-order modes, Leaky waves.

I. INTRODUCTION AND BACKGROUND

The capability of focusing radiation in near-field regions is a fundamental feature for several modern applications, such as medical imaging, wireless power transfer, near-field probing, etc.. Free-diffraction beam-like solutions to the Helmholtz equation, represented by Bessel beams [1], furnish very inviting field profiles in these contexts. Ideally, a Bessel beam does not exhibit diffractive spreading along its axis of propagation, even though this would require an infinite aperture. However, it has been demonstrated [1] that a finite-aperture approximation of a Bessel beam can possess a diffraction-free propagation behavior over a long distance, the so-called non-diffractive range. In particular, zeroth-order Bessel beams are the only ones which exhibit a narrow but intense central peak, which makes them extremely interesting in the aforementioned applications. In optics, such beams have been realized using different methods [2],[3], but all the proposed solutions have been based on the scalar theory.

In order to avoid the limitations due to the paraxial approximation, a low-profile low-cost solution in the microwave frequency region was investigated in [4], using a full vector approach. In that experiment, a zeroth-order Bessel beam was generated through the excitation of the

lowest-order TM leaky-wave mode into a radial waveguide loaded with a suitable impedance sheet. Thanks to the design rules provided in [4], Bessel beams of arbitrary transverse size can simply be synthesized by correctly choosing the thickness of the substrate and the equivalent impedance of the artificial surface. However, extending this design at higher frequencies by simply scaling the configuration would lead to an extremely thin structure, giving rise to various practical mechanical problems and excessive ohmic losses.

In this frame, the present work wishes to investigate the possibility of achieving a Bessel beam launcher through the excitation of higher-order leaky-wave modes, thus avoiding the above-mentioned drawbacks. We will therefore show how it is possible to efficiently design a Bessel-beam launcher through the excitation of the second-order leaky-wave mode in such structures. In Sec. II, the basic analysis of the launcher is presented, introducing also new efficient and accurate design formulas. In Sec. III, relevant numerical results are shown for the realization and test of a prototype working around 40 GHz. Conclusions are drawn in Sec. IV.

II. DESIGN ANALYSIS OF A MM-WAVE BESSEL BEAM LAUNCHER

As is known, a grounded radial waveguide loaded with an upper capacitive impedance sheet (as sketched in Fig. 1) can support an azimuthally invariant TM-polarized fast leaky-wave mode. Moreover, a fully vector wave analysis [4] has shown that the z -component of the electric field assumes a J_0 profile (zeroth-order Bessel function of first-kind) when a circular metallic rim is placed in one of the zeroes of the J_0 function. Suitable design equations, which express h (the thickness of the substrate) and X_s (the reactive value of the equivalent surface impedance) in terms of $k_\rho = \beta_\rho - j\alpha_\rho$ (the radial complex wavenumber) have also been derived directly from the dispersion equation. It is worth noting that the phase (β_ρ) and the attenuation (α_ρ) constants of the radial wavenumber in this case are directly related to the fundamental features of the Bessel beam (i.e., non-diffractive range and beamwidth).

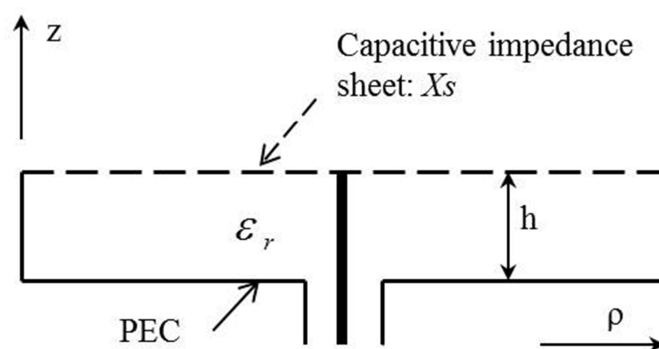


FIG. 1 – Leaky radial waveguide loaded with an upper impedance sheet.

The design equations given in [4] are strictly valid for the lowest-order TM leaky-wave mode. As also stated above, it is seen that, when designing a Bessel beam launcher in a higher range of frequencies, the use of the aforementioned closed-form equations would lead to impractical values for both substrate thickness and surface impedance.

One strategy to overcome this issue is represented by the generation of a Bessel beam through the excitation of a higher-order leaky mode. To this aim, we have solved the dispersion equation of the relevant layered structure over a wide range of frequencies, assuming for this specific design $h = 3.175$ mm and $X_s = -j 25 \Omega$ (see also Appendix for some details on parameters):

$$Y_{air} + Y_s - jY_0 \epsilon_r \cot(k_{z1} h) = 0 \quad (1)$$

where $Y_s = -j/X_s$ is the equivalent admittance of the artificial surface, Y_0 and Y_{air} are the characteristic admittances in the slab and air, respectively, and k_{z1} is the vertical wavenumber in the slab.

Due to space limits, we cannot show here the interesting results of this dispersion analysis. Nevertheless, the most important aspect emerging from this investigation is that, as frequency reaches the value around 40 GHz, the fundamental TM leaky mode becomes a bounded surface wave and hence it does not contribute anymore to radiation. On the other hand, the second-order leaky-wave mode reaches a complex value with $k_\rho = 0.8 - j0.007$, becoming well suitable for our applications.

III. RESULTS FOR A MM-WAVE LAUNCHER PROTOTYPE

It should be emphasized that the efficient design of a Bessel beam launcher through the excitation of the second-order leaky-wave mode requires new closed formulas, which involve the modal index of the leaky waves. The main steps to obtain these formulas are summarized in the Appendix. Once the spectral content of the Bessel beam is fixed, the design equations provide the correct values of the parameters h and X_s .

A millimeter-wave 40-GHz launcher was simulated with the CAD tool COMSOL Multiphysics, neglecting the actual implementation of the artificial surface. Some results for the near-field distribution are presented in Fig. 2(a). As expected, a proper Bessel beam is generated around the frequency of 40 GHz. The beam remains well confined within the non-diffractive range $z_{ndr} = 2.23\lambda$, beyond which the main beam starts to widen. This model was then verified with all the realistic details (artificial surface, presence of glue, etc.) by means of the CAD tool HFSS.

Based on the described closed-form expressions, whose validity was confirmed by the simulation results, it has been possible to design and then manufacture a millimeter-wave launcher prototype, as shown in Fig. 2(b).

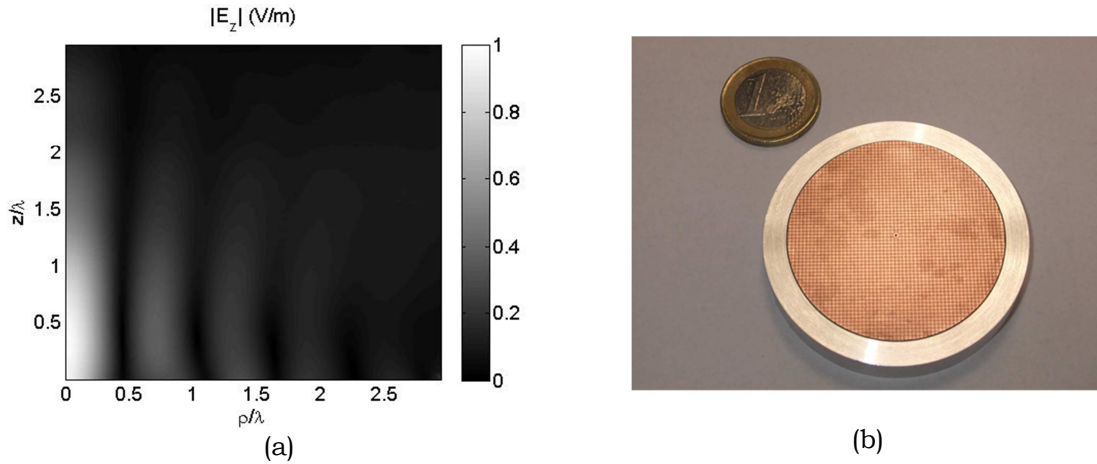


FIG. 2 – a) A plot of the Bessel-beam behavior of E_z on ρz -plane around 40 GHz. b) Prototype of the manufactured mm-wave launcher.

IV. CONCLUSION

A very promising near-field non-diffractive system based on higher-order leaky-wave modes has been presented, suitably designed, and tested. The results have confirmed the focusing capabilities as in similar microwave launchers, but in higher frequency ranges at millimeter waves, with reduced ohmic losses and fabrication complexity.

APPENDIX

In the previous sections, we found specific values for h and X_s : this choice was related to the excitation of the second-order leaky-wave in our structure, which generates a Bessel beam with $k_\rho = 0.8 - j0.007$ at the frequency of 40 GHz, as desired. In order to find these values, we have rearranged the terms of (1), approximating the cotangent function with its first-order Laurent series expansion:

$$Y_{air} + Y_s - \frac{jY_0 \epsilon_r}{k_{z1} h - n\pi} = 0 \quad (2)$$

where n represents the modal index of the leaky modes. Separation of (2) in its real and imaginary part leads to a pair of closed-formulas for h and X_s , not reported here for space limitations.

REFERENCES

- [1] J. Durnin, "Exact solutions for nondiffracting beams. I. The scalar theory," *J. Opt. Soc. Amer.*, vol. 4, no. 4, pp. 651–654, Apr. 1987.
- [2] J. Turunen, A. Vasara, and A. T. Friberg, "Holographic generation of diffraction-free beams," *Appl. Opt.*, vol. 27, no. 19, pp. 3959–3962, Oct. 1988.
- [3] W. B. Williams and J. B. Pendry, "Generating Bessel beams by use of localized modes," *J. Opt. Soc. Amer. A.*, vol. 22, no. 5, pp. 992–997, May 2005.
- [4] M. Ettore and A. Grbic, "Generation of propagating Bessel beams using leaky-wave modes," *IEEE Trans. Antennas Propag.*, vol. 60, no. 8, pp. 3605–3605, Aug. 2012.

RADIOFREQUENCY POWER COUPLED TO HIGH-DENSITY PLASMAS FOR DRIVING CURRENT IN THERMONUCLEAR REACTORS

L. Amicucci ^(1,2), A. Cardinali ⁽¹⁾, C. Castaldo ⁽¹⁾, R. Cesario ⁽¹⁾,
A. Galli ⁽²⁾, F. Napoli ⁽³⁾, G. Schettini ⁽³⁾, A. A. Tuccillo ⁽¹⁾

⁽¹⁾ ENEA – Unità Tecnica Fusione, Centro Ricerche Frascati,
Via E. Fermi 45, 00044 Frascati, Rome, Italy

⁽²⁾ Università “Sapienza” di Roma – Dipartimento di Ingegneria
dell’Informazione, Elettronica e Telecomunicazioni, Rome, Italy

⁽³⁾ Università Roma Tre –

Dipartimento di Ingegneria Elettronica, Rome, Italy

luca.amicucci@enea.it

Abstract

A fundamental problem in the research on thermonuclear fusion energy is to control, in steady state, the radial profile of the current for magnetically trapped toroidal plasmas. This is necessary for maintaining stability and thermal insulation required by fusion gain in plasmas which, obtained by intrinsically pulsed device, require the non-inductive current fraction to be set independently of achieved regime. Microwave power at several gigahertz, launched by phased arrays of rectangular waveguide antennas, is capable to drive current via the lower hybrid current drive (LHCD) effect, whose extrapolation to reactor grade high plasma density has been problematic for a long time. Recently, the Frascati Tokamak Upgrade assessed a method for reducing the broadening of launched spectrum, which prevents the power penetrating to the plasma core. We summarize the progresses for understanding how enabling the LHCD effect in the dense and hot reactor plasmas, thus making the non-inductive current profile effectively controllable by the antenna parameters.

Index Terms – Magnetized plasmas, Tokamak, RF propagation.

I. INTRODUCTION

The main activity for the research on energy by thermonuclear fusion of hydrogen is based on the tokamak concept, which is utilized in the next international experiment ITER (International Thermonuclear Experiment Reactor) and in other existing experiments, e.g., FTU (Frascati Tokamak Upgrade) [1] and JET (Joint European Torus). In a tokamak, the deuterium gas is led to the status of hot plasma magnetically trapped into a toroidal vacuum chamber. The plasma ring works as secondary coil of a transformer which is capable delivering a current of several mega-amperes, heating the plasma up to hundred millions of degrees.

Such strong heating is necessary for approaching the fusion conditions, which require ions to win the Coulomb repulsion and, consequently, enable the strong nuclear interaction to fuse deuterons and produce helium and a huge energy. Since the strong nuclear interaction is the most intense force existing in nature, and the gain in bounding energy per mass unity is maximum for helium nuclei produced by deuterons, the energy provided by fusion, instead of that from fission, should be retained as the *true* nuclear energy.

A major problem for this research consists in how controlling the radial profile of the plasma column current density, as this is necessary for sustaining towards steady-state, stable and thermally well-insulated plasmas. Tokamaks produce, indeed, plasmas only in transient regime that is not suitable for a reactor, and the non-inductive current self-produced by transport mechanism of particles, via the bootstrap effect that occurs in toroidal plasmas, should be however aided by tools independent of the reached regime.

Two problems persisted for long time preventing the LHCD tool to be considered of practical use for a reactor: *i*) the difficult extrapolation of the LHCD effect at reactor graded high densities due to non linear effects of plasma edge; *ii*) the strong wave damping which would produce the LH power deposition too at the periphery in the hot plasma of reactor [2]. The RF-produced plasma current would be thus determined by these effects rather than the antenna parameters (i.e., the coupled RF power and the phasing between the waveguide arrays) as required for active current drive.

We review in this context the important progresses recently performed at Frascati and the further understanding which is still necessary to be achieved in order to solve the fundamental problem of current drive in a tokamak reactor.

II. CURRENT DRIVE PRODUCED BY LAUNCHED ELECTROMAGNETIC WAVES

The importance of driving non-inductive current for a fusion reactor plant is shown by experiments demonstrating that the thermal insulation of the plasma column is improved when micro-turbulence and magneto-hydrodynamic instabilities (which represent the major cause of heat and particle loss from the core) are suppressed. This condition is reached by sustaining, during a tokamak plasma discharge, a suitable radial profile of current density. This goal represents a true challenge mainly in the outer radial half of plasma, as the tools envisaged so far for a reactor could not satisfy such request.

The active control of plasma current profile should be in principle produced in a reactor by means of RF power at a few gigahertz, which can be coupled to plasma by means of antennas consisting in phased arrays of rectangular waveguides, working in fundamental TE_{10} mode.

Figure 1 shows the launcher in operation on FTU (Frascati Tokamak Upgrade) capable of coupling to the plasma about 1 MW of power at the frequency of 8 GHz.

This antenna couples RF power to lower hybrid (LH) plasma waves, which are natural modes that propagate in magnetized high density plasma: $f_{pe} > f_0$, where f_{pe} is the electron plasma frequency and f_0 is the operating frequency. Therefore, LH waves are useful to penetrate in the core of a reactor grade plasma, which requires high densities even at the plasma edge, namely, $n_{e_{0.8}} \approx 0.8 \times 10^{20} \text{m}^{-3} - 1 \times 10^{20} \text{m}^{-3}$ at the normalized minor radius $r/a \approx 0.8$, and at the centre: $n_{e0} \approx n_{e_{0.8}}$ ($r = a$ is the plasma minor radius at the last closed magnetic surface). Due to the nature of quasi-electrostatic slow waves, the LH waves can drive current via the lower hybrid current drive (LHCD) effect [3,4]. This phenomenon is originated by Landau damping on electrons at relatively high velocity in the tail of the distribution function, i.e., for wave phase velocity: $v_{F//} \equiv c/n_{//} \approx (2.5 \div 4)v_{the}$, where $n_{//}$ is the wave-number component parallel to the equilibrium magnetic field, v_{the} and c are the electron thermal velocity and the light speed, respectively [5].

In the following we address the recent understanding on issues mentioned in Sec. I, which prevent the practical use of lower hybrid current drive in a reactor.

In experiments, the LHCD effect was observed to occur only at relatively low plasma densities (about $0.4 \times 10^{20} \text{m}^{-3} - 0.6 \times 10^{20} \text{m}^{-3}$). This problem was solved by a method assessed on FTU [6], based on previous theoretical predictions that, under relatively high temperature of plasma edge, non-linear effects of physics of the edge [7,8], preventing the penetration of the coupled LH power to the core, should be strongly reduced [9,10]. With operating electron temperatures at the plasma edge (T_{e_edge}) higher of the order of 50% than in the standard regime, clear effects of LH current drive and a markedly reduced spectral broadening have been observed, as shown in the comparable results of Fig. 2. This condition, useful for enabling the LHCD effect at high plasma density, should be naturally met in reactor.

Further studies are in progress at Frascati aimed at assessing how enabling the LHCD effect in the hot plasma core of reactor.



FIG. 1 – Waveguide antenna of the lower hybrid current drive experiment on the Frascati Tokamak Upgrade (FTU).

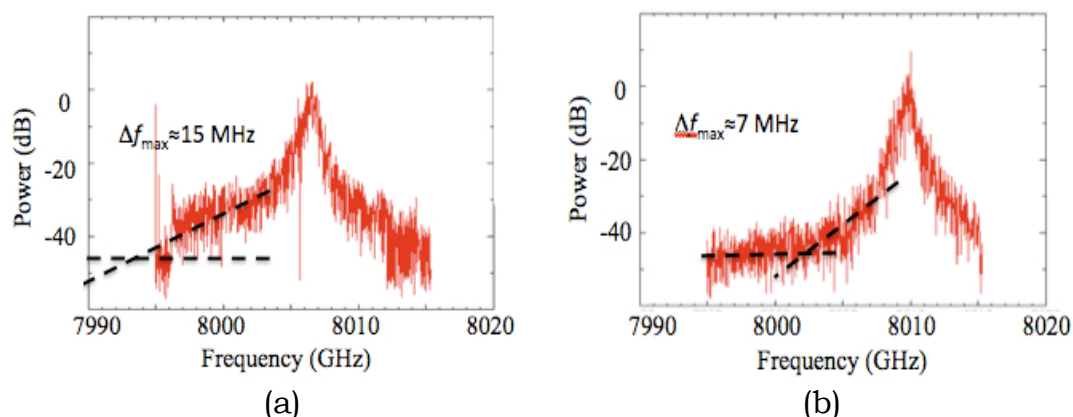


FIG. 2 – (a) Spectrum measured by an RF probe located outside the machine during the FTU experiment in standard operating conditions with line averaged plasma density: $1.0 \times 10^{20} \text{ m}^{-3}$.

The broadening at about 30 dB below the pump power peak is 15 MHz. This effect is expected to be accompanied by a PI-produced $n//$ broadening of the antenna spectrum from $n// \approx 2$ to $n// \approx 30$.

(b) Same of Fig. 2a but line averaged plasma density: $1.8 \times 10^{20} \text{ m}^{-3}$ operating with higher temperature at the plasma periphery.

A much less spectral broadening than in Fig 2a occurs.

In this case, PI-produced $n//$ is expected to be reduced to $n// \lesssim 10$.

III. CONCLUSION

Progress made on FTU has demonstrated that non-linear phenomena of plasma edge, broadening the launched antenna spectrum and thus preventing the use of LHCD effect at high plasma densities, should be naturally avoided in a reactor, thanks to high temperature envisaged at the plasma periphery. Further studies are in progress for assessing how to possibly drive current in the core of reactor by means of waveguide-type antennas.

REFERENCES

- [1] A. A. Tuccillo et al., 23rd IAEA FEC, Paper OV/4-2, Daejon, Rep. of Korea, 11-16 October 2010.
- [2] J. Garcia et al., *Nucl. Fusion*, **48**, 075007, 2008.
- [3] N. J. Fisch, *Phys. Rev. Letters*, **41**, 873-876, 1978.
- [4] S. Bernabei et al., *Phys. Rev. Letters*, **49**, 1255-1258, 1982.
- [5] M. Brambilla, *Kinetic Theory of Plasma Waves*, Oxford Press, 1999.
- [6] R. Cesario et al., *Nature Comm.*, **1**, 5, 55, 2010.
- [7] C. S. Liu and V. K. Tripathi, *Physics Reports*, **24**, 1709, 1984.
- [8] M. Porkolab, *Phys. Fluids*, **17**, 1432-1442, 1974.
- [9] R. Cesario et al., *Phys. Rev. Letters*, **92**, 17, 175002, 2004.
- [10] R. Cesario et al., *Nucl. Fusion*, **54**, 043002, 2014.

ELECTROMAGNETIC BACKSCATTERING MODELS FOR A COUPLE OF BUILDINGS

A. Ciotola, G. Di Martino, A. Iodice, D. Riccio, G. Ruello

University of Naples Federico II

alessio.ciotola-gerardo.dimartino-antonio.iodice-daniele.riccio-giuseppe.ruello@unina.it

Abstract

The presence of buildings generates some linear bright features in SAR images. Such lines are derived from the radar signal bouncing on buildings and ground. In this paper we propose an electromagnetic backscattering model able to interpret those linear structures relevant to multiple reflection mechanism involving a couple of buildings. The model has been tested in an actual case providing good results.

Index Terms– Electromagnetic scattering, Geometrical Optics, Physical Optics, urban areas,

I. INTRODUCTION

The metric resolution achievable with most modern Synthetic Aperture Radar (SAR) sensors, allows us recognizing buildings in SAR images. Unfortunately, typical distortions introduced by SAR geometry and multipath phenomenon among closely spaced buildings, makes SAR images very difficult to be interpreted by a visual inspection. Then we need effective electromagnetic models describing the field backscattered from buildings in order to support interpretation and information retrieval. The main features revealing the buildings presence in SAR images are bright linear structures: they are relevant to radar signal multiple bounce. A typical example is the well-known double reflection line arising from the dihedral structure formed by a building's wall and the ground in front of it. Other linear features correspond to signal multiple reflection between two or more buildings. In this paper we introduce an innovative backscattering model that generalize to a couple of buildings the one previously presented in [1] and [2], which described the field backscattered from an electromagnetic isolated building.

II. MULTIPLE REFLECTION SCATTERING MODEL

In the case of an electromagnetic isolated building the only linear structure in SAR image derives from the double bounce on the structure visualized in Fig.1(a) in which a vertical wall and a rough soil

form a dihedral structure [1]-[2]. But now we focus on the structure pictured in Fig.1(b) constituted by the walls of two close buildings and the rough surface between them. The signal multiple reflection causes other bright linear structure that are added to the double reflection phenomenon. The model we propose decomposes the problem in three pieces of information: the order of reflection n , i.e. the number of bounces that the signal experiments, the backscattering position in the natural SAR coordinates (azimuth, range), and the backscattering radiometric value, presented in term of Radar Cross Section (RCS). Multiple reflection RCS is evaluated within a sound physical framework [1] under Kirchhoff approximations, together with Physical Optics and Geometric Optics. Some simplified geometric hypothesis are assumed, as building's walls being flat and aligned with sensor flight direction. Fig.2 reports an example of multiple reflection of order 4 (a) and of order 6 (b). All the rays involved in the phenomenon have the same path of the green one and so the return range coordinate corresponds to the point indicated with o' . Anyhow, if o is the ground range coordinate of the base of the second wall, the n -order multiple reflection contribute will be located at coordinate

$$o' = o + (n/2 - 1)d$$

where d is the distance between buildings. Then its RCS has the following expression:

$$\sigma^0 = 2h_{equivalent} |S_{ij}|^2 l \tan \vartheta \exp(-4k^2 \sigma^2 \cos^2 \vartheta) \sum_{m=0}^{\infty} \frac{(2k\sigma \cos \vartheta)^2 k^2 L^2}{m! 4m}$$

where σ and L are rough surface, variance and correlation length [3], respectively, ϑ is the incidence angle, k is the electromagnetic wavenumber and l the buildings length in the azimuth direction; $h_{equivalent}$ is an appropriate height, (see Fig. 2), whose evaluation is presented in this paper as summarized in Table1. It depends on buildings heights, h_1 and h_2 , their relative distance d , and the order of reflection n . These dependencies are made explicit in the second column of Table 1 while in the first column the conditions for their existence are reported. Finally S_{ij} is the scattering matrix which takes into account the polarization, the order of reflection and the wall's electromagnetic properties, i.e. dielectric constant and conductivity.



FIG. 1– (a) Dihedral structure formed by an isolated building and the ground; (b) case of two close buildings

III. EXAMPLE

The proposed scattering model has been integrated in a SAR simulator and tested in an actual case, i.e. over the Business District Centre of Naples. Fig.3(b) reports the comparison between the real SAR image (bottom) and the simulated one (top) while in Fig.3(a) it could found involved buildings enumerated. Correspondent multiple reflection lines are highlighted in rectangles and linked by an arrow.

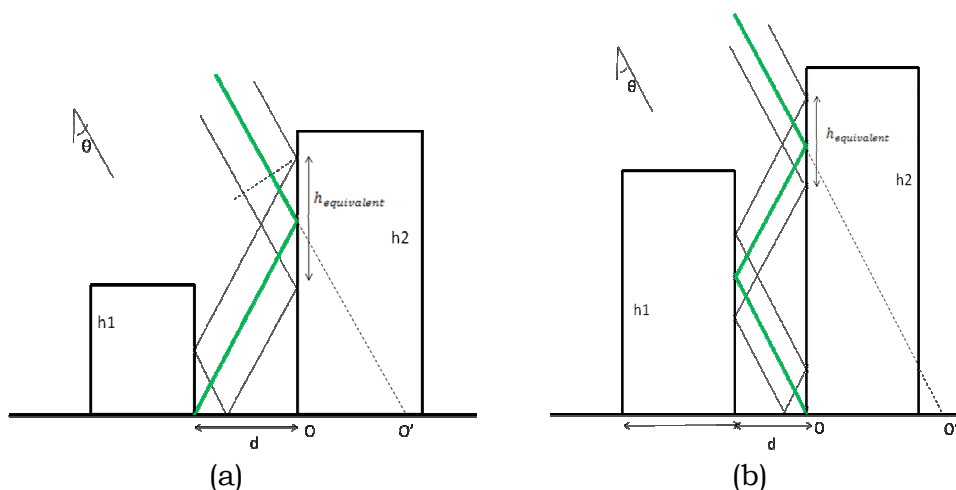


FIG. 2—fourth- (a) and sixth- (b) order reflection contributions.

TABLE I - CONDITIONS FOR MULTIPLE REFLECTIONS AND H-EQUIVALENT

Existence conditions	$h_{equivalent}$
$h_2 > (n/2 - 1)d \cot \vartheta$	If
$(n/2 - 2)d \cot \vartheta < h_1 < (n/2 - 1)d \cot \vartheta$	$(h_2 - h_1) > d \cot \vartheta$ $h_{equivalent} = 2 \cdot (h_1 - d \cot \vartheta)$
	If
	$(h_2 - h_1) < d \cot \vartheta$ $h_{equivalent} = 2 \cdot (h_2 - (n/2 - 1)d \cot \vartheta)$
$h_2 > (n/2 - 1)d \cot \vartheta$	If
$(n/2 - 2)d \cot \vartheta < h_1 < (n/2)d \cot \vartheta$	$(h_2 + h_1) > (n - 1)d \cot \vartheta$ $h_{equivalent} = nd \cot \vartheta - 2h_1$
	If
	$(h_2 + h_1) < (n - 1)d \cot \vartheta$ $h_{equivalent} = 2 \cdot (h_2 - d \cot \vartheta)$

In particular one bright line is related to double reflection between building 1 and the surrounding ground; another bright line reflects the fourth-order reflection relevant to building 1 and 2, and the last bright

line is relevant to a sixth-order phenomenon relevant to the same buildings.

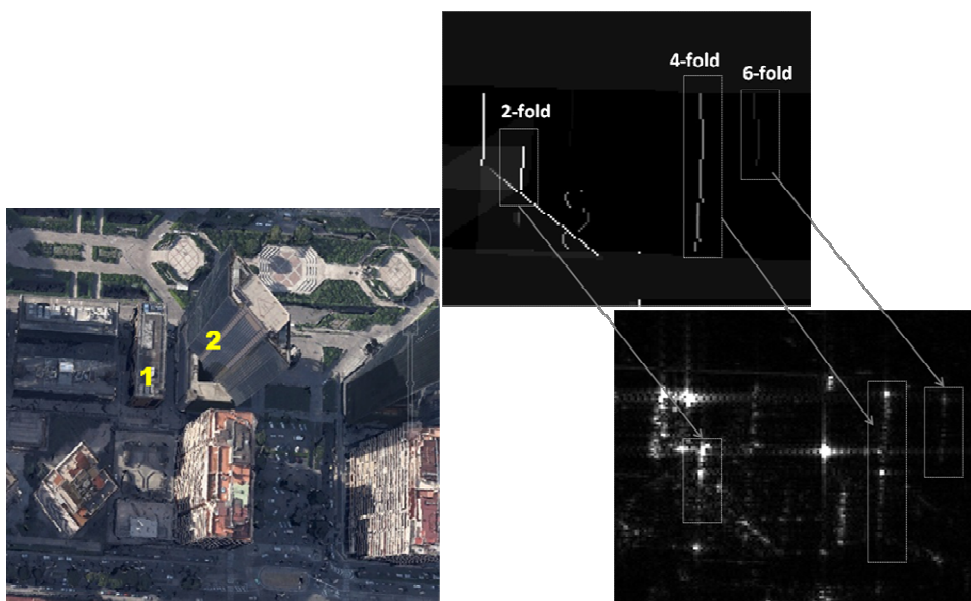


FIG. 3– Comparison between simulated and real image (b); buildings involved (a) in multiple reflection phenomenon

IV. CONCLUSION

In this paper we propose a novel scattering model which describes linear bright structures in SAR images due to the interaction returns relevant to two close buildings. The model provides conditions that defines the existence of such structures and the evaluation of their RCS expressed in closed form and depending on a few parameters. Its simplicity makes this model as a good candidate for analyzing complex urban scenarios in remote sensing applications and for the realization of SAR simulation tool over urban areas. Exposed tests show the capability of the model to predict the existence of multiple reflection contributions and its radiometric behavior.

REFERENCES

- [1] G.Franceschetti, A.Iodice, D.Riccio, "A Canonical Problem in Electromagnetic Backscattering from Buildings", *IEEE Transactions on Geoscience and Remote Sensing*, GE-40, 1787-1801, aug. 2002.
- [2] G.Franceschetti, A.Iodice, D.Riccio, G.Ruello, "SAR Raw Signal Simulation for Urban Structures", *IEEE Transactions on Geoscience and Remote Sensing*, GE-41, 1986-1995, sept. 2003.
- [3] G.Franceschetti, D.Riccio, "Scattering, Natural Surfaces and Fractals", Academic Press, Burlington, MA (USA), , pp.304, jan.2007.

EPSILON-NEAR-ZERO BASED ANTENNAS

L. La Spada^(1,2), L. Vegni⁽¹⁾

⁽¹⁾ Department of Engineering, University of Roma Tre, Via Vito Volterra 62, Rome 00146, Italy

⁽²⁾ School of Electronic Engineering and Computer Science, Queen Mary University of London, London, E1 4NS, United Kingdom

luigi.laspada@uniroma3.it, vegni@uniroma3.it

Abstract

In this paper new kind of ENZ-based antennas are presented. Three structures are considered: the classical PEC antennas, the dielectric dipole covered by Epsilon Near Zero (ENZ) material and the PEC+ENZ cover antenna.

The main crucial aspects concerning this paper are the following: the possibility to reproduce the same behavior of a classical half-wavelength dipole also for shorter dimensions, and the capability to guide the displacement current not only in straight paths but also in curved and bended shapes.

The proposed structure offers great potential in a wide variety of practical application fields such as detection and sensing, communications applications.

Index Terms – Epsilon-Near-Zero materials, Antennas, Sensing, Telecommunications applications

I. INTRODUCTION

Nowadays it is common knowledge that antennas, in the RF and Microwave regimes are a well-established technology, designed to convert confined signals into electromagnetic waves that can propagate in the free space, and vice versa. Over the years, several researches have been conducted on such a topic leading to a great evolution in antenna technology and in all its relevant applications. Recent progress in the metamaterial field allows the possibility of enhancing their performances, especially in the microwave, infrared and optical frequency range. Typically, metamaterial-based antennas have been designed by using double-negative (DNG) [1], negative permittivity (ENG) [2], or negative permeability (MNG) [3,4] materials. The newly nanofabrication techniques and the use of metamaterials and plasmonics open new possibilities to built-up antennas in the infrared and optical regime, leading to an enhancement of their properties [5]. Recently, the so-called epsilon-near-zero (ENZ), a particularly class of metamaterials, become a topic of great research interest [6]. In this regard several theoretical and numerical works on ENZ-based antennas can be found in literature, in order to improve its input impedance, bandwidth, directivity and gain [7]. Despite this interest, no one to the best of our knowledge has studied how to use ENZ materials to replicate the electromagnetic behavior of an antenna in the infrared and optical regime. Considering this, the aim of this paper is to design a new kind of ENZ antenna. This paper is organized as follows: first of all a brief overview of the general operation pattern of the following structure: ENZ+AIR antenna, ENZ+PEC Antenna is shown. Secondly, relevant

differences between optical and conventional antenna operation are pointed out. Finally, conclusions are drawn in the final section.

II. THE ENZ ANTENNAS

Figure 1 shows the structures under study: the ENZ+AIR antenna is characterized by a cylindrical air dipole with radius $a=\alpha\lambda_p$, length $l=\beta\lambda_p$, embedded in a concentric ENZ material cylinder as cover, whose thickness is $s=\gamma\lambda_p$, where λ_p is the plasma frequency of the ENZ material. The ENZ permittivity is described by the complex dielectric permittivity $\epsilon_{ENZ}(\omega)=\epsilon_0(\epsilon_r(\omega)-j\epsilon_i(\omega))$ and magnetic permeability $\mu_{ENZ}=\mu_0\mu_r$ (being $\mu_r=1$ the relative magnetic permeability of the free space and $\omega=2\pi f$ is the frequency in rad/s). The antenna system is excited by a discrete port placed between two circular metallic plates in the middle of the dipole. The metallic plates are filled by the ENZ material too, whose thickness is $d=\delta\lambda_p$. Let's assume the surrounding region as free space with electric permittivity ϵ_0 and magnetic permeability μ_0 . Same operation pattern can be obtained for the second case study: the traditional PEC antenna covered by the ENZ layer.

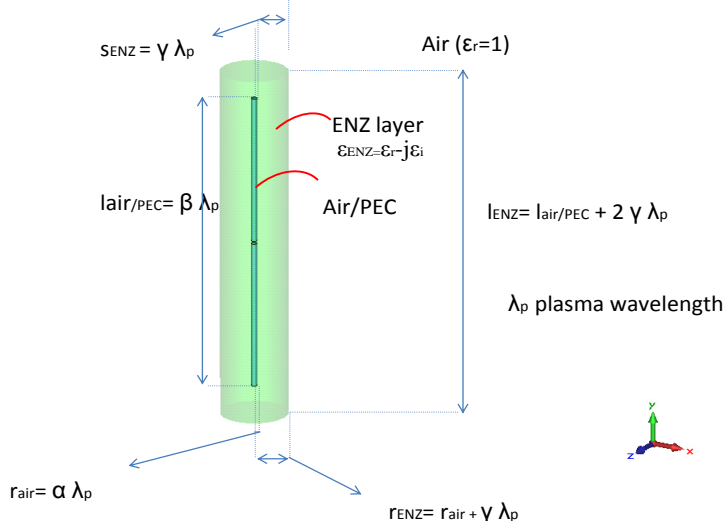


FIG. 1 – AIR/PEC+ENZ Antennas Operation patterns

We simulated the electromagnetic field distribution of the considered structures by using the commercial electromagnetic software CST Microwave Studio [8]. The results are shown in Figure 2, where a comparison of the far-field properties between the classical PEC dipole and the AIR+ENZ antenna is reported. What we have obtained is that:

- the displacement current is predominantly longitudinal, strongest at the center of the cross section, flowing forward along the air structure, strictly confined in the air dipole.
- the phase has little changes from the source to the top/bottom of the dipole, without leaking into the air region. Whereas is transversally directed in the ENZ shell.

From the uniform phase over along all the cross section of the dipole derives that:

- a) the electric and magnetic field distribution, around the dipole, remind those of a regular metallic wire at radiofrequencies;
- b) a strong uniform displacement current flowing inside the dipole. A negligible current flow across the ENZ region, due to the different values of permittivity in the two regions.
- c) negligible amplitude decay and radiation losses, due to the fact that the ENZ shell acts as a perfect magnetic conductor reducing the field to zero outside the air dipole.

The uniform (displacement/conduction) current distribution in the antenna system leads to two important aspects:

- 1) the possibility to reproduce the same behavior of an half-wavelength dipole (and all its relevant aspects in terms of impedance and gain) also for shorter dimensions.
- 2) the possibility to guide the displacement current not only in straight path but also in curved and bended shapes: the displacement current can be tailored and shaped using properly designed structures analogous to what happened in metallic wire for the conduction currents. It means that it is possible to transfer the classical metallic ring concepts to the higher frequencies (infrared and visible), obtaining the same electromagnetic behavior.

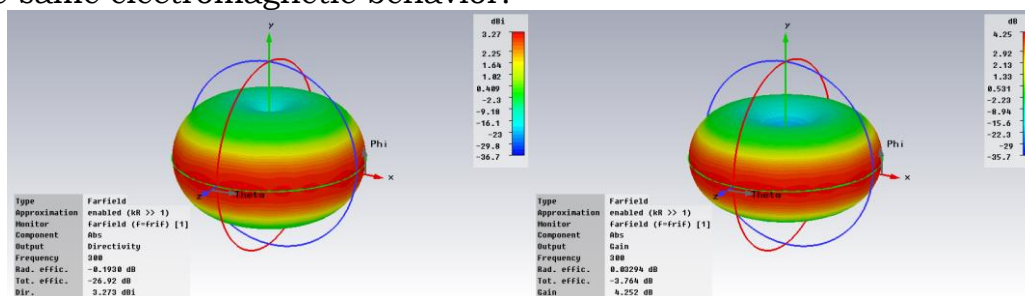


FIG. 2 – Far-field radiation properties for (a) PEC dipole, (b) ENZ+AIR dipole

III. CONCLUSIONS

The aim of the paper was to design a new kind of ENZ antenna. We revisit the RF and Microwave antenna concepts and bring them to the higher frequency (infrared and optics), by exploiting the extraordinary ENZ material properties. The main crucial aspects concerning this study can be summarized as follows:

- the possibility to reproduce the same behavior of a classical half-wavelength dipole also for shorter dimensions.
- the possibility to guide the displacement current not only in straight paths but also in curved and bended shapes. It means that it is possible to transfer the classical metallic ring concepts to the higher frequencies (infrared and visible), obtaining the same electromagnetic behavior.

Our results pave the way for new interesting and relevant applications in a variety of fields of optics, sensing, communications and nanodevices.

REFERENCES

- [1] R.W. Ziolkowski and A.D. Kipple "Application of double negativematerials to increase the power radiated by electrically small antennas", IEEE Trans. Antennas Propag., vol. 51, no. 10, pp.2626-2640, 2003.
- [2] R.W. Ziolkowski and A. Erentok "Metamaterial-based efficient electrically small antennas," IEEE Trans. Antennas Propag., vol. 54, no. 7, pp.2113-2130, 2006.
- [3] F. Bilotti, A. Alù, and L. Vegni "Design of miniaturized metamaterial patchantennas with μ -negative loading", IEEE Trans. Antennas Propag., vol. 56, no. 6, pp.1640-1647, 2008.
- [4] P.Y. Chen and A. Alù; "Sub-wavelength elliptical patch antenna loaded with μ -negative metamaterials," IEEE Trans. Antennas Propag., vol. 58, no. 9, pp.2909-2919, 2010.
- [5] M. Agio "Optical antennas as nanoscale resonators," Nanoscale, vol. 4, no. 3, pp.692-706, 2012.
- [6] R.W. Ziolkowski, "Propagation in and scattering from a matched metamaterial having a zero index of refraction," Phys. Rev. E, vol.70, pp. 046608-1-12, 2004.
- [7] A. Alù and N. Engheta, "Theory, Modeling and Features of Optical Nanoantennas," IEEE Trans. Antennas Propag., vol. 61, no. 4, pp.2909 -2919 2010.
- [8] CST STUDIO SUITE™ 2013, CST of America, Inc., www.cst.com.

METAMATERIAL-BASED ELECTROMAGNETIC WAVE ABSORBER

L. La Spada^(1,2), L. Vegni⁽¹⁾

⁽¹⁾ Department of Engineering, University of Roma Tre, Via Vito Volterra
62, Rome 00146, Italy

⁽²⁾ School of Electronic Engineering and Computer Science, Queen Mary
University of London, London, E1 4NS, United Kingdom

luigi.laspada@uniroma3.it, vegni@uniroma3.it

Abstract

In this paper, an analytical and numerical study of a new type of electromagnetic absorber, operating in the infrared and optical regime, is proposed. The absorber consists in a planar layered structure with an isotropic epsilon-near-zero (ENZ) material and a Split-Ring-Resonator (SRR), both placed over a perfect conductor (PEC) metal plate. Absorption is obtained by exploiting the combination of both ENZ and SRR materials properties. The main issue is to absorb the incident electromagnetic wave in the broadest angle range possible. Such configuration permits to improve the absorber performances. In particular, an absorption in a wide angle range (0° - 80°), for different resonant frequencies (multi-band) with a large frequency bandwidth (wide-band) for small structure thicknesses ($d=\lambda_p/4$) is demonstrated, compared to the conventional absorbers working at the same frequencies.

Index Terms – Epsilon-Near-Zero Materials, Split-Ring-Resonator, Electromagnetic Wave Absorbers, Sensing, Telecommunications Applications

I. INTRODUCTION

A near unity absorber is a device in which all incident radiation is absorbed at the operating frequency, meanwhile Transmission, Reflection and Scattering are zero. Initial interests in electromagnetic wave absorbers were largely in the microwave range. They are used in both improving radar performance and providing wave suppression against radar systems for military aims [1]. First resonant absorbers were proposed from Salisbury, Jaumann, and Dällenbach who independently, created similar devices for electromagnetic wave absorbers [2]. Other types of resonant electromagnetic wave absorbers are the crossed grating absorber [3] and the Circuit Analog (CA) absorbers (an extension of the Salisbury screen) [2]. Examples of broadband absorbers are geometric transition and low-density absorbers [2]. Recently, the advent of metasurfaces permitted to enhance all the aforementioned devices performances. Metamaterial-based absorber designs have been proposed in the microwave frequency regime [4], at millimeter waves [5], THz [6], infrared [7], and optical wavelengths [8]. Recent evidence suggests that good absorption could be obtained by using ENZ (Epsilon-Near-Zero) materials [9,10].

From what we have seen so far, the major issues in the electromagnetic absorber design concern satisfying the following requirements:

- Small thickness: most of the presented absorbers require a thickness at least around $\lambda/4$

- Broad angle range: the absorption is required at all angle of incidence;
 - Broad bandwidth and multi-resonant behavior: wide the bandwidth of the single resonant frequency and/or create multiple resonant bands with the wider bandwidth possible
 - Scaling the structure: the possibility to replicate the same behavior and performances in all the electromagnetic spectrum frequency ranges
- The main goal, not easily achievable, is to satisfy all the features listed above at the same time.

Considering all these issues, in this paper, by combining the particular properties of ENZ materials and metasurfaces, we propose the design of an electromagnetic absorber, in order to satisfy all the mentioned requirements at the same time.

II. THE METAMATERIAL-BASED ELECTRCOMAGNETIC WAVE ABSORBER

The structure under study is show in Figure 1. An isotropic ENZ material slab with a thickness d is placed on top of an infinitely extended perfect electric conductor (PEC) sheet. On the ENZ slab a metasurface (i.e. a Split-Ring-Resonator, SRR) is deposited. The top layer and the ENZ slab are entitled as region 1 and region 2, respectively. Let's assume the region 1 as free space with electric permittivity ϵ_0 and magnetic permeability μ_0 . The ENZ material is described by the electric permittivity $\epsilon_{ENZ}(\omega) = \epsilon_0(\epsilon_r(\omega) - j\epsilon_i(\omega))$ and magnetic permeability $\mu_{ENZ} = \mu_0\mu_r$ with $\mu_r = 1$ the relative magnetic permeability of the free space and $\omega = 2\pi f$ is the frequency (rad/s). The structure is excited by an electromagnetic plane wave, having the electric field and the propagation vector \mathbf{k} inclined to the ground plane with a generic Angle Of Incidence (AOI) α . In this way, there is always an electric field component that can excite the SRR. A wave may be reflected (r), transmitted (t), or absorbed (a), with their relationship given as $a = 1 - t - r$. In our case, due to the presence of the PEC, the transmission coefficient t is zero, so the corresponding absorption a is related to the reflection coefficient as $a = 1 - |r|^2$. As a consequence the absorption is obtained when the coefficient r approaches to 0.

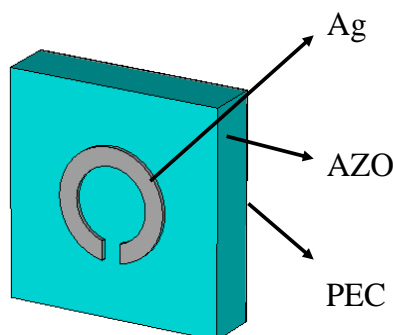


FIG. 1 – Metamaterial-based Electromagnetic Wave Absorber operation pattern

We developed an analytical approach to find the reflection coefficient r , in order to link the absorption properties to the electromagnetic material characteristics (ENZ and SRR), the angle of incidence (α) and the geometrical parameters of ENZ and SRR (the ENZ layer thickness D , the SRR radius R , the SRR gap G , the SRR layer thickness T and the SRR strip width W). The corresponding reflection coefficient formula reads:

$$r = \frac{a_4 \rho^4 + a_3 \rho^3 + a_2 \rho^2 + a_1 \rho + a_0}{b_4 \rho^4 + b_3 \rho^3 + b_2 \rho^2 + b_1 \rho + b_0} \quad (1)$$

being $\rho = d_{\text{tot}}/\lambda_r$ (where $d_{\text{tot}} = D + T$, λ_r is the resonant wavelength) and the coefficients are a function (not simple) of all the geometrical and electromagnetic parameters listed above of the ENZ and SRR.

Analytical model and the results obtained by full-wave simulations are compared. Simulations are performed by using a frequency domain solver, implemented by the finite integration commercial code CST Microwave Studio [11]. In Figure 2 the reflection coefficient spectra for the proposed structure is presented.

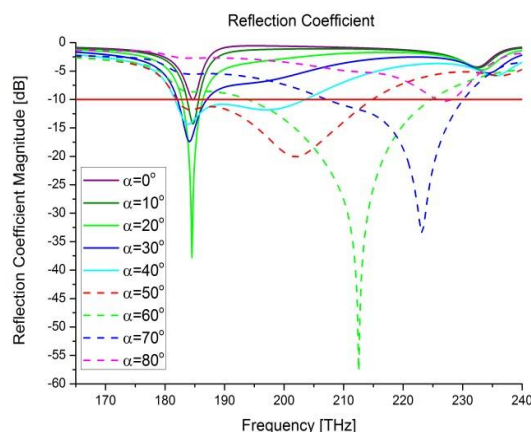


FIG. 2 – Multi-frequency and wideband absorption behavior of the proposed structure ($d_{\text{tot}}/\lambda_p = 0.25$)

III. CONCLUSIONS

The combination of the potential role of ENZ and SRR materials to design a new electromagnetic absorber was investigated. Such materials, thanks to their peculiar properties, path new ways forward the design of electromagnetic absorbers, satisfying specific requirements. In this regard, first of all a new analytical model, describing the electromagnetic absorption characteristics of the structure (in terms of magnitude, bandwidth and frequency position) was presented. The proposed model is compared to the results obtained by full-wave simulations. Good agreement among analytical and numerical results was obtained.

Full-wave simulations have confirmed the ability of the proposed configuration to behave as a multi-band and broadband absorber in a wide range of angle of incidence for small thicknesses.

The proposed structure offers great potential in a wide variety of practical application fields such as to build-up selective thermal emitters, for detection and sensing, for imaging and defense applications.

REFERENCES

- [1] B.A. Munk, *Frequency Selective Surfaces*, John Wiley & Sons, New York 2000.
- [2] W.H. Emerson, "Electromagnetic wave absorbers and anechoic chambers through the years," *IEEE Transactions on Antennas and Propagation*, vol. 21, no. 4, pp. 484–490, 1973.
- [3] B. Munk, P. Munk, J. Pryor, "On Designing Jaumann and Circuit Analog Absorbers (CA Absorbers) for Oblique Angle of Incidence," *IEEE Transactions on Antennas and Propagation*, vol. 55, no. 1, pp. 186–193, 2007.
- [4] N.I. Landy, S. Sajuyigbe, J. J. Mock, D. R. Smith, W. J. Padilla, *Phys. Rev. Lett.*, vol. 100, 207402, 2008.
- [5] A.I.M. Ayala, Master of Science Thesis, Tufts University, USA, 2009.
- [6] H. Tao, N.I. Landy, C. M. Bingham, X. Zhang, R. D. Averitt, W. J. Padilla, "A metamaterial absorber for the terahertz regime: Design, fabrication and characterization," *Opt. Exp.*, vol. 16, 7181, 2008.
- [7] X. Liu, T. Starr, A.F. Starr, W.J. Padilla, "Infrared spatial and frequency selective metamaterial with near-unity absorbance," *Phys. Rev. Lett.*, vol. 104, 207403, 2010.
- [8] K. Aydin, V.E. Ferry, R. M. Briggs, H.A. Atwater, "Broadband, polarization-independent resonant light absorption using ultrathin, plasmonic super absorbers," *Nat. Comm.*, vol. 2, 517, 2011.
- [9] S. Feng, and K. Halterman, "Coherent perfect absorption in epsilon-near-zero metamaterials," *Phys. Rev. B*, vol. 86, no. 16, pp. 165103-1-6, 2012.
- [10] S. Zhong and S. He, "Ultrathin and lightweight microwave absorbers made of μ -near-zero metamaterials", *Nature Scientific Reports*, vol. 3, 2083, pp. 1-4, 2013.
- [11] CST STUDIO SUITE™ 2013, CST of America, Inc., www.cst.com.

RADIATION FROM VERTICAL DIPOLES IN THE PRESENCE OF HOMOGENIZED OMNIDIRECTIONAL METASURFACES

D. Di Ruscio, P. Burghignoli, P. Baccarelli, A. Galli

Department of Information Engineering, Electronics and
Telecommunications, Sapienza University of Rome
Via Eudossiana 18, 00184 Rome, Italy
diruscio/burghignoli/etc@die.uniroma1.it

Abstract

Radiation from vertical sources placed inside a grounded dielectric slab covered with a thin microstructured metal screen with annular geometry is studied. The screen is represented by a locally homogenized surface impedance dyadic. We propose both analytical and numerical models for the calculation of the far-field pattern. The results are validated through rigorous full-wave approaches.

Index Terms – Equivalent networks, homogenization, metasurfaces, method of moments, omnidirectional antennas.

I. INTRODUCTION

Planar structures with annular geometry excited by azimuthally symmetric sources have received considerable interest in different applications (see, e.g., [1] and references therein).

The aim of this work is to characterize this type of structures both analytically and numerically using homogenization concepts. The first case studied is that of a radially uniform metasurface for which the local surface impedance is independent of the radial coordinate. The case of a radially non-uniform metasurface is considered next, with emphasis on a piecewise constant dependence on the radial coordinate.

II. ANALYSIS

The reference structure, shown in Fig.1(a) with the relevant polar coordinate system (ρ, ϕ) , is a grounded dielectric slab of thickness h and relative permittivity ϵ_r , covered by a thin metal screen with annular geometry (i.e., an *annular metasurface*). The structure is excited by an omnidirectional source, like a vertical electric or magnetic dipole (VED or VMD, respectively) embedded within the slab and placed along the z axis.

The screen is locally linearized and homogenized; the resulting surface impedance dyadic $\underline{\mathbf{Z}}_s^{\text{lin}}(\mathbf{k}'_t; \rho)$, \mathbf{k}'_t being the transverse wavenumber of the

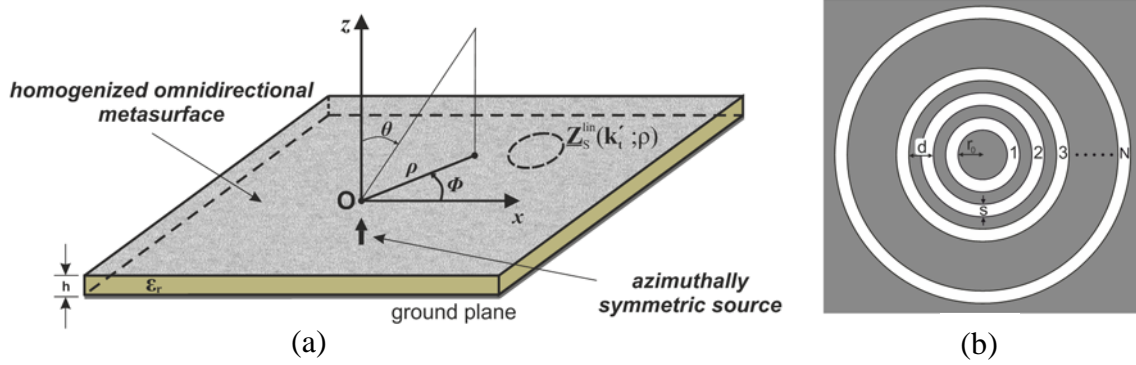


FIG. 1 – (a) A grounded dielectric slab covered with an annular metasurface; (b) geometry of the metasurface considered in this work: d is the period, r_0 is the internal radius of the first slot, s is the constant width of the slots and N is the number of slots.

local field, is assumed to be independent of the ϕ coordinate. However, in what follows the $\underline{Z}_s^{\text{lin}}$ will be considered independent of the wavenumber as well. Examples of linearized structures which admit such representation are capacitive slot gratings (narrow slots, TM fields) and inductive slot gratings (narrow strips, TE fields), as in Fig.1(b) (for other examples see [2]).

The rotational symmetry of the problem decouples Maxwell equations into separate equations for TM^z and TE^z fields; assuming for simplicity that the metasurface does not couple the polarizations, the two cases can be studied separately.

A. Radially Constant Metasurfaces

If the homogenized surface impedance is independent of the radial coordinate ρ , i.e., $\underline{Z}_s^{\text{lin}}(\rho) = \text{const}$, the field radiated by a VED or VMD can be calculated in closed form on the basis of a transverse equivalent network (TEN) model of the structure. The model is based on the assumption that the local interaction of a cylindrical wave and the annular metasurface can be treated as the interaction of the locally linearized plane wave with the locally linearized structure. Assuming that the latter can be represented through the scalar impedances Z_s^{TM} and Z_s^{TE} , respectively for TM and TE fields, the metasurface can be modeled through a spectral impedance dyadic given by:

$$\underline{Z}_s = Z_s^{\text{TM}}(k_\rho) \mathbf{u}_0 \mathbf{u}_0 + Z_s^{\text{TE}}(k_\rho) \mathbf{v}_0 \mathbf{v}_0 \quad (1)$$

where $k_\rho = |\mathbf{k}_t|$, $\mathbf{u}_0 = \mathbf{k}_t / k_\rho$ and $\mathbf{v}_0 = \mathbf{z}_0 \times \mathbf{u}_0$. The absence of translational invariance in the annular geometry does not allow for expressing in the spectral domain the tangential electric field as the dot product of (1) and

of the surface current for general fields. However, (1) is used here only for modeling the interaction of the metasurface with omnidirectional cylindrical waves. For those waves, a TEN model can be established, in which the metasurface is represented by a single shunt impedance Z_S^{TM} or Z_S^{TE} . The far field can then be determined using reciprocity, adopting as a test source in the far field a magnetic or an electric ring.

B. Radially Variable Metasurfaces

In this case the radially non-uniform impedance of the metasurface prevents from establishing a simple TEN model. The analysis is then based on a suitable generalization of the method-of-moments formulation developed in [3] for the treatment of annular slots in a perfectly conducting plane. However, in this case the continuity of the tangential magnetic fields across the slots is replaced by an impedance boundary condition (IBC).

III. RESULTS

To validate the homogenization model based on (1), two kinds of numerical tests were performed on the structure in Fig. 1.

First, the TEN model has been improved with a physical optics (PO) approach to take into account edge diffraction due to substrate truncation [4]. As it can be seen in Fig. 2, as the number of considered periods increases, the PO solution converges to the TEN model solution for both polarizations.

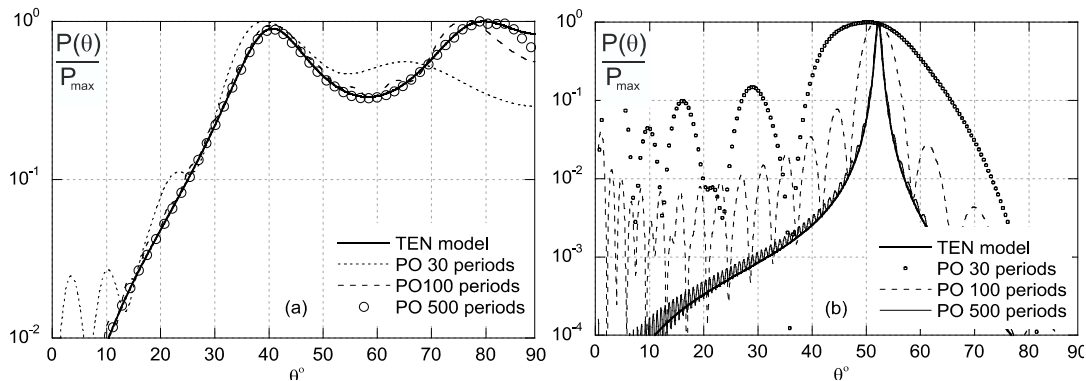


FIG. 2 – Radiated normalized power versus angle of observation θ in degrees.

(a) TM: $h=14.37$ mm, $f=16$ GHz, $r_0=3$ mm, $\epsilon_r=1$, $d=3$ mm, $s=0.25$ mm.

(b) TE: as in the TM case but with $s=2.75$ mm.

Subsequently, by considering the MoM formulation that implements the IBC (IBC-MoM), the results have been compared both with the PO approach and with full-wave numerical simulations in FEKO (see Fig. 3). All the results are in excellent agreement for both polarizations.

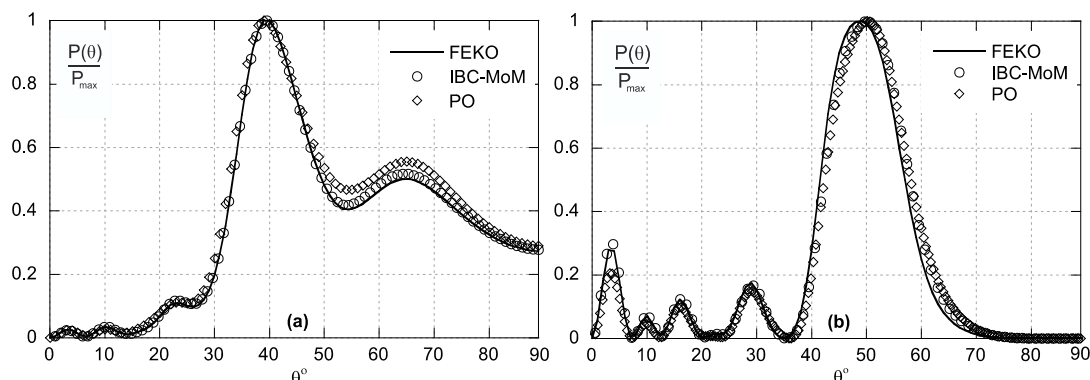


FIG. 3 – Radiated normalized power versus angle of observation θ in degrees. (a) TM: as in Fig.2(a) but $N=30$. (b) TE: as in Fig.2(b) but $N=30$.

IV. CONCLUSION

In this work radiation from vertical dipoles placed inside a grounded slab covered with an omnidirectional metasurface has been studied and an unconventional use of the surface impedance dyadic has been proposed. The study has been carried out both analytically, with reference to a TEN model improved with a PO approach, and numerically through the use of a specific MoM formulation. Both the MoM and TEN-PO results are in good agreement with those obtained with independent full-wave simulation software (FEKO).

REFERENCES

- [1] F. Ares, G. Franceschetti, J. Mosig, S. Vaccaro, J. Vassallo, and E. Noreno, "Satellite communication with moving vehicles on Earth: Two prototype circular array antennas," *Microw. Opt. Technol. Lett.*, vol. 39, n. 1, pp. 14-16, Oct. 2003.
- [2] O. Luukkonen, C. R. Simovski, G. Granet, G. Goussetis, D. Lioubtchenko, A. Räsänen, and S. A. Tretyakov, "Simple and accurate analytical model of planar grids and high-impedance surfaces comprising metal strips or patches," *IEEE Trans. Antennas Propag.*, vol 56, n. 6, pp. 1624-1632, Jun. 2008.
- [3] D. Di Ruscio, P. Burghignoli, P. Baccarelli, D. Comite, and A. Galli, "Spectral method of moments for planar structures with azimuthal symmetry," *IEEE Trans. Antennas Propag.*, vol. 62, n. 4, April 2014 (to appear).
- [4] H. Ostner, E. Schmidhammer, J. Detlefsen, and D. R. Jackson, "Radiation from dielectric leaky wave antennas with circular and rectangular apertures," *Electromagnetics*, vol 17, n. 5, pp. 505-535, 1997.

ON THE APPLICATIONS OF A PARTICULAR ELECTRIC-MAGNETIC UNIAXIAL LOSSY MEDIUM

M. Khalid

Department of Information Engineering, Electronics and
Telecommunications, "La Sapienza" University of Rome,
Via Eudossiana 18, 00184 Roma, Italy
muhammad.khalid@uniroma1.it

Abstract

In this paper the reflection behavior of a SH/DB interface between an isotropic medium and a particular electric-magnetic uniaxial lossy medium is presented. This SH/DB boundary medium in the perspective of an absorbing material is also analyzed. The uniaxial lossy material can be characterized by the complex diagonal permittivity and permeability tensors. The electromagnetic response of this medium is investigated by arbitrarily choosing the different directions of the optic axis and the incident wave vector. Numerical results are presented and some interesting properties of this interface are noted.

Index Terms – Boundary conditions, uniaxial lossy media, SH/DB boundary, metamaterials.

I. INTRODUCTION

Perfectly Matched Layer (PML) is a free-space simulation technique widely used for solving unbounded electromagnetic problems numerically. The PML shows zero reflection which is independent of incident angle, frequency and polarization of impinging wave [1, 2]. The realization of this absorbing layer has been suggested in terms of a uniaxial lossy material with the following properties:

$$\underline{\underline{\mu}} = \eta_1^2 \underline{\underline{\varepsilon}} \quad \text{and} \quad \varepsilon_t \varepsilon_z = \varepsilon_1^2 \quad (1)$$

where ε_1 is the permittivity and η_1 is the impedance of the isotropic medium matched with the uniaxial material characterized by $\underline{\underline{\varepsilon}}$ and $\underline{\underline{\mu}}$ tensors. Moreover, the subscripts t and z represent transverse and axial components of the permittivity with respect to the surface normal.

On the contrary, for a DB medium introduced in [3], the reflection factor is zero only at normal incidence and approaches unity for any other incident angle. The realization of the DB boundary has been suggested in terms of a uniaxial medium with the components of both permittivity and permeability orthogonal to the interface approaching zero. In a very recent paper [4], a strange and interesting analogy between a PML and a DB medium has been presented. By assuming the loss factor α to be very small, the parameters of the uniaxial material able to realize a DB boundary have been approximated as,

$$\varepsilon_t \approx \varepsilon_1 M(1+i\alpha) \quad \text{and} \quad \varepsilon_z \approx \frac{\varepsilon_1}{M} \quad (2)$$

where M is the magnitude of the permittivity components. A medium with the above mentioned parameters is not a PML as the second condition in Eq. (1) is not fulfilled. However, for $\alpha \ll 1$, the interface of such a medium shows almost zero reflection and approaches a PML as α goes to zero. A medium with these properties has been called an approximate Perfectly Matched Layer (a-PML) medium in [4]. It is also important to note that for large values of M the medium characterized by (2) acts as a particular DB medium and concurrently as a PML medium when $\alpha = 0$.

The DB medium is a special case of the more general SH/DB boundary medium introduced in [5]. The realization of the SH/DB boundary has been suggested by means of a uniaxial material with the components of both permittivity and permeability in the direction of optic axis approaching zero. In the present paper, the behavior of a SH/DB interface separating an isotropic and a particular electric-magnetic uniaxial lossy medium with optic axis lying in an arbitrary direction is investigated.

II. ELECTRIC-MAGNETIC UNIAXIAL LOSSY MEDIUM

Let us presume that the electric-magnetic uniaxial lossy medium with SH/DB interface is defined by the following parameters,

$$\epsilon_\tau = \epsilon_1 M(1+i\alpha) \quad \text{and} \quad \epsilon_c = \frac{\epsilon_1}{M}(1+i\beta) \quad (3)$$

where, τ and c indicate orthogonal and axial directions with respect to the optic axis and β represents the losses. Now, consider a plane wave travelling in an isotropic medium (Medium 1) incident on an interface with an electric-magnetic uniaxial lossy medium (Medium 2) as shown in Fig. 1. The incident wave vector k_i makes an angle θ_i with the surface normal. The tangential component of vector k_i makes an angle ϕ_i with the x-axis while ψ is the angle between the optic axis c and the z-axis.

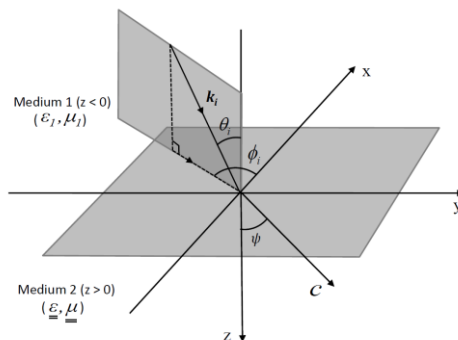


FIG. 1 – Geometry of the problem

It is found that the SH/DB boundary medium with the optic axis in a generic direction shows very interesting properties. Due to lack of space, only results are presented here while the expressions for the reflection coefficients are explicitly presented in [6]. The reflection response of the interface is shown in Figs. 2(a) and 2(b) respectively when the plane of

incidence and the plane containing optic axis are parallel ($\phi_i = 90^\circ$) and are orthogonal ($\phi_i = 0^\circ$) to each other. From these results, it can be noted that the SH/DB medium behaves as an absorbing material only when the optic axis is perpendicular to the interface, i.e., $\psi = 0$ (DB medium) and the interface suddenly changes its behavior from a perfect transmitter to a perfect reflector as ψ increases.

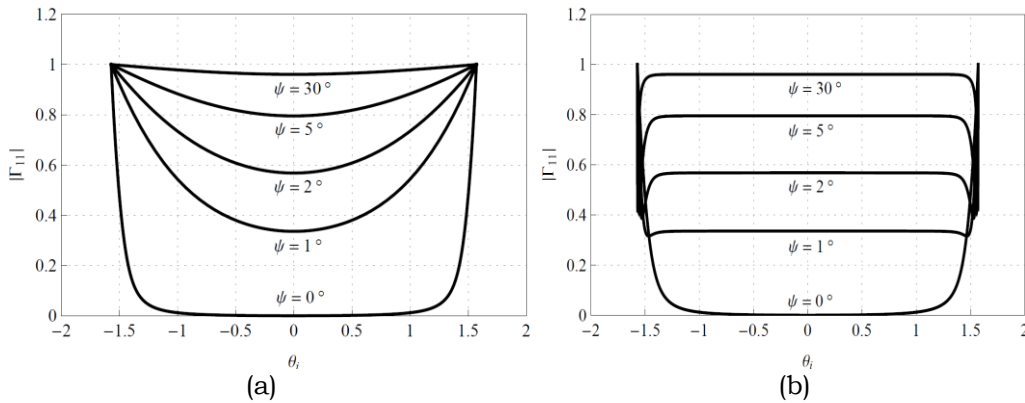


FIG. 2 – Amplitudes of reflection coefficients Γ_{11} (a) $\phi_i = 90^\circ$ and (b) $\phi_i = 0^\circ$ for different values ψ when $\varepsilon_1 = \mu_1 = 1$, $\underline{\underline{\mu}} = \underline{\underline{\varepsilon}}$, $\alpha = \beta = 0.01$ and $M = 100$.

Now, let us analyze the case when the plane of incidence is neither parallel nor perpendicular to the plane containing optic axis. Let us split this situation into two parts: when $\phi_i < 45^\circ$ and when $\phi_i \geq 45^\circ$. Considering the first case when $\phi_i < 45^\circ$, the reflection coefficients Γ_{11} and Γ_{12} are given in Fig. 3. In this case, an important property can be noted that there exists an incident angle for which the co-component of the impinging wave is totally transmitted while the cross component is totally reflected. This Brewster's angle like effect may have potential applications. The reflection behavior of the medium when $\phi_i \geq 45^\circ$ is shown in Fig. 4.

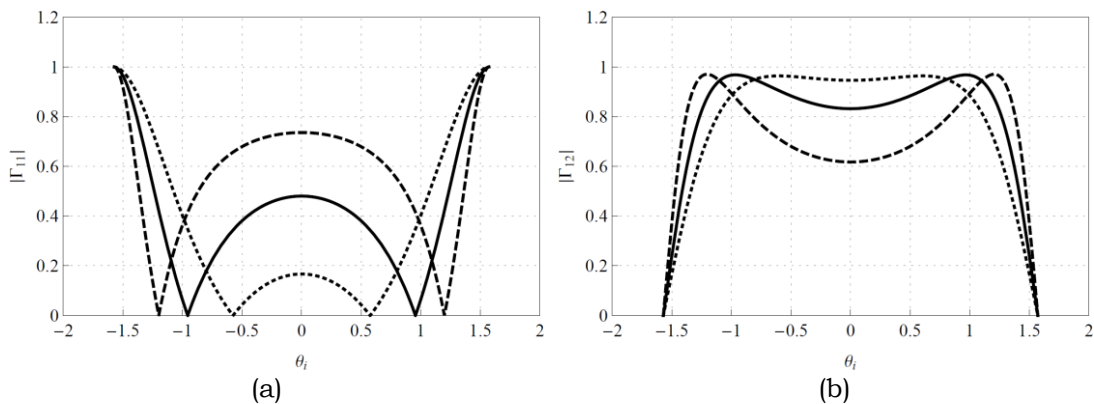


FIG. 3 – Amplitudes of reflection coefficients (a) Γ_{11} and (b) Γ_{12} when $\varepsilon_1 = \mu_1 = 1$, $\psi = 30^\circ$, $\underline{\underline{\mu}} = \underline{\underline{\varepsilon}}$, $\alpha = \beta = 0.01$, $M = 100$ and $\phi_i = 20^\circ$ (solid), $\phi_i = 30^\circ$ (dashed), $\phi_i = 40^\circ$ (dotted).

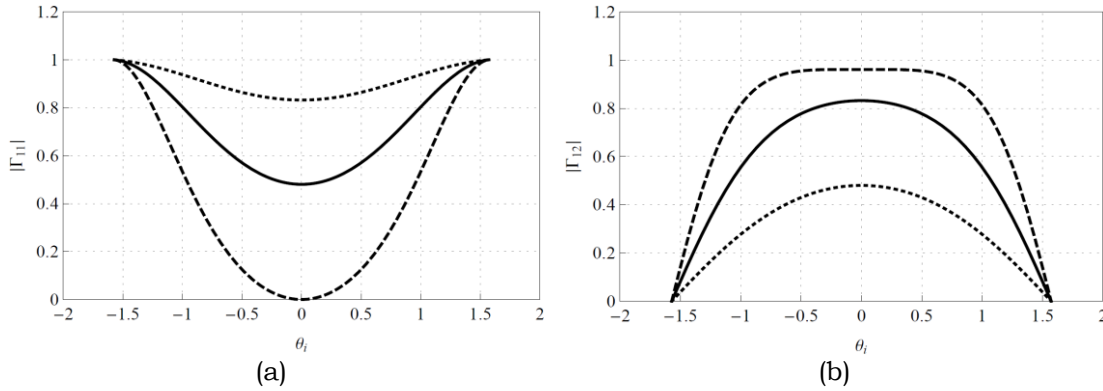


FIG. 4 – Amplitudes of reflection coefficients (a) Γ_{11} and (b) Γ_{12} when $\varepsilon_1 = \mu_1 = 1$, $\psi = 30^\circ$, $\underline{\underline{\mu}} = \underline{\underline{\varepsilon}}$, $\alpha = \beta = 0.01$, $M = 100$ and $\phi_i = 45^\circ$ (solid), $\phi_i = 60^\circ$ (dashed), $\phi_i = 75^\circ$ (dotted).

III. CONCLUSIONS

The SH/DB interface between an isotropic medium and a particular electric-magnetic uniaxial lossy medium is investigated. It is found that the SH/DB boundary medium can behave as an absorbing material only when the optic axis is in the direction of surface normal vector. Another important result is that depending on the direction of the optic axis, the same interface can be used as a perfect transmitter or as a perfect reflector. Moreover, Brewster's angle like effect is also observed when the co-component of the incident field is totally transmitted while the cross component is totally reflected. This novel electric-magnetic uniaxial lossy material with the SH/DB interface may have potential applications and must be deeply analyzed in future works.

REFERENCES

- [1] Z. S. Sacks, D. M. Kingsland, R. Lee, and J. F. Lee, "A perfectly matched anisotropic absorber for use of an absorbing boundary condition", *IEEE Transactions on Antennas and Propagation*, vol. 43, pp. 1460-1463, 1995.
- [2] S. D. Gedney, "An anisotropic perfectly matched layer-absorbing medium for truncation of FDTD lattices", *IEEE Transactions on Antennas and Propagation*, vol. 44, pp. 1630-1639, 1996.
- [3] I. V. Lindell and A. H. Sihvola, "Electromagnetic boundary and its realization with anisotropic metamaterials", *Phys. Rev. E*, vol. 79, 026604, 2009.
- [4] N. Tedeschi, F. Frezza, and A. Sihvola, "On the Perfectly Matched Layer and the DB boundary condition", *J. Opt. Soc. Am. A*, vol. 30, pp. 1941-1946, 2013.
- [5] N. Tedeschi, F. Frezza, and A. Sihvola, "Reflection and Transmission at the interface with an electric-magnetic uniaxial medium with applications to boundary conditions", *IEEE Transactions on Antennas and Propagation*, vol. 61, pp. 5666-5675, November 2013.
- [6] F. Frezza, M. Khalid, and N. Tedeschi, "On a lossy electric-magnetic uniaxial medium and its applications to metamaterials and boundary conditions", *IEEE Transactions on Antennas and Propagation*, submitted for publication, 2014.

A HYBRID ALGORITHM FOR OVERCOMING THE BRANCH AMBIGUITY PROBLEM IN THE RETRIEVAL OF THE EQUIVALENT PARAMETERS OF A DOUBLE NEGATIVE METAMATERIAL

A. Sgrò⁽¹⁾, D. De Carlo⁽¹⁾, G. Angiulli⁽¹⁾

⁽¹⁾ Department DIIES, University Mediterranea
Via Graziella 1 – Loc. Feo di Vito, 89122 Reggio Calabria, Italy
{annalisa.sgro, domenico.decarlo, giovanni.angiulli}@unirc.it

Abstract

Over the last years the interest on double negative (DNG) metamaterials is noticeably increased due to their revolutionary properties. Researchers have been working on methods for retrieving their effective electric permittivity ϵ_{eff} and magnetic permeability μ_{eff} . Among these, the scattering parameter retrieval (SPR) method can be considered the primary choice to accomplish this task, despite some limitations including the so-called “branch ambiguity” problem. In this work a numerical study of an algorithm for overcoming this issue, is presented.

Index Terms – DNG metamaterials, effective material parameters, branch ambiguity problem.

I. INTRODUCTION

During the last decade, there has been growing interest in the scientific community on metamaterials [1]. Roughly speaking, a metamaterial is a man-made material designed by embedding specific inclusions, periodically arranged, in a host medium in order to obtain a structure with desired properties in its response to an outer electromagnetic field [2]. In a metamaterial both the size of the inclusions and the period of the lattice are made larger than the wavelength at the inclusion's resonance, and so a homogenized description applies to it, allowing the characterization of its electromagnetic properties in term of conventional homogeneous material parameters [2]. If both electrical permittivity ϵ_{eff} and magnetic permeability μ_{eff} are negative at the same frequency, the metamaterial is referred to as a double negative (DNG) metamaterial [2]. In designing and optimizing a DNG metamaterial structure an effective and robust method able to retrieve the associated effective parameters ϵ_{eff} , μ_{eff} is required [1]. Among the various procedures introduced in literature, the scattering parameter retrieval (SPR) method has become the main tool to accomplish this task [1]. Nonetheless its popularity, this method is affected by the so-called “branch ambiguity” problem. It is related to the choice of the branch of the complex logarithmic function involved in the evaluation of the complex refractive index N_{eff} characterizing the DNG metamaterial under study [1], [3], [4]. Several methods have been introduced in literature in order to face this issue [1], and very recently a couple of

promising algorithms have been proposed [3], [4]. The first is based on the Kramers-Kronig relations [3], whereas the second exploits the phase unwrapping method [4]. Despite their effectiveness both the methods are characterized by some limitations. In this work, we propose to link them in a simple way realizing so a hybrid method able to overcome their inherent limitations.

II. BASIC THEORY

In what follows only a brief account of the branch ambiguity problem [1] and of the related resolution methods [3], [4] considered in this study is given. In order to retrieve the effective parameters of a DNG metamaterial, this can be considered equivalent to a homogeneous slab of thickness d_{eff} , having an electrical permittivity ϵ_{eff} and magnetic permeability μ_{eff} . For a uniform plane wave that impinges normally on the slab, it can be shown that the complex refractive index N_{eff} and the wave impedance Z_{eff} of the slab are related to the scattering coefficients S_{11} and S_{21} as follows (the time-harmonic dependence $e^{-j\omega t}$ is assumed and suppressed throughout) [1], [3], [4]

$$e^{jN_{eff}k_0d_{eff}} = \frac{S_{21}}{1-S_{11}R_{01}} \quad R_{01} = \frac{Z_{eff}-1}{Z_{eff}+1} \quad Z_{eff} = \pm \sqrt{\frac{(1+S_{11})^2 - S_{21}^2}{(1-S_{11})^2 - S_{21}^2}} \quad (1)$$

The complex refractive index $N_{eff} = n_{eff} + j\kappa_{eff}$ results

$$n_{eff} = \frac{1}{k_0d_{eff}} \left[\arg\left(\frac{S_{21}}{1-S_{11}R_{01}}\right) + 2m\pi \right] \quad \kappa_{eff} = \frac{1}{k_0d_{eff}} \left(-j \ln \left| \frac{S_{21}}{1-S_{11}R_{01}} \right| \right) \quad (2)$$

where $\ln(\cdot)$ is the complex natural logarithm, $\arg(\cdot)$ is the principal branch of $\ln(\cdot)$ whereas the term $2m\pi$, $m \in \mathbb{Z}$ denotes the secondary branches of the logarithmic function. It can be noticed as the imaginary part of the complex refractive index, the extinction coefficient κ_{eff} , is uniquely determined, while the real part, the refractive index n_{eff} , results undetermined because it is affected by the branches of the logarithmic function, i.e. its computation is afflicted by a “branch ambiguity”. Following [3], [4] this issue can be basically solved in two way. The first is based on the requirement that the response of the DNG metamaterial to an outer electromagnetic field should be causal. This constraint implies that the real and the imaginary parts of N_{eff} are univocally linked by means of the Kramers-Kronig relations. Since κ_{eff} is not affected by the branches of the complex logarithm, n_{eff} can be unambiguously derived from it by evaluating the following integral (in the principal value sense)

$$n_{eff}^{KK}(\omega') = n_{\infty} + \frac{2}{\pi} \wp \int_0^{\infty} \frac{\omega \kappa_{eff}}{\omega^2 - \omega'^2} d\omega \quad (3)$$

As shown in [3], the relation (3) provided a guideline for the correct choice of the index m in (2). The second way enforces the continuity of the refractive index n_{eff} unwrapping it by means of a suitable stepwise function which selects the proper index m in (2) making the complex logarithmic function single valued. Once univocally evaluated N_{eff} (using one of the methods succinctly described above) the equivalent parameters ϵ_{eff} and μ_{eff} are simply computed as

$$\epsilon_{eff} = \frac{N_{eff}}{Z_{eff}}, \quad \mu_{eff} = N_{eff} Z_{eff} \quad (4)$$

III. THE HYBRID ALGORITHM

By a comparison among the performances of the two methods [3], [4], it appears that the Kramers-Kronig algorithm i) is able to give accurate numerical results for n_{eff} , ii) provides the upper limit frequency f_{upp} for which the effective medium theory applies iii) turns to be computationally very expensive. For what concerns the phase unwrapping method we have that it, i) is computationally very light, ii) does not provide any information regarding f_{upp} , and consequently it can give an erroneous reconstruction of the refraction index n_{eff} for frequencies exceeded f_{upp} . On the basis of the above considerations a simply hybrid algorithm with combines both methods, having the aim of overcome their limitations, is proposed. The hybrid algorithm uses the unwrapping phase method [4] for a fast computation of the refraction index n_{eff} , while exploits the Kramers-Kronig method [3] to validate the correctness of the results obtained. This is made through a comparison between the values of n_{eff} given by the two methods at the upper end of the frequency band of interest. If any discrepancies are found, the hybrid algorithm stops. Otherwise, using a binary search algorithm the comparison is carried out until the upper limit frequency f_{upp} is established, so discarding the results given by the phase unwrapping algorithm over this frequency value. As a test case we computed the refractive index for a DNG metamaterial composed by three unit cells presented in [3]. In figure (1) and Table I are reported results for the retrieved refractive index n_{eff} and the CPU time involved in the retrieval. All computation have been carried out on a machine mounting an Intel Core Duo P8700 2.53 GHz and equipped with 4 GB RAM using Ansys HFSS. It can be noticed as the hybrid algorithm precisely locates the upper limit frequency f_{upp} thus allowing to discard the unphysical behavior of n_{eff} given by the phase unwrapping method, providing a

reduction of the CPU time of two order of magnitude compared with Kramers-Kronig simulations.

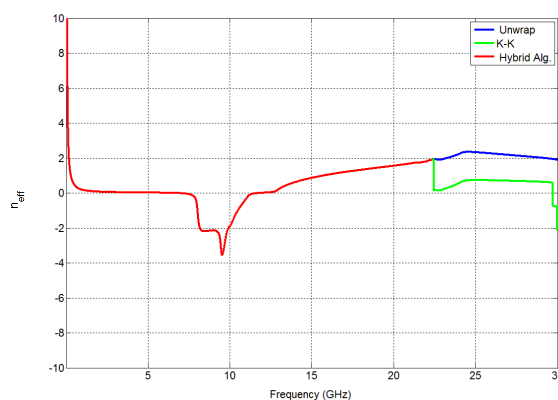


FIG. 1 – Retrieved refractive index for a DNG metamaterial presented in [3].

TABLE I – CPU TIME

Method	Cpu Time (sec)
Kramers-Kronig	3.434
Phase Unwrapping	0.033
Hybrid Algorithm	0.065

IV. CONCLUSION

In this work a hybrid algorithm to overcome the branch ambiguity issue related the effective parameter evaluation for a DNG metamaterial has been presented. Future work is aimed at the integration of the propose algorithm in a framework devoted to the fast design of DNG structures.

REFERENCES

- [1] S. Arslanagic, T. V. Hansen, N. A. Mortensen, A. H. Gregersen, O. Sigmund, R. W. Ziolkowski, and O. Breinbjerg, “A review of the scattering-parameter extraction method with clarification of ambiguity issues in relation to metamaterial homogenization,” *IEEE Antennas and Propagation Magazine*, vol. 55(2), pp. 91-106, 2013.
- [2] L. Solymar, E. Shamonina, *Waves in Metamaterial*, Oxford University Press, 2009.
- [3] Z. Szabò, G. Park, R. Hedge and E. Li, “ A unique extraction of metamaterial parameters based on Kramers-Kronig relationship,” *IEEE Transactions on Microwave Theory and Techniques*, vol. 58(10), pp. 2646-2653, 2010.
- [4] J. J. Barroso, U. C. Hasar, “Resolving phase ambiguity in the inverse problem of transmission/reflection measurement methods,” *Journal of Infrared, Millimeter, and Terahertz Waves* , vol. 33(6), pp.857-866, 2011.

USE OF METAMATERIALS TO IMPROVE ELECTRICAL AND RADIATING PERFORMANCES OF HORN ANTENNAS

M. Barbuto^(1,2), F. Bilotti⁽¹⁾, A. Monti^(1,2),
D. Ramaccia⁽¹⁾, and A. Toscano⁽¹⁾

⁽¹⁾ Department of Engineering, “Roma Tre” University, Rome (Italy)

⁽²⁾ “Niccolò Cusano” University, Rome (Italy)

Abstract

In this contribution, we present some metamaterial-based devices able to improve the performances of horn antennas in different applicative scenarios. In particular, we show how it is possible to (a) design a compact horn by using an annular epsilon-near-zero metamaterial lens; (b) increase the signal-to-noise ratio of receiving systems exploiting filtering metamaterial-inspired modules; (c) dramatically reduce the blockage effects from obstacles placed in the near-field of the antenna using cloaking technologies. The effectiveness of the proposed components has been checked through proper full-wave simulations and/or experimental measurements.

Index Terms – Metamaterials, horn antennas, Cloaking.

I. INTRODUCTION

Horn antennas are widely used in different application fields (satellite systems, radars, directive radio-links, etc.) due to their appealing electrical and radiating properties [1]. However, depending on the particular application, some of the inherent characteristics of horn radiators may limit their performances.

In fact, since the gain of a horn antenna is inherently related to its physical dimensions, high gain horns are typically heavy and rather bulky components. Therefore, the availability of compact horn antennas exhibiting gain performances comparable to the ones of regular and even optimum horns would represent a remarkable achievement in the field.

Moreover, especially in receiving satellite systems, signals have a narrower bandwidth compared to the one of the used feeding horns. A filtering module, thus, is usually required to reduce the out-of-band noise contribution. Therefore, the availability of a low insertion loss filtering module integrated within the horn would reduce the space occupancy, without affecting the in-band performances.

Finally, we consider the co-siting problem consisting in sharing communication platforms among different antennas. In fact, due to the stringent space-saving requirements, it is rather common that a support structure, or another antenna, must be placed in front of the horn aperture, resulting in a serious degradation of both the electrical and the radiating performances of the antenna.

In this contribution, we propose three different approaches based on the use of metamaterial concepts to overcome the mentioned issues.

II. BROADBAND COMPACT HORN ANTENNAS

We present a metamaterial-based solution to reduce horn length without affecting the radiating performances. Starting from the theoretical study of an epsilon-near-zero (ENZ) slab, we have recently proposed a novel metamaterial flat lens [2], which is a combination of a conventional dielectric material and an ENZ artificial material. When such a lens is plugged on the aperture of a shortened horn, the radiation performances are comparable to the ones of the corresponding optimum horn over a broad frequency range. The idea behind the operation of the lens is that the ENZ material is able to accelerate the phase-fronts of the field where they are more curved, returning, thus, flat phase-fronts at the antenna aperture.

As an example, in Fig. 1a, we show a pyramidal horn (aperture length A and height B) capped by our proposed lens consisting of a conventional epsilon-positive material (central part) and two different wire-mediums (WM) implementing the ENZ metamaterial able to flatten the phase-fronts on the E- and H-plane, respectively.

As shown in Fig. 2, the broadside realized gain of the shortened antenna (blue line) is comparable to the one of the corresponding (twice longer) optimum horn (black line). These results confirm the expected operation of the lens.

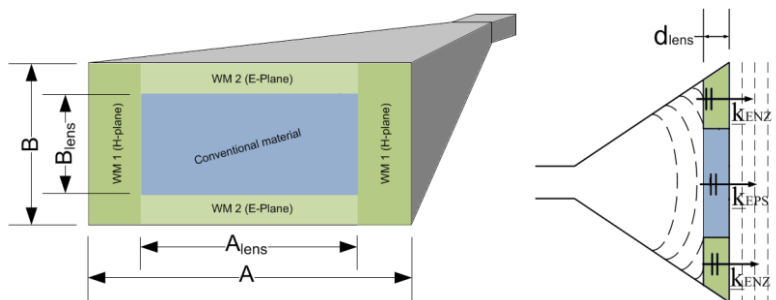


FIG. 1 – (a) Prospective view of a short horn antenna loaded with a flat metamaterial lens. (b) Side view and representation of the phase-fronts before and after the lens.

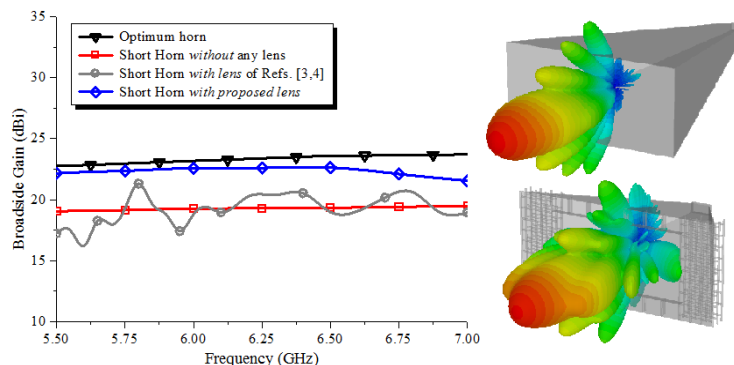


FIG. 2 – (a) Broadside gain of different horns as a function of the frequency; (b) 3D gain of optimum (up) and proposed shortened horn (down) at 6 GHz.

III. SELF-FILTERING CIRCULARLY POLARIZED HORN ANTENNA

In order to reduce the operating bandwidth of a horn and increase the signal-to-noise ratio, we have recently proposed a solution implementing a planar all-metallic filtering module with polarization transforming capabilities [2].

In particular, the filtering module is implemented in the antenna shown in Fig. 1 consisting in a standard corrugated conical horn with a complementary electrically small resonator integrated at its throat and working in circular polarization.

In Fig. 2, we report matching and polarization properties of the antenna. The numerical and experimental results confirm the filtering and polarization transforming capabilities of the proposed module.

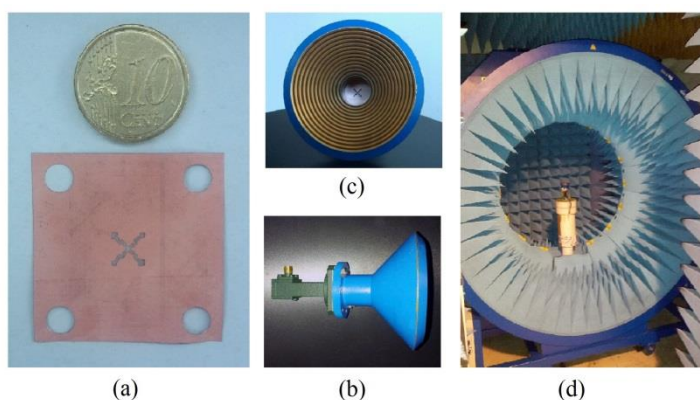


FIG. 2 – (a) Photograph of the proposed filtering module, (b)-(c) side and front view, respectively, of the antenna, (d) the antenna in the near-field measurement system.

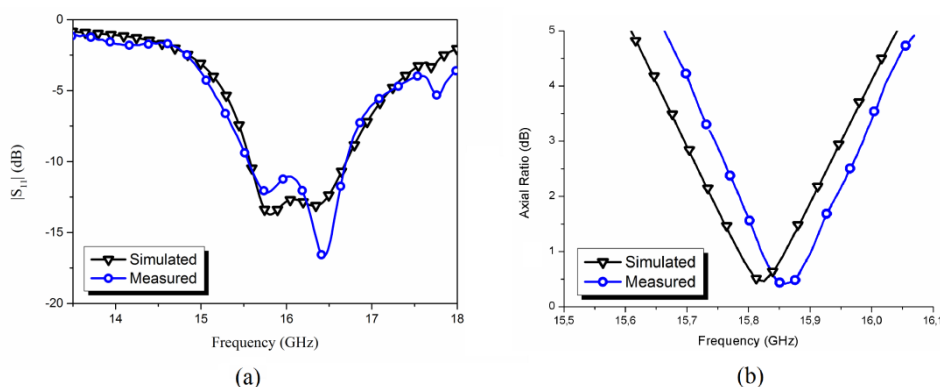


FIG. 3 – Reflection coefficient amplitude (a) and axial ratio for the main beam direction (b) of the self-filtering circularly polarized horn antenna.

IV. REDUCTION OF THE BLOCKAGE EFFECT

In this Section, we consider the scenario depicted in the inset of Fig. 4(a) where the horn antenna is obstructed by an array of densely packed metallic cylinders placed in close proximity of the aperture. The presence of such obstacles dramatically deteriorates the antenna

electrical and radiating performances (see the results of the full-wave simulations reported in Fig. 4(a) - continuous line). Exploiting the mantle cloaking concept, it is possible to make the array of cylinders invisible to the horn antenna within a frequency band, restoring, thus, its original performances. Using a proper analytical model of the structure, followed by a numerical refinement procedure, we have designed an anisotropic metasurface able to provide a cloaking effect within the operating bandwidth of the horn for both TM and TE incidence [4]. Such covers have been conformally applied to the individual cylinders of the array (see Fig. 4(b)). The results of the full-wave simulations shown in Figs. 4(a) and 4(b) confirm the validity of the proposed approach and the effectiveness of the design. A dramatic improvement of the antenna impedance matching and of the antenna gain, in fact, has been obtained. Please note that, since the designed covers work for dual-polarization, they properly operate for any arbitrary orientation between the horn antenna and the cylinder array.

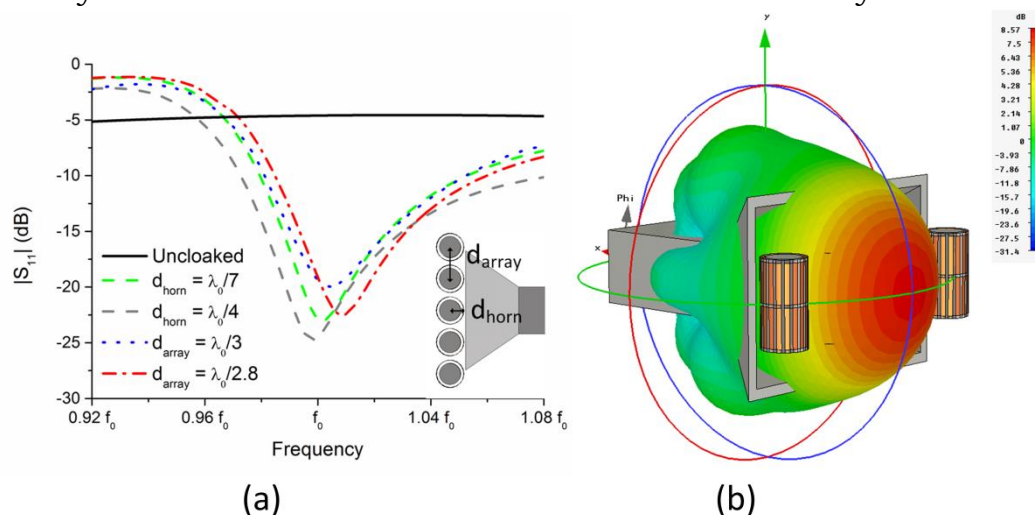


FIG. 4 – (a) Reflection coefficient amplitude of the horn antenna in the uncloaked and cloaked cases and (b) gain pattern in the cloaked case.

REFERENCES

- [1] C.A. Balanis, *Antennas Theory: Analysis and Design*, 3rd Ed., New York: Wiley & Sons, 2005.
- [2] D. Ramaccia, F. Scattone, F. Bilotti, and A. Toscano, "Broadband Compact Horn Antennas by using EPS-ENZ Metamaterial Lens", *IEEE Trans. Antennas Propag.*, vol. 61, No. 6 pp. 2929 - 2937, June 2013.
- [3] M. Barbuto, F. Trotta, F. Bilotti, and A. Toscano, "A combined bandpass filter and polarization transformer for horn antennas," *IEEE Antennas and Wireless Propagation Letters*, Vol. 12, pp. 1065-1067, 2013.
- [4] A. Monti, J. Soric, A. Alù, A. Toscano, and F. Bilotti, "Anisotropic Mantle Cloaks for TM and TE Scattering Reduction," *submitted to IEEE Trans. Antennas Propag.*

CHIPLESS RFID WITH METASURFACES

F. Costa⁽¹⁾, S. Genovesi⁽¹⁾, A. Monorchio⁽¹⁾, G. Manara⁽¹⁾

⁽¹⁾ Dipartimento di Ingegneria dell'informazione, Università di Pisa,
Via G. Caruso 16, 56122 Pisa, Italy
filippo.costa@iet.unipi.it

Abstract

The most relevant properties of spectral domain chipless RFID based on High-Impedance Surfaces are described. Two different detection mechanisms based on co-polar absorption and cross-polar reflection are presented.

Index Terms – Chipless RFID, Electromagnetic Absorbers, Frequency Selective Surfaces (FSS), High Impedance Surfaces (HIS).

I. INTRODUCTION

Barcode is today the most popular method of labeling objects but it has significant limitations when applied to manufacturing automation, gate access control and anti-counterfeiting (short-range readability, non-automated tracking, operation in harsh environments, etc.).

To achieve the next leap forward in supply chain efficiency, many organizations are turning to Radio Frequency Identification (RFID) [1]. Application of RFID to consumer packaged goods, postal items, drugs and books is feasible only if tag prices drop to under one cent including the cost of fitting them in place. After significant investments the price of tags decreased but it is still not competitive when compared to barcodes (the cost of passive tags started at US\$0.05 each for very large quantities but special tags can cost more than one euro). Indeed, the presence of the integrated circuit poses a lower bound to the cost of tags.

As a consequence in the last few years efforts have been put in developing chipless RFID tags with no ICs, which means that the main cost of the tag is being removed [2]. The potentially revolutionary aspect of chipless tags is that, eventually, they could be printed directly on products and packaging for 0.1 cents and then replace ten trillion barcodes yearly. IDtechEx Ltd, a company which provides independent market research on emerging technologies, predicted that chipless RFID can lead to an exponential growth of radio frequency identification technologies [3]. Chipless RFID is a new technology which is still in the infancy, and many products have not left the prototyping cycle. Two general types of RFID tags can be identified: time domain (TD)-based and spectral (frequency) signature-based chipless RFID tags.

The first class of chipless tags encodes the information in time domain (TD). The most popular tag classifiable as chipless RFID tag is the surface acoustic wave (SAW) tag [4] which has been commercialized in nineties with a moderate success because of high realization costs. Another promising technology for TD tags is represented by Thin Film Transistor Circuits (TFTCs) which are being developed using organic or printed inorganic semiconductors [3].

The second class of chipless tags encodes data into the spectrum using resonant structures where a bit is associated with the presence or absence of a resonant peak at a predetermined frequency. The advantages of these tags are that they are fully printable and extremely low cost. After initial designs based on multiple antennas accorded on multiple frequencies [5], a different design approach based on two orthogonally polarized antennas with a series of resonators in between were proposed [6] but the information is encoded within the antenna component of the radar cross section. The structural component of RCS, which is a major scattering contribution is a disturb for this tag design.

Finally, chipless tags can be designed by using several resonators of different size [7]. This category of chipless tags has recently gained most of the attention since information is advantageously contained in the structural component of RCS. None of the proposed designs based on multi-resonators has showed scalability potentials mainly because the disposition of resonators one close to another creates harmful destructive interferences when the number of bit increases. Our proposal is to employ multi-resonant high-impedance surfaces to design chipless tags. The periodic arrangement provides several advantages with respect to classical designs.

II. PROPOSED CHIPLESS TAGS AND ENCODING SCHEMES

The proposed chipless RFID tag consists of a Frequency Selective Surface (FSS) printed on top of a grounded substrate. The unit cell of the periodic surface must be a multi-resonant element since the chipless tag encodes the information in the spectral domain. One suitable element for achieving multi-resonant behavior is the concentric-loop element. A 3D sketch of the proposed tag is reported in Fig. 1a.

The structure, differently from literature available designs, can be rapidly analyzed as an infinite extent surface by using a Periodic Method of Moment (PMM). Moreover, the structure can also be efficiently modeled by using an equivalent circuit approach [8]. For practical need, the periodic impedance surface is truncated to few unit cells without altering the frequency position of the resonances. The number of unit cells employed determines the average value of Radar Cross Section (RCS) and therefore the read range. Bit encoding can be obtained in different ways: the first option is to encode information in

the co-polar component of the reflection coefficient by using the peculiar multi-frequency absorption properties of the designed surface [9]. If the suitable amount of loss is introduced in the resonant structure, a perfect absorption can be achieved in correspondence of the resonance frequency. An alternative method is to exploit the de-polarizing properties of these surfaces which are able to produce a positive reflection peak in correspondence of every resonance frequency. Such method is particularly useful when the tag is mounted on metallic objects [10], [11]. Indeed, while the electromagnetic echo of a metallic surface increases proportionally to its dimensions, it does not have any cross-polarized component. This means that tags can be detected, without any signal deterioration, even if the metallic surface is big.

As an example in Fig. 1b the normalized co-polar reflection of the tag measured in free space and cross-polar reflection coefficient of a 5 bit HIS tag placed on a metallic door are reported. The 3x3 HIS tag is interrogated with a dual-polarized horn antenna. The five absorption peaks of the multi-resonant impedance surface are correctly retrieved when the tag is measured in free space. However, when the tag is accommodated on the metallic door the co-polar reflection coefficient is not anymore intelligible as the tag but the five resonant peaks in cross-polarized reflected signal are well visible.

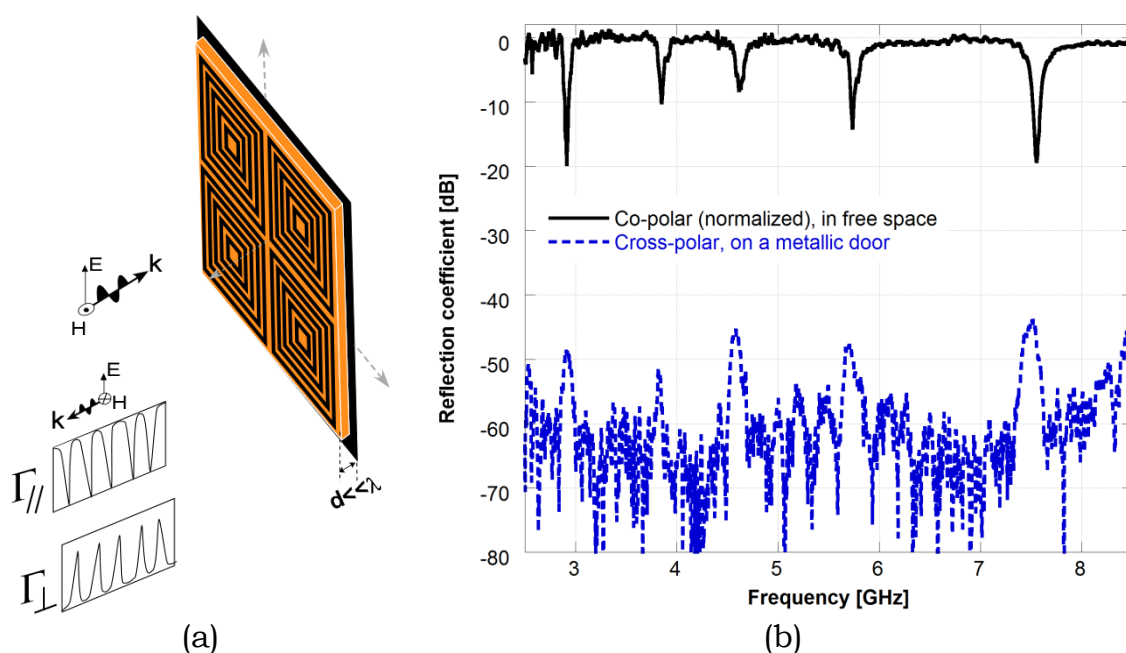


Fig. 1 – 3D sketch of the chipless RFID working principle (a) and measured co-polar and cross-polar scattering of a 5 bit chipless RFID at a 25 cm distance (b).

III. CONCLUSION

Promising properties of chipless technology are exposed and the importance of employing impedance periodic surfaces as chipless transponders is also remarked. Relevant properties of the High-Impedance Surfaces employed as a spectral domain chipless RFID transponder are described. Two different detection mechanisms based on co-polar absorption and cross-polar reflections are summarized. It is pointed out that the cross-polar detection technique reduces the read range of the tag but it provides important benefits such as the reduced sensitivity to multipath and robust reading performance when the tag is accommodated on metallic objects.

REFERENCES

- [1] K. Finkenzeller, *RFID Handbook: Radio-Frequency Identification Fundamentals and Applications*. Hoboken, NJ: Wiley, 2004.
- [2] S. Preradovic, N. Karmakar "Chipless RFID – Barcode of the future", *IEEE Microwave Magazine*, vol. 11, no. 7, pp. 87-97, December 2010.
- [3] R. Das and P. Harrop, "Printed and chipless RFID forecast, technology & players 2009-2019" (IDTechEx, 2010).
- [4] V. Plessky, L. Reindl, "Review on SAW RFID Tags", *IEEE Trans. Ultrason. Ferroelectr. Freq. Control*, 2010, 57, (3), pp. 654 –668.
- [5] B. Shao, Q. Chen, Y. Amin, R. Liu, L. R. Zheng "Chipless RFID tags fabricated by fully printing of metallic inks", *Annals of Telecommunications-(Annales des Télécommunications)*, vol. 68(7-8), pp. 401-413, 2013.
- [6] S. Preradovic, I. Balbin, N. C. Karmakar, G. F. Swiegers, "Multiresonator-based chipless RFID system for low-cost item tracking", *IEEE Trans. on Microwave Theory and Tech.*, vol. 57, no. 5, pp: 1411-1419, May 2009.
- [7] A. Vena, E. Perret, S. Tedjini, "Chipless RFID Tag Using Hybrid Coding Technique", *IEEE Trans. on Microwave Theory and Tech.*, vol. 59, no. 12, pp: 3356-3364, 2011.
- [8] F. Costa, S. Genovesi, A. Monorchio, "On the Bandwidth of High-Impedance Frequency Selective Surfaces," *IEEE Antennas Wireless & Propag. Lett.*, vol. 8, pp. 1341-1344, 2009.
- [9] F. Costa, S. Genovesi, A. Monorchio, "A Chipless RFID based on Multi-Resonant High-Impedance Surfaces" *IEEE Transactions on Microwave Theory and Techniques*, vol. 61, no. 1, pp. 146-153, 2013.
- [10] F. Costa , S.Genovesi, A. Monorchio, "Chipless RFID trasponders by using multi-resonant High-Impedance Surfaces" *Proceedings of 2013 URSI International Symposium on Electromagnetic Theory (EMTS)*, Hiroshima, Japan 20 - 24 May, pp. 401-403, 2013.
- [11] F. Costa, S. Genovesi, A. Monorchio, "Reading Chipless RFID Located on Metallic Platforms by using Cross-Polar scattering" *2014 XXXIth URSI General Assembly and Scientific Symposium (URSI GASS)*, August 2014.

A MORTAR-ELEMENT METHOD FOR THE ANALYSIS OF CYLINDRICAL GUIDING STRUCTURES

A. Tibaldi^(1,2) and G. Addamo⁽²⁾

⁽¹⁾ Dipartimento di Elettronica e Telecomunicazioni, Politecnico di Torino, Corso Duca degli Abruzzi 24, 10129, Torino, Italy

⁽²⁾ Consiglio Nazionale delle Ricerche, Istituto di Elettronica e di Ingegneria dell'Informazione e delle Telecomunicazioni (CNR-IEIIT), Torino, Italy

alberto.tibaldi@polito.it

Abstract

In this work a novel formulation for the analysis of structures with axial symmetry is presented. A multi-domain spectral method based on mortar-matching is developed. The technique is applied to the analysis and design of smooth-wall horn antennas. A comparison of the simulation results obtained with this numerical scheme and with a mode-matching code is presented.

Index Terms – Spectral-element methods, multi-beam antennas

I. INTRODUCTION

Multi-beam antenna systems are widely used to cover a well-defined geographical region with several beams generated by an array of radiators which feed a reflecting surface [1]. Thanks to their potential characteristics in terms of matching, low cross-polarization levels and high efficiency, smooth-walls circular horn antennas are optimal candidates as array elements. These devices are composed by a cascade of slope discontinuities designed in order to excite the desired field configuration. A classical analysis procedure consists of considering a staircase approximation of the profile that is, then, analyzed as a cascade of circular waveguide steps; each step is described by its generalized scattering matrix (GSM) that is obtained, for example, by the mode matching technique [2].

In this work a novel formulation for axially symmetrical structures is presented and applied to the efficient analysis of these antennas, since staircase approximations are avoided. The solution scheme is based on the mortar-element method (MEM) [3],[4]. This technique has been exploited for the design of a high performance multi-beam antenna in Q band. A comparison between the reflection coefficient simulated with the MEM code and with a code based on a coupled integral equation formulation [5] is reported.

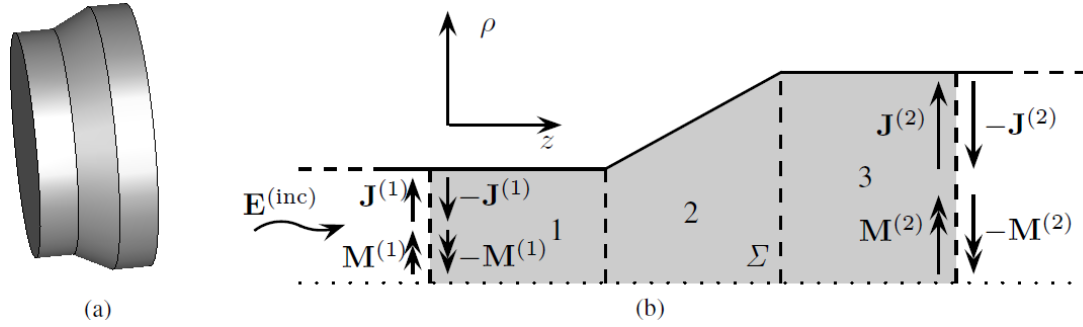


FIG. 1 – Left (a): 3d view of a slope discontinuity. Right (b): (z, ρ) plane section of the slope. The grey internal region Σ is divided in three patches separated by the dashed lines to apply the multi-domain strategy. $\mathbf{J}^{(1,2)}$ and $\mathbf{M}^{(1,2)}$ are the equivalent electric and magnetic current densities.

II. DESCRIPTION OF THE METHOD

The scattering problem has been solved exploiting the Equivalence Theorem and the domain decomposition. The analysis of each slope discontinuity is divided in two sub-problems by introducing two couples of equivalent electric and magnetic current densities $\mathbf{J}^{(1,2)}$ and $\mathbf{M}^{(1,2)}$ at each access port (see Fig. 1b). In the first sub-problem the field is non-zero only at the access ports and it is described by modal expansion. In the second one the field is non-zero only in the internal region and the electromagnetic problem is solved by means of a multi-domain spectral method. An equivalent circuit for the n -th mode is introduced by exploiting the classical line transmission formalism, as shown in Fig. 2. The generators are related to the projection of $\mathbf{J}^{(1,2)}$ and $\mathbf{M}^{(1,2)}$ on the circular waveguide modes.

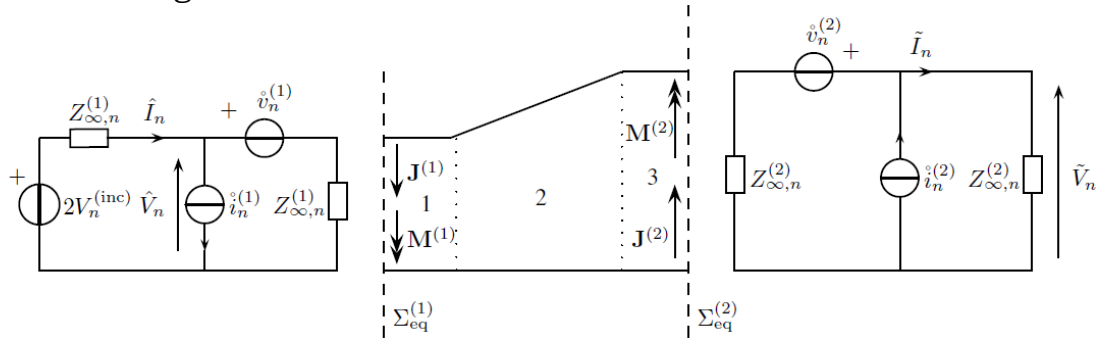


FIG. 2 – Equivalent circuit for the n -th mode of the circular access waveguides; $Z_{\infty,n}^{(1,2)}$ are the relevant characteristic impedances at the access ports; the sources are related to the equivalent current densities; $V_n^{(\text{inc})}$ is the incidence voltage of the n -th mode.

Focusing on the internal region, since the device exhibits axial invariance (see Fig. 1a) and the incident mode has $e^{+jm\varphi}$ azimuthal dependence, it is possible to derive the electric and magnetic fields $\mathbf{E}_t = \{E_\rho, E_z\}$ and $\mathbf{H}_t = \{H_\rho, H_z\}$ transverse to the $\hat{\boldsymbol{\phi}}$ direction, as functions of E_φ and H_φ , from four of the curl Maxwell's equations. By projecting

the remaining two equations on two sets of entire-domain basis functions $v_\beta^{(e)}$ and $v_\beta^{(h)}$ and by applying the Stokes theorem:

$$jkY \iint_{\Sigma} E_\varphi v_\beta^{(e)} dz d\rho + \iint_{\Sigma} \left[H_\rho \frac{\partial v_\beta^{(e)}}{\partial z} - H_z \frac{\partial v_\beta^{(e)}}{\partial \rho} \right] dz d\rho = \oint_{\gamma_\Sigma} (\mathbf{H}_t v_\beta^{(e)}) \cdot d\mathbf{s} \quad (1a)$$

$$-jkZ \iint_{\Sigma} H_\varphi v_\beta^{(h)} dz d\rho + \iint_{\Sigma} \left[E_\rho \frac{\partial v_\beta^{(h)}}{\partial z} - E_z \frac{\partial v_\beta^{(h)}}{\partial \rho} \right] dz d\rho = \oint_{\gamma_\Sigma} (\mathbf{E}_t v_\beta^{(h)}) \cdot d\mathbf{s} \quad (1b)$$

where Σ is the solution domain as indicated in Fig. 1 and γ_Σ is its boundary. By substituting the expressions of the four components in the equations (1a-1b), a vector differential problem with unknowns E_φ and H_φ is obtained. According to the mortar-element method, the domain Σ is divided in sub-domains as shown in Fig. 1 in order to generate ad-hoc entire-domain basis functions $u_\alpha^{(e)}$ and $u_\alpha^{(h)}$ used to expand the unknowns. Both expansion and test functions satisfy PEC boundary conditions at the metallic domain boundaries and continuity conditions at the edges of adjacent sub-domains. The synthesis of these functions is obtained by means of a basis recombination approach based on the singular value decomposition (SVD) [4]. This procedure leads to the following algebraic system:

$$\begin{bmatrix} jkY\mathbf{A}^{(e,e)} & jm\mathbf{A}^{(e,h)} \\ jm\mathbf{A}^{(h,e)} & -jkZ\mathbf{A}^{(h,h)} \end{bmatrix} \begin{bmatrix} \mathbf{c}^{(e)} \\ \mathbf{c}^{(h)} \end{bmatrix} = \begin{bmatrix} \mathbf{b}^{(e)} \\ \mathbf{b}^{(h)} \end{bmatrix} \quad (2)$$

where the vector $\mathbf{c}^{(e)}$ and $\mathbf{c}^{(h)}$ contain the unknown coefficients of the expansion functions for E_φ and H_φ , respectively; the terms $\mathbf{b}^{(e)}$ and $\mathbf{b}^{(h)}$ refer to the incident field at the access ports. The terms of the moment matrix are given by double integrals which are singular in $\rho = m/k$. A special numerical scheme has been developed in order to achieve a fast and accurate computation of this terms.

Note that in the case $m = 0$ the moment matrix is block-diagonal and the vector problem decouples in two scalar (TE and TM) sub-problems. Similarly, the continuity equation can be written as:

$$\mathbf{F} \mathbf{c} = \mathbf{D} \mathbf{x} + \mathbf{E} \mathbf{V}^{(inc)} \quad (3)$$

where \mathbf{F} contains the projection integrals of the MEM basis functions on the access waveguide modes, \mathbf{D} and \mathbf{E} derive from the solution of the circuit of Fig. 2, \mathbf{x} is the vector of the coefficients of the current densities and the vector $\mathbf{V}^{(inc)}$ is related to the incident field. Once the solution of (2) and (3) is obtained, the generalized scattering matrix (GSM) is calculated from the electric and magnetic current densities.

III. RESULTS

The numerical method described in section II has been used to design a high efficiency smooth-wall horn antenna operating in Q-band ([39,48] GHz). The profile geometry of the antenna is shown in Fig. 4, the input and output diameters are 6.8 mm and 50 mm. In Fig. 4 is reported a comparison between the simulated reflection coefficient obtained using the MEM code with 289 basis function for each slope discontinuity and with a code based on a coupled integral equation technique (CIET) [5]. The good agreement between the two curves confirms the validity of the proposed analysis method.

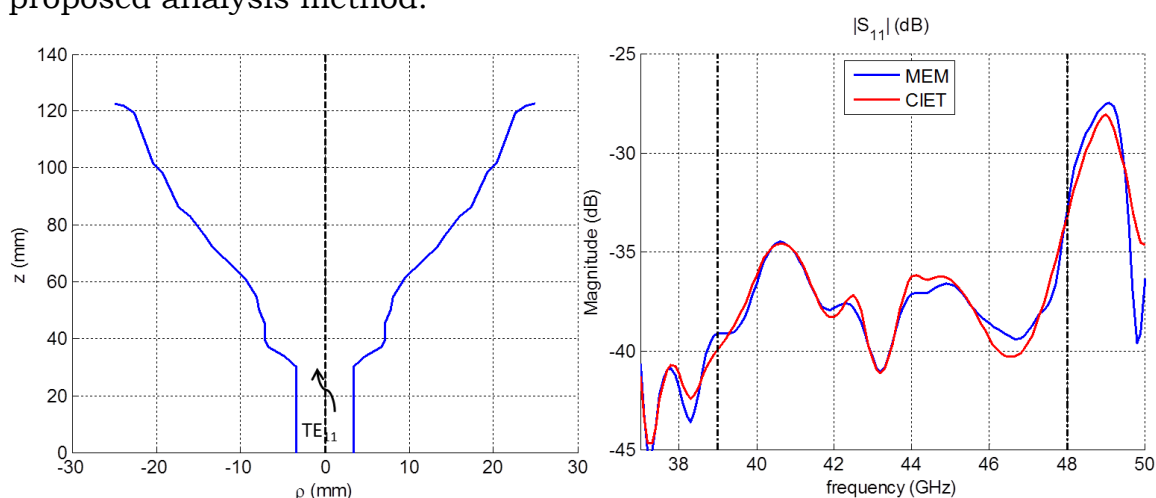


FIG. 3 – Reflection coefficient for the TE₁₁ mode. The blue and red curves refer to the MEM and CIET methods, respectively. The vertical black lines show the operating band of the antenna.

REFERENCES

- [1] S. K. Rao, "Design and analysis of multiple-beam reflector antennas," *IEEE Antennas Propagation Magazine*, vol. 41, no. 4, pp. 53-59, Sep. 1999.
- [2] K. K. Chan and S. K. Rao, "Design of high efficiency circular horn feeds for multibeam reflector applications," *IEEE Transaction Antennas Propagation*, vol. 56, no. 1, pp. 253-258, Jan. 2008.
- [3] C. Canuto, M. Y. Hussaini, A. Quarteroni and T. Zang, "Spectral methods: evolution to complex geometries and applications to fluid dynamics," Berlin, Germany: Springer-Verlag, 2007.
- [4] O. A. Peverini, G. Addamo, G. Virone, R. Tascone and R. Orta, "A spectral-element method for the analysis of 2-D waveguide devices with sharp edges and irregular shapes," *IEEE Trans. Microwave Theory Techniques.*, vol. 59, no. 7, pp. 1685-1695, July 2011.
- [5] G. Addamo, O. A. Peverini, G. Virone, R. Tascone and R. Orta, "Model-order reduction technique for the efficient analysis of complex waveguide structures – an application to the design of corrugated horns," *IEEE Antennas Wireless Propagation Letters*, vol. 8, 2009.

SOURCE STIRRING ANALYSIS FOR REVERBERATION CHAMBERS

G. Cerri⁽¹⁾, A. De Leo⁽¹⁾, V. Mariani Primiani⁽¹⁾, P. Russo⁽¹⁾

⁽¹⁾ Department of Information Engineering, Università Politecnica delle Marche, Via B. Bianche, 60131 Ancona, Italy
g.cerri@univpm.it

Abstract

The source stirring technique for reverberation chambers (RC) is obtained by several monopole antennas located on the chamber walls. The stirring action is accomplished subsequently feeding each antenna pairs covering all possible combinations. Antennas are fed by real generators and their length is not negligible with respect to the wavelength. An efficient way, that improves the modal series convergence, is presented to compute the electromagnetic field inside the large shielded room. Results are checked by means of typical RC parameters such as the cumulative distribution function (CDF), the polar plot of each field components and field uniformity. Out-of-phase dipole feeding allows to improve field uniformity especially in the lower frequency range.

Index Terms – reverberation chamber; source stirring; cavity modes; series convergence.

I. INTRODUCTION

The main aim of a Reverberation Chamber (RC) is to achieve a statistical field uniformity, isotropy, and random polarization in all the working volume. This effect can be obtained in different way: historically one or more stirrers were introduced into the chamber, and the efficient of the stirring effect depends on the shape [1] and numbers [2] of mechanical stirrer used. In recent past different type of stirring were proposed in literature, in order to reduce the measurement time or the complexity of the measurement. Among these proposals the authors demonstrate, theoretically and experimentally, the possibility of using the source stirring, based on the use of several active antennas, as an alternative for reverberating a cavity.

In this way reverberation is obtained by managing the overall energy delivered to the chamber. Source stirring feasibility was demonstrated by a rigorous electromagnetic model [3-4] and validated by measurements [5]. The antennas used in previous works were 20 conical broadband antennas, fed two at a time in order to achieve a large number of field configuration inside the chamber. The antennas were positioned on the walls of a 1 m³ metallic cubic box and the cables used to feed each antenna were placed inside the box in order to reduce the load effect of all the cables on the Q factor of the cavity.

In the present work an alternative antenna positioning is presented. The antennas used in this work are linear dipoles, in order to have a simple

structure that can be simulated analytically. The dipoles are placed on the chamber wall and they are fed two at a time. The advantage of this configuration is the possibility of increase the working value and to eliminate the feeding cables inside the chamber. Moreover this particular configuration can be used to analyze the possibility of using the source stirring for reverberating the chamber at low frequency. The results are checked by means of typical RC parameters such as the cumulative distribution function (CDF), the polar plot of each field components and field uniformity.

II. MODELLING

A rectangular cavity of dimensions a , b , c is excited by many monopoles of length L on its walls, Fig. 1.

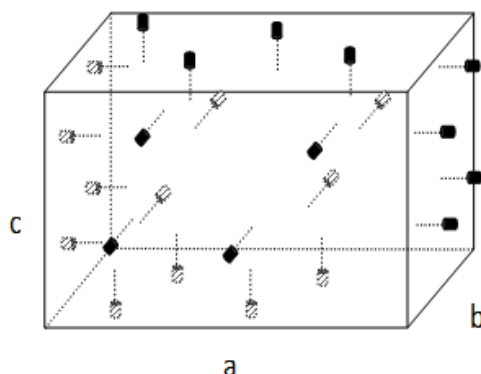


FIG. 1 - Rectangular cavity with the monopoles placed on the walls.

The geometry of the structure allows us to express in a closed form the field inside the chamber using the well-known formulation of the interior problem for resonant cavities [6].

Assuming electric sources only, the electric field expression is given by

$$\vec{E} = -\frac{1}{j\omega\epsilon} \sum_m \frac{\int_V \vec{J} \cdot \vec{f}_m dV}{\int_V |\vec{f}_m|^2 dV} \vec{f}_m - j\omega\mu \sum_m \frac{\int_V \vec{J} \cdot \vec{e}_m dV}{(k_m^2 - \tilde{k}^2) \int_V |\vec{e}_m|^2 dV} \vec{e}_m \quad (1)$$

Where \vec{f}_m and \vec{e}_m are irrotational and TE, TM divergenceless electric eigenvectors respectively.

A sinusoidal current distribution is considered to flow along the conductor of each antenna; for example a monopole in the y - z wall is characterized by the following current density:

$$\vec{J}(x) = I_0 \frac{\sin[k(L-x)]}{\sin(kL)} \delta(y-y_p) \delta(z-z_q) \hat{x} \quad (2)$$

Where I_0 is the current at the antenna feeding point, and $(0, y_p, z_q)$ are the coordinates of the antenna entry point. Also in this case similar expressions can be written for all the other antennas. Using (2) all

terms of (1) are evaluated analytically. A speed up procedure was developed in [7] in order to calculate the slow convergence triple series in (1).

III. RESULTS

The antennas are considered fed two a time for a total of 1891 combinations. In order to check the stirring capability of the proposed method, the classical statistical tools were applied to the results obtained. The Cumulative Distributions Functions (CDF's) for the electric field calculated in the point (3.5m, 2.5m, 1.5m) is shown in Fig. 2. All values are mean normalized. Obtained results match well the expected distributions.

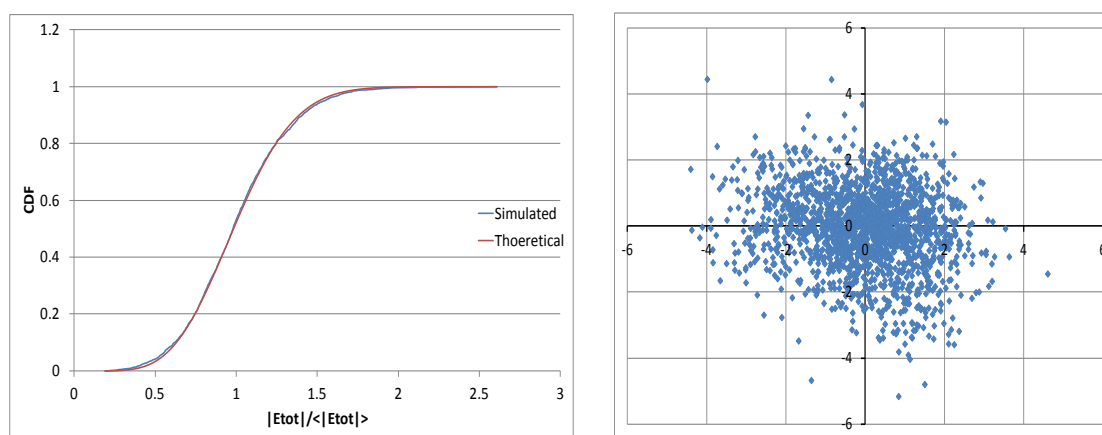


FIG. 2 – Cumulative distribution function and Polar Plot for the total electric field at point (3.5, 2.5, 1.5) m for 1.371GHz

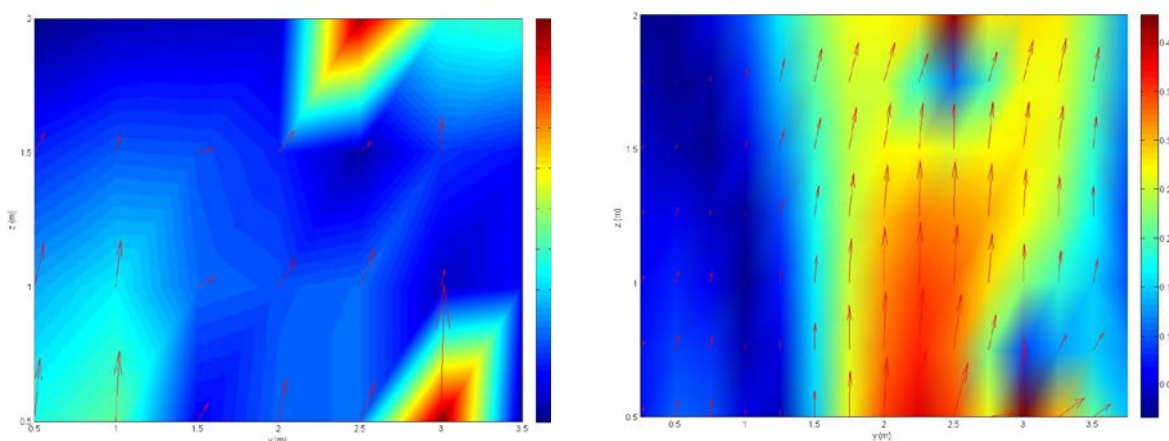


FIG. 3 – Electric field map obtained feeding the same two antennas by in-phase (left) and by out-of-phase (right) signals

The previous analysis makes use of the magnitude of each field components and of the total field. On the other hand, the adopted model is able to separately compute both real and imaginary part of the electric field. The availability of this information allows us to better analyze how the phase of each field value is distributed over the complex plane. As an example, Fig. 2 reports the polar plot for the E_x components.

Fig. 3 compares the electric field map obtained feeding the same two antennas by in-phase and by out-of-phase signals. The improvement in the field intensity and uniformity in the considered transversal section of the chamber is evident.

This alternative feeding way could be useful in the lower frequency range where the chamber becomes undermoded.

IV. CONCLUSIONS

A novel source stirring technique based on the placement of 62 dipoles fed two a time for a total of 1891 combination was presented. The field computation is based on the well known formulation of the interior problem for resonant cavities, and the presented results, in particular the CDF and the polar plot graphics, demonstrate the field uniformity inside the chamber.

REFERENCES

- [1] J. Clegg, A.C. Marvin, J.F. Dawson, S.J. Porter, "Optimization of stirrer designs in a reverberation chamber," *IEEE Trans. on Electromagnetic Compatibility*, vol.47, no.4, pp. 824- 832, Nov. 2005
- [2] F. Moglie, V. Mariani Primiani, "Analysis of the Independent Positions of Reverberation Chamber Stirrers as a Function of Their Operating Conditions," *IEEE Trans. On Electromagnetic Compatibility*, vol.53, no.2, pp.288-295, May 2011
- [3] G. Cerri, V. Mariani Primiani, S. Pennesi, P. Russo, "Source stirring mode for reverberation chambers", *IEEE Trans. On Electromagnetic Compatibility*, vol. 47, no. 4, pp. 815-823, Nov. 2005.
- [4] G. Cerri, V. Mariani Primiani, C. Monteverde, P. Russo "A Theoretical Feasibility Study of a Source Stirring Reverberation Chamber" *IEEE Trans. on Electromagnetic Compatibility*, vol.51, n.1, pp. 3-11, Feb. 2009.
- [5] V. Mariani Primiani, P. Russo, G. Cerri, "Design and Testing of an Antenna System for the Source Stirring Technique in Reverberation Chambers", *Journal of Electromagnetic Waves and Applications*, vol. 26, n. 7, pp. 837-850, 2012
- [6] Van Bladel, *Electromagnetic Fields*, Second Edition, John Wiley & Sons, 2007, pp. 509-562.
- [7] Russo, P. , Primiani, V.M. , Cerri, G., "An efficient model for the field analysis in source stirred reverberation chambers" 2013 International Symposium on Electromagnetic Compatibility, EMC Europe 2013; Brugge; Belgium; 2 - 6 September 2013; Pages 420-424, ISBN: 978-146734979-6

MODELING THE ELECTROMAGNETIC FIELD IN ANISOTROPIC INHOMOGENEOUS MAGNETIZED PLASMA OF ECR ION SOURCES

G. Torrisi^(1,2), D. Mascali⁽¹⁾, L. Neri⁽¹⁾, G. Sorbello^(1,3), L. Celona⁽¹⁾, G. Castro⁽¹⁾, L. Di Donato^(1,3), T. Isernia⁽²⁾ and S. Gammino⁽¹⁾

⁽¹⁾ INFN - Laboratori Nazionali del Sud,
Via S. Sofia 62, 95125 Catania, Italy
peppetorrisi@lns.infn.it

⁽²⁾ Università Mediterranea di Reggio Calabria, Dipartimento di
Ingegneria dell'Informazione, delle Infrastrutture e dell'Energia
Sostenibile, Via Graziella, 89100 Reggio Calabria, Italy;

⁽³⁾ Università degli Studi di Catania, Dipartimento di Ingegneria Elettrica
Elettronica ed Informatica, Viale Andrea Doria 6, 95125 Catania, Italy

Abstract

We present a numerical approach to solve the 3D Maxwell-Lorentz system with the aim of investigating the interaction of the electromagnetic waves with the magnetized non-homogeneous plasma produced inside Electron Cyclotron Resonance Ion Sources. The FEM COMSOL Multiphysics® software was used to compute the electromagnetic field in a cavity filled by the anisotropic-inhomogeneous plasma, described by a full non-uniform dielectric tensor in "cold plasma" approximation. The full-wave solution is then coupled to an "in-Matlab" developed kinetic code based on a PIC – Particle-In-Cell strategy, solving the Newton-Lorentz equation of motion for plasma electrons. Our model explains the experimentally observed frequency sensitivity and gives a relevant contribution to the challenging goal of predicting the electron/ion dynamics in ECR plasmas.

Index Terms – anisotropic media, full wave simulation, FEM, plasma kinetic

I. INTRODUCTION

Electron Cyclotron Resonance Ion Sources (ECRIS) [1] are devices used for the production of intense currents of highly charged ions by a magnetically confined plasma, heated by some kW of microwave power in the 2.45-28 GHz frequency range. Wave propagation modelling in magnetized plasma – including the coupling with the Newton-Lorentz equations of motion – represents a powerful tool for a better understanding of the physical phenomena occurring in the ECRIS plasma-filled resonant cavity, and a necessary step towards future developments and further optimization of advanced ECRIS.

II. COUPLED ELECTROMAGNETIC AND PARTICLE MOTION MODEL

Considering the plasma as a dispersive medium modelled as a cold magneto-fluid with collisions, Maxwell's equations, in the case of

harmonic time dependence $e^{j\omega t}$, read as:

$$\nabla \times \mathbf{E}(\mathbf{r}) = -j\omega \mathbf{B}(\mathbf{r}) \quad (1)$$

$$\nabla \times \mathbf{H}(\mathbf{r}) = j\omega \bar{\bar{\epsilon}}(\mathbf{r}) \cdot \mathbf{E}(\mathbf{r}) \quad (2)$$

where the tensorial relation $\bar{\bar{\epsilon}} \cdot \mathbf{E}$ describes the field-plasma interaction. Hereby we will apply the "cold plasma" approximation, (i.e. $v_\phi \gg v_{th}$, being v_ϕ the wave's phase speed and v_{th} the electron thermal speed), considering the actual magneto-static structure of an ECRIS (minimum-B configuration, see [2] for $B_{x,y,z}$ components) that is not uniform nor axis-symmetric. $\bar{\bar{\epsilon}}(\mathbf{r})$ depends in a complex way from the magnetostatic field $\vec{B}_0(\mathbf{r})$ and the local electron density $n_e(x,y,z)$, (details in [2]).

Full wave simulations are carried out, through the COMSOL Multiphysics FEM solver, considering the geometry shown in Fig. 1 (a) with an initial electron density $n_e(x,y,z)$ and the above described "cold plasma" model. Since nearby the resonance surface, individuated from the iso-surface $|\vec{B}_0| = B_{ecr} = \frac{m_e}{e} \omega$, the permittivity $\bar{\bar{\epsilon}}$ varies widely, in such narrow region the mesh needs to be finer and to achieve this, the ECR iso-surface has been used also to start the mesh construction and growth (Fig. 1(b)).

III. FULL-WAVE AND PARTICLES MOTION 3D SIMULATION SETUP

The electromagnetic field $\{\mathbf{E}(\mathbf{r}), \mathbf{H}(\mathbf{r})\}$ solution is coupled to a 3D kinetic Matlab[®] code that is based on a numerical particles-in-cell method that simulates a plasma as a collection of N macro-particles, (being N much

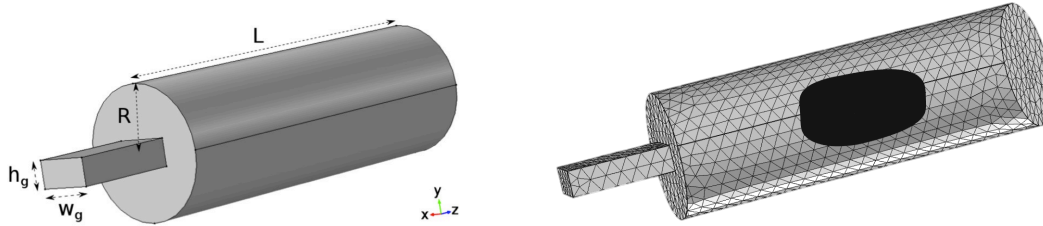


FIG. 1 - (a) Simulated Geometry: Cavity and waveguide.

(b) Non-uniform mesh density: it is finer nearby the ECR layer.

smaller than real plasma particles), with corresponding spatial coordinates and momenta described by the functions $\mathbf{r}_i(t)$ and $\mathbf{p}_i(t)$ for i^{th} particle. We considered a plasma consisting of a single species only (electrons), whose trajectories obey the Lorentz single particle equation of motion, considering electro-static (Spitzer) collisions at 90° :

$$\frac{d\mathbf{p}_i(t)}{dt} = q[\mathbf{E}(\mathbf{r}_i(t), t) + \mathbf{v}_i(t) \times \mathbf{B}(\mathbf{r}_i(t), t)] \quad (3)$$

The kinetic code, following the relativistic Boris scheme [3], solves the

equation of motion (3) of each single macroparticle for its entire life (i.e. until they impinge on the chamber walls), accumulating the electron density in a 3D grid; the output of the kinetic code is a new map for the local electron density $n_e(x,y,z)$ to be used for computing $\bar{\epsilon}(\mathbf{r})$ and the electromagnetic field $\{\mathbf{E}(\mathbf{r}), \mathbf{H}(\mathbf{r})\}$. This loop should run until a convergence is reached. Hereby we show results up to step 1, i.e. after the evaluation of the magnetized plasma action on RF and vice-versa.

IV. NUMERICAL RESULTS AND DISCUSSION

Figures 2(a) and 2(b) illustrate the COMSOL outputs for either electric field distribution and power dissipation into the cavity (and the plasma in particular). At step 0, a preformed plasma is assumed to influence the wave propagation, reaching a density of $0.7n_{\text{cutoff}}$ inside the volume embedded by the ECR surface. The profile of the ECR region has been put in evidence in figures 2. Even if partially perturbed by the plasma, the electric field structure resembles the standing wave feature of the inner-cavity modes. The electric field strength inside the cavity appears enhanced by the presence of the plasma and, as expected, the largest fraction of input power is absorbed at ECR (55% of the total input power). This field was used to calculate the electron motion. In Fig. 3 the electron density distribution is represented over the ECR isomagnetic surface as well as over planar sections.

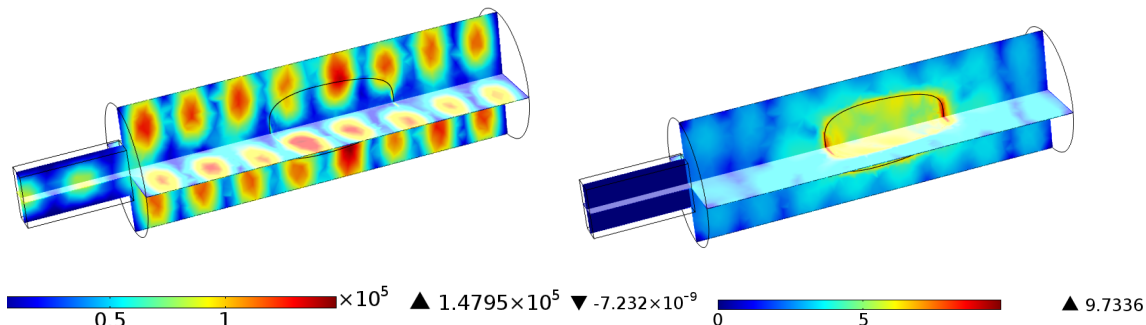


FIG. 2 - (a) Electric field into the plasma filled cavity (b) RF power dissipated into the plasma filled cavity.

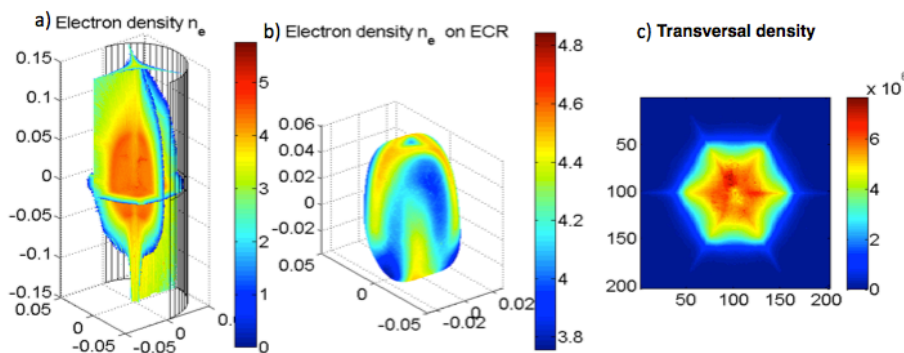


FIG. 3 Total electron density n_e

This results highlight very interesting effects: i) the overall structure of the plasma assumes an hexagonal shape in agreement with the few available imaging results [4]; ii) the electrons (see fig. 3) accumulate mostly inside the volume limited by the ECR surface, forming a high density plasma core that can be named as “plasmoid”, surrounded by a rarefied halo; iii) a density depletion region appears in the quasi-axial region, and it may be the responsible of hollow shapes in the transversal ion beam intensity plots, often observed in ion transport beam lines; iv) although the modal field distribution is perturbed by the medium, a standing wave pattern still persists in the plasma filled cavity as we can see in Fig. 2, and this may explain the sensitivity to the frequency tuning [5] manifested by many ECRIS.

V. CONCLUSION

The synergic (full wave plus kinetic) approach represents a considerable step forward with respect to other approaches already attempted in the past, when oversimplified models (assuming single mode refractive indexes, e.g. of R-waves [6]) have been adopted. Additional steps will be needed to exhaustively model the plasma dynamics until the ion beam formation [7], which is the final goal of our activity. (ARES-ENSAR Grant agr. 262010 7th FP; RDH experiment funded by Gr. V-INFN).

REFERENCES

- [1] R. Geller, "Electron cyclotron resonance ion sources and ECR plasmas", *Inst. of Phys.*, (1996).
- [2] G. Torrisci, D. Mascali, G. Sorbello, L. Neri, L. Celona, G. Castro, T. Isernia, S. Gammino, "Full-wave FEM simulations of electromagnetic waves in strongly magnetized non homogeneous plasma", *Journal of electromagnetic wave and application (JEWA)*, in press (2014).
- [3] C. K. Birdsall, A. B. Langdon, "Plasma physics via computer simulation" (*Taylor and Francis*, New York 2005) p. 356-35.
- [4] S. Biri, A. Valek, T. Suta, E. Takács, Cs. Szabó, L. T. Hudson, B. Radics, J. Imrek, B. Juhász, and J. Pálinkás, "Imaging of ECR plasmas with a pinhole x-ray camera" *Rev. Sci. Instrum.* 75, 1420, (2004).
- [5] L. Celona, Ciavola G., Consoli F., Gammino S., Maimone F., Mascali D., Spädtke P, Tinschert, "Observations of the frequency tuning effect in the 14 GHz CAPRICE ion source", *Rev. Sci. Instrum.* 79, 023305, (2008).
- [6] E. G. Evstatiev, V. A. Svidzinski, J. A. Spencer, and J. S. Kim, "Analytical and numerical modeling of radio frequency electron cyclotron resonance power absorption within the cold plasma picture" *Rev. Sci. Instrum.* 85, 02A503 (2014).
- [7] D. Mascali, S. Gammino, L. Celona, G. Ciavola, "Towards a better comprehension of plasma formation and heating in high performances electron cyclotron resonance ion sources", *Rev. Sci. Instrum.* 83, 02A336 (2012).

ASSESSMENT OF THE PERFORMANCES OF GMRES(R) USING A DOMAIN DECOMPOSITION APPROACH AS A PRECONDITIONER

L. Ntibarikure, G. Pelosi, S. Selleri

Department of Information Engineering, University of Florence
Via di Santa Marta 3, 50139 Florence, Italy
[laurent.ntibarikure, giuseppe.pelosi, stefano.selleri]@unifi.it

Abstract

Some analyses concerning the performances of the GMRES(r) iterative solver with a Domain Decomposition based preconditioner are presented. Convergence is analyzed and results discussed.

Index Terms – Finite Elements, Domain decomposition, Smart antennas, mobile ad-hoc networks, planar antennas, finite elements.

I. INTRODUCTION

The most important limit of numerical full-wave electromagnetic analyses is the limitation of computational resources. Truly large, complex problems are limited, at least when trying to fit all the problem in memory at a time and, even if one had infinite computational resources, many algorithms, like the linear system solvers, would require a huge amount of time. The problem is common to most numerical techniques inasmuch most of them reduce the electromagnetic problem to a linear system of equations, but this paper will focus on the Finite Elements (FE) method.

To overcome the resources problem, parallel processing needs to be considered, splitting system matrix filling and system solution over multiple computers interconnected through a high speed network. Iterative solvers, which are the most appealing for their reduced memory requirements and relative speed in solution, can anyway be too time consuming if the problem size grows since the number of iteration required grows with system dimensions.

Among the methods developed to increase the computational efficiency of FE analysis, domain decomposition (DD) methods have found noticeable interest in the last decade. They allow to analyze a whole problem upon partitioning it and computing solutions for each smaller problem. Then, all the solutions are “connected” in order to recover the effective solution within the whole domain. Relying on a *divide et impera* scheme, these methods are de facto intrinsically parallelizable.

While DD will provide a suitable parallelization for matrix filling and solving, it can also be used as an efficient starting point for block subdivision of the system matrix for block Jacobi or Gauss-Seidel preconditioning.

$$P_J = \underbrace{\begin{bmatrix} B_{11} & 0 & \dots & 0 \\ 0 & B_{22} & 0 & \dots & 0 \\ 0 & 0 & B_{33} & & \vdots \\ \vdots & \vdots & & \ddots & 0 \\ 0 & 0 & \dots & 0 & B_{NN} \end{bmatrix}}_{\text{Block Jacobi}}; \quad P_{GS} = \underbrace{\begin{bmatrix} B_{11} & 0 & \dots & 0 \\ B_{21} & B_{22} & 0 & \dots & 0 \\ B_{31} & B_{32} & B_{33} & & \vdots \\ \vdots & \vdots & & \ddots & 0 \\ B_{N1} & B_{N2} & \dots & B_{NN-1} & B_{NN} \end{bmatrix}}_{\text{Block Gauss Seidel}} \quad (2)$$

Being B_{ij} the corresponding block of the system matrix (1). Since preconditioning matrix need to be inverted, the Jacobi preconditioner requires the inversion of N small matrices, while the Gauss-Seidel one requires the inversion of a block triangular matrix which has a computational cost comparable to a direct solution of the whole problem. It can anyway be shown [3] that the inverse of the block triangular (2) can be computed sequentially on the basis of the residual computed in the GMRES(r) algorithm, hence speeding up the process.

III. NUMERICAL RESULTS

The block preconditioning is here applied to the problem of a WR-90 waveguide segment 240mm long and discretized in 20.602 tetrahedra. As a first series of tests the domain is partitioned in two roughly equal (10.489 and 10.113 tetrahedra) subdomains. Fig. 2 shows convergence data without preconditioning over the full domain and with the two preconditioners for each of the two DD schemes for GMRES(100), that is bases for solution projection are restarted every 100 iteration. Table I clearly show the edge of the preconditioning schemes in general, and of the Gauss-Seidel preconditioner in particular. As a further set of tests, the problem under analysis was solved for increasing number in domain subdivision, from 2 to 4,8,12 and 16, each roughly sharing the same number of degrees of freedom. Fig. 3 shows convergence data.

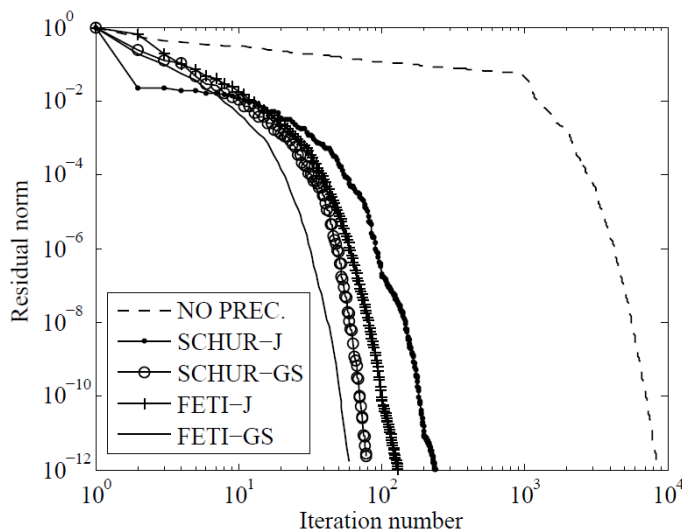


FIG. 2 – Comparison between the two DD schemes applied to the two preconditioners analyzed in the text and the full domain unpreconditioned solution.

TABLE I – TIMES AND MEMORY REQUIREMENTS FOR DIFFERENT GMRES(100) RUNS AT 10GHZ.

Solver	Iterations	Time (s)	Peak Memory (MB)
<i>No preconditioner</i>	8459	276	68.2
<i>Schur-Jacobi</i>	238	160	68.6
<i>GMRES(r)</i> <i>Schur-GS</i>	78	54.5	69.1
<i>FETI Jacobi</i>	130	90	69.7
FETI-GS	58	41.8	69.2

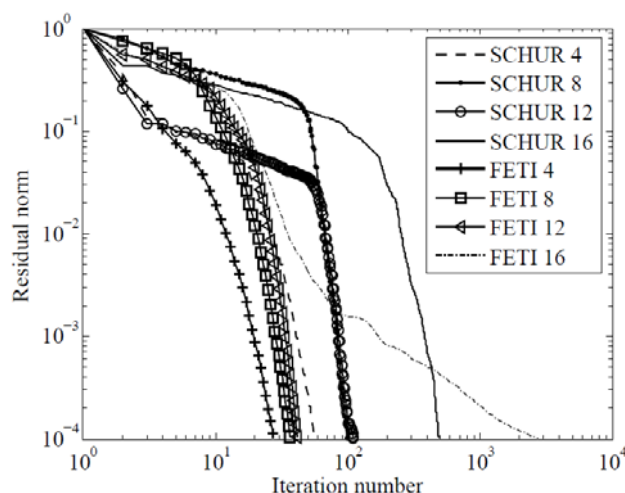


FIG. 3 – Comparison between the two DD schemes, applied to the Gauss-Seidel preconditioner, for 4,8,12 and 16 subdomains.

IV. CONCLUSION

The block subdivision of the FE system matrix arising from a DD subdivision is exploited as a basis to construct block-preconditioners. Numerical results shows the excellent reduction in computing times, especially when using the Gauss-Seidel preconditioner.

REFERENCES

- [1] T. P. A. Mathew, *Domain Decomposition Methods for the Numerical Solution of Partial Differential Equations*. Berlin, D: Springer-Verlag, 2008.
- [2] G. Guarnieri, G. Pelosi, L. Rossi, S. Selleri, "A Domain Decomposition Technique for Finite Element Based Parametric Sweep and Tolerance Analyses of Microwave Passive Devices," *International Journal of RF and Microwave Computer Aided Engineering*, Vol. 19, No. 3, pp. 328-337, 2009.
- [3] C. Farhat, F.-X. Roux, "A method of finite element tearing and interconnecting and its parallel solution algorithm," *International Journal for Numerical Methods in Engineering*, Vol. 32, no. 6, pp. 1205-1227, 1991.
- [4] Y.Saad, *Iterative Methods for Sparse Linear Systems*, 3rd ed., Philadelphia, PA: SIAM, 2000.

A NEW APPROACH THE ANALYSIS OF SECTORIAL ELLIPTIC WAVEGUIDES

Alessandro Fanti ⁽¹⁾, Giuseppe Mazzarella ⁽¹⁾

Department of Electrical and Electronic Engineering
University of Cagliari, 09123, Piazza d'Armi, Cagliari, Italy
[alessandro.fanti, mazzarella}@diee.unica.it](mailto:{alessandro.fanti, mazzarella}@diee.unica.it)

Abstract

We present a frequency domain finite difference approach in curvilinear coordinates to the computation of the modes of ridged elliptic waveguides. The use of an elliptic mesh allows to avoid the staircase approximations of the boundary, providing a very effective and accurate procedure.

Index Terms – Cutoff frequency, Finite Difference Frequency Domain, Microwave Components, Microwave Filters, Ridged Waveguides, Waveguide Modes

I. INTRODUCTION

Application of ridged circular and elliptic waveguides (REW) [1] can be found in many components like filters, matching networks, orthomode transducers, polarizers and circulators that are widely used in satellite and terrestrial communication systems [2-6]. Low-cost design, small size, and optimum performance of these components are essential to satisfy today's stringent payload requirements. For an elliptical waveguide, the analytic computation of modes is the hardest, and most accurate, approach since the mode distribution can be expressed in terms of Mathieu Functions [7], and the eigenvalues are the well-known zeroes of these functions. An analytical, closed form solution exists also for elliptic waveguides, and has been found by Chu [8] since the 30's. Unfortunately, the field distribution is described by the Mathieu functions, whose numerical evaluation is very cumbersome. The best approach seems the expansion of those functions in a series of (more tractable) Bessel functions [9]. Aim of this work is to devise a FDFD approach for REWs, tailored to the structure, but as simple as the standard one in the formulation. Use of a suitable elliptical grid (which perfectly fits the waveguide boundary) allows to evaluate the REW modes with the required accuracy using order of magnitude less points than the standard approach. By generalizing a solution already used in [10] for elliptic regular waveguide. The proposed approach has been validated by comparison with analytical results [11].

II. DESCRIPTION OF THE TECHNIQUE

Let us consider a ridged elliptic waveguide . Both TE and TM modes can be found from a suitable scalar eigenfunction, solution of the Helmholtz equation:

$$\nabla_t^2 \phi + k_t^2 \phi = 0 \tag{1}$$

with the boundary conditions (BC)

$$\begin{aligned} \frac{\partial \phi}{\partial n} &= 0 \quad (TE \text{ modes}) \\ \phi &= 0 \quad (TM \text{ modes}) \end{aligned} \tag{2}$$

at the boundary of the ridged waveguide. Both the equation (1) and the BC (2) can be replaced by a discretized version looking for the eigenfunction values at a suitable set of sampling points, and therefore replacing derivatives with finite approximations. The standard solution is to use a rectangular set of sampling points but this forces to replace the curved boundary with a staircase approximation. This approximation results in a low accuracy (using a coarse grid), or in an heavy computational load (using a very fine grid). We propose here to select a set of sampling points located on the elliptic coordinates framework.

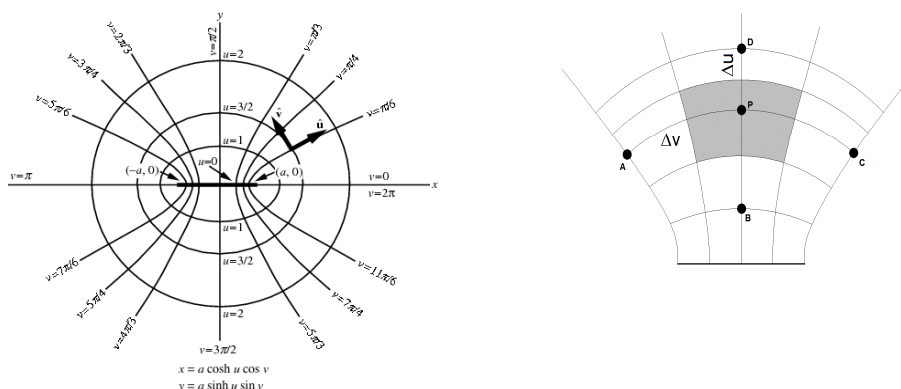


FIG. 1 – a) Geometry of the elliptic coordinates. b) Internal point of the elliptic coordinates grid TE and TM

Chose a regular spacing on the coordinate lines, with step $\Delta u, \Delta v$. Letting $\phi_{pq} = \phi(p\Delta u, q\Delta v)$ the eigenvalues equation (1) should be:

$$\frac{1}{a^2 (\sinh^2 p\Delta u + \sin^2 q\Delta v)} \cdot \left[\frac{\partial^2 \phi}{\partial u^2} + \frac{\partial^2 \phi}{\partial v^2} \right]_{pq} = -k_t^2 \phi_{pq} \tag{3}$$

In this case it is simpler to discretize (1) using a Taylor expansion, for each internal point P since the term in brackets expanded exactly as in a rectangular grid:

$$\left[\frac{\partial^2 \phi}{\partial u^2} + \frac{\partial^2 \phi}{\partial v^2} \right] = \frac{1}{\Delta v^2} \cdot \phi_A + \frac{1}{\Delta u^2} \cdot \phi_D + \frac{1}{\Delta v^2} \cdot \phi_C + \frac{1}{\Delta u^2} \cdot \phi_B - \left(\frac{2}{(\Delta u)^2} + \frac{2}{(\Delta v)^2} \right) \cdot \phi_P \tag{4}$$

Equation (4) cannot be used for the two foci, for points between them and for external points. For a point P lying on the segment joining the

two foci we can integrate (1) $\int \nabla_t^2 \phi dS = -k_t^2 \int \phi dS \theta$ and apply the Gauss theorem to obtain:

$$\int_{\Gamma_F} \frac{\partial \phi}{\partial n} \cdot dl = -k_t^2 \int_{S_F} \phi dS, \quad (5)$$

wherein S_F is the cell surface, and Γ_F is the cell boundary.

In the elliptic grid used for a REW, we have two types of boundary points: the radial ones (P in Fig. 2a) and the angular ones (P in Fig. 2b).

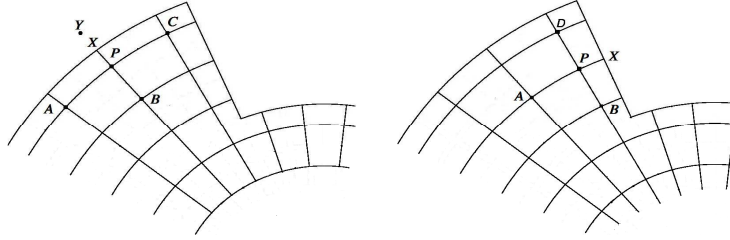


FIG. 2 – a) Geometry pertinent to the first type of boundary point P. b) Geometry pertinent to the second type of boundary point P.

The TE boundary condition can be enforced in the same way for both types of boundary points, so we describe it only for a radial one (Fig. 2a). The boundary point X in Fig. 2a is not a discretization point. Therefore, use of the Taylor expansion would require an extrapolation of $\phi(r)$ outside the sampling region, using either ϕ_x or ϕ_y to enforce the boundary condition $\partial\phi/\partial n=0$. Actually, we can use a FDFD approximations for the normal derivative on the waveguide boundary $\partial\phi/\partial n|_x \simeq (\phi_x - \phi_p)/(\Delta r/2)$, and (4) is replaced by:

$$\frac{\phi_A}{\Delta v^2} + \frac{\phi_C}{\Delta v^2} + \frac{\phi_B}{\Delta u^2} - \left(\frac{1}{\Delta u^2} + \frac{2}{\Delta v^2} \right) \phi_P \simeq -k_t^2 \phi_P^2 \quad (6)$$

In the same way, for P in Fig. 2b we get:

$$\frac{\phi_A}{\Delta v^2} + \frac{\phi_D}{\Delta u^2} + \frac{\phi_B}{\Delta u^2} - \left(\frac{2}{\Delta u^2} + \frac{1}{\Delta v^2} \right) \phi_P \simeq -k_t^2 \phi_P^2.$$

III. RESULTS

In the simulations presented in this section we will consider a sector of elliptic ridged waveguide. All dimensions have been normalized to the minor semi-axis of the ellipse. We compare the FDFD procedure has been assessed against a [11]

TABLE 1: RELATIVE ERROR FOR THE ANALYTICAL [11] AND NUMERICAL (FDFD) NORMALIZED CUT-OFF WAVELENGTHS λ_c/a FOR AN ELLIPTIC SECTORAL GUIDE WITH $u_1 = 0.1$, $u_2 = 0.5$ AND $v_1 = -50^\circ$, $v_2 = 50^\circ$ AND $\Delta u = 0.01$, $\Delta v = 0.0087$

<i>TE</i>	λ_c/a [11]	λ_c/a Our Code	Relative Error %	<i>TM</i>	λ_c/a [11]	λ_c/a Our Code	Relative Error %
1	2.656401	2.656379	0.000817	1	14.283213	14.280883	0.016315
2	6.836981	6.836780	0.002943	2	14.299466	14.297680	0.012488
3	9.544562	9.543917	0.006760	3	19.561598	19.553527	0.041260

IV. CONCLUSION

We have proposed a FDFD to the computation of the modes of an elliptic sectoral guide. A elliptic mesh has been used in order to avoid staircase approximations of the boundary. The proposed approach has been validated by comparison with the results of [11].

ACKNOWLEDGEMENT

Alessandro Fanti gratefully acknowledges Sardinia Regional Government for the financial support of her Post Doc fellowship (P.O.R. Sardegna F.S.E. Operational Programme of the Autonomous Region of Sardinia, European Social Fund 2007-2013 - Axis IV Human Resources, Objective 1.3, Line of Activity 1.3.1.).

REFERENCES

- [1] A. A. El-Sherbiny , "Cutoff wavelengths of ridged, circular, and elliptic guides," *IEEE Trans. Microwave Theory Tech.*, Vol. 21, pp. 7-12, Jan. 1973.
- [2] A. E. Williams and A. E. Atia, "Dual-Mode canonical waveguide filters", *IEEE Trans. Microwave Theory Tech.*, Vol. 25, No. 12, pp. 1021-1026, Dec. 1977.
- [3] R. Behe and P. Brachat, "Compact duplexer-polarizer with semicircular waveguide," *IEEE Trans. Antennas Propagat.*, Vol. 39, pp. 1222-1224, Aug. 1991.
- [4] B. V. de la Filolie and R. Vahldieck, "Coaxial and circular waveguide band-pass filters using printed metal inserts," *IEEE MTT-S Int. Microwave Symp. Dig.*, 1992, pp. 905-908.
- [5] J. Huang, R. Vahldieck, and H. Jin, "Computer-aided design of circular ridged waveguide evanescent-mode bandpass filters using the FDTLM method," *IEEE MTT-S Int. Microwave Symp. Dig.*, 1993, pp. 459-462.
- [6] U. Balaji and R. Vahldieck, "Mode matching analysis of circular-ridged waveguide discontinuities," *IEEE Trans. Microwave Theory Tech.*, Vol. 46, pp. 191-195, Feb. 1998.
- [7] N. Marcuvitz, *Waveguide Handbook*, Peregrinius, London, 1986.
- [8] L. J. Chu, "Electromagnetic waves in elliptic hollow pipes of metal," *J. Appl. Phys.*, Vol. 9, 583-591, 1938.
- [9] J. G. Kretzschmar, "Wave propagation in hollow conducting elliptical waveguides," *IEEE Trans. Microwave Theory Tech.*, Vol. 18, pp.547-554, 1970.
- [10] A. Fanti, G. Mazzarella, G. Montisci, and G. A. Casula, "Computation of the Modes of Elliptic Waveguides with a Curvilinear 2D Frequency-Domain Finite-Difference Approach," *Progress In Electromagnetics Research M*, Vol. 26, 69-84, 2012.
- [11] G. Amendola, G. Di Massa, G. Angiulli, "Elliptic-hyperbolic waveguides," *Journal of Electromagnetic Waves and Applications*, Vol. 14, issue 11, pp. 1473-1487. 2000

BEAM COUPLING IMPEDANCE SIMULATION AND RF MEASUREMENTS OF A PASSIVE EXTRACTION SEPTUM FOR PARTICLE ABSORBING IN THE CERN PROTON SYNCHROTRON

S. Persichelli⁽¹⁾⁽²⁾, M. Migliorati⁽¹⁾⁽²⁾

⁽¹⁾ CERN Beam Department Geneva, Switzerland

⁽²⁾ SBAI Department, University "La Sapienza", Via A. Scarpa 14/16 - 00161 Rome
serena.persichelli@cern.ch

Abstract

We present a study of the beam coupling impedance due to trapped modes of a new protection septum that will be installed in the CERN Proton Synchrotron (PS) during the Long Shutdown 1 (LS1). The interaction between the particle field and the discontinuities inside the septum generates electromagnetic fields localized in a particular region inside the device. These resonances, producing narrow peaks in the coupling impedance, can be potential source of beam instabilities for high intensity particle accelerators like PS. The final outcome of these studies is the basis for the acceptance of the septum installation in section 15 of the PS ring.

Index Terms – Beam coupling impedances, RF measurements, trapped modes.

I. INTRODUCTION

The CERN Proton Synchrotron (PS) belongs to the Large Hadron Collider (LHC) injector chain, producing high intensity and brightness beams for collision in the LHC [1]. Combinations of septa are frequently used to inject and extract beams for each experiment. A high level of activation of the magnetic septum in the PS straight section 16, has been observed. The solution adopted consists in installing a dummy septum [2] in straight section 15 of the PS ring, a protection passive device, provided by a thin metallic blade intercepting the beam during the rise time of the kickers.

II. BEAM COUPLING IMPEDANCE SIMULATIONS

The interaction between a beam and its surroundings space can be described in terms of beam coupling impedance. The longitudinal impedance accounts for the energy lost by a point test charge because of the electromagnetic field of a leading particle [3].

CST Particle Studio Wakefield Solver has been used to obtain the wake potential generated by an ultra-relativistic pencil beam with no transverse size circulating inside the septum. Fig.1 shows the real part of the longitudinal impedance due to trapped modes excited by a bunch of rms length 26 cm and charge $q = 1$ nC, circulating 5 mm away from the axis of the copper blade.

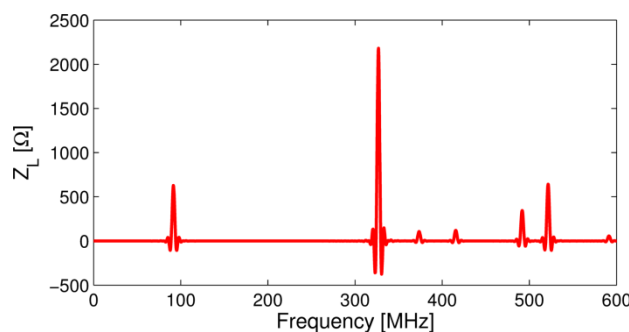


FIG. 1 – Longitudinal impedance during extraction (beam circulating at 5 mm from the blade) evaluated with CST Particle Studio.

The wake potential has been evaluated through the Direct Integration Method. Perfect electric conductor (PEC) has been defined on all the outer surfaces, except for the beam entrance and exit planes that have been defined as open boundaries (perfect matching layer). Longitudinal impedance has been evaluated at different distances from the location of the blade. We observed that trapped modes frequencies, correspond to the eigenvalues of the closed structure; frequencies do not depend on the beam position respect to the blade, while the amplitudes of several peaks increase as the relative distance between the beam and the blade is decreasing. During extraction, while the beam covers 90 mm in about 6 ms to approach the blade, the maximum of the impedance peaks' amplitude is reached. This effect is due to the strong electromagnetic field trapped at the edges of the metallic blade after the passage of the beam. CST Microwave Studio frequency domain simulations have been performed to crosscheck results obtained from time domain. Q factor, shunt impedance R_s , and $\frac{R}{Q}$ can be calculated post-processing the Eigenmode simulation. The first trapped mode excited by the beam resonates at 118 MHz with a Q factor of 2616 and shunt impedance evaluated at extraction of 50 k Ω . Between the nominal and the extraction positions, the shunt impedance increases of a factor 600. The amplitude of the impedance's peaks in Fig. 1 does not correspond to the shunt impedance of each resonance, since the saturation of the peaks is reached when the simulation is performed with a wake length of about 7 km. Such a time consuming simulation has been performed and fits with the shunt impedance evaluated by the Eigenmode solver.

III. TRAPPED MODES DAMPING SOLUTIONS

Two proposals of modifications of the inner design have been studied to damp the 118 MHz mode.

Since the resonance at 118 MHz is mainly localized in the gap between the RF been screen and the support table, the first solution consists of inserting sliding metallic contacts among them, canceling the mode at 118 MHz.

The second solution consists in the insertion of a block of ferrite TT2-111R: this solution will not have the effect of canceling the mode, but will reduce the shunt impedance and Q factor of the mode itself and, as a consequence, the impact on PS coupled bunch instability [4]. Ferrite has to be placed where the magnetic field is stronger; therefore, we suggested installing a brick of $24 \times 7 \times 395 \text{ mm}^3$ between the displacement system and the impedance screen, providing a reduction of shunt impedance of a factor 600 for the 118 MHz mode. Since the 118 MHz mode falls inside the PS bunch extraction spectrum with power of -20 dB, the deposited heating would be about 3.6 W [5], and the foreseen cooling system should easily cope with it.

As an outcome of these studies, the decision has been taken to install the sliding contacts between the RF beam screen and the support table. The option of installing a block of ferrite is left as a fall back solution to be implemented only in case of failure of sliding contacts.

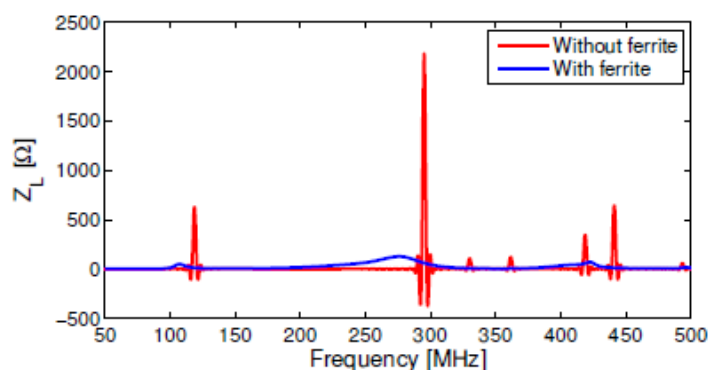


FIG. 2 – Comparison between longitudinal impedance evaluated at extraction with CST Particle Studio with and without ferrite.

IV. RF IMPEDANCE MEASUREMENTS

Impedance measurements with coaxial wire method have been performed [6], allowing to excite in the device under test an electromagnetic field similar to the one generated by an ultra-relativistic point charge. The impedance has been measured stretching a metallic wire of 0.5 mm radius inside the septum, modeling a TEM-like coaxial line; the wire is then connected to two matching resistors to consider the effect of the mismatch at the beginning and at the end of the perturbed transmission line, and finally welded to a suco-box. This setup allows measuring the transmission coefficient S_{12} by means of a vector network analyzer (VNA). The impedance for three positions of the wire/beam respect to the extraction blade has been measured, while the position of the blade was fixed. In Fig. 3 is shown the comparison of the impedance measurement for the three wire positions. The first trapped mode has a frequency of 270 MHz, thus indicating that the sliding fingers are working as expected on canceling the mode at 118 MHz. Measurements have also been compared with simulations performed with CST Microwave Studio Frequency domain solver, adding the

metallic wire in the geometry and calculating the scattering parameters on the entrance and exit port of the device under test, simulating the measurement setup. Measurements and simulations agree on the frequency of the first trapped mode resonating in the septum. Nonetheless, the measurements results confirmed that the dummy septum can be safely installed in the PS ring and that the insertion of ferrite is not needed.

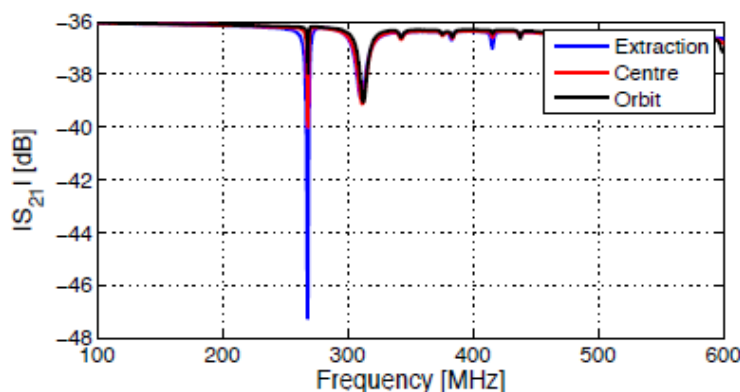


FIG. 3 – S_{12} coefficient measured for three positions of the wire respect to the extraction blade.

V. CONCLUSION

We have characterized the beam coupling impedance due to trapped modes of a dummy septum to be installed in the CERN Proton Synchrotron (PS). Simulations with CST Microwave Studio and Particle Studio, together with theoretical calculations for the coupled bunch instability and RF measurements have been performed. Preventive actions to reduce the instabilities have been suggested and implemented in the final design of the septum, as an outcome of the impedance studies.

REFERENCES

- [1] M. Migliorati, S. Persichelli et al., "Beam-wall interaction in the CERN Proton Synchrotron for the LHC upgrade", *Phys. Rev. ST Accel. Beams*, 16 3 2013.
- [2] M. Giovannozzi et al., "Implementation details of the PS dummy septum for mitigating irradiation of the magnetic septum for fast extractions towards the SPS", CERN-ATS-Note-2013, to be published.
- [3] L. Palumbo and V.G. Vaccaro, "Wake field and impedances", Fifth Advanced Accelerator Physics Course, CERN Accelerator School (CAS), (1995).
- [4] H. Damerau et al., "Longitudinal coupled bunch instabilities in the CERN PS", CERN-AB-2007-051.
- [5] B. Salvant, "Beam induced heating", Proceedings of LHC Beam Operation Workshop, Evian (2012).
- [6] A. Mostacci et al., "RF coupling impedance measurements versus simulations", Proceedings of Workshop on Beam Dynamics in Future Hadron Colliders and Rapidly Cycling High-Intensity Synchrotrons, Geneva (2004).

NOVEL FD-BPM FORMULATION FOR THE ANALYSIS OF GRAPHENE-ASSISTED OPTICAL DEVICES

A. D. Capobianco⁽¹⁾, A. Locatelli⁽²⁾, C. De Angelis⁽²⁾
S. Boscolo⁽³⁾, M. Midrio⁽³⁾

- (1) Dipartimento di Ingegneria dell'Informazione, Università di Padova
Via Gradenigo 6/b, 35131 Padova, Italy
adc@dei.unipd.it
- (2) Dipartimento di Ingegneria dell'Informazione, Università di Brescia
Via Branze 38, 25123 Brescia Italy
- (3) Dipartimento di Ingegneria Elettrica Gestionale e Meccanica
Università di Udine, Via delle Scienze 206, 33100 Udine, Italy

Abstract

We propose a novel finite-difference beam propagation method capable of dealing with the discontinuity of the tangential component of the magnetic field induced by bidimensional graphene layers. In stark contrast with conventional numerical solvers, this approach does not require a discretization step as small as a fraction of the atomic thickness of graphene, allowing ultrafast simulation times. The validity of the method is proved by propagating the plasmonic supermodes of two coupled graphene layers.

Index Terms – Graphene, plasmonics, beam propagation method, finite difference methods.

I. INTRODUCTION

The recent advances in theoretical and experimental studies concerning graphene have opened up new scenarios in the field of photonics, envisaging the birth of novel applications which exploit the peculiar properties of this 2D fascinating material. Existing full-wave numerical solvers can still be used, as long as graphene is modeled as a sub-nanometer layer [1]. As a consequence, discretization steps smaller than its atomic thickness (0.34nm) are required, leading to an unacceptable computational burden. It has recently been demonstrated in the literature [2] that the discontinuity of the tangential magnetic field component induced by the currents flowing on a bi-dimensional graphene layer can be treated as a boundary condition instead of considering a volumetric layer of graphene in the problem. To the best of our knowledge, this idea has never been exploited to realize a highly efficient field propagator specifically tailored for graphene-based devices. In this paper we propose a novel finite-difference formulation of the second derivative of the tangential component of the magnetic field, which exhibits discontinuities due to the surface currents flowing on the graphene layers. The algorithm has been validated by propagating the supermodes of two coupled graphene layers, and by comparing these data with known results.

II. NUMERICAL FORMULATION

We consider planar and piecewise constant dielectric structures where x and z are the transverse and the propagation directions respectively, with no variation in the y coordinate. With these assumptions and focusing our attention on harmonic TM waves, the propagation of the H_y component of the magnetic field, under the paraxial approximation, obeys the Schroedinger equation:

$$-2j\kappa_0 n_0 \frac{\partial H_y}{\partial z} + \frac{\partial^2 H_y}{\partial x^2} + \kappa_0^2 (n^2(x) - n_0^2) H_y = 0, \quad (1)$$

where κ_0 is the wave-number in vacuum, n_0 is a reference refractive index and $n(x)$ is the refractive index profile. If a sheet of graphene is introduced within the geometry (see Fig. 1), a discontinuity of the tangential component of the magnetic field is induced by the surface currents flowing on the graphene layer:

$$H_y|_R - H_y|_L = j\omega\epsilon_0 \epsilon_{gr\Sigma} E_z|_{R,L}, \quad (2)$$

where $\epsilon_{gr\Sigma}$ is the relative surface dielectric constant of graphene and subscripts R and L refer to right and left graphene boundaries.

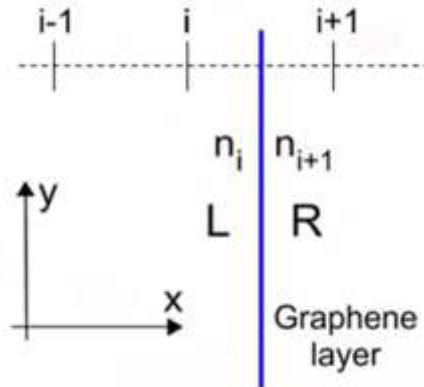


FIG. 1 – Schematic view of the transverse discretized domain.

Moreover, whenever a dielectric discontinuity occurs, the following equation derived from Maxwell equations holds at the corresponding boundary:

$$\left. \frac{\partial H_y}{\partial x} \right|_R = \frac{n^2|_R}{n^2|_L} \left. \frac{\partial H_y}{\partial x} \right|_L, \quad (3)$$

In order to model the effects of graphene-induced surface currents and dielectric discontinuities, special care must be devoted to the finite-

difference implementation of the second derivative with respect to the transverse coordinate x , since samples fall before and after a graphene layer or a dielectric discontinuity. Following the procedure described by Stern in the Appendix of [3], and labeling for the sake of simplicity H_y as H , and E_z as E , the finite-difference approximation of the second derivative of the magnetic field component, evaluated at point i with a dielectric interface or a graphene layer in-between points i and $i+1$ (see Fig. 1) can be written as:

$$\left. \frac{\partial^2 H}{\partial x^2} \right|_i = \frac{H_{i-1} - 2H_i + H_{i+1}^*}{\Delta x^2}, \quad (4)$$

where Δx is the transverse step and the superscript $*$ is introduced to indicate that a discontinuity between points i and $i+1$ must be taken into account. Now using the Taylor series expansion for H and the finite-difference approximation for its first derivative we can get:

$$H|_R = \frac{H_{i+1} + H_i^*}{2}, H|_L = \frac{H_{i+1}^* + H_i}{2} \quad (5)$$

$$\left. \frac{\partial H}{\partial x} \right|_R = \frac{H_{i+1} - H_i^*}{\Delta x}, \left. \frac{\partial H}{\partial x} \right|_L = \frac{H_{i+1}^* - H_i}{\Delta x} \quad (6)$$

By substituting Eq. (5) in Eq. (2), and Eq. (6) in Eq. (3) we can write that:

$$(H_{i+1} + H_i^*) = (H_{i+1}^* + H_i) + 2j\omega\epsilon_0\epsilon_{gr\Sigma} E|_L, \quad (7)$$

$$(H_{i+1} - H_i^*) = n_{i+1}^2 / n_i^2 (H_{i+1}^* - H_i) \quad (8)$$

After some algebra and using Maxwell equations, it is possible to formulate Eq. (4) in terms of "regular" H_{i-1}, H_i and H_{i+1} samples weighted with coefficients depending on the refractive indexes and on the relative surface dielectric constant of graphene.

III. NUMERICAL ASSESSMENT

We considered the directional coupler which has already been thoroughly analyzed in [2]. Two graphene monolayers are placed with a spacing d among them. These are immersed in a uniform dielectric medium with relative dielectric constant $\epsilon_s = 2.25$, and a bias voltage is applied between the sheets with the goal of tuning the bi-dimensional complex conductivity of graphene. The dependence of the beat length L_B on the chemical potential μ_C has been systematically investigated

by using our BPM technique, always comparing these results with the reference solution provided by the dispersion relations of the supermodes. In Fig. 2 the beat length as a function of the chemical potential is depicted when $d = 15\text{nm}$ and μ_c is varied between 0.1 and 0.16eV . It is straightforward to see that light propagation performed by using our BPM technique predicts a field evolution inside the benchmark structure which is in excellent agreement with the analytical estimates of L_B , and this constitutes a strong validation of the proposed method.

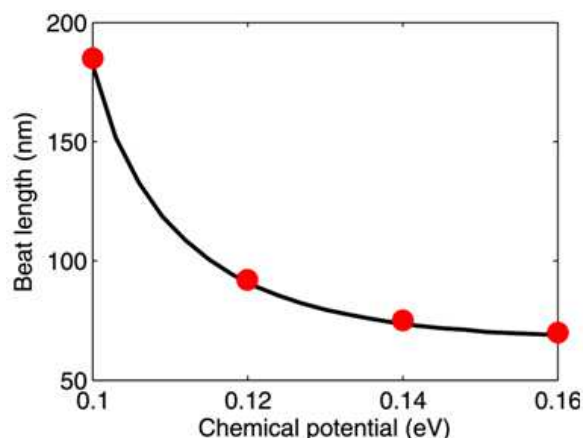


FIG. 2 – Beat length as a function of the chemical potential evaluated from the BPM (red circles) and from the analytical formulas (black solid line).

IV. CONCLUSION

We have described a novel finite-difference beam propagation method which efficiently deals with the discontinuity of the tangential magnetic field component induced by the surface currents flowing on bi-dimensional graphene layers. We have demonstrated that this BPM algorithm allows ultra-fast and accurate analysis of complex graphene-based plasmonic devices.

REFERENCES

- [1] A. Vakil and N. Engheta, “Transformation Optics Using Graphene,” *Science*, vol. 332, no. 6035, pp. 1291-1294, Jun. 2011.
- [2] A. Auditore, C. De Angelis, A. Locatelli, and A. B. Aceves, “Tuning of surface plasmon polaritons beat length in graphene directional couplers,” *Opt. Lett.*, vol. 38, no. 20, pp. 4228–4231, Oct. 2013.
- [3] M. S. Stern, “Semivectorial polarised finite difference method for optical waveguides with arbitrary index profiles,” *IEE Proc.*, vol. 135, no. 1, pp. 56-63, Feb. 1988.

GRAPHENE-BASED ONE-DIMENSIONAL GRATING FOR ENHANCED ABSORBERS

M. Grande⁽¹⁾, M.A. Vincenti⁽²⁾, T. Stomeo⁽³⁾, G. V. Bianco⁽⁴⁾, D. de Ceglia⁽²⁾, G. Magno⁽¹⁾, V. Petruzzelli⁽¹⁾, G. Bruno⁽⁴⁾, M. De Vittorio^{(3),(5)}, M. Scalora⁽⁶⁾ and A. D'Orazio⁽¹⁾

⁽¹⁾ Dipartimento di Ingegneria Elettrica e dell'Informazione (DEI), Politecnico di Bari, Via Re David 200, 70125 Bari, Italy

⁽²⁾ National Research Council, Charles M. Bowden Research Center, RDECOM, Redstone Arsenal, Alabama 35898-5000 – USA

⁽³⁾ Center for Bio-Molecular Nanotechnologies, Istituto Italiano di Tecnologia (IIT), Via Barsanti, 73010 Arnesano (Lecce), Italy

⁽⁴⁾ Institute of Inorganic Methodologies and of Plasmas, IMIP-CNR, Via Orabona 4, 70126 Bari, Italy

⁽⁵⁾ National Nanotechnology Laboratory (NNL), CNR-Istituto Nanoscienze, Dip. Ingegneria dell'Innovazione, Università Del Salento, Via Arnesano, 73100 Lecce, Italy

⁽⁶⁾ Charles M. Bowden Research Center, RDECOM, Redstone Arsenal, Alabama 35898-5000 – USA

grande@deemail.poliba.it

Abstract

We report on the design and optimization of a one-dimensional (1D) dielectric grating that incorporates a monolayer graphene. The 1D grating is designed in order to support guided mode resonances that efficiently interact with the monolayer graphene achieving an enhanced absorption. The numerical findings, based on the Rigorous Coupled-Wave Analysis, reveal that a single layer of graphene suffices to absorb about 60% of the impinging light in the visible range for both the TE and the TM polarizations over a narrow bandwidth of few nanometers.

Index Terms – Graphene, absorption, dielectric grating, guided resonances, Fano resonances.

I. INTRODUCTION

Graphene is a single atomic layer of graphite that consists of very tightly bonded carbon atoms organised into a hexagonal lattice [1]. Graphene shows an sp^2 configuration that leads to a total thickness of about 0.34 nm. This two-dimensional nature is responsible of the very exceptional electrical, mechanical and optical properties shown by this material. In particular, it has been theoretically and experimentally demonstrated that the absorption of a monolayer graphene does not depend on the material parameters but only on the fundamental constants since it is equal to $\pi\alpha$ (defined by the fine structure constant $\alpha = e^2 / \hbar c$) that corresponds to about 2.3% over the visible range [2].

Even if this constant value is very high if compared with other bulk materials, graphene absorption can be boost and enhanced combining this two-dimensional material with photonic [3] and plasmonic [4] nanostructures.

In this paper, we will exploit guided mode resonances [5], excited in a one-dimensional dielectric grating, to enhance light absorption in the monolayer graphene. Guided mode resonances define optical modes with complex wavenumber, typically leaky modes, which are strongly confined in the 1D grating. Forced excitation [6] of these lattice modes may be triggered by phase-matching to incident plane waves. The interaction between these discrete modes and the out-of-plane radiation continuum gives rise to narrowband and asymmetric spectral features, also known as Fano resonances [5-8].

II. RESULTS

Figure 1 shows the sketch of the proposed device that consists of a one-dimensional grating made of Polymethyl-methacrylate (PMMA) stripes deposited on a Silicon Nitride (SiN) slab that is supported by a glass substrate. The monolayer graphene is sandwiched between the PMMA layer and the SiN slab forcing it to interact with the guided mode resonances. Finally, the periodicity p , the PMMA width w_{PMMA} and the SiN slab thickness t_{SiN} are set equal to $0.4 \mu\text{m}$, $0.2 \mu\text{m}$ ($p/2$) and $0.1 \mu\text{m}$, respectively. It is worth stressing that the PMMA width and the SiN slab thickness are chosen in order to satisfy technological constraints.

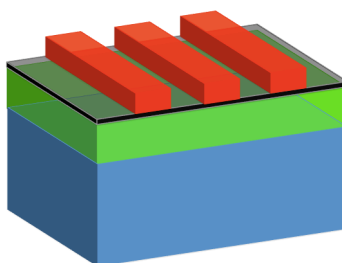


FIG. 1 – Sketch of the proposed device: PMMA stripes (red) on silicon nitride slab (green) grown on silicon dioxide substrate (blue). The black thin layer indicates the monolayer graphene.

The one-dimensional grating has been simulated by means of the Rigorous Coupled-Wave Analysis (RCWA) in the visible range. The dispersion for the different dielectric media has been taken into account through the Sellmeier equation. The monolayer graphene has been modelled as reported in [9].

The spectral response of the optimized configuration has been investigated for both the TE and the TM polarizations as shown in Figure 2. In particular, the plots in Figures 2(a)-(c) clearly illustrate the asymmetric Fano resonances when the monolayer graphene is not considered. On the other hand, when the graphene is considered it is possible to achieve almost the same absorption (about 60%) for both the

polarizations (see Figures 2(b) and (d)). However, the resonances for TE and TM polarizations show different Full-Width at Half Maximum (FWHM) (6 nm and 3 nm, respectively) and central wavelengths. The dissimilarities are due to the different values of complex wavenumbers of TE and TM modes.

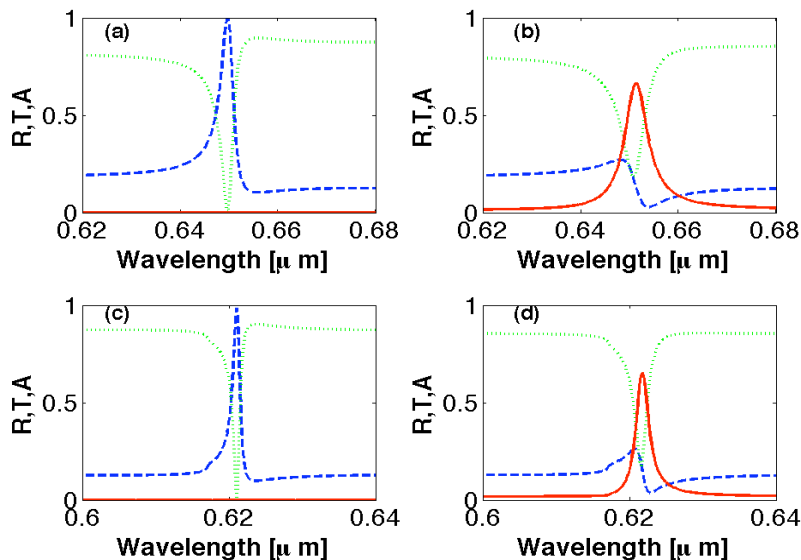


FIG. 2 – Reflection (blue dashed curve, labelled R), transmission (green dotted curve, labelled T) and absorption (red solid curve, labelled A) spectra for the 1D grating when $p= 400$ nm, $t_{PMMA}= 200$ nm, $w_{PMMA}=200$ nm, $t_{SiN}= 100$ nm for the TE polarization (a)-(b) and TM polarization (c)-(d) without (a)-(c) and with (b)-(d) the monolayer graphene, respectively.

Finally, the effects of the technological tolerances on the device performance have been investigated by varying the PMMA thickness.

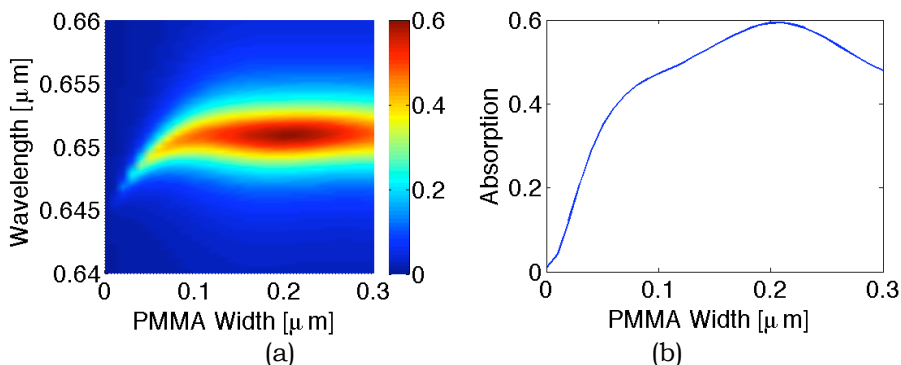


FIG. 3 – (a) Absorption map for the 1D grating ($p= 400$ nm, $w_{PMMA}= 0.2$ μm and $t_{SiN}= 0.1$ μm) when the PMMA thickness t_{PMMA} is varied between 0 nm and 0.3 μm for the TE polarization; (b) Maximum absorption versus the PMMA thickness in the range of interest.

In particular, Figure 3(a) shows the absorption map of the 1D grating when the PMMA thickness t_{PMMA} is varied in the range 0-0.3 μm . The maximum absorption is about 60% and it is achieved for $t_{PMMA} = 0.2$ μm

(Figure 3(b)). Moreover, Figure 3(b) also reveals that the absorption is not very sensitive to the PMMA layer thickness in the range $0.15 \mu\text{m}$ - $0.25 \mu\text{m}$ since it does not vary too much (less than 10%).

III. CONCLUSION

In conclusion, we have reported on the design and the optimization of a one-dimensional dielectric grating based absorber that incorporates a monolayer graphene. The periodic structure has been designed in order to excite guided mode resonances in the visible range. The numerical simulations reveal that a single layer of graphene suffices to absorb about 60% of the impinging light in the visible range for both the TE and the TM polarizations over narrow bandwidths. These results are very promising since the proposed configuration is based on a very simple geometry and shows low sensitivity to the geometrical parameters, hence significant robustness in terms of fabrication tolerances. Finally, the proposed device could be efficiently exploited as a building block for innovative absorbers or photo-detectors where the 1D grating is integrated with active materials.

ACKNOWLEDGEMENTS

This research was performed while the authors M. A. Vincenti and D. de Ceglia held National Research Council Research Associateship awards at the U. S. Army Aviation and Missile Research Development and Engineering Center. M. Grande thanks the U.S. Army International Technology Center Atlantic for financial support (W911NF-13-1-0434).

REFERENCES

- [1] K. S. Novoselov, et al, "Electric Field Effect in Atomically Thin Carbon Films", *Science* 306, 666 (2004).
- [2] R. R. Nair, et al, "Fine Structure Constant Defines Visual Transparency of Graphene", *Science* 320, 1308 (2008).
- [3] M. A. Vincenti, et al, "Nonlinear control of absorption in one-dimensional photonic crystal with graphene-based defect", *Optics Letters* 38, 3550 (2013).
- [4] M. Grande, et al., "Fabrication of doubly resonant plasmonic nanopatch arrays on graphene", *Applied Physics Letters* 102, 231111 (2013).
- [5] R. Magnusson and S. S. Wang, "New principle for optical filters," *Appl. Phys. Lett.*, vol. 61, p. 1022, (1992).
- [6] A. Hessel, A. A. Oliner, "A New Theory of Wood's Anomalies on Optical Gratings", *Appl. Opt.* 4, 1275 (1965).
- [7] U. Fano, "Effects of Configuration Interaction on Intensities and Phase Shifts," *Phys. Rev.*, vol. 124, p. 1866, 1961.
- [8] S. Fan and J. D. Joannopoulos, "Analysis of guided resonances in photonic crystal slabs," *Phys. Rev. B*, vol. 65, p. 235112, 2002.
- [9] M. Bruna and S. Borini, "Optical constants of graphene layers in the visible range", *Appl. Phys. Lett.* 94, 031901 (2009).

MATERIAL-BY-DESIGN FOR ADVANCED ELECTROMAGNETIC DEVICES

G. Oliveri

ELEDIA Research Center @ DISI, University of Trento
Via Sommarive 5, 38123 Trento, Italy
giacomo.oliveri@unitn.it

Abstract

The System-by-Design (SbD) Paradigm is exploited in this work for the synthesis of complex electromagnetic devices. This approach is aimed at the design, definition, and integration of heterogeneous components to yield user-desired performance in a task-oriented manner. To achieve this goal, the design process is modeled in the SbD paradigm as a combination of elementary functional blocks devoted to the synthesis/analysis of each sub-part of the overall device. Such a choice enables the designer to easily identify different trade-off solutions in the synthesis procedure in terms of complexity, speed, effectiveness, and reliability. To illustrate the SbD method, a numerical validation is carried out concerning the synthesis of an inhomogeneous lens for enhancing the radiation performance of conformal phased arrays.

Index Terms – System-by-Design; Optimization Strategies; Electromagnetic Devices; Metamaterials; Artificial Lenses.

I. INTRODUCTION AND RATIONALE

Modern wireless and remote sensing systems are often required to fit several contrasting constraints (e.g., EM performance, size, costs, fabrication complexity) which can be met only by a combination of several effective sub-components (e.g., antenna elements, radome, feeding networks). As a consequence, the derivation of innovative techniques to handle the synthesis of a large set of interconnected sub-systems is mandatory in this field [1]. However, most design approaches are based on independent procedures in which each sub-system is optimized neglecting the methods adopted in rest of the overall system [1]. Unfortunately this guideline does not fully exploit the degrees-of-freedom (DoFs) available in the design process, since it neglects the inter-correlations between the different sub-components of the EM device [1]. To overcome this issue, the so-called *SbD* Paradigm [1] has been recently introduced as a new methodological approach in which current and innovative methods, algorithms, architectures, and solutions can be merged to enable the development of innovative, affordable, and reliable complex systems [1]. Indeed, the main objective of *SbD* Paradigm is the exploitation, the customization, and the innovation of synthesis/analysis methodologies acting as enabling tools for the effective development of integrated design procedures comprising several equivalent functionalities. More in detail, the *SbD* Paradigm is

based on the representation of the synthesis procedure as a flowchart (Fig. 1) which can comprise *Synthesis Blocks* (e.g., “Evolutionary Optimization Algorithm” – Fig. 1), that are responsible for configuring a part/sub-part of the system starting by means of suitable optimization strategies [2][3], as well as *Analysis Blocks* (e.g., “Fast EM Simulation”, “Homogenization Technique” – Fig. 1), that are devoted to determining the features of a part/subpart of the system. Thanks to such a representation, the arising design technique enables the choice of the optimal trade-off (e.g., in terms of accuracy vs. computational complexity) solution in the selection of the algorithms/methodologies to be used for designing each functional sub-component [4]-[11].

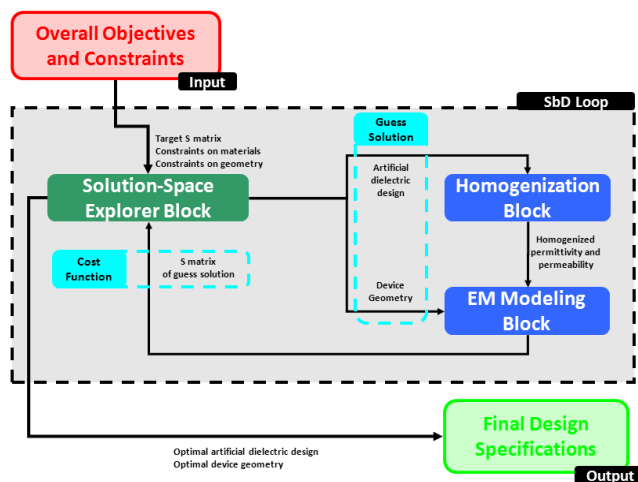


FIG. 1 – System-by-Design loop as applied to the design of an EM device.

In the following, the application of the *SbD* paradigm to the design of an inhomogeneous lens to be used to enhance the radiation features of conformal phased arrays will be discussed.

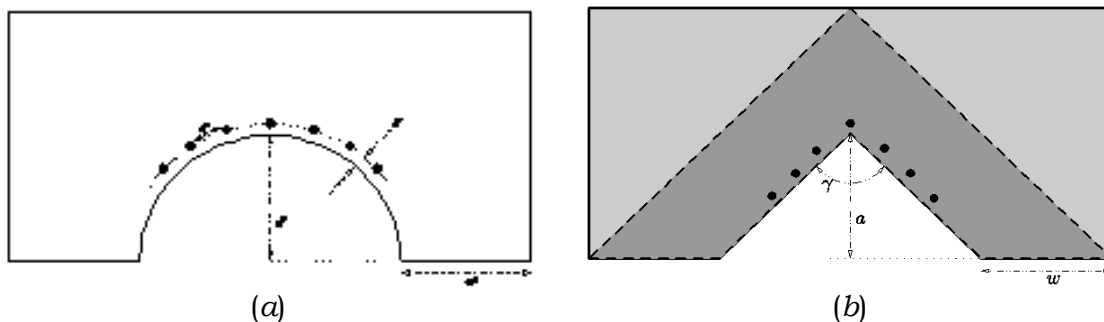


FIG. 2 – Geometry of the problem: (a) synthesis

II. APPLICATION OF SB D TO DESIGN OF LENSES FOR CONFORMAL ARRAYS

Consider the synthesis of an inhomogeneous anisotropic lens to be combined with a corner-conformal phased array [Fig. 2(b)], whose aim is

to manipulate the field radiated by the arrangement so that it fits that of the corresponding circular *target* layout [Fig. 2(a)]. With reference to the flowchart in Fig. 1, the application of the *SbD* paradigm to such a problem considers the following choices:

1. *Homogenization Technique* - not included since the lens is characterized by inhomogeneous permittivity and permeability tensors, and no homogenization is possible in such a case;
2. *Fast EM simulation* - to efficiently determine the electromagnetic features of the antenna plus the lens [Fig. 2(b)] and evaluate the associated “cost function” (difference between expected and obtained far field), a 2D FEM technique is adopted;
3. *Evolutionary optimization algorithm* - to update the guess solution a combination of an evolutionary algorithm (aimed at controlling the lens geometry) and of a quasi-conformal transformation optics (QCTO) [6] (that configure the dielectric tensors) is adopted.

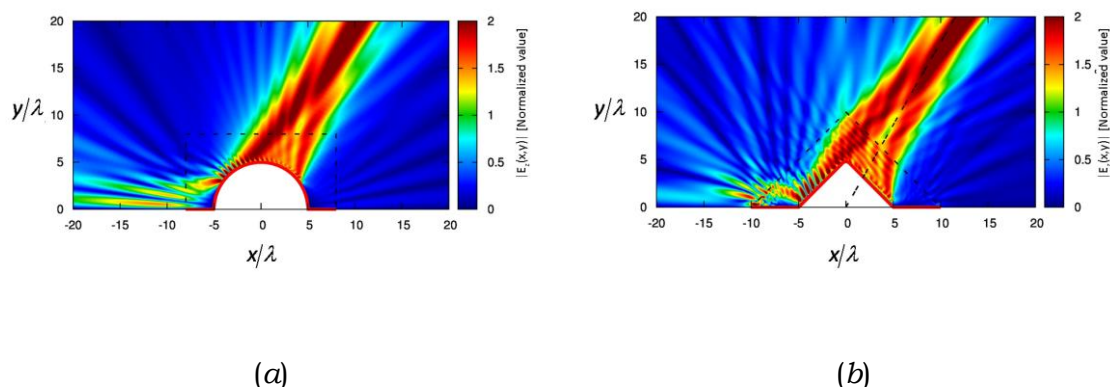


FIG. 3 – Amplitude of the z -component of radiated field for the (a) target circular array of Fig. 2(a), and (b) conformal arrangement coated with the designed lens of Fig. 2(b).

To illustrate the effectiveness of the resulting *SbD* loop, the design of a 2D lens coating an $N=20$ element array steered at 60 [deg] has been numerically carried out. In such a case, the *target* array is a half-wavelength spaced arrangement with unitary excitations [Fig. 2(a)], and the layout to be designed is conformal to a 90 [deg] corner [Fig. 2(b)]. By iteratively executing the loop in Fig. 1, a final arrangement is obtained whose radiated field [Fig. 3(b)] closely resembles the target performance [Fig. 3(a)] thanks to the presence of the designed inhomogeneous lens. The effectiveness of the *SbD* method is confirmed by the fact that the designed arrangement yields a very similar mainbeam and sidelobe pattern outside the lens region (Fig. 3), as expected.

III. CONCLUSION

The System-by-Design Paradigm is adopted for the synthesis of complex electromagnetic devices, in order to model the EM design process as a combination of elementary functional blocks devoted to the

synthesis/analysis of each sub-part of a complex system. To illustrate the SbD method, the synthesis of an inhomogeneous lens for conformal array applications is carried out.

ACKNOWLEDGEMENT

This work has been partially supported by the EMERALD project funded by the Autonomous Province of Trento – Calls for proposal “Team 2011”.

REFERENCES

- [1] A. Massa, G. Oliveri, P. Rocca, and F. Viani, “*System-by-Design: A new paradigm for handling design complexity*”, *8th European Conf. Antennas and Propagation (EUCAP 2014)*, The Hague, The Netherlands, Apr. 6-11, 2014.
- [2] P. Rocca, M. Benedetti, M. Donelli, D. Franceschini, and A. Massa, “Evolutionary optimization as applied to inverse problems,” *Inverse Problems* vol. 25, 123003, pp. 1-41, Dec. 2009.
- [3] P. Rocca, G. Oliveri, and A. Massa, “Differential Evolution as applied to electromagnetics,” *IEEE Antennas Propag. Mag.*, vol. 53, pp. 38-49, Feb. 2011.
- [4] G. Oliveri, L. Manica, and A. Massa, “Synthesis of multi-layer wideband WAIM coatings for planar phased arrays within the system-by-design framework,” *IEEE Trans. Antennas and Propag.*, submitted, 2014.
- [5] L. Manica, M. Carlin, I. Malcic, G. Oliveri, and A. Massa, “Wideband multi-layer WAIM design and optimization”, *8th European Conf. Antennas and Propagation (EUCAP 2014)*, The Hague, The Netherlands, Apr. 6-11, 2014.
- [6] E. T. Bekele, G. Oliveri, J. P. Turpin, D. Werner, A. Massa, “Design of metamaterial-coated arrays through quasi-conformal transformation optics”, *8th European Conf. Antennas and Propagation (EUCAP 2014)*, The Hague, The Netherlands, Apr. 6-11, 2014.
- [7] E. T. Bekele, G. Oliveri, E. Martini, S. Maci, and A. Massa, “A material-by-design strategy for the design and optimization of multisurface-metamaterial polarizers”, *8th European Conf. Antennas and Propagation (EUCAP 2014)*, The Hague, The Netherlands, Apr. 6-11, 2014.
- [8] G. Oliveri, E. T. Bekele, D. H. Werner, J. P. Turpin, and A. Massa, “Generalized QCTO for metamaterial-lens-coated conformal arrays,” *IEEE Trans. Antennas Propag.*, in press.
- [9] G. Oliveri, P. Rocca, M. Salucci, E. T. Bekele, D. H. Werner, and A. Massa, “Design and synthesis of innovative metamaterial-enhanced arrays,” *IEEE International Symposium on Antennas Propag. (APS/URSI 2013)*, Orlando, Florida, USA, Jul. 7-12, 2013.
- [10] I. Martinez, A. H. Panaretos, D. H. Werner, G. Oliveri, and A. Massa, “Ultra-thin reconfigurable electromagnetic metasurface absorbers,” *7th European Conf. Antennas and Propagation (EUCAP 2013)*, Gothenburg, Sweden, April 8-12, 2013.
- [11] G. Oliveri, “Improving the reliability of frequency domain simulators in the presence of homogeneous metamaterials - A preliminary numerical assessment,” *Progress In Electromagnetics Research*, vol. 122, pp. 497-518, 2012.

CHARACTERIZATION OF NANOCOMPOSITES BASED ON MWCNTs FOR RADAR ABSORBING APPLICATIONS

M. Miscuglio⁽¹⁾, M. Hajj Yahya ⁽¹⁾, P. Savi ⁽¹⁾,
M. Giorcelli ⁽²⁾, A. Tagliaferro ⁽²⁾

⁽¹⁾ Department of Electronic and Telecommunication, Politecnico di Torino, Corso Duca degli Abruzzi 24, 10129 Torino, Italy

⁽²⁾ Department of Applied Science and Technology, Politecnico di Torino, Corso Duca degli Abruzzi 24, 10129 Torino, Italy,
patrizia.savi@polito.it

Abstract

A wide band microwave characterization of nanocomposites based on commercial multiwall carbon nanotubes (MWCNTs) and epoxy resin is presented. Field Emission Scanning Electron Microscopy is used for morphological samples analysis of nanocomposites and MWCNTs. Complex permittivity is measured using a commercial dielectric probe and a Network Analyzer. The reflection coefficient of a single-layer structure backed by a metallic plate was simulated taking into account the value of the measured permittivity and compared with RCS measurements.

Index Terms – Carbon nanotubes, nanocomposites, permittivity measurements, radar absorbing materials.

I. INTRODUCTION

Carbon nanotubes (CNTs) have been used intensively as a filler in a variety of polymers. Their outstanding mechanical, electrical and thermal properties allow them to enhance the properties of the material in which they are used as a filler. Recently, CNT composites have been proposed as microwave absorbers [1,2] and for shielding applications [3,4]. For these applications, the ability consist into tailor the values of complex permittivity. This is obtained with an opportune mixing of appropriate polymer matrix and selected concentration of a particular type of CNTs.

In this paper, Nanoconposites (NCs) based on multi wall CNTs (MWCNTs) and epoxy resin were prepared using an in-situ polymerization process. Complex permittivity of pristine polymer matrix and NCs with different MWCNTs concentration was measured using a commercial dielectric probe. Starting from the knowledge of the permittivity values of NCs with different weight percentage of MWCNTs, the reflection coefficient of a one-layer of given thickness (d), backed by a metallic plate was computed and the results compared with RCS measurements.

II. NANOCOMPOSITES CHARACTERISTICS

Nanocomposites were prepared starting from a commercial thermosetting resin (Epilox®, Leuna, Germany) and MWCNTs (NTX-4 Nanothinx, Rio Patras, Greece). The polymer matrix is a bi-component system formed by a resin and a hardener. It was chosen among other polymers because it is thermoset and can withstand high temperatures.

MWCNTs (diameters in the range 6-10 nm and length $>10 \mu\text{m}$) were dispersed in Epilox in various concentrations (1wt.%, 3wt.% 5wt.%) (details in [5]) and the degree of dispersion analysed by a Field Emission Scanning Electron Microscopy (FESEM Zeiss Supra-40). Fesem images of MWCNTs and NCs at 3wt% of MWCNTs are reported in Fig. 1.

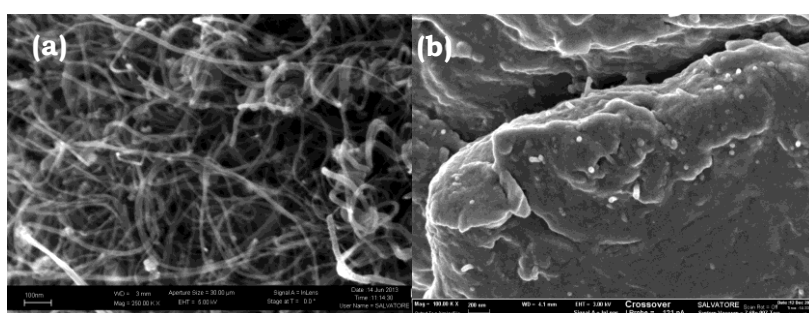


FIG. 1 – FESEM images of (a) MWCNTs used as filler and (b) cryo-fractured NC surface.

III. RESULTS

The complex permittivity was measured by using a commercial probe (Agilent 85070D) and a Network Analyser (E8361A). A standard calibration short/air/water was performed before each measurement. The real part of permittivity and the AC electrical conductivity are shown in Fig. 2. As it was expected, higher values of both real permittivity and AC conductivity are observed for increasing wt% of CNTs loading.

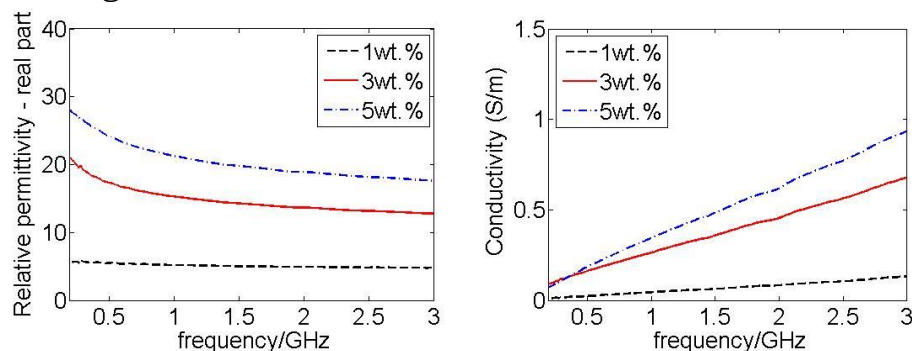


FIG. 2 – Measured permittivity and AC electrical conductivity of samples with different MWCNTs concentrations.

A plane wave with parallel (TM) and perpendicular (TE) polarization incident on a one-layer structure was considered, and a transmission line model applied to evaluate the reflection coefficient (see Fig.3). Results obtained considering a one-layer of thickness $d = 2\text{mm}$ and normal incidence are shown in Fig. 4 (red line). As it was expected, the increase of the relative permittivity values with the concentration produces a minimum in the reflection coefficient. For 3% concentration a peak of -17dB at 6GHz is obtained. Radar Cross Section (RCS) of samples of small dimensions backed by a metallic plane was measured in an anechoic chamber. The measurement setup is shown in Fig.4 (left panel). A preliminary result is shown in the figure (black line, right panel) and compared with the simulated data.

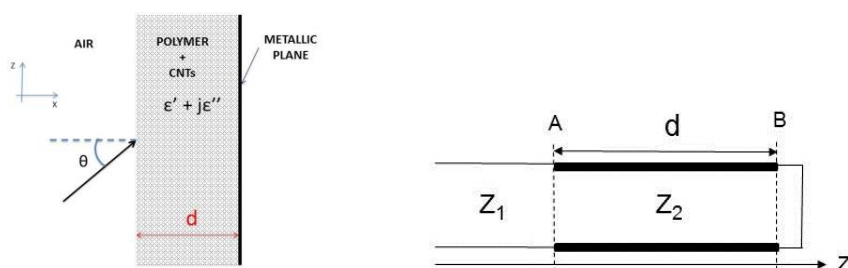


FIG. 3 – One-layer backed by a metallic plate (left panel). Transmission line model (right panel).

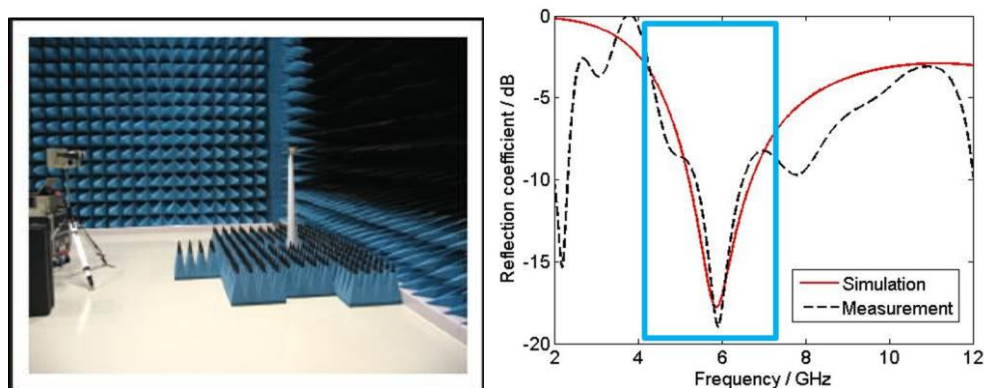


FIG. 4 – RCS measurement setup (left panel). Comparison between the simulated (red) and measured (black) reflection coefficient (right panel).

IV. CONCLUSIONS

In this paper NCs based on epoxy resin and MWCNTs in different concentrations (1,3,5 wt. %) were made. Their complex permittivity was measured with a commercial probe and network analyzer. Our study

clearly shows that the values of complex permittivity increase by increasing the filler concentration. A one-layer structure backed by a metallic plate with a plane wave incidence was modelled with a transmission line approach. The reflection coefficient, for normal and oblique incidence, was calculated by considering in the model the measured permittivity values and results compared with RCS measurements. Measurement and simulation values are in agreement and reach a value of -17 dB at 6 GHz for NC with 3% of MWCNTs.

Analysis of nanocomposites with MWCNTs of different lengths and diameters and design of a two-layer absorber are foreseen.

ACKNOWLEDGEMENT

Authors would like to thank A. Delogu, W. Ferrarese and M. Mwanya (SELEX SE) for the RCS measurements. Salvatore Guastella for FESEM Analysis and Nanothinx for MWCNTs supply.

REFERENCES

- [1] A. Saib, L. Bednarz, R. Daussin, C. Bailly, X. Lou, J.M. Thomassin, et al., "Carbon nanotube composites for broadband microwave absorbing materials," *IEEE Trans. on Microwave Theory Tech.* 2010, pp. 2745–2754, 2010.
- [2] D. Micheli, R. Pastore, C. Apollo, M. Marchetti, G. Gradoni, V. Mariani Primiani, F. Moglie, "Broadband electromagnetic absorbers using carbon nanostructure-based composites," *IEEE Trans. on Microwave Theory and Techniques* 2011, vol. 59, pp. 2633-2646, 2011.
- [3] I.M. De Rosa, F. Sarasini, M.S. Sarto, A. Tamburrano, "EMC Impact of Advanced Carbon Fiber/Carbon Nanotube Reinforced Composites for Next-Generation Aerospace Applications," *IEEE Trans. on Electromagnetic Compatibility*, vol. 50, pp. 556-563, 2008.
- [4] M.Y. Koledintseva, J. Drewniak, R. DuBro, " Modeling of shielding composite materials and structures for microwave frequencies, " *Progress In Electromagnetics Research B*, vol. 15, pp. 197-215, 2009.
- [5] P. Savi, M. Miscuglio, M. Giorcelli, A. Tagliaferro, "Analysis of microwave absorbing properties of epoxy MWCNT composites," *Progress In Electromagnetics Research Letters*, vol. 44, pp. 63-6, 2014.

GRAPHENE-ASSISTED AMPLITUDE AND PHASE MODULATION IN SILICON PHOTONICS

M. Midrio⁽¹⁾, P. Galli⁽²⁾, M. Romagnoli⁽³⁾, L. C. Kimerling⁽⁴⁾, J. Michel⁽⁴⁾

⁽¹⁾ Dipartimento di Ingegneria Elettrica, Gestionale e Meccanica,
Università degli Studi di Udine, 33100 Udine, Italy

⁽²⁾ Bell Labs, Alcatel Lucent, 20871 Vimercate (MB), Italy

⁽³⁾ CNIT, 56124 Pisa, Italy, romagnoli@cnit,

⁽⁴⁾ MIT, Cambridge, MA 02139, USA

Abstract

Graphene based phase ($V_{\pi}L\pi = 0.0022 \text{ Vcm}$) or amplitude ($0.23 \text{ dB}/\square m$) modulation can be separately achieved by only changing modulator DC bias. We show an example of 64-APSK modulator for short reach single waveguide low energy 200Gb/s interconnection.

Index Terms – Modulators, Integrated optoelectronic circuits, Integrated optics materials, Optical communications.

I. INTRODUCTION

Recently a single and double sheet of graphene on a silicon waveguide has been reported to provide an efficient low power consumption electro absorption modulation^{1,2}. This mechanism is based on interband transitions of photogenerated electrons that induce absorption. However, biasing the graphene layers to raise the Fermi level to an energy larger than half of the photon energy brings graphene to a transparent condition and to a change of index of refraction as well^{3,4}. By choosing therefore a suitable bias, the graphene modulator can be switched from pure amplitude to pure phase modulation.

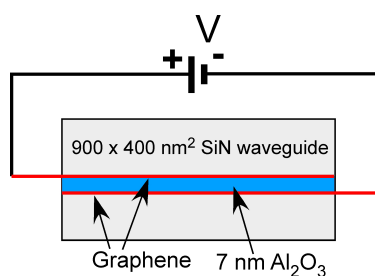


FIG. 1 – Graphene-SiN waveguide cross section. Cladding material is SiO₂.

This new property that is specific of graphene opens a new scenario for efficient complex modulation format transmitters. In this paper we will report on the characteristics of phase and amplitude response of a TE mode in a SiN nanowire waveguide and in a microring where two layers of graphene are embedded in the waveguide core, and spaced by 7nm of

Al₂O₃ insulating layer to form a MOS capacitor (see Fig.(1)).

Short distance interconnections are presently based on parallel optics that involves a number of optical fibers or waveguides equal to the number of transmitters, or single WDM channels that use only one fiber/waveguide. We propose a simple approach to increase the bandwidth density that can be added to currently used interconnection schemes. We will report on an example of miniaturized and energy efficient 3x33Gb/s transmitter based on a N-APSK modulation format, in particular on asynchronous 4-ASK and 16-DQPSK. Finally we will discuss the energy/bit required by the proposed modulator.

II. THEORY

A remarkable and unique property of graphene is that its complex conductivity can be tuned, even at optical frequencies, by varying the applied chemical potential (μ_c), i.e. by adding or removing charges from the graphene sheet. In the waveguide of Fig.(1), the two graphene layers together with a 7nm thick Al₂O₃ layer form a capacitor, and charges can be added or removed by applying a suitable voltage across it. The relationship between the chemical potential and the applied voltage reads as⁴ $V \approx 10.3 \mu_c^2 + 2|\mu_c|$. The dependence of the graphene's complex conductivity (σ) on frequency (ω), temperature (T) and applied chemical potential has been discussed in several papers⁵. It reads as:

$$\sigma_R = \sigma_0 \left(\tanh \frac{\hbar\omega + 2\mu_c}{4k_B T} + \tanh \frac{\hbar\omega - 2\mu_c}{4k_B T} \right), \quad \sigma_I = \sigma_0 \left(\frac{4\mu_c}{\pi\omega} - \frac{1}{2\pi} \log \frac{(\hbar\omega + |2\mu_c|)^2}{(\hbar\omega + |2\mu_c|)^2 + (2T)^2} \right) \quad (1)$$

where \hbar and k_B are the reduced Planck's and Boltzmann constants, respectively, and $\sigma_0 \approx 6.08 \times 10^{-5}$ Siemens. The relative dielectric constant of graphene is simply related to the imaginary part of its conductivity as follows⁴ $\epsilon_r = 1 + \sigma_I / (\omega\epsilon_0)$ with $\epsilon_0 = 8.85 \times 10^{-12}$ F/m. Fig.(2.a) shows the real conductivity and relative dielectric constant for $\hbar\omega \approx 0.8$ eV (corresponding to a free-space wavelength of 1550 nm) vs the voltage applied to the capacitor formed by the two graphene layers of Fig.(1) in the voltage range of interest for this paper. It may be seen from the inset of the figure that when the applied voltage changes from roughly 2 to 3.5 V, a large variation of the real part of graphene's conductivity is observed. In the same voltage range, the imaginary part changes as well (see eqs.(1) and (3)), leading to both amplitude and phase modulation to an optical signal travelling into the waveguide. When the applied voltage exceeds 3.5 V, the real part drops to negligible values: graphene behaves in this regime as an optically transparent material. Any further change of the conductivity will now reflect on the dielectric constant only, eventually leading to phase modulation of the travelling optical signal.

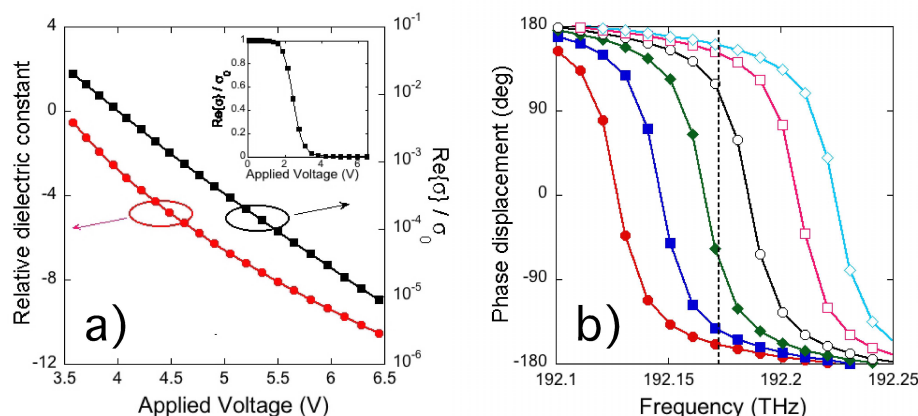


FIG. 2 – a) Red curve (left axis): relative dielectric constant of graphene vs. applied voltage. Black curve (right axis): real part of the graphene conductivity for free-space wavelength equal to 1550 nm. Inset: same quantity on a broader range of applied voltages. b) Phase shift across a 12 μm radius microring based on the graphene-SiN waveguide shown in Fig.(1) when the applied voltage ranges from 4.3V (red curve) to 5.8 V (cyan curve) at 0.3 V steps.

III. PHASE MODULATION WITH ALL-PASS MICRORING FILTERS AND AMPLITUDE MODULATION WITH A STRAIGHT WAVEGUIDE

Fig.(2.b) shows the behavior of a 12 μm radius microring phase modulator based on the graphene-SiN waveguide cross section shown in Fig.(1). The phase shift ψ vs. frequency is shown for applied voltages ranging from 4.3V to 5.8 V at steps of 0.3 V. It can be seen that wide phase modulation can be achieved upon application of a relatively small change of applied voltage. At any given frequency, π phase shift requires a variation of the applied voltage in the order of 0.3V.

From these values we evaluate an effective voltage-length product as small as $V_{\pi}L_{\pi} = 0.0022 \text{ Vcm}$. The energy consumption is evaluated from a capacitance $C=0.85\text{pF}$ and results $\Delta E_{\pi}=0.65\text{pJ}$ for π modulation.

Whereas, when graphene is biased in the chemical potential range $|\mu_c| < 0.5\text{eV}$, that is with an applied voltage lower than 3.5V, interband transitions and absorption occur whereas phase changes become negligible. In our example, when the chemical potential $|\mu_c|$ changes between 0.3eV and 0.5eV (corresponding to a change of the applied voltage between 1.5V and 3.5 V) an induced loss $\Delta\alpha_{\square\square} = 0.23\text{dB}/\square\text{m}$ may be obtained. In order to obtain an attenuation of 1 dB a waveguide length of 4.3 μm is hence required. The energy consumption is evaluated from a capacitance $C = 49\text{fF}$ and evaluates to $\Delta E_{\square\square}=122\text{fJ}$. Each additional dB of attenuation adds a $C = 49 \text{ fF}$ capacitance in parallel, and 122fJ of energy consumption.

IV. N-APSK MODULATOR

To exploit the advantage of phase modulation in increasing the channel density bandwidth, a complex modulation format combining phase and amplitude modulation has to be implemented. As an example we propose a scheme that enables the transmission of a multi-level signal obtained through the multiplexing of two asynchronous and independent optical streams. The multi-level signals are implemented with a $N = 64$ -symbol APSK (N-APSK) modulation format, derived from two streams implemented with differential quadrature 16-PSK (DQPSK) and 4-ASK modulation, respectively. The transmitter scheme includes a cascade of two microring phase modulators for the DQPSK modulation followed by a straight waveguide amplitude modulator for the 4ASK modulation. One microring is used to induce a $\pm\pi/2$ phase shift, while the second one is used to induce $\pm 15\pi/16$ (16-PSK) phase shift. The amplitude modulator has to provide a maximum of 6dB for the four level 4-ASK format. The receiver scheme would include a splitter to send the multiplexed multi-level signal to both the DQPSK and ASK receivers. This modulation scheme is particularly suitable for short distance interconnections as it is non-coherent, the ASK and PSK are asynchronous, and the demodulation scheme is simple. Assuming a symbol rate of 33GBd/s the energy required to drive a microring phase modulator is 640fJ/bit from $-\pi/2$ to $+\pi/2$ phase shift. The energy consumption of the amplitude modulator to achieve 6dB modulation is 720fJ/bit. The overall consumption is 2pJ/bit for the 64-APSK (200Gb/s) yielding, at a base rate of 33GBd/s, a required power of 66mW.

V. CONCLUSIONS

We reported on the possibility of using graphene in SiN waveguides to achieve either pure amplitude or phase modulation. We showed an effective phase modulation efficiency $V_{\pi}L_{\pi} = 0.0022$ Vcm and amplitude efficiency $\Delta\alpha_{\text{opt}} = 0.23\text{dB}/\mu\text{m}$. We evaluated the exploitation of phase/amplitude modulation with two examples of N-APSK modulation formats and we showed that the real advantage of introducing phase modulation is for large constellations

REFERENCES

- [1] M. Liu et al., Nature, Vol. **474**, p. 64 (2011).
- [2] M. Liu et al., Nanoletters, Vol. **12**, p. 1482 (2012).
- [3] C. Xu et al., Opt. Expr., Vol. **20**, p. 22398 (2012).
- [4] M. Midrio et al., to be published in Photon. Res. Journal (2014).
- [5] L. Falkowski et al., Phys. Rev. B, Vol. **76**, p. 153410 (2007)

REMOTE RETUNING OF X-BAND MINI WEATHER RADAR USING GROUND CLUTTER ECHOES

S. Bertoldo⁽¹⁾, C. Lucianaz⁽¹⁾, O. Rorato⁽¹⁾, M. Allegretti⁽²⁾, G. Perona⁽³⁾

⁽¹⁾ Department of Electronic and Telecommunication, Politecnico di Torino
Corso Duca degli Abruzzi 24, 10129, Torino, Italy
silvano.bertoldo@polito.it, claudio.lucianaz@polito.it

⁽²⁾ Envisens Technologies s.r.l.,
Via Menotti 4, 10138, Torino, Italy
marco.allegretti@polito.it

⁽³⁾ CINFAI, local unit c/o Politecnico di Torino
Corso Duca degli Abruzzi 24, 10129, Torino, Italy
giovanni.perona@polito.it

Abstract

The magnetron of a X-band mini weather radar could drift mainly due to external factors such as temperatures, humidity etc. The central frequency of the radar receiver filter must remain perfectly aligned with the magnetron generated frequency in order to receive the maximum power and avoid rain underestimation problems. This work describe a simple and cheap technique developed to remote retuning a X-band weather radar using ground clutter echoes acquired during clear sky days. By statistically analyzing the power distributions of ground clutter echoes observed in clear sky conditions, it is possible to control the radar stability over a long time interval and to retune the radar. The technique is described and several results are reported.

Index Terms – Ground clutter echoes, Radar tuning, X-band weather radar.

I. X BAND RADAR NETWORK

Radar meteorology has always been one of the major research topics for the the Remote Sensing Group (RSG) of Polytechnic of Turin, local unit of CINFAI (Consorzio Interuniversitario per la Fisica delle Atmosfere e delle Idrosfere). Its own X-band mini radar system was developed in the past years in collaboration with Envisens Technologies s.r.l., spinoff of Polytechnic of Turin [1].

The first fully operational network of mini radars was set up starting from 2010 and now, in 2014, it is made up by 8 radar systems (Fig. 1): one in Turin town, Italy (2010), in Aosta Valley, Italy (2011), in Foggia, Italy (2012), in Palermo, Italy (2012), two in Israel in collaboration with the Hebrew University of Jerusalem (2012), one near Nizza Monferrato in Piedmont Region, Italy (2012) and one in Parma, Italy (2013).

Each radar acquires the real time maps and send them to a specific server where some specific services and applications have been implemented. Processed radar maps can be browsed on the official network web site (meteoradar.polito.it) where they are projected over a cartographic system. On the server side, specific applications and services are running [2].

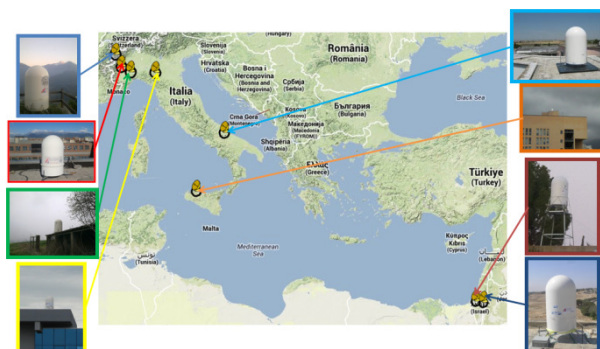


FIG. 1 – The X-band mini weather radar network in March 2014.

The radars are exclusively devoted to rain measurement and reach good performance thanks also to some specific developed calibration procedures.

II. THE “DETUNING” PROBLEM

To assure good performances in detection and measurement of rain, it is not only important that the radar is well calibrated, but it is necessary to control the stability of the overall radar system components. These sub-systems may suffer for some degradations due both to external factors, such as temperature fluctuations, humidity etc, and to equipment ageing and related issues.

Among all these problems, the frequency drifts of the magnetron is very common because all the radars are installed in open field and are exposed to different, and often extreme, weather conditions. In order to receive the maximum power back scattered by the rain cells, it is important that the receiver filter central frequency is completely aligned with the transmitted frequency by the magnetron, in order to avoid the so called “detuning” problem.

III. GROUND CLUTTER ECHOES TO DETECT A “DETUNING” CONDITION

According to RCA (Relative Calibration Adjustment) algorithm described in [3], originally proposed for a S-band ground radar, the Probability Distribution Function (PDF) of the clutter echo and, consequently, the corresponding Cumulative Distribution Function (CDF), should significantly change only if modifications on the radar systems occurred.

It is demonstrated in [4] that it is possible to use clutter echoes acquired during clear sky days, and properly statistically analyzed, to control the radar stability also for X-band mini weather radar. In particular an experiment is described: the radar receiver filter is intentionally detuned to establish which are the best statistical indicators to check if the system is properly working.

X-band mini weather radar receiver central frequency is controlled by a 8-bit register, and its value can be remotely modified. If a radar is supposed to be detuned, it is possible to turn off the clutter filter (usually enabled) and acquire clutter maps during clear sky days varying the value of such filter, in order to track the drifts of the magnetron.

To retune the radar using ground clutter echoes, the procedure is the following (note that all the operations can be done remotely and last less than 2 hours, thanks to the flexibility and the high configurability of the system):

- A set of clutter maps is acquired for different receiver filter code value (10 - 15 maps for each value are enough);
- considering each set of clutter maps acquired with different receiver filter code value, the CDFs are computed;
- A possible radar detuning condition is checked by observing the mean values.
- In case of system detuning, the losses are evaluated considering the difference between the mean value of the CDFs.
- The register filter code value for which the 90th percentile (and consequently the mean) reaches its maximum is the new value to be written in the register, in order to restore the tuning and track the magnetron drifts.

IV. EXAMPLE OF REMOTE RETUNING OF GILAT (ISRAEL) RADAR

The radar in Gilat (Israel) was installed in October 2012 within a scientific cooperation program between Italy and Israel.

After one year, during November 2013, the radar was heavily underestimating the rain. It was supposed to be detuned and the remote retuning procedure was applied during a clear sky day.

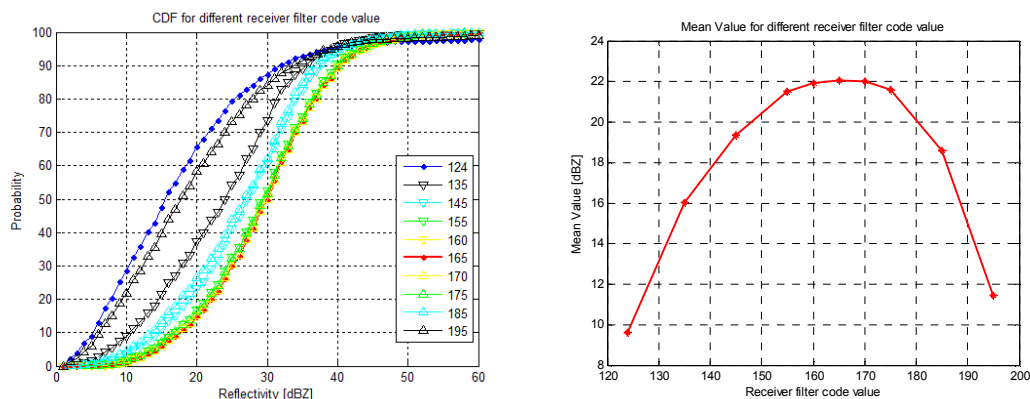


FIG. 2 – CDFs for different receiver filter code value on the left (a), and mean of the different distributions obtained with different receiver filter code value on the right (b).

The CDFs were evaluated it was immediately noticed that the radar was detuned: the receiver filter code value set during the installation was 124, blue line, and the new value for tuning was 165, red line (Fig. 2 (a)). According to the information provided by the analysis of the mean of the different distributions, the system was losing about 12 dB (Fig. 2 (b)).

The X-band mini weather radar was remotely retuned by setting the new receiver filter code value. The radar was then restarted with the clutter filter enabled in order to get only backscattered echoes coming from rain cells.

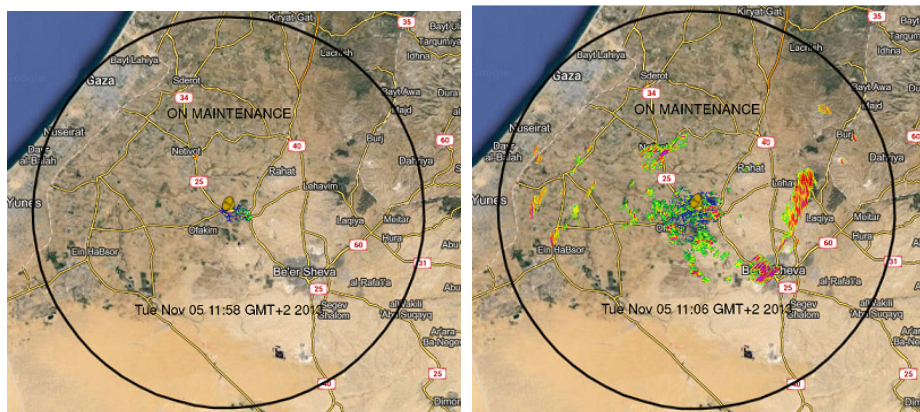


FIG. 3 – Example of clutter maps in detuning on the left (a) with receiver filter code value equal to 124, and after the retuning operation on the right (b) with receiver filter code value equal to 165. It is clear that the radar was heavily detuned because before the retuning operation the clutter echoes were very low.

V. CONCLUSION

A procedure to remote retune a X-band mini weather radar system is presented together with its application on an operative radar installation. The procedure is simple, does not require any additional software with respect to the standard software package to control the radar system (therefore it is cheap), and does not require too much time to be executed. The procedure works well and allow to retune a radar when a frequency drift of the magnetron occurs. Since this experience, the algorithm is periodically applied to compensate seasonal drift due to the mean temperature variations keeping the radar calibrated for rain estimation within a 2 dB interval.

REFERENCES

- [1] M. Gabella, R. Notarpietro, S. Bertoldo, A. Prato, C. Lucianaz, O. Rorato, M. Allegretti and G. Perona, “A Network of Portable, Low-Cost, X-Band Radars”, *Doppler Radar Observations - Weather Radar, Wind Profiler, Ionospheric Radar, and Other Advanced Applications*, Dr. Joan Bech Ed., InTech, 2012, pp 175-202.
- [2] S. Bertoldo, C. Lucianaz, O. Rorato, M. Allegretti, A. Prato, G. Perona, “An operative X-band mini-radar network to monitor extreme rainfall events with high time and space resolution”, *Engineering technology and applied science research*, vol. 2(4), pp 246-250, 2008.
- [3] D. S. Silberstein, D. B. Wolff, D. A. Marks, D. Atlas and J. L. Pippitt, “Ground Clutter as a Monitor of Radar Stability at Kwajalein, RMI”, *Journal of Atmospheric and Oceanic Technology*, vol. 15(11), pp 2037-2045, 2008.
- [4] S. Bertoldo, R. Notarpietro, M. Branca, G. Dassano, C. Lucianaz, O. Rorato, M. Allegretti, “Characterization of the receiver filter of a X-band weather radar to improve the performance of an application to control the radar stability”, *International Conference in Electromagnetics in Advanced Applications*, Cape Town, South Africa, September 2nd – 7th, 2013, pp. 1040-1043.

ELECTROMAGNETIC-BASED APPROACH FOR RGB REPRESENTATION OF SAR MULTITEMPORAL DATA

D. Amitrano, G. Di Martino, A. Iodice, D. Riccio, G. Ruello

Department of Electric Engineering and Information Technology,
Università degli Studi di Napoli Federico II, Naples, Italy
{donato.amitrano; gerardo.dimartino; iodice; daniele.riccio;
ruello}@unina.it

Abstract

In this paper we present an innovative approach for interpretation, processing and representation of multi-temporal SAR images. The proposed approach includes three blocks of activities concerning data calibration, adaptive processing and user-based representation. The knowledge of electromagnetic models guides the production of RGB maps, whose interpretation does not require specific expertise in remote sensing. The method is presented with the support of a case study concerning the production of land cover maps in a rural context.

Index Terms – Synthetic aperture radar, multitemporal processing, RGB representation.

I. INTRODUCTION

Despite the huge amount of available data and scheduled missions, the use of SAR data in applicative scenarios is still limited. The main constraints to a full exploitation of the potentiality of SAR are the lack of reliable interpretation models and the limited efficiency of methods that should present the retrieved information with universally recognized symbolism [1].

This paper presents a new approach for addressing these issues, shading light on the importance of electromagnetic models for both image interpretation and data representation. The proposed 3 steps multi-temporal adaptive processing (MAP3) defines the processing needed for the production of new multi-temporal products. MAP3 aims at obtaining a set of spatially, temporally and radiometrically comparable images, whose appropriate combination provide user-friendly maps. In section II, the rationale of the proposed approach is discussed. In Section III, the obtained RGB products are presented. Discussion of the results and the concluding remarks are provided in Section IV.

II. RATIONALE

The block diagram of Fig. 1 describes the rationale of the proposed approach, made of three blocks of processing. The pre-processing chain

includes data coregistration, despeckling and calibration, providing as output a set of comparable images. The obtained images are then combined in order to retrieve the physical information that is object of analysis. The last block involves the processing devoted to appropriately represent the estimated information, providing products that could be read and comprehended by users with no experience with SAR images.

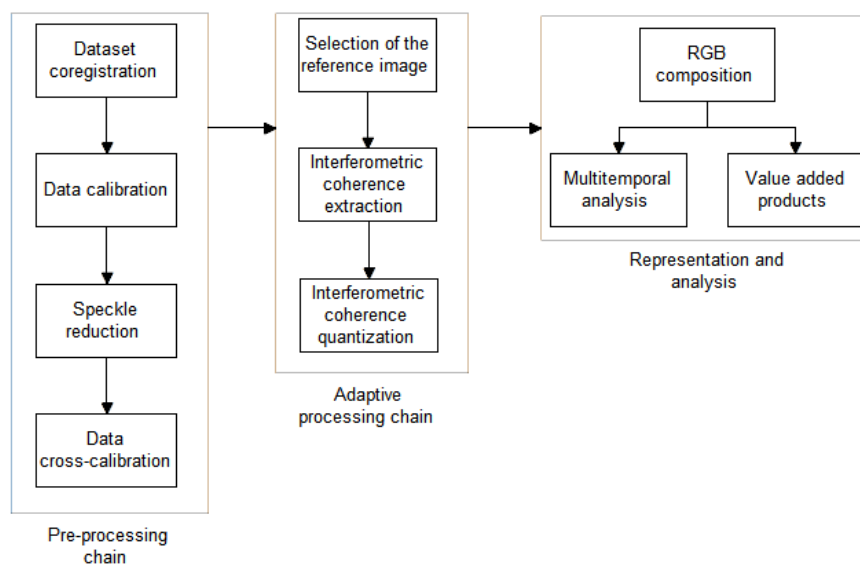


FIG. 1 – Block diagram of the proposed method.

The design of the blocks was guided by six properties: (i) reproducibility; (ii) automation: a minimum number of parameters to be set up by the users; (iii) adaptability: the processing should be suitable for a large number of applications; (iv) reversibility: the processing chain should preserve the electromagnetic and physics characteristics of the analyzed scene, giving rise to invertible models; (v) visualization: the output maps should be comfortable with human view and help the visual extraction of information; (vi) interpretation: the obtained maps and value added products should be easily interpreted by a large variety of scientists and researchers belonging to different disciplinary sectors.

Knowledge of the electromagnetic propagation and scattering models is needed in order to combine the images of the time series in a color composite view. In fact, the data should be expressed in a common scale with a number of levels (usually 256) suitable with human visual perception. Blind methods existing in literature tried to solve the problem with percentile-based histogram clipping and rescaling. But, in time-variant scenarios (for example, in monitoring agricultural cycles), this method could lead to alteration of the amplitude ratios between different images and to misclassification of the required features.

In our approach, in order to guarantee a reliable criterion of comparability between a series of images, we impose the conservation of the amplitude ratios, ensuring that the histogram clipping is performed at the same amplitude level for all the elements of the time series.

Under the hypothesis that the calibration step provides perfectly calibrated images, the proposed method guarantees the balance of the channels involved in the RGB composition. The choice of the clip level is guided by electromagnetic backscattering models.

III. RGB PRODUCTS

The rationale described in Section II has been tested on a set of 15 COSMO-SkyMed stripmap images with 3 meters of spatial resolution acquired in the North of Burkina Faso, a semi-arid region where a 3 months wet and a 9 months dry seasons characterize the climate [2]. We loaded on red, green and blue bands the coherence map, the test image and a reference image acquired at the end of the dry season, respectively. The band-color association facilitates the association between the displayed colors and the physical characteristics of the scene. The clip level has been chosen in order to enhance the evolution of vegetation during the year. In Fig. 2 a full resolution detail of the intensity of a single SAR image, acquired in August (during the wet season) is compared with the corresponding MAP3 product.

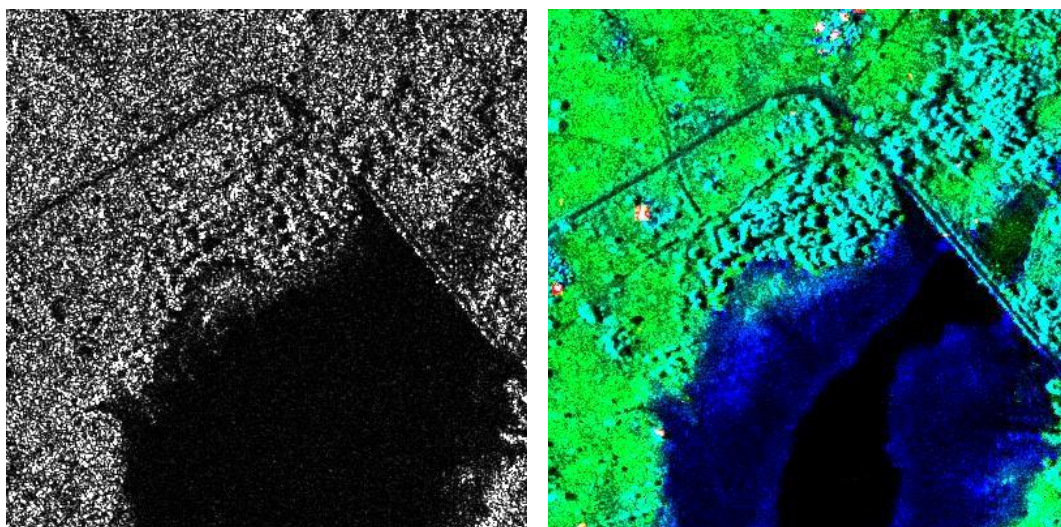


Fig. 2 – Single SAR image intensity (left) and MAP3 result (right).

The interpretation of Fig. 2b, where vegetation is mapped in green and water in blue, does not require any *a priori* knowledge of the electromagnetic mechanisms that govern the formation of the SAR image, despite they were essential for their construction.

An RGB image for each acquisition was provided, allowing a monitoring of the land cover on a 40 x 40 km² area. The proposed approach allows to show the growth of vegetation, because it determines an enhancement of the electromagnetic backscattering during the wet season, as shown in Fig. 3. In the dry season image, the cyan is the dominant color because the electromagnetic response of the two scenes

is almost unchanged, except for the areas in which the counter-season agriculture is exercised.

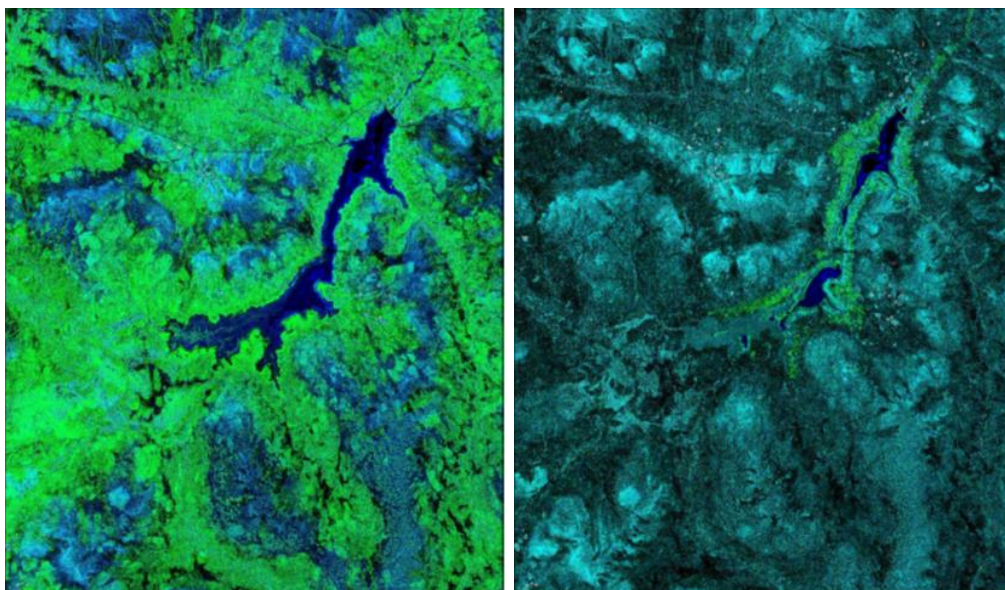


FIG. 3 – Comparison between MAP3 products relative to wet (left) and dry season (right) acquisitions.

IV. CONCLUSION

In this paper we presented a new approach for processing a set of multi-temporal SAR images and producing RGB products. The method is based on three blocks of processing and provides products that can be easily read by potential beneficiaries, with no expertise in electromagnetics or remote sensing. Appropriate electromagnetic models guide the choice of the tuning parameters that allow to adapt the processing to specific applications.

ACKNOWLEDGEMENT

The SAR images were provided by the Italian Space Agency (ASI) under the aegis of the 2007 COSMO-SkyMed AO Project ‘Use of High-Resolution SAR Data for Water Resource Management in Semi-Arid Regions’.

REFERENCES

- [1] V. Madhok and D. A. Landgrebe, “A Process Model for Remote Sensing Data Analysis,” *IEEE Trans. Geosci. Remote Sens.*, vol. 40, no. 3, pp. 680–686, 2002.
- [2] D. Amitrano, G. Di Martino, A. Iodice, G. Ruello, F. Ciervo, M. N. Papa, and Y. Koussoubé, “Effectiveness of High-Resolution SAR for Water Resource Management in Low-Income Semi-Arid Countries,” *Int. J. Remote Sens.*, vol. 35, no. 1, pp. 70–88, 2014.

ELECTROMAGNETIC MODEL FOR SAR SHAPE FROM SHADING

G. Di Martino, A. Di Simone, A. Iodice, D. Riccio, G. Ruello

Department of Electric Engineering and Information Technology,
Università degli Studi di Napoli Federico II, Naples, Italy
gerardo.dimartino@unina.it; al.disimone@studenti.unina.it; {iodice;
daniele.riccio; ruello}@unina.it

Abstract

In this paper we introduce a novel approach to Synthetic Aperture Radar (SAR) Shape from Shading (SfS) based on sound electromagnetic models. In particular, fractal geometry is used to model the shape of natural surfaces, which are here of concern. The electromagnetic scattering mechanisms are described through the Small Perturbation Method (SPM) evaluated for fractal surface models, and a simple SAR image model is used. This direct model is then inverted to recover the local terrain slope and hence the underlying topography. The algorithm is applied to an actual Cosmo/SkyMed SAR image of the Vesuvius Volcano and the main results and limits of the proposed SAR SfS technique are discussed.

Index Terms – Electromagnetic scattering, fractals, shape from shading, Synthetic Aperture Radar.

I. INTRODUCTION

Up to now, many techniques aimed at retrieving surface elevation profiles have been developed, namely stereoscopy [1], interferometry [2], radarclinometry (or shape from shading) [3], [4] and polarimetry [5]. Unlike the other techniques, which require (a minimum of) two complex SAR images possibly acquired at the same time, SfS is applicable when limited data and resources are available – only one intensity image is needed – and a very rough estimate of the topography is required.

In the scientific literature the widespread use of the Lambertian reflectivity function [5] (or its generalization [3]) makes surface modeling unnecessary. However, this model is very inaccurate in describing scattering from natural surfaces in the microwave region, where SAR sensors usually operate [3]. In general, the lack of an adequate electromagnetic modeling step is one of the main weaknesses of existing SfS techniques.

In this paper the general SAR SfS problem is decomposed in two steps: first of all, a direct model linking the SAR image intensity to the parameters of interest, i.e., the local range and azimuth slopes, is developed introducing proper models both for natural surfaces and for electromagnetic scattering description; in particular, we use fractal geometry to describe the shape of natural surfaces [6]. Finally, an inversion procedure is set up in order to invert the forward model and estimate the underlying topography.

II. DIRECT MODELS

In this section the rationale for expressing the link between SAR image intensity and local slopes of the surface is presented. In particular, the proposed direct model is divided in three steps:

- *Surface model*

The natural surface under study is properly modeled using fractal geometry; in particular, a fractional Brownian motion (fBm) is used [6]:

$$\Pr\{z(x, y) - z(x', y') < \bar{\zeta}\} = \frac{1}{\sqrt{2\pi s \tau^H}} \int_{-\infty}^{\bar{\zeta}} \exp\left(-\frac{\zeta^2}{2s^2 \tau^{2H}}\right) d\zeta \quad (1)$$

where τ is the distance between the two considered points of coordinates (x, y) and (x', y') ; H is the Hurst coefficient ($0 < H < 1$); s is the incremental standard deviation.

- *Scattering model*

In general, only approximate analytic solutions to the scattered field are achievable for natural surfaces. In this work the scattering mechanisms are described through the SPM for fBm surfaces because of its simplicity and range of validity adequate to SAR applications [7]:

$$\sigma_{mn}^0 = 2\pi 8k^4 \cos^4 \theta |\beta_{mn}|^2 \frac{S_0}{(2k \sin \theta)^{2+2H}} \quad (2)$$

wherein k is the electromagnetic wavenumber of the incident field; S_0 is the spectral amplitude of the fBm surface; β_{mn} is a reflection coefficient depending on transmitted and received signal polarization and the radar look angle θ .

- *Imaging model*

The intensity of a SAR image can be assumed as the amount of electromagnetic energy backscattered from the resolution cell. Assuming a small-slopes regime for the surface a first-order approximation of the image intensity can be evaluated with regard to the local range slopes of the observed surface p (in a first order approximation no dependence on the azimuth slopes is present [8]):

$$I = G|a_0 + a_1 p| \quad (3)$$

III. MODEL INVERSION

The main objective of shape from shading is to invert Eq. (3) and, consequently, recover the 3-D shape of the illuminated surface. To this aim we propose a two-step approach:

- First, exploiting the independence of SAR image intensity from azimuth local slopes in a first-order approximation (see Eq. (3)), it is

possible to solve Eq. (3) for the unique unknown p , obtaining an initial estimate of the height map through independent slope integration in the range direction. In this step we use the mean value of H estimated from the image using the technique introduced in [8].

- Due to the independent integration in the range direction, the reconstructed DEM presents unnatural patterns along the range axis. Then, in order to reintroduce azimuth slopes and reduce the lineage, we propose a very simple regularization procedure based on Bayesian Minimum Mean Squared Error (MMSE) estimation.

IV. EXPERIMENTAL RESULTS

The result obtained applying the proposed technique on a Cosmo/SkyMed stripmap SAR image (Fig. 1) of the Somma-Vesuvius volcanic complex, close to Naples, Italy, are presented in Fig 2. In particular, profiles of the estimated and real DEMs are reported, where the better estimation result provided by the fractal model with respect to the Lambertian one is clearly visible, especially in the azimuth cut.

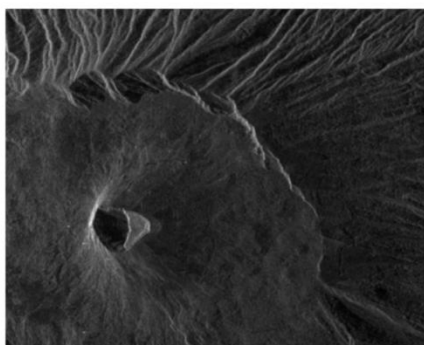
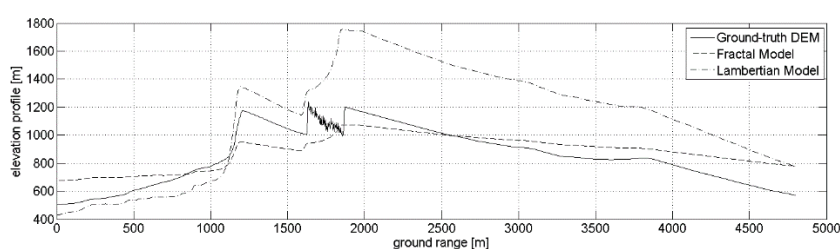
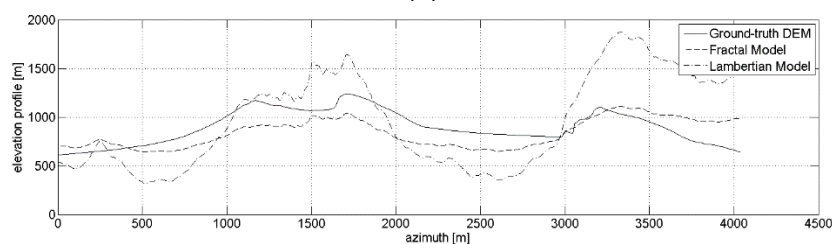


FIG. 1 – Cosmo/SkyMed SAR image of the Vesuvius.



(a)



(b)

FIG. 2 – Range (a) and azimuth (b) cuts comparison of the actual and estimated SfS DEMs using Lambertian and Fractal model.

V. CONCLUSION

In this paper a novel model-based shape-from-shading technique applied to SAR images of natural surfaces has been developed. The contribution of this work is the prominent role of electromagnetic modeling, trying to stimulate a new perspective in the complex world of SAR shape from shading.

The present paper shows that, with a better modeling of surface and scattering mechanisms, a reliable DEM estimation is possible also with very simple and low computational complexity inversion technique.

Before applying the proposed SFS technique, the identification of homogenous segments through segmentation could be a reasonable means to ensure an accurate elevation reconstruction over a wide area.

Another key issue to deal with is speckle [9]; in this direction, a despeckling algorithm suitable for fractal surfaces could be a further development in the near future.

References

- [1] U. R. Dhond and J.K. Aggarwal, "Structure from stereo – a review," *IEEE Transactions on Systems, Man and Cybernetics*, vol. 19, no. 6, pp. 1489-1510, Nov. 1989.
- [2] D. Massonnet and T. Rabaute, "Radar interferometry: limits and potential," *IEEE Trans. Geosci. Remote Sens.*, vol. 31, no. 2, pp. 455-464, 1993.
- [3] D. N. Ostrov, "Boundary Conditions and Fast Algorithms for Surface Reconstructions from Synthetic Aperture Radar Data," *IEEE Trans. Geosci. Remote Sens.*, vol. 37, no. 1, pp. 335-346, Jan. 1999.
- [4] B. K. P. Horn and M. J. Brooks, *Shape From Shading*. Cambridge: MA: MIT Press, 1989.
- [5] X. Chen, C. Wang, and H. Zhang, "DEM Generation Combining SAR Polarimetry and Shape-From-Shading Techniques," *IEEE Geoscience and Remote Sensing Letters*, vol. 6, no. 1, pp. 28-32, Jan. 2009.
- [6] G. Franceschetti and D. Riccio, *Scattering, Natural Surfaces and Fractals*. Burlington: MA: Academic, 2007.
- [7] G. Franceschetti, A. Iodice, S. Maddaluno, and D. Riccio, "A Fractal-Based Theoretical Framework for Retrieval of Surface Parameters from Electromagnetic Backscattering Data," *IEEE Trans. Geosci. Remote Sens.*, vol. 38, no. 2, pp. 641-650, Mar. 2000.
- [8] G. Di Martino, D. Riccio, and I. Zinno, "SAR Imaging of Fractal Surfaces," *IEEE Trans. Geosci. Remote Sens.*, vol. 50, no. 2, pp. 630-644, Feb. 2012.
- [9] G. Di Martino, G. Poggi, D. Riccio, and L. Verdoliva, "Effects of despeckling on the estimation of fractal dimension from SAR images," in *Geoscience and Remote Sensing Symposium (IGARSS)*, 2013, pp. 3950-3953.

TELAER : AN ITALIAN INTERFEROMETRIC AIRBORNE SAR SYSTEM

S.Perna^(1,2), P.Berardino⁽²⁾, C.Esposito^(2,3), G.Fornaro⁽²⁾, A.Gifuni⁽¹⁾,
G.Jackson^(1,2), A.Pauciullo⁽²⁾, R.Lanari⁽²⁾

⁽¹⁾ DI, Università degli Studi di Napoli “Parthenope”
Centro Direzionale Is.C4, Napoli, Italy
[perna,gifuni}@uniparthenope.it](mailto:{perna,gifuni}@uniparthenope.it)

⁽²⁾ IREA, National Research Council
Via Diocleziano 328, Napoli, Italy.
[berardino.p,esposito.c,fornaro.g,jackson.g,pauciullo.a,lanari.r}@irea.cnr.it](mailto:{berardino.p,esposito.c,fornaro.g,jackson.g,pauciullo.a,lanari.r}@irea.cnr.it)

⁽³⁾ DING, Università degli Studi del Sannio
Piazza Roma, 21, Benevento, Italy

Abstract

In this contribution we show the capabilities of the X-band TELAER airborne Synthetic Aperture Radar (SAR) system.

More specifically, this TELAER system has recently been upgraded according to an Italian National Research Council (CNR) funding. Moreover, CNR has entrusted the Institute for Electromagnetic Sensing of the Environment (IREA) for managing all the activities related to such a system upgrading. Thanks to this upgrading, the TELAER SAR system is now equipped with a multi-antenna configuration that allows carrying out single-pass interferometry.

Bench-tests and flight-tests, aimed at evaluating the performances achievable with the upgraded system, were carried in January and February 2013. In this contribution we show some results achieved during these tests.

Index Terms – Synthetic Aperture Radar (SAR), Airborne SAR systems, SAR Interferometry.

I. INTRODUCTION

The aim of this paper is to present the capabilities of the TELAER airborne Synthetic Aperture Radar (SAR) system recently upgraded to the interferometric mode [1].

TELAER is an Italian airborne X-Band SAR system, whose main parameters are listed in Table I. It is mounted onboard a LearJet 35A aircraft. Originally equipped with a single TX/RX antenna, it now operates in single-pass interferometric mode thanks to a system upgrading funded by the CNR, via the MIUR, in the frame of a cooperation with the Italian Agency for Agriculture Subsidy Payments (AGEA). In particular, CNR has entrusted the Institute for Electromagnetic Sensing of the Environment (IREA) for managing all the activities, included the final tests, relevant to the system upgrading. According to such a system upgrading, two additional receiving X-band

antennas have been installed in order to allow, simultaneously, single-pass *Across-Track* and *Along-Track* interferometry [1].

The system upgrading has been completed in January 2013; bench-tests and flight-tests have been then carried out in order to assess the achievable performances. Some preliminary results relevant to these tests are discussed in the next section.

II. BENCH-TESTS AND FLIGHT-TESTS: RESULTS

Before carrying out the flight-tests, bench-tests have been carried out to assess the stability of the upgraded radar system. Amongst these bench-tests, we focus on the antenna measurements carried out in the anechoic chamber of the Dipartimento di Ingegneria of the Università degli Studi di Napoli “Parthenope”. In particular, we have accurately measured the Phase Center (PC) of the three TELAER antennas. This, indeed, has a twofold aim. First, it allows evaluating the flatness of the antenna phase pattern, which is a key constraint in radar applications [2]. Second, during the SAR focusing step [2], accurate knowledge of the antenna PC is necessary to precisely apply motion compensation procedures [3]-[5].

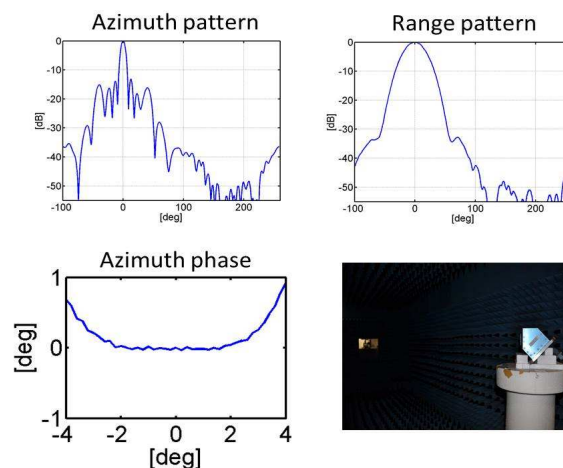


FIGURE 1 Relevant to the measurements carried out in anechoic chamber on one X-band antenna of the TELAER airborne SAR system.

The PC has been evaluated through the method shown in [6]. This allowed obtaining the results reported in the bottom-left plot of Figure 1, where it is shown the antenna phase pattern (in the azimuth direction) measured in the anechoic chamber by placing the Antenna Under Test (AUT) over a rotating column (bottom-right) with the rotation axis passing exactly through the estimated PC. It can be seen that within the azimuth beam (which is about 8° wide) the azimuth phase is very stable, since its variations are on the order of fractions of degree and reach 0.7° only at the very edge of the main beam. Figure 1 shows also the azimuth (top-left) and range patterns (top-right) of the AUT.

Turning to the flight-tests, they were carried out over the Napoli area. Main mission parameters are listed in Table II. Figure 2 shows one

multi-look amplitude image, characterized by a resolution of 4m×4m, of an acquired strip. Figure 3a shows the high resolution (0.5m×0.5m) image relevant to the patch highlighted in Figure 2. Figure 3b shows instead the single-pass interferogram relevant to the patch of Figure 3a. Interestingly, in both Figures 3a and 3b it is possible to identify particular features of the buildings, clearly visible in the corresponding Google Earth image (shown in Fig. 3c) relevant to the considered area.

TABLE I - PARAMETERS OF THE UPGRADED TELAER SAR SYSTEM

Wavelength	0.0314 m
Transmitted Bandwidth	100 – 400 MHz
PRF	200-16000 Hz
Standard Swath width	2-10 Km
# of receiving antennas	3
Resolution	0.5-5 m
Polarization	HH

TABLE II - MISSION PARAMETERS

Height of ambiguity at mid range	83 m
Mean aircraft altitude	4000 m
Mean aircraft velocity	125 m/s
Look angle at mid range	45°
Mid slant range	5260 m



FIGURE 2 –Amplitude multi-look image of a 7 km long patch of the entire (22 km) acquired strip. Ground range extension: 2 km. Geometric resolution: 4m×4m.

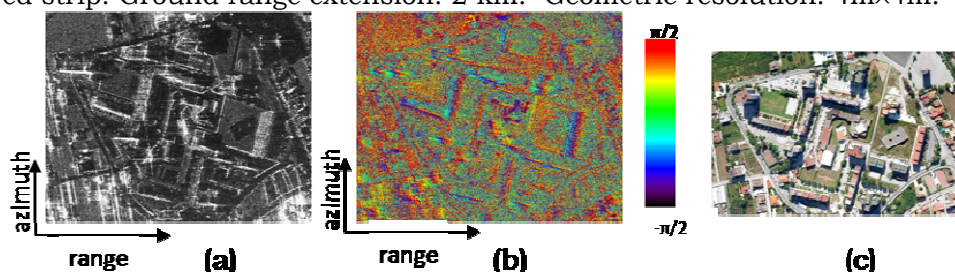


FIGURE 3 –High resolution amplitude image (a) and interferogram (b) relevant to the area highlighted in the bottom-left part of Fig.2. Geometric resolution: 0.5m×0.5m. Google Earth image of the same area (c).

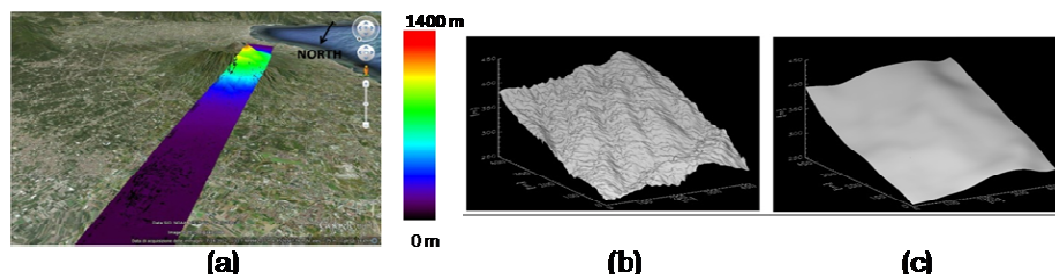


FIGURE 4 –TELAER InSAR DEM (1m×1m of resolution) relevant to the entire strip acquired by the system (a); the DEM has been geocoded and superimposed on a Google Earth image. Comparison between the TELAER InSAR DEM (b) and the SRTM DEM (c) relevant to a small patch 400m×400m of the strip shown in (a).

The achieved $1\text{m}\times 1\text{m}$ final InSAR Digital elevation Model (DEM) is shown in Figure 4a: it is relevant to the entire (22 km) acquired strip and it is superimposed on a Google Earth image. To have just an idea of the achieved resolution and accuracy, we present in Figures 4b and 4c a comparison between the obtained DEM and the easily available world-wide Shuttle Radar Topography Mission (SRTM) one (characterized by $90\text{m}\times 90\text{m}$ resolution). A deeper analysis on the vertical and horizontal accuracies of the achieved DEM has been carried out by exploiting GPS measurements on corner reflectors, and an available LIDAR DEM of the same area. Corresponding results will be included in the final contribution.

III. CONCLUSION

We have described some results relevant to the bench-tests and flight-tests carried out in the frame of the recent upgrading of the TELAER airborne SAR system.

In particular, it has been shown that the phase pattern of the TELAER antennas is very stable, since its variations within the main lobe are on the order of fractions of degree.

Moreover, we have shown some results relevant to a single-pass InSAR acquisition carried out, during the flight-tests, over the Somma Vesuvius volcanic complex. In particular, it has been shown that the obtained high resolution (that is, $0.5\text{m}\times 0.5\text{m}$) interferograms are extremely accurate. Moreover, we have shown the achieved single pass InSAR DEM ($1\text{m}\times 1\text{m}$ of resolution) of the illuminated area.

The shown single-pass interferometric capabilities, along with the intrinsic flexibility of airborne platforms, render the TELAER airborne SAR system a powerful instrument for fast generation of high resolution DEMs, even in natural disaster scenarios. Accordingly, this system can play today a key role for the monitoring of natural hazards, especially if properly integrated with other remote sensing sensors.

REFERENCES

- [1] S. Perna et al, "Capabilities of the TELAER airborne SAR system upgraded to the multi-antenna mode", *In Proceedings IGARSS 2012 Symposium*, Munich, 1545 – 1548, 2012.
- [2] G. Franceschetti, and R.Lanari, Synthetic Aperture Radar Processing, *CRC PRESS*, New York, 1999.
- [3] G.Fornaro, G.Franceschetti, S.Perna, "Motion Compensation Errors: Effects on the Accuracy of Airborne SAR Images," *IEEE Trans. Aerosp. Electron. Syst.*, 41, 2005.
- [4] G.Fornaro, G.Franceschetti, S.Perna, "On Center-Beam Approximation in SAR Motion Compensation", *IEEE Geosci. Remote Sens. Lett.*, vol. 3, Issue 2, pp. 276 – 280, 2006.
- [5] S.Perna, V.Zamparelli, A.Pauciullo, G.Fornaro, "Azimuth-to-Frequency Mapping in Airborne SAR Data Corrupted by Uncompensated Motion Errors," *IEEE Geosci. Remote Sens. Lett.*, 10, 6, 2013.
- [6] S.Perna, C.Esposito, A.Pauciullo, P.Romano, A.Gifuni, "A fast approach for antenna phase center evaluation", *accepted to IGARSS 2014 Symposium*, 2014.

GNSS-R SIGNAL STRENGTH SENSITIVITY TO SOIL MOISTURE

R. Notarpietro, Y. Pei, P. Savi

Department of Electronic and Telecommunications, Politecnico di
Torino, Corso Duca degli Abruzzi 24, 10129 Torino, Italy,
riccardo.notarpietro@polito.it

Abstract

GNSS Reflectometry is an emerging technique used for the remote sensing of soil surface. In this work, a bi-static radar equation method was implemented for remote sensing of soil. A portable GNSS-R receiver was used during various in situ measurements campaign. Left Hand Circularly Polarized (LH) reflected signals were processed to extract Delay Doppler Maps (DDMs) and corresponding Delay Waveforms (DWs) by means of an open-loop approach. Signal to Noise Ratios (SNRs) time series were estimated from non-coherent integrated Delay Waveforms. The signal strength sensitivity to different soil moisture levels, i.e. different SNRs levels in input, was verified.

Index Terms – GNSS-Reflectometry, Remote Sensing, Delay Doppler Maps.

I. INTRODUCTION

Recently, the use of reflected Global Navigation Satellite Systems (GNSS) signals to extract information about the Earth's surface, named GNSS Reflectometry (GNSS-R) has been introduced [1-3]. Exploiting a bistatic geometry approach, the GNSS satellites act as transmitters while an aircraft or a Low Earth Orbit satellite are the receiving platforms. Comparing it with other existing satellite scatterometric, radiometric and radar applications, GNSS-R remote sensing has several advantages: its passive working principle requires no transmitters except GNSS satellites; thanks to the global and full-time coverage provided by GNSS satellites, very dense multi-static radar measurements at L-band can be performed; the technique works in all-weather conditions since L-band signals are used.

In this paper, GNSS reflected signals measured on different types of terrain by a portable GNSS-R receiver based on a Software Defined Radio solution are analyzed. A receiver connected to a down-looking Left Hand Circularly Polarized antenna for the reception of reflected L1 GPS signals was developed. Digital samples collected were processed into Delay Doppler Maps (DDMs) and Delay Waveforms exploiting a fully open loop scheme, in order to evaluate Signal to Noise Ratios

(SNRs) time series, without the necessity to wait for standard GNSS close loop acquisition and tracking.

The system was tested with in situ measurements on a mostly sand terrain, whose water content was varied from dry to completely wet conditions, to evaluate its effectiveness in detecting different soil moisture levels.

II. MEASUREMENT SYSTEM

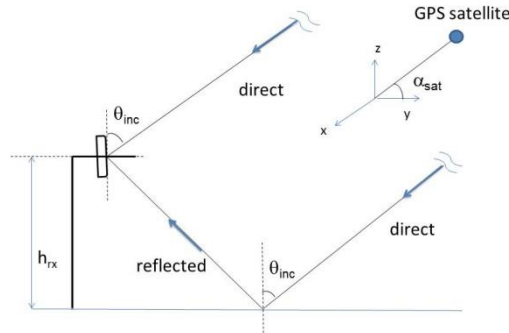


FIG. 1 – Sketch of the geometry

GNSS-R uses a bi-static radar geometry, since the transmitter and the receiver are not co-located. In our experiment, GPS satellites are seen as the active sources-transmitters, while the receiver was placed at a given height from the terrain (see Figure 1). A nadir-pointing antenna collecting reflected Left Hand Circularly Polarized GPS signals was mounted on the receiver. The total received power P_S (coherent signal power) can be expressed by the following simplified equation [4]:

$$P_S = \frac{\Phi_{peak} \cdot P_N}{G_D} \tag{1}$$

being Φ_{peak} the absolute Signal to Noise ratio defined as the ratio between the pure signal and the noise powers, that can be evaluated considering the normalized Delay Waveform; G_D is the processing gain (~ 30.1 dB) due to the de-spread of the GPS Coarse Acquisition code; P_N is the input noise power:

$$P_N = kT_N B_w \tag{2}$$

where k is the Boltzmann’s constant, $k=1.380 \times 10^{-23}$ J/K, T_N the estimate of the receiver noise equivalent temperature and $B_w=1/T_I$ is the signal bandwidth determined by the coherent integration time T_I (1 ms in our case). In particular, the noise floor $\overline{P_N}$ can be estimated as the DW

averaged level computed over a region of delays where no signal Φ_{peak} is present. Therefore, the SNR obtained by the measurement can be easily derived as follows:

$$\Phi_{peak} = \frac{1 - \overline{P_N}}{\overline{P_N}}, \quad (3)$$

Data stored during the measurements were post-processed implementing an open-loop GPS data acquisition. For each available satellite, correlation of raw data with a replica of the transmitted GPS C/A code locally generated by a software routine, in both delay and Doppler frequency shift domains was evaluated. Non-coherent integration (500ms was chosen) was performed by summing several consecutive DDM in order to mitigate the fading or speckle noise caused by the random scattering. From the non-coherently integrated DDM, the Delay Waveform (DW) - the entire correlation function containing the maximum value evaluated in function of the time (range) - was extracted. Corresponding SNR time series were estimated every 500ms.

III. RESULTS

Several measurements campaign were performed in order to verify the sensitivity of the receiver (in terms of estimated SNRs level) to different soil moisture levels. The measurement setup is shown in Figure 2 (left panel). The receiver was placed at a height of 3m from the ground. During the experiment, three consecutive data acquisitions of 40 s each were performed. In the first time slot, the soil was almost dry, then, in the second time slot, the condition was changed from dry to almost wet, and in the third time slot to soaking wet. Figure 2 (right panel) shows the estimated positions of specular reflection points for each satellite in view. The black circle is the LH receiving antenna footprint projected into the ground. Blue circles are the First Fresnel zone areas related to the position of each specular reflection point. The wet area was between the points related to signals coming from GPS Space Vehicle (PRN) 24 (black dots) and PRN15 (green dots). The movement of the specular points is shown with a sample time of 5 min, being the completely bold dot the first one. In Figure 3 the corresponding SNRs time series are shown. Data from time interval spent in changing the soil conditions are not shown. During dry soil conditions SNRs were small for both satellite signals, while they were increasing coherently with the terrain moistening.

IV. CONCLUSION

Reflected GPS signals were collected by a fully software receiver in a static condition by using a LH antenna. An open loop approach was

applied for calculating SNR of reflected GPS signals. A good correlation between the values of SNR and the flooding state of the terrain was obtained. Other measurements campaign are foreseen using both LH and RH polarization, and an algorithm for permittivity retrieval will be tested.

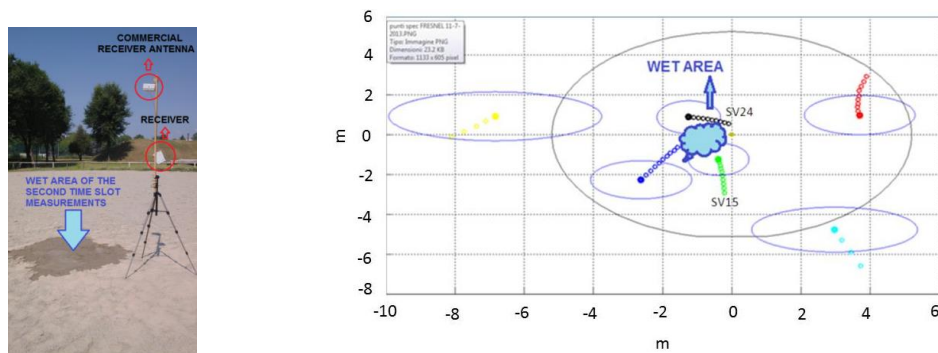


FIG. 2 – Measurements setup (left panel). Distance of specular reflection points from the receiver (right panel).

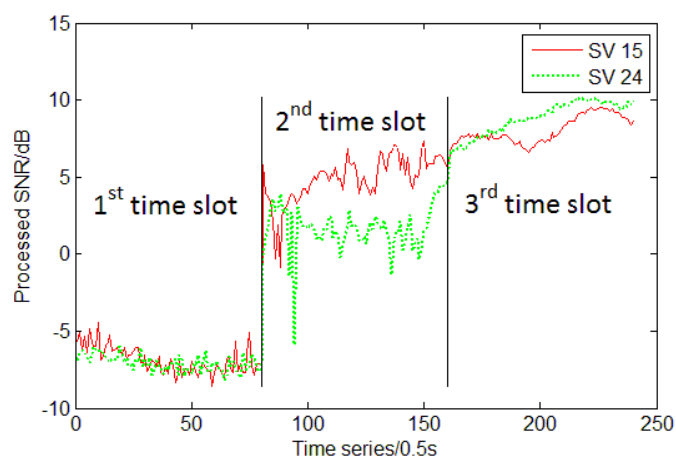


FIG. 3 – SNR time series (red: satellite 15, green: satellite 24).

REFERENCES

- [1] S. Jin, E. Cardellach, F. Xie, , “GNSS Remote Sensing. Theory, Methods and Applications,” Springer, 2014.
- [2] A. Egido, M. Caparrini, G. Ruffini, S. Paloscia, E. Santi, L. Guerriero, N. Pierdicca, N. Floury, “Global navigation satellite systems reflectometry as a remote sensing tool for agriculture,” *Remote Sensing*, vol. 4, pp. 2356-2372, 2012.
- [3] N. Rodriguez-Alvarez, A. Camps, M. Vall-llossera, et al., , “ Land geophysical parameters retrieval using the Interference Pattern GNSS-R technique,” *IEEE Transactions on Geoscience and Remote Sensing*, vol. 49, pp. 71–84, 2011.
- [4] Y. Pei, R. Notarpietro, P. Savi, M. Cucca, F. Dosis, “ A fully software GNSS-R receiver for soil monitoring,” *International Journal of Remote Sensing*, vol. 35 n. 6, pp. 2378-2391, 2014.

MODELING THE POLARIMETRIC RESPONSE TO ATMOSPHERIC PRECIPITATION ON SYNTHETIC APERTURE RADAR IMAGERY OVER OCEAN

F. Polverari^{1,2}, S. Mori^{1,2}, L. Pulvirenti^{1,3}, N. Pierdicca¹,
F.S. Marzano^{1,2}

(¹) Department of Information Engineering, Electronics and Telecommunications (DIET), Sapienza University of Rome, Via Eudossiana 18, 00184 Rome, Italy
polverari@diet.uniroma1.it

(²) CETEMPS, University of L' Aquila, Via Vetoio 1, 67100 L'Aquila, Italy
marzano@diet.uniroma1.it

(³) CIMA Research Foundation, Via Armando Magliotto 2, 17100 Savona, Italy
luca.pulvirenti@cimafoundation.org

Abstract

The polarimetric synthetic aperture radar (SAR) response at frequencies above the C-band, has proved to be affected by atmospheric events so that they can be used to extract information useful for studying weather conditions and climate changes. A microwave model for simulating the Normalized Radar Cross Section (NRCS) over sea surface, due to atmospheric precipitation, has been developed based on the model set up over bare soil. In this work, the main results obtained by considering a realistic scenario, using the wind vectors extracted by the System for Atmospheric Modeling (SAM) data to realize the synthetic surface model, are shown. The sea surface response has been performed using the SEAWIND2 software, which is able to simulate the scatterometer backscattering coefficient.

Index Terms – Atmospheric precipitation, polarimetric modeling, polarimetric synthetic aperture radar, sea surface.

I. INTRODUCTION

Spaceborne synthetic aperture radars (SARs) allow the observation of the Earth surface at very high spatial resolution of about few hundred of meter. The development of fully-polarimetric SAR systems, which take into account all the different polarization states of the electromagnetic field of the received and transmitted signals, allows to obtain more accurate information of the scattering properties of the target. Thus, in many applications of Earth observation, polarimetric SAR data offer an opportunity to perform a complete characterization and quantitative analysis of the observed scene. In this respect,

polarimetric SAR data have shown a good potentiality to better understand the atmospheric processes especially in retrieving precipitation measurements using X-band SARs [1], as well as in identifying different species of cloud hydrometeors using Ka-band. In particular, even if SARs are not designed for atmospheric observations, the response of such operating systems, at frequency above the C-band, have demonstrated to be significantly affected by atmospheric precipitation occurrence within the field of view, as observed by [1], [2].

II. POLARIMETRIC SAR RESPONSE MODEL

The SAR response due to precipitation has two main contributions such as: the surface contribution, which is the radar return obtained from the ground and the volume contribution obtained by the scattering of the hydrometeors.

To describe such effects, we have considered a two-dimensional shape model of the precipitating cell, where the cell is supposed to be divided in two layers: the liquid and frozen hydrometeors. Assuming a wave-plane incident approximation, a rectilinear coordinate l - t in the cross-track plane x - z can be defined such that l is the longitudinal coordinate along the plane-wave direction and t is the transverse coordinate with respect to l . The model is shown in Fig. (1).

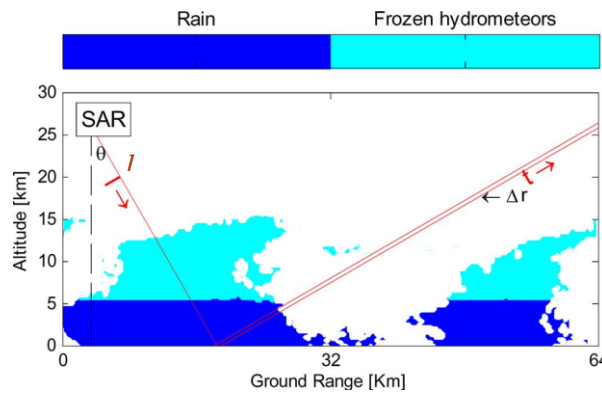


FIG. 1 – Schematic view of the used SAR response model due to a liquid and snow precipitation cross section. The two-layers distribution consists of: “precipitating liquid water” (in blue) below the “precipitating ice water”, (cyan).

In this perspective, considering the two-way path attenuation factor through the precipitating atmosphere, the polarimetric Normalized Radar Cross Section observed by the SAR can be defined as follows [3]:

$$\sigma_{SARpq}(x, y) = 4\pi \left\langle \left| S_{SARpq} \right|^2 \right\rangle = \sigma_{SFRpq}(x, y) + \sigma_{VOLpq}(x, y) \tag{1}$$

where p and q represent the radar receive and transmit linear polarization, S_{SARpq} is the element of the backscattering complex matrix, the $\langle \rangle$ is the ensemble averaging and σ_{SFRpq} , σ_{VOLpq} are the "surface-

driven" and the "volume-driven" polarimetric backscattering sections, respectively. The detailed expression of both contributions is given by

$$\sigma_{SRFpq}(x, y) = \sigma_{pq}^{ground}(x, y) \exp \left(- \int_{\Delta l(x,y)} k_{qq}(l) dl - \int_{\Delta l(x,y)} k_{pp}(l) dl \right) dt \quad (2)$$

$$\sigma_{VOLpq}(x, y) = \text{sen } \theta \int_{\Delta l(x,y)} \eta_{pq}(t) \exp \left(- \int_{\Delta l(t)} k_{qq}(l) dl - \int_{\Delta l(t)} k_{pp}(l) dl \right) dt \quad (3)$$

where σ_{pq}^{ground} is the surface backscattering coefficient, η_{pq} is the radar volume reflectivity, k is the specific attenuation, θ is the off-nadir angle [deg], whereas Δl and Δt are the longitudinal (radial) and transverse path increments along l and t , respectively.

Many recent works have discussed the SAR response at X-band due to the large availability of new data offered by missions equipped with instruments operating in this band (e.g. TerraSAR-X/TanDEM-X, COSMO-SkyMed missions). These analyses have been performed considering the SAR return over bare soil in order to avoid the complex effects of other kind of surfaces [3]. However, bare soil is not the unique scenario in which the SAR systems can operate, thus, we have continued this analysis with the aim to model the polarimetric SAR response at both X and Ka band when different surfaces occur. In particular, we have focused our attention to the effects of sea surface.

III. SENSITIVITY ANALYSIS TO THE SEA SURFACE AND CONCLUSIONS

To develop a realistic surface model, we have used the System for Atmospheric Modeling (SAM) data referring to the experiment conducted for the Kwajalein Atoll (Marshall Islands) during 23 July-15 September 1999 [4]. In particular, the SAM sea-surface wind vectors over ocean have been used to simulate the sea surface response. Such response has been realized using the SEAWIND2 software [5], which is able to provide scatterometer numerical simulations using a two-scale model. The obtained results of the surface response are shown in Fig 2.

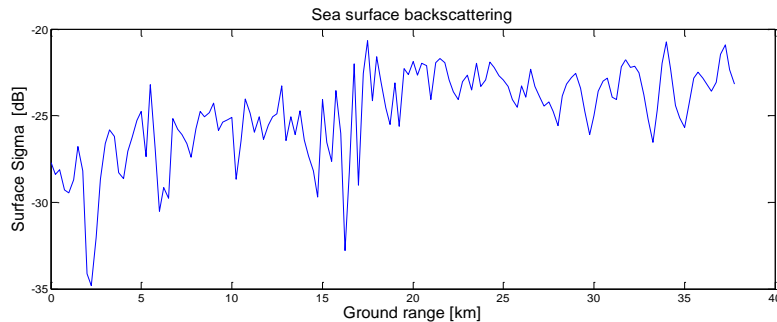


FIG. 2 – Sea surface response at X-band and hh polarization

The simulated polarimetric SAR response due to a uniform-shaped cell system horizontally delimited by $x_L = 24$ km and $x_R = 30$ km, in hh polarization for the described surfaces, is illustrated in Fig. 3.

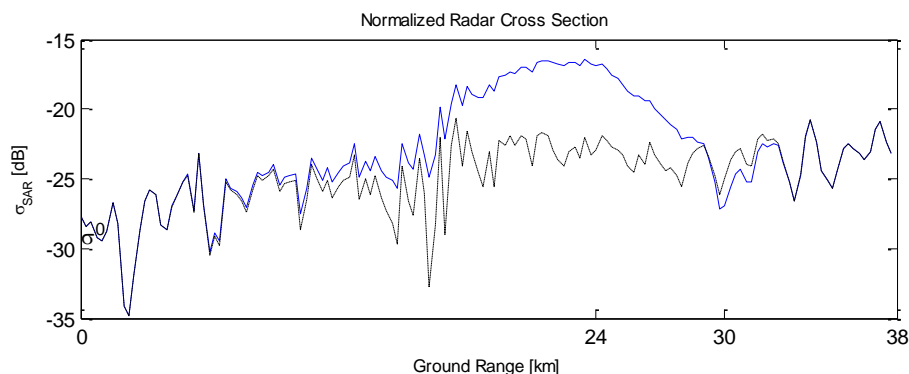


FIG. 3 – Polarimetric SAR response over sea surface (blue) at X-band and hh polarization compared to the surface response (black).

The NRCS trend shows values greater than the background σ_{ground} due to the volume scattering from cloud-top hydrometeors. Moving within the rain-cloud cell, the NRCS decreases since the backscattering is attenuated by rain and it approaches to a minimum value. Once the signal leaves the cloud cell, the NRCS returns to the background value. This trend is very similar to the SAR response over land but it is different from the obtained values.

In conclusion, the proposed model is able to characterize the SAR response due to atmospheric precipitation over sea in a realistic surface scenario so that it can be useful for future applications and studies.

IV. REFERENCES

- [1] Atlas D., R.K. Moore, "The measurement of precipitation with synthetic aperture radar", *J. Atmos. and Ocean Tech.*, vol. 4, pp. 368-376, 1987
- [2] Marzano, F.S.; Mori, S.; Weinman, J.A., "Evidence of Rainfall Signatures on X-Band Synthetic Aperture Radar Imagery Over Land", *Geoscience and Remote Sensing, IEEE Transactions on*, vol.48, no.2, pp.950,964, Feb. 2010
- [3] Marzano, F.S.; Mori, S.; Weinman, J.A.; Montopoli, M., "Modeling Polarimetric Response of Spaceborne Synthetic Aperture Radar Due to Precipitating Clouds From X- to Ka-Band", *Geoscience and Remote Sensing, IEEE Transactions on*, vol.50, no.3, pp.687,703, March 2012
- [4] P. N. Blossey, C. S. Bretherton, J. Cetrone, and M. Khairoutdinov, "Cloudresolving model simulations of KWAJEX: Model sensitivities and comparisons with satellite and radar observations," *J. Atmos. Sci.*, vol. 64, no. 5, pp. 1488–1508, 2007
- [5] Pierdicca, N.; Pulvirenti, L., "Comparing Scatterometric and Radiometric Simulations With Geophysical Model Functions to Tune a Sea Wave Spectrum Model", *Geoscience and Remote Sensing, IEEE Transactions on*, vol.46, no.11, pp.3756,3767, Nov. 2008

MONITORING OF TISSUE SHRINKAGE DURING A MICROWAVE THERMAL ABLATION PROCEDURE

L. Farina⁽¹⁾, N. Weiss⁽²⁾, Y. Nissenbaum⁽³⁾, M. Cavagnaro⁽¹⁾, V. Lopresto⁽⁴⁾, R. Pinto⁽⁴⁾, N. Tosoratti⁽⁵⁾, C. Amabile⁽⁵⁾, S. Cassarino⁽⁵⁾, S.N. Goldberg⁽³⁾⁽⁶⁾

⁽¹⁾ Dept of Information Engineering, Electronics and Telecommunications, Sapienza University of Rome, Roma, Italy
farina@diet.uniroma1.it

⁽²⁾ Dept of Biomedical Engineering, Technion IIT, Haifa, Israel

⁽³⁾ Dept of Radiology, Hadassah Medical Center, Hebrew University, Jerusalem, Israel

⁽⁴⁾ Technical Unit of Radiation Biology and Human Health, Casaccia Research Centre, ENEA, Rome, Italy

⁽⁵⁾ R&D Unit, HS HOSPITAL SERVICE SpA, Aprilia, Italy

⁽⁶⁾ Dept of Radiology, Beth Israel Deaconess Medical Center, Boston, MA, USA

Abstract

The purpose of this study was to investigate the structural and dynamical changes that occur in a biologic tissue during a microwave ablation treatment, with particular focus on the contraction phenomenon observed in clinical practice and in experimental investigations. The experiments were conducted inserting an interstitial microwave antenna in specimens of ex vivo bovine liver and radiating different power levels (20 - 80 W) for 10 minutes. 2 to 8 lead markers ($d = 1.4 \pm 0.1$ mm) were placed into the tissue, close to the antenna, and were tracked in real-time under CT control. The collected images demonstrate that the tissue shrinkage is the result of a complex and hardly predictable rotatory and translational motion, strictly linked with the heterogeneous nature of the biological tissue.

Index Terms – Ex vivo studies, Microwave thermal ablation, Tissue shrinkage, X-ray CT imaging

I. INTRODUCTION

Microwave (MW) thermal ablation is a minimally-invasive procedure used in the treatment of unresectable tumors. Thermal ablation therapies rely on the interaction between a physical energy and the tissue to heat the target cells up to irreversible injury: irreversible cellular damage is obtained increasing the tissue temperature to 46 °C for 60 minutes or to 50 – 52 °C for 4 - 6 minutes. Increasing the temperature up to 60 °C leads to almost instantaneous coagulation and above 100 °C the tissue boils, vaporizes, and carbonizes. In MW ablation the heat source is an electromagnetic field in the microwave frequency range (typically 915 MHz or 2.45 GHz) [1].

Great accuracy in the delivery of the microwave electromagnetic field and a well-understanding of the behavior of the biological tissue during the heat treatment is required to control the ablated volume and destroy as less normal tissue as possible. To this end, recent research has been devoted to characterization of how dielectric and thermal properties change as a function of the increasing temperature [2]-[4]. However, in the clinical practice and in experimental investigations, tissue shrinkage was observed and reported showing that the zone of ablation measured at the end of the thermal procedure probably corresponds to a different and greater area of the underlying tissue [5]-[7].

This study investigates the structural and dynamical changes that occur in a biological tissue during a microwave ablation treatment in real-time. To this end, spherical lead markers had been placed into the tissue close to the radiating antenna, and their motion has been tracked during the heating phase of treatment by CT scanning. The experimental set-up was optimized at the Technical Unit of Radiation Biology and Human Health (UT-BIORAD), ENEA Casaccia (Italy), while the experiments under CT controls have been carried out at the Applied Radiology Laboratory, Hadassah Hebrew University Medical Center (Israel).

II. MATERIALS AND METHODS

An internally cooled 14G MW ablation antenna (HS Amica probe 14G, HS Hospital Service S.p.A., Rome, Italy) was used. This applicator is made by an asymmetrical dipole with a miniaturized choke, which limits the back heating effects, and a pointed capacitive cap, that allows an easier insertion of the applicator [8]. The applicator is internally cooled via a fully automated peristaltic pump and connected to a generator (HS Amica GEN H 1.0, HS Hospital Service S.p.A, Rome, Italy) via a coaxial cable.

Before the CT trials, the experimental set-up was optimized by identifying spherical lead markers which would not influence the antenna behavior nor the temperature distribution, and at the same time should be easily identifiable in the CT images and easily located in pre-defined positions around the radiating antenna. As a result of the set-up optimization, a plastic box, substantially transparent to MW radiation, was designed to contain the tissue specimen and provide an accurate and repeatable positioning both of the antenna and markers. The plastic box was constructed to permit the straightforward insertion of the MW antenna parallel to the working plane; moreover, a grid of holes was made on three sides of the box allowing reliably placements of the markers in several defined positions. The selected markers were spherical in shape ($d = 1.4 \pm 0.1$ mm). An optimum number between 2 to 8 was considered to track the tissue modifications within the zone of maximum power deposition (and hence region of greatest tissue change).

In the real-time experimental trials, the set-up was placed into a CT gantry (Brilliance iCT Philips Healthcare, Cleveland, OH, USA), and the MW antenna was allowed to radiate different power levels (20 - 80 W) for 10 minutes. CT scans were obtained every 29 seconds, thus allowing to dynamically track the markers movements during the 10 minutes ablation procedure. Finally, the specimen was extracted and sectioned along the antenna axis to visually evaluate the obtained ablated area.

III. RESULTS

Although a local overheating of the lead markers and of the surrounding tissue was observed, the area involved was very small so that it could be concluded that the markers do not influence the antenna behavior, nor the shape of the radiated electromagnetic field or the ablated zone.

Fig. 1 shows two CT images referring to an experiment conducted placing two markers close to the antenna, and radiating 60 W for 10 minutes. The two CT scans show a slice orthogonal to the antenna axis before the beginning of the ablation procedure, and at the end of the heating time. The white dots in the figure represent the more reflecting objects, i.e. the antenna (central dot) and the two markers. Comparing the two images, a complex rotatory displacement can be noted.

In order to better investigate the behavior of the tissue, the collected data were processed with a purposely developed MATLAB routine with the aim of tracking the 3D markers motion as a function of time (Fig. 2).

IV. CONCLUSIONS

The structural changes undergone by a biological tissue during a MW thermal ablation procedure have been recorded through real time CT monitoring. Results show that these changes are linked to a complex rotatory phenomenon, which finally results in the shrinkage of the treated biological tissue. These complex modifications of the tissue close to a radiating antenna will likely need to be taken into account for future methods of real-time ablation monitoring and improved assessment of thermal ablation treatments efficacy.

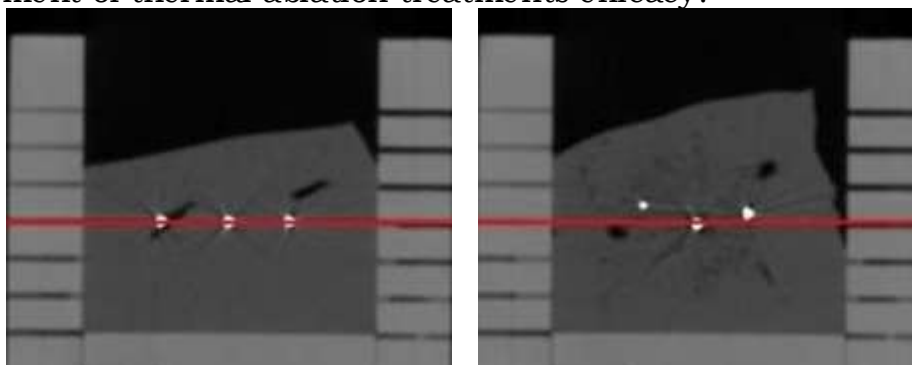


FIG. 1 – CT images obtained during a 60 W MW ablation procedure. (a) $t = 0$ s, beginning of the experiment; (b) $t = 600$ s, end of the experiment.

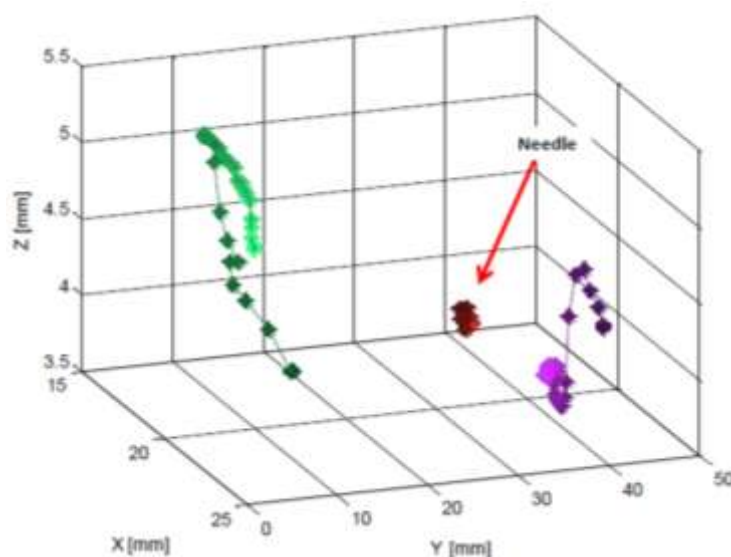


FIG. 2 – 3D view of the temporal kinetic of the markers during a 60 W MW ablation procedure (darker color at the beginning of the experiment).

REFERENCES

- [1] M. Ahmed, C.L. Brace, F.T. Lee, Jr and S.N. Goldberg “Principles of and Advances in Percutaneous Ablation,” *Radiology*, vol. 258(2), pp.351-369, 2011.
- [2] D. Yang, M.C. Converse, D.M. Mahvi and J.G. Webster “Measurement and Analysis of Tissue Temperature During Microwave Liver Ablation,” *IEEE Transactions on Biomedical Engineering*, vol. 54(1), pp. 1382-1388, 2011.
- [3] Z. Ji and C.L. Brace “Expanded modeling of temperature-dependent dielectric properties for microwave thermal ablation,” *Physics in Medicine and Biology*, vol.56, pp. 5249– 5264, 2011.
- [4] V. Lopresto, R. Pinto and M. Cavagnaro “Experimental characterisation of the thermal lesion induced by microwave ablation,” *International Journal of Hyperthermia*, vol. 30(2), pp. 110-118, March 2014.
- [5] C.L. Brace, T.A. Diaz, J.L. Hinshaw and F.L. Lee Jr “Tissue Contraction Caused by Radiofrequency and Microwave Ablation: A Laboratory Study in Liver and Lung”, *Journal of Vascular and Interventional Radiology*, vol. 21, pp. 1280–1286, 2010.
- [6] C.M. Sommer, S.A. Sommer, T. Mokry, T. Gockner, D. Gnutzmann, N. Bellemann et al. “Quantification of tissue shrinkage and dehydration caused by microwave ablation: experimental study in kidneys for the estimation of effective coagulation volume,” *Journal of Vascular and Interventional Radiology*, vol. 24, pp. 1241- 1248, 2013.
- [7] C. Rossmann, E. Garrett-Mayer, F. Rattay and D. Haemmerich “Dynamics of tissue shrinkage during ablative temperature exposures,” *Physiological Measurement*, vol. 35, pp. 55-67, 2014.
- [8] M. Cavagnaro, C. Amabile, P. Bernardi, S. Pisa and N. Tosoratti “A Minimally Invasive Antenna for Microwave Ablation Therapies: Design, Performances, and Experimental Assessment,” *IEEE Transactions on Biomedical Engineering*, vol. 58, pp. 949-959, 2011.

NANOSCALE IMAGING THROUGH OPTICAL FIBER EXTRINSIC MICRO-CAVITY SCANNING MICROSCOPY

A. Di Donato⁽¹⁾, T. Pietrangelo⁽²⁾, D. Mencarelli⁽¹⁾, M. Farina⁽¹⁾

⁽¹⁾ Department of Information Engineering, Ancona Polytechnic University of Marche, 60131 Ancona, Italy

⁽²⁾ Department of Neuroscience and Imaging, Università “G. d’Annunzio”, Chieti, Italy
a.didonato@univpm.it

Abstract

In this work we present a novel kind of scanning probe microscope carried out through an optical fiber extrinsic micro-cavity. The micro-cavity is realized by approaching a single mode fiber to a sample placed on piezo-scanner. The probe is fed by a low-coherence source and measurement of the reflected optical intensity is acquired by optical spectrum analyzer. The transverse resolution is not defined by the numerical aperture of the fiber and consequently by the conventional Rayleigh limit, but it is a function of the transverse electromagnetic field inside the micro-cavity. The lens-free system paves the way towards quantitative measurements not only in air but also in liquid environment.

Index Terms – Scanning Microscopy, Optical Micro-Cavity, Infrared Imaging, Fiber Optics.

I. INTRODUCTION

Thanks to their high sensitivity, Fabry-Perot optical cavities have always been applied in the realization of sensors. They were also exploited to measure refractive index of optical glasses, to realize sensors with sub-nanometer resolution, and lastly in scanning probe microscopy [1-3], to monitor the displacement of cantilevers. This work describes a scanning probe microscopy technique based on optical fiber micro-cavity, in which a cleaved single mode fiber is approached to a surface under investigation. The interaction between the sample and probe occurs at distance of tens of microns. The interfering signal directly comes from the micro-cavity in which the diffracted field experiences multiple reflections and interferences. Contrast phase images, reflectivity and topographic information can be investigated by means of the optical fiber itself without the use of lens. Variations of cavity response are induced by changes of the surface permittivity and micro-cavity dimension. The main electromagnetic parameters change periodically making the relation between them and the physical quantity to be measured, non-linear. Although the technique proposed features some analogies with similar scanning techniques, such as Synthetic Aperture Radars, Spectral Optical Coherence Tomography

(OCT) or Scanning Near-Field Optical Microscopy (SNOM) [4,5], it has some aspects that distinguish it from these.

II. THE SYSTEM

In Fig. 1 we report the optical system for the scanning probe microscope. A SLED diode source at 850 nm (bandwidth FWHM = 40 nm) feeds a broad band directional coupler that provides separation between transmitted and reflected waves. The latter is split by a further coupler that directs the signal to a photo-detector and an Optical Spectrum Analyzer (OSA) with a resolution of about 0.23 nm. The sample is placed on a piezo-scanner that controls the position with nanometric resolution in the plane and in the normal direction. The cleaved fiber (Numerical Aperture = 0.10 – 0.14, Mode Field Diameter = 5.6 μm) is mounted on a fixed head. The piezo approaches the sample making a cavity with dimension of tens of microns.

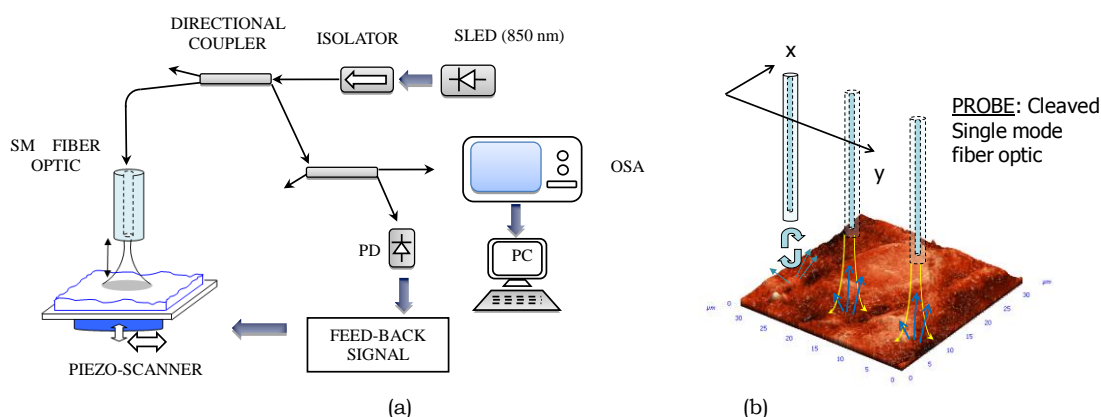


FIG. 1 – Micro-Cavity Scanning Probe set-up.

In Fig. 2 we report the data acquisition process. The spectrum acquired at each point is analyzed in the time domain, following a method similar to the one introduced in Scanning Microwave Microscopy and in a previous work [6]. By recording the behavior of the peak of the cavity response in the time domain, we can acquire contrast phase information. The latter is a function of the effective refractive index of the sample, as well as of the surface topography, according to the relation introduced in [7]. The spectrum acquired by the OSA in the wavelength domain is mapped to the spatial frequency domain, interpolated by a polynomial algorithm and transformed into time/spatial domain. Following this method we can describe the behavior of the micro-cavity, and in particular changes of the peak-amplitude and peak-position of the spatial domain response, due to variations of the fiber-sample distance and surface permittivity.

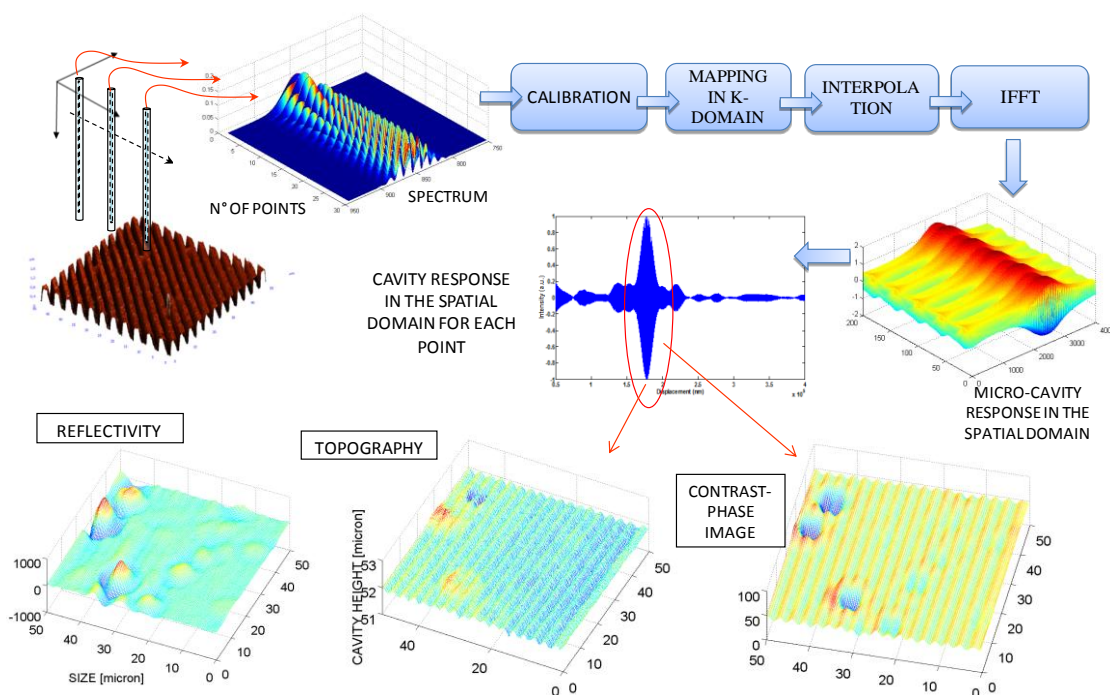


FIG. 2 – Data acquisition scheme. The images are related to a AFM calibration grating made in SiO₂ with a step height equal to about 100 nm with a period of 3 μm.

III. RESULTS

Measurements were performed over surfaces having different level of reflectivity, such as Atomic Force calibration gratings, whose surfaces are realized in SiO₂, and biological samples, as reported in Fig. 3.

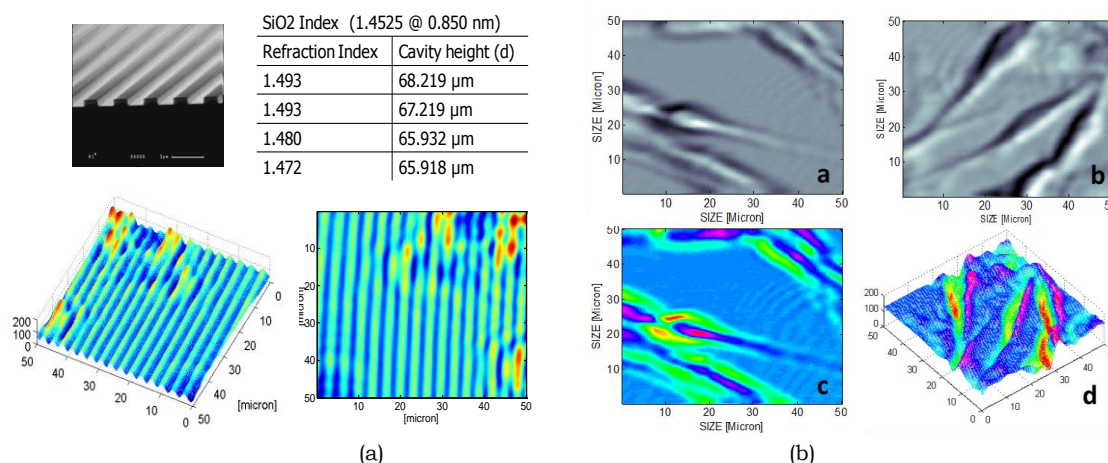


FIG. 3 – Quantitative imaging at nanoscale: (a) Contrast-phase images of AFM calibration grating in SiO₂ over a Si wafer with step height of about 500 nm and 3 micron pitch (b) Infrared images of undifferentiated myoblasts. (up) maps of reflectivity, (down) contrast-phase maps.

The calibration grating allows to define the resolution of the system along the normal direction (affected by different factors, such as the laser source bandwidth and piezo drift) and in transverse plane (it is equal to around $1\mu\text{m}$ [7]). In addition, the Contrast-phase images show an higher sensitivity respect to reflectivity and topographic maps, especially in liquid environment [8]. This aspect is relevant, especially for biological applications, where the sample (cells and other biological materials), are bound to be kept in osmotic equilibrium or in their buffer.

IV. CONCLUSION

According to the results reported, we have demonstrated how the high sensitivity of micro-cavity can allow to realize infrared imaging at nanometric scale for different kinds of reflective surface and different environmental conditions.

REFERENCES

- [1] Yu, B., et al., "Analysis of fiber Fabry-Perot interferometric sensors using low-coherence light sources," *IEEE Journal of Lightwave Technology*, Vol. 24 , No. 4, 1758-1767, Apr. 2006.
- [2] Zhou, X. and Q. Yu, "Wide-range displacement sensor based on fiber-optic Fabry-Perot interferometer for subnanometer measurement," *IEEE Sensors Journal*, Vol. 11 , No. 7, 1602-1606, Jul. 2011.
- [3] Chen, J. H., J. R. Zhao, X. G. Huang, and Z. J. Huang, "Extrinsic fiber-optic Fabry-Perot interferometer sensor for refractive index measurement of optical glass," *Applied Optics*, Vol. 49, No. 29, 5592-5596, Oct. 2010.
- [4] Daniels, D. J., *Ground Penetrating Radar*, 2nd Edition, IET, London, 2007.
- [5] Bouma, B. and G. Tearney, *Handbook of Optical Coherence Tomography*, Marcel Dekker, 2002.
- [6] Farina, M., et al., "Disentangling time in a near-field approach to scanning probe microscopy," *Nanoscale*, Vol. 3, No. 9, 3589-3593, Sep. 2011.
- [7] A. Di Donato, A. Morini, and M. Farina, "Optical Fiber Extrinsic Micro-Cavity Scanning Microscopy", *Progress In Electromagnetics Research*, Vol. 133, pp. 347-366, 2013.
- [8] A. Di Donato, T. Pietrangelo, A. Anzellotti, T. Monti, A. Morini and M. Farina, "Infrared imaging in liquid through an extrinsic optical microcavity," *Optics Letters*, Vol. 38, Issue 23, pp. 5094-5097 (2013)

A MM-WAVE 2D ULTRA-WIDEBAND RADAR FOR BREAST TUMOUR IMAGING

S. Moscato⁽¹⁾, G. Matrone⁽¹⁾, M. Pasian⁽¹⁾, A. Mazzanti⁽¹⁾, M. Bozzi⁽¹⁾, L. Perregrini⁽¹⁾, F. Svelto⁽¹⁾, G. Magenes⁽¹⁾, P. Arcioni⁽¹⁾, and P. Summers⁽²⁾

(1) Department of Electrical, Computer, and Biomedical Engineering
University of Pavia, via Ferrata 6 – Pavia – Italy

(2) Division of Radiology IEO – Istituto Europeo di Oncologia
Milano – Italy

Abstract

This paper presents the preliminary design of a mm-wave Ultra-Wideband (UWB) imaging system for breast cancer screening. The proposed architecture could be an innovative solution to achieve the high imaging resolution required without risks for the patient. The 20-40 GHz frequency band used in the presented system guarantees both high cross and range resolutions performance. A prototype aimed to generate 2D images is manufactured and measured using a mm-wave vector network analyzer. The scattering matrix is then post-processed to elaborate a high-resolution image of the targets. Experimental results show that in free space 3 mm cross and 8 mm range resolutions were achieved, which is promising for future developments.

Index Terms – antenna array, bioengineering, breast cancer, microwave imaging, mm-wave, radar, tumour.

I. INTRODUCTION

Breast cancer ranks fifth of all diseases as a cause of death from cancer in women. However, if the cancer is detected early enough, surgery to completely remove the tumour mass has a consequent 5-year survival rate of more than 80% [1]. X-ray mammography is the commonly used technique for breast screening but it is not without risks, very uncomfortable and it is not failsafe. A mm-wave breast imaging system is a very feasible alternative: it combines the resolution advantages of mammogram with the absence of risks for the patient. Employing a frequency range from 20 to 40 GHz, the radar can provide resolutions down to few millimetres, suitable for breast cancer detection and imaging, together with an acceptable penetration in human tissues.

Microwave and mm-wave radar techniques detect the backscattered power in the medium due to discontinuities in the dielectric constant ϵ_r . By this method, the position of the discontinuity could be computed. This methodology is also suitable for breast cancer detection because of the contrast between tumour tissues against fat [2] in microwave region.

In the literature, the lower frequencies of the microwave band have been exploited in several prototypes to produce three dimensional breast images [3-4]. This band involves wavelengths down to few centimeters which guarantees a significant penetration of the electromagnetic field in human tissues. In the other hand, the relatively low frequency poses limitation on the achievable resolutions. Furthermore, also E-band imaging

systems have been developed, but their use is best suited for the detection of concealed weapons [5].

The novel contribution of this work is the development of a mm-wave radar imaging system with a 20 GHz bandwidth centred at 30 GHz, which can potentially be employed for breast imaging and cancer detection. This band allows us high range and cross resolution with respect to existing systems and to achieve adequate penetration in the human tissues [6]. In this paper, the design of a preliminary imaging system is presented. Instead of a complete system, this system is based on a synthetic aperture realized by the shifting of two antennas for 2D imaging. The intended targets were synthetic objects in free-space. This configuration allowed us to evaluate all the critical system aspects.

II. DESIGN OF THE MM-WAVE RADAR

The stepped frequency continues wave (SFCW) approach was chosen for the imaging system. It considers the antenna-target-antenna electromagnetic system as a linear transfer function, defined by the S parameters. The architecture of the synthetic antenna array sets the performance of the imaging system in terms of cross-resolution while the frequency bandwidth (BW) sets the range resolution [5]. Another feature is the non-ambiguous range (RNA): it arises from the frequency discretization process. The free space within the RNA is the only one that has a physical meaning, beyond the RNA take place infinite replicas.

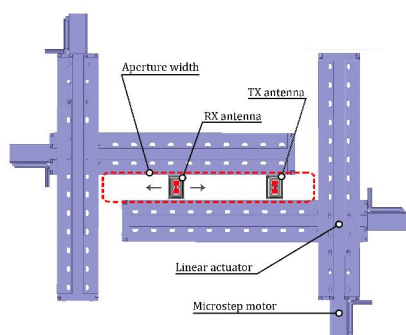


FIG. 1: – A schematic top view of the setup.

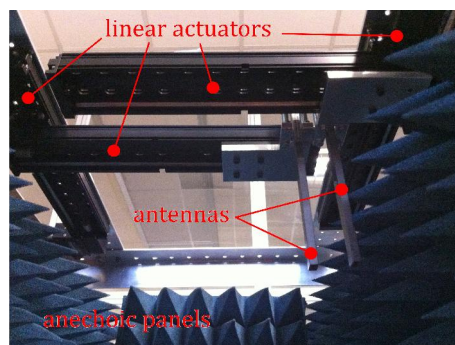


FIG. 2: – Lateral view of the setup.

The proposed 20 GHz bandwidth needs suitable broadband antennas. In this preliminary design, the radiators were two truncated double-ridge waveguides in order to exploit a monomodal band from 18 to 40 GHz. Another issue concern the antenna-to-target distance. The biomedical constrains lead to focus the EM fields very close to the antennas thus the working region is in deep near field. Nevertheless, the radiators distance is related to the presence of grating lobes and the -3 dB beamwidth is directly controlled by the total aperture width. The maximum synthetically aperture achievable with the experimental setup was 200 mm. The best performance was reached with 35 radiators with variable reciprocal spacings, obtained with four linear actuators crossed (by this way, the experimental setup can be extended to generate 3D images), as shown in Figure 1. Physically, the minimum separation between adjacent antennas

was limited to 25 mm by flange transition hindrance. Subsequent steps, achieved with the coordinate shifting, were reduced to 5 mm. The measurements are demanded to a mm-wave vector network analyzer (VNA) while the radiators, directed towards the floor, were fastened to the carriage of linear actuators (as shown in Figure 2). Moreover, in order to save the total measurement time, the symmetry of S matrix can be exploited and the number of acquisitions dramatically diminishes.

Other critical aspects concern the weakness of the signal received, the large mutual coupling XT (due to the low spacings between radiators) and the collected phases affected by waveguide propagation and spurious back-scattering. In order to avoid the aforementioned issues, two more measurements are demanded: one without targets in order to calibrate the environment and XT , and the second one with a calibration standard for which the transfer function is analytically known (i.e. a copper plane). The equation that summarizes the entire calibration process is stated below:

$$H_t = \frac{(H_A H_S H_A + H_A H_{XT} H_A) - (H_A H_{XT} H_A)}{H_r / H_p}$$

where H_t is the final calibrated transfer function of the interested target, H_A is the antenna response, H_S is the measured transfer function of the target and H_{XT} is the frequency domain XT contribution. Finally, H_r is the analytical S matrix of calibration standard and H_p is the measured one. Furthermore, when dealing with a real scenario, artefacts due to air-skin reflections will also need to be considered and minimized, i.e. through a dielectric coupling medium.

III. EXPERIMENTAL RESULTS

The multistatic DMAS algorithm, originally conceived in [7] for microwave breast imaging, was used for image reconstruction. Among the algorithms proposed in the literature, the DMAS allows to achieve a better SNR and dynamic range [6], but at the expense of high computational resources. Backscattered signals were obtained by first convolving the measured S matrix with the input excitation signal (a 30 GHz modulated Gaussian pulse with 20 GHz of BW). Then, using the amplitude and phase of each processed signal, the intensity of each focal point can be calculated. It is computed by multiplying together each signal that arises from each pair of antennas. Finally, the signals are summed and squared. To achieve the image, an envelope detection is applied together with a log compression.

Two small fragments of corrugated paper formed the targets and were placed close to the edges of the array, at distance of 110 mm far from the antenna array plane (Figure 3). The targets and their positions were chosen in order to highlight the system as they have small dimensions and low dielectric contrast. Figure 4 represents the 2D image produced of the above target configuration. The targets are well identified and their positions are well detected. The high resolution image confirms the key points of the proposed architecture: the capability to detect targets down to 2 mm diameter, a very high dynamic range.

IV. FUTURE DEVELOPMENTS

In this paper a mm-wave UWB radar for breast imaging was presented and a preliminary 2D high-resolution measurement described. The performance are promising for breast imaging applications and for 3D improvements. Furthermore, more developments are foreseen and they regarding the adoption of a fully integrated antenna array and several speed-up techniques in imaging formation and post-processing.

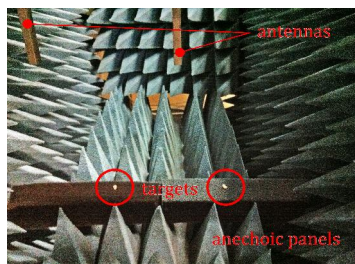


FIG. 3: – Measurement scenario: lateral view. The targets are the white dots.

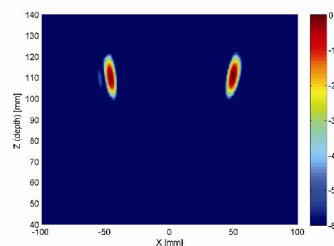


FIG. 4: – Final image of two small dielectric spheres at 110 mm from the antennas.

REFERENCES

- [1] National Cancer Institute at the National Institutes of Health, website: <http://www.cancer.gov/>. Accessed March 2014.
- [2] X. Li, S. K. Davis, S. C. Hagness, D. W. Van der Weide, and B. D. Van Veen, "Microwave Imaging via Space-Time Beamforming: Experimental Investigation of Tumor Detection in Multilayer Breast Phantoms," *IEEE Transactions on Microwave Theory and Techniques*, Vol. 52, No. 8, pp. 1856-1865, August 2004.
- [3] M. Klemm, I. J. Craddock, J. A. Leendertz, A. Preece, and R. Benjamin, "Radar-Based Breast Cancer Detection Using a Hemispherical Antenna Array - Experimental Results," *IEEE Transactions on Antennas and Propagation*, Vol. 57, No. 6, pp. 1692-1704, June 2009.
- [4] M. O'Halloran, E. Jones, and M. Glavin, "Quasi-Multistatic MIST Beamforming for the Early Detection of Breast Cancer," *IEEE Transactions on Biomedical Engineering*, Vol. 57, No. 4, pp. 830-840, April 2010.
- [5] S. S. Ahmed, A. Schiessl, and L. P. Schmidt, "A Novel Fully Electronic Active Real-Time Imager Based on a Planar Multistatic Sparse Array," *IEEE Transactions on Microwave Theory and Techniques*, Vol. 59, No. 12, pp. 3567-3576, December 2011.
- [6] S. Moscato, G. Matrone, M. Pasian, et al., "A mm-Wave 2D Ultra-Wideband Imaging Radar for Breast Cancer Detection," *International Journal of Antennas and Propagation*, vol. 2013, Article ID 475375, 8 pages, 2013.
- [7] H. B. Lim, N. T. Nhung, E. P. Li, and N. D. Thang, "Confocal Microwave Imaging for Breast Cancer Detection: Delay-Multiply-and-Sum Image Reconstruction Algorithm," in *IEEE Transactions on Biomedical Engineering*, Vol. 55, No. 6, pp. 1697-1704, June 2008.

**A COMPARISON OF SIMPLE MODELS TO EVALUATE DIELECTRIC
PROPERTIES OF HUMAN TISSUES AT 2.45 GHz
FROM WATER CONTENT**

M. Cavagnaro⁽¹⁾, F. Frezza⁽¹⁾, R. Laurita⁽¹⁾, M. Tannino⁽¹⁾

⁽¹⁾ Dept. of Information Engineering, Electronics and
Telecommunications, “La Sapienza” University, Rome, Italy
marco.tannino@diet.uniroma1.it

Abstract

Aim of the work is to define a parametric model to evaluate the dielectric properties of human tissues in the microwave range starting from the tissue's water content. A qualitative validation comparing the data obtained from the model with those available in the literature has been performed.

Index Terms – water content; dielectric properties; microwaves; predicting model.

I. INTRODUCTION

The field of personalized care in medicine can take great advantages from the development of models of the specific patient with the related pathology. Particularly, in microwave thermal ablation therapies, dielectric models of the patient could be used to optimize the treatment through numerical simulations [1].

A semi-automatic procedure to develop a dielectric model of the human body was proposed in [2,3]. This procedure evaluates the water content of body tissues starting from MRI (Magnetic Resonance Imaging), then the electric permittivity and conductivity are estimated using a direct proportionality with the water content [2]. Recently new measurements of the dielectric properties of body tissues have been performed [4] and the measured data have been interpolated as a function of the frequency according to the Cole-Cole model [6] (on line version [7]). Accordingly, the proportionality between water content and dielectric properties should be validated with the newly measured data. Moreover, in [5] it is shown that the relationship between the dielectric parameters and the water content in tissues depends on the frequency. In this work the possibility to correlate tissue' dielectric properties values with water content is tested. In the next sections the Cole-Cole model will be reported first, then the relationships between water content and dielectric properties will be addressed from an analytical and mathematical point of view. Afterwards, the obtained model will be compared with the data predicted in [7] for different tissues. The accuracy of the results will be examined, and potential improvements will be suggested.

II. METHODS

Eq. (1) reports the complex dielectric permittivity of a tissue as a function of the frequency as given by the Cole&Cole model [6]. Table I shows the parameters in Eq. (1).

$$\varepsilon^*(\omega) = \varepsilon_\infty + \sum_{k=1}^4 \frac{\varepsilon_k}{1 + (j\omega\tau_k)^{(1-\alpha_k)}} + \frac{\sigma_i}{j\omega\varepsilon_0} \quad (1)$$

TABLE I - COLE-COLE PARAMETERS

Parameter	Description
$\Delta\varepsilon_k$	Difference between max. and min. values of the ε_k for the k^{th} relaxation interval
τ_k	Time constant for the k^{th} relaxation, equal to $1/(2\pi f_{r,k})$ with $f_{r,k}$ the k^{th} relaxation frequency
α_k	Measured extension of the dispersion in the k^{th} interval
σ_i	Static ionic conductivity
ε_∞	Permittivity at infinite frequency
ω	Angular frequency
ε_0	Vacuum permittivity

Usually, 4 relaxation processes are considered to characterize the dielectric properties of human tissues from a few kHz to several GHz, for a total of 14 parameters that should be calculated. These parameters, described in [4], can be readily obtained on line [7].

In case one considers a narrow frequency range, e.g. around a few GHz, the summation could be reduced to a single term. Moreover, neglecting α_k from (1), the Debye formula will be derived. In this case, the number of parameters in (3) can be reduced to 4: ε_∞ , τ , ε_s and σ_i . To identify these parameters, a fitting procedure is used starting from the dielectric properties' values reported in [7] and obtained through Eq. (1). In particular, the (non-linear) least squares algorithm is applied to evaluate τ and ε_s from the real part of ε_∞^* and σ_i from its imaginary part. Then, a relationship between the tissue water content, x , and the constants just identified has been searched for. The tissue water contents used in the following discussion have been taken from [8]. In [4] ε_∞ assumes only two values: 4 or 2.5, for tissues with high and low (less than 50%) water content, respectively. The same assumption has been used in the present work. ε_s and σ_i will be studied looking for a linear relationship with the water content, while with reference to τ , both a constant value and a linear relation will be studied.

III. RESULTS

Table II shows the human tissues and their water content [8] used to test the considered model. In [8], the tissue's water content is given as a range and/or as the most probable value (shown in brackets in Table II). Therefore, in the following, several points for the same tissue have been considered to identify the regression parameters. Moreover, it must be noted that different tissues have the same water content but different ϵ_s , as e.g. muscle, liver, spleen and kidney (Figure 1).

TABLE II – TISSUE WATER CONTENT

Tissue	Water Content
Cerebro Spinal Fluid	99
Brain (Grey Matter)	83-86
Brain (White Matter)	68-77
Fatty Adipose	11.4-30.5 (21.2)
Gall Bladder	64-81.5
Kidney	72.3-80.5 (76.6)
Liver	72.8-75.6 (74.5)
Muscle (Skeletal)	70-78.6 (74.1)
Spleen	72-79 (77)
Stomach	60-78 (75)
Tendon	63
Bone (Cortical)	12-15
Cartilage	55-85 (72)

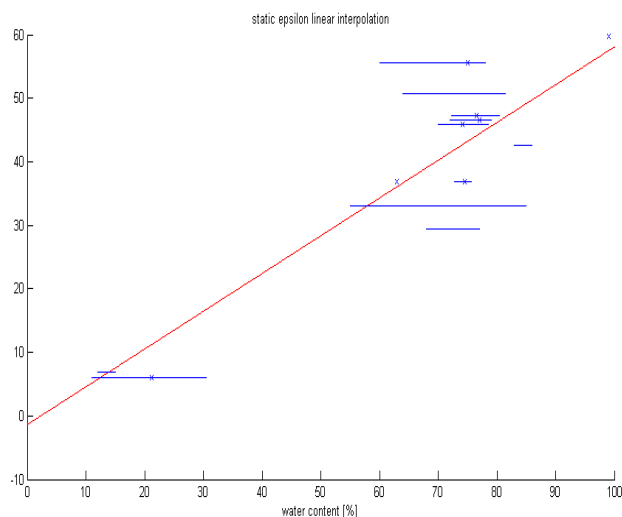


Fig. 1 - Static dielectric constant (ϵ_s) [7] as a function of the water content [8]

To validate the model, the dielectric properties have been evaluated at 2.45 GHz following the proposed procedure and compared with those reported in [7]. The lowest error is obtained for tissues with high water content: e.g. the error was lower than 10% for tendon. However, the

agreement is worse for the tissues with low water content and for brain matter: in this case errors as high as 20-30% have been obtained.

IV. CONCLUSION

A simple model to evaluate the dielectric properties of human tissues starting from their water content has been proposed. The obtained results show a good agreement between the values predicted by the model and those reported in the literature only for tissues with high water content. The analysis performed showed that the dielectric properties effectively depend on the tissue's water content but that more inputs beyond the whole percentage of water in a tissue should be used.

To improve the model, work is ongoing to differentiate the several phases for water recognizable in a tissue (i.e. free and bound water), which show a different behavior under the action of an electromagnetic field, and consequently different dielectric properties. These phases can be discriminated using new MRI sequences as the balanced Steady State Free Precession (bSSFP) used in [9].

REFERENCES

- [1] M. Cavagnaro, C. Amabile, P. Bernardi, S. Pisa, and N. Tosoratti, "A minimally invasive antenna for microwave ablation therapies: design, performances, and experimental assessment," *IEEE Trans. on Biomed. Eng.*, vol. 58, no. 4, pp. 949-959, 2011.
- [2] M. Mazzurana, L. Sandrini, A. Vaccari, C. Malacarne, L. Cristoforetti, and R. Pontalti, "A semi-automatic method for developing an anthropomorphic numerical model of dielectric anatomy by MRI," *Phys. Med. Biol.*, vol. 48, pp. 3157-3170, 2003.
- [3] M. Cavagnaro, F. Frezza, R. Laurita, F. Mangini, and A. Palombo, "From Magnetic Resonance Imaging to dielectric properties of tissues," *Biophysics & Bioeng. Letters*, vol. 4, no. 2, pp. 1-6, 2011.
- [4] S. Gabriel, R. W. Lau, and C. Gabriel, "The dielectric properties of biological tissues: III. Parametric model for the dielectric spectrum of tissues," *Phys. Med. Biol.* 1996, Vol. 41, pp. 2271-2293.
- [5] M. P. Robinson, J. Clegg, and D. A. Stone, "A novel method of studying total body water content using a resonant cavity: experiments and numerical simulation," *Phys. Med. Biol.* 2003, Vol. 48, pp. 113-125.
- [6] R. H. Cole and K. S. Cole, "Dispersion and Absorption in Dielectrics," 1941, Vol. 9, pp. 341-352.
- [7] <http://niremf.ifac.cnr.it/tissprop/htmlclie/htmlclie.htm>, *IFAC - Istituto Fisica Applicata Nello Carrara*.
- [8] F. A. Duck, "Physical Properties of Tissue: A Comprehensive Reference Book," Bath Academic Press, 1990.
- [9] M. Gloor, K. Scheffler, and O. Bieri, "Quantitative Magnetization Transfer Imaging Using Balanced SSFP," *Mag. Res. Med.*, vol. 606, pp. 91-700, 2008.

CONTRAST AIDED BLIND FOCUSING OF THE ELECTROMAGNETIC FIELD FOR MICROWAVE HYPERTHERMIA

G. Bellizzi⁽¹⁾, O. M. Bucci^{(1),(2)}

⁽¹⁾ DIETI Università di Napoli Federico II, Via Claudio 21, 8125
Napoli, Italia

⁽²⁾ IREA-CNR, Via Diocleziano 324, 80124 Napoli, Italia
bucci@unina.it

Abstract

The paper presents a novel approach of focused microwave hyperthermia based on the use of contrast agents. The idea is to induce a detectable and localized contrast change in the target and exploit this variation for the synthesis of the excitations of the antenna array employed for the focusing. In particular, the excitations are determined through a fast and effective processing of the differential scattering matrix, obtained by the difference of two scattering matrixes measured, by the same antenna array used for the focusing, before and after a localized change of contrast the target contrast. As a result, the approach is computationally effective and totally blind, not requiring any a priori knowledge of the electric and geometric features of the region to be treated.

Index Terms – Blind focusing, contrast agents, focused microwave hyperthermia, micro and nano-composites.

I. INTRODUCTION

Focused Microwave Hyperthermia (FMH) is a modality of hyperthermia where the selective heating of the malignant tissue (target) is achieved by focusing the microwave radiation emitted by an array of antennas, located outside the region to be treated [1]. From the electromagnetic standpoint, one of the main goal in FMH is to determine the excitations of the antennas which assure the focusing of the electric field in the target. To this end, several effective approaches have been proposed. However, the most of them require some a priori information, such as the geometric and electric features of the region to be treated, which are not easily and quickly obtainable and are unavoidably affected by uncertainty which could significantly degrade the actual performances. Accordingly, an effective approach which does not need such information would be desirable.

The aim of this communication is to promote an innovative approach of FMH, presented for the first time in [2] and currently under review in [3], which exploits the same antenna array radiating the field to collect the information for its proper focusing. The idea is to induce a *localized* and detectable change of the electric contrast in the target and to measure the resulting variation of the scattered field for the synthesis of the excitations of the antennas. Due to the *localized* character of the induced contrast change, the optimal excitation vector is the first right

singular vector of the *differential* scattering matrix, obtained as difference of two scattering matrixes measured, by the antenna array itself, before and after the change of the target contrast. Accordingly, the approach is computationally effective and totally blind, not requiring any a priori knowledge on the electric and geometric features of the region to be treated. Further details and numerical results on the effectiveness of the approach, besides those provided in Section IV of this paper, can be found in the preliminary works [2]-[3].

II. FORMULATION OF THE APPROACH

The proposed approach is based on the fact that the difference between the fields due to a given Tx antenna of the array, before and after a *localized* change of the contrast in the target, is practically the same radiated by a proper elementary source located inside the target. Therefore, for the reciprocity, back-propagating such *difference field*, i.e. feeding the antenna array with an excitation vector proportional to the complex conjugate of the vector of the *difference field* samples measured by the antenna array itself, it results in a field mainly focused on the target. Obviously, the field focused is the electric or the magnetic field depending on the nature, electric or magnetic, of the contrast change.

Comparable or even better focusing performance are achieved if, instead of the field samples due to a single Tx antenna, one considers the *differential* scattering matrix, say \underline{S} , obtained by the difference of two scattering data matrixes measured by the antenna array itself before and immediately after the contrast change. In this case, the optimal excitation vector is simply the right singular vector associated to the largest singular value of \underline{S} . Since \underline{S} is a measured datum, the focusing is achieved without requiring any a priori knowledge on the geometry and permittivity of the region to be treated.

III. CONTRAST AGENTS

An effective way to change the contrast of the target is by inserting into the target micro or nano-composites, like microbubbles [4], carbon nanotubes [5] and nanoparticle [6], in form of suspensions. These composites are very attractive for our purpose for their reduced sizes which make their infusion minimally invasive, for the possibility of a their biological functionalization which increase their biocompatibility and cellular uptake, and for the remarkable electromagnetic response in the microwave frequency range. Concerning the last feature, In Table I we report, for a frequency of 1.5 GHz, typical values of contrast variation achievable by exploiting microbubbles and carbon nanotubes. These values come from experimental characterizations [4], [5].

TABLE I - ELECTRIC AND MAGNETIC CONTRAST CHANGE, AT 1.5 GHz, FOR SOME CONTRAST AGENTS

Contrast agents (concentration)	Electric (χ_ϵ) and magnetic (χ_μ) contrast change
Microbubbles (10% by volume)	$\chi_\epsilon=-0.14$, $\chi_\mu=0$
Carbon nanotubes (1 mg/cm ³)	$\chi_\epsilon=0.12-i0.06$, $\chi_\mu=0$

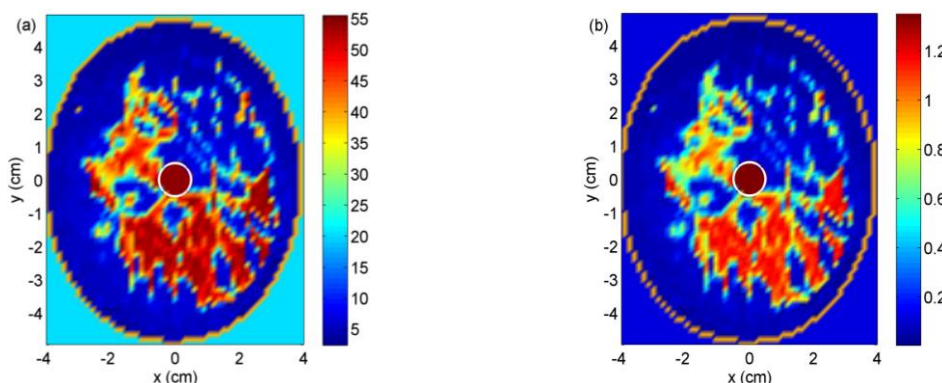


FIG. 1 – Relative permittivity (a) and effective conductivity (b) maps, at 1.5 GHz, of the adopted 2D breast model (white circles delimit the target).

IV. NUMERICAL ASSESSMENT

To show the effectiveness of the approach, a 2D numerical analysis, completing that already reported in [2]-[3], has been carried out. To this purpose, a slice of a realistic breast model [7], having a malignant inclusion of 10 mm in size, has been considered in the simulations (see Fig. 1(a)-(b)). The antenna array is made of $N=18$ ideal z -directed currents wires, located along a circle of radius $R=10$ cm, surrounding the breast. The overall system is embedded in an infinitely extended medium, acting as matching medium, having relative permittivity $\epsilon_r=20$ and conductivity $\sigma=0.13$ S/m, which are the values measured for water-oil emulsions at the working frequency $f=1.5$ GHz.

Fig. 2(a) shows the results of the approach, in terms of (normalized) power distribution dissipated in the breast by the applied electric field, when the contrast change is induced by using microbubbles (see Table I). For comparison, in Fig. 2(b) we also report the results of a standard time reversal approach, obtained by assuming the target embedded in a homogeneous medium with the permittivity of the matching medium. As it can be seen, in case (a) the power dissipation is mainly concentrated in the target, while in case (b) the focusing is practically lost. This result confirms the effectiveness of the approach. Additional results, not reported for brevity, will be presented at the conference.

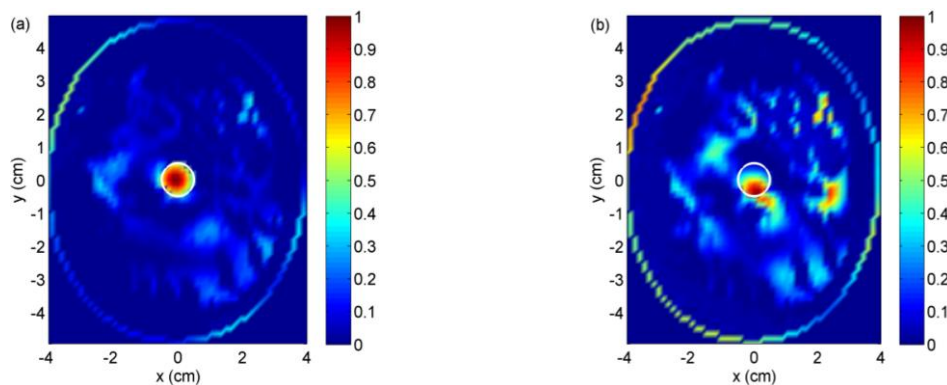


FIG. 2 – Normalized electric power distribution dissipated in the breast: (a) our approach; (b) time reversal approach (white circles delimit the target).

ACKNOWLEDGEMENT

This work is partially supported by the Italian Ministry of University and Research under the project MERIT.

REFERENCES

- [1] W. Rao., Z. S. Deng and J. Liu, “A review of hyperthermia combined with radiotherapy/chemotherapy on malignant tumors”, *Crit Rev Biomed Eng.*, vol. 38, pp. 101-116, Gen. 2010.
- [2] G. Bellizzi and O.M. Bucci, “Blind Focusing in Microwave Hyperthermia by Target Contrast Variation”, 8th EuCAP, The Hague, April 5-11 2014.
- [3] G. Bellizzi and O.M. Bucci, “Blind Focusing of Electromagnetic Fields in Hyperthermia Exploiting Target Contrast Variations”, *IEEE Trans. Biomed. Eng.*, under review.
- [4] A. Mashal, J. H. Booske, and S. C. Hagness, “Toward contrast-enhanced microwave-induced thermoacoustic imaging of breast cancer: a experimental study of the effects of microbubbles on simple thermoacoustic targets”, *Phys. Med. Biol.*, vol. 54, pp. 641-650, Feb. 2009.
- [5] A. Mashal, B. Sitharaman, X. Li, P. K. Avti, A. V. Sahakian, J. H. Booske and S. C. Hagness, “Toward carbon-nanotube-based theranostic agents for microwave detection and treatment of breast cancer: enhanced dielectric and heating response of tissue-mimicking materials”, *IEEE Trans. Biomed. Eng.*, vol. 57, pp. 1831-1834, Aug. 2010.
- [6] G. Bellizzi and O.M. Bucci, “A novel measurement technique for the broadband characterization of diluted water ferrofluid for biomedical applications”, *IEEE Trans Magn.*, vol. 49, pp. 2903-2912, June 2013.
- [7] E. Zastrow, S. K. Davis, M. Lazebnik, F. Kelcz, B. D. Van Veen, and S. C. Hagness, “Database of 3D grid-based numerical breast phantom for use in computational electromagnetic simulations”, available at <http://uwcem.ece.wisc.edu/home.htm>

EXPLOITING COMPRESSIVE SENSING IN MNP ENHANCED MWI FOR BREAST CANCER IMAGING

M. Bevacqua⁽¹⁾ and R. Scapaticci⁽²⁾

⁽¹⁾ DIIES, Univ. Mediterranea di Reggio Calabria, Italy
(martina.bevacqua@unirc.it)

⁽²⁾ CNR-IREA, Naples, Italy (scapaticci.r@irea.cnr.it)

Abstract

Magnetic nanoparticles have been recently proposed as contrast agent in microwave breast cancer imaging. As a matter of fact, being human tissues non-magnetic, their use would allow achieving a reliable and specific diagnosis of breast cancer, by pursuing the reconstruction of a magnetic contrast into a totally electric scenario. In this communication, we investigate the adoption of compressive sensing as imaging strategy, which has been recently considered to solve linear problems in which the unknown is sparse. In this respect, the low amount of nanoparticles actually targetable assures that the problem to be faced in MNP enhance MWI is linear. In addition, being the magnetic contrast associated to the targeted tumour small and localized, the sought unknown function is also intrinsically sparse.

Index Terms—breast cancer imaging, compressive sensing, magnetic nanoparticles, microwave imaging

I. INTRODUCTION

In the last years, thanks to the evidence that human tissues exhibit different electric properties at microwaves as a function of their typology and physio-pathological status, Microwave Imaging (MWI) has gained an increasing interest in medical imaging applications. The most extensively investigated field in biomedical diagnostics has been breast cancer imaging, but notwithstanding the efforts of researchers among the world, the expected breakthrough is not yet come and MWI is still far from its application in the clinical practice. The main reason of this circumstance can be found in recent studies on the electric properties of mammary tissues [1], which have outlined that the electric contrast between healthy fibroglandular tissues and cancerous ones is not as high as initially thought, thus completely impairing the possibility of a reliable diagnosis. To overcome this drawback, the adoption of magnetic nanoparticles (MNP) has been recently proposed as contrast agent [2]. The innovative aspect of this technique is the adoption of properly functionalized magnetic nanoparticles able to selectively target tumoral cells, creating a localized magnetic contrast in the malignant tissues (because of the non-magnetic nature of human body). By doing so, the cancer imaging is pursued as the reconstruction of a magnetic contrast embedded into an electric scenario. However, only a low amount of MNP can be actually targeted so the signal scattered by the MNP targeted

tumor is several order lower than the field scattered by the breast. Accordingly, in order to extract the useful signal from the measured data, a differential measurement strategy is exploited, taking advantage of the possibility of modulating the magnetic response of MNP at microwaves by means of an external polarizing magnetic field (PMF). On the other hand, the low magnitude of the induced magnetic contrast, allows to simplify the imaging task. As a matter of fact, the inverse scattering problem can be reliably modeled using the distorted Born approximation, which entails that the imaging problem is turned into a linear and ill-posed one. While a robust imaging procedure for this kind of problem has been recently proposed [3], the linearity of the problem, jointly with the consideration that possible tumors targeted by MNP represent small and localized anomalies into the breast, led us to investigate the adoption of Compressive Sensing (CS) techniques for the imaging task, with the aim of achieving a better resolution with respect to the previously proposed strategy.

II. FORWARD PROBLEM

Due to the low magnitude of the induced magnetic contrast, it is possible to model the scattering phenomenon which takes place in MNP enhanced MWI by means of the distorted Born approximation, i.e., assuming that the induced magnetic anomaly does not perturb the field due to the electric scenario.

Accordingly, by omitting some unessential factors and assuming M transmitting probes and M receiving probes working at the angular frequency ω , the generic element $\Delta E_s(r_v, r_m)$ of the $M \times M$ differential data scattering matrix is given by [2,3]:

$$\Delta E_s(r_v, r_m) = \int_{\Omega} \mathbf{G}^{EM}(r_m, r) \Delta \chi_{\mu}(r) \mathbf{H}_i(r, r_v) dr = \mathcal{L}^{EM} \Delta \chi_{\mu} \quad v, m = 1, \dots \quad (1)$$

wherein Ω denotes the region hosting the breast, r_m denotes the receiving probe position and r_v is the position of the transmitting one. $\mathbf{G}^{EM}(r_m, r)$ is the electric-magnetic Green's function of the reference scenario, i.e., the electric field in r_m generated by an elementary magnetic source in r . $\mathbf{H}_i(r, r_v)$ is the magnetic "incident" field into the electric scenario, i.e., the magnetic field generated by an electric source located in r_v in the point $r \in \Omega$, in presence of the breast, but without any magnetic anomaly. Due to the reciprocity principle, $\mathbf{G}^{EM}(r_m, r) = \mathbf{H}_i^T(r, r_v)$, where the superscript T denotes the transpose matrix. Finally, $\Delta \chi_{\mu}$ represents the differential magnetic contrast, i.e., the susceptibility variation due to the change of the PMF intensity between the two stages of the measurement. As can be seen from eq. (1), the data to unknown relationship is linear, as the operator \mathcal{L}^{EM} does not depend on the unknown $\Delta \chi_{\mu}$.

III. RETRIEVAL BY CS THEORY

In the last years, CS [4] has become an increasingly relevant paradigm in the signal processing and recovery community.

Part of its success is due to the fact that CS theory, guarantees an accurate reconstruction of the unknown even if the number of measurements is much lower than the overall number of coefficients representing the unknown. These achievements are obtained exploiting the concept of “sparsity”, where sparsity means that the unknown function can be represented through a limited number of nonzero coefficients in a given basis.

In MWI problems the amount of non-redundant information, which can be collected, is bounded [5], so CS paradigm can be definitely attractive, as it could improve the accuracy of inversion procedures or drive the design of simpler and cheaper measurement set-ups.

On the other side, CS theory is well developed for the case of linear problem. This represents a fundamental difficulty on a possible application of CS to the area of MWI. However, in this particular application, the unknown is intrinsically sparse in the voxel basis, i.e. it can be represented by means of a limited number of voxels and, moreover, the relationship between data and unknowns can be considered linear, as stated in the previous section. Therefore, CS can represent an effective and reliable procedure to accurately recover the electromagnetic properties of the induced magnetic anomaly.

Let us consider the problem (1). According to CS theory, it can be solved by means of the following optimization constrained problem [6]:

$$\min_{\Delta\chi_\mu} \|\Delta\chi_\mu\|_{l_1} \quad \text{subject to} \quad \|\mathcal{L}^{EM} \Delta\chi_\mu - \Delta\mathbf{E}_s\|_{l_2} \leq \epsilon \quad (2)$$

Notably, the number of differential data $\Delta\mathbf{E}_s$, i.e. $M \times M$ can be (much) less than the overall number of voxels of the investigated scenario, but sufficiently larger than the number of nonzero elements of $\Delta\chi_\mu$.

IV. A PRELIMINARY NUMERICAL EXAMPLE

As a preliminary example, we have applied the above described procedure against an anthropomorphic breast phantom (ID 070604PA2 from <http://uwcem.ce.wisc.edu/home.htm>). The breast is immersed in a homogeneous lossless matching medium, whose relative permittivity is $\epsilon_b=25$. The domain Ω is probed by means of 24 z-directed electric dipoles, working at ≈ 2 GHz, and evenly spaced on three circumferences surrounding Ω . Transmitting and receiving probes are located at the same positions. The tumor, modeled as a spherical inclusion of radius 0.5 cm, has approximately the same electric features of the fibroglandular tissue and a magnetic contrast between the two stages of

the measurement of $|\Delta\chi_\mu|=0.0094$ has been considered. In this preliminary example, the exact knowledge of the breast under test has been assumed. In Fig.1a is shown the normalized reconstruction obtained via CS, while, for the sake of comparison, in Fig.1b the corresponding TSVD normalized reconstruction is reported, where the occurrence of spurious spots appears as a consequence of the low number of transmitting and receiving probes. Further details and results concerning our analysis will be presented at the conference.

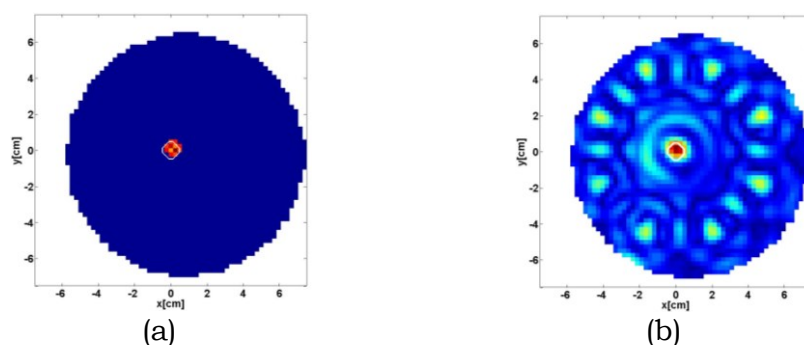


FIG. 1 – Normalized reconstructions of the absolute value of the magnetic contrast (a) via CS, (b) via TSVD. SNR=70dB.

ACKNOWLEDGEMENT

The authors want to acknowledge Professor O.M. Bucci, Professor T. Isernia and Dr L. Crocco for the fruitful discussions, which inspired the writing of this communication.

REFERENCES

- [1] M. Lazebnik et al., “A large-scale study of the ultra wideband microwave dielectric properties of normal, benign and malignant breast tissue obtained from cancer surgeries”, *Phys. Med. Biol.*, vol. 52, pp. 6093–6115, 2007.
- [2] G. Bellizzi, O. M. Bucci, I. Catapano, “Microwave Cancer Imaging Exploiting Magnetic Nanoparticles as Contrast Agent”, *IEEE Trans. On Biomed. Eng.*, vol. 58, no.9, pp.2528-2536, Sept. 2011.
- [3] R. Scapaticci, G. Bellizzi, I. Catapano, L. Crocco, O.M. Bucci, “An Effective Procedure for MNP-Enhanced Breast Cancer Microwave Imaging”, *Trans. on Biomed. Eng.*, vol. 61, pp. 1071-1079, 2014.
- [4] Donoho D., “Compressed sensing,” *IEEE Trans. Inf. Theory*, vol. 52, n. 4, pp. 1289–1306, 2006.
- [5] O. M. Bucci and T. Isernia, “Electromagnetic inverse scattering: Retrievable information and measurement strategies”, *Radio Sci.*, vol. 32, pp. 2123–2138, 1997.
- [6] Chen S., Donoho D., M. Saunders D., “Atomic decomposition by basis pursuit”, *SIAM J. Sci. Comput.*, vol. 20, n. 1, pp. 33–61, 1999.

OBSERVING SCATTERED FIELDS IN VIEW AND FREQUENCY DIVERSITIES

M. A. Maisto⁽¹⁾, R. Solimene⁽¹⁾, R. Pierri⁽¹⁾

⁽¹⁾ Department of Industrial and Information Engineering,
Via Roma 29, 81031 Aversa, Italy
mariaantoniamaisto@unina2.it

Abstract

In this paper the role of view and frequency diversities in linear inverse scattering problems is analyzed in terms of the singular values behavior of the pertinent scattering operators. In order to obtain analytical results, the analysis is developed within a two-dimensional scalar far-zone configuration.

Index Terms – Diversities- Inverse scattering- NDF -SVD.

I. INTRODUCTION

Linear inverse electromagnetic scattering problems amount to inverting an integral equation of the first kind for an object function which is related to the scatterer's features like the shape, the support, the dielectric contrast, etc. It is known that probing the scattering scene at different angles of incidence (multi-view configuration) or at different frequencies (multi-frequency configuration) can improve the achievable performance. However, some degree of *redundancy* can be expected as not all the data are necessarily independent. The focus here is on establishing the role played by the diversities on the singular values behavior. To this end, the problem is addressed under the canonic scattering scenario depicted in Fig. 1.

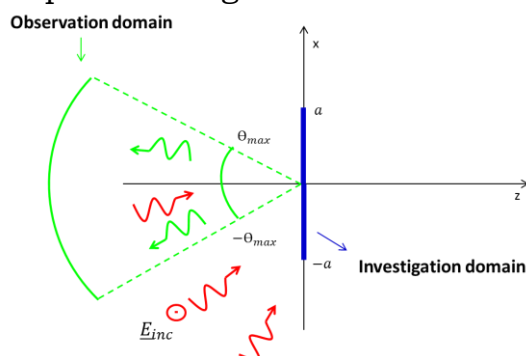


FIG. 1 –Pictorial view of the scattering configuration considered in this paper.

In detail, the scattering domain is assumed to be a strip $I = [-a, a]$ along the x -axis illuminated by plane waves. The scattered field is collected in far-zone within the observation angular sector $\Omega_o = [-u_{max}, u_{max}]$, so that $u_o = \sin\theta_o \in \Omega_o$. Invariance is assumed along the plane wave polarization direction which in turn is orthogonal to the strip. Accordingly, the study is developed for a two-dimensional scalar configuration. When a view diversity is employed, the scattered field is collected for different

incidence directions $u_i = \sin\theta_i \in \Omega_i$, with $\Omega_i \subseteq \Omega_o$. In the case of frequency diversity, the frequencies are taken uniformly within the band $\Omega_{k_o} = [k_{omin}, k_{omax}]$. The reaming of the paper is organized as follows. In sections 2 and 3 report results concerning the cases of view and frequency diversities, respectively. Finally, conclusions end the paper.

II. VIEW DIVERSITY

Consider the view diversity. Let us assume that Ω_i be a discrete subset of Ω_o . In particular, say M (assumed odd) the number of views which are taken by uniformly sampling Ω_o . The pertinent scattered operator then writes as:

$$\mathcal{A}_i: \chi(x) \in \mathcal{L}_l^2 \rightarrow E_s(u_o, u_{in}) = \int_{-a}^a \chi(x) e^{jk_o(u_o - u_{in})x} dx \in \mathcal{L}_{(\Omega_o \times \Omega_i)}^2 \quad (1)$$

where k_o being the wavenumber. In order to estimate the singular system of (1), it is convenient to study the eigen-spectrum of the associated operator $\mathcal{A}_i^\dagger \mathcal{A}_i$, with \mathcal{A}_i^\dagger being the adjoint operator of \mathcal{A}_i [1]. In this case it results

$$\mathcal{A}_i^\dagger \mathcal{A}_i = \sum_{m=1}^{2M-2} \frac{2\pi}{k_o} P_1 \mathcal{B}_{\tilde{\Omega}_m} P_1 \quad (2)$$

with $\tilde{\Omega}_m = [-2k_o u_{max}(m-1)\Delta, -2k_o u_{max} + m\Delta]$ and $\Delta = 2k_o u_{max}/(M-1)$.

Applying same arguments in [2], it can be foreseen that the singular values exhibit $M-1$ steps where the first knee occurs at $N_1 = [4c_M/\pi]$, with $c_M = a\Delta/2$. The successive m -th step is comprised between the indexes $N_m = N_1 + \sum_{l=0}^{m-2} l[4c_M/\pi]$ and $N_m + [4c_M/\pi]$, for $m \in \{2, 3, \dots, M-1\}$. Moreover, on each step the singular values are equal to $\sqrt{(M-m)2\pi\lambda_n(c_M)/k_o}$. This result is very well verified by the example reported in Fig.2.

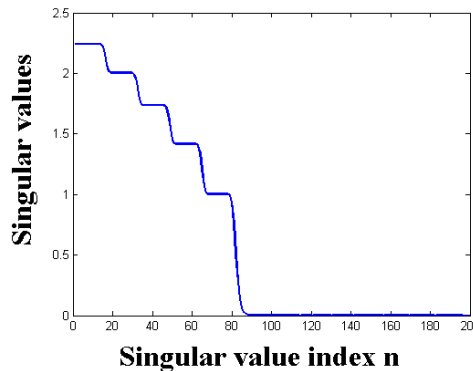


FIG. 2 –Singular value behavior for six angles of incidence, $\Omega_o = [-1,1]$ and $a = \frac{20\pi}{k_o}$. As can be seen, the foreseen five steps are well evident.

In fact, the singular values exhibit the expected $M-1=5$ steps. Moreover, also their value estimation through $\sqrt{(M-m)2\pi\lambda_n(c_M)/k_o}$ is in strict accordance to the numerical result. For example, on the first step, the previous formula returns 2.23 which well agrees with 2.24 given by the numerical simulation.

Note that, for only two views at $(-1,1)$, the singular values exhibit a single step ($N = [2c/\pi]$) with the flat part equals to $\sqrt{\frac{2\pi}{k_o} \lambda_n(c)}$, with $c = 2k_o u_{max} a$. Of course, this single-step behavior allows to identify N as the

number of degrees of freedom which results ideally independent on the noise (see Fig. 3). Hence, the use of more views does not increase the NDF but only the numerical value of the singular values. This is important in the inversion as this entails more stability.

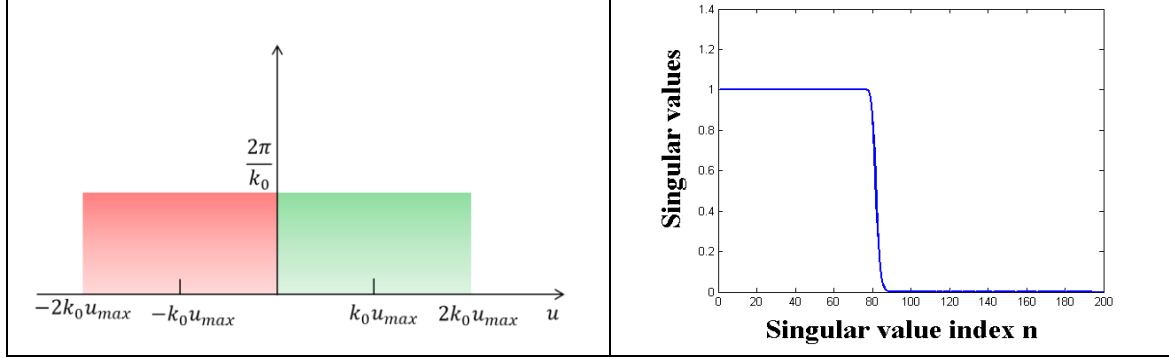


FIG. 3 – The case of two angles of incidence $\Omega_i = (-u_{max}, u_{max}) = (-1, 1)$. The left panel gives a pictorial view of the frequency bands corresponding to each view.

The right panel reports the singular value of the scattering operator for

$$\Omega_0 = [-1, 1] \text{ and } a = \frac{20\pi}{k_0}.$$

III. FREQUENCY DIVERSITY

Let us assume that the frequency of the incident waves can assume discrete values, so that Ω_{k_0} consists of M frequencies k_{om} taken uniformly between $[k_{omin}, k_{omax}]$ at a step of $\Delta = (k_{omin}, k_{omax}) / (M - 1)$. The scattering operator particularizes as

$$\mathcal{A}_f: \chi(x) \in \mathcal{L}_f^2 \rightarrow E_s(u_o, k_{on}) = \int_{-a}^a \chi(x) e^{jk_{on}(u_o)x} dx \in \mathcal{L}_{(\Omega_o \times \Omega_{k_o})}^2 \quad (3)$$

As before, we consider the operator $\mathcal{A}_i^\dagger \mathcal{A}_i$ and study its eigen-spectrum. Accordingly, it results that

$$\mathcal{A}_f^\dagger \mathcal{A}_f = \sum_{m=1}^M \frac{2\pi}{k_{om}} P_1 \mathcal{B}_{\Omega_m} P_1 \quad (4)$$

where now $\Omega_m = [-k_{om}u_{max}, k_{om}u_{max}]$. For the sake of simplicity, from now on, we assume that $u_{max} = 1$ so that $\Omega_m = [-k_{om}, k_{om}]$. The operator $\mathcal{A}_i^\dagger \mathcal{A}_i$ can be conveniently rearranged as

$$\mathcal{A}_f^\dagger \mathcal{A}_f = 2\pi \sum_{m=1}^3 \frac{1}{k_{om}} P_1 \mathcal{B}_{\Omega_m} P_1 + \sum_{m=2}^M 2\pi \sum_{l=m}^M \frac{1}{k_{ol}} (P_1 \mathcal{B}_{\tilde{\Omega}_m} P_1 + P_1 \mathcal{B}_{\hat{\Omega}_m} P_1) \quad (5)$$

where $\tilde{\Omega}_m = [k_{omin} + (m - 1)\Delta, k_{omin} + m\Delta]$ and $\hat{\Omega}_m = [-k_{omin} - m\Delta, -k_{omin} - (m - 1)\Delta]$. Therefore, exploiting the results presented in [2], as long as $c_M = \frac{a\Delta}{2} \gg 1$ and $ak_{omin} \gg 1$, the $\lambda_n[\mathcal{A}_f^\dagger \mathcal{A}_f]$ exhibit M steps with knees occurring at $N_m = \left\lfloor \frac{2ak_{omin}}{\pi} \right\rfloor + (m - 1) \left\lfloor 2 \frac{a\Delta}{\pi} \right\rfloor$. Moreover, on the m -th step the numerical value is $2\pi \sum_{l=m}^M \frac{1}{k_{ol}}$. The example reported in Fig. 4 refers to the case of $M = 3$ and shows how the theory agrees very well with the numerical results. The expected three steps are evident. Also it can be easily checked the accordance between the numerical and the theoretical values of the $\sigma_n[\mathcal{A}_f]$.

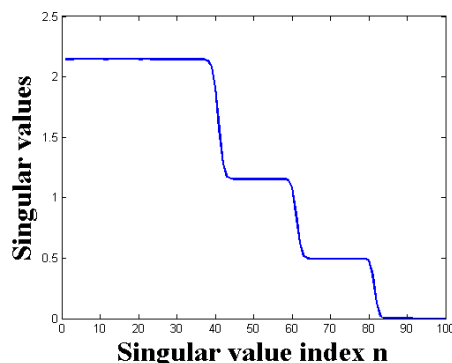


FIG. 4 –Singular value behavior of \mathcal{A}_f for the case of $M = 3$ frequencies

$$k_{\min}, 1.5k_{\min} \text{ and } 2k_{\min}, k_{\min} = 2\pi m^{-1} \text{ and } a = \frac{20\pi}{k_0}.$$

Eventually, it can be concluded that while the maximum number of significant singular values of the scattering operator depend on the highest adopted frequency, by using more frequencies (lower than the highest one) shapes the singular value behavior so that it resemble a staircase.

IV. CONCLUSION

In this contribution, we presented some our recent results about the study of linear scattering operators. Our aim is to highlight the role played by the parameters of the scattering configuration on the performance achievable. In particular, we focused on the singular value behavior of such operators as they are linked to all the most used metrics (such as NDF, resolution, information content [3]) which actually are employed to assess the achievable performance in linear inverse scattering problems. The obtained results show that in order to increase the NDF to the largest extent two *extremal* views and the highest adopted frequency are sufficient. By further increasing views (within the angular corner bounded by the two extremal views) or adding frequencies (below the highest one) does not lead to an increase in the NDF, but entails an increase of the numerical values of the singular values. Moreover, having fixed the noise, higher singular values can lead to a more stable inversion procedure. We advice the reader that while the proposed procedure can be applied to other scattering configurations (multi-dimensional cases that will be shown during presentation) as well, the obtained results pertain to the particular cases addressed herein.

REFERENCES

- [1] M. Bertero and P. Boccacci, "Introduction to linear inverse problem in imaging", (IOP, Bristol 1998)
- [2] Raffaele Solimene, Maria Antonia Maisto and Rocco Pierri, "The role of diversity on the singular values of linear scattering operators: the case of strip objects", *J. Opt. Soc. A*, Vol. 30, Issue 11, pp. 2266-2272 (2013).
- [3] E. De Micheli and G. A. Viano, "Metric and probabilistic information associated with Fredholm integral equations of the first kind," *J. Int. Eq. Appl.* vol. 14, pp. 283-310 (2002)

A NUMERICAL MICROWAVE TOMOGRAPHIC ALGORITHM TO IMPROVE RECONSTRUCTION OF BURIED OBJECTS

D. Comite⁽¹⁾, A. Galli⁽¹⁾, I. Catapano⁽²⁾, F. Soldovieri⁽²⁾

- ⁽¹⁾ Department of Information Engineering, Electronics and Telecommunications (DIET), “Sapienza” University of Rome
Via Eudossiana 18, 00184 Rome, Italy
comite@diet.uniroma1.it , galli@diet.uniroma1.it
- ⁽²⁾ IREA, Istituto per il Rilevamento Elettromagnetico dell’Ambiente,
C.N.R. – Via Diocleziano 328, 80127 Naples, Italy
catapano.i@irea.cnr.it , soldovieri.f@irea.cnr.it

Abstract

An original implementation of a tomographic approach is presented and tested in order to improve considerably the accuracy of reconstruction for unknown buried objects using typical Ground Penetrating Radar (GPR) systems. A customized ‘synthetic setup’ is carried out by means of a numerical tool, capable of accounting for the specific features of the antenna system and of the signals used for the illumination. Such a tool allows for a reliable and efficient computation of both the incident and the backscattered field distributions in the region of interest. Therefore a fully-numerical data processing, based on the Born approximation and exploiting the computed incident field, is adopted to enhance the accuracy of the inverse problem solution. Examples of imaging of buried targets illustrate the improvements achieved through this technique compared to standard approaches, in terms of definition and resolution features.

Index Terms – GPR, inverse problems, numerical tools, target imaging.

I. INTRODUCTION

In a variety of civil, geophysical, and planetary applications, Ground Penetrating Radar (GPR) techniques are extensively used with the aim of locating and imaging shallow buried targets [1]. The possibility to obtain for the reconstructed images reliable information on the geometrical and physical features of the targets depends both on the quality of the data collected by means of GPR systems and on the wave propagation model on which the imaging procedure is based.

In this context, in the last years some of the Authors developed and extensively tested a ‘microwave tomographic approach’ to face classes of problems concerning target reconstruction applicable in typical GPR configurations [2]. In this frame, in the present paper we analyze further improvements that can be achieved when the distinctive features of the real antenna system are adequately taken into account in the imaging process. In order to accurately estimate the incident and scattered fields, which have to be considered in the imaging procedure, an electromagnetic (EM) computer-aided-design (CAD) simulation of the scenario under test is exploited and suitably implemented [1,3].

II. A FULLY NUMERICAL IMPLEMENTATION FOR TARGET RECONSTRUCTION

Our investigation is focused here on a reference scenario constituted by two half-space media, describing a typical environment (e.g., air/soil) in which a ground-coupled radar operates by moving close to the interface in one or two directions, and gathers signals backscattered by unknown targets. A suitable CAD implementation (based on CST Microwave Studio) has been developed for such analysis [1]. As a reference, in Fig. 1(a), a monostatic configuration is displayed, with an interfacial movable GPR radiator (e.g., a Vivaldi antenna) detecting a buried target (dielectric or metallic) in a ground medium. For each position on the surface, a signal waveform (e.g., a Gaussian pulse) is radiated and collected. The bandwidth is equal to 0.5–3 GHz, and the antenna scans along x direction with a step fixed to 3 cm. Fig. 1(b) shows the amplitude of the received signal in grey scale along time for different scanning locations, after a regularization ('background removal') [3]. Such an image is the 'synthetic' B-scan cross section (radargram) obtained with the simulation tool and looks like a typical output achievable by GPR instruments. Typical hyperbolic signature can be recognized, with the position of the signal maxima correctly located.

As is known, the imaging reconstruction is related to an ill-posed inverse scattering problem, whose solution can be found under specific approximations (Kirchhoff, Born, etc.) [2],[3]. An integral equation connects the problem data (concerning the incident and scattered EM fields) to an unknown 'contrast function', which is related to the probed scatterer. Such an equation accounts for the involved EM interaction (generally of dyadic type) between radiation and probed structures. We recall next just the basic characteristics of the problem, omitting the analytical details derivable from a number of related works [2,3].

In the standard microwave tomographic approach, the probing signal (input data) is modeled in a simple form as a time-harmonic electric field, which is radiated by an elementary current line oriented along one direction. This ideal configuration is chosen to simplify the features of a real GPR dipole-like antenna [2].

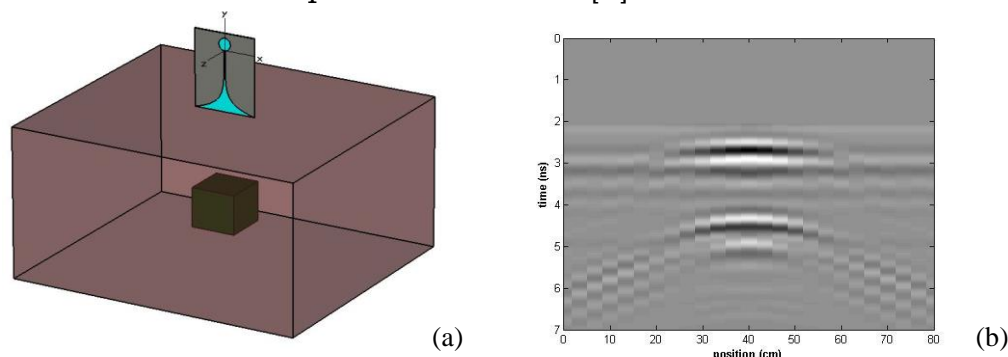


FIG. 1 – (a) GPR synthetic setup: view of a movable ground-coupled system (based on a Vivaldi antenna) with an unknown buried target. (b) Plot of regularized radargram for a basaltic cube ($\epsilon_r = 6.7$, $\mu_r = 1$, $\sigma = 0$) of side $l = 13$ cm, placed at an interfacial depth $d = 18$ cm.

For each position of the antenna on the surface, the backscattered signal is gathered at discrete frequencies uniformly distributed inside the signal spectrum. From the solution of the relevant integral equation the contrast function of the target is then achieved.

It should be reminded that different issues affect the accuracy of the reconstruction with this standard approach. In particular, the incident field distribution of the current line radiating in free space is clearly different from the one due to an actual GPR transmitting system. Moreover, by choosing the transmitting antenna very close to the interface, it is assumed that the Green's function is calculated for a fully-homogeneous medium (the ground).

These critical assumptions are herein removed by facing the imaging problem with a fully-numerical approach that accounts for the real distribution of the incident and scattered fields. Specifically, a fundamental improvement of the proposed numerical implementation is represented by the substitution of the 'ideal' incident field of the standard approach, due to a filamentary current line, with the 'real' field generated by the chosen specific GPR antenna, which also operates in an inhomogeneous environment.

The relevant linear integral equation [2] is given in a matrix form and the solution is reached by the inversion of a suitable discretized operator, faced here by means of a scheme based on Truncated Singular Value Decomposition (TVSD) [2,3].

III. IMAGING RESULTS AND DISCUSSION

To assess the features of our implementation, various numerical tests have been performed, comparing in particular the results of two- and three-dimensional imaging with what obtainable through standard approaches. We illustrate here a reference case of 2D reconstruction for a buried target with the GPR Vivaldi antenna in the air/ground scenario as given in Fig. 1. It should be noted that such a configuration is quite 'challenging' for the imaging process, in connection with the choices of interfacial antennas and of shallow scatterers having both location and size comparable to the wavelengths of the probing signal.

Reconstructed distributions of permittivity for a cubic dielectric target are given in Fig. 2 with color-plot maps in a central cross section (2D view in the xz plane). Fig. 2(a) shows the imaging that is derived through the standard tomographic approach in equivalent conditions, whilst the imaging by our fully-numerical implementation is in Fig. 2(b).

As a basic comment of such results, it can be seen that the quality of reconstruction is manifestly better in the latter case, showing in particular a much more defined location of the stronger backscattering effect due to the upper side and relevant edges of the cube.

The scattering effect of the lower side of the cube is also more correctly predicted by our improved approach, taking properly into account the dielectric contrast between ground medium and target. Such improvements are related to our more adequate description of the effective illumination (the ‘focused’ field distribution of the Vivaldi antenna here) if compared to the ideal one of the standard approach (the ‘isotropic’ distribution of the filamentary current line). The spatial resolution of the proposed fully numerical technique is also better, allowing for a more accurate estimation of the target shape and size. This is particularly manifest in the tests performed accounting for multiple close objects to be detected.

Additional examples, omitted here for space limitation, further assessing the advantages of the considered approach will be possibly provided at the conference.

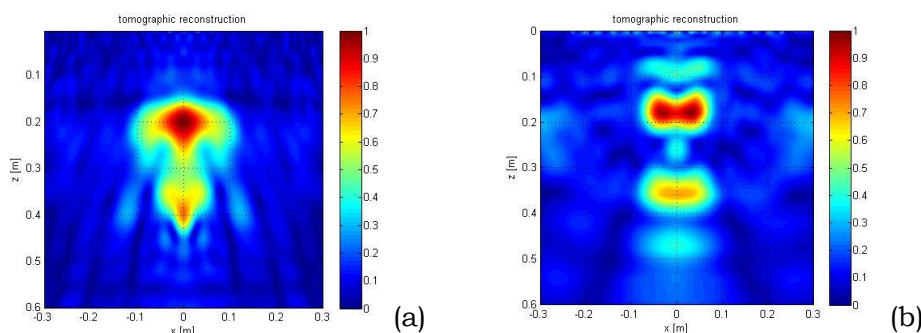


FIG. 2 – Normalized contrast function for a buried basalt cube in a sandy soil.
 (a) Imaging with a ‘standard tomographic approach’ (current line source).
 (b) Imaging with the proposed ‘synthetic implementation’ (Vivaldi antenna).

IV. CONCLUSION

A novel implementation, based on a tailored simulation setup, has been proposed for a tomographic approach to analyze target reconstruction in complex GPR scenarios. A fully-numerical solution of the inverse problem has been achieved, allowing for a more realistic description of the problem with respect to standard approaches that need significant idealizations. The improvements in the accuracy of the proposed algorithm have been presented and discussed in useful reference cases.

REFERENCES

- [1] G. Valerio et al., “GPR detectability of rocks in a Martian-like shallow subsoil: a numerical approach,” *Planet. Space Sci.*, vol. 62, Mar. 2012.
- [2] G. Leone and F. Soldovieri, “Analysis of the distorted Born approximation for subsurface reconstruction: Truncation and uncertainties effect,” *IEEE Trans. Geosci. Remote Sens.*, vol. 41, no. 1, Jan. 2003.
- [3] A. Galli et al., “3D imaging of buried dielectric targets with a tomographic microwave approach applied to GPR synthetic data,” *Int. J. Antennas Propag.*, art. ID 610389, 2013.

INNOVATIVE PASSIVE TECHNIQUES FOR CROWD OPPORTUNISTIC WIRELESS LOCALIZATION

F. Viani

ELEDIA Research Center @DISI, University of Trento
Via Sommarive 5, I-38123 Trento, Italy
federico.viani@disi.unitn.it

Abstract

The localization of crowd in large areas is of paramount importance in many application fields, ranging from security and flow management up to advertising and marketing. Standard approaches for crowd localization are mainly based on dedicated technologies, such as video surveillance systems and image processing techniques. However, high complexity, costs, and privacy issues often limit the diffusion of such solutions. In this work, an alternative approach based on the opportunistic exploitation of existing wireless infrastructures is proposed for the localization of passive (i.e., transceiver-free) crowds. The localization problem has been recast as an inverse problem. Toward this end, customized methodologies have been studied for the real-time processing of wireless signals and the reconstruction of the presence, density, and movement of crowd. A selected set of experimental results are reported and discussed to assess the potentialities and limitations of the opportunistic passive wireless localization principle.

Index Terms – Crowd management, inverse problems, passive localization, target tracking.

I. INTRODUCTION

Crowd localization and management has become a significant research challenge because of the increasing need of centralized supervision of people in large spaces, such as shopping malls, exhibitions, airports, etc., in order to prevent critical situation as well as to plan and optimize advanced services to end users. One of the main challenge is to effectively detect and localize the crowd moving within the monitored areas, by limiting the invasiveness, the cost, and the complexity of the system. In this work, an alternative solution for the flexible and inexpensive implementation of a crowd localization system exploiting the existing wireless infrastructures is proposed. Nowadays, wireless networks and devices are more and more diffused, both in private and public spaces to provide free connection to web-based services, as well as for pervasive monitoring of heterogeneous parameters, within the so-called smart homes and smart cities [1]. Such wireless technologies, like WiFi and wireless sensor networks (WSNs) [2], have been exploited in an opportunistic way to acquire information about the crowd. More in

detail, the proposed approach implements the passive wireless localization principle [3][4] exploiting the available received signal strength indicator (RSSI) measured by most of the commercial wireless devices in order to reconstruct the characteristics of the domain under investigation and thus of the crowd presence and position. A multi-step procedure for the (a) detection, (b) density estimation, and (c) localization of crowd has been studied and validated. The preliminary outcomes of the experimental activities carried out both in controlled and non-controlled environment have been shown to give some insight about the envisaged potentialities in real-world applications.

II. PROBLEM FORMULATION

Let us consider a two-dimensional investigation domain Ω where a set of N wireless devices are deployed in known positions $\underline{r}_n, n = 1, \dots, N$, $\underline{r} = (x, y)$ being the position vector. Every device acts as transmitter and receiver, as well. When the n -th device is transmitting, an incident field $\xi_n^{inc}(\underline{r})$ is generated, it propagates throughout the domain where background objects and obstacles exist, and is received by the remaining $N - 1$ devices, in positions $\underline{r}_m, m = 1, \dots, N - 1$. In presence of crowd, the measured field is

$$\xi_n^{tot}(\underline{r}_m) = \xi_n^{inc}(\underline{r}_m) + \int_{\Omega_T} J_T(\underline{r}') G(\underline{r}' | \underline{r}_m) d\underline{r}' \quad n = 1, \dots, N; m = 1, \dots, N - 1 \quad (1)$$

where $J_T(\underline{r})$ is an equivalent source induced on the target (Ω_T being the target domain) by virtue of the incident field, and G is the free-space Green function. The crowd localization problem has been reformulated as the inverse problem of estimating the equivalent source $J_T(\underline{r})$ starting from the knowledge of the total measured field $\xi_n^{tot}(\underline{r}_m)$.

As a matter of fact, the field transmitted by the n -th transmitter and measured by the m -th receiver can be expressed as the complex open circuit voltage

$$\tilde{V}_{m,n} = \xi_n^{tot}(\underline{r}_m) \cdot l_m^{eff} + \eta_m = V_{m,n} e^{j\phi_{m,n}} \quad n = 1, \dots, N; m = 1, \dots, N - 1 \quad (2)$$

where l_m^{eff} is the antenna effective length of the m -th receiver and η_m the additive noise term. Accordingly, starting from the received power $\|\tilde{V}_{m,n}\|^2$ the available RSS indicator $RSS_{m,n} = 10 \log_{10} \|\tilde{V}_{m,n}\|^2$, usually represented in logarithmic scale, is derived.

In presence of crowd, both magnitude and phase of $\tilde{V}_{m,n}$ are affected due to the scattering of human bodies, that reflects in RSSI perturbations. Such perturbations can be mostly characterized by $\overline{RSS}_{m,n} = (1/K) \sum_{k=1}^K RSS_{m,n}(t_k)$ and $Var_{m,n} = E[RSS_{m,n}(t) - \overline{RSS}_{m,n}]$ statistical indicators, $t_k, k = 1, \dots, K$ being the considered time instants of acquisition. It has to be noticed that $Var_{m,n}$ is more sensitive to moving

crowd, while static configuration are better represented by changes in $\overline{RSS}_{m,n}$. Starting from the real-time analysis of RSSI, the following three-step (ordered by increasing complexity) procedure has been defined.

Step 1 - Crowd detection. Background subtraction techniques have been applied to enhance the contrast between the reference field propagation (absence of crowd) and the total field measured in presence of crowd. This first step gives a simple and raw binary information about crowd absence or presence within the domain Ω .

Step 2 - Crowd density estimation. Starting from the principle that total RSSI variance $Var_{m,n}$ $m = 1, \dots, N - 1; n = 1, \dots, N$ measured in presence of crowd can be approximated as a linear combination of the variance caused by each person [5], the density of the crowd has been estimated by processing the variance patterns. The output of this step is a percentage value of density, ranging from 0% (absence of crowd) up to 100% (predefined maximum number of persons within Ω).

Step 3 - Crowd localization. A spatial relation among all the $N \times (N - 1)$ wireless links exists according to the known positions of the wireless devices. This relation reflects on the statistical indicators $\overline{RSS}_{m,n}$ and $Var_{m,n}$, which have been given in input to a customized learning-by-example (LBE) technique, able to learn the complex relation between RSSI spatial perturbations and position of crowd within Ω . To this end, the domain has been discretized in a finite set of cells and the probability that the crowd belongs to one cell has been evaluated.

III. PRELIMINARY RESULTS

The proposed localization system has been experimentally validated in a real indoor scenario. A WiFi network ($f = 2.4GHz$) composed by $N=12$ access points has been adopted as reference wireless technology. The size of the domain Ω has been set to $50 \times 50 m^2$. Different crowded situations, besides the reference background, have been considered to test all the aforementioned steps (detection, density, localization). As for the detection phase, 2% of false detections has been obtained over a total number of $L=50$ tests. An example of RSSI behavior of one link perturbed by the entrance of $P=2$ persons within Ω is shown in Fig. 1(a). As it can be noticed, the effect on the RSSI variance has been clearly detected. Regarding the density estimation, a resolution of $\pm 16\%$ has been obtained ($P=90$ being the predefined maximum number of persons).

Finally, the most complex step of crowd localization, has been solved by means of a customized support vector machine (SVM) classifier (trained offline and only once) able to estimate the probability of crowd presence within a finite set of $C=25$ cells, each cell corresponding to a class. An example of probability map of crowd presence is shown in Fig. 1(b), the white dots being the actual crowd position.

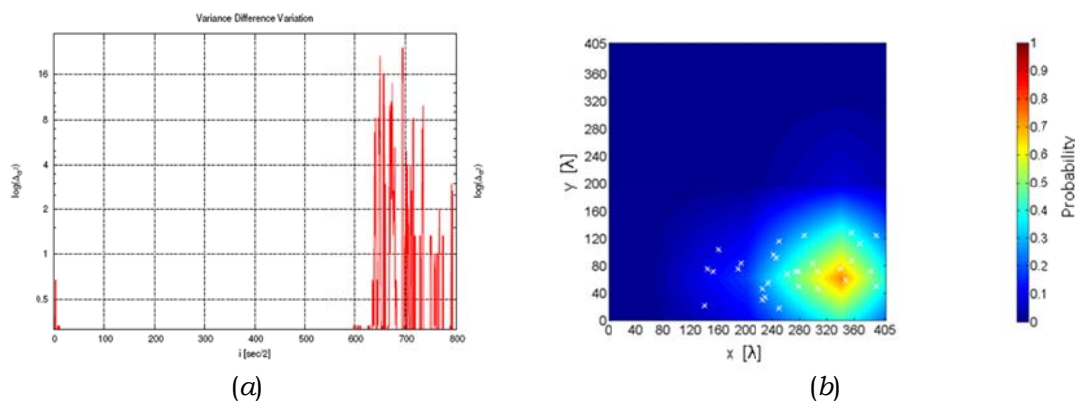


FIG. 1 – RSSI analysis for crowd binary detection (a) and probability map of crowd presence (b).

IV. CONCLUSION

In this work, the opportunistic exploitation of existing wireless infrastructures has been introduced for the passive localization of crowds in large indoor scenario. The proposed approach represents an alternative solution to complex and expensive monitoring systems and its adoption can be envisaged in a variety of application fields. The preliminary validation has shown the technological and methodological feasibility in the detection, density estimation, and localization of moving crowds. Further studies will be focused on the system robustness and on the long-term validation in real crowded test sites.

REFERENCES

- [1] F. Viani, F. Robol, A. Polo, P. Rocca, G. Oliveri, and A. Massa, "Wireless architectures for heterogeneous sensing in smart home applications – concepts and real implementations", *Proc. IEEE*, vol. 101, no. 11, pp. 2381-2396, Nov. 2013.
- [2] M. Benedetti, L. Ioriatti, M. Martinelli, and F. Viani, "Wireless sensor network: a pervasive technology for earth observation," *IEEE J. Sel. Topics Appl. Earth Observ.*, vol. 3, no. 4, pp. 488-496, 2010.
- [3] F. Viani, P. Rocca, G. Oliveri, D. Trincherio, and A. Massa, "Localization, tracking, and imaging of targets in wireless sensor networks: An invited review", *Radio Sci.*, vol. 46, no. 5, art. no. RS5002, Sep. 2011.
- [4] F. Viani, P. Rocca, M. Benedetti, G. Oliveri, and A. Massa, "Electromagnetic passive localization and tracking of moving targets in a WSN-infrastructure environment", *Inverse Problems*, vol. 26, no. 074003, pp. 1-15, 2010.
- [5] J. Wilson and N. Patwari, "See through walls: motion tracking using variance-based radio tomography networks," *IEEE Trans. Mobile Comput.*, vol. 10, no. 5, pp. 612-621, May 2011.

DIRECT AND INVERSE SCATTERING OF AXIALLY MOVING MULTILAYER ELLIPTIC CYLINDERS

M.Pastorino, M. Raffetto, and A. Randazzo

Department of Electrical, Electronic, Telecommunication
Engineering, and Naval Architecture (DITEN), University of Genoa
Via Opera Pia 11a, 16145, Genoa, Italy
{matteo.pastorino; mirco.raffetto; andrea.randazzo}@unige.it

Abstract

An efficient recursive procedure is generalized to solve electromagnetic direct scattering problems in the presence of axially moving multilayer elliptic cylinders. The new procedure is then exploited to define two inverse scattering procedures whose target is the reconstruction of the velocity and permittivity profiles of multilayer elliptic cylinders. Starting from the same measurements of the scattered field, it is shown that the reliability of the two procedures depend on the magnitude of the velocities of the layers. Preliminary results are then discussed.

Index Terms – Direct scattering problem, inverse scattering problem, moving media, reconstruction of permittivity and velocity profiles, elliptic cylinder.

I. INTRODUCTION

This paper deals with the scattering problem involving multilayer dielectric targets in which one or more layers are moving in the axial direction, even at relativistic velocities. The importance of this topic is well recognized in several areas, including astrophysics, nuclear fusion, as well as in several engineering fields. We consider here the case of multilayer cylinders with confocal elliptic cross sections under plane wave illumination conditions, in order to take advantages of an effective series solution for the forward scattering problems in the presence of cylinders at rest which has been previously developed by the authors [1]. Electric or magnetic line sources can be considered as well [2], [3].

The purpose of the paper is twofold. First of all we discuss the direct scattering problem. The iterative formulation in [1], [4], is modified in order to take account of the possible stationary axial velocities of the different layers. The topic has been discussed in [2] and some numerical results are reported in Section III. Successively, the direct scattering solution is used to define an iterative inverse scattering procedure aimed at retrieving both the permittivity profile and the velocities of the various layers starting from measurements of field samples performed outside the target. To this end, a proper cost function is defined and minimized by using a stochastic approach. The mathematical formulation is outlined in Section II. Some initial results are reported in Section III, whereas some conclusions are drawn in Section IV.

II. OUTLINE OF MATHEMATICAL FORMULATION

We refer to an N -layer elliptic cylinder hosted in vacuum. The z axis is placed along its axis, while in the transverse plane we use the elliptic coordinates (u, v) . We denote by d and a_i , $i = 1, \dots, N$, the semifocal distance and the semimajor axes of the elliptical interfaces, respectively. Each layer is made up of a linear, homogeneous and isotropic medium, characterized in its rest frame by $\varepsilon_{r,i} \in \mathbb{R}$, $i = 1, \dots, N$, and μ_0 , and can present a constant axial speed $\beta_i = v_{z,i}/c_0 \in \mathbb{R}$, $i = 1, \dots, N$, with respect to the selected reference frame, where c_0 is the speed of light in vacuum.

In the electromagnetic scattering problems we assume that the incident field is time-harmonic and independent of the z coordinate. Since all media are linear and the boundaries, the constitutive parameters and the axial velocities are stationary, all fields will be time-harmonic everywhere and the common factor $e^{j\omega t}$ is suppressed. Moreover, since, in addition to the previously recalled properties, the incident field is independent of the z coordinate we obtain that the solution, in each homogeneous medium, is independent of the axial coordinate as well. The solution we obtain in this way in each layer has then to be joined through the continuity of the tangential components of the electric and magnetic fields at the dielectric interfaces. In particular, in any layer of the scatterer, the axial components $E_z^i(u, v)$ and $H_z^i(u, v)$, $i = 1, \dots, N$, satisfy the two-dimensional Helmholtz equation in which the coefficient take account of the features of the possibly moving medium [2]. For the scattered components $E_z^{scat}(u, v)$ and $H_z^{scat}(u, v)$ the same result is easily deduced since the external medium is at rest in the adopted reference frame. Now we can expand all these field components in terms of Mathieu functions [2]. All the other components can be deduced from $E_z^i(u, v)$ and $H_z^i(u, v)$, for the i th layer, $i = 1, \dots, N$, or $E_z^{scat}(u, v)$ and $H_z^{scat}(u, v)$ for the scattered field in the external medium. Thus, we can generalize the efficient procedure defined in [1] and define another efficient procedure able to solve the problem of interest [2].

As for the inverse scattering procedure we define an investigation domain (where the axially moving cylinder is placed) and a set of probes to measure the arrays $E_{z,m,s,\mathbf{x}}^{measured}$ and $H_{z,m,s,\mathbf{x}}^{measured}$ ($m = 1, \dots, M$), for any illuminating field ($s = 1, \dots, S$) and for any scatterer configuration \mathbf{x} . For any trial solution $\bar{\mathbf{x}}$ the forward scattering procedure determines the arrays $E_{z,m,s,\bar{\mathbf{x}}}^{forward}$ and $H_{z,m,s,\bar{\mathbf{x}}}^{forward}$. Any optimization procedure able to minimize a cost function defined by considering $|E_{z,m,s,\mathbf{x}}^{measured} - E_{z,m,s,\bar{\mathbf{x}}}^{forward}|$ and $|H_{z,m,s,\mathbf{x}}^{measured} - H_{z,m,s,\bar{\mathbf{x}}}^{forward}|$ can be used. In particular, in this work we exploit the Artificial Bee Colony algorithm (ABC; a swarm optimization method inspired by the foraging behavior of honey bees).

The previous considerations do not take account of the specific inverse problem we have at hand. However, one can easily deduce that, in the presence of a TM (TE) incident field, small values of β_i , $i = 1, \dots, N$, affect E_z (H_z) in a way proportional to their square values and H_z (E_z) in a

way proportional to their values. Thus, in addition to the usual approach to solve the optimization problem, which considers all unknowns at the same time, we can define a two-step approach. In the first step the algorithm has to find all unknowns except for the values β_i , $i = 1, \dots, N$, by using just the measures of E_z (H_z), as if the media were at rest. The second step of this approach is devoted to the estimate of β_i , $i = 1, \dots, N$, by an inverse scattering procedure working just on H_z (E_z). It can be shown that the two-step approach is more efficient and reliable provided that $\max_{i=1, \dots, N} |\beta_i| \leq 0.1$ and $\varepsilon_{r,i}$ of the moving media are not too large.

III. NUMERICAL RESULTS

As a first example we consider a pipeline, that is a two-layer elliptic cylinder ($N = 2$), characterized by $d = 0.2\lambda_0$, $a_1 = 0.3\lambda_0$, $a_2 = 0.4\lambda_0$, $\varepsilon_{r,1} = 5$, $\varepsilon_{r,2} = 2$, $\beta_2 = 0$. The stationary and uniform axial speed of the inner material is considered to vary in the range $0.001 \leq \beta_1 \leq 0.2$. The scatterer is hosted in vacuum and is illuminated by a TM plane wave propagating in the \hat{x} direction. In Fig. 1 we show the magnitudes of E_z and H_z along the line $y = -x$ for different values of β_1 . The results are calculated by truncating all series expansions after the first 8 terms. This number is sufficiently large to give stable solutions. The results for $|E_z|$ are not strongly affected by β_1 . This is the reason why we report just the behavior of this quantity for $\beta_1 = 0.001$ and $\beta_1 = 0.2$. On the contrary, the figure clearly shows the effect of β_1 on $|H_z|$.

As for the performances of the two approaches to the inverse scattering problem discussed in Section II, we consider again a pipeline. In order to ease the task we consider also the following fixed quantities: the cylinder center of gravity is placed on the center of the investigation domain, $d = 0.15\lambda_0$, $a_1 = 0.25\lambda_0$, $a_2 = 0.3\lambda_0$, $\beta_2 = 0$. In this example the unknowns to be determined are just $\varepsilon_{r,1} = 4$, $\varepsilon_{r,2} = 2$, and $\beta_1 = 0.05$. Four illuminating TM plane waves whose directions of propagation are uniformly distributed in $[0, 2\pi)$ are considered. For every view the axial components of the electric and magnetic fields are measured on 90 measurement points, placed on a circle of radius λ_0 . All measured data are corrupted by a zero mean value Gaussian noise (having a variance corresponding to $SNR = 20$ dB). The following values for the parameters of the ABC algorithm are considered: maximum number of iterations $I_m = 100$; stop condition at I_m or when no improvements occur for last 20 steps; 10 executions are performed; number of bees for the two-step procedure equal to 12; number of bees for the general single step procedure $B_n = 16$. Many runs stop with very large errors when the general single step procedure is executed by using $B_n = 12$. The results obtained by using the two-step procedure are: mean number of iterations: 72.2 (step 1), 63.4 (step 2); mean relative errors: 0.9% ($\varepsilon_{r,1}$), 4.0% ($\varepsilon_{r,2}$), 1.1% (β_1). The corresponding results obtained by using the general procedure are: mean number of iterations: 85.8; mean relative errors:

1.8% ($\varepsilon_{r,1}$), 5.2% ($\varepsilon_{r,2}$), 1.7% (β_1). Other results obtained for $\beta_1 \leq 0.01$ show that the two-step procedure works and the general one fails in many cases (the percentage of the failures is more or less proportional to $1/\beta_1$).

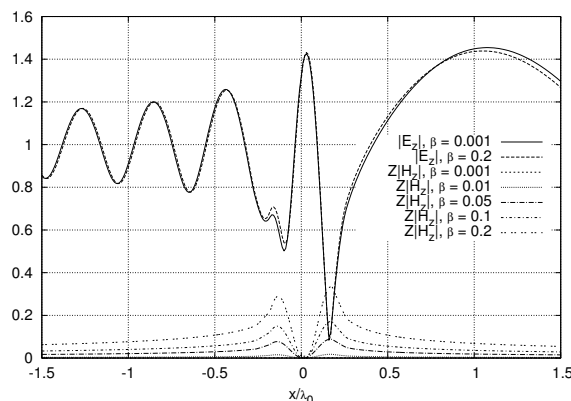


FIG. 1 – Magnitude of E_z and $\sqrt{\mu_0/\varepsilon_0}H_z$ along the line $y = -x$.

IV. CONCLUSIONS

In this paper an efficient recursive procedure is used to solve the direct scattering problem by axially moving multilayer elliptic cylinders. This solution is used to develop an inverse scattering method aimed at retrieving the velocity and permittivity profiles starting from measurements performed around the target. Two approaches have been developed, whose reliability depend on the magnitude of the velocities of the layers. Some preliminary results have been provided.

REFERENCES

- [1] S. Caorsi, M. Pastorino, and M. Raffetto, "Electromagnetic Scattering by a Multilayer Elliptic Cylinder Under Transverse-Magnetic Illumination: Series Solution in Terms of Mathieu Functions," *IEEE Transactions on Antennas and Propagation*, vol. 45 (6), pp. 926–935, Jun. 1997.
- [2] M. Pastorino and M. Raffetto, "Scattering of Electromagnetic Waves From a Multilayer Elliptic Cylinder Moving in the Axial Direction," *IEEE Transactions on Antennas and Propagation*, vol. 61 (9), pp. 4741–4753, Sep. 2013.
- [3] M. Pastorino, M. Raffetto, and A. Randazzo, "Two-Dimensional Green's Function for Scattering and Radiation Problems in Elliptically-Layered Media," *IEEE Transactions on Antennas and Propagation*, vol. 62 (4), pp. 2071–2080, Apr. 2014.
- [4] M. Pastorino, M. Raffetto, and A. Randazzo, "Electromagnetic Scattering by Lossy Multilayer Elliptic Cylinders," *IEEE Microwave and Wireless Components Letters*, Submitted.

SYNTHETIC EXPERIMENTS AND FIELD CONDITIONING AS AN EFFECTIVE APPROACH TO INVERSE SCATTERING

M. Bevacqua⁽¹⁾, L. Di Donato⁽²⁾, L. Crocco⁽³⁾, T. Isernia^(1,3),

⁽¹⁾ DIIES, Univ. Mediterranea di Reggio Calabria, Italy,
(martina.bevacqua, tommaso.isernia)@unirc.it

⁽²⁾ DIEEI, Univ. di Catania, Italy, loreto.didonato@dieei.unict.it

⁽³⁾ CNR-IREA, Naples, Italy, crocco.l@irea.cnr.it

Abstract

In this paper, two new solution procedures, based on a suitable pre-processing of the original scattered field data, are introduced in order to deal with inverse scattering problems. The two approaches allow to considerably simplify the research of the inverse problem solution.

Index Terms – contrast source approximations, contrast source conditioning, inverse scattering problem, synthetic experiments.

I. INTRODUCTION

In inverse scattering problems, known the incident fields and the measurements of the corresponding scattering fields, one aims to reconstruct the geometry and electromagnetic properties of an unknown scattering object. Because of the very many possible applications, this class of problems represents an area of relevant interest in applied electromagnetics. On the other side, because of ill-posedness and nonlinearity, the development of inversion procedures allowing to reconstruct the unknown target in an effective and reliable way, still represents a challenging and difficult task.

In this paper two new effective inversion procedures, based on suitably designed synthetic experiments, are proposed and discussed.

II. STATEMENT AND PECULIARITIES OF THE PROBLEM

Let us consider, in a 2-D geometry, an unknown nonmagnetic object embedded in an homogeneous lossless medium of electromagnetic features μ_b and ε_b , with compact support Ω . Let us suppose that some antennas are located in far-field on a closed curve Γ and irradiate a set of incident fields with TM polarization. The corresponding scattered fields are measured by some receiver antennas located on Γ . The equations describing the scattering problem for each ν -th illumination condition read:

$$E_s^{(\nu)}(r) = k^2 \int_{\Omega} G(r, r') W^{(\nu)}(r') dr' = \mathcal{A}_e[W^{(\nu)}] \quad r \in \Gamma, r \notin \Omega \quad (1.a)$$

$$\begin{aligned}
W^{(v)}(r) &= \chi(r)E_i^{(v)}(r) + \chi(r)k^2 \int_{\Omega} G(r,r')W^{(v)}(r')dr' \\
&= \chi E_i^{(v)} + \chi \mathcal{A}_i[W^{(v)}], \quad r \in \Omega
\end{aligned} \tag{1.b}$$

where $E_i^{(v)}(\cdot)$, $E_s^{(v)}(\cdot)$ and $W^{(v)}(\cdot)$ are the incident, scattered field and the contrast source induced in Ω , respectively, $k = \omega\sqrt{\mu_b\epsilon_b}$ is the wavenumber in the host medium, $G(r,r')$ is the Green's function pertaining to the homogeneous background, $\chi(\cdot)$ is the contrast function, \mathcal{A}_e and \mathcal{A}_i are the integral radiation operators. In (1) both $W^{(v)}(\cdot)$ and $\chi(\cdot)$ represent the unknowns of the problem, respectively.

Let us note that the amount of non-redundant information which can be collected is bounded [1] and, so, only a finite number of independent experiments and measurements can be made.

III. "SYNTHETIC" EXPERIMENTS

As described in [1], the solution of inverse scattering problems can take advantage from multiple (or multiview) experiments, i.e., from considering N fields with different directions ϑ_v impinging on the targets. Due to the linearity of the scattering phenomena, a superposition of these incident fields with known coefficients α_v , i.e.:

$$E_{inc,synthetic}(r) = \sum_{v=1}^N \alpha_v E_i(r, \vartheta_v) \tag{2}$$

gives rise to a scattered field and an induced contrast current which are the (same) superposition respectively, of the corresponding scattered fields and of the corresponding contrast currents respectively, i.e.:

$$W_{synthetic}(r) = \sum_{v=1}^N \alpha_v W(r, \vartheta_v) \tag{3.a}$$

$$E_{s,synthetic}(\varphi) = \sum_{v=1}^N \alpha_v E_s(\vartheta_v, \varphi) \tag{3.b}$$

where φ denotes the direction in which the scattered field is measured.

So, by means of several re-arrangements of the original experiments, one is able to build a set of new, 'synthetic', experiments that do not require new physical measurements. Hence, the two equations (3) represent a different manner to consider (and 're-weight') the collected information, provided that they have been properly chosen in order to avoid any loss of information.

IV. TWO NEW SOLUTION PROCEDURES BASED ON CONDITIONING OF CONTRAST SOURCES

An interesting chance arises from the possibility of ‘conditioning’ the contrast sources induced inside the object by means of a suitable “design” of the synthetic experiments. In fact, as these latter are also unknowns of the inverse problem, the enforcement and exploitation of some peculiar properties can simplify the solution task.

Amongst the several possibilities, let us consider the establishing of a circular symmetry of the currents around some ‘pivot points’ r_p inside the object. In fact, such a behavior can be easily enforced by requiring the same kind of symmetry on the scattered fields. Then, besides the linearized approach already successfully considered in [2], one has at least two innovative and effective solution procedures tackling the problem in its full non linearity.

A) A new regularized contrast source inversion scheme

Let us suppose to use a contrast source inversion procedure as in [3], and to apply it to a properly designed set of synthetic experiments satisfying the above quoted circular symmetry requirement. Then, in the different synthetic experiments one can enforce a circular symmetry of the contrast sources around different points r_p belonging to the target by simply adding a penalty term in the objective functional [3]. In practice, one will require contrast sources with minimal azimuthal slope rate, so that the penalty term will be expressed as:

$$\Phi = \sum_{p=1}^P \tau_p \Pi_p \left\| \frac{\partial W_{\text{synthetic}}^{(p)}}{\partial \phi_p} \right\|^2 \quad (4)$$

where (ϕ_p, ρ_p) is the local polar reference system centered on each pivot point r_p , Π_p represents a binary mask function that accounts for the imposition the penalty term only in a circular neighborhood of the pivot point, and τ_p is a non-negative weighting parameter.

B) An algebraic inversion method

Let us consider a set of points r_p belonging to the support of the object and such that the contrast function is slowly variable around them so that, in a first instance, the medium can be considered locally homogeneous. Then, in a sufficiently small neighborhood, one can represent the contrast source as a superposition of Bessel functions [4] as:

$$W_{\text{synthetic}}^{(p)} = \sum_{n=-\infty}^{+\infty} a_n J_n(k_p \rho_p) e^{jn(\phi_p - \frac{\pi}{2})} \quad (5)$$

where a_n is an amplitude coefficients and k_p is the “local” wavenumber in the pivot point r_p . As the currents are circularly symmetric, they can be approximated by means of the Bessel function of zero order, the only term in (5) which does not exhibit any angular variations with ϕ_p . This also implies that the currents are somehow ‘focused’ in r_p .

Moreover, thanks to the truncated Multiplication Theorem [5] of the Bessel function, the induced currents are rewritten in terms of the “local” values of contrast χ_p in the pivot point, i.e.:

$$W_{synthetic}^{(p)} \approx a_0^{(p)} \left\{ J_0(k|r - r_p|) - \frac{1}{2}k|r - r_p|J_1(k|r - r_p|)\chi_p + \frac{1}{8}(k|r - r_p|)^2 J_2(k|r - r_p|)\chi_p^2 \right\} \quad (6)$$

The equation (6) represents a new approximation of the currents which, (by neglecting the currents far from the considered pivot point where the contrast sources are actually focused), allows to formulate the inverse scattering problem in terms of a diagonal system of third degree algebraic equations. Obviously, this leads to a very fast inversion procedure.

V. CONCLUSION

Two new inversion approach, based on the condition of the contrast source by synthetic experiments, have been briefly described. The first one aims to regularize the inverse problem, looking for contrast currents without angular variations, while, in the second approach the inverse problem is recast into a diagonal system of third degree algebraic equations.

Further details on these approaches and on the synthetic experiments, together with examples, will be presented at the Conference.

REFERENCES

- [1] O. M. Bucci and T. Isernia, “Electromagnetic inverse scattering: Retrievable information and measurement strategies”, *Radio Sci.*, vol. 32, pp. 2123–2138, 1997.
- [2] L. Crocco, L. Di Donato, I. Catapano, and T. Isernia, “The linear sampling method as a way to quantitative inverse scattering”, *IEEE Trans. Antennas Propag.*, 60(4) 1844-1853, Apr. 2012.
- [3] P. M. van den Berg and R. E. Kleinman, “A contrast source inversion method”, *Inv. Probl.*, vol. 13, n. 6, p. 1607, 1997.
- [4] D. S. Jones, “Acoustic and *Electromagnetic Waves*”, Oxford, England: Clarendon Press, 1986.
- [5] M. Abramowitz, I. A. Stegun, “Handbook of Mathematical Functions with Formulas, Graphs, and Mathematical Tables”, New York, Dover Publications, 1964.

A PRINTED LPDA FED BY A COPLANAR WAVEGUIDE FOR WIDEBAND APPLICATIONS

Giovanni Andrea Casula⁽¹⁾, Giorgio Montisci⁽¹⁾, Giuseppe Mazzarella⁽¹⁾,
Paolo Maxia⁽¹⁾

⁽¹⁾ Dipartimento di Ingegneria Elettrica ed Elettronica of the
University of Cagliari, Italy
a.casula@diee.unica.it, giorgiom@diee.unica.it,
mazzarella@diee.unica.it, paolo.maxia@diee.unica.it

Abstract

A printed Log-periodic dipole array (LPDA), operating between 3 and 6 GHz, and fed with a coplanar waveguide, is presented. The antenna has been designed using CST Microwave Studio 2012, and then realized. The proposed antenna can be used for broadband applications in the whole operating frequency band (3-6 GHz), with a very good input matching and a satisfactory end-fire radiation pattern.

Index Terms – Log-periodic arrays, Coplanar waveguide, Wideband Antennas.

I. INTRODUCTION

A log-periodic antenna is a broadband directional antenna whose properties are regularly repetitive as a logarithmic function of the excitation frequency. Even the lengths and spacing of the elements of a log-periodic antenna increase logarithmically from one end to the other. This kind of antenna is useful in all the applications requiring a wide range of frequencies to be covered while still having moderate gain and directionality. The individual elements of a log-periodic antenna are usually dipoles, as in log-periodic dipole arrays (LPDAs). In a LPDA, alternating elements must be driven with 180 degrees of phase shift from one to another, therefore the LPDA produces an end-fire radiation pattern. In a wired LPDA this phase shift is normally implemented by connecting individual elements to alternating wires of a balanced transmission line. On the other hand, for printed LPDAs, an appropriate feeding network must be designed in order to excite each element with the requested phase. Log-periodic dipole arrays (LPDAs) using cylindrical dipoles are extensively used as wideband antennas, and their design can be performed following the suggestions given by Carrel [1]. LPDA can be designed with a bandwidth up to a decade, and with a typical gain around 10 dBi. Therefore, log-periodic (LP) concept has been used with different implementations in the past years, and, among them, printed LP arrays are very promising due to their low cost and weight, although their realization can be difficult, since all dipoles must be fed (and with alternate sign) by a Paired Strip (PS) [2], and some dipoles should be very thin and short. An important and critical task

the designer has to overcome during the design of printed log-periodic arrays is the modeling of the feeding network. The implementation of the wideband matching of a LPDA is typically obtained with an infinite balun, which in wire LPDAs is achieved with a coaxial cable passed through one of the antenna booms and connected to the narrow side of the antenna, while in printed LPDAs is obtained soldering the outer conductor of a coaxial cable to the bottom layer of the LPDA, and connecting the inner conductor to the top layer of the antenna using a via inside the substrate. However, this feeding technique presents some difficulties, in fact the soldering over all the antenna layout can be very hard to realize, and can compromise both the radiation pattern and the antenna matching. To overcome such problems, the solution is a fully planar feeding network without any shorting pins. Thus, we investigate in this work the electromagnetic behavior of a new feeding technique, using a coplanar waveguide (CPW) cut into one of the PS, while the other PS is floating. Coplanar waveguides have already been employed to feed printed antennas [3-4]. The aim of this work is to create a sort of “flat” coaxial cable in one of the LPDA layers, and a balun at its end. The balun is obtained using a via-hole between the CPW and the strip on the other side of the slab, and an “open” termination of the two ground conductors of the CPW. The LPDA array has been designed using CST MICROWAVE STUDIO 2010, a general purpose software for the 3D electromagnetic simulation of microwave components.

II. ANTENNA DESIGN

The dipoles of the printed LPDA, shown in Fig.1, are alternately connected on the two lines of the PS, fed by a coplanar waveguide printed within one strip. The structure is very close to a standard (namely, wire) LPDA, and therefore the standard strategy to design an LPDA can be used [1], though with some modifications. The design specifications of the proposed LPDA antenna are its operating bandwidth and directivity. The design parameters are the spacing factor, $\sigma = S_n/4L_n$, and the log-period, $\tau = L_{n+1}/L_n$ (see Fig. 1a), which are selected by using Carrel design curves for the specified bandwidth and directivity [1]. In our case, we require an average directivity of 9 dB in the bandwidth 3-6 GHz, therefore, following the design rules given by Carrell [1], the number of elements must be equal to $N=11$, the log-period must be $\tau=0.88$, and the spacing factor must be $\sigma=0.16$. In order to obtain an easy matching with the standard SMA connectors, we choose for the GCPW feeding line a characteristic impedance equal to 50Ω . Therefore, the CPW parameters a and b , shown in Fig. 1(b), are computed using the well-known CPW design equations [5]. Since the printed LPDA lies on a dielectric substrate, the geometric parameters of this antenna cannot be computed as in the case of a standard wire LPDA [1], which radiates in free space, and their values heavily depend

on the LPDA substrate. We have chosen ARLON AD450 as dielectric substrate, a low loss material (whose dielectric loss tangent is $\delta = 0.0035$), with a dielectric permittivity $\epsilon_r = 4.5$ and a thickness of 1.524 mm, while the thickness of the metallization is $t = 0.035$ mm. The CPW parameters a and b , required to get $Z_0 = 50 \Omega$, are: $a = 1.05$ mm, $b = 1.5$ mm. The total width c of the CPW feeding line has been chosen equal to the width of the PS corresponding to an equivalent impedance of 50Ω : $c = 3.9033$ mm. At the lowest operating frequency (3 GHz), the active region includes only the dipole N (the longest one), which therefore must be resonant at this frequency. Since the resonant resistance of this dipole must be 50Ω , both the length L_N and the width W_N of it have been evaluated using a cut-and-try procedure on CST Microwave Studio. Then, we obtain $L_N = 17.5$ mm and $W_N = 2.87$ mm. The lengths and widths of the other dipoles are computed by using the well-known expressions for LPDAs [1]: $L_{n+1}/L_n = 1/\tau$, $n=1, \dots, 10$. The same equation can be used in order to compute the dipole widths and spacings. In Fig. 1e the geometry of the dipoles is reported. The shown spacings are computed using the aperture angle α , according to [1]. The aim of this work is to implement a flat coaxial cable by using a coplanar waveguide as feeding network of a log-periodic antenna. Therefore, the central conductor of the coplanar waveguide must be connected, through a via-hole, to the bottom layer of the PS (as indicated in Fig. 1), so that a single progressive wave propagates on the PS itself toward the largest dipole. In this way, the CPW termination acts as a balun, as long as the two ground lines of the CPW end abruptly (as in Fig. 1d). The starting length of the final termination L_H of the CPW (see Fig. 1a) has been chosen equal to half a wavelength at the central frequency of 4.5 GHz. This value has been then optimized, and the best input matching has been obtained for $L_H = 22.97$ mm.

III. RESULTS

The LPDA antenna, designed in Section II, has been manufactured (see Fig. 1d) and fully characterized. In Fig. 2a, the simulated and measured frequency responses of the input reflection coefficient are shown, and the broadband input matching specification between 3 and 6 GHz is fulfilled, with a very good agreement between simulation and measurement. As a matter of fact, the input matching range extends well beyond 6 GHz, and the -10 dB antenna bandwidth approximately extends from 2.5 to 7.5 GHz. In Fig. 2b, the antenna gain (both evaluated by CST and measured) as function of the frequency is reported. The antenna gain is quite stable over the required frequency range, with an average value equal to 6.85 dB. Therefore, the proposed LPDA can be successfully used as a broadband antenna in the frequency range 3-6 GHz, with a relative bandwidth greater than 33%.

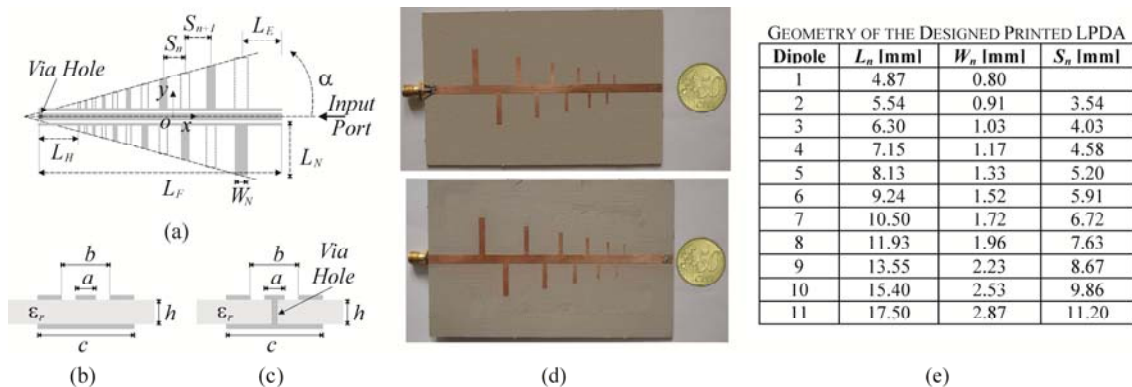


FIG. 1 – (a) Antenna Layout (Top Layer); (b) Coplanar Waveguide transverse section at the input port; (c) Coplanar Waveguide view at the via-hole section; (d) Photo of the LPDA antenna; (e) Geometry of the designed printed LPDA.

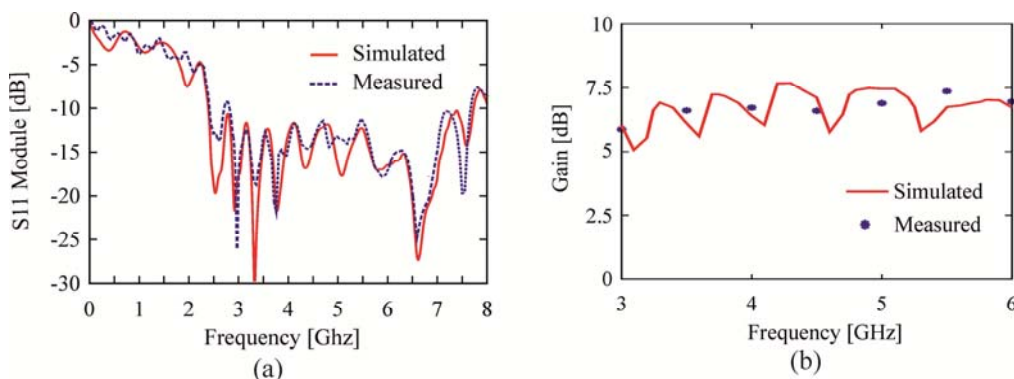


FIG. 2 – (a) Reflection coefficient; (b) Gain in the endfire direction of the designed LPDA antenna shown in Fig. 1.

IV. CONCLUSION

A printed log-periodic dipole array with a new feeding technique, operating between 3 and 6 GHz, has been designed and analyzed using CST. The directivity, the return loss and the radiated electric field in the design bandwidth are similar to other solutions employing the coaxial cable feeding. On the other hand, the proposed configuration has a simple realization, avoiding manufacturing time and problems due to soldering of the coaxial cable, with low cost and compact size, and is easy to connect with the external SMA connectors.

REFERENCES

[1] R. Carrel, “The Design of Log-Periodic Dipole Antennas,” IRE International Convention Record, Vol.9, March 1961, pp. 61-75.
 [2] H.A. Wheeler, “Transmission properties of parallel strips separated by a dielectric sheet,” IEEE Trans. Microw. Theory Tech., vol.13, pp. 172-176, 1965.
 [3] S.Y. Chen, P.H. Wang, P. Hsu, “Uniplanar Log-Periodic Slot Antenna Fed by a CPW for UWB Applications,” IEEE Ant. and Prop. Letters, vol.5, 2006.
 [4] S.H. Kim, J.H. Choi, J.W. Baik, Y.S. Kim, “CPW-fed Log-Periodic Dumb-Bell Slot Antenna Array,” Electronic Letters, vol. 42, no. 8, April 2006.
 [5] B.C. Wadell, Transmission Line Desing Handbook, Artech House, 1991.

A NUMERICAL METHOD TO ACCOUNT FOR DIGITALLY-MODULATED CARRIERS IN TIME-MODULATED ANTENNA ARRAYS

D. Masotti⁽¹⁾, P. Francia⁽¹⁾, F. Mastroi⁽²⁾, A. Costanzo⁽²⁾, V. Rizzoli⁽¹⁾

⁽¹⁾ DEI, University of Bologna
Viale Risorgimento 2, 40136 Bologna, Italy

⁽²⁾ DEI, Cesena Campus, University of Bologna
Via Venezia 52, 47521 Cesena, Italy
diego.masotti@unibo.it

Abstract

The paper shows a circuit-level/electromagnetic co-simulation tool for the rigorous analysis of time-modulated arrays in presence of digitally modulated carriers. The Harmonic Balance (HB) technique is used for the accurate description of the nonlinearities, and is combined to the full-wave description of the radiating array. The resulting large dimension of the solving system is efficiently managed by the further deployment of a model-order reduction HB technique. The developed tool overcomes simplifying assumptions of previous approaches and its effectiveness is verified with numerical examples in both modulated and unmodulated carrier cases.

Index Terms – Harmonic balance technique, nonlinear simulation, time-modulated arrays

I. INTRODUCTION

In time-modulated arrays (TMAs) the time-sequence pattern used to pilot the nonlinear switch at each antenna port is exploited as a further degree of freedom in the radiation surface engineering. The almost unlimited combinations of: (i) “switch-on” interval durations (as in Variable Aperture Size (VAS) solutions [1]), (ii) rising and falling instants choice (as in Binary Optimized Time Sequences (BOTS) [2] or Pulse Shifting (PS) [3] solutions), make TMAs a highly versatile and agile system, ideal for Cognitive and Software-Defined Radio applications.

In spite of the importance of these systems, the available design approaches do not consider the electro-magnetic (EM)-couplings between the different parts of the system, the nonlinear nature of these arrays, and their actual operation in modern telecommunication links.

In this paper we extend the approach presented in [4] by exploiting the versatility of the Harmonic Balance (HB) technique in order to simultaneously manage the modulation laws of both the bias sources driving the switches and the digitally modulated carrier.

II. NUMERICAL APPROACH DESCRIPTION

The HB method is a powerful numerical tool which can be easily used for the rigorous co-simulation of time-modulated linear arrays by combining it with full-wave solvers for the EM description of the

antenna elements. According to piecewise HB principles [4] a TMA can be described as any nonlinear system, i.e. by considering a linear subnetwork (the array and its feeding network) and a nonlinear subnetwork (the nonlinear switches).

If we consider a sinusoidal steady-state regime, described by a set (say n_H) of harmonics of a fundamental (angular) frequency ω_0 , a generic signal $s(t)$ of the nonlinear radiating system can be expressed as a combination of its harmonic phasors S_k by

$$s(t) = \text{Re} \left[\sum_{k=0}^{n_H} S_k \exp(jk\omega_0 t) \right] \quad (1)$$

In the case of an antenna array subsystem with n_A excitation ports, due to the superposition principle, the far field radiated by the array at the fundamental frequency ($k = 1$) may be cast in the form

$$\mathbf{E}(r, \theta, \phi; \omega_0) = \frac{\exp(-j\beta r)}{r} \bullet \sum_{i=1}^{n_A} \left[\hat{\theta} A_{\theta}^{(i)}(\theta, \phi; \omega_0) + \hat{\phi} A_{\phi}^{(i)}(\theta, \phi; \omega_0) \right] \mathbf{I}_1^{(i)} \quad (2)$$

where $\hat{\theta}, \hat{\phi}$ are unit vectors in the θ, ϕ direction of the spherical reference system, $\mathbf{I}_1^{(i)}$ is the phasor of the current at the i -th port of the array at ω_0 , and $A_{\theta}^{(i)}, A_{\phi}^{(i)}$ are the scalar components of the normalized field, generated once for all by the EM simulation of the given array.

III. TMA SIMULATION WITH SINUSOIDAL CARRIERS

The rigorous co-simulation of TMAs by taking into account the time modulation of the bias sources driving the switches can be carried out by resorting to the modulation-oriented harmonic-balance (MHB) method [4]. If the bias voltages are periodic sequences of rectangular pulses with repetition time T_s and modulation frequency $\omega_s = 2\pi/T_s$, according to MHB principles (i.e. provided that $\omega_0 \gg \omega_s$, always valid in practical applications), for the current signals at the i -th antenna port, we have

$$i^{(i)}(t, t_s) = \text{Re} \left[\sum_{k=0}^{n_H} \mathbf{I}_k^{(i)}(t_s) \exp(jk\omega_0 t) \right] \quad (3)$$

where t_s is the slow envelope time of the switches modulation law, t is the fast carrier time, and $\mathbf{I}_k^{(i)}(t_s)$ is the time-dependent complex k -th current envelope (or modulation law). Of course the time-dependent far-field envelope may be computed by exploiting the “modulated” version of (2), similar to (3) [4].

IV. TMA SIMULATION WITH DIGITALLY MODULATED CARRIERS

The traditional approach to system analysis under digitally modulated RF drive is again the MHB method, but it cannot be applied in the specific case: here the fundamental angular frequencies of the two-tone

steady state are the RF carrier ω_0 and the diode switching frequency ω_S , and the digital modulation is applied to the former. The problem obviously arises from the fact that the digital modulation bit rate B_D is usually such that $\omega_S/2\pi \ll B_D$, so that circuit envelope analysis requires time-domain convolution to compute the linear subnetwork response, and thus becomes very inefficient [5]. In order to overcome this difficulty, we may replace the aperiodic sequence of modulating bits by a periodic signal generated by repeating a basic random sequence of N bits. The integer N should be large enough to allow the statistical properties of the real signal to be accurately reproduced by the periodic sequence. The fundamental angular frequency of this signal is $\omega_D = 2\pi B_D/N$ and t_D is the corresponding envelope time. In this way each physical quantity supported by the system, e.g. the radiated field, is described as a three-tone quasi-periodic signal with a discrete spectrum whose lines are located at $\Omega_{k_0, k_S, k_D} = k_0 \omega_0 + k_S \omega_S + k_D \omega_D$, where k_0, k_S, k_D are integer harmonic numbers. In this way the problem solution is demanded to the ability of the HB algorithm to handle large numbers of spectral lines. The numerical solution strategy adopted is based on an evolution of the model-order-reduction techniques introduced in [5].

Therefore the current at the i -th array port under digitally modulated drive may be expressed in the form

$$i^{(i)}(t, t_j, t_m) = \text{Re} \left[\sum_{k_0, k_j} \mathbf{I}_{k_0, k_j}^{(i)}(t_m) \exp \left\{ j(k_0 \omega_0 t + k_j \omega_j t_j) \right\} \right] \quad (4)$$

where j and m stands for S and D in any combination. The corresponding far-field can be obtained by an equation similar to (2) with the constant phasor $\mathbf{I}_1^{(i)}$ replaced by the time-dependent phasor $\mathbf{I}_{k_0, k_j}^{(i)}(t_m)$. If $j = S$ and $m = D$ the far-field envelope $E_{k_0, k_S}^{(i)}(t_D)$ reproduces the digitally modulated law. Similarly, $E_{k_0, k_D}^{(i)}(t_S)$ represents the far-field envelope of the switching modulation sequence, in presence of a digitally modulated carrier. The results for $k_0=1, k_D=0$ provide the waveform at the fundamental frequency ω_0 .

V. CO-SIMULATION RESULTS

The TMA system we consider consists of a 16-monopole planar linear array with corporate microstrip feed network, operating at $\omega_0 = 2\pi * 2.45 \text{GHz}$. The substrate is a 0.635 mm-thick Taconic RF60A ($\epsilon_r = 6.15, \tan\delta = 0.0028 @ 10 \text{GHz}$). The array elements are aligned along the x -axis and the element spacing is $\lambda/2$, according to a standard broadside solution [4].

The adopted switching modulation frequency for the Schottky diodes is $\omega_S = 2\pi * 12 \text{kHz}$. The 2.45GHz carrier is modulated according to the 16-QAM modulation format: a sequence of 512 bits (with oversampling

4, i.e. 2048 samples) with bit rate 25.6Mb/s is considered, thus providing a modulation frequency $\omega_D = 2\pi \cdot 50\text{kHz}$.

As an example of application the case of a VAS pulse sequence reproducing the Dolph-Chebyshev pattern with side lobe level (SLL)=-30dB is considered. The inset of Fig. 1 shows the corresponding symmetric periodic sequence of the “switch-on” intervals as a function of the diode numbers. The number of spectral lines of the entire spectrum is about 193,000, corresponding to an HB solving system of more than 6,000,000 scalar unknowns. Fig. 1(a) shows the xz plane radiation patterns of the TMA driven by a 0dBm 16-QAM carrier, at the fundamental ($k_S=0$) and the two switching modulation harmonics ($k_S=1,2$). The effect of the modulation is evident from inspection of Fig. 1(b) reporting the corresponding patterns for an unmodulated carrier at the same input power level.

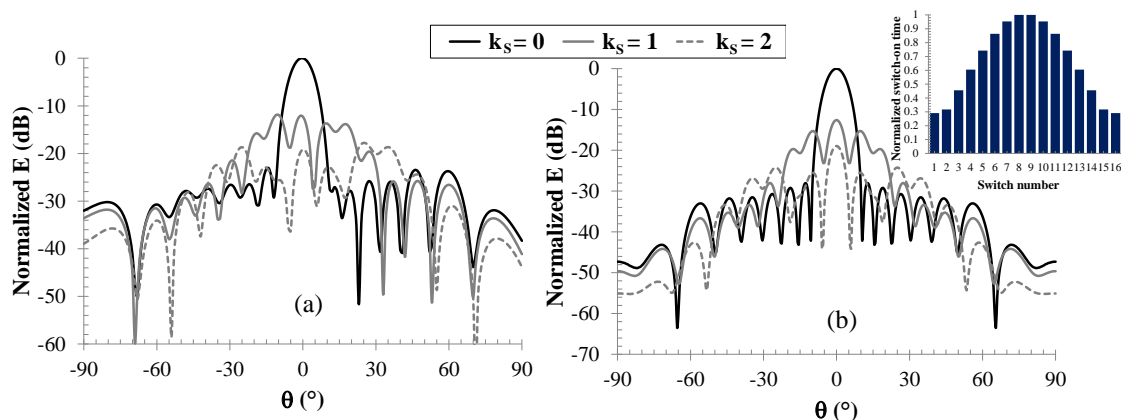


FIG. 1 – Normalized radiation pattern at the fundamental and first two harmonics for a VAS control sequence (switches excitation pattern shown in the inset): (a) under digitally modulated drive; (b) under sinusoidal excitation.

REFERENCES

- [1] W. H. Kummer, A. T. Villeneuve, T. S. Fong, and F. G. Terrio, “Ultra-low sidelobes from time-modulated arrays,” *IEEE Trans. on Ant. and Prop.*, vol. AP-11, no. 6, pp. 633-639, Nov. 1963.
- [2] S. Yang, Y. B. Gan, A. Qing, and P. K. Tan, “Design of a uniform amplitude time-modulated linear array with optimized time sequences,” *IEEE Trans. on Ant. and Prop.*, vol. 53, no. 7, pp. 2337-2339, July, 2005.
- [3] L. Poli, P. Rocca, L. Manica, and A. Massa, “Pattern synthesis in time-modulated linear arrays through pulse shifting,” *IET Microwaves, Antennas & Propagation*, vol. 4, no. 9, pp. 1157-1164, Sept. 2010.
- [4] D. Masotti, P. Francia, A. Costanzo, and V. Rizzoli, “Rigorous Electromagnetic/Circuit-Level Analysis of Time-Modulated Linear Arrays,” *IEEE Trans. on Ant. and Prop.*, vol. 61, no. 11, 2013, pp. 5465-5474.
- [5] V. Rizzoli, F. Matri, A. Costanzo, and D. Masotti, “Harmonic Balance Algorithms for the Circuit-Level Nonlinear Analysis of UWB Receivers in the Presence of Interfering Signals”, *IEEE Trans. Computer-Aided Design of Integrated Circuits and Systems*, vol. 28, no. 4, April 2009, pp. 516 - 527.

A MICROWAVE DISPLACEMENT SENSOR SYSTEM EXPLOITING ELECTROMAGNETIC INTERFEROMETRY

A. Costanzo ⁽¹⁾, M. Fantuzzi⁽²⁾, D. Masotti ⁽²⁾, V. Rizzoli⁽²⁾

⁽¹⁾ DEI, Cesena Campus, University of Bologna
Via Venezia 52, 47521 Cesena, Italy

⁽²⁾ DEI, University of Bologna
Viale Risorgimento 2, 40136 Bologna, Italy
alessandra.costanzo@unibo.it

Abstract

The paper describes a possible circuit implementation of a low-cost, non-invasive sensor system for wireless structural monitoring. It consists of a two-tags array and one reader: the former is the sensor placed on the structure to be monitored, the latter is placed in a predetermined position with respect to the array phase center. The simple operating principle of the system exploits the far-field array-factor definition, in particular the positions, on the reader side, of the nulls of the received radiation surface. A proof of concept of the sensor is experimentally demonstrated for two operating frequencies, 2.45 and 5.8 GHz.

Index Terms – Displacement sensor, antenna array, interferometry, RFID.

I. INTRODUCTION

Modern displacement sensors are invasive components which need to be embedded in the material of the structure to be monitored. The solution we present represents an important step in the direction of a low-cost, easily-mounting sensor system. It consists of a couple of microwave antennas with known excitations, equipped with onboard sources (for preliminary tests) or remotely supplied (in final realization). A custom reader device is placed in a precise position with respect to the sensor, and receives the electromagnetic (EM) field radiated by the sensor: the sharp slope of the nulls of the corresponding radiation surface is exploited. A comparison with a priori stored EM-simulated data allows to easily recover the actual reciprocal position of the sensor tags and, thus, to know the status of the monitored portion of the building. The operating principle is thus based on reverse engineering of the well-known concept of antenna array factor. The accuracy of the displacement sensor here presented is directly related to the wavelength of the radiated field. Therefore, in order to measure deformations in the millimeter range the RFID tags need to operate at the microwave band: two measurement examples at 2.45 GHz and 5.8 GHz are presented for comparison.

II. SENSOR OPERATING PRINCIPLE AND EXPERIMENTAL VALIDATION

The sensor under exam consists of a simple broadside array of two patch antennas, aligned along z-axis as indicated in Fig. 1(a). From

inspection of Fig. 1(b), reporting the array factor (AF) dependence on the elevation θ , the strong dependence of the first nulls position on the array elements spacing L_a , in a narrow θ range, is evident. This property suggests the idea on which the new displacement sensor system is based: the inversion of the map provided by Fig. 1(b) allows to obtain, in a very accurate way, the reciprocal position of the two antennas by the knowledge of the θ value corresponding to the nulls.

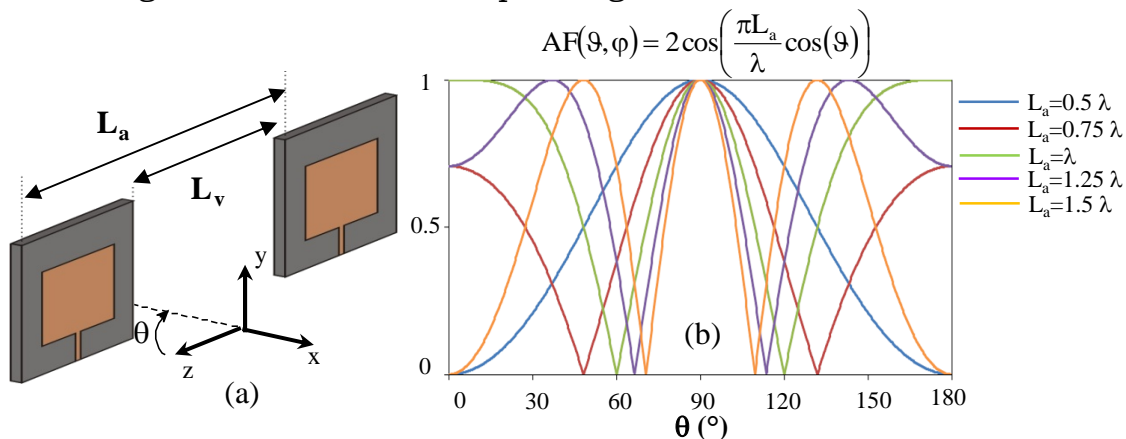


FIG. 1 – (a) Array of two patch antennas and parameters definition; (b) normalized AF of the array vs. elevation θ for different elements spacing.

By means of a full-wave simulator it is possible to accurately simulate the actual sensors system in order to take into account the EM couplings between them. Fig. 2 reports the predicted field received by the reader at a distance $x=10$ m, at the same height of the sensors ($y=0$), moving along the z axis, for the patch array of Fig. 1(a), operating at 2.45 GHz, for several normalized displacements $L_x=L_a/\lambda-0.5$.

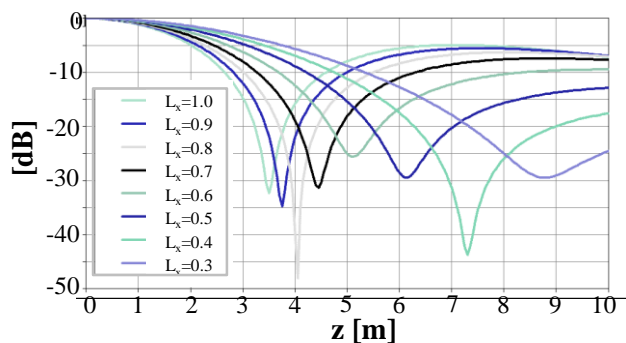


FIG. 2 – Normalized field received by a moving reader for different sensors spacing.

As a first experimental validation two tests have been performed in an outdoor environment with the two couples of patch antennas resonating at 2.45 GHz and 5.8 GHz, respectively. The antennas are placed on a wooden support with moving cursors, in order to vary their distance and to easily measure it by means of a precision caliper. The support is then attached on a building wall at 1.8 m from the ground.

The reader is at a distance of $x=5$ m from the building at the same sensor height ($y=0$). It is equipped with a broadband log-periodic 8-dB gain antenna, and is moved parallel to yz -plane to detect the electromagnetic field nulls. The transmitted power is 10 dBm, roughly corresponding to -68 dBm and -75 dBm of received power in correspondence of the EM-field nulls at the two operating frequencies, in free-space conditions. Remote distance estimations are obtained by comparing reader measurements with the stored database available from the modeling procedure. Referring to Fig. 1(a), L_v is the sensors displacement to be measured: if L_{ve} is the estimated value stored in the database, we are able to define the measurement relative error

$$\Delta L_v \% = 100 \cdot |L_v - L_{ve}| / L_v \quad (1)$$

This test has been carried out for several different situations and Table I reports the corresponding measurement results obtained at the two different operating frequencies. It clearly demonstrates that the system accuracy is very promising: deformations in the millimeter range can be easily detected. Furthermore, the higher is the frequency, the lower is the measurement error.

TABLE I – MEASUREMENT CAMPAIGNS

@ 2.45 GHz			
$L_x [\lambda]$	$L_v [mm]$	$L_{ve} [mm]$	$\Delta L_v \%$
0.4	35.00	34.31	1.97
0.64	64.75	66.28	2.36
0.72	74.00	74.82	1.11
0.80	84.00	84.53	0.63
0.4	35.00	34.31	1.97
@ 5.8 GHz			
0.66	25.00	24.76	0.96
0.71	27.50	27.36	0.51
0.76	30.00	30.01	0.03
0.81	32.50	32.54	0.09
0.66	25.00	24.76	0.96

III. SYSTEM IMPLEMENTATION

The new sensor concept has been patented [1]. The engineering process of both the tags and the reader circuits are currently under development. In this paper we briefly describe the 5.8 GHz sensor design: in order to be energy aware, the sensor is based on an active two-element antenna array normally in sleep mode, and activated by injection locking techniques. In our design the sensor antennas must be able to manage two cross-polarized signals: one to receive the injection locking signal (horizontally polarized), the other to send the oscillators output to be decoded as structural conditions (vertically polarized). According to the operating principle described in section II, the moving

reader is able to detect the minimum of the sensor array reply, and a Personal Digital Assistant (PDA) elaborates the data to retrieve the sensor displacement information.

The optimum system operating condition should consider two exactly in-phase sensors reply. Instead of satisfying this difficult constrain, we have evaluated the effect of phase-unbalance between the two tags [2]: an encouraging 1% increment of the relative error (1) has been detected for a high 30° phase unbalance.

The compact layout of the self-oscillating antenna is obtained by exploiting the multilayered architecture of Fig. 3(a): a 1.52 mm-thick Neltec NY9208 substrate ($\epsilon_r = 2.08$) supporting the patch (Fig. 3(b)) is stacked on the slotted ground of a 0.635 mm-thick substrate of Taconic RF-60 ($\epsilon_r = 6.15$) for the oscillator circuit (Fig. 3(c)). The adopted hole-shaped antenna topology allows to reach an isolation better than -25 dB in the operating frequency bandwidth. For the accurate design of the ILO is fundamental to exploit well-established CAD techniques for autonomous nonlinear circuits based on the combination of harmonic-balance method and bifurcation theory [3]. As an example, for 13 dBm of power transmitted by a signal generator 0.8 m far from the antenna, the simulated stable locking range is represented by the frequency band from 5.8 to 5.837 GHz.

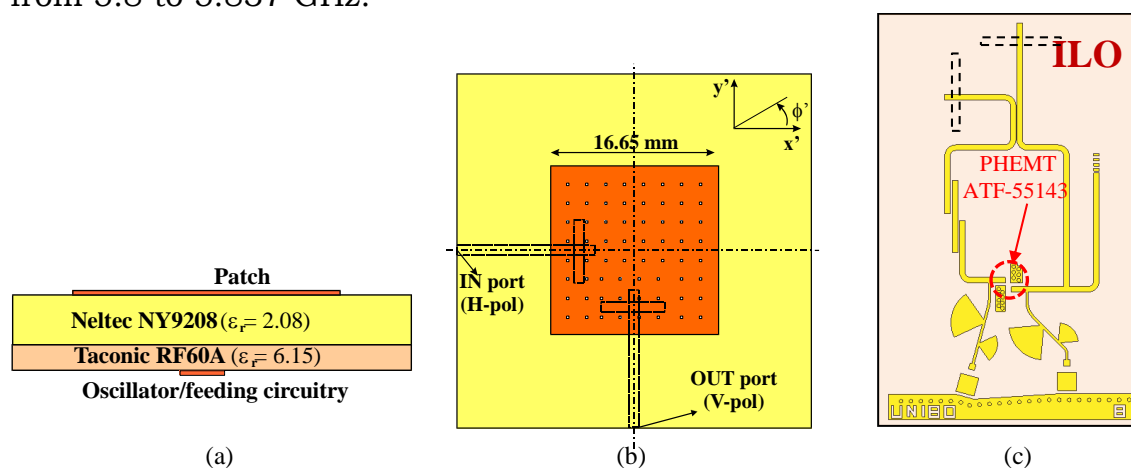


FIG. 3 – System layout: (a) stack-up; (b) antenna layer; (c) ILO layer.

REFERENCES

- [1] A. Costanzo, A. Benedetti, V. Rizzoli, "Method and system for remote monitoring deformations of a structure", patent no. US 8,410,924 B2, Apr. 2 2013.
- [2] V. Rizzoli, A. Costanzo, E. Montanari, and A. Benedetti, "A New Wireless Displacement Sensor Based on Reverse Design of Microwave and Millimeter-Wave Antenna Array", *IEEE Sensors Journal*, Vol. 9, No. 11, Nov. 2009, pp. 1557 – 1566.
- [3] V. Rizzoli, A. Costanzo, and D. Masotti, "Coupled nonlinear/electromagnetic CAD of injection-locked self-oscillating microstrip antennas", *Int. Journal RF and Microwave Computer-Aided Eng.*, vol. 13, Sept. 2003, pp. 398-414

POSITIONING ERRORS COMPENSATION IN A NONREDUNDANT SPHERICAL NF-FF TRANSFORMATION: EXPERIMENTAL EVIDENCES

F. D'Agostino, F. Ferrara, C. Gennarelli, R. Guerriero, M. Migliozi

D.I.In., Università di Salerno, via Giovanni Paolo II, 132 - 84084 Fisciano, Italy
{fdagostino, flferrara, cgennarelli, rguerriero, mmigliozi}@unisa.it

Abstract

An effective technique to compensate the positioning errors in a spherical near-field – far-field (NF-FF) transformation for quasi-planar antennas is proposed and experimentally validated. It relies on a nonredundant sampling representation of the voltage measured by the probe obtained by adopting a very flexible antenna modelling. The singular value decomposition method is applied to retrieve the NF data at the points fixed by the sampling representation from the acquired nonuniformly spaced ones. Once the uniform data have been recovered, those needed by the classical spherical NF-FF transformation are efficiently evaluated by using an optimal sampling interpolation algorithm.

Index Terms – antenna measurements, NF-FF transformations, spherical scan, non-redundant representations of electromagnetic fields, positioning errors compensation.

I. INTRODUCTION

An efficient near-field–far-field (NF-FF) transformation with spherical scanning for quasi-planar antennas has been recently developed [1] by considering the antenna under test (AUT) as enclosed in a double bowl, i.e., a surface Σ formed by two circular bowls with the same aperture diameter, but eventually different bending radii. Such a technique is based on the nonredundant sampling representations of the radiated electromagnetic (EM) fields [2] and allows to reduce in a significant way the number of needed NF data, without losing the efficiency of previous approaches. Unfortunately, due to an inaccurate control of the positioning systems, it may be unpractical to get uniformly spaced NF measurements. On the other hand, the samples position can be accurately read by optical devices. Accordingly, the development of an efficient algorithm for an accurate and stable reconstruction from nonuniform data is relevant. Since a direct reconstruction from nonuniform samples is not advisable, a convenient strategy [3] is to recover the uniform samples from the nonuniform ones and then determine the value at any point of the scanning surface by an accurate and stable optimal sampling interpolation (OSI) formula. An approach based on an iterative technique, which converges only if it's possible to build a biunique correspondence associating at each uniform sampling point the nearest nonuniform one, has been proposed to reconstruct the uniform samples in the case of cylindrical and FF spherical surfaces [3]. A technique based on the use of the singular value decomposition (SVD) method to compensate the positioning errors in the spherical NF-FF transformation for long antennas has been recently developed and compared with the iterative one [4]. It allows to exploit the data redundancy to increase the stability of the algorithm, but can be usefully applied only if the uniform samples reconstruction can be reduced to the solution of two independent one-dimensional problems.

Aim of this work is to extend the SVD based approach for compensating the positioning errors to the spherical NF-FF transformation for quasi-planar antennas [1] and to provide its experimental validation, which will be carried out at the UNISA Antenna Characterization Lab.

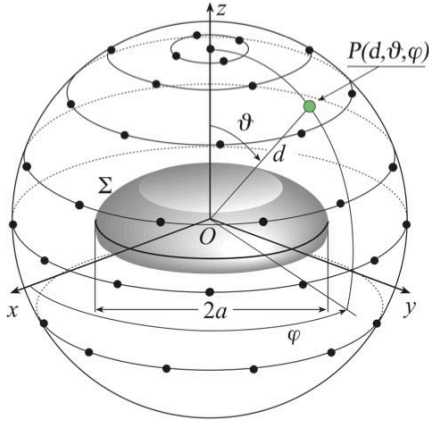


FIG. 1 – Spherical scanning for a quasi-planar antenna.

II. NONREDUNDANT SAMPLING REPRESENTATION ON A SPHERE

Let us consider a quasi-planar AUT enclosed in a double bowl Σ and a nondirective probe scanning a sphere of radius d in the NF region, and adopt the spherical coordinate system (r, ϑ, φ) to denote an observation point P (Fig. 1). Since the voltage V measured by such a probe has the same effective spatial bandwidth of the field, the nonredundant sampling representation of EM fields [2] can be applied to it. Accordingly, let us introduce the “reduced voltage” $\tilde{V}(\xi) = V(\xi) e^{j\gamma(\xi)}$, where $V(\xi)$ is the voltage V_1 or V_2 measured by the probe or by the rotated probe, $\gamma(\xi)$ is a proper phase

function, and ξ is an optimal parameter used to describe each of the curves C (meridians and parallels) representing the sphere. The error, occurring when $\tilde{V}(\xi)$ is approximated by a bandlimited function, becomes negligible as the bandwidth exceeds a critical value W_ξ [2]. Therefore, it can be effectively controlled by choosing a bandwidth $\chi'W_\xi$, with $\chi' > 1$.

The bandwidth W_ξ and parameterization ξ relevant to a meridian, and the corresponding phase function γ are [1, 2]:

$$W_\xi = \beta \ell' / 2\pi ; \quad \gamma = (\beta/2)[R_1 + R_2 + s'_1 - s'_2] ; \quad \xi = (\pi/2\ell')[R_1 - R_2 + s'_1 + s'_2] \quad (1)$$

where β is the wavenumber, ℓ' the length of the curve C' intersection between the meridian plane through the observation point P and Σ , $R_{1,2}$ are the distances from P to the tangency points $P_{1,2}$ on C' , and $s'_{1,2}$ are their curvilinear abscissae. On a parallel, the function γ is constant and it is convenient to choose the angle φ as parameter. The expressions of the bandwidth W_φ and of the quantities in (1) as function of the double bowl parameters (aperture diameter $2a$, and bending radii c and c' of the upper and lower arcs) are reported in [1]. The voltage at P on the meridian at φ can be determined [1] via the OSI expansion

$$\tilde{V}(\xi(\vartheta), \varphi) = \sum_{n=n_0-q+1}^{n_0+q} \tilde{V}(\xi_n, \varphi) \Omega_N(\xi - \xi_n, \bar{\xi}) D_{N''}(\xi - \xi_n) \quad (2)$$

wherein $2q$ is the number of the retained intermediate samples $\tilde{V}(\xi_n, \varphi)$, i.e., the voltage values at the intersection points between the meridian through P and the sampling parallels, $n_0 = \text{Int}(\xi/\Delta\xi)$, $\bar{\xi} = q\Delta\xi$, and

$$\xi_n = n\Delta\xi = 2\pi n / (2N'' + 1) ; \quad N'' = \text{Int}(\chi N') + 1 ; \quad N' = \text{Int}(\chi' W_\xi) + 1 \quad (3)$$

Moreover, $D_{N''}$ and Ω_N are the Dirichlet and Tschebyscheff sampling functions [1, 2], $\text{Int}(x)$ denotes the integer part of x , $N = N'' - N'$, and $\chi > 1$ is an oversampling factor which controls the truncation error. The intermediate samples are given by:

$$\tilde{V}(\xi_n, \varphi) = \sum_{m=m_0-p+1}^{m_0+p} \tilde{V}(\xi_n, \varphi_{m,n}) \Omega_{M''}(\varphi - \varphi_{m,n}, \bar{\varphi}) D_{M''}(\varphi - \varphi_{m,n}) \quad (4)$$

wherein $2p$ is the number of the retained reduced samples $\tilde{V}(\xi_n, \varphi_{m,n})$ on the parallel fixed by ξ_n , $m_0 = \text{Int}(\varphi/\Delta\varphi_n)$, $\bar{\varphi} = p\Delta\varphi_n$, and

$$\varphi_{m,n} = m\Delta\varphi_n = 2\pi m / (2M_n'' + 1); \quad M_n'' = \text{Int}(\chi M_n') + 1; \quad M_n' = \text{Int}[\chi^* W_\varphi(\xi_n)] + 1 \quad (5)$$

$$\chi^* = 1 + (\chi' - 1) [\sin \vartheta(\xi_n)]^{-2/3}; \quad M_n = M_n'' - M_n' \quad (6)$$

III. RECONSTRUCTION OF THE UNIFORM SAMPLES

Let us suppose that, apart the sample at the pole $\vartheta = 0$, the nonuniformly distributed samples lie on parallels not regularly spaced. In such a case, the recovery of the uniform samples reduces to the solution of two independent one-dimensional problems. In both the cases, let us also assume that at each uniform sampling position corresponds at least a nonuniform one whose distance is less than one half the uniform spacing, thus avoiding a strong ill-conditioning of the related linear system. The regularly spaced $2M_k'' + 1$ samples on a nonuniform parallel at $\vartheta(\eta_k)$ are retrieved as follows. Given a sequence of $J_k \geq 2M_k'' + 1$ nonuniform sampling points (η_k, ϕ_j) on it, the corresponding voltage $\tilde{V}(\eta_k, \phi_j)$ can be expressed in terms of the uniform ones via expansion (4). A linear system $\underline{A} \underline{x} = \underline{b}$ is so obtained, where \underline{b} is the sequence of the known nonuniform samples $\tilde{V}(\eta_k, \phi_j)$, \underline{x} is that of the unknown uniform ones $\tilde{V}(\eta_k, \varphi_{m,k})$, and \underline{A} is a $J_k \times (2M_k'' + 1)$ matrix, whose elements are $a_{jm} = \Omega_{M_k}(\phi_j - \varphi_{m,k}, p\Delta\varphi_k) D_{M_k}(\phi_j - \varphi_{m,k})$ and are zero if the index m is out of the range $[m_0(\phi_j) - p + 1, m_0(\phi_j) + p]$. The best least squares approximation of such a system is obtained via the SVD method. Once the uniform samples on the nonuniform parallels have been retrieved, expansion (4) is applied to get the samples $\tilde{V}(\eta_k, \varphi)$ at the intersection points between these parallels and the meridian through P . Obviously, these last samples are nonuniform. Accordingly, the voltage at P can be obtained by first retrieving the uniform intermediate samples via SVD and then interpolating them via the expansion (2). Once the uniform samples have been so obtained, the NF data needed by the spherical NF-FF transformation [5] can be accurately recovered via (2) and (4).

IV. EXPERIMENTAL RESULTS

The proposed NF-FF transformation has been experimentally validated in the anechoic chamber available at the UNISA Antenna Characterization Lab, provided with a roll over azimuth spherical NF facility system. The considered AUT is a standard gain horn with aperture $19.4\text{cm} \times 14.4\text{cm}$, located on the plane $z = 0$ of the reference system (Fig. 1) and operating at 10 GHz. Such an AUT has been fitted by a double bowl modelling with $a = 12.5\text{ cm}$, $c = 3.0\text{ cm}$, and $c' = 3.0\text{ cm}$. The probe voltages have been collected by an open-ended WR90 rectangular waveguide on irregularly spaced parallels lying on a sphere of radius $d = 72.2\text{ cm}$. The distances between each nonuniform parallel and the associated uniform one and those between the nonuniform sampling points and the corresponding uniform ones on them are random variables uniformly distributed in $(-\Delta\xi/2, \Delta\xi/2)$ and $(-\Delta\varphi_n/2, \Delta\varphi_n/2)$, respectively.

The amplitudes of the reconstructed voltages V_1 and V_2 relevant to the meridians at $\varphi = 0^\circ$ and $\varphi = 90^\circ$ are compared in Figs. 2 and 3 with those directly measured. At last, the FF patterns in the principal planes E and H obtained from the nonuniform NF data are compared in Figs. 4 and 5 with those (references) obtained from the NF data directly measured on the classical spherical grid. In both the cases, the software package MI-3000 of MI Tech-

nologies, implementing the classical NF–FF transformation [5], has been used to get the FF reconstructions. As can be seen, all the reconstructions are very accurate, in spite of the severe values of the considered positioning errors.

It is worth noting that the number of employed samples is 1 514, less than one half that (3 280) needed by the standard spherical scanning technique [5].

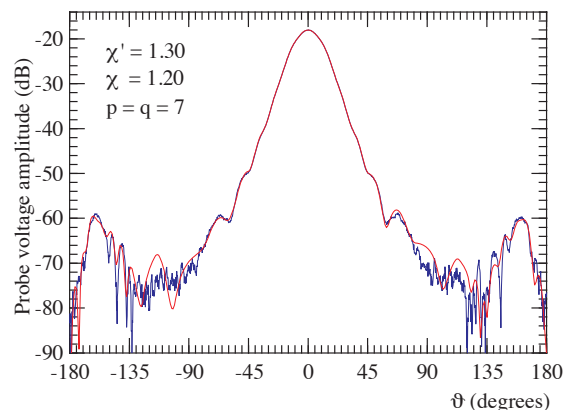


FIG. 2 – Amplitude of V_1 on the meridian at $\varphi = 0^\circ$. Blue line: measured. Red line: recovered from irregularly spaced NF data.

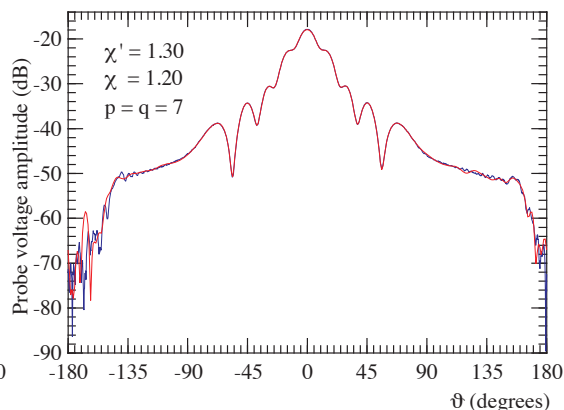


FIG. 3 – Amplitude of V_2 on the meridian at $\varphi = 90^\circ$. Blue line: measured. Red line: recovered from irregularly spaced NF data.

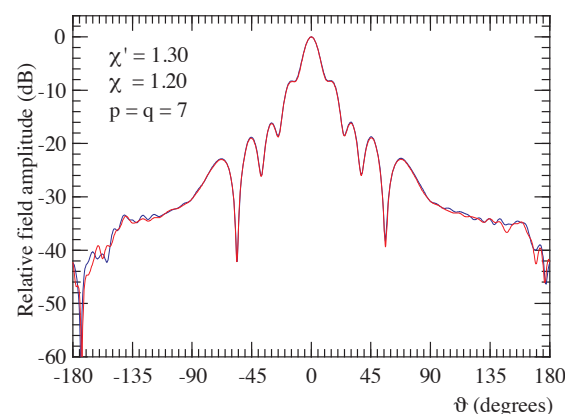


FIG. 4 – E-plane pattern. Blue line: reference. Red line: recovered from irregularly spaced NF data.

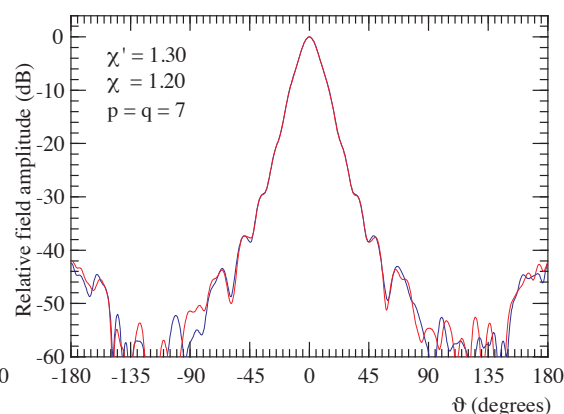


FIG. 5 – H-plane pattern. Blue line: reference. Red line: recovered from irregularly spaced NF data.

REFERENCES

- [1] F. D'Agostino, F. Ferrara, C. Gennarelli, R. Guerriero, and M. Migliozi, "Effective antenna modellings for a NF–FF transformation with spherical scanning using the minimum number of data," *Int. Jour. Antennas Prop.*, vol. 2011, ID 936781, 11 pages.
- [2] O.M. Bucci, C. Gennarelli, and C. Savarese, "Representation of electromagnetic fields over arbitrary surfaces by a finite and nonredundant number of samples," *IEEE Trans. Antennas Prop.*, vol. 46, pp. 351-359, March 1998.
- [3] O.M. Bucci, C. Gennarelli, G. Riccio, and C. Savarese, "Electromagnetic fields interpolation from nonuniform samples over spherical and cylindrical surfaces," *IEE Proc. Microw. Antennas Prop.*, vol. 141, pp. 77-84, April 1994.
- [4] F. D'Agostino, F. Ferrara, C. Gennarelli, R. Guerriero, M. Migliozi, "Two techniques for compensating the probe positioning errors in the spherical NF–FF transformation for elongated antennas," *The Open Electr. Electron. Eng. Jour.*, vol. 5, pp. 29-36, 2011.
- [5] J. Hald, J.E. Hansen, F. Jensen, and F.H. Larsen, "Spherical near-field antenna measurements," J.E. Hansen Ed., Peter Peregrinus, London, 1998.

A SIMPLE AND EFFECTIVE ALGORITHM FOR THE POWER SYNTHESIS OF RECONFIGURABLE ARRAYS WITH NEAR-FIELD NULLS

G. Buttazzoni⁽¹⁾, R. Vescovo⁽¹⁾

(1) Department of Engineering and Architecture, University of Trieste
Via A. Valerio 10, 34127 Trieste, Italy
giulia.buttazzoni@phd.units.it, vescovo@units.it

Abstract

A powerful iterative method is presented for the synthesis of arbitrary reconfigurable antenna arrays. The algorithm yields very good results also for arrays consisting of a large number of elements. The reconfigurability is achieved by phase-only control. The excitation amplitudes may be different for different array elements, and are not pre-assigned, but are optimized. Furthermore, the electric field vanishes in a number of prescribed points located in the near-field region, so that a strong field reduction is obtained in a neighborhood of them.

Index Terms – Antenna arrays, near-field nulls, phase only control, power synthesis, reconfigurability.

I. INTRODUCTION

Antenna arrays consisting of several elements are very common structures in many applications, such as radars, satellites and wireless communications. One of their attracting features is the reconfigurability, that is, the capability of generating different radiation patterns by suitably modifying the phase of the excitations. However, the possible presence of metallic structures close to the antenna can interfere modifying the radiated patterns. A possible approach to reduce this effect consists in reducing the radiated field in the zone where an interfering object is located [1-5]. Given an arbitrary array, the algorithm here proposed allows to synthesize a number of desired phase-only reconfigurable patterns, in such a way that the corresponding near-fields vanish at suitably chosen points close to the antenna, thus reducing the near-field in a neighborhood of them.

II. PROBLEM FORMULATION AND SOLVING PROCEDURE

With reference to a Cartesian system $O(x, y, z)$, let us consider an antenna array of arbitrary geometry, consisting of N arbitrary radiating elements. The radiation pattern in the generic direction φ of the xy -plane, and the electric field at a point \vec{r} , produced by the excitation vector $\mathbf{i} = [i_1, \dots, i_N]^T$, are given, respectively, by:

$$F(\mathbf{i}; \varphi) = \sum_{n=1}^N i_n f_n(\varphi) \quad (1)$$

$$\vec{E}(\mathbf{i}; \vec{r}) = \sum_{n=1}^N i_n \vec{E}_n(\vec{r}) \quad (2)$$

where $f_n(\varphi)$ and $\vec{E}_n(\vec{r})$ are, respectively, the array pattern and the electric field corresponding to the excitation vector $\mathbf{e}_n = [0, \dots, 1, \dots, 0]^T$ having unity in the n -th position. We want to find S excitation vectors $\mathbf{i}_s = [i_{1s}, \dots, i_{Ns}]^T$ ($s = 1, \dots, S$) such that the s -th radiation pattern $F(\mathbf{i}_s; \varphi)$ belong to a suitable mask $K_s = \{f(\varphi): K_{1s}(\varphi) \leq |f(\varphi)| \leq K_{2s}(\varphi)\}$, where $K_{1s}(\varphi)$ and $K_{2s}(\varphi)$ are the lower and the upper bound, respectively, of the

mask. Furthermore, we require that each of the S array patterns can be transformed into any of the others by modifying only the excitation phase of each array element, and keeping the excitation amplitude constant (phase-only control). Finally, we impose that the electric field radiated by the array with the excitation vector \mathbf{i}_s , $\vec{\mathbf{E}}(\mathbf{i}_s; \vec{\mathbf{r}})$, be zero in M suitable points $\vec{\mathbf{r}}_m$ ($m = 1, \dots, M$) located in the near-field region. If such points are close to each other, then the field reduction is achieved in a neighborhood of them. This problem can be formalized as follows: find \mathbf{i}_s in such a way as to satisfy the following constraints:

$$F(\mathbf{i}_s; \varphi) \in K_s, \quad s = 1, \dots, S \tag{3}$$

$$|i_{n1}| = \dots = |i_{nS}|, \quad n = 1, \dots, N \tag{4}$$

$$\vec{\mathbf{E}}(\mathbf{i}_s; \vec{\mathbf{r}}_m) = 0, \quad s = 1, \dots, S, m = 1, \dots, M \quad (M < N/3) \tag{5}$$

The method of solution that we are presenting is an evolution of that in [5], and is based on the alternating projections method. We introduce the set $\mathcal{H} = \{\tilde{\mathbf{h}} = (g_1(\varphi), \dots, g_S(\varphi), \mathbf{h}_1, \dots, \mathbf{h}_S)\}$, with $g_s(\varphi)$ an arbitrary complex scalar function defined in the interval $[-\pi, \pi]$ with square integrable modulus, and $\mathbf{h}_s = [h_{1s}, \dots, h_{Ns}]^T$ a column vector with N arbitrary complex components. We define the scalar product between two elements $\tilde{\mathbf{h}}, \tilde{\mathbf{h}}' \in \mathcal{H}$ as: $\langle \tilde{\mathbf{h}}, \tilde{\mathbf{h}}' \rangle_{\mathcal{H}} = \sum_{s=1}^S (\langle g_s(\varphi), g'_s(\varphi) \rangle + \mathbf{h}_s^H \mathbf{h}'_s)$, where $g'_s(\varphi)$ and \mathbf{h}'_s are the components of $\tilde{\mathbf{h}}'$, $\langle g_s(\varphi), g'_s(\varphi) \rangle = \int_{-\pi}^{\pi} g_s(\varphi) g'^*_s(\varphi) d\varphi$, where the asterisk denotes the complex conjugate, and the superscript H denotes transpose conjugate. The scalar product yields the norm and the distance in the classical way. In \mathcal{H} we now introduce the subsets: $\mathcal{K} = \{\tilde{\mathbf{k}} = (f_1(\varphi), \dots, f_S(\varphi), \mathbf{k}_1, \dots, \mathbf{k}_S) : f_s(\varphi) \in K_s, |k_{n1}| = \dots = |k_{nS}|, n = 1, \dots, N, s = 1 \dots S\}$, $\mathcal{W} = \{\tilde{\mathbf{w}} = (F(\mathbf{w}_1; \varphi), \dots, F(\mathbf{w}_S; \varphi), \mathbf{w}_1, \dots, \mathbf{w}_S)\}$, and $\mathcal{Z} = \{\tilde{\mathbf{z}} = (F(\mathbf{z}_1; \varphi), \dots, F(\mathbf{z}_S; \varphi), \mathbf{z}_1, \dots, \mathbf{z}_S) : \vec{\mathbf{E}}(\mathbf{z}_s; \vec{\mathbf{r}}_m) = 0, s = 1, \dots, S, m = 1, \dots, M\}$. The elements of \mathcal{K} consist of S arbitrary complex scalar functions and of S arbitrary complex column vectors satisfying (3) and (4), respectively. The elements of \mathcal{W} consist of S array patterns and of S excitation vectors that produce such patterns. The set \mathcal{Z} consists of those elements of \mathcal{W} whose electric field vectors satisfy condition (5). It is evident that each element belonging to the intersection $\mathcal{K} \cap \mathcal{Z}$ (if any) is a solution to our problem. Since such intersection may be empty, we consider, as a solution, an element of \mathcal{K} minimizing the distance from \mathcal{Z} . The solution is sought starting from a suitable point $\tilde{\mathbf{k}}_0 \in \mathcal{K}$, and following the iteration scheme:

$$\tilde{\mathbf{k}}_{n+1} = T_{\mathcal{K}} T_{\mathcal{Z}} \tilde{\mathbf{k}}_n, n = 0, 1, 2, \dots \tag{11}$$

where $T_{\mathcal{K}}$ and $T_{\mathcal{Z}}$ are the projectors onto the sets \mathcal{K} and \mathcal{Z} , respectively. Formulas for implementing them can be deduced by following [5]. By definition of distance, and due to $T_{\mathcal{K}}$ and $T_{\mathcal{Z}}$ being two projectors, it results $\rho_n \geq \rho_{n+1}$, where ρ_n is the distance from $\tilde{\mathbf{k}}_n$ to \mathcal{Z} . Thus, (11) generates a sequence of points $\tilde{\mathbf{k}}_n$ of \mathcal{K} which are closer and closer to \mathcal{Z} . We stop the procedure at a point $\tilde{\mathbf{k}}_n^o = (f_1^o(\varphi), \dots, f_S^o(\varphi), \mathbf{k}_1^o, \dots, \mathbf{k}_S^o)$ such that: $\rho_n < \varepsilon$ or $(\rho_{n-1} - \rho_n)/\rho_n < \delta$, with ε and δ suitable thresholds. As optimal excitation vectors we consider the S vectors \mathbf{k}_s^o . Such vectors satisfy (4),

being elements of \mathcal{K} . However, the functions $f_s^o(\varphi)$ are not array patterns. The optimal array patterns and the radiated fields are calculated replacing \mathbf{i} with \mathbf{k}_s^o in (1) and (2), respectively. Thus, constraints (3) and (5) are satisfied only approximately. However, the accuracy is very good, as will be shown below. The extension to the 3D-case is straightforward.

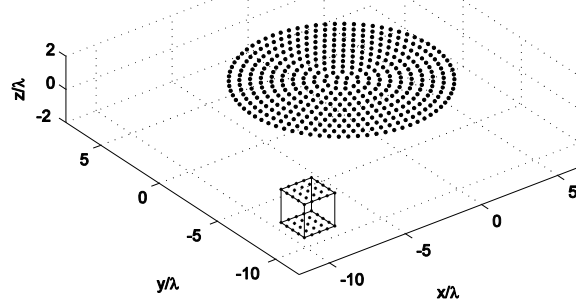


FIG. 1 – Geometry of the problem: array of $N = 429$ elementary vertical dipoles equally spaced on 11 rings in the xy -plane; $M = 50$ equally spaced null points on the top and bottom faces of the cube $-10.5\lambda \leq x, y \leq -8.5\lambda, z = \pm\lambda$

III. NUMERICAL EXAMPLE

We posed the problem of synthesizing by phase-only control $S = 4$ patterns belonging to the masks of Fig. 2. The geometry of the example is shown in Fig. 1. In order to quantify the field reduction obtained by imposing the near-field nulls, we first solved the problem without imposing condition (5) (“reduced” problem). Then, also the constraint in (5) was taken into account (“complete” problem). As it was to be expected, constraint (4) was satisfied exactly. Condition (3) was very well approximated, also in the complete problem, as it can be seen in Fig. 2, as well as constraint (5). Precisely, in the complete problem the maximum near-field amplitude in the constraint points exhibited a 50.03 dB reduction with respect to that of the reduced problem. Fig. 3 shows the contour plots of the electric field amplitude on a portion of the xy -plane for $s = 1$ (worst case), showing a strong amplitude reduction obtained in the complete problem in a neighborhood of the null points. Subsequently, for both the reduced and the complete problem, we also evaluated the field amplitudes on a mesh of $\lambda/8$ -spaced points in the cube of Fig. 1, whose top and bottom faces are the two sub-regions containing the null points, obtaining a reduction of the maximum amplitude of 48.25 dB and a reduction of the mean amplitude of 43.06 dB. Such high values show the great improvement obtained by imposing the nulls.

IV. CONCLUSION

The presented algorithm allows to synthesize a number of radiation patterns for an arbitrary reconfigurable antenna array, with phase-only control, simultaneously reducing the near-field amplitude in a region close to the antenna. The near-field reduction is obtained by imposing that the field vanishes at a prescribed number of suitably located points. In such a way, strong reductions can be obtained with low computational times (reduced problem: 1.78 seconds; complete problem: 30.19 seconds).

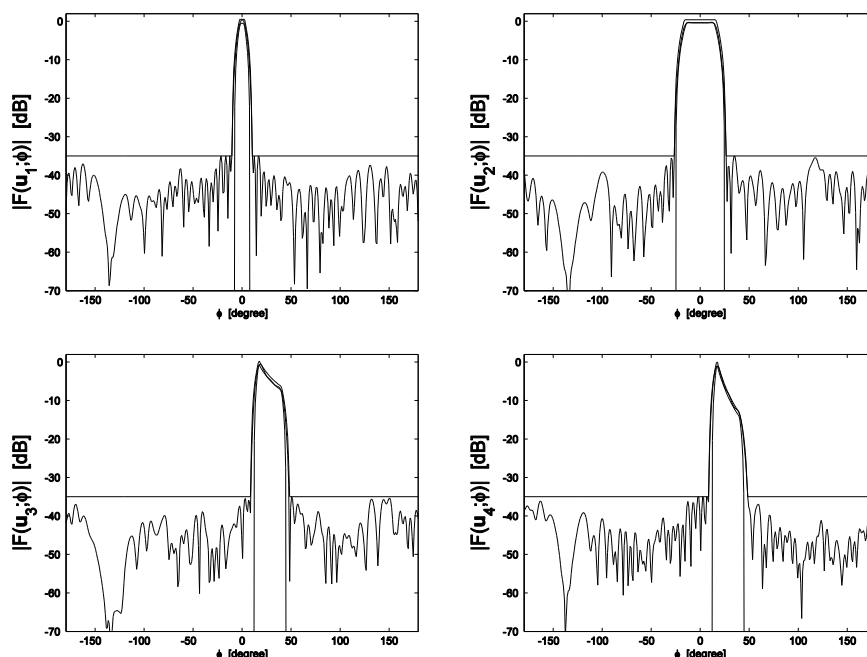


FIG. 2 – Assigned masks and synthesized patterns (complete problem).

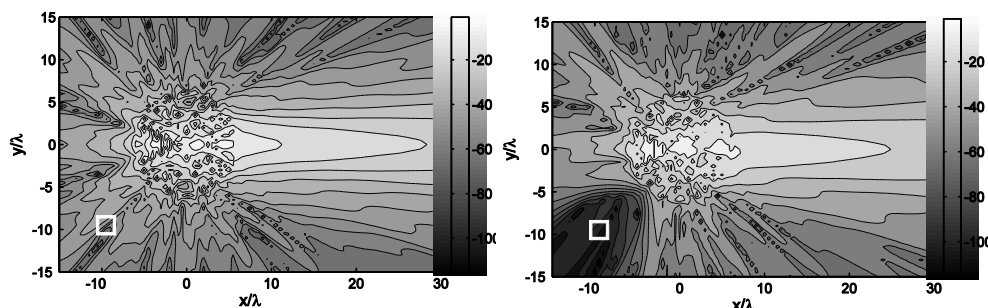


FIG. 3 – Contours of the electric-field amplitude for $s = 1$ on a portion of the xy -plane, obtained in the reduced (left) and in the complete (right) problem.

REFERENCES

[1] Steyskal, H., “Synthesis of antenna patterns with imposed nearfield nulls,” *Electron. Lett.*, Vol. 30, No. 24, 2000–2001, 1994.

[2] Landesa, L., F. Obelleiro, J.L. Rodriguez, J.A. Rodriguez, F. Ares, and A.G. Pino, “Pattern synthesis of array antennas with additional isolation of near field arbitrary objects,” *Electron. Lett.*, Vol. 34, No. 16, 1540–1542, 1998.

[3] Comisso, M., and Vescovo, R., “3D Power Synthesis with reduction of Near-Field and Dynamic Range Ratio for Conformal Antenna Arrays,” *IEEE Trans. Antennas Propag.*, Vol. 59, No. 4, 1164–1174, 2011.

[4] Buttazzoni, G., and Vescovo, R., “Power Synthesis for Reconfigurable Arrays by Phase-Only Control With Simultaneous Dynamic Range Ratio and Near-Field Reduction,” *IEEE Trans. Antennas Propag.*, Vol. 60, No. 2, 1161–1165, 2012.

[5] Vescovo, R., “Power pattern synthesis for antenna arrays with null constraints in the near-field region,” *MOTL*, Vol. 44(6), pp. 542–545, 2005.

UAV-BASED ANTENNA VERIFICATION SYSTEM: EXTRACTED AUT PATTERN

F. Paonessa⁽¹⁾, G. Virone⁽¹⁾, O. A. Peverini⁽¹⁾, G. Addamo⁽¹⁾, R. Orta⁽¹⁾,
R. Tascone⁽¹⁾ and P. Bolli⁽²⁾

⁽¹⁾ Istituto di Elettronica ed Ingegneria dell'Informazione e delle
Telecomunicazioni (IEIIT), Consiglio Nazionale delle Ricerche (CNR)
C.so Duca degli Abruzzi 24, 10129 Torino, Italy
fabio.paonessa@ieiit.cnr.it

⁽²⁾ Osservatorio Astrofisico di Arcetri (OAA),
Istituto Nazionale di Astrofisica (INAF)
Largo Enrico Fermi 5, 50125 Firenze, Italy

Abstract

A novel far-field antenna pattern verification system based on a flying test source has been recently published [1]. It directly performs the antenna validation considering the received power level at the antenna port. This paper discusses an extraction procedure to obtain the antenna pattern from such measured data. Significant results obtained on a log-periodic antenna operating at 408 MHz are also reported.

Index Terms – Antenna radiation pattern, UAV

I. INTRODUCTION

The UAV-based antenna verification system in [1] exploits a micro Unmanned Aerial Vehicle (UAV) equipped with a continuous-wave RF transmitter and a dipole antenna (Fig. 1a).

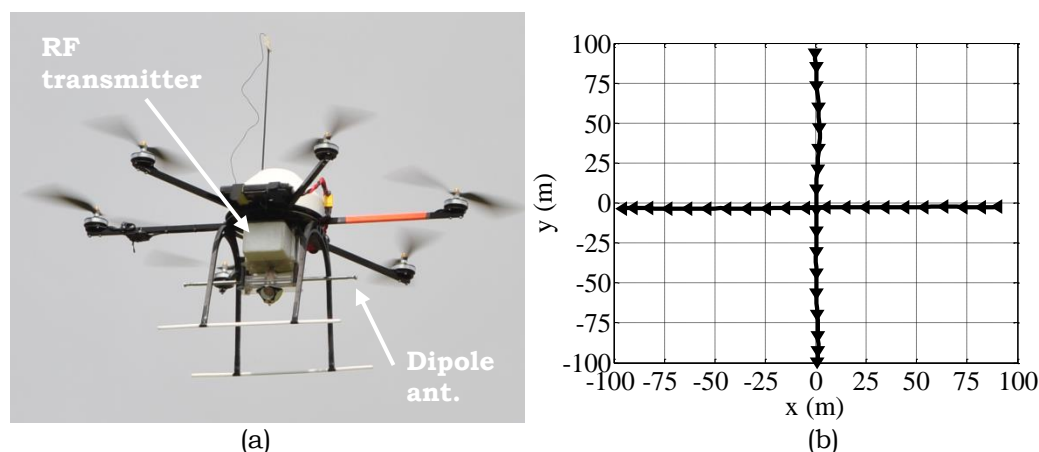


FIG. 1 – (a) UAV equipped with the RF transmitter and the dipole antenna.
(b) Projection on the horizontal plane of two UAV flight paths above the AUT:
quasi-E-plane (vertical line); quasi-H-plane (horizontal line).

This setup operates as a far-field source that is used to characterize the Antenna Under Test (AUT) on the ground by executing autonomous, constant-height flights above it [2]. This solution is suitable to characterize low-frequency antennas and arrays in their operative conditions (with soil ground).

A total station [1] is used to track the flying test source with centimetric accuracy, whereas its orientation is recorded by the onboard Inertial Measurement Unit (IMU). The AUT output power is measured through a spectrum analyzer. All the data are synchronized with the GPS clock. This paper describes the extraction technique that is used to extract the AUT pattern from the above mentioned data.

II. EXTRACTION OF THE AUT PATTERN

As reported in [1], the flights are performed following quasi-rectilinear paths above the AUT. In Fig. 1b, the AUT is placed in the center of the reference system, it is oriented towards the zenith and its E -plane is aligned along the y -axis. On the contrary, a quasi-rectilinear path along x -axis mainly corresponds to the H -plane. The nominal orientation α_0 of the test source (dipole) relative to the y -axis, also called bearing angle, is set to 0° or 90° to execute a co-polar or a cross-polar scan, respectively.

In order to extract the AUT pattern from the received signal at the AUT port, the Friis equation is conveniently written as

$$g_{AUT}(\hat{r})M(\hat{r}) = \frac{P_R(\underline{r})}{P_S \cdot g_S(\hat{r}, \alpha, \beta, \gamma) \cdot G_R} \left(\frac{4\pi R}{\lambda} \right)^2 \quad (1)$$

where g_{AUT} is the gain of the AUT, the unit vector \hat{r} identifies a specific observation direction in the AUT spherical reference system, M is the polarization mismatch, P_R is the measured received power at AUT port, $\underline{r} = R\hat{r}$ is the distance vector from the AUT to the test source measured by the total station, G_R contains both the LNA gain and the cable losses. P_S and $g_S(\hat{r}, \alpha, \beta, \gamma)$ are the source power and its radiation pattern, respectively. The angles α , β and γ , called bearing, pitch and roll, describe the orientation of the test source measured by the IMU. It should be noted that the real bearing angle α can be slightly different from the above mentioned set-point α_0 (few degrees).

The polarization mismatch in Eq. (1) can be written as a function of the polarization vector components of both test source and AUT, relative to the third Ludwig polarization basis [3] in the AUT reference system

$$M = |\hat{p}_S \cdot \hat{p}_{AUT}|^2 = |p_S^{co} p_{AUT}^{co} + p_S^x p_{AUT}^x|^2 \quad (2)$$

where the superscripts co and x identify the co-polar and cross-polar components, respectively.

Owing to the two-fold symmetry of the test source, its cross-polar component value approaches zero in its principal planes. Therefore,

when $\alpha_0 = 0^\circ$ (co-polar orientation), $p_S^x \approx 0$ and $p_S^{co} \approx 1$, hence $M \approx |p_{AUT}^{co}|^2$. In this case, the first member of Eq. (1) becomes the co-polar pattern $g_{AUT}^{co} = g_{AUT}(\hat{r})|p_{AUT}^{co}|^2$ that can be estimated through the second member of the equation. In other words, the AUT pattern g_{AUT}^{co} is computed by removing the simulated contributions of the source pattern g_S , the path loss and the constants $P_S G_R$ from the measured received power P_R .

On the contrary, when the test sources is rotated of 90° ($\alpha_0 = 90^\circ$, cross-polar orientation), the polarization vector components of the test source in the AUT reference system become $p_S^x \approx 1$ and $p_S^{co} \approx 0$. Since in this case $M \approx |p_{AUT}^x|^2$, the first member of Eq. (1) becomes the cross-polar pattern $g_{AUT}^x = g_{AUT}(\hat{r})|p_{AUT}^x|^2$.

III. EXPERIMENTAL RESULTS

The extraction procedure has been applied to the measurements in Fig. 8 and 9 of [1], performed on a log-periodic antenna at 408 MHz, which has been used to estimate the accuracy of the system. The results for both the H -plane and the E -plane are reported in Fig. 2 as a function of the zenith angle.

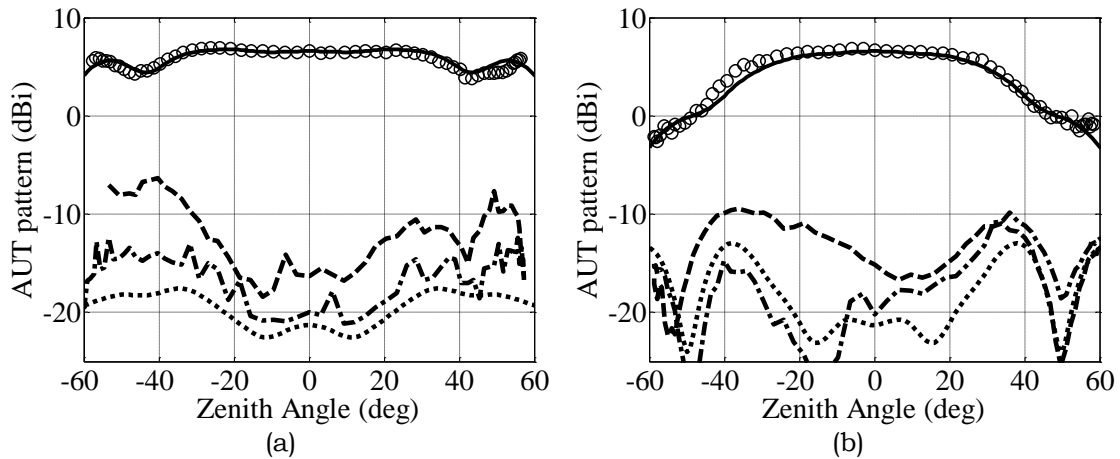


FIG. 2 – Extracted AUT pattern for the log-periodic antenna at 408 MHz.

(a) H -plane, (b) E -plane. Co-polar meas. (circles); co-polar sim. (solid); cross-polar meas. (dashed); cross-polar sim. (dotted); cross-polar sim. on the quasi- E/H -planes (dash-dotted).

The agreement is very good for the co-polar scans. It should be noted that, with the formulation of section II, all the errors of the system are implicitly attributed to the AUT. This is negligible for co-polar measurements but leads to an overestimation of the cross-polar level. The simulated cross-polar values have been computed on both the ideal E/H -planes and the quasi- E/H -planes. In the latter, the real position of the test source and its orientation angles have been inserted in the first

member of Eq. (1). The lateral deviation angle of the quasi-planes from the ideal ones is within 2° , with a RMS value of 1° .

Finally, Fig. 3 shows the contributions g_s and path loss that have been used to extract the H -plane co-polar pattern of Fig. 2a. Since the height of the test source is almost constant, the path loss changes during the flight. The contribution $P_S G_R$ has a measured value of +24.6 dBm.

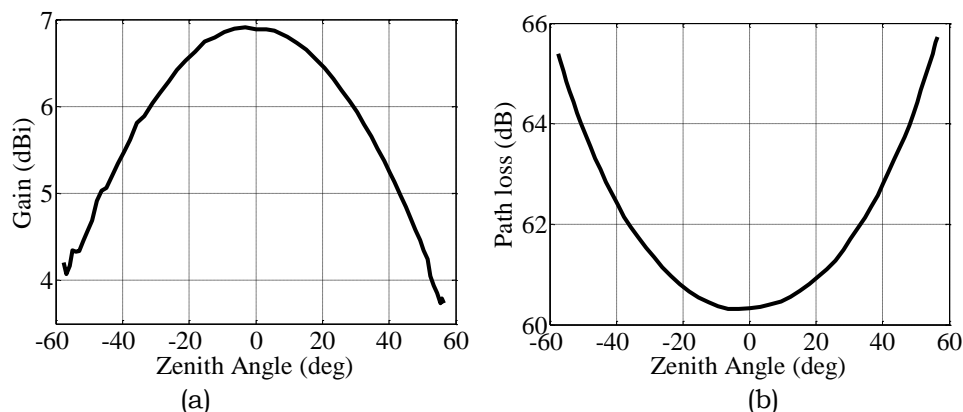


FIG. 3 – Simulated contributions of Eq. (1) to the H -plane co-polar pattern of Fig. 2a. (a) Source antenna pattern g_s . (b) Path loss.

IV. CONCLUSION

A proper formulation to extract the AUT radiation pattern from the received power pattern has been presented. The obtained results for a log-periodic antenna at 408 MHz show a good accuracy for co-polar scans, generally within 1 dB. The same technique has also been used in [4] to obtain the embedded element patterns and the overall radiation pattern of a small low-frequency array.

REFERENCES

- [1] G. Virone, A. M. Lingua, M. Piras, A. Cina, F. Perini, J. Monari, F. Paonessa, O. A. Peverini, G. Addamo, and R. Tascone, "Antenna Pattern Verification System Based on a Micro Unmanned Aerial Vehicle (UAV)," *IEEE Antennas and Wireless Propagation Letters*, vol. 13, pp. 169-172, Jan 2014.
- [2] F. Chiabrando, A. Lingua, and M. Piras, "Direct Photogrammetry Using UAV: Tests and First Results," *ISPRS Archives*, vol. XL-1/W2, pp. 81-86, *UAV-g2013*, Sept 4-6 2013, Rostock, Germany.
- [3] A. C. Ludwig, "The definition of cross polarization," *IEEE Transaction on Antennas and Propagation*, vol. 21, pp. 116-119, Jan 1973.
- [4] G. Virone *et al.*, "UAV-based Radiation Pattern Verification for a Small Low-Frequency Array," *IEEE International Symposium on Antennas and Propagation and USNC-URSI National Radio Science Meeting 2014*, July 6-12 2014, Memphis, Tennessee, USA.

RESEARCH ACTIVITIES ON UHF RFID SYSTEMS AT THE UNIVERSITY OF PISA - RESEARCH UNIT

A. Buffi, A. Michel, R. Caso, A. D'Alessandro, A. Baroni, P. Nepa
Department of Information Engineering, University of Pisa, Italy
Via Caruso 16, 56122 Pisa, Italy
[a.buffi](mailto:a.buffi@iet.unipi.it), [a.michel](mailto:a.michel@iet.unipi.it), [r.caso](mailto:r.caso@iet.unipi.it), [a.dalessandro](mailto:a.dalessandro@iet.unipi.it), [p.nepa](mailto:p.nepa@iet.unipi.it),
a.baroni@for.unipi.it

Abstract

An overview of the most recent research activities on UHF RFID systems at the Department of Information Engineering, University of Pisa, is here presented. Focus is on the design of antennas for desktop readers and portable readers, together with new radio-localization techniques for RFID-based smart storage spaces (drawers, shelves) and conveyor belts.

Index Terms – UHF RFID systems, printed antenna design, smart shelves, smart conveyor belts, tag localization, near-field antennas.

I. INTRODUCTION

In the last decades, Radio Frequency Identification (RFID) systems at the UHF band are reaching increasing attention for automatic authentication and management processes (e.g. logistics, anti-counterfeiting, access control, airport baggage management), as well as for localization and tracking of tagged items in location-aware based applications. With respect to the firstly widespread HF RFID systems, UHF RFID systems have the advantages of higher data rate, higher read rate, higher read range, smaller tags. In such framework, our research activities are mainly focused to the design of ad-hoc and novel reader antennas, and the development of RFID-based smart spaces (e.g. drawers, shelves, conveyor belts) with tag localization capabilities.

II. UHF RFID READER ANTENNA DESIGN

In UHF RFID applications based on passive tags, the reader antenna represents one of the system key elements that can be tailored to meet customer requirements. Depending on the application at hand, the reader antenna can be either far-field (FF) or near-field (NF) oriented.

In NF UHF RFID systems, the reader antenna is required to detect tags close to its surface, thus a uniform, relatively high-amplitude field is of interest in the near-field region, also with a low far field gain (to avoid false positive readings). In [1]-[3], the authors suggested the employment of travelling wave antenna (TWA) technology with a meandered geometry, to achieve an as homogeneous as possible field amplitude distribution, for all field components, on the antenna surface. Also, the antenna is easily scalable since its length and shape are not strictly related to the operating frequency (not-resonating structure), and it represents a low-cost, wideband and low-profile solution that can be easily integrated into the reader casing. A first

design consisted of a meandered Coplanar Waveguide (CPW) transmission line divided into a forward branch and a backward branch, which fits desktop reader size of $275 \times 135 \times 10 \text{ mm}^3$ [1]. The CPW line has been realized on a 0.73mm-thick FR4 substrate, and is ended on a matched load to avoid a standing wave (non-uniform) near-field pattern on the antenna surface. A metallic reflector has also been added in order to make the reader performance quite independent of the material properties of the desk the reader lie on. An upgraded design has been developed by exploiting the same technology, but in a 2×2 array configuration [2]-[3], to get field distributions more confined and maximized in the desktop reader central area. In both configurations, a reliable tag detection is guaranteed in any point on the antenna surface, with a detection range up to a few tens of centimeters from the antenna surface. It is worth noting that for NF oriented antennas, performance parameters are different from the conventional ones for FF antennas [4]-[5].

In the framework of multi-function RFID portable readers, the authors have recently proposed a compact dual-band antenna that allows to add a 2.4 GHz wireless link to transfer tag collected data toward a local server (for data storage and processing). The proposed circularly-polarized antenna consists of a combination of four meandered monopoles (UHF RFID radio link) and a miniaturized patch (WLAN at 2.4 GHz) that share the same surface of a $60 \times 60 \text{ mm}^2$ FR4 substrate. The four meandered dipoles are fed through a series feeding network, to implement sequential rotation technique. Despite of the limited antenna volume, satisfactory performance in terms of both axial ratio and antenna gain have been obtained [6]-[7].

III. UHF RFID SMART SYSTEMS

The continuous developments of the UHF RFID technology also allow the implementation of additional services for Item Level Tagging (ILT) applications. In this context, RFID-based smart storage spaces have been conceived. In [8], a classification method has been implemented for tagged items localization in a large drawer. The drawer sub-region the tag belongs to is estimated by the exploitation of the RSSI (Received Signal Strength Indicator) data acquired during the drawer opening/closing natural operations. Indeed, during drawer movements, the relative position of tag and reader antenna changes, so allowing to collect a large number of RSSI data, then increasing the amount of information made available to the RSSI-based classification algorithm. With respect to other available solutions, the proposed technique does not require multiple antennas for each single drawer or any mechanical system for assisted sliding actions. Thus, the method represents a low-cost and easily deployable solution with only one reader antenna for each drawer, which can be applied to relatively large storage systems. Classifications results related to a $80 \times 40 \text{ cm}^2$ drawer with 42 tagged boxes show that an overall accuracy (number of correctly classified tags

with respect to the total number of identified tags in the scenario) greater than 90% can be reached, by considering a drawer subdivision into two regions. The idea of enhancing the number of the classification algorithm input features (reliable RSSI values) has been also adopted in UHF RFID smart shelves. The main idea is exemplified in [9], with reference to a smart bookshelf system. Two off-the-shelf reader antennas attached to the bookshelf columns, one in front of the other, are used as an alternative to large-area thin planar antennas integrated onto the shelf surface. By both sequentially fed and contemporarily fed the two antennas, several RSSI data are acquired and then employed in a clustering algorithm. Classification results related to a 97 cm-length shelf with 24 tagged books show that an overall accuracy close to 90% can be reached by considering a shelf subdivision into three regions. Besides, the authors have also developed and patented [10] a phase-based localization technique for tagged items moving along a conveyor belt [11]-[13]. The latter is based on a synthetic-array approach that takes advantage of the fact that the tagged items move along a conveyor belt whose speed and path are known *a priori* (knowledge-based approach). Design guidelines for the geometrical and electrical parameters of the proposed localization system have been derived by using numerical results from a ray-based indoor propagation model developed at the research unit [14]. The complex amplitude of the tag backscattered signal is estimated accounting for wave reflections from the floor, ceiling and lateral walls, as a function of the tag position along the conveyor belt. Moreover, exhaustive measurement campaigns in real scenarios have proved that the technique is robust with respect to multipath phenomena and it is able to determine the position of all tags within the reader antenna beam with centimeter accuracy [13]. The proposed localization method can be applied in any scenario with a relative motion between reader antenna and tagged objects, if path and speed are known *a priori* (e.g. for localization of tagged sheets and garments in automated industrial laundries). It is worth noting that all the proposed classification/localization methods can be implemented with common commercial UHF RFID readers, antennas and tags (EPC Gen 2 protocol).

IV. CONCLUSIONS

A synthetic overview of the most recent results on UHF RFID systems activities at the Department of Information Engineering of the University of Pisa has been presented. Work in progress is about a new modular antenna, which will extend the read range to include the radiative near-field region of the desktop reader antenna. The latter could be a series-fed combination of a travelling wave antenna and a low-gain resonating antenna, which share the desktop reader volume [15]. Furthermore, the employment of the proposed phase-based localization technique to discriminate between tags moving along the conveyor and static tags (namely tags located out of the conveyor belt)

tags is under investigation. Finally, the characterization of RFID readers is going to be analyzed experimentally, to define consistent operating procedures.

ACKNOWLEDGEMENTS

The authors would like to thank the C.A.E.N RFID, Viareggio, Italy, for the technical and financial support to the development of RFID-based smart storage spaces; also, the authors acknowledge the “Fondazione Cassa di Risparmio di Pisa” for the financial support to the research activity devoted to tag localization on conveyor belts (SARFID project – Nov. 2012-Nov.2015).

REFERENCES

- [1] A. Michel, A. Buffi, R. Caso, P. Nepa, G. Isola, H.T. Chou, “Design and Performance Analysis of a Planar Antenna for Near-Field UHF-RFID Desktop Readers”, *APMC*, pp. 1019-1021 December 2012.
- [2] A. Michel, R. Caso, A. Buffi, P. Nepa “An array of meander Travelling Wave Antennas for near-field UHF-RFID readers”, *IEEE AP-S Int. Symp.*, 2013.
- [3] A. Michel, R. Caso, A. Buffi, P. Nepa, “Meandered TWAS array for near-field UHF RFID applications”, *Electronic Letters*, vol. 50, pp. 17-18, 2014.
- [4] A. Buffi, P. Nepa, G. Manara, “Analysis of near-field coupling in UHF-RFID systems”, *IEEE-APS APWC*, pp. 931-934, September 2011.
- [5] A. Buffi, A. Michel, R. Caso, P. Nepa, “Near-field coupling in UHF-RFID systems”, *URSI Int. Symp. on EM Theory (EMTS)*, pp. 408-411, May 2013.
- [6] R. Caso, A. Michel, M.R. Pino, P. Nepa, “Dual-Band UHF-RFID/WLAN Circularly Polarized Antenna for Portable RFID Readers”, to appear on *IEEE Transactions on Antennas and Propagation*, 2014.
- [7] R. Caso, A. Michel, M.R. Pino, P. Nepa, “Performance comparison between an UHF RFID antenna for portable reader and its UHF RFID/WLAN dual-band version”, *URSI-GASS*, Beijing, China, August 2014.
- [8] A. D’Alessandro, A. Buffi, P. Nepa, G. Isola, “RFID-Based Smart Shelving Storage Systems”, *APMC*, pp. 1034-1036, December 2012.
- [9] A. D’Alessandro, A. Buffi, P. Nepa, G. Isola, “A localization technique for smart bookshelves based on UHF-RFID systems”, *IEEE AP-S Int. Symposium*, pp. 1112-1113, July 2013.
- [10] P. Nepa, F. Lombardini, A. Buffi, “Method for determining the location of a moving RFID tag,” EP2533173 (A1), IP: University of Pisa, 2012.
- [11] P. Nepa, F. Lombardini, A. Buffi, “Location and Tracking of UHF-RFID Tags”, *IEEE-APS APWC*, pp. 1062-1065, September 2011.
- [12] P. Nepa, F. Lombardini, A. Buffi, “Location and tracking of items moving on a conveyor belt and equipped with UHF-RFID tags”, *IEEE AP-S*, July 2012.
- [13] A. Buffi, A. Baroni, P. Nepa, “Experimental validation of phase-based localization of UHF-RFID tags moving on a conveyor belt”, *IEEE AP-S Int. Symposium*, pp. 2319-2320, July 2013.
- [14] A. Buffi, P. Nepa, G. Manara, “An indoor propagation model for development and testing of UHF-RFID tag localization techniques”, *Int. Conference on Electromagnetics in Advanced Applications*, September 2013.
- [15] A. Michel, R. Caso, A. Buffi, P. Nepa, G. Isola, “Modular antenna for reactive and radiative near-field regions of UHF-RFID desktop readers”, *URSI-GASS*, Beijing, China, August 2014.

ENERGY HARVESTING FROM ELECTROMAGNETIC EMISSIONS OF COMPACT FLUORESCENT LAMPS

Giuseppina Monti, Fabrizio Congedo, Paola Arcuti, Luciano Tarricone

Department of Innovation for Engineering, University of Salento
Via per Monteroni, 73100 Lecce, Italy
[giuseppina.monti](mailto:giuseppina.monti@unisalento.it); [paola.arcuti](mailto:paola.arcuti@unisalento.it); [fabrizio.congedo](mailto:fabrizio.congedo@unisalento.it);
[luciano.tarricone](mailto:luciano.tarricone@unisalento.it)@unisalento.it

Abstract

This paper presents a novel device for energy harvesting of Radio Frequency (RF) emissions of Compact Fluorescent Lamps (CFLs). The proposed device consists of a capacitively loaded spiral loop and an RF-to-DC converter. A near-field magnetic coupling is exploited for power generation from spurious emissions of CFLs. Results of experimental tests performed with a 30 W CFL are reported and discussed demonstrating that up to 0.61 mW can be generated.

Index Terms – Compact Fluorescent Lamps, Energy Harvesting, Near-Field Magnetic Coupling, Spiral Loop.

I. INTRODUCTION

Energy harvesting technologies are a promising solution for providing low-power sensors with the energy they need to operate. Accordingly, in the last years several devices optimized to capture the electromagnetic (EM) energy available in the environment have been presented in the literature [1-6]. Most of these devices are based on a far-field coupling with Electromagnetic (EM) waves emitted by wireless communication systems. To this regard, the key device is a rectenna (rectifying antenna) consisting of an antenna and a Radio Frequency (RF)-to-Direct-Current (DC) rectifier. However, this approach allows to generate a DC power insufficient for energizing sensors of interest in real world practical applications. In fact, from experimental studies, values of DC power of the order of microwatt are demonstrated.

This is an obvious result of the very low values of EM power density available for harvesting in common indoor environments and related to wireless systems. Conversely, some electronic devices generate relatively strong low frequency spurious emissions.

In particular, Compact Fluorescent Lamps (CFLs), commonly adopted for artificial lighting of indoor environments, emit in the frequency range from a few tens to some hundreds of kHz [7-8], thus representing an attractive source for harvesting applications.

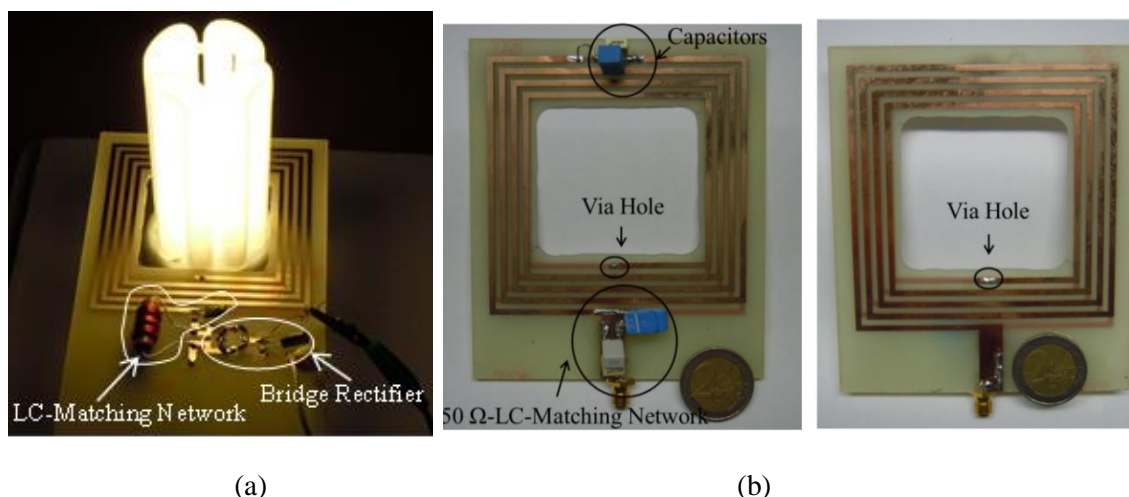


FIG. 1 – (a) Photograph of the proposed harvester when coupled with a 30 W CFL. (b) Front and back view of the 50 Ω matched realization of the resonator adopted for measurements by means of a HP E4411B spectrum analyzer of the harvested spectrum.

Accordingly, in this paper a device for power generation by spurious emissions of CFLs is presented. The proposed harvester uses a resonant loop inductively coupled with the magnetic field emitted by CFLs.

Experimental tests are reported and discussed. It is shown that up to 0.61 mW can be obtained from a 30 W CFL, thus demonstrating that the proposed device represents an optimum candidate for energizing sensors for home monitoring applications.

II. HARVESTER DESIGN AND EXPERIMENTAL TESTS

The layout of the proposed harvester is reported in Fig. 1a. It consists of two basic elements: a resonator, inductively coupled with the magnetic field emitted by CFL and a full-wave bridge rectifier, which converts the Alternate-Current (AC) signal collected by the resonator into a DC one. An LC-matching network was added so as to guarantee the maximum power transfer between the resonator and the rectification circuit.

The geometry of the resonator can be observed in Fig. 1b. It consists of a 4-turn spiral coil loaded by a lumped tuning capacitor so to resonate at about 50 kHz where, as explained in the following, a peak of the power collected by the harvester was observed.

The design process was carried out as follows. Firstly, we realized a network matching the resonator to the input impedance of a HP E4411B spectrum analyzer (i.e., a 50 Ω impedance); a photograph is given in Fig. 1b. This realization was used to evaluate the power that the harvester is able to deliver to a matched load when coupled with a CFL. The experimental setup is shown in Fig 2a, while the power

spectrum received with the HP E4411B spectrum analyzer is given in Fig. 2b.

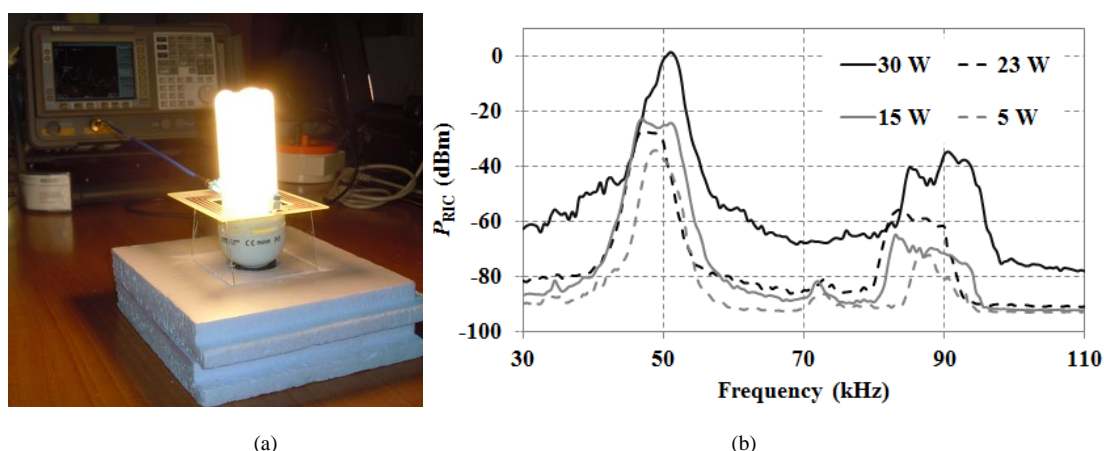


FIG. 2 – (a) Experimental setup used to estimate the RF spectrum received by the proposed harvester when coupled with CFLs with a power consumption from 5 W to 30 W. (b) Spectrum measured with the HP E4411B spectrum analyzer.

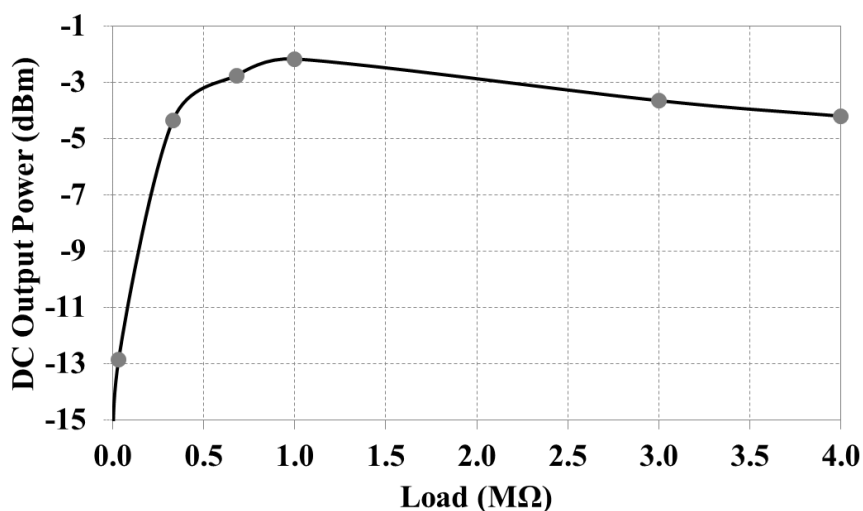


FIG. 3 – Measured DC output power. Data obtained for different values of the load by coupling the proposed harvester with a 30 W CFL.

The spectrum of the signal received in the case of coupling with a 30 W warm white Beghelli CFL (see the black curve in Fig. 2b) was used to optimize the bridge rectifier by means of circuital simulations. Referring to the use of the proposed scavenger for energizing low-power sensors for home automation, a 1 $M\Omega$ load was adopted. The values calculated this way for the inductance and the capacitance of the LC matching network in Fig. 1a are 2.5 mH and 5.6 nF, respectively. The DC-pass smoothing capacitor of the bridge rectifier was set at 1 μ F.

Finally, measurements of the DC power were carried out for different values of the load; corresponding results are given in Fig. 3. It can be noticed that the proposed device is able to deliver up to 0.61 mW fulfilling the low-power consumption of a sensor for home monitoring applications

III. CONCLUSION

A novel device able to generate up to 0.61 mW from electromagnetic spurious emission of compact fluorescent lamps has been presented. Reported experimental data demonstrate that the proposed device is an optimum candidate for powering sensors for home monitoring applications.

REFERENCES

- [1] N. Md. Din, C. K. Chakrabarty, A. Bin Ismail, K. K. A. Devi, and W.-Y. Chen, "Design of RF energy harvesting system for energizing low power devices," *Progr. In Electrom. Research*, vol. 132, pp. 49-69, 2012.
- [2] G. Monti, F. Congedo, D. De Donno, and L. Tarricone, "Monopole-based rectenna for microwave energy harvesting of UHF RFID systems", *Progr. In Electrom. Research C*, vol. 31, pp. 109-121, 2012.
- [3] G. Monti and F. Congedo, "UHF rectenna using a bowtie antenna," *Progr. In Electrom. Research C*, vol. 26, pp. 181-192, 2012.
- [4] G. Monti, L. Corchia, and L. Tarricone, "ISM band rectenna using a ring loaded monopole," *Progress In Electrom. Research C*, vol. 33, pp. 1-15, 2012.
- [5] Z. W. Sim, R. Shuttleworth, M. J. Alexander, and B. D. Grieve, "Compact patch antenna design for outdoor RF energy harvesting in wireless sensor networks," *Progr. In Electrom. Research*, vol. 105, pp. 273-294, 2010.
- [6] D. Bouchouicha, F. Dupont, M. Latrach, and L. Ventura, "Ambient RF energy harvesting," in *Proc. ICREPQ'10*, 2010, Granada, Spain, pp. 1-5.
- [7] T. Letertre, F. Gaudaire, A. Azoulay, A. Destrez, and C. Martinsons, "Characterization of compact fluorescent lights RF emissions in the perspective of human exposure," in *Proc. 2009 EMC*, 2009, Kyoto, Japan, pp. 473-476.
- [8] G. Schmidt and I. Berta, "Radiated radiofrequency emission from the plasma of compact fluorescent lamps," *I.J.PEST*, vol. 5, no. 1, pp. 84-92, 2011.

WIRELESS SENSOR NETWORK PLANNING WITH ELECTROMAGNETICS

Gerardo Di Martino, Antonio Iodice, Daniele Riccio, Giuseppe Ruello

Department of Electric Engineering and Information Technology,
Università degli Studi di Napoli Federico II, Naples, Italy
{gerardo.dimartino; iodice; daniele.riccio; ruello}@unina.it

Abstract

We present an electromagnetic propagation software tool able to help planning and deployment of wireless sensor networks (WSN) in an outdoor environment. The tool is based on a ray-tracing algorithm for the evaluation of electromagnetic propagation in a built-up area, and on additional software modules that use the output of the electromagnetic solver to generate nodes' connectivity matrix, to compute individual nodes' coverage areas, and to identify the best locations where gateways can be placed. The presented tool is able to deal with the electromagnetic propagation issues involved in WSN planning and deployment, and it is conceived as a part of an overall WSN deployment, planning, and commissioning & maintenance tool.

Index Terms – Diffraction, electromagnetic wave propagation, ray tracing, wireless sensor networks.

I. INTRODUCTION

Simulation tools may be very helpful to designers of wireless sensor networks (WSN). Indeed, currently many wireless network simulation tools are publicly available, among which, for instance, OMNeT++ [1], TOSSIM [2]. However, all of them rely on very simple, heuristic propagation models that do not account for the detailed description of the surrounding environment and obstacles. On the other hand, electromagnetic propagation prediction tools accounting for complex outdoor environment do exist, see for instance [3]-[6]. However, they are tailored for radio and television broadcasting or cellular telephony systems, or Wi-Fi, and have not been employed in the framework of WSN planning.

In this work we present a software tool able to help planning and deployment of WSN in a complex outdoor environment. The core of the tool is an electromagnetic solver that employs a ray-tracing algorithm for the evaluation of electromagnetic propagation in a built-up area. It is substantially based on the methods described in [5]-[6], with some modifications to tailor it to the WSN case and to adapt the format of input and output to more widespread standards. This electromagnetic solver allows computation of the electromagnetic field in a built-up area, when the three-dimensional (3-D) topography (terrain height profile and buildings) of the considered city area is prescribed, as well as the radiating sources (locations, input power and antenna radiation

diagram of WSN nodes). The solver considers both reflected and diffracted rays, although a "fast mode" only considering reflected rays may be also selected. The output of the solver is the electromagnetic field intensity on a 3-D grid in the considered area: it can be directly displayed to the WSN designer, or it can be provided as an input to additional modules of the software tool, that use it to generate nodes' connectivity matrix, to compute individual node's coverage areas, and to identify the best locations where gateways can be placed, according to different WSN planning scenarios, as described in the next sections.

The presented tool is able to deal with the radio-frequency (RF) propagation issues involved in WSN planning and deployment, so that in the following we will refer to it as "RF tool". However, it is conceived as a part of an overall WSN deployment, planning, and commissioning & maintenance (DPCM) tool that is being developed in the framework of a European project [7]. In particular, the RF tool is directly interfaced with a Graphic User Interface (GUI) and with a network simulator, which takes care about protocols, data throughput, etc.

II. ELECTROMAGNETIC SOLVER

The proposed RF tool is composed of an electromagnetic solver and of three additional modules, namely a "connectivity matrix" module, a "coverage" module, and a "gateway positioning" module.

The electromagnetic solver input is a digital description of the scene and of the transmitting antenna. The scene description is provided by a file in kml (Keyhole Markup Language) format describing the buildings, and a raster file describing the terrain topography (Digital Terrain Model, DTM). Default values of buildings' walls and terrain relative permittivity and conductivity can be selected according to the area typology (historical area, residential area, business district). Antenna description is provided by means of its position and pointing, radiated power, polarization and radiation diagram.

Our solver is based on a 3-D space analysis similar to that of [5]-[6]. A ray-tracing algorithm is employed that considers direct, reflected and diffracted rays. Reflections are treated by using Geometrical Optics (GO), whereas diffraction is evaluated by using the Uniform Theory of Diffraction (UTD). Since most of the computational load is due to diffracted rays, the user can optionally select a "fast mode" that only considers direct and reflected rays.

The solver output is a 3-D map of the field levels produced by the transmitting antenna in the considered area. In fact, the electromagnetic field is computed on regular 2-D grids ("layers") placed on surfaces at different fixed heights above the ground (or above the roof, if the grid point is in correspondence of a building). This output is stored in a geotiff format file, and can be displayed by the GUI and/or passed to the additional software modules.

III. ADDITIONAL MODULES

The “connectivity matrix” module takes N simulated field maps produced by the electromagnetic solver and extracts the field values radiated by each antenna (node) at the locations of all other antennas (nodes). A "connectivity matrix" is then obtained, which is stored in a json (JavaScript Object Notation) file. If desired, and if a receiver field threshold level is defined, this matrix can be immediately translated into a binary matrix whose non-zero elements can be displayed by the GUI as arcs connecting corresponding nodes (see Fig.1).

The “coverage” module, by using the field map relative to a transmitting node, produced by the electromagnetic solver, and given a receiver threshold, computes the coverage area of the considered node, stored as the list of output grid points for which the field level is higher than the receiver threshold. The coverage area can be displayed by the GUI (see Fig.2).

Finally, let us consider the “gateway positioning” module. Inputs of this module are N simulated field maps produced by the electromagnetic solver (one for each transmitting node) and a gateway receiver threshold. First of all, the module finds the grid points, if any, for which all the N field levels are higher than the threshold. These are "candidate points" for the gateway positioning. Among these points, the module determines the best gateway position by using one of the following criteria, selectable by the user.

- "Median" criterion: the grid point such that the median value of the N field levels is the highest is chosen.
- "90%" criterion: for each grid point, the field value exceeded by the 90% of the N field levels is computed; the grid point such that this value is the highest is chosen.
- "Minimum" criterion: the grid point such that the minimum of the N field levels is the highest is chosen.

If no candidate point is found, the set of N nodes is split into different subsets (clusters) such that for each subset at least one candidate point is present. For each cluster of nodes, the best gateway position is determined as described above (see Fig.3).

IV. CONCLUSION

An electromagnetic propagation software tool able to help planning and deployment of WSN in a complex outdoor environment has been presented. It is being currently employed, as a part of an overall WSN DPCM tool, in actual case-studies within a European project.

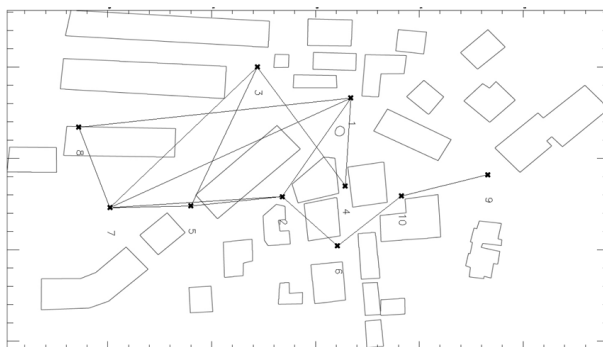


FIG. 1 – Connectivity maps for a 10-node WSN in the suburbs of Naples, Italy.

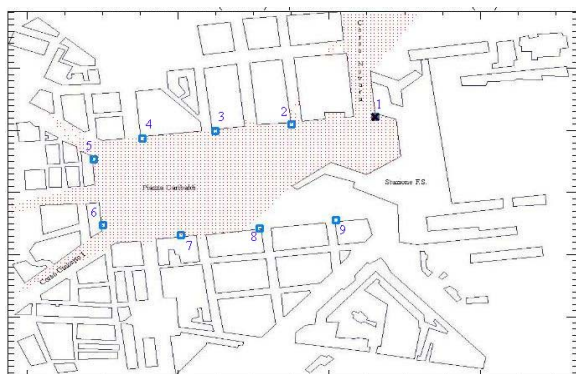


FIG. 2 – WSN in the area of Naples Central Station. Coverage map for node 1.

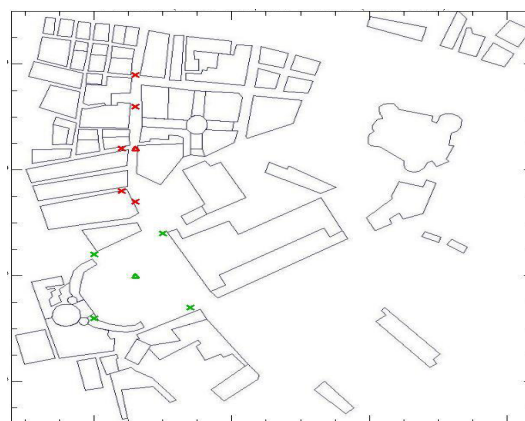


FIG. 3 – WSN in the area of Naples city centre. Cluster A (green) and cluster B (red) nodes (crosses) and gateways (triangles).

ACKNOWLEDGEMENT

This work has been supported by the ARTEMIS Joint Undertaking (EU) and by the Italian Ministry of University and Scientific Research, within the WSN - DPCM project.

REFERENCES

- [1] <http://www.omnetpp.org/>
- [2] P. Levis, N. Lee, M. Welsh, and D. E. Culler, "TOSSIM: accurate and scalable simulation of entire TinyOS applications", *Proceedings of SenSys*, Los Angeles (USA), 2003, pp. 126-137.
- [3] EdxPro, <http://www.edx.com/products/signalpro.html>
- [4] WinProp: Software tool for the planning of radio communication networks, <http://www.awe-communications.com/>
- [5] G. Franceschetti, A. Iodice, D. Riccio, G. Ruello, "A Tool for Planning Electromagnetic Field Levels in Urban Areas", *Proceedings of the Antennas and Propagation Society International Symposium*, Monterey (USA), 2004, pp. 2211-2214.
- [6] G. Franceschetti, P. Imperatore, A. Iodice, D. Riccio, "Radio-Coverage Parallel Computation on Multi-Processor Platforms", *Proceedings of the 39th European Microwave Conference*, Rome (Italy), 2009, pp. 1575-1578.
- [7] <http://www.wsn-dpcm.eu/>

MINIATURIZED FRACTAL-SHAPED REFLECTARRAYS FOR WIDE-ANGLE FIXED-BEAM APPLICATIONS

S. Costanzo, F. Venneri

DIMES - Università della Calabria
Via P. Bucci, cubo 41D, 87036 Rende (CS), Italy
costanzo@deis.unical.it

Abstract

The intrinsic miniaturization capabilities of fractal geometries are applied in this work to design a reduced size reflectarray unit cell, potentially offering the ability to focalize the reflected field along very wide angles off-broadside. A Minkowski fractal shaped patch is proposed as reflectarray radiator, with a properly fixed reduced side length and a variable scaling factor as phase tuning parameter. The proposed approach is applied to design a X-band $0.3\lambda \times 0.3\lambda$ fractal reflectarray cell giving a 320° phase agility. A reflectarray prototype of 15×15 radiators is considered as validation example, and the measured radiation patterns are reported to demonstrate the reflectarray capability to point the main lobe at a wide direction off-broadside, equal to 50° .

Index Terms – Fractals, microstrip antennas, reflectarrays.

I. INTRODUCTION

Reflectarrays are very compact reflector antennas based on the use of a microstrip array illuminated by a primary antenna [1]. They offer the best features of microstrip technology as well as the advantages given by parabolic reflectors. Many different reflectarray configurations have been proposed in literature. Each of them is based on the concept to control the phase of the field reradiated by the single unit cell composing the array. The phase tuning is typically realized by changing the size, the shape and/or the position of each radiator [1]. Reflectarray elements can also be integrated with tunable components, such as MEMs [1] or varactors [2, 3], in order to actively control the phase delay. The phase tuning mechanism proposed in this work is based on the use of a Minkowski square patch with a fixed side length and a variable insets size, i.e. a different scaling factor, giving a full phase range. The adopted configuration allows to obtain a significant reduction in the patch size [4], thus offering the opportunity to deal with an array grid having very small inter-element spacing. As a consequence of this, reflectarrays with a main beam directed along a very wide angular position off-broadside can be usefully designed. The proposed approach is adopted to obtain a small X-band $0.3\lambda \times 0.3\lambda$ reflectarray cell giving a full phase range [5]. Then, the miniaturized unit cell is applied to synthesize a 15×15 reflectarray prototype, with a main beam directed along a wide angular position equal to 50° , in the H-plane. The antenna

is successfully tested into the Microwave Laboratory at University of Calabria, demonstrating the effectiveness of the proposed approach.

II. UNIT CELL DESIGN

The proposed unit cell is based on the use of the Minkowski fractal patch in Fig. 1. It is characterized by a beginning square element of dimensions $L \times L$ (Fig. 1(a)), which is reshaped as follows: a smaller square of side SL is removed from the center of each square patch side (Fig. 1(b)), where S is the scaling factor ranging from 0 up to $L/3$. By applying the described construction rule to each side of the structure in Fig. 1(b), the 2nd iteration patch is obtained (Fig. 1(c)).

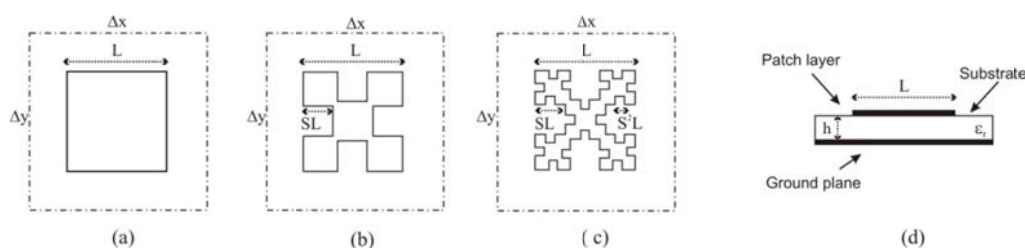


FIG. 1 – Geometry of fractal unit cell: (a) generator square patch; (b) 1st iteration fractal patch; (c) 2nd iteration fractal patch; (d) layers stratification

The main benefit due to the use of fractal geometries in the design of microstrip antennas is that more electrical length can be fitted into a smaller physical area [4]. In the case of the Minkowski fractal patch (Fig. 1(b, c)), for example, the resonant length is longer with respect to the square patch side length L (Fig. 1(a)), as demonstrated by the following equation [4]:

$$L_n = (1 + 2S)^n L \quad (1)$$

where n is the iteration number and L_n is the resonant length of the patch generated at the n^{th} iteration. The increased electrical length of fractal patch (1) leads to a lower resonant frequency, thus the fractal antenna size must be reduced in order to obtain the resonance at the desired working frequency. Keeping in mind relation (1), the phase tuning of the Minkowski reflectarray cell is realized by varying the scaling factor S , while the patch size L is properly fixed in order to match the resonance condition at the working frequency f_0 , for a suitable value of S , giving the desired miniaturization level. The proposed phase tuning approach is adopted to design a 10 GHz reflectarray unit cell printed on a substrate with $\epsilon_r = 2.33$ and $h = 0.762\text{mm}$ (Fig. 1(d)). The cell size is initially set to a value $\Delta x \times \Delta y = 0.6\lambda \times 0.6\lambda$ at f_0 . The analysis is performed by adopting the infinite array approach and assuming a normally incident plane wave. A 10 GHz resonant square patch with $L = 9.215\text{mm}$ is considered as generator element for the fractal cell design (Fig. 1(a)), while the scaling factor S is

varied from 0 up to 0.25. The simulated reflection phase curves, obtained for different values of S, are reported in Fig. 2(a), for both the 1st and the 2nd iteration patch. A full phase variation range is obtained in both cases, when considering an operating frequency around 9 GHz. Furthermore, it can be observed that, for increasing values of S, much lower resonating frequencies are obtained for the fractal patches, moving from the square patch resonant value of 10 GHz down to 8 GHz (1st iteration patch) and 7.5 GHz (2nd iteration patch), which are equivalent to a 20% and a 25% size reduction, respectively. This last behaviour demonstrates the miniaturization capability of the proposed fractal element, which becomes more relevant when a greater value of S is considered and/or the fractal construction is progressively reiterated. To obtain a reflectarray cell giving a full phase range at the design frequency $f_0 = 10\text{GHz}$, the side length of the 1st iteration patch is properly decreased to the value $L = 7.6\text{mm}$, thus obtaining a reduced size $0.3\lambda \times 0.3\lambda$ elementary cell. The fractal patch is dimensioned in order to resonate at f_0 when the scaling factor S is fixed to 0.2. The phase curve of the new reduced cell, computed for different values of the scaling factor S, is reported in Fig. 2(b). In this case, the frequency swing due to the variation of S is centered around 10 GHz, and a phase range of about 320° can be observed in the neighbourhood of f_0 . The designed cell is experimentally tested with a far-field measurement setup [3], obtaining a good agreement between measured and simulated phase curves, as demonstrated in Fig. 2(c).

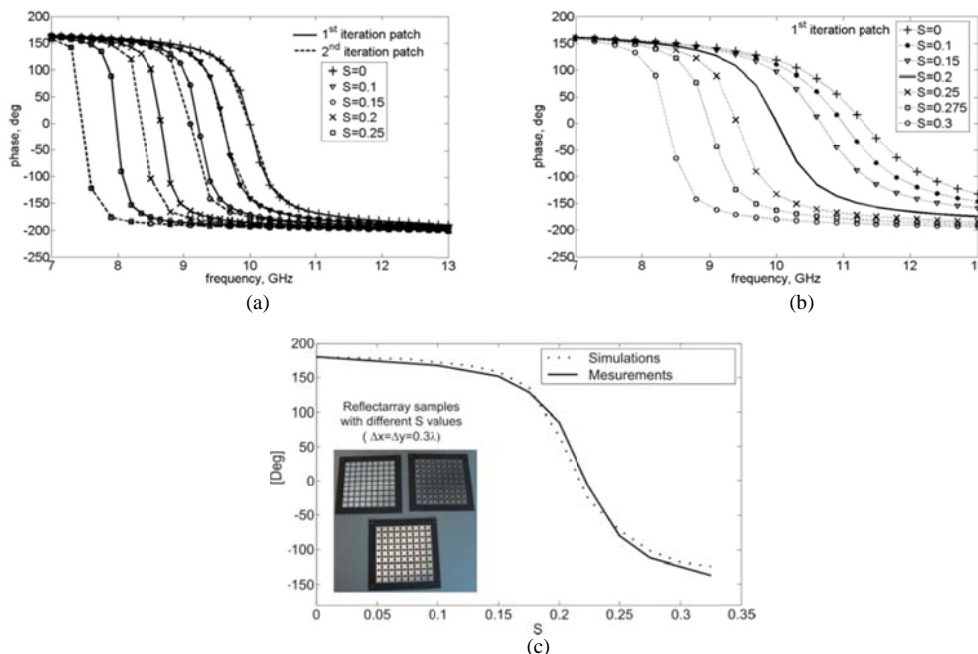


FIG. 2 – Phase curves - phase vs. frequency for different values of S: (a) $L=9.215\text{mm}$, $\Delta x \times \Delta y = 0.6\lambda \times 0.6\lambda$ and (b) $L=7.6\text{mm}$, $\Delta x \times \Delta y = 0.3\lambda \times 0.3\lambda$; (c) comparison between simulated and measured phase curve vs. scaling factor S at 10 GHz.

III. DESIGN OF A WIDE-ANGLE FIXED-BEAM REFLECTARRAY PROTOTYPE

The proposed $0.3\lambda \times 0.3\lambda$ fractal unit cell is adopted to synthesize a 10 GHz reflectarray with 15×15 radiators, illuminated by an offset X-band horn. The antenna is designed to point the main beam along 50° off-broadside in the xz -plane (Fig. 3(a)). A synthesis algorithm [2] is adopted to compute the scaling factor S for each array element. The realized antenna (Fig. 3(a)) is tested into the Microwave Laboratory at University of Calabria. Fig. 3(b) shows a good agreement between measured and simulated radiation patterns, having a main lobe along the desired direction. Furthermore, the lack of grating lobes demonstrates the effectiveness of the proposed approach in the design of reflectarrays with wide beam scan angles.

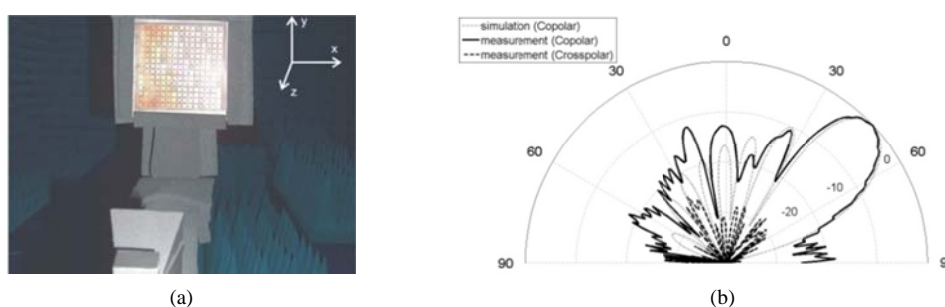


FIG. 3 – (a) Reflectarray prototype; (b) Simulated and measured radiation patterns.

IV. CONCLUSION

A miniaturized fractal configuration has been proposed in this work as reflectarray unit cell. First, a 10 GHz fractal reflectarray element, embedded into a small $0.3\lambda \times 0.3\lambda$ cell, has been designed. Then, a 15×15 reflectarray prototype has been successfully realized and tested, showing the effectiveness of the proposed configuration.

REFERENCES

- [1] J. Huang, J. Encinar, "Reflectarray antennas", Wiley-IEEE Press, 2008.
- [2] F. Venneri, S. Costanzo, G. Di Massa, "Design and validation of a reconfigurable single varactor-tuned reflectarray", *IEEE Trans. Antennas Propag.*, 2013, 61, (2), pp. 635-645.
- [3] F. Venneri, S. Costanzo, G. Di Massa, "Reconfigurable Aperture-Coupled Reflectarray Element Tuned by a Single Varactor Diode", *Electronics Letters*, 2012, 48, pp. 68-69.
- [4] J. P. Gianvittorio, Y. Rahmat-Samii, "Fractal antennas: A novel antenna miniaturization technique, and applications", *IEEE Antennas Propag. Mag.*, 2002, 44, (1), pp. 20-36
- [5] S. Costanzo, F. Venneri, "Fractal shaped reflectarray element for wide angle scanning capabilities", *Proc. 2013 IEEE AP-S Int. Symp.*, Orlando, USA.

DATA MODEL FOR THE EXCHANGE OF AUGMENTED GEOMETRICAL INFORMATION: DESIGN AND IMPLEMENTATION

F. Rossi⁽¹⁾, M. Sabbadini⁽²⁾, F. Mioc⁽³⁾

⁽¹⁾ Department of Information Engineering, Padova University,
Via Gradenigo 6/b, 35131 Padova, Italy, rossifra@dei.unipd.it

⁽²⁾ ESA, Noordwijk, The Netherlands, Marco.Sabbadini@esa.int

⁽³⁾ MVI, Pomezia, Italy, francesca@mioc.info

Abstract

About a decade ago the EDX Group was formed aiming at a common language for data exchange in electromagnetic modelling. The language is constituted by three main components, the core one consists in a set of Data Dictionaries defining the meaning of the data and the associated conventions. The others are the XML-based syntax and the software library to actually exchange the data. The implementation of the Structure Data Dictionary is outlined here, including all geometrical information and the related physical details needed by antenna design tools. To help an organized and complete development of the data model a Python-based prototype tool, with a minimalistic CAD, was created and exploited to generate in an easy way some complex test case of the Structure Data Dictionary, one of them is reported as an example.

Index Terms - Data model, data exchange, EDX, electromagnetic modelling

I. INTRODUCTION

The electromagnetic design process is typically based on rather elaborated procedures. One of the main reasons is that a full design cycle involves many different modelling tools each one featuring its own data model and conventions. The resulting translations are very time-consuming and obstruct a smooth development of space antenna solution. A problem especially felt in the space applications domain.

Over a decade ago, the Antenna Centre of Excellence (ACE) and the European Antenna Modelling Library (EAML) team established a joint Working Group to develop the Electromagnetic Data Exchange language (EDX). The work has been supported by the European Space Agency (ESA) as well as, later on, by the European Association on Antennas and Propagation (EurAAP).

The EDX language, first established in 2005, aims at being a reference for data exchange among electromagnetic modelling tools. It is composed by three main components: an Electromagnetic Mark-Up Language (EML) that specifies how the information is organised and formulated in a file, a software library, called Electromagnetic Data Interface (EDI) supporting uniform access to data, and a collection of Electromagnetic Data Dictionaries (EDDs) that define the information needed to fully describe physical structures and quantities.

This paper describes the design and the testing that has led to the draft of another dictionary, the Structure EDD (S EDD). Its purpose is to provide for an organized and complete description of physical structures, including not only purely geometrical information but also other data usually required for electromagnetic modelling [1], e.g. material properties and a description of the antenna ports. The draft is actually a complete dictionary, which has also been verified on a rather extensive set of examples of increasing complexity.

II. STRUCTURE DATA DICTIONARY: DESIGN

The Structure Data Dictionary allows the complete and organized definition of all physical details of an electromagnetic model. To achieve a good level of completeness and generality there is need of multiple description of the same objects (many meshes with different accuracy, both CSG and boundary representation, etc.). The description must also relieve the human reader from inspecting long lists of raw geometry data to understand the content. A highly structured data model with layered structure (Fig. 1) has been chosen to this end.

The current layers are: Objects, Geometry, Topology, Materials and Parameters. They correspond to EML Folders (an XML element defined by the language). More can be added in the future if need arises thanks to the modularity of the whole structure.

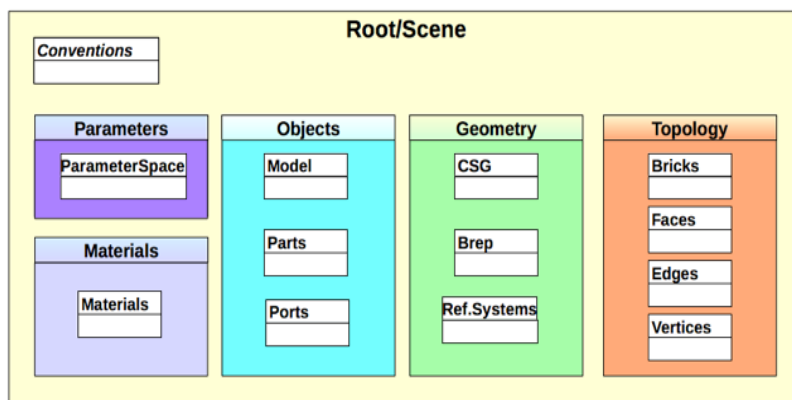


FIG. 1 – Structure data dictionary: general overview.

The Object layer is the entry point of data set and outlines its logical hierarchical structure, allowing a robust handling of very complex structures. It reflects the spontaneous high-level way of describing a complex object from the general structure down to the smallest details.

The Geometry layer contains three groups of classes (other type of XML elements): the ReferenceSystems, the CSGElements and the BRep. These groups of data provide a full geometric description using both CSG and BRep definition [2]. They also include the information needed for a proper use of the corresponding meshes in the modelling tools, so as to enable simple validity checking.

The Topology layer contains the six classes required for the 4D-BRep representation, an extension of the Winged-Edge structure allowing a full navigation of both surface and volumetric meshes.

The Materials layer, instead, is a collection of lists catering for the description of the electromagnetic properties of three groups of materials allowing the description of homogeneous materials and sheet boundaries as well as descriptions based on scattering matrices.

Finally, the Parameters layer contains a single class which instances are lists of parameters with their definition, intended for use in the geometry description to support full parameterisation of the models.

III. STRUCTURE DATA DICTIONARY: IMPLEMENTATION

Naturally the data model has undergone a refinement process and a Python-based software prototype was implemented to test the growing data structure and to efficiently create examples for this purpose. The utility was developed focusing on Objects, Geometry and Topology and it is logically divided into three main parts: the EDX S I/O BackEnd, the DMF Loader and the GEO Modeller.

The EDX S I/O BackEnd includes a library of I/O functions to access, both in reading and writing any EML data. The inherently hierarchical XML data are directly mapped into a tree-like data structure.

The DMF Loader is a lexical and syntactical analyser. It takes as input the formal definition of the EDD [4] and checks if the input file matches its lexicon and syntax. If so, it encodes it into a logical sequence (an ordered Python dictionary) used to drive the I/O module.

The GEO Modeller is the core S-EDD-specific part and mainly consists in a library of topological and geometrical functions devoted to the manipulation of geometries and all related data.

Several examples of increasing complexity were used to perform tests checking completeness and correctness of both the tool and the S EDD. A typical test includes the creation of an empty model to which shapes are added in sequence. The model is then displayed, the EDX data file written and the internal storage reset. Afterward the data file is read back and the model rebuilt and displayed.

Robustness and performance were also tested using some large examples. Here we consider a simplified version of a generic satellite shown in Fig. 2 (a), containing almost a thousand elementary shapes. The structure is comprised of a body, two solar panels, two centred reflector antennas (bottom-right inset) on the top, three offset ones on the two sides, two feed horns on the front edge illuminating the reflectors beneath and an array (top-left inset) on the back illuminating the other. The feeders are too small to be visible on the full model.

Thousands of raw data are written and then read back for this satellite model. Coincidence of the initial and final model, Fig. 2 (b), ensures completeness and correctness of data structures.

Lower level tests were made initially to verify the correctness of the logic by verifying all the internal data structures in detail.

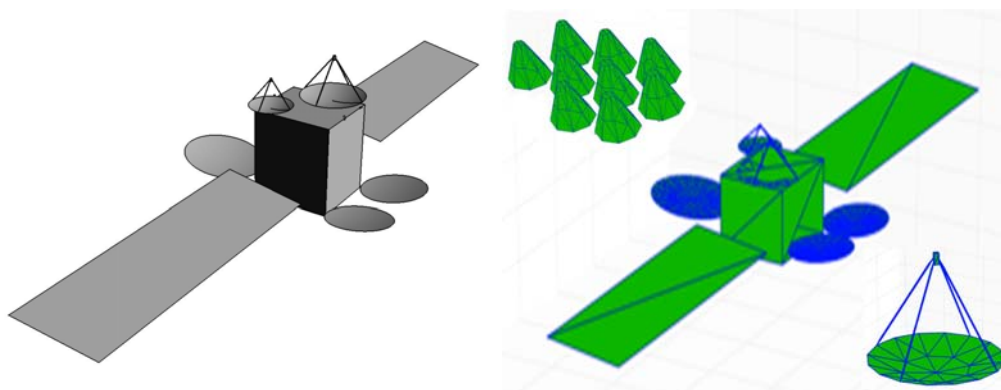


FIG. 2 – Satellite example: (a) CAD version, (b) GeoModeller visualization, with details of the feed array (top left) and centre-feed reflector.

IV. CONCLUSION

The Structure Data Dictionary (S EDD) has been successfully developed exploiting an ad-hoc Python-based software prototype as part of the continuing development of the EDX language.

The S EDD has reached a rather stable draft version, to be publicly reviewed as part of the EurAAP activities. The prototype utility will be consolidated in parallel, addressing speed optimization and complete handling of non-geometric information. The improved version is likely to become part of in some commercial tools for space antenna design.

ACKNOWLEDGEMENT

The work described was made partly possible thanks to the funds provided by the European Space Agency as part of the European Antenna Modelling Library project.

The work of F. Rossi was supported by independent funds provided IDS, MVI and TICRA in the form of a joint study grant.

REFERENCES

- [1] F. Mioc, M. Sabbadini, P.E. Frandsen, “Proposal for a new advanced Structure and Mesh Data Dictionary for the Electromagnetic Data Exchange”, *Proc. EuCAP*, Gothenburg, April 2013.
- [2] M. Sabbadini, “Electromagnetic Data Exchange Dictionary Declaration Language”, Issue 0, Version B, *ESA*, Noordwijk, The Netherlands, November 2008.

EBG-BASED SPATIAL FILTERS FOR DIRECTIVE ANTENNAS: A COMPARISON BETWEEN TWO DIFFERENT MECHANISMS

S. Ceccuzzi⁽¹⁾, L. Pajewski⁽¹⁾, C. Ponti⁽¹⁾, G. Schettini⁽¹⁾

⁽¹⁾ Department of Engineering, Roma Tre University,
Via Vito Volterra 62, 00146 Roma, Italy
silvio.ceccuzzi@uniroma3.it

Abstract

We present a comparison between two different mechanisms using Electromagnetic Band Gap (EBG) materials to enhance the directivity of a primary radiator. By means of two-dimensional periodic structures, which respectively work inside and at the edge of the bandgap, only a small portion of the wavenumber spectrum is selected. The benchmark is carried out against triangular arrangements of alumina cylinders, excited by a 8 GHz, TM-polarized, infinitely long current wire. A large set of geometries has been optimized to elucidate the best working range of the two methods. The first one is shown to reach the highest performance for long layers, while being outranked by the second mechanism when short layers are considered.

Index Terms – EBG, periodic structures, directive antenna, spatial filter

I. INTRODUCTION

Periodic physical properties in space allow the control of particle motion: this principle applies to electrons within a periodic electrostatic potential as well as to photons, i.e. electromagnetic waves, in photonic crystals [1]. This behaviour triggered a remarkable interest and an intense research towards the so-called Electromagnetic Band-Gap (EBG) materials that in the last three decades have been applied to a wide range of devices such as shields, filters, waveguides, antennas [2].

Concerning antennas, EBGs can be designed to be a passive medium able to shape the antenna radiation pattern, standing out as an attractive solution when the use of several radiators with their own feeding networks is not suggested. In this sense a well-known configuration is the resonator antenna [3] made by a ground plane and an EBG layer working in the bandgap. The primary source is located inside this interspace, which acts like a crystal defect and produces a transmission peak in the bandgap. A different method using an EBG working at the edge of the bandgap was proposed [4]. It requires the primary source to be embedded in the periodic structure to excite a crystal mode instead of a defect one. We will refer to the former and latter configuration as the *cavity* and *embedded source* method.

Recently we presented a preliminary comparison between the two mechanisms [5]. In this paper we overcome some limits of that work by carrying out a benchmark against a larger set of two-dimensional

geometries consisting of dielectric cylinders with identical radius and relative permittivity. Rods are arranged in a triangular lattice and excited by a line current aligned with their axis.

II. THEORETICAL BACKGROUND AND BENCHMARK SETUP

Despite based on different physical behaviours, the two methods can be seen as filters in the spectrum of the in-plane wavevector, being the one contained in the plane orthogonal to the cylinder axis. We refer to a current wire placed in the origin and aligned with the z -axis and to a space and time dependence equal to $I_0 e^{j(\omega t - k_z z)}$. The field radiated by this source is TM-polarized and can be expressed through the vector potential as a summation of the following family of solutions to the Helmholtz equation in cylindrical coordinates:

$$\mathbf{A}_m = \hat{z} A_{z,m} = \hat{z} \left[C_1 H_m^{(1)}(k_t \rho) + C_2 H_m^{(2)}(k_t \rho) \right] \cdot \left[D_1 \cos(m\phi) + D_2 \sin(m\phi) \right] e^{-jk_z z} \quad (1)$$

being ρ and ϕ the polar in-plane coordinates, k_t the in-plane wavenumber and $H_m^{(1)}$ and $H_m^{(2)}$ the m -th Hankel functions of the first and second kind, respectively. In an unbounded vacuum without scatterers, a line source features $C_1 = 0$ and $m = 0$, while the integration constants are $C_2 D_1 = A_0 = -j0.25\mu_0 I_0$. So in far region:

$$\mathbf{E} = -I_0 \sqrt{\frac{jk_t \mu_0}{8\pi \varepsilon_0}} \frac{e^{-jk_t \rho}}{\sqrt{\rho}}, \quad \mathbf{H} = \sqrt{\frac{\varepsilon_0}{\mu_0}} \hat{\rho} \times \mathbf{E} \quad (2)$$

which is a TEM wave that does not depend on ϕ , namely the line source uniformly excites the k_t space, generating an omnidirectional radiation pattern in the H -plane.

The EBG-based techniques for directivity enhancement shape this uniform spectrum. In the case of the cavity method, the structure behaves like a Fabry-Perot interferometer, so that very few components of the wavevector are enhanced, whereas the others are impaired. With reference to the embedded source approach, instead, the crystal works in a region of the Brillouin diagram, where only a small portion of the wavevector spectrum is allowed.

These concepts are clarified in Fig. 1, where the filtering behaviour of two structures with infinite layers of rods is reported. Our benchmark is performed at 8 GHz using triangular arrangements of cylinders with diameter $d = 5.6$ mm and dielectric constant $\varepsilon_r = 9$. The distances between rods have been preliminarily designed as reported in Fig. 1.

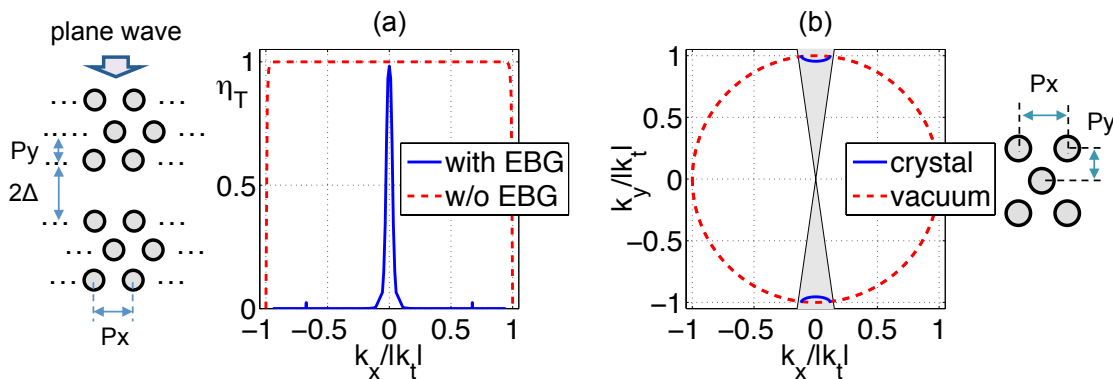


FIG. 1 – (a) Transmission efficiency versus angular spectrum in a vacuum and in the EBG structure sketched aside ($P_x = 15.4$ mm, $P_y = 13.4$ mm, $\Delta = 20.4$ mm); (b) constant-frequency band diagram in a vacuum and in the lattice sketched aside ($P_x = 18.8$ mm, $P_y = 18.4$ mm).

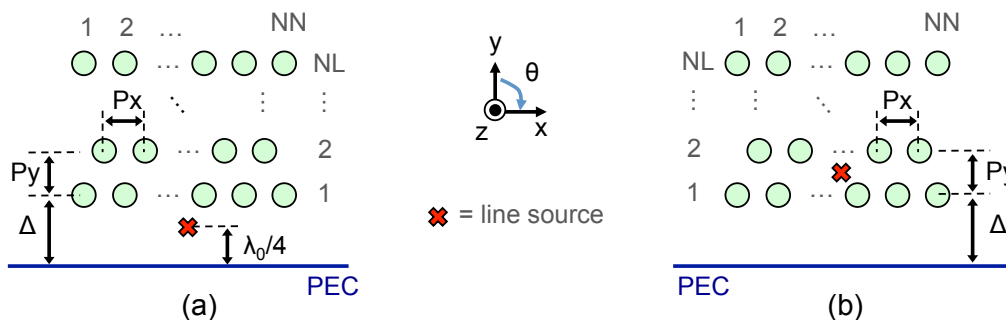


FIG. 2 – Finite-size geometries for the triangular arrangement of cylinders in the cavity (a) and in the embedded source (b) method.

Spatial filters are up-down symmetric so that a ground plane is needed to suppress downward propagating waves. Moreover layers have to be truncated because real antennas are finite in extent and the primary source has to be placed. Finite-size geometries are shown in Fig. 2. Truncation and boundary effects introduce small changes of the structure behaviour so that an optimization is needed to maximize the directivity. The optimization has been carried out for a set of geometries with number of layers ranging from 2 to 4 and number of rods per layer ranging from 2 to at least 50 with steps of 2.

III. RESULTS

The directivity of optimized geometries is plotted in Fig. 3 versus the number of rods in the longest layer. For the same NL, at low abscissa values the embedded source configuration is more directive, but the curves quickly saturate and are overpassed by the directivities of the cavity method at higher abscissa values.

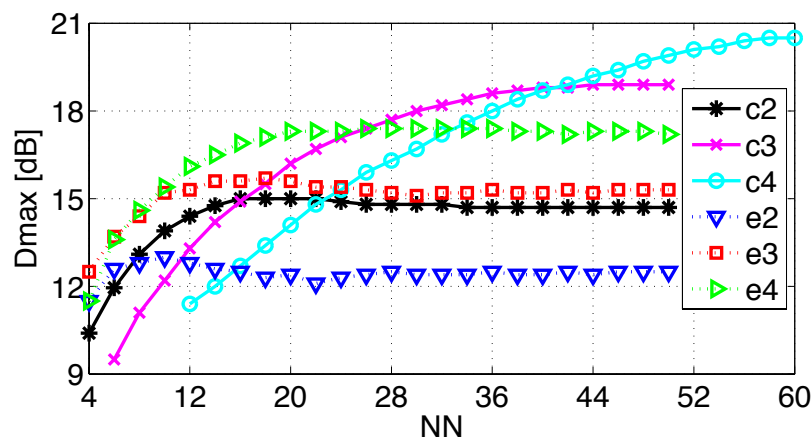


FIG. 3 – Maximum directivity vs. NN (see Fig. 2); curve acronyms consist of a letter (c=cavity, e=embedded source) and a number (=NL).

IV. CONCLUSION

Two EBG-based methods for the directivity enhancement of a primary, omnidirectional source have been benchmarked against triangular arrangements of infinite dielectric cylinders. The one, i.e., the resonator antenna, relies on a defect mode and achieves the highest directivity when long layers are used, standing out as the ideal candidate for low-profile devices. The other, i.e., the embedded source configuration uses a crystal mode and results more suitable for compact structures.

REFERENCES

- [1] J. D. Joannopoulos, R. D. Meade, and J. N. Winn, *Photonic crystals: molding the flow of light*, Princeton: Princeton University Press, 2nd ed., 2008.
- [2] P. de Maagt, R. Gonzalo, Y. C. Vardaxoglou, and J.-M. Baracco, "Electromagnetic bandgap antennas and components for microwave and (sub)millimeter wave applications," *IEEE Transactions On Antennas and Propagation*, vol. 51(10), pp. 2667–2677, Oct. 2003.
- [3] C. Cheype, C. Serier, M. Thèvenot, T. Monédière, A. Reineix, and B. Jecko, "An electromagnetic bandgap resonator antenna," *IEEE Transactions On Antennas and Propagation*, vol. 50 (9), pp. 1285–1290, Sep. 2002.
- [4] S. Enoch, G. Tayeb, and D. Maystre, "Dispersion diagrams of Bloch modes applied to the design of directive sources," *Progress In Electromagnetic Research*, vol. 37, pp. 61–81, 2002.
- [5] S. Ceccuzzi, L. Pajewski, C. Ponti, and G. Schettini, "Directive propagation in two EBG structures: A comparison," in *IEEE MTT-S International Microwave Symposium Digest (IMS)*, 2013, pp. 1–4.

INNOVATIVE WIRELESS SOLUTIONS FOR SMART CITIES

E. Giarola⁽¹⁾, S. Marchesi⁽²⁾, A. Polo⁽¹⁾, F. Robol⁽¹⁾, F. Viani⁽¹⁾,
L. Zappini⁽²⁾, A. Zorer⁽³⁾, and A. Massa⁽¹⁾

⁽¹⁾ ELEDIA Research Center @DISI, University of Trento
Via Sommarive 5, I-38123 Trento, Italy
andrea.massa@ing.unitn.it

⁽²⁾ Agenzia Centrale Unica Emergenza, Provincia Autonoma di Trento
Via Roma 50, I-38122 Trento, Italy
luisa.zappini@provincia.tn.it

⁽³⁾ Trentino Network S.r.l.
Via G. Pedrotti 18, 38121 Trento, Italy
alessandro.zorer@trentinonetwork.it

Abstract

In the last years, more and more attention has been focused on the adoption of wireless systems as a flexible and scalable backbone for the implementation of innovative and advanced services in smart cities. In this framework, the ELEDIA Research Center of the University of Trento has studied, designed, and developed heterogeneous solutions for improved awareness of operators and decision makers in the monitoring, supervision, control, and management of territory, public and private spaces, citizens, and environment. Such solutions exploit the wireless communications in combination with intelligent methods in order to provide advanced services as applied to many application fields, like environment monitoring, natural hazard prevention, fleet management, indoor localization, energy management in smart districts and buildings. In this paper, a review of the last advances have been reported and discussed.

Index Terms – Distributed monitoring, smart cities, wireless localization, wireless sensor networks.

I. INTRODUCTION

Wireless technologies are playing a key role in creating more instrumented and interconnected urban environments. The resulting so-called smart cities present a more efficient management of resources and a consequent increased quality of life for the city inhabitants. Although the wireless infrastructures and devices still represent the main issue in the development of distributed monitoring systems, many challenges are recently focused on the development of next-generation services able to leverage the heterogeneous information acquired by the increasing number of wireless sensors and instruments. Toward this end, smart strategies and algorithms have been developed for the real-time and efficient processing of data, for fast analysis and visualization. Most of the innovative applications related to smart cities and societies present stringent requirements in terms of simplicity and low

computational load, to enable effective control and usage also from mobile devices such as smartphones and tablets. Within this scope, the ELEDIA Research Center has investigated various technological and methodological solutions that offer to end users a quick access to highly representative information, as the results of efficient correlation and fusion of many data streams coming from distributed wireless systems. This work aims at reviewing the recent applications of such intelligent wireless systems with reference to real deployments and experimental validations to give some insights about the implemented solutions.

II. SEMANTIC WIRELESS LOCALIZATION

Most of the next-generation services need real-time information about user presence, movement, and behavior. The ELEDIA Research Center has recently developed many localization approaches that implement the so-called semantic wireless localization (SWL) paradigm whose underlying idea is that *“the best position estimation is not the most accurate one, but one that provides the highest informative contribution respect to the context”*. This basic concept has been integrated in both active and passive [1][2] localization systems to (i) enhance the localization accuracy of moving targets, and (ii) reconstruct their profiles starting from the study of their movement indicators. Toward this end, the information inferred from the human-environment relations have been processed by learning-by-example methods that learn positions and trajectories respect to the objects and characteristics of the scenario at hand [3]. Such knowledge has been also exploited to enhance the awareness about the usage of a known area, if and how the users occupy it, and to provide statistics about past and present activities. The same principles have been also applied to the management of fleets, composed by vehicles and operators localized thanks to heterogeneous wireless technologies, including TETRA terminals [4]. Decision support systems for the optimal selection of resources during civil protection missions have been experimentally tested, using real location information of the TETRA network deployed in Trentino, Italy, thanks to the collaboration with Trentino Network S.r.l. and Centrale Unica Emergenza of the Autonomous Province of Trento.

III. DISTRIBUTED WIRELESS SENSING

Heterogeneous integrated smart systems based on wireless sensor network (WSN) technology have been developed at the ELEDIA Research Center of the University of Trento [5][6]. One of the key features of WSNs as applied to distributed monitoring is that, while the capabilities of each single sensor node is limited, the implementation of cooperative

schemes throughout the whole network enables the solution of even complex tasks. Among them, some examples of WSN-based systems experimentally applied to the localization of people [7][8] and wildlife [9] have been proposed. More recently, the WSN backbone as well as the investigated sensing technologies have been customized for monitoring superficial movements of the soil [10]. The relative positions of wireless sensor nodes deployed where high probability of landslide exists is carefully monitored to forecast dangerous events. Multiple sensors like ultrasound, laser, high precision GPS, for the precise measurement of relative distances between the nodes of the network and the absolute positions respect to reference targets have been integrated in a prototype system. Experimental results have been obtained on a real test site, in Rendena Valley, Trentino, Italy, thanks to the collaboration of the Geological Department and the Centrale Unica Emergenza (CUE) of the Autonomous Province of Trento. The acquired information have been organized in a structured and large database that collects many heterogeneous streams of real-time data. Such information have been processed by data fusion techniques and represented through a simple and user-friendly application for smartphone and tablets, called SEMPLICE, in order to guarantee a constant access to the highly important monitored data.

IV. SMART GRIDS AND BUILDINGS

The concept of smart grid has been analyzed not only from the energetic viewpoint. The integration and reuse of existing components within smart buildings have been addressed [1]. Collecting, connecting, reusing, combining and semantically aggregating disjoint information extracted from a plethora of sources, such as information generated by users (e.g. through social networks), captured from sensors or made available by public authorities is one of the key challenges that has been investigated.

Interoperable wireless infrastructures exploiting new trends of the future Internet and open data have been adopted to create context-aware services and applications of relevance to families, citizens, and large crowds. Preliminary applicative frameworks have been developed for the real-time analysis of such information coming from multi-scale domains (apartment, building, district, city, etc.) and finally useful for energy management systems.

V. CONCLUSION

In this paper, the recent wireless solutions studied at the ELEDIA Research Center for the development of more intelligent and smart

environments have been reviewed. Adaptive, learning, cognitive and bio-inspired systems as well as distributed and embedded control and sensing have been studied and tested as an important avenue for the medium to long term development of the next-generation smart cities.

REFERENCES

- [1] F. Viani, F. Robol, A. Polo, P. Rocca, G. Oliveri, and A. Massa, "Wireless architectures for heterogeneous sensing in smart home applications – concepts and real implementations", *Proc. IEEE*, vol. 101, no. 11, pp. 2381-2396, Nov. 2013.
- [2] F. Viani, P. Rocca, G. Oliveri, D. Trincherò, and A. Massa, "Localization, tracking, and imaging of targets in wireless sensor networks: An invited review", *Radio Sci.*, vol. 46, no. 5, art. no. RS5002, Sep. 2011.
- [3] F. Viani, A. Polo, F. Robol, G. Oliveri, P. Rocca, and A. Massa, "Crowd detection and occupancy estimation through indirect environmental measurements", *2014 European Conference on Antennas and Propagation (EUCAP)*, (The Hague, The Netherlands), 6-11 Apr. 2014.
- [4] A. Polo, F. Robol, C. Nardin, S. Marchesi, A. Zorer, L. Zappini, F. Viani, and A. Massa, "Decision support system for fleet management based on TETRA terminals geolocation", *2014 European Conference on Antennas and Propagation (EUCAP)*, (The Hague, The Netherlands), 6-11 Apr. 2014.
- [5] M. Benedetti, L. Ioriatti, M. Martinelli, and F. Viani, "Wireless sensor network: a pervasive technology for earth observation," *IEEE Journal of Selected Topic in Applied Earth Observation and Remote Sensing*, vol.3, no. 4, pp. 488-496, 2010.
- [6] F. Viani, M. Salucci, F. Robol, E. Giarola, and A. Massa, "WSNs as enabling tool for next generation smart systems," *Atti XIX Riunione Nazionale di Elettromagnetismo (XIX RiNEm)*, Roma, pp. 393-396, 10-14 Sep. 2012.
- [7] F. Viani, P. Rocca, M. Benedetti, G. Oliveri, and A. Massa, "Electromagnetic passive localization and tracking of moving targets in a WSN-structured environment", *Inverse Problems*, vol. 26, no. 074003, pp. 1-15, 2010.
- [8] F. Viani, E. Giarola, A. Polo, G. Vannuccini, L. Longo, and A. Massa, "Decision support system for museum management through distributed wireless sensing," *Museums and the Web (MWF 2014)*, Florence, Italy, Feb. 19-21, 2014.
- [9] F. Viani, F. Robol, M. Salucci, E. Giarola, S. De Vigili, M. Rocca, F. Boldrini, G. Benedetti, and A. Massa, "WSN-based Early Alert System for Preventing Wildlife-Vehicle Collisions in Alps Regions – From the Laboratory Test to the Real-World Implementation," *2013 European Conference on Antennas and Propagation (EUCAP)*, (Gothenburg, Sweden), pp. 38-41, 8-12 Apr. 2013.
- [10] F. Viani, F. Robol, A. Polo, E. Giarola, and A. Massa, "Localization strategies in WSNs as applied to landslide monitoring," *2013 American Geophysical Union Fall Meeting*, San Francisco, USA, Dec. 9-13, 2013.

ENTROPY BASED CLUTTER MITIGATION IN TWI

A. Cuccaro⁽¹⁾, R. Solimene⁽¹⁾, R. Pierri⁽¹⁾

⁽¹⁾Department of Industrial and Information Engineering,
Second University of Naples,
Via Roma 29, 81031, Aversa Italy
antonio.cuccaro@unina2.it

Abstract

A clutter rejection method based on data entropy is compared to other literature methods such as the average trace subtraction, the differential approach, and the subspace projection method. It is shown that the entropy-based method is as effective as the other methods in removing front wall contribution, but at same time, it avoids unwanted filtering of the field scattered by the targets.

Index Terms – Clutter rejection, linear inverse scattering, through-wall imaging (TWI).

I. INTRODUCTION

In through-wall imaging (TWI), the wall introduces clutter signals that often overwhelm the target ones: therefore, clutter rejection methods are required. Subtracting background measurements (i.e., without scattering objects) allows a perfect clutter removal. However, in realistic cases, background measurements are hardly available.

Rejection clutter is achieved by tailoring a filtering procedure on the features that make targets different from the wall. When targets consist of *animate* scatterers, their movements can be exploited to tune a Doppler filter as in a moving target indicator. For stationary scatterers, there are many methods for mitigating clutter already present in the literature [1]-[3]. The simplest way to achieve that is to subtract from the data the average (over the number of sensors) trace (*average trace subtraction*). However, spatial filtering also acts on the target fields; hence, some compensation procedures are required to restore the point spread function (PSF).

Time-of-arrival considerations suggest adopting a *time gating* procedure to erase wall reflection. Basically, as the wall signals arrive before, the clutter can be removed by withdrawing the “first part” of the collected data. This solution appears very appealing as unwanted filtering is avoided. The major problem here is that the field scattered by targets in close proximity of the wall can be erased as well. What is more, for a layered background medium, target signals may overlap in time to clutter. Therefore, in this case, the issue to be tackled concerns the automatic selection of the window within which the signal must be “silenced”. In order to address this problem, it is observed that, when a multimonostatic configuration is employed, the field reflected from a layered background medium has a strong *similarity* over different sensor positions [4]. Here, the entropy-based windowing proposed in [4]

is checked against synthetic data compared to common average trace subtraction method.

II. CLUTTER REJECTION METHODS

The scenario consists of a three-layered medium. The first and the third layers are assumed to be the free-space. The second layer is representative of a laterally homogeneous wall. Targets are represented in terms of spatially localized in-homogeneities and may be present in the third region within the investigation domain D .

Upon discretizing time, data can be conveniently arranged in an $N \times M$ matrix as $\underline{e} = [\underline{e}_0, \dots, \underline{e}_m, \dots, \underline{e}_{M-1}]$, where N and M are the number of sensor positions and time samples, respectively, and the column represents the data collected over the measurement positions at the m -th time sample.

A. Average Trace Subtraction (AV)

According to the measurement configuration, it is noted that the clutter contribution ideally does not vary with the antenna location (while target signals indeed do). Therefore, eliminating wall reflection from (1) is equivalent to separate constant from non constant signals across the array. In its simplest form, this can be achieved by subtracting from each trace the average (over sensors' positions) one. This can be done in time or equivalently in frequency domain. In particular, in the time domain, one obtains

$$e_{AV}(n, m) = e(n, m) - \bar{e}(m) \quad m = 0, 1, \dots, M - 1 \quad (1)$$

where $\bar{e}(m)$ is the average trace, the couple (n, m) denotes elements of data matrix \underline{e} and the subscript AV in (1) reminds that the average trace subtraction algorithm is used. The Fourier transform along cross range of the decluttered signal e_{AV} for the m -th time sample can be written as

$$\hat{e}_{AV}(k_x, m) = \hat{e}(k_x, m) - \bar{e}(m) \frac{\sin(N\Delta_x k_x/2)}{\sin(\Delta_x k_x/2)} e^{-j[\Delta_x k_x(N-1)/2]} \quad (2)$$

where k_x is the spatial frequency and $\Delta_x < 2\pi/k_x$ with k_0 being the free-space wavenumber. As is clear from (2), average trace subtraction entails rejecting the low-frequency spatial spectrum of target signals as well.

B. Time Gating Based on Entropy Criterion

The assumption that the clutter has a similar behavior over each time trace can also be exploited to properly define a windowing strategy

for mitigating it. In this case, the window function has to be supported over those instants of time where trace similarity is low [4]. This idea was adopted by employing an entropy-based metric in order to discriminate between clutter and target signals. Let us construct the normalized time traces as

$$e_{Nz}(n, m) = \frac{|e(n, m)|}{\sum_{l=0}^{N-1} |e(l, m)|} \quad m = 0, 1, \dots, M - 1 \quad (3)$$

where $e_{Nz} \geq 0$ and $\sum_{n=0}^{N-1} e_{Nz}(n, m) = 1 \forall m$. Therefore for each instant of time, (3) is a probability density function. If we define entropy measure as

$$\epsilon_s(m) = -\sum_{n=0}^{N-1} e_{Nz}(n, m) \log e_{Nz}(n, m) \quad (4)$$

the clutter signals are expected to give large values of $\epsilon_s(m)$, whereas the target signals give low value of $\epsilon_s(m)$. Hence, in order to get rid of the clutter, a window which eliminates signals for instants of time where $\epsilon_s(m)$ is high can be set up so that

$$e_w(n, m) = W(m)e(n, m) \quad (5)$$

with

$$W(m) = \begin{cases} 0 & \text{if } \epsilon_s(m) \geq \alpha \log(N - 1) \\ 1 & \text{elsewhere} \end{cases} \quad (6)$$

where $\log(N - 1)$ is the maximum entropy and $\alpha < 1$ is a tolerance threshold.

III. COMPARATIVE ANALYSIS

We consider a multimono-static measurement configuration: the reflected field is collected at the same position as the source, while the latter moves over a set of $N = 64$ different uniform positions ($= 0.02 m$) in order to synthesize a measurement line $\Sigma = [-0.64, 0.64]m$. The target resides within investigation region $D = [-0.64, 0.64] \times [0.2, 1]m^2$. The wall consists of a homogeneous dielectric layer of thickness $d = 0.2 m$ and dielectric permittivity $\epsilon_w = 5.9$. As the imaging algorithm presented in [4] is used, after the clutter has been mitigated, time domain data (returned by the forward solver) are transformed in the frequency domain. A frequency band of $[0.5, 2.5]$ GHz is employed. As scatterer is considered a metallic ellipse at a distance $0.1 m$ from wall and with minor and major axes equal to $0.1 m$ and $0.5 m$, respectively. Basically, this scatterer has the spatial spectrum more *concentrated* around the zero frequency. By looking at Fig. 1, it is seen that the target is detected in all of the images.

However, now the entropy time gating clearly outperforms the AV methods and gives a reconstruction nearly identical to the ideal one (compare Fig. 1(a) and Fig. (c)). In fact, the filtering introduced by the AV

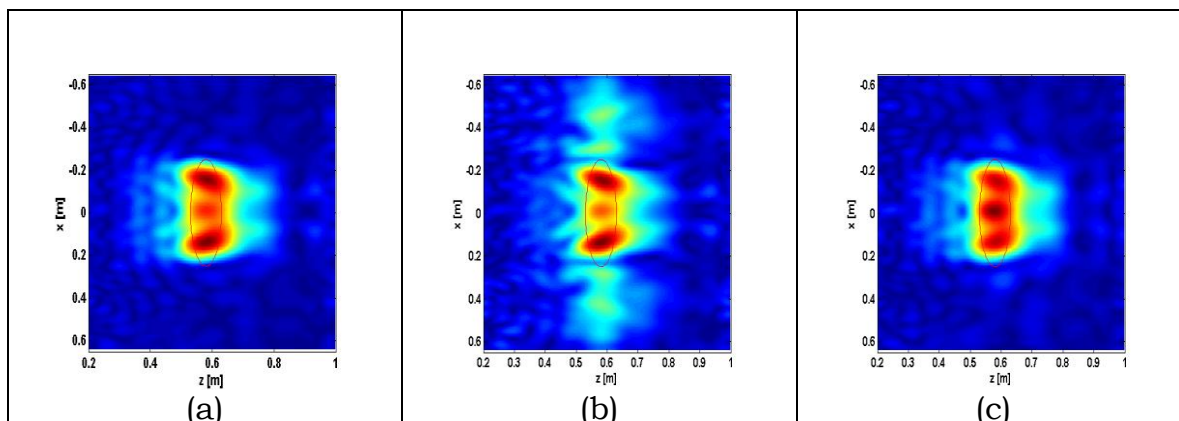


FIG. 1 – Extended target reconstructions. (a) Background subtraction. (b) Average trace subtraction. (c) Entropy criterion.

methods entails that the side of the scatterer (which has a low spectral content) is removed in the reconstructions. A detailed analysis of the comparison between the different algorithms is made in [5].

IV. CONCLUSION

A new clutter rejection method based on a data entropy time gating procedure is introduced and compared to known literature method average trace subtraction.

It has been shown that the proposed method works as well as the other technique in removing wall contribution. However, it avoids filtering of the low spatial frequency content. Therefore, it allows to reach better reconstruction specially for targets which have significant low spectral content.

REFERENCES

- [1] Y. Yoon and M. Amin, "Spatial filtering for wall-clutter mitigation in through-the-wall radar imaging," *IEEE Trans. Geosci. Remote Sens.*, vol. 47, no. 9, pp. 3192–3208, Sep. 2009.
- [2] M. Dehmollaian, M. Thiel, and K. Sarabandi, "Through-the-wall imaging using differential SAR," *IEEE Trans. Geosci. Remote Sens.*, vol. 47, no. 5, pp. 1289–1296, May 2009.
- [3] F. Tivive, M. Amin, and A. Bouzerdoum, "Wall clutter mitigation based on eigen-analysis in through-the-wall radar imaging," in *Proc. Int Conf. Digital Signal Process.*, Corfu, Greece, pp. 1–8, 2011.
- [4] R. Solimene and A. D'Alterio, "Entropy based clutter rejection for intra-wall diagnostics," *Int. J. Geophys.*, vol. 2012, pp. 418084-1–418084-7, 2012.
- [5] R. Solimene, A. Cuccaro, "Front Wall Clutter Rejection Methods in TWI", *IEEE Geosci. and Remote Sens. Letters*, Vol. 11, no. 6, pp. 1158-1162, 2014.

ACKNOWLEDGMENT

This work was supported by the European Regional Development Fund (ERDF) POR Campania FSE 2007/2013 – "EMBEDDED SYSTEM".

NANOPARTICLE STUDIES FOR BIOMEDICAL APPLICATIONS

Renato Iovine, Richard Tarparelli, Lucio Vegni

Department of Engineering, "Roma Tre" University
Via Vito Volterra 62, 00146 Rome, Italy
renato.iovine@uniroma3.it

Abstract

In this contribution we review some research activities recently developed at Roma Tre University in the field of plasmonic nanoparticles for biomedical applications. We show a sensing platform, operating in the visible and near-infrared frequency regime suitable for ultrasensitive DNA alterations recognition. The proposed application is verified through numerical results, expressed in terms of Extinction-Cross Section. We show that the proposed approach is able to detect DNA alterations, based on LSPR phenomenon.

Index Terms – Functionalized Nanoparticles, LSPR, BRCA1, ultrasensitivity.

I. INTRODUCTION

In the last few years several studies have been carried out in the area of nanostructures. In particular, metal nanoparticles, due to their optical properties, became suitable for biosensing applications [1]. Their optical properties arise from the interaction between the incident electromagnetic field and the metal nanostructure electrons, in the VIS (Visible) and NIR (Near InfraRed) frequency regime. When a nanoparticle is exposed to an electromagnetic source, a collective electrons oscillation, arises on metal nanoparticles and the electromagnetic field response is highly localized near the nanostructure. This phenomenon is called LSPR (Localized Surface Plasmon Resonance) [2]. Although several researches have focalized the attention on the experimental evaluation of nanoparticle electromagnetic characteristics not enough is known about the possibility to control the physical phenomenon.

Starting from this scenario, our research activities deal with the development of new analytical models and numerical analysis in order to describe electromagnetic properties of metallic nanoparticles suitable for biomedical applications.

This review paper shows our proposal to detect multi DNA alterations, with original nanoparticles configurations. In Section II, the electromagnetic properties of metallic nanoparticles are evaluated in terms of extinction cross-section properties. Finally, conclusions are drawn at the end of the paper.

II. ELECTROMAGNETIC PROPERTIES OF METALLIC NANOPARTICLES

In order to study the electromagnetic field distribution and the extinction cross-section spectra when an electromagnetic field interacts with a metallic nanoparticle, we have developed quasi-static model and performed full-wave simulations for several shape, as shown in Fig.1(a) (e.g. sphere, rod, cube, elliptical cylinder). A good agreement among these approaches was obtained as shown in Fig. 1(b) [3].

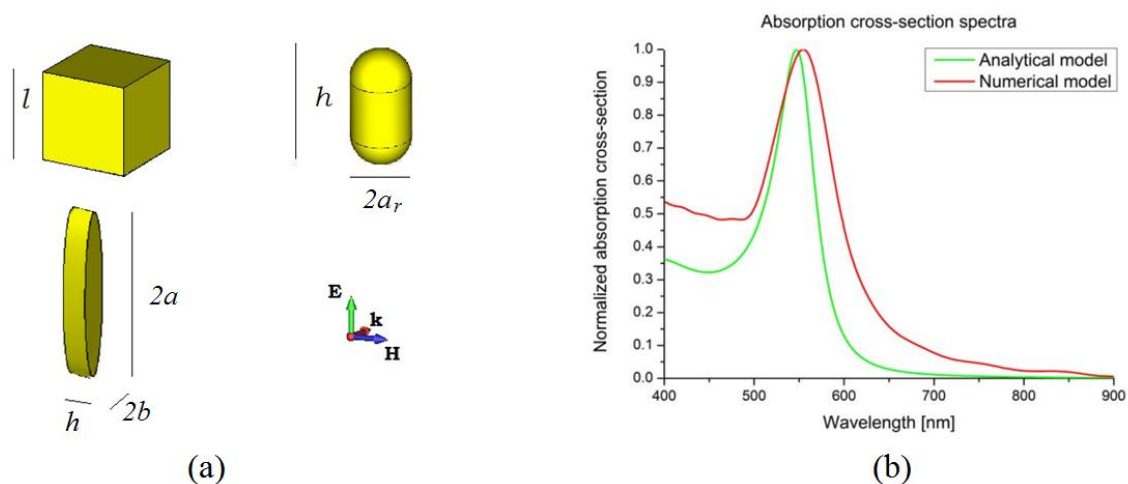


FIG. 1 – (a) Geometrical sketch of the nanoparticles: cube, rod, and elliptical cylinder. (b) An example of comparison among analytical and numerical results for cube particle with $l = 80 \text{ nm}$.

III. MULTI DETECTION OF DNA ALTERATIONS

In order to provide the multi-detection of DNA alterations, we have designed the geometrical parameters of cube, rod, elliptical cylinder particles in order to resonate at different frequencies [4].

For this purpose we have assumed the following geometrical parameters for the selected particles: (1) the nanocube with $l=51 \text{ nm}$, (2) the nanorod with $h=64 \text{ nm}$, $a_r=18 \text{ nm}$, and (3) the elliptical cylinder nanoparticle with $a=35 \text{ nm}$ and $b=7 \text{ nm}$ and $h=10 \text{ nm}$. In this condition the cube, rod and elliptical cylinder nanoparticles resonate at 542 nm , 671 nm and 808 nm respectively. For such nanoparticles configurations, we have shown how the multi-detection condition for DNA alterations can be established.

It is well known that various shapes of nanoparticles can be functionalized with single DNA sequences [5]. We have considered the nanoparticles functionalized with the corresponding DNA Probe Sequence (PS) of alternative splicing junctions of BRCA1, as shown in Fig. 2(a).

The three corresponding DNA Capture Sequences (CS) of alternative splicing junctions of BRCA1 are allocated on three square gold patches deposited on silica substrate as shown in Fig. 2(b). The geometry of the silica substrate has been chosen for $a=600 \text{ nm}$, $b=200 \text{ nm}$, $c=20 \text{ nm}$ and $d=150 \text{ nm}$.

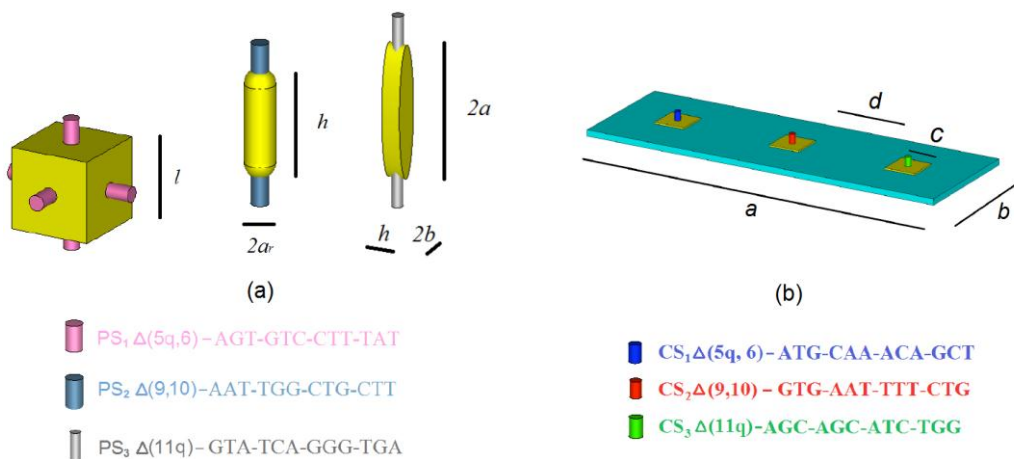


FIG. 2 – (a) Schematic model of functionalized nanoparticles with corresponding Probe Sequences. (b) Unit cell of the sensing platform, functionalized with three different Capture Sequences.

In order to test the proposed platform, extensive numerical analysis have been conducted through full-wave simulation [6].

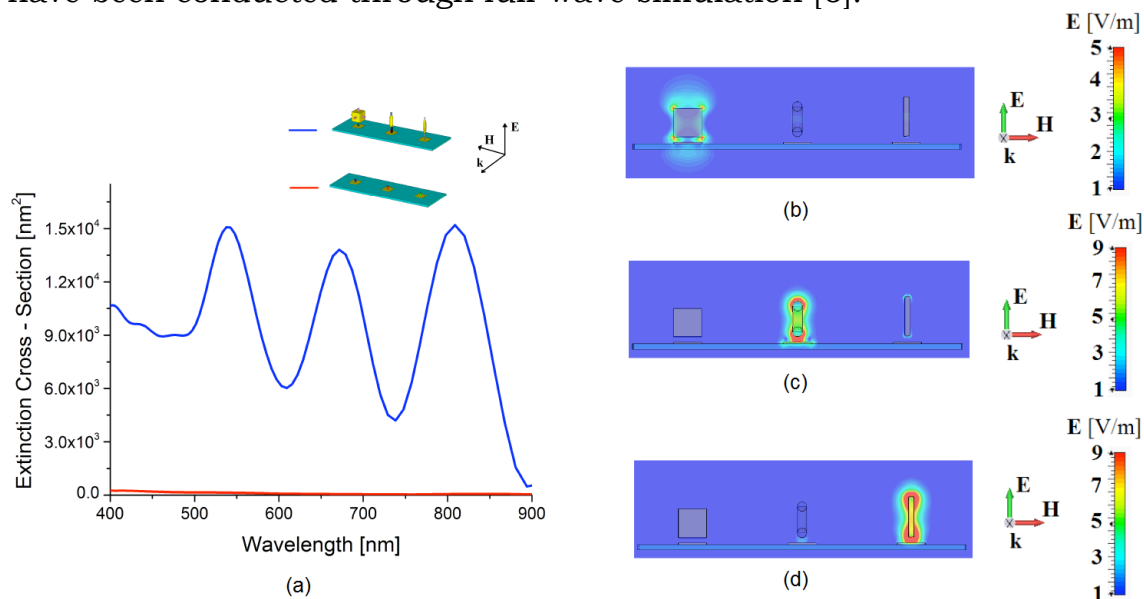


FIG. 3 – (a) Extinction Cross-Section spectra when all the target sequences are bound. Near electric field distribution of the sensing platform at (b) the cube resonant wavelength (542 nm), (c) the rod resonant wavelength (671 nm), and (d) the elliptical cylinder resonant wavelength (808 nm).

The sensing platform is excited by an impinging plane wave, having the electric field parallel to the principal axis of the particles. The excitation is employed to analyze the electromagnetic properties, in terms of extinction cross-section. In the simulations we have assumed (i) for gold the experimental values of the complex permittivity reported in [7], (ii) for silica a complex refractive index $n=1.44+ i0$ according to [8] and (iii) an in silico replica of BRCA1 alternative splice variant as reported in [9].

In Fig. 3(a) the extinction cross-section is shown, for the case of three nanoparticles bindings. Obviously the sensor is able to recognize also no binding (see the red line in Fig. 3(a)). Fig. 3(b), 3(c) and 3(d) show the near electric field distributions at the corresponding resonant wavelength of nanocube, nanorod and elliptical cylinder particles respectively. Such results confirm us that the coupled effects among near nanoparticles are negligible and also each nanoparticle shows near electric field enhancement at the proper resonant wavelength.

IV. CONCLUSION

In this contribution research activities in the field of plasmonic nanoparticles for biomedical applications, conducted at Roma Tre University are presented. We have reviewed our recently theoretical study in order to investigate alternative gene splicing of BRCA1. The proposed design has the potential to reveal alternative splicing profile of different genes without the use of labels through the exploitation of LSPR phenomenon.

REFERENCES

- [1] G. Doria, J. Conde, B. Veigas, L. Giestas, C. Almeida, M. Assunção, J. Rosa and P. V. Baptista, "Noble Metal Nanoparticles for Biosensing Applications," *Sensors*, vol 12(2), pp. 1657-1687, February 2012.
- [2] J. Zhao, X. Zhanf, C. R. Yonzon, A. J. Haes, and R. P. Van Duyne, "Localized surface plasmon resonance biosensors," *Nanomedicine*, vol. 1(2), pp. 219-228, 2006.
- [3] L. La Spada, R. Iovine, and L. Vegni, "Nanoparticle Electromagnetic Properties for Sensing Applications," *Advances in Nanoparticles*, vol. 1(2), pp. 9-14, August 2012.
- [4] R. Iovine, V. Loscri, S. Pizzi, R. Tarparelli, and A. M. Vegni, "Model of Multi-Source Nanonetworks for the Detection of BRCA1 DNA Alterations Based on LSPR Phenomenon," *Advances in Nanoparticles*, vol. 2(4), pp. 301-312, November 2013.
- [5] D. Graham, K. Faulds, D. Thompson, F. Mackenzie, R. Stokes and A. Macaskill, "Functionalized nanoparticles for nucleic acid sequence analysis using optical spectroscopies," *Biochemical Society Transaction*, vol. 37(2), pp. 441-444, 2009.
- [6] CST (2012), *Microwave Studio 2012*, Computer Simulation Technology. Available: www.cst.com
- [7] P. B. Johnson and R. W. Christy, "Optical constants of the noble metals," *Physical Review B*, vol. 6(12), pp. 4370-4379, 1972.
- [8] P. K. Jain, K. S. Lee, I. H. El-Sayed, and A. El-Sayed, "Calculated absorption and scattering properties of gold nanoparticles of different size, shape, and composition: Applications in biological imaging and biomedicine," *J. Phys. Chem. B*, vol. 110(14), pp. 7238-7248, 2006.
- [9] L. Sun, C. Yu, and J. Irudayaraj, "Raman multiplexers for alternative gene splicing," *Analytical Chemistry*, vol. 80(9), pp. 3342-3349, 2008.

EXPERIMENTAL GENERATION AND MEASUREMENT OF ORBITAL ANGULAR MOMENTUM RADIO WAVES

F. Spinello^{(12)*}, E. Mari⁽²⁾, G. Parisi⁽²⁾, F. Tamburini⁽²⁾, F. Romanato⁽²³⁾
and C. G. Smeda⁽²⁾

⁽¹⁾ Department of Information Engineering, Padova University
Via Gradenigo 6/b, 35131 Padova, Italy

⁽²⁾ Twist Off s.r.l., Via della Croce Rossa 112, 35131 Padova, Italy

⁽³⁾ Department of Physics and Astronomy, Padova University
Via Marzolo 8, 35131 Padova, Italy

*spinello@dei.unipd.it

Abstract

In this paper we consider conformal parabolic antennas that radiate electromagnetic waves with a quantity of Orbital Angular Momentum (OAM) different from zero. Laguerre Gauss beams are used, as an optimum approximation, to describe the generated fields and to investigate its properties. Moreover we present the measurements of the radiated far field amplitude and phase distributions and we compare them with simulated one. We also measure other interesting antenna's parameters, such as Return Loss and Insertion Loss, in order to verify some peculiar properties of OAM beams.

Index Terms – Radio Orbital Angular Momentum, Conformal Antennas, Vortex wave, Laguerre Gauss Beam

I. INTRODUCTION

Wireless systems are nowadays used more and more for an ever-growing range of applications in everyday life. As a consequence the electromagnetic (EM) spectrum is becoming very crowded, leading to the saturation of the available frequency bands. To overcome this problem scientists and engineers are studying various techniques to exploit the spectrum in a better way. One of such techniques is the use of electromagnetic waves with a quantity of Orbital Angular Momentum (OAM) different from zero.

Laguerre-Gauss (LG) beams are known to carry OAM and are solutions of the Maxwell's equations under the paraxial approximation[1]. LG beams are characterized by a donut distribution of the field intensity and by a helical phase front. Considering a 3D space with cylindrical coordinates r , φ and z , a LG beam of parameters l and p is described by Eq. (1) where $w(z)$ is the beam waist radius, $L_l^p(\cdot)$ the correspondent generalized Laguerre polynomial and $k = 2\pi/\lambda$ the wave number. The quantities $R(z)$ and $\xi(z)$ are the radius of curvature of the wave-front and the Gouy phase shift respectively. The parameter l gives the number of twists of the helical phase-front within a wavelength while the parameter p is the number of radial nodes present in the LG mode.

$$E_{pl}(r, \phi, z) \propto \frac{1}{w(z)} \left(\frac{r\sqrt{2}}{w(z)} \right)^{|l|} L_l^p \left(\frac{2r^2}{w(z)} \right) e^{-r^2/w(z)^2} e^{\frac{-ikr^2}{2R(z)}} e^{-i(2p+|l+1)\xi(z)} e^{-il\phi} \quad (1)$$

LG beams are particularly interesting because they are an orthogonal basis. For this reason they could be exploited to implement a channel multiplexing on the same frequency and with the same wave polarization. In fact, for example, two LG beams with different values of the parameter l are orthogonal to each other:

$$\int_0^{2\pi} \int_0^{\infty} E_{p_1 l_1}(r, \phi, z) E_{p_2 l_2}(r, \phi, z) dr d\phi = 0 \quad (2)$$

Another peculiar property of LG beams is the fact that they reverse their OAM value sign when reflecting on a conductive surface. This is due to boundary conditions that have to be satisfied in the reflection process.



Figure 1: A) Examples of LG beams amplitude and phase distributions for beams with $p=0$ and $l=-1, 0, +1, +2$ and $+3$; B) and C) Examples of conformal parabolic reflector

II. OAM BEAMS GENERATION

The generation of LG beams, in the radio domain, can be done with various techniques, such as: dielectric masks, conformal antennas and arrays [2]. In our experiments we used a modified prime focus parabolic antenna, represented in Fig. 1B-C.

In transmission, the twisted reflector converts the field generated by the feeder into a helical beam with the desired OAM value. The behavior of such reflector can also be understood thinking that it acts as a phase mask. When used as receiving antenna, impinged upon by an on-axis LG beam, similarly, it acts as an inverse phase mask as long as all the received beam is collected. To control the value of the OAM that can be generated or received it is sufficient to change the propeller pitch of the twisted reflector. For a more in-depth description see [3]. We designed antennas to produce fields with a quantity of OAM equal to $+1$ and -1 . From now on these devices will be called, for simplicity, “ $l=+1$ ” or “ $l=-1$ ” antenna; instead a standard antenna will be called “ $l=0$ ”.

III. MEASUREMENTS AND RESULTS

First of all we report the measurements of the EM radiation in the *far field zone* generated by the $l=-1$ antenna. We used the setup of Fig. 2. A continuous wave (CW) signal at 17.2GHz of a standard commercial radio is used as reference for the Vector Network Analyzer (VNA) and to feed the conformal antenna under test. The antenna is angularly

rotated around its support and the generated field is sampled with a horn connected to the VNA.

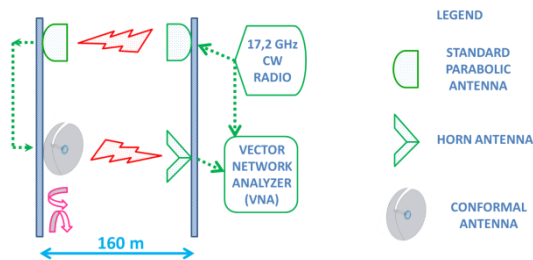


Figure 2: Far field measurements setup.

With this system we are able to directly and instantly map both the amplitude and the phase distributions of the radiated field. The measured maps and the simulated one are reported in Fig. 3.

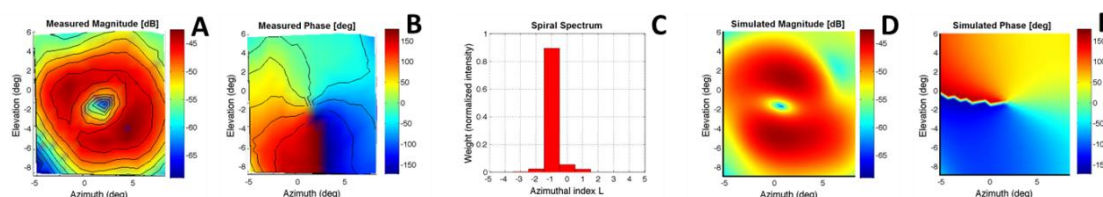


Figure 3: Far field amplitude: A) measured, D) simulated. Far field phase B) measured, E) simulated. C) Spiral spectrum calculated on measured data.

From the processing of the acquired data, with the calculation of the spiral spectrum[5], that is a Fourier transform in the angular domain, we also verified the value of the carried OAM. Analogous results has been obtained from the measurements on the $l=+1$ antenna.

Then, we measured the *Return Loss (RL)* of an $l=+1$ and an $l=0$ antenna. The devices were individually fed by a 17.2 GHz CW signal radiated in a reflection-less environment; the measurements were made using the VNA. Subsequently, we placed a brass plate directly in front of the antennas and repeated the measurements. The results are reported in Table I.

Table I: Measurements of Return Loss

Antenna under test	RL [dB]	Antenna status
$l=0$	13.7	Free to radiate
$l=0$	2.3	Shielded with brass plate
$l=+1$	14.2	Free to radiate
$l=+1$	16.2	Shielded with brass plate

The most interesting figure is the value of the RL of the conformal antenna corked with the brass plate. This is due to the fact that the incident wave, generated with the $l=+1$ parabola, reverses its OAM’s sign when reflecting on the brass plate. For this reason the reflected wave cannot be correctly detected from the same antenna. This phenomenon is a direct consequence of the orthogonality of OAM states.

Another quantity evaluated is the *Insertion Loss (IL)* between $l=0$, $l=+1$ and $l=-1$ antennas. The Tx and Rx antennas were placed at a distance

of about 0.5 m from each other; the measure was obtained again through the VNA. The results are reported in Table II.

As can be seen, the value of IL is low between identical antennas and high between different ones. Still again, this is due to the action of the conformal reflectors that, acting as phase masks both in transmission and reception, exploit the orthogonality between different OAM states. For further information on all the results see[4].

Table II: Measurement of Insertion Loss

Tx Antenna	IL [dB]	Rx Antenna
l=0	3.3	l=0
l=+1	3.2	l=+1
l=+1	18.6	l=0
l=+1	26.2	l=-1

IV. CONCLUSIONS

In this work we have examined antennas able to generate an EM field with OAM. We have tested these devices measuring, for the first time in the radio domain, both the amplitude and the phase distributions of the radiated field. In addition, with the evaluations of RL and IL, we have also verified some peculiar characteristic of EM waves carrying OAM such as: change of OAM's sign during reflection and orthogonality between different OAM states. The results of this work constitute an additional step in the investigation on the physical generation of EM waves with OAM in the radio domain. They can also be used to evaluate some properties of OAM that can be exploited in telecommunication in order to improve the electromagnetic spectrum efficiency.

V. ACKNOWLEDGEMENT

The authors acknowledge M. Oldoni, R. Ravanelli, P. Coassini of SIAE Microelectronics and its financial support and collaboration.

VI. REFERENCES

- [1] Allen, L., Beijersbergen, M. W., Spreeuw, R. J. C., & Woerdman, J. P. (1992). Orbital angular momentum of light and the transformation of Laguerre-Gaussian laser modes. *Physical Review A*, 45(11), 8185-8189.
- [2] Thidé, B., Then, H., Sjöholm, J., Palmer, K., Bergman, J., Carozzi, T. D., ... & Khamitova, R. (2007). Utilization of photon orbital angular momentum in the low-frequency radio domain. *Physical review letters*, 99(8), 087701.
- [3] Trinder, J. R., patent WO 2005069443 A1 - Parabolic reflector (2005)
- [4] Tamburini, F., Thidé, B., Mari, E., Parisi, G., Spinello, F., Oldoni, M., ... & Romanato, F. (2013). Tripling the capacity of a point-to-point radio links by using electromagnetic vorticity. Submitted to *Nature Scientific Reports*.
- [5] Torner, L., Torres, J., & Carrasco, S. (2005). Digital spiral imaging. *Optics express*, 13(3), 873-881.

HOMWORK OPEN-SOURCE PLATFORM (HOP) TO TEST THE STUDENTS' KNOWLEDGE IN ELECTROMAGNETICS

L.Zappelli

Department of Information Engineering, Università
Politecnicadelle Marche, Ancona, Italy

l.zappelli@univpm.it

Abstract

An Open-source platform for homework assignment and correction is presented and discussed. The platform was used during the academic course in Fundamentals of Electromagnetics at the Università Politecnica delle Marche, Ancona, Italy. Statistics on the marks obtained by the students showed that the homework undoubtedly enhanced the students' knowledge.

Index Terms – Homeworks, open-source platform, teaching.

I. INTRODUCTION

One of the most common problems when teaching in Universities is the assessment of what the students learn during the academic courses. Another interesting aspect is related to testing the students on the course contents. Unfortunately, for many courses the current tendency is to assess the students' knowledge only through a written session, with less possibility to evaluate their real understanding of the subjects. This limited examination is a consequence of the large number of students, especially on the basic courses, such as Physics and Fundamental of Mathematics, that would make running both a written and an oral session extremely time-consuming. Hence, only a written session is currently preferred. This choice produces a distortion in the evaluation of the students. The solution to these problems could be to run a written/oral session combined with successfully completed homework assignments. The homework can cover all the course topics and only those students who have successfully completed all the assignments will be allowed to sit the written (and oral, if applicable) exam: this approach should prevent the inadequate assessment previously discussed. Unfortunately, this approach is time consuming: for example, for a group of 50 students, hypothesizing 9 homework assignments, one for each course topic, based on about 10 questions for each assignment, the teacher should prepare and correct 4500 questions. Moreover, to prevent students from cribbing solutions, each assignment should have the same questions (to avoid discrepancy in the evaluation) but with different data values, increasing the time that the teacher must spend on correcting the work.

The solution lies in using the web resources, creating an on-line procedure to assign, complete and correct homework, just as the

function “merge mail/data” of the word processors. Hence, a homework web platform is needed that requires only the problem-form (the problem without data value, for example “Given $x=.$ and $y=.$, find $z=x+y$ ”) and combines the problem-form with a csv file, loaded by the teacher, containing the data for each student (in this case, 2 data, the values for x and y , for 50 students, i.e. 100 data). Similarly, for the solution to the question, the teacher should load onto the web platform a csv file containing the 50 solutions for z . The web platform should use the loaded solution file to correct the homework assignment solved by the student.

II. HOMEWORK PLATFORM

The proposed solution for the assignment of on-line homework is based on a php developed code and it has been named HOP (Homework Open-source Platform). HOP is divided into three “interfaces”: student “interface”, teacher “interface” and web “interface”.

Student “interface”

The aim is to assign homework to the students, that can be completed at home without any time constraints. Each student is assigned the same homework text but with a different set of data randomly chosen from a set of n_c homework “copies”, in order to prevent cribbing and to foster autonomous assignment completion (assignment phase). When the student has completed the homework, he enters the answers using an online mask (solution phase) and receives the correct solution with a final mark (mark phase). The teacher can decide whether the assignment can end with the final mark, that may be lower or higher than the threshold, fixed at 6 with a default maximum mark of 10, or whether the assignment must be repeated by the student. In the latter case, if the final mark is lower than 6/10, the student must repeat assignment, but with a different set of data, i.e. he receives a different homework “copy”. Hence, he must complete all the questions again because the question data are different. The flow chart shown in Fig. 1.a describes this procedure.

Teacher “interface”

The teacher “interface” is managed by the teacher who must set the number of homework assignment, n_h , that students must complete, and the homework “copy” number, n_c (50 by default). Homework “copies” are a set of n_c homework assignments with the same text but different data values contained in the questions. Therefore, for the i -th homework assignment, the teacher must select the n_p problem-forms, the n_q questions for each problem, their marks and the measurement units of the answers. The flow chart shown in Fig. 1.b describes this procedure.

Web “interface”

The flow chart shown in Fig. 1.c describes the procedures of the HOP “core” (assignment phase, completion phase and mark phase of the homework assignment). After the sign in and login procedures, the choice of the homework to be completed is proposed to the user (the i -th

homework). The data acquisition procedures are then activated and the files needed for each problem of the i -th homework assignment are read and used in the following steps. The user decides whether the assignment of a new copy of the i -th homework or the resolution of the homework must be chosen. In the assignment procedure (the left side in Fig. 1.c), the php codes randomly assign the j -th homework “copy” to the user. The homework text can then be visualized, with the help of the previously acquired data. The user prints or saves the homework assignment and completes it at home with no time constraints.

In the solution procedure (the right side in Fig. 1.c), the “copy” index (j) of the assigned homework is read and is used to visualize the homework with as many selection fields as the number of questions. For each selection a number of numerical solutions are proposed and the user must choose only one of them. In the mark procedure, the correction is made by comparing the chosen solution with the right ones, stored in the files $sol_k.csv$, and the final mark is assigned. If the mark is lower than the threshold set by the Administrator (default 6) with respect to the maximum mark for each assignment (default 10), and the Administrator has chosen the “repeat” mode (the user must successfully complete each assignment), the php codes invite the user to repeat the homework with a new copy assignment (dotted line in Fig. 1.c).

III. HOP IN ELECTROMAGNETICS

HOP has been used on the Electromagnetics course at the Università Politecnica delle Marche and 9 homework assignments on the topics: Mathematics prerequisites, Coulomb's law, Gauss's law, Electrostatic potential and work, Ohm's law, Ampere's law, Faraday's law, Boundary conditions and Plane wave. The percentage distribution of the marks for the successfully completed assignments is shown in Tab. I: more than 60% of the students who successfully completed the 9 assignments obtained a mark of more than 8/10 (sum of the last two rows). It is interesting to compare these marks with the mark obtained at the final written examination. 70.27% of the students passed the written examination at the first attempt, with the mark distribution shown in Tab. II. In this table, the ratio between the mark obtained for the final written examination, M_w , and the average mark obtained by each student for the 9 assignments, M_H , is reported in the ranges shown in the first row. About 22% of the students passed the written examination with a mark greater than M_H (fourth column) and about 66% of the students with a mark greater than $0.9M_H$ (44%+22%). These simple statistics confirm the importance of homework assignments in order to achieve a high percentage of success in the written examination

A survey was completed by the students and their answers are shown in Fig. 2. The students appreciated the possibility to do assignments during the academic course and this in itself can be considered as a positive result. The students seem to accept extra hours of study if this leads to a more thorough understanding of the course topics. HOP can

be downloaded at [1] and it can be freely used. Moreover, on request, the Author can share the 9 homework assignments in Electromagnetics [2] (interested reader can sign in with any four-digits SIN in the sign-in form of [2]).

REFERENCES

- [1] <http://leibniz.dii.univpm.it/zappelli/HOPdownload.html>
- [2] <http://leibniz.dii.univpm.it/zappelli/HOPFE/login.php>

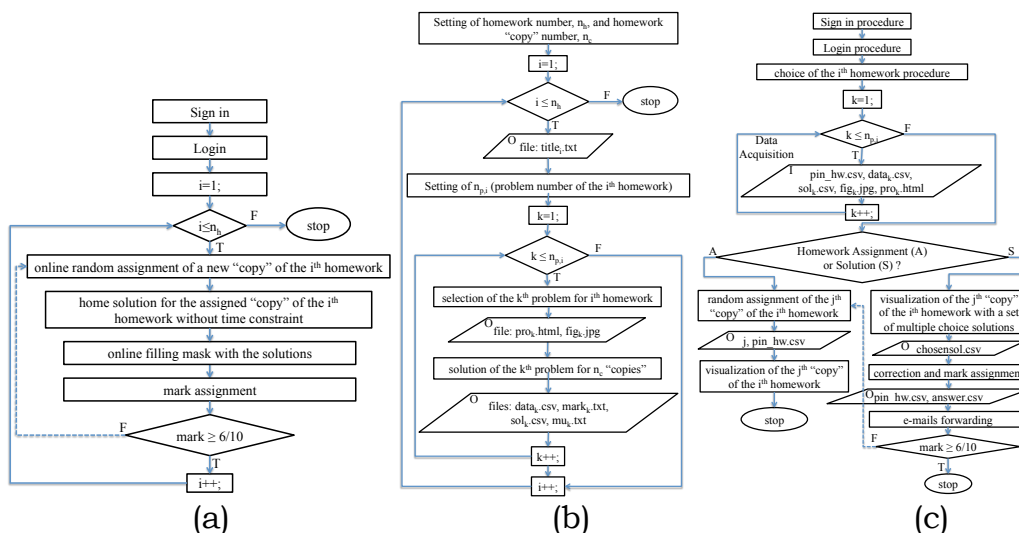


Fig. 1: Flow charts describing the student, teacher and web interfaces.

TABLE I - PERCENTAGE DISTRIBUTION OF MARKS FOR THE 9 SUCCESSFULLY COMPLETED ASSIGNMENTS.

Mark range	Homework assignment nr.								
	1	2	3	4	5	6	7	8	9
6-6.99	14	12	13	21	1	17	19	9	11
7-7.99	24	18	15	12	5	18	5	12	16
8-8.99	20	32	12	32	1	25	19	24	34
9-9.99	42	38	60	35	93	40	57	55	39

TABLE II - PERCENTAGE DISTRIBUTION OF THE MARK OBTAINED FOR THE FINAL WRITTEN EXAMINATION, M_w , COMPARED WITH THE AVERAGE MARK OBTAINED BY EACH STUDENT FOR THE 9 ASSIGNMENTS, M_H .

M_w/M_H	<0.8	0.8-0.9	0.9-1	>1
% students	20	14	44	22

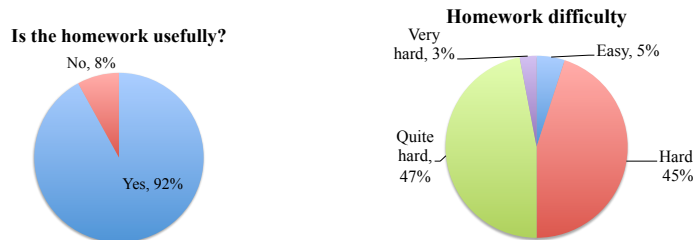


Fig. 2: Results of the survey completed by the students.

WIDEBAND THz TIME DOMAIN SPECTROSCOPY SET-UP BASED ON ULTRAFast PULSED LASER: MODEL AND EXPERIMENTS

A. Tomasino⁽¹⁾, S. Stivala⁽¹⁾, A. C. Busacca⁽¹⁾, A. C. Cino⁽¹⁾, M. Peccianti⁽²⁾,
and R. Morandotti⁽³⁾

⁽¹⁾ DEIM - Department of Energy, Information engineering and
Mathematical models, University of Palermo, Viale delle Scienze
Bldg. 9, 90128, Palermo, Italy

⁽²⁾ Dept. Of Physics and Astronomy, University of Sussex, Falmer,
Brighton BN1 9QH, UK

⁽³⁾ INRS-Énergie, Matériaux et Télécommunications, 1650 Blvd
Lionel Boulet, Varennes (Québec), J3X1S2, Canada
salvatore.stivala@unipa.it

Abstract

We present an analytical model describing the full electromagnetic propagation in a THz Time Domain Spectroscopy (THz-TDS) laser based system. We pay particular attention to the modelling of the time-frequency behavior of all the stages, which compose our experimental set-up. In particular, our model takes into account the following features: pump beam focusing into the generation crystal; phase-matching between pump and THz pulses inside both the generation and detection crystals; chromatic dispersion and absorption inside the materials; Fabry-Perot effect in both the crystals; diffraction along the propagation, focalization and overlapping between THz and probe beams; Electro-Optic Sampling. The data obtained from our experimental set-up are in optimum agreement with simulations, so proving the effectiveness of our model.

Index Terms – Nonlinear Optics, Terahertz, Ultrafast Photonics.

I. INTRODUCTION

Generation and detection of THz electromagnetic waves has been arousing an ever-increasing interest in the last decade, since recent studies demonstrated that THz spectroscopy could reveal useful information on the conformational stage of many molecules, potentially enabling their discrimination in various compounds [1]. Moreover, the negligible ionization power of THz radiations, compared to both optical and X-rays, makes them perfectly suitable for biological applications and imaging. The most challenging technology development still concerns the area of THz sources and detectors, since both wide band and high power are often required at the same time. Optical Rectification (OR) combined with Electro-Optic Sampling (EOS) detection scheme is still considered the most suitable configuration in high energy pulsed THz systems. Herein, we present an analytical model able to simulate the full electromagnetic propagation, which

takes place in the THz-TDS set-up sketched in Fig. 1, employing ZnTe crystals [2].

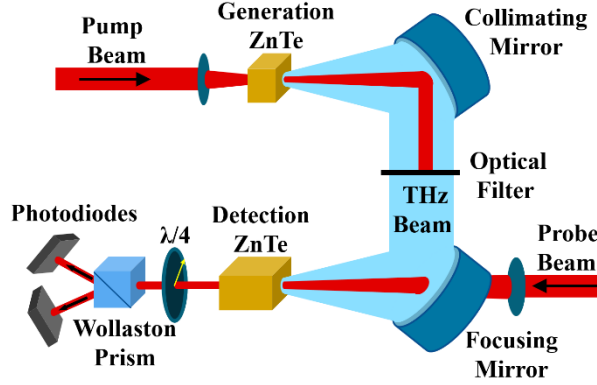


FIG. 1 – Sketch of the experimental THz-TDS set-up.

II. OPTICAL RECTIFICATION AND THz WAVES PROPERTIES

Optical Rectification occurs inside a nonlinear crystal with a nonzero second-order optical susceptibility $\chi^{(2)}$. Briefly, when an ultrashort laser pulse -with linewidth $\Delta\omega$ - impinges on such a material, OR performs a mixing of the frequencies within each pulse, generating a low frequency ($0 < \Omega < \Delta\omega$) radiation, that is the THz pulse. Our model starts on solving the nonlinear Helmholtz equation [3]:

$$\left[\frac{\partial^2}{\partial z^2} + \frac{\Omega^2}{c^2} n_{THz}^2(\Omega) \right] E_{THz}(z, \Omega) = \frac{\chi^{(2)}(\Omega)}{c^2} \int_{-\infty}^{+\infty} \frac{\partial^2 |E_{PP}(t)|^2}{\partial t^2} e^{-i\Omega t} dt, \quad (1)$$

where n_{THz} is the THz refractive index of ZnTe, E_{PP} is the instantaneous pump electric field, E_{THz} is the THz electric field, with the following simplifications: (i) the pump pulse only gives rise to OR, thus neglecting any other nonlinear process; (ii) the second derivative of the pump envelope with respect to time can be neglected, since it contains several cycles of the optical carrier (slowly varying envelope approximation, SVEA); (iii) both the beams are considered plane waves, being their diffraction lengths much larger than the crystal thickness. SVEA does not hold for the THz wave, since the generated THz bandwidth is comparable to its central frequency, thus resulting in a time-varying THz wave envelope along the propagation. According to the above-mentioned conditions, the expression for the generated THz electric field wave is [4]:

$$E_{THz}(z, \Omega) \propto \frac{\chi^{(2)}(\Omega) E_0^2 \tau_0}{W_{PP}^2 (n_{THz}^2(\Omega) - n_g^2)} \exp\left(-\frac{\tau_0^2 \Omega^2}{4}\right) \left[\frac{e^{\frac{n_{THz} \Omega z}{c}}}{2} \left(1 - \frac{n_g}{n_{THz}}\right) + \frac{e^{-\frac{n_{THz} \Omega z}{c}}}{2} \left(1 + \frac{n_g}{n_{THz}}\right) - e^{-\frac{n_g \Omega z}{c}} \right], \quad (2)$$

where n_g is the group index, τ_0 is the transform-limited pulse duration, E_0 is the magnitude of the optical pulse and w_{PP} is the pump waist size.

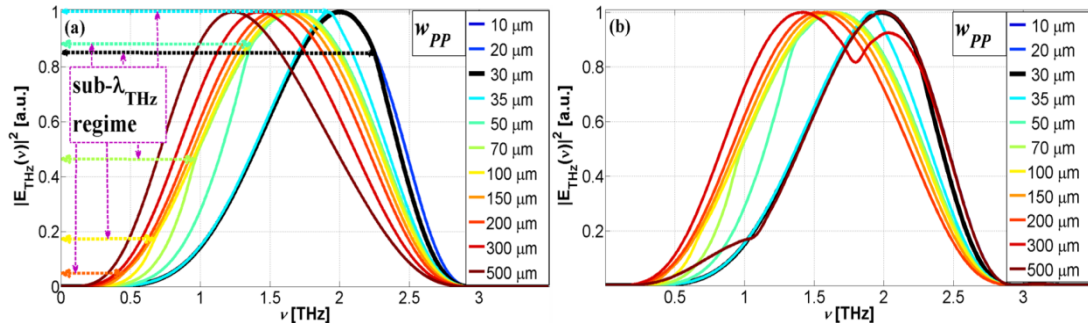


FIG. 2 – Frequency behavior of the (a) collecting and (b) focusing stages at varying w_{PP}

From Eq. (2), the THz waveform results from the interference among three waves: the first one is backward, while the other two are forward. The Gaussian term acts as a low pass filter: the wider the bandwidth, the shorter τ_0 . Anyway, the actual bandwidth mostly depends on the chosen crystal, since the coefficient in Eq. (2) is a frequency-dependent function, accounting for phase-matching (PM) between THz and optical pulses, dispersion and resonant absorption inside the crystal, the last two not negligible because of the ultrashort nature of the pump pulse.

III. PROPAGATION EFFECTS AND ELECTRO-OPTIC SAMPLING

The normal incidence at the crystal-air interface and the Fabry-Perot (FP) effect inside the material could be formalized by considering the dispersion of the Fresnel reflection and transmission coefficients within the THz band. Diffraction outside the crystal is a more delicate issue. If we consider the THz beam as the overlapping among many single-frequency beams, it is found out that lower frequencies follow Bethe's theory of diffraction, because of the sub-wavelength source size ($w_{PP}/\sqrt{2}$) [5], resulting in a beam spreading more pronounced than what Rayleigh law predicts. Thus, the field-rate gathered by the collecting stage mostly depends on the mirror diameter and it results the richer in the low-frequency spectrum, the greater w_{PP} , as shown in Fig 2(a). Conversely, Fig. 2(b) shows how the second mirror could perform a spectrum reshape depending on w_{PP} , since the focusing effect is stronger for wide rather than for thin beams. EOS is a coherent detection technique based on the Pockels effect, and it could be modeled by means of relations similar to the OR case, taking into account (i) dispersion and absorption inside the detection crystal; (ii) FP inside the detection crystal (iii) finite pulse duration of the probe beam; (iv) phase-mismatch between probe and THz pulses. Moreover, only those THz frequencies, whose spot size is overlapped with the probe one, could be detected.

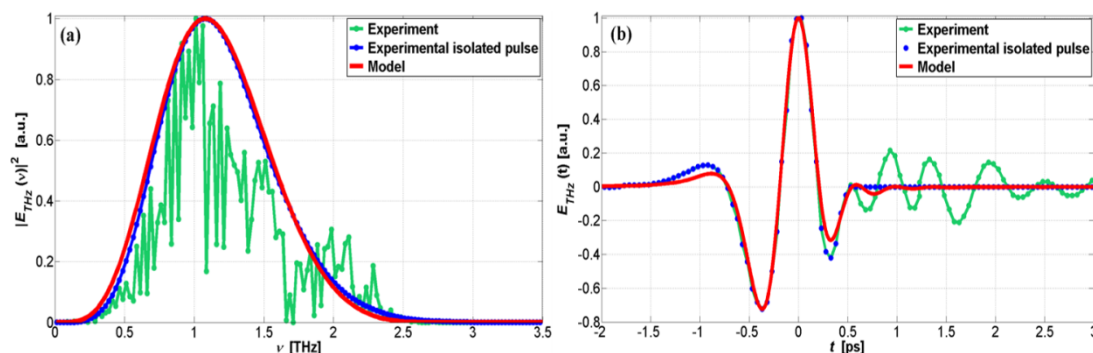


FIG. 3 – Comparison between (a) the spectra and (b) the waveforms.

IV. CONCLUSION

Figure 3 shows the comparison between the results of our simulations (red solid lines) and the experimental data (green circles), though the latter are affected by some unwanted phenomena, mainly related to the observation window size and the laboratory atmosphere. So, in order to make a convenient comparison with the model, we first isolated the fundamental w -shaped pulse (blue circles in Fig. 3(b)) in the time domain and then calculated the corresponding spectrum (plotted in blue circles in Fig 3(a)). The optimum agreement between the latter and the model (red lines) proves its effectiveness, with particular regard to the PM condition and the sub-wavelength generation regime.

REFERENCES

- [1] N. Horiuchi, "Terahertz technology: Endless applications," *Nature Photonics*, vol. 4(1), p. 140, Mar. 2010.
- [2] A. Tomasino, A. Parisi, S. Stivala, P. Livreri, A. C. Cino, A. C. Busacca, M. Peccianti, R. Morandotti, "Wideband THz Time Domain Spectroscopy based on Optical Rectification and Electro-Optic Sampling," *Scientific Reports*, vol. 3, pp. 3116-3124, Oct. 2013.
- [3] Y. J. Ding, "Quasi-Single-Cycle Terahertz Pulses Based on Broadband-Phase-Matched Difference-Frequency Generation in Second-Order Nonlinear Medium: High Output Powers and Conversion Efficiencies," *IEEE Journal of Selected Topics Quantum Electronics*, vol. 10(5), pp. 1171, Oct. 2004.
- [4] J. Faure, J. Van Tilborg, R. A., Kaindl, W. P. Leemans, "Modelling laser-based table-top THz sources: Optical rectification, propagation and electro-optic sampling," *Optics Quantum Electronics*, vol. 36, pp. 681-697, May 2004.
- [5] M. Peccianti, M. Clerici, A. Pasquazi, L. Caspani, S. P. Ho, F. Bucchieri, J. Ali, A. Busacca, T. Ozaki and R. Morandotti, "Exact Reconstruction of THz Sub- λ Source Features in Knife-Edge Measurements," *IEEE Journal of Selected Topics Quantum Electronics*, vol. 19(1), pp. 8401211, Feb. 2013.

A STATISTICAL MODEL FOR THE PROPAGATION THROUGH WAVE CHAOTIC SYSTEMS

G. Gradoni^(1,2)

⁽¹⁾ School of Mathematical Sciences, University of Nottingham
University Park, NG7 2RD Nottingham, United Kingdom
gabriele.gradoni@nottingham.ac.uk

⁽²⁾ Institute for Research in Electronics and Applied Physics,
University of Maryland
Paint Branch Drive, 20742 College Park, United States of America
ggradoni@umd.edu

Abstract

A statistical model based on wave chaos theory, the random coupling model, has been developed and validated for semi-open irregular cavities. We show how the model can be extended to study complicated scenarios involving interconnected cavities. Finally, we discuss the experimental activity conducted by independent research groups in order to validate the model. Those validations involve mode-stirred reverberation chambers, of fundamental importance in electromagnetic compatibility and emulation of modern wireless communication channels.

Index Terms – Cavity; random matrix theory; statistical electromagnetics; aperture

I. INTRODUCTION

Wave chaos and disorder occur in cavities with either irregular and smooth wall geometries. The fundamental ingredient for such disorder to occur is the chaotic dynamics of underlying ray trajectories. Wave chaotic behavior finds a convenient description in terms of statistical theories. The nature of the interaction between electromagnetic (EM) radiation and semi-open systems is characterized by two components: an average contribution expressing the direct (or prompt) scattering amplitude, and a delayed (or equilibrated) amplitude related to the reflection and the absorption of the cavity field, given by the difference between actual and average field. The first component is slowly varying in frequency, and gets developed through semiclassical methods; the second component is related to rapid system fluctuations (highly sensitive to frequency) that are described by the random matrix theory (RMT). For complex cavities, the random coupling model (RCM) describes the chaotic cavity behavior through the universal fluctuation laws given by the RMT [1].

I. RANDOM COUPLING MODEL

Consider a cavity with either (convex) smooth or irregular boundary geometry. The RCM uses two statistical prescriptions inspired by wave chaos to describing the impedance matrix of antennas radiating inside

the cavity. Typically, in the high frequency limit, the propagation throughout a closed cavity undergoes a chaotic ray dynamics. The eigenmode topologies are highly delocalized and sensitive to boundary perturbations. In a statistical perspective, the local mode amplitude can then be replaced by a random superposition of N plane waves. In the limit $N \rightarrow \infty$ the local mode amplitudes assumes zero mean Gaussian distribution. In the semiclassical limit, the system is large with respect to the wavelength, and then the complexity of the problem arises from the many independent volumes developing self-averaging (coherent interference) behavior, leading to incoherent propagation. This behavior is characterized by many degrees of freedom, and thus is best described by statistical fluctuations. Those fluctuations follow universal laws that reflect the symmetry of the system under investigation, and depend on a few scalar parameters of clear physical meaning. We now assume that a lossy irregular cavity hosts both antennas and apertures, making it semi-open. Then, we construct hybrid input $\underline{\phi}$ and output $\underline{\psi}$ vectors by combining aperture voltages with antenna port currents, and aperture currents with antenna port voltages, respectively

$$\underline{\phi} = \begin{bmatrix} \underline{V}_A \\ \underline{I}_P \end{bmatrix}, \quad \underline{\psi} = \begin{bmatrix} \underline{I}_A \\ \underline{V}_P \end{bmatrix}. \quad (1)$$

It has been proved that the linear relation between vector in (1), $\underline{\psi} = \underline{T} \cdot \underline{\phi}$, can be written in compact form as [2]

$$\underline{T} = i\Im(\underline{U}) + [\Re(\underline{U})]^{1/2} \cdot \underline{\xi} \cdot [\Re(\underline{U})]^{1/2}, \quad (2)$$

where, in case antenna ports and apertures are completely separated

$$\underline{U} = \begin{bmatrix} \underline{Y}^{rad} & \underline{0} \\ \underline{0} & \underline{Z}^{rad} \end{bmatrix}. \quad (3)$$

In (3), the block diagonal matrix is made of free-space aperture radiation admittance \underline{Y}^{rad} and free-space antenna radiation impedance \underline{Z}^{rad} matrix. The fluctuating part of (2), representing the chaotic scattering throughout the cavity, is defined as the summation over irregular modes, i.e., whose behavior is wave chaotic and the related statistics are regulated from the two RCM prescriptions, viz.,

$$\underline{\xi} = \frac{i}{\pi} \sum_n \frac{w_n \tilde{w}_n}{(K_0^2 - K_n^2 + i\alpha)}, \quad (4)$$

where $K_0^2 = k_0^2 / \Delta k^2$, Δk^2 is the average mode-to-mode spacing in the cavity spectrum, k_n are cavity mode wavenumbers, and α is the loss parameter accounting for internal distributed losses

$$\alpha = \frac{k_0}{\Delta k^2 Q}, \quad (5)$$

where Q is the average mode quality factor, and k_0 is the excitation wavenumber. In (4), \underline{w}_n is a vector of uncorrelated, zero-mean, unit width Gaussian random variables, and k_n are eigenvalues of a large random matrix selected from the Gaussian orthogonal ensemble (GOE). The fluctuation of those eigenvalues, reproduced by the RMT, is universal and reflects the symmetry of the system. In this picture, energy equipartition is assumed for the closed (unperturbed) cavity. The fluctuation matrix $\underline{\xi}$ has the physical meaning of coupling antenna current profiles with aperture basis functions.

The general form in (2) can be used to study linear chains of interconnected cavities. Specifically, in the scenario where two irregular cavities are interconnected through an aperture, the transfer function between transmit and receive antennas can be calculated. In the realistic assumption of high-loss condition for both the cavities, we obtain the approximation

$$H_{TR}(k_0) = \frac{Z_L}{2(Z_L + Z^{rad,(2)})Z^{rad,(1)}} \underline{C}_{PA}^{(1)} \cdot [\underline{Y}^{rad,(1)} + \underline{Y}^{rad,(2)}] \cdot \underline{C}_{AP}^{(2)}, \quad (6)$$

where the aperture (port)-port (aperture) coupling vectors read

$$\underline{C}_{PA}^{(1)} = \left[\Re(Z^{rad}) \right]^{1/2} \cdot \underline{\xi} \cdot \left[\Re(\underline{Y}^{rad}) \right]^{1/2}, \quad (7.a)$$

$$\underline{C}_{AP}^{(2)} = \left[\Re(\underline{Y}^{rad}) \right]^{1/2} \cdot \underline{\xi} \cdot \left[\Re(Z^{rad}) \right]^{1/2}. \quad (7.b)$$

Monte Carlo simulations of (6) (with $\alpha^{(1)}, \alpha^{(2)} > 1$ to emulate high-losses) reproduce the experimental observation of a double Rayleigh fading for reverberation chamber field.

II. EXPERIMENTAL VALIDATIONS

The natural laboratory frameworks for the validation of the RCM are the mode-stirred electromagnetic enclosures. Inherently, the generalized formulation of the RCM for 3D cavities in (2) can be considered a unified RC model [2]. Recently, full-wave numerical simulations of a large RC highlight remarkable deviations, some unexpected, from idealized field/power statistics. It is found that those deviations are strongly dependent on both frequency and distributed losses. The RCM predictions confirm, and explain on a physical basis, the rejection rates of goodness-of-fit tests as performed on scattering parameters at those RC operations [3]. This evidence constitutes the basis for the explanation of an optimal max-to-mean ratio [4]. Those experiments have been conducted in a two-port mode-stirred RC. Further experiments performed in a multiport (multi-antenna) RC highlight the degradation of multivariate normality of complex scattering parameters

in RC. With the help of the RCM, it has been found that this phenomenon occurs at high-loss operation of irregular cavities, and is enhanced by an increasing number of mutually coupled elements in the transmit and receive antenna arrays [5]. This finding is crucial in the understanding of MIMO channels for next generation wireless communications. Further experimental validations of the RCM are ongoing. Those involve aperture mediated coupling, useful to emulate fading in the outdoor (indoor)-to-indoor handover.

III. CONCLUSION

The random coupling model has been successful in reproducing experimental observations performed in reverberation chambers of different dimensions and operated at different conditions. In particular, deviations from idealized statistics due to either very low or very high distributed losses have been confirmed, as well as non-multivariate Gaussianity in the emulation of multiple-input multiple-output wireless channels through high-loss RC with coupled elements in the antenna array. Wave chaotic cavities interconnected through arbitrary apertures are modeled through an extension of the random coupling model. The cavity-to-cavity transfer function reproduce and extend numerical and experimental observations for different aperture dimensions.

ACKNOWLEDGEMENT

Financial support from US AFOSR, ONR, and Italian Telecom Italia Lab, Grant "RCM for Semi-open Wireless Electromagnetic Environments".

REFERENCES

- [1] G. Gradoni, J.-H. Yeh, B. Xiao, T. M. Antonsen, S. M. Anlage, and E. Ott, "Predicting the statistics of wave transport through chaotic cavities by the random coupling model: A review and recent progress," *Wave Motion*, Available online 19 Feb. 2004,
- [2] G. Gradoni, T. M. Antonsen, S. M. Anlage, and E. Ott, "A statistical model for the excitation of cavities through apertures," *IEEE Transactions on Electromagnetic Compatibility*, submitted, Feb. 2014.
- [3] G. Gradoni, V. Mariani Primiani, and F. Moglie, "Dependence of Reverberation Chamber Performance on Distributed Losses: a Numerical Study," *Electromagnetic Compatibility (EMC), 2014 IEEE International Symposium on*, August 3-7 2014, Raleigh (NC), United States of America.
- [4] G. Gradoni, V. Mariani Primiani, and F. Moglie, "Effect of losses on the maximum-to-mean value in a mode-stirred reverberation chamber," *Electromagnetic Compatibility (EMC EUROPE), 2012 International Symposium on*, September 1-4 2014, Gothenburg, Sweden.
- [5] G. Gradoni, X. Chen, T. M. Antonsen, S. M. Anlage, and E. Ott, "Random Coupling Model for Wireless Communication Channels," *Electromagnetic Compatibility (EMC EUROPE), 2012 International Symposium on*, September 1-4 2014, Gothenburg, Sweden.

ELECTROMAGNETIC TECHNOLOGY FOR VISUALLY IMPAIRED PEOPLE

V. Di Mattia

Dipartimento di Ingegneria dell'Informazione,
Università Politecnica delle Marche
Via Breccie Bianche, 60131, Italy
v.dimattia@univpm.it

Abstract

This contribution discusses the experimental and theoretical studies concerning the design of an electromagnetic assistive technology to the mobility of visually impaired subjects. The system has to detect potentially dangerous obstacles and to alert the user in advance, so as to avoid collisions and to allow safely and independently walking even in unfamiliar environments. In this contest, an electromagnetic model able to solve the problem of obstacles detection even at large distances has been implemented as support tool to define system parameters and performances. Moreover a laboratory prototype of an EM cane has been realized and tested with a blind end-user, with encouraging results and interesting hints for future developments.

Index Terms – Assistive technologies, electromagnetic travel aid, blind people

I. INTRODUCTION

Mobility in unknown environments is an extremely difficult task for visually impaired and blind people and very often it requires the use of assistive devices. The most used is still the white cane, which can only provide alerts for obstacles in front of the user's feet (<1m), without any protection against obstacles on the upper part of the body and without information regarding their speed, volume, and distances [1]. In order to overcome such limitations many Electronic Travel Aids (ETAs) have been proposed during last decades. Most of them are based on the transmission of an energy wave and the detection of echoes from objects present along user's pathway, mainly using optical or ultrasonic emitter/receiver transducers [2]. Despite recent improvements, these devices still present some drawbacks and recognized limitations [2-4].

The main aim of this paper is to summarize the research activities concerning the study and the design of a novel system to improve the autonomy and self-confidence of visually impaired subjects during mobility in unfamiliar environments. The new system is based on electromagnetic (EM) technology, never used before for this purpose.

II. AN EXPERIMENTAL PRELIMINARY STUDY

To start, an experimental comparison between performances of a laboratory EM system and an ultrasonic system, which is a golden standard among ETAs, has been carried out. The aim was twofold: to investigate the potentialities and to highlight the peculiarities of an EM system to be used for this specific application [5].

Results showed that the EM system is able to detect all the obstacles, and in some cases its performances are even higher respect to those of the ultrasonic system. Moreover, its performances still remain high even in uncontrolled environments although irregular ground, trees and other elements create cluttering effects.

III. THE EM MODEL AND THE SYSTEM PROTOTYPE

In order to optimize system parameters, it could be useful to study many different scenarios, testing and comparing antennas performances in detecting several types of objects. This is not easily achievable in reality, but it may be possible by simulating the scattering problem using numerical codes. Nevertheless, the discretization of a volume containing the antenna and the obstacle may require an extremely high computational cost due to: complex geometries of the objects under test and thus the high resolution required to represent small details; the large distances involved, up to 3-5m from the sensor; the high working frequency (required to reduce system dimensions).

Therefore the idea has been to implement a novel approach to divide the whole scattering problem into a small number of sub-problems and solve some of them by analytical methods and the others by numerical codes, taking the advantages of both. To this end, an EM model has been implemented to approximate the field radiated from an antenna only in a portion of space close to an obstacle. The hypothesis is that the field radiated in a generic point P (x,y,z) nearby the objects, can be expressed as the sum of a few functions, easily to be handle as sources in commercial EM software:

$$\mathbf{E}_{app}(t, r; \theta, \phi) = \sum_{n=1}^N \mathbf{f}_n \left(t - \frac{x \sin \theta_n + y \sin \phi_n + z \cos \theta_n \cos \phi_n}{c} \right)$$

where c is the speed of light and $\theta_n \phi_n$ are the angular coordinates.

In order to find the \mathbf{f}_n functions, a matching point technique has been implemented, based on the knowledge of the actual field just in N points, properly chosen close to the object, where the \mathbf{E}_{app} is forced to be equal to the actual field [6]. It is worth noting that the method represents an approximation of the Angular Plane Wave Spectrum theory generally used to represent the field radiated in the whole space, characterized by a slow convergence and by the use of a large number of plane waves. On the contrary, the model proposed focuses its attention only on a portion of space close to the obstacle, using a smaller number of plane waves. Finally, they can be used as sources to solve the scattering problem without simulating the antenna, with clear advantages in terms of computational cost and time for solution. The method has been tested to solve scenario consisting of a double ridge horn antenna and a metallic obstacle (at a distance of 3.5m). The far field radiated from the antenna has been analytically approximated as the one radiated from an equivalent aperture over a metallic plane:

$$\mathbf{E}_{\text{radiate}} = (r, \theta, \phi, f) \cong j \frac{2\pi}{kr} e^{-jkr} E_0 2\pi f \sqrt{2\pi t_0} e^{-\frac{1}{2}\left(\frac{f}{f_0}\right)^2} \frac{\pi ab}{2\lambda^2} \frac{\sin\left(\frac{\pi b\alpha}{\lambda}\right)}{\left(\frac{\pi ab}{\lambda}\right)} \frac{\cos\left(\frac{\pi a\beta}{\lambda}\right)}{\left(\frac{\pi}{2}\right)^2 - \left(\frac{\pi a\beta}{\lambda}\right)^2}$$

where a and b are the aperture dimensions, α and β are the direction cosines and λ is the minimum wavelength.

Then, using the EM model, the $\mathbf{E}_{\text{radiated}}$ has been sampled with $N=5$ plane waves, used to solve 5 scattering problems by commercial software simulating only the obstacle. The 5 echoes obtained have been summed to find the total echo in antenna direction. If desired, it is possible to simulate the antenna with the total echo impinging on its aperture to find the voltage signal at antenna port. Fig. 1 shows a comparison between the signal obtained and the one measured in our laboratory reproducing the same set up. The fidelity, defined as the correlation among the approximated and the measured voltage signal, is more than 80% and it is a very satisfying result considering all the approximations introduced. Changing some parameters the fidelity can be increased at the expense of the computational cost and the time for solution. Then, system parameters have to be defined as a trade off between desired accuracy and complexity of solution. The model needs to be further improved considering more complex scenarios.

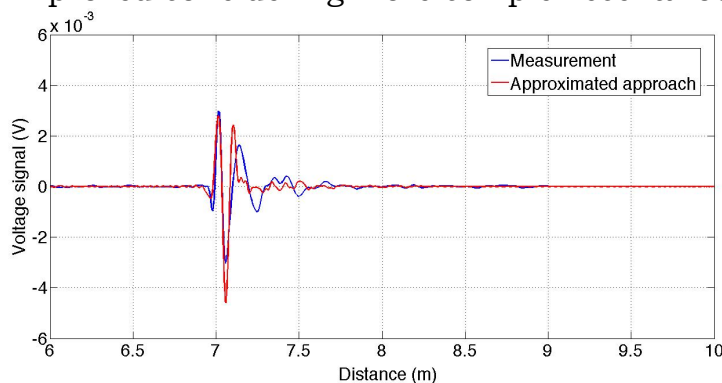


Fig. 1 Comparison with experimental result.

On the base of the encouraging results obtained in the preliminary studies, a prototype system based on EM pulses has been designed, realized and tested with a blind volunteer [7,8]. The prototype consists of a homemade helical antenna, a portable Vectorial Network Analyzer (VNA) and a laptop. The antenna receives the sum of all the echoes coming from the surrounding and the VNA calculates the S_{11} coefficient for each frequency in the band of interest; a MATLAB code gets the data from the VNA, calculates the Inverse Fast Fourier Transform (IFFT) and compares the signal in time with a prefixed threshold, producing an acoustic alarm when it is exceeded.

After a detailed characterization of the portable EM system in presence of one or more obstacles, the most significant tests have been conducted thanks to the collaboration of a blind volunteer. According to

user's feedbacks the system needs to be optimized in terms of: signal processing to increase walking speed; dimensions to reduce weight and improve portability; user interface, because a vibro-tactile signal is preferred respect to acoustic alarms.

To date, new antenna designs based on printed technology are under investigation. The main requirements that the radiating element should satisfy are: working at high frequencies to reduce dimensions, with evident comfort for the user, flexible and small structure easily integrable with microwave circuits and feeding lines; a wide band to ensure a good spatial resolution; a radiation pattern narrow on the horizontal plane to discriminate the obstacle direction and wide over vertical plane to protect all the user's height. Finally the penetrability of common fabric from EM waves paves the way for a full wearable ETA, improving acceptability and usability.

IV. CONCLUSION

In this paper the studies concerning the design of an EM travel aid for visually impaired users have been briefly described. In particular the advantages of using the EM technology have been highlighted and some aspects related to the solution of the EM problem of obstacles detection have been preliminary investigated. Moreover, a prototype has been realized and tested with a blind volunteer with encouraging results. The system is now under optimization, to: 1) reduce dimension and weight; 2) speed up system response; 3) improving signal processing and user interface providing suitable acoustic/tactile signals.

V. REFERENCES

- [1] B. B. Blasch et al., *Foundation of Orientation and Mobility*, 2nd ed., New York: AFB Press, 1997
- [2] U. R. Roentgen et al., "Inventory of electronic mobility aids for visually impaired persons—A literature review," *J. Vis. Impairment Blindness*, vol. 102, no. 11, pp. 702–724, 2008.
- [3] National Research Council, *Electronic Travel Aids: New Directions for Research*, Nat. Acad. Press, Washington D.C., 1986
- [4] D. Dakopoulos and N. G. Bourbakis, "Wearable obstacle avoidance electronic travel aids for blind: A survey," *IEEE Trans. Syst., Man, Cybern. C, Appl. Rev.*, vol. 40, no. 1, pp. 25–35, Jan. 2010
- [5] L. Scalise et al., "Experimental investigation of electromagnetic obstacle detection for visually impaired users: a comparison with ultrasonic system", *IEEE Transactions on Instrumentation and Measurement*, vol. 61, issue 11, pp. 3047-3057, Nov. 2012.
- [6] V. Di Mattia et al., "An Efficient Numerical-Analytical Tool for Time Domain Obstacle Detection", *IET Science, Measurement and Technology*, October 2013.
- [7] V. Di Mattia et al., "Electromagnetic Travel Aid for Visually Impaired Users", *Electromagnetics in Advanced Applications (ICEAA), 2013 International Conference on*, pp.1408,1411, 9-13 Sept. 2013.
- [8] <http://www.youtube.com/watch?v=AyUngKPWtyE>

THE ITALIAN CONTRIBUTION TO THE LOW FREQUENCY APERTURE ARRAY OF THE SQUARE KILOMETER ARRAY

P. Bolli⁽¹⁾, G. Bianchi⁽²⁾, A. Lingua⁽³⁾, J. Monari⁽²⁾, M. Murgia⁽⁴⁾, F.
Perini⁽²⁾, G. Pupillo⁽²⁾, F. Schillirò⁽²⁾, G. Tartarini⁽⁵⁾, G. Virone⁽⁶⁾

⁽¹⁾ Astrophysical Observatory of Arcetri, INAF
Largo E. Fermi 5, 50125 Florence, Italy
pbolli@arcetri.inaf.it

⁽²⁾ Institute of Radio Astronomy, INAF
Via P. Gobetti 101, 40129 Bologna, Italy

⁽³⁾ Department of Environment, Land and Infrastructure
Engineering, Polytechnic of Turin
Corso Duca degli Abruzzi 24, 10129 Turin, Italy

⁽⁴⁾ Astronomical Observatory of Cagliari, INAF
Via della Scienza 5, 09047 Selargius (CA), Italy

⁽⁵⁾ Department of Electrical, Electronic and Information Engineering,
University of Bologna
Viale Risorgimento 2, 40136 Bologna, Italy

⁽⁶⁾ Institute of Electronics, Computer and Telecommunication
Engineering, CNR
Corso Duca degli Abruzzi 24, 10129 Turin, Italy

Abstract

The Italian National Institute for Astrophysics (INAF) represents Italy as one of the eleven Full Members in the Square Kilometer Array (SKA) Organization. The SKA is an ambitious project of the worldwide astrophysical community. Among the several work packages composing the complex project, INAF plays a key role in the Low-Frequency Aperture Array (LFAA). This instrument consists of 256.000 antenna elements with digital beam forming. INAF is actively contributing in several technological aspects of the LFAA: antenna calibration procedures, optimization of antenna element, design of both analog receiving system including data transportation and digital back-end for data acquisition. In parallel, INAF is also investigating the technology for LFAA by using two small-scale demonstrators installed in the Italian radio telescope sites: Medicina and Sardinia Array Demonstrators.

Index Terms – Radio Astronomy, Aperture Arrays.

I. INTRODUCTION

The SKA (Square Kilometer Array, www.skatelescope.org) represents one of the largest projects in astrophysics aimed to answer fundamental questions [1]. By using the largest collecting area ever built, this new huge instrument will observe the Universe in the lower part of the radio window where the atmosphere is transparent, between 50 MHz up to 20 GHz. The instrument will be based on several receiving concepts to cover the almost 3 decades of frequency bandwidth. The telescope facilities for the first phase of the project, which should start with full science operations in 2020, consists of a Low-Frequency Aperture Array (LFAA, see Fig. 1) and a mid-frequency array of dishes equipped with phased array feeds, both arrays to be built in Australia, and a mid-frequency array of parabolic reflectors (dishes) to be built in South Africa. In this paper, we will focus to the LFAA system where the Italian contribution is remarkable. The LFAA is aimed to cover the low frequency range of SKA, 50 – 350 MHz and is scientifically mainly driven by probing the Dark Ages, the Epoch of Reionization, the Galaxy Evolution and Cosmology observing the highly red-shifted hyperfine spin-flip (21 cm) transition from neutral hydrogen.



FIG. 1 – Artistic view of the LFAA. Courtesy of the SKA Organization.

II. LOW-FREQUENCY APERTURE ARRAYS

Even if the LFAA activity officially started at the end of 2013 with the kick-off meeting of the international Consortium AADC (Aperture Array Design and Construction), a long research path have been followed since many years by the members of the Consortium. The LFAA system indeed capitalizes the experience acquired with several precursors developed by different research institutes like AAVP [2], LOFAR (www.lofar.org), LWA (<http://www.phys.unm.edu/~lwa>), and MWA (<http://mwatelescope.org>). The aperture array approach radically changes the concept of a radio telescope, classically intended as a huge reflector antenna mechanically steerable. It consists indeed of an

extremely large number of low-directive antennas whose beam are electronically combined to form few highly directive beams in the sky. The large field-of-view of each element allows to beam-form the array in a wide portion of the sky.

Basically, the LFAA system will consist in 2^{18} log-periodic dual-polarized antennas arranged in a very compact configuration with 75% of the antennas packed within a 2 km diameter core and the remaining collecting area situated on three spiral arms, extending out to a radius of 50 km and enabling higher spatial resolution observations. The system sensitivity will be $\sim 1000 \text{ m}^2/\text{K}$ at frequencies above 110 MHz at the zenith. After an analogic pre-conditioning of the incoming signals, data are transported to the beam-formers and then to a central signal processing building, where they will be channelized and cross-correlated with each other. Finally, output data from the correlator are sent to the science data processing center. Further detailed technical specifications of the instrument can be found in [2].

The Italian contribution to the AADC Consortium is broad and mainly addressed to the following work packages [3-5]:

- Antenna and low noise amplifier, whose goal is to develop an antenna and associated low noise amplifier optimized to the specification of SKA. The Italian contribution includes also the use of an Unmanned Aerial Vehicle system for characterizing and calibrating both the antenna element and the array patterns.
- Receiver (with the role of leading the task) includes the development and design of the LFAA receiver architecture based on the assumption that the digital conversion is in a central housing far away from the antennas. The receiver encompasses all the analogic blocks distributed from the output of the low-noise amplifier to the input of Analog-Digital converter, including also the Radio-Over-Fibre technology which is a promising technology for data transportation over long distances.
- Signal processing. Beam-forming, cross-correlation, channels equalization and all the data processing will be performed digitally with state of the art technology.

III. NATIONAL PROJECTS IN THE LFAA CONTEXT

Since many years, INAF is acquiring experience in advanced technologies addressed to the observation of the sky at low radio frequencies. Several national projects have been funded together with collaborations established with Universities and other research institutes to create a national skilled team for contributing to SKA. The main two projects currently in progress at Italian level are (see Fig. 2):

- The Medicina Array Demonstrator (MAD) experiment focuses on small antenna array calibration and beam-forming. MAD is a regularly spaced array arranged in a 3x3 rhomboidal

configuration based on dual-polarized Vivaldi antennas, which was also included in Aperture Array Verification Program of SKA.

- The Sardinia Array Demonstrator (SAD) funded by the Regione Sardegna aims to install at the Sardinia Radio Telescope site 128 Vivaldi antennas distributed between a core and few more distant satellite regions.



FIG. 2 – (left) Medicina Array Demonstrator; (right) possible distribution of the antennas of the Sardinia Array Demonstrator.

ACKNOWLEDGMENT

The authors are grateful to their collaborators: F. Govoni, M. Schiaffino, G. Bianchi, A. Mattana, G. Naldi, S. Rusticelli, A. Tibaldi, F. Paonessa, Z. Farooqui, R. Tascone, O. A. Peverini, G. Addamo, M. Piras, A. Cina, P. Maschio and B. Horea.

REFERENCES

- [1] P.E. Dewdney, P.J. Hall, R.T. Schilizzi, T.J.L.W. Lazio, “The Square Kilometre Array”, *Proc. IEEE*, vol. 97, n. 8, 2009.
- [2] J.G. bij Vaate, et al., “Low frequency aperture array developments for phase 1 SKA”, *Proc. General Assembly and Scientific Symposium, XXXth URSI Istanbul*, 13-20 Aug. 2011.
- [3] J. Monari, et al., “Aperture Array for Low Frequency: the Vivaldi solution,” *Electromagnetics in Advanced Applications (ICEAA)*, 66-69, 2013.
- [4] G. Virone, et al., “Antenna Pattern Verification System Based on a Micro Unmanned Aerial Vehicle (UAV),” *IEEE Antennas and Wireless Propagation Letters*, vol. 13, 169-172, Jan. 2014.
- [5] F. Chiabrando, A. Lingua, M. Piras, “Direct photogrammetry using UAV: Tests and first results”, *International archives of the photogrammetry, remote sensing and spatial information sciences*, vol. XL-1/W2, G. Grenzdörffer and R. Bill, UAV-g2013, 81-86, 4-6 Sept. 2013.

BIT ERROR RATE EVALUATION OF A SILICON-ON-INSULATOR OPTICAL-NETWORK-ON-CHIP ROUTER

A. Parini^(1,2), A. Annoni⁽³⁾, F. Morichetti⁽³⁾, A. Melloni⁽³⁾, G. Bellanca⁽¹⁾

⁽¹⁾ Dipartimento di Ingegneria, Università degli Studi di Ferrara,
Via Saragat 1, Ferrara 44122, Italy

⁽²⁾ Laboratory of Micro and Submicro Enabling Technologies
of the Emilia-Romagna Region (MIST E-R), Ferrara, Italy

alberto.parini@unife.it

⁽³⁾ Dipartimento di Elettronica, Informazione e Bioingegneria,
Politecnico di Milano, Via Ponzio 34/5, Milano 20133, Italy

Abstract

In this contribution, we present the outcomes of a joint activity between the PHOTONICA FIRB 2008 and the SAPPHIRE PRIN 2009 Projects. In particular, we characterize a four-input four-output microring-based integrated router, designed for optical networking at chip level. The switching performance of the device are tested through Bit Error Rate measurements in two dual configurations: single channel 10 Gbit/s, and 3-channels WDM 10 Gbit/s. BER curves show that a low rejection on filter elements, induced by fabrication issues, mostly penalize the channels associated with through paths, while keeping channels associated to drop paths almost unaffected.

Index Terms – Optical Networks on Chip, Photonic Integrated Circuits, Silicon-on-Insulator, Bit-Error-Rate.

I. INTRODUCTION

Optical Networks-on-Chip (ONoCs) are a promising paradigm to interconnect a large number of processing cores at chip level. On-chip optical networking aims at achieving, at a micrometric scale, the well assessed advantages of long-distance fiber communications. More specifically, the integration of a photonic layer in a heterogeneous electronic platform can improve the overall performance of the system, in terms of transmission bandwidth and power budget. Microring-based networks, as the one presented in this contribution, implement a selective routing between different cores by exploiting a wavelength dependent resonance mechanism. Alternatives topologies involve, for example, the use of Mach-Zehnder modulators.

Here, we report on Bit-Error-Rate measurements performed on a Silicon on Insulator (SOI) microring router enabling a WDM-type communication between four nodes [1].

II. 4 × 4 GWOR STRUCTURE

The left panel of Fig. 1 shows the analyzed 4 inputs 4 outputs Generic Wavelength-routed Optical Router (4 × 4 GWOR) structure [2]; in the right panel of the same figure is presented a microscope image of the

actual fabricated sample. The router is composed of four pairs of rings arranged at the four corners of a square layout. The rings labeled R1 have a radius of 20 μm , whereas the ones labeled R2 have a radius of 18 μm . The network is topologically invariant under step rotations of 180°, and each orthogonal input port differs only for the first encountered routing ring.

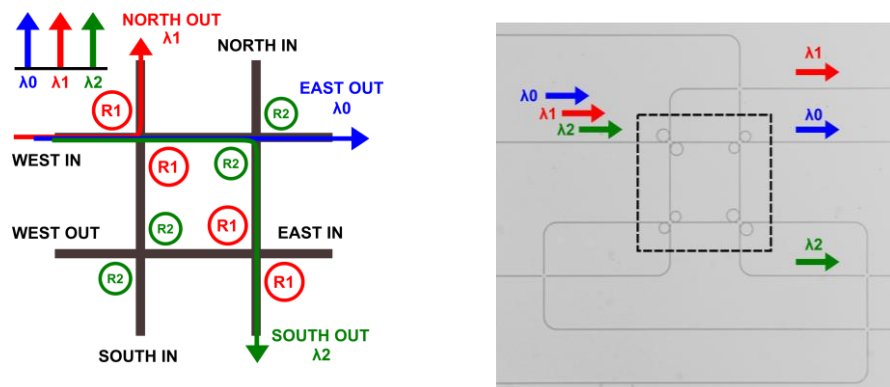


Fig. 1 – (Left) GWOR topology with four input and four output ports. The wavelength dependent routing is achieved through the choice of different radii for rings R1 and R2. (Right) microscope image of the fabricated device.

Thanks to this topological invariance, we decided to characterize the device using the West-In port. By injecting in this input three signals with different wavelengths, namely λ_0 , λ_1 and λ_2 , the routing paths inside the device are the following:

- λ_0 is a through wavelength for both R1 and R2 ring pairs; consequently, the signal at this wavelength is directly routed from West-In to East-Out;
- λ_1 is a drop wavelength for the R1 rings; the associated data stream is then redirected toward the North-Out port;
- λ_2 is a drop wavelength for the R2 ring family, but not for the R1 one; the associated data stream is therefore routed to the South-Out port.

U turn paths, i.e. West In to West Out, are topologically forbidden (a computational core, in fact, does not need to communicate with itself).

III. DEVICE FABRICATION AND BER EVALUATIONS

The component has been designed by following the building block approach proposed in the framework of the SAPPHIRE PRIN 2009 Italian Research Project, and by exploiting the photonic library of the ASPIC® software [3]. The device has been fabricated at the James Watt Nanofabrication Center of the University of Glasgow (JWNC). The overall footprint of the GWOR core is of about 0.8 mm².

We evaluated the power penalty for a Bit Error Rate ranging between 10⁻⁴ and 10⁻¹⁰, with respect to the Back to Back (B2B) experiment. When evaluating the BER in WDM configuration, a comb of three modulated signals is injected simultaneously into the West-In port

(black solid line in panel (a) of Fig 2). Each wavelength corresponds to one of the three previously described routing paths of the device, namely: $\lambda_0 = 1551.32$ nm (through path between the West-In and the East-Out ports), $\lambda_1 = 1552.11$ nm (resonance of the R1 pairs) and $\lambda_2 = 1553.13$ nm (resonance of the R1 pairs).

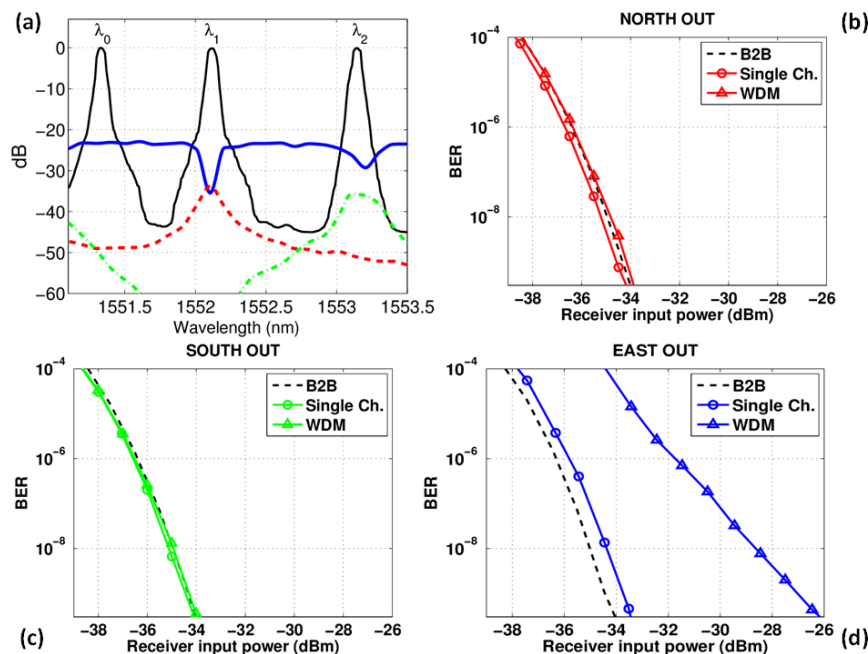


FIG. 2 – (a) Spectra of the three output ports of the device (blue solid line for East-Out, red dashed line for North-Out and green dash-dotted line for South-Out), together with the spectra of the three laser sources used for the WDM BER evaluations (black solid line). (b) (c) (d) BER curves in single channel and in 3-channel WDM configurations.

Results obtained for the different routing paths are summarized hereafter:

NORTH OUT: The routing wavelength associated with this port is λ_1 , while λ_0 and λ_2 represent the interfering signals, when operating in WDM configuration. Panel (b) of Fig. 3 shows the BER curves obtained in single channel (red line with circles) and in WDM (red line with triangles) operation, respectively. At a BER of 10^{-9} , the power penalty measured in the WDM configuration with respect to the single channel one is only 0.4 dB; therefore, it is possible to assert that the associated routing path is substantially robust with respect to crosstalk from the other channels.

SOUTH OUT: The associated wavelength is now λ_2 , whereas λ_0 and λ_1 are the interfering WDM signals. From the measured transmission spectrum in reported in the (a) panel of Fig. 3 (green dash-dotted line) one can see that the rejection of λ_0 with respect to λ_2 is 15 dB, whereas the rejection of λ_1 is more than 25 dB. As a consequence of the high selectivity of this channel, the crosstalk can be considered negligible. This is confirmed by the corresponding WDM BER curve,

which does not show any significant penalty with respect to the one measured in single channel configuration.

EAST OUT: This output port is a through-path for both R1 and R2 ring families. The associated wavelength is now λ_0 , while λ_1 and λ_2 are the interfering WDM signals. The BER of the single channel shows no significant penalties with respect to the B2B experiment. On the contrary, when operating in WDM regime, the BER curve exhibits a power penalty of 7 dB, (for a BER of 10^{-9}), which is induced by the strong crosstalk of the interfering channels. The low performance on this path is determined by the poor rejection of the north-eastern R2 ring couple. In fact, by observing the East-Out transmittance curve in panel (a) of Fig. 3 (blue solid line) one can note that the relative rejection of λ_2 with respect to λ_0 is of only 3 dB (right notch in the curve). Due to this poor rejection, a high fraction of the λ_2 signal is not filtered out and remains on the bus waveguide, giving rise to interference on this output. To assure a better performance on this path, the selectivity of R2 nodes needs to be increased.

IV. CONCLUSION

The switching capabilities of a SOI 4×4 GWOR device have been evaluated through BER measurements. Comparisons between BER curves in single and WDM multichannel operative conditions enable a clear understanding of the main sources of transmission quality deterioration. Results show that a poor rejection of a switching node, reasonably due to fabrication issues, introduces a crosstalk power penalty of 7 dB on the through path, while leaving almost unaffected the corresponding drop path.

ACKNOWLEDGEMENT

This work is the outcome of the collaboration between the PHOTONICA FIRB 2008 and the SAPPHIRE PRIN 2009 Projects, and is supported by the Italian Ministry of the University and Research. Alberto Parini thanks the Programma Operativo FESR 2007-2013 of the Emilia Romagna Region - Attività I.1.1 for the financial support to his research activity. We acknowledge the support from the technical staffs of JWNC at Glasgow University and of CNRS-FOTON Laboratory - Lannion (France)

REFERENCES

- [1] A. Parini *et al.*, "BER Evaluation of a Passive SOI WDM Router," IEEE Phot. Techn. Lett., vol. 25, no. 23, pp. 2285-2288, Dec. 2013.
- [2] X. Tan *et al.*, "A generic optical router design for photonic network-on-chips," IEEE Journal Lightwave. Technology, vol. 30, no. 3, pp. 368 - 376, Feb. 2012.
- [3] ASPIC: <http://www.aspicdesign.com>

ELECTROMAGNETIC INTERACTION WITH AN ALIGNMENT OF SPHERES WITHIN A HOST SPHERE

F. Mangini

Department of Information Engineering, Electronics
and Telecommunications, "La Sapienza" University of Rome,
Via Eudossiana 18, 00184 Rome, Italy, fabio.mangini@uniroma1.it

Abstract

In this paper, we consider the interaction of a uniform electric field with a dielectric host sphere containing a series of aligned perfect electric conductor spheres. We propose a static approach in order to calculate the external electric field, the polarizability and the effective permittivity of this spherical system, afterwards the study is extended to the quasi-static case, providing the quasi-static rule for this particular system. A Matlab code is implemented, where a suitable truncation criterion of the system has been adopted. We analyze the behavior of the scattering parameters as a function of the dimension, position and number of the spherical inclusions.

Index Terms – Effective permittivity, homogenization model, polarizability, quasi-static approximation.

I. INTRODUCTION

In the present paper, we propose a homogenization model of aligned Perfect Electric Conductor (PEC) spheres embedded in a dielectric host sphere, in order to deduce the properties of the scatterer as a homogenized sphere. The effective-medium analysis of a composite sphere has been previously attempted in [1].

We intend to understand the role of the presence of the inclusions on the effective-medium parameters.

In Section 2, we present the static model of the aligned spherical inclusions embedded in a dielectric sphere and we obtain an analytical expression for the polarizability and for the effective permittivity. Moreover, we validate the static results through comparisons with a Finite-Element Method based software. Furthermore, we present a parametric study to clarify the role of the inclusions on the polarizability. Finally, in Section 3, the conclusions are drawn.

II. ELECTROSTATIC MODEL AND VALIDATION

We consider L PEC spheres with a radius R_{c_j} , respectively, in a dielectric host sphere with a radius R_s (Fig. 1); the center of the host sphere coincides with the origin of the Cartesian system. The other spheres are centered in the origin O_j of a local reference system. The main reference system is chosen so that the z -axis coincides with the external electric field $\underline{E}_0 = E_z \underline{z}_0$. Since the system is in azimuthal symmetry, the potential function is independent of φ .

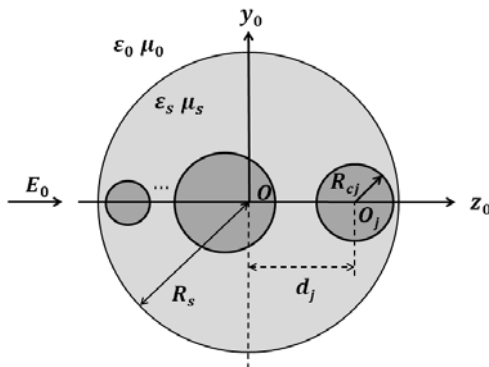


FIG. 1 – Statement of the problem.

We define the properties of the medium where the spheres system is immersed with the electromagnetic constants ϵ_0, μ_0 and $\sigma_0 = 0$, and for the dielectric sphere ϵ_s, μ_s and $\sigma_s = 0$. The potential function in spherical coordinates of the external field is [2]:

$$\Phi_0(\underline{r}) = \sum_{n=1}^{\infty} [E_n R_n(\underline{r}) \delta_{n1} + b_n^0 I_n(\underline{r})] \tag{1}$$

with $R_n(\underline{r}) = r^n P_n(\cos \vartheta)$, $I_n(\underline{r}) = r^{-(n+1)} P_n(\cos \vartheta)$: the Regular and Irregular solid harmonics, respectively, and δ_{n1} known as delta of Kronecker.

Similarly, doing the same reasoning for the region inside the host sphere, we obtain for the electrostatic potential $\Phi_s(\underline{r})$:

$$\Phi_s(\underline{r}) = \Phi_s(\underline{r}) + \sum_{j=1}^L \Phi_{c_j}(\underline{r}_j) = \sum_{n=1}^{\infty} \left[a_n^s R_n(\underline{r}) + \sum_{j=1}^L b_n^{c_j} I_n(\underline{r}) \right] \tag{2}$$

We have expressed the field as a superposition of the field incoming in the center of the host sphere and of the fields outgoing from each of the spheres centered in their local reference system. To solve the problem we have to impose the boundary conditions on all the surfaces [3], i.e.:

$$\begin{cases} \Phi_0(\underline{r}) = \Phi_s(\underline{r}) + \sum_{i=1}^L \Phi_{c_i}(\underline{r}) & \text{for } r = R_s \\ \epsilon_0 \nabla \Phi_0(\underline{r}) = \epsilon_0 \nabla \left[\Phi_s(\underline{r}) + \sum_{i=1}^L \Phi_{c_i}(\underline{r}) \right] & \text{for } r = R_s \\ \Phi_s(\underline{r}_j) + \Phi_{c_j}(\underline{r}_j) + \sum_{i=1, i \neq j}^L \Phi_{c_i}(\underline{r}_j) = 0 & \text{for } r = R_{c_j} \end{cases} \tag{3}$$

with $j = 1, \dots, L$. We note in all the equations that the potentials are expressed in their local reference system. To achieve this translation we can use the Morse-Feshbach formula [4]. Choosing the truncation criterion for the summation, changing the order of sums, interchanging the indices, replacing the equations in the boundary condition and applying the orthogonality properties of the Legendre functions, we obtain:

$$\begin{cases} \frac{b_n^0}{R_s^{2n+1}} - a_n^s - \sum_{i=1}^L \sum_{v=1}^N \frac{b_v^{ci}}{R_s^{2n+1}} \binom{n}{n-v} z_i^{n-v} = -E_n \delta_{n1} \\ -N_n \frac{b_n^0}{R_s^{2n+1}} - \varepsilon a_n^s + N_n \varepsilon \sum_{i=1}^L \sum_{v=1}^N \frac{b_v^{ci}}{R_s^{2n+1}} \binom{n}{n-v} z_i^{n-v} = -E_n \delta_{n1} \\ \sum_{v=n}^N a_v^s \binom{v}{v-n} z_j^{v-n} + \frac{b_n^{cj}}{R_{cj}^{2n+1}} + \sum_{i=1 \neq j, v=1}^L \sum_{v=1}^N \frac{b_v^{ci}}{R_{cj}^{2n+1}} \binom{n}{n-v} z_i^{-(n+v+1)} = 0 \end{cases} \quad (4)$$

with $\varepsilon = \varepsilon_s/\varepsilon_0$ (dielectric contrast), $N_n = (n+1)/n$, $E_1 = -E_0$, z_i the share along z of the center of the i -th sphere. Solving this system we obtain the coefficients of the series expansion of the electrostatic potential. In our case, because of the axial symmetry, the electric field E_0 generates a dipole perturbation in the sphere's surroundings; therefore, the polarizability and the effective permittivity can be written as [5]:

$$\alpha = 4\pi\varepsilon_0 \frac{b_1}{E_0}, \quad \varepsilon_{eff} = \varepsilon_0 + \frac{\alpha/V}{1 - \alpha/(3\varepsilon_0 V)} \quad (5)$$

respectively and where V is the volume of the external sphere.

We consider for all following results the case of an external sphere with a ratio between the radius and the wavelength equal to 10^{-4} , so as to verify the quasi-static approximation rule, besides we choose as the truncation criterion that proposed by [1]. In Fig. 2, we have shown, to validate the model, the comparison between the electric fields along a line of coordinate $(x; y) = ([-R_s, 0]; -1.5R_s)$ obtained with Matlab and Comsol in the case of four inclusions. The radii are $R_{cj} = R_s/8$ and the distances from the origin are $d_1 = -0.75$, $d_2 = -0.25$, $d_3 = 0.25$, and $d_4 = 0.75$, respectively. The internal spheres are embedded in a dielectric sphere $\varepsilon_s = 2.25$ immersed in air and the external electric field is $E_0 = 1$ V/m. As can be seen, the match between the results of the electric field is excellent, then the model is representative of the phenomenon taken into consideration, moreover the quasi-static approximation rule has been respected.

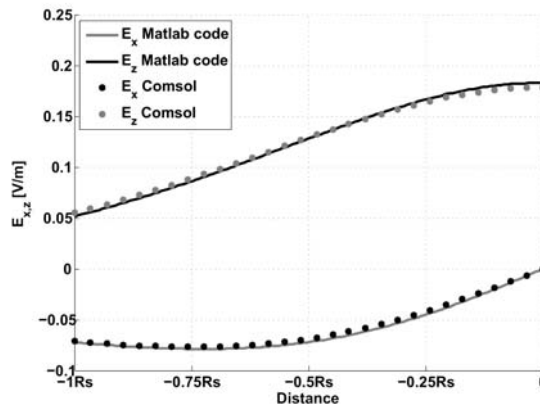


FIG. 2 – Electric field components computed along a line of coordinate $(x; y) = ([-R_s; 0]; -1.5R_s)$, in the case of four internal spheres in a dielectric host sphere.

To clarify the role of the geometrical characteristics, we consider the case of a single sphere PEC, let us consider the case of two internally tangential spheres, with the radius of the internal sphere varying from zero to the radius of the host sphere (Fig. 3.a). The permittivity of this object must vary from $\epsilon_s = 4$ to $\epsilon_s = \infty$. In Fig. 3.b, we can see that the effective permittivity, as a function of the radius of the inclusion, grows extremely slowly with the inclusion's radius until $R_c = 0.75R_s$. Beyond that, the increase becomes more nonlinear and tends to infinity.

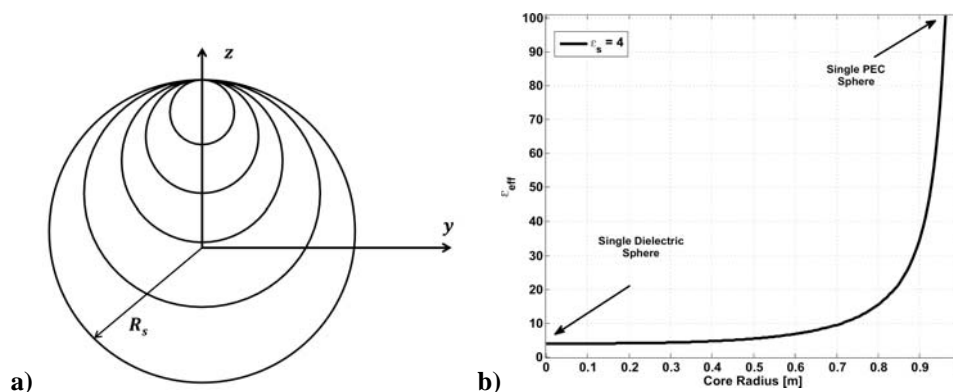


FIG. 3. a) Geometry and b) effective permittivity of two internally tangential spheres as a function of the internal radius.

III. CONCLUSION

In this paper, we studied the behavior of a system consisting of a series of aligned spheres in a dielectric host sphere in the presence of a uniform electric field. A quasi-static analysis has been developed in order to obtain the external electric field, the polarizability and the effective permittivity of the system. A comparison has been presented to validate the results. We found that the polarizability of the two eccentric spheres is affected mostly by the radius of the internal sphere and weakly by the internal sphere's position.

REFERENCES

- [1] F. Mangini, N. Tedeschi, F. Frezza, and A. Sihvola, "Electromagnetic interaction with two eccentric spheres," *J. Opt. Soc. Am. A*, vol. 31(4), 9 pp., 2014.
- [2] J.A. Stratton, *Electromagnetic Theory*, McGraw-Hill, New York and London, 1941.
- [3] B. N. Cuffin, "Eccentric Spheres Models of the Head," *IEEE Transactions on Biomedical Engineering*, vol. 38(9), pp. 871-878, 1991.
- [4] P. M. Morse and H. Feshbach, *Methods of Theoretical Physics*, Part II, McGraw-Hill, New York, Toronto and London, 1953.
- [5] A. Sihvola, *Electromagnetic mixing formulas and applications*, The Institution of Electrical Engineers, London, United Kingdom, 1999.

A CONVERGENCE STUDY BETWEEN THE MODELS OF A MULTILAYER SPHERE AND A RADIAL UNIAXIAL SPHERE

F. Mangini* and N. Tedeschi

Department of Information Engineering, Electronics
and Telecommunications, "La Sapienza" University of Rome,
Via Eudossiana 18, 00184 Rome, Italy, *fabio.mangini@uniroma1.it.

Abstract

A multilayer sphere with a fixed external radius and with an arbitrary number of layers is presented as a possible realization of a Radial Uniaxial (RU) sphere. In particular a layered sphere with two alternating materials is taken into account. The well-known quasi-static model for the polarizability of the multilayer sphere is considered. The limits in which the multilayer sphere can be considered as a Radial Uniaxial sphere are discussed, we consider different kinds of stratification, keeping constant either the thickness, or the area, or the volume, and in each case a convergence rule for the RU model is presented. Moreover, different techniques are shown for layering the spheres and it is found which of them is convenient in terms of convergence speed.

Index Terms – Homogenization model, Multilayer sphere, Radial Uniaxial sphere, Polarizability.

I. INTRODUCTION

The electromagnetic interaction by a multilayer sphere is widely studied in the literature, because of its interest from the point of view of both theory and applications [1]. Also, the RU structures have been widely studied because of their application to the metamaterial design and in particular to the electromagnetic cloaking [2].

The main purpose of the present paper is to understand the limits in which a stratified sphere with a fixed external radius can be considered homogenized in a RU sphere, by varying the number of the internal layers. We take a layered sphere with two alternating materials, i.e., with only two values of the permittivity.

In Section 2, a quasi-static analysis of a multilayer sphere is performed and the polarizabilities of different kinds of multilayer spheres are calculated, the homogenization procedure is presented. Moreover, the validation and the study of the convergence of the homogenized RU model by a comparison are reported. Finally, in Section 3, the conclusions are drawn.

II. HOMOGENIZATION MODEL

Let us consider a multilayer sphere of alternating relative permittivity ε_1 and ε_2 , immersed in a vacuum (Fig. 1). In the following, the permittivity of the cover layer is always called ε_1 . The radius of the external sphere is fixed and equal to a_1 and the other internal radii are:

$a_k = a_1(N - k + 1)/N$ i.e., initially, we consider the case of equidistant layers. The number of layers N is arbitrary. To obtain the dipole moment of this multilayer sphere, the static problem of an external field $\underline{E}_z = E \underline{z}_0$ must be faced. To solve the problem, we apply the transmission-line method [3], i.e. the Laplace equation $\nabla^2 \Phi(\underline{r}) = 0$ has to be solved in spherical coordinates for the electric potential in all the subregions: $\Phi(\underline{r}) = (-C_i r + D_i r^{-2}) \cos \vartheta$. Applying the boundary conditions on all the layers, we obtain [3]:

$$\begin{pmatrix} C_0 \\ D_0 \end{pmatrix} = \prod_{i=0}^{N-1} \begin{bmatrix} M_{11} & M_{12} \\ M_{21} & M_{22} \end{bmatrix} \begin{pmatrix} C_N \\ 0 \end{pmatrix} \tag{1}$$

where, ϵ_0 is the vacuum's permittivity, and V is the volume of the external sphere. From the knowledge of the polarizability, it is easy to obtain an expression of the effective permittivity of the multilayer sphere [4]: $\epsilon_{eff} = \epsilon_0 + \alpha/[V - \alpha/(3\epsilon_0)]$. The quasi-static model allows us to consider the multilayer sphere as an isotropic sphere with the permittivity.

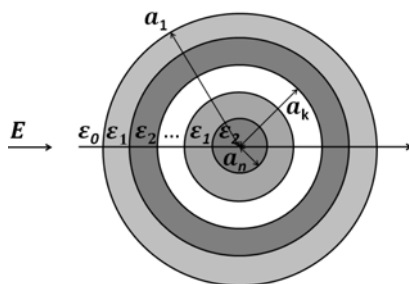


Fig. 1 – Geometry of the problem.

A different model of the multilayer sphere is the RU sphere. In the literature, a layered sphere with two permittivities ϵ_1 and ϵ_2 has been considered as a homogeneous sphere with a tensorial permittivity in a spherical reference frame, as follows [5]: $\underline{\underline{\epsilon}} = \epsilon_r \underline{u}_r \underline{u}_r + \epsilon_\tau \underline{I}_\tau$, where: \underline{u}_r is the unit vector in the radial direction, $\underline{I}_\tau = \underline{I} - \underline{u}_r \underline{u}_r$ is the tangential unit tensor. The quantities ϵ_r and ϵ_τ are the relative permittivities in the radial and tangential directions, respectively. The expressions of the radial and tangential permittivities, found in the literature, as a function of the permittivities of the layers in a multilayer sphere, are the following [6]: $\epsilon_r = 2\epsilon_1\epsilon_2/(\epsilon_1 + \epsilon_2)$, $\epsilon_\tau = (\epsilon_1 + \epsilon_2)/2$.

Moreover, the RU sphere can be represented with a polarizability and with an effective permittivity as follows [11]:

$$\alpha_{RU} = 3 \frac{\epsilon_{RU} - 1}{\epsilon_{RU} + 2}, \quad \epsilon_{RU} = \frac{\epsilon_r}{2} \left(-1 + \sqrt{1 + 8 \frac{\epsilon_\tau}{\epsilon_r}} \right) \tag{2}$$

As a first result, we want to show five values of polarizability (Fig. 2) in the following cases: two concentric spheres, with $\epsilon_1 = 2$ and $\epsilon_2 = 4$ and

viceversa; a RU sphere, analyzed with the formula (2); a multilayer sphere, as a function of the number of the layers, with $\epsilon_1 = 2$ and $\epsilon_2 = 4$. The radius of the sphere is considered of $a_1 = \lambda_0 10^{-3}$ to respect the quasi-static approximation rule, with λ_0 the wavelength in the air.

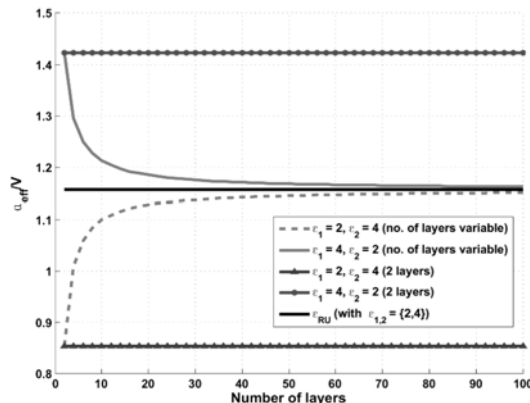


Fig. 2 – Polarizability as a function of the number of layers, with $\epsilon = \{2, 4\}$.

From Fig. 2, we can see that the value of the permittivity of the external sphere has a great weight on the polarizability. Both the cases of two concentric spheres are bounded between these two values: in the case with the external sphere with permittivity $\epsilon_1 = 2$ the polarizability is $a = 0.85$, and in the case with $\epsilon_1 = 4$ it is $a = 1.42$. On the other hand, the polarizability of the RU sphere takes a value $a = 1.16$, see Eq. (2), that is an intermediate value between the previous two cases. Considering now the case of the multilayer sphere, we can see that if $\epsilon_1 = 2$, the polarizability starts from the value $a = 0.85$ and suddenly increases to the polarizability of the RU sphere. On the other hand, if we consider a multilayer sphere with an external layer with $\epsilon_1 = 4$, the polarizability starts from the value $a = 1.42$ and suddenly decreases to the polarizability of the RU sphere. As a consequence, the error in considering a multilayer sphere as a RU sphere decreases when the number of layers grows. The polarizability of the multilayer sphere approaches the polarizability of the RU sphere from greater or lower values depending on the permittivity of the external layer.

Until now, we considered a multilayer sphere with equidistant layers. We considered other two possibilities: one of them is the case in which each layer has the same volume, and the other possibility is the same-area rule, i.e. we consider that each sphere has an increase of surface equal to the previous sphere, in formula: $a_k = a_1(N - k + 1)^{1/3} / N$, $a_k = a_1(N - k + 1)^{1/2} / N$, respectively. In Fig. 3, the difference between the effective permittivity of a RU sphere and that of a multilayer sphere as a function of the number of layers, with $\epsilon_1 = 2$ and $\epsilon_2 = 4$, is shown with the three different rules. As can be seen, the speed of the convergence varies with the rule type, i.e., the convergence with the same-area rule is quicker than that with the same-distance rule and the same-volume rule is quicker than the same-area rule.

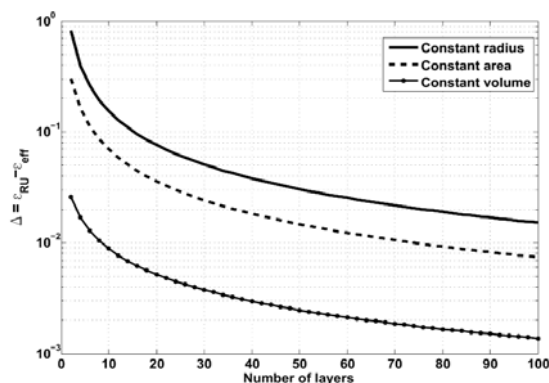


Fig. 3 – Difference between the effective permittivities of a RU sphere and of a multilayer sphere as a function of the number of layers with $\epsilon = \{2, 4\}$ in three different cases: same-distance rule, same-area rule, and same-volume rule.

III. CONCLUSION

In this paper, we presented a quasi-static model for the analysis of the electric potential in the presence of a multilayer sphere with an arbitrary number of layers with two alternating values of permittivity. We found closed-form expressions for the polarizability and the effective permittivity of the multilayer sphere. Moreover, we analyzed the convergence of the polarizability of the multilayer sphere to the expected value of the effective polarizability of a RU sphere. We demonstrated how the polarizability of a multilayer sphere suddenly tends to the polarizability of a RU sphere when increasing the number of layers. Furthermore, we considered three different ways to choose the distance between the layers, and we checked the speed of convergence of the three methods, finding in the same-volume rule the best choice.

REFERENCES

- [1] X. Zhou and G. Hu, "Design for electromagnetic wave transparency with metamaterials," *Phys. Rev. E*, vol. 74, 026607, 8 pp., 2006.
- [2] J.B. Pendry, D. Shurig, and D.R. Smith, "Controlling electromagnetic fields," *Science*, vol. 312, pp. 1780-1782, 2006.
- [3] A. Sihvola and I.V. Lindell, "Transmission line analogy for calculating the effective permittivity of mixtures with spherical multilayer scatterers," *J. Electromag. Waves Appl.*, vol. 2(8), pp. 741-756, 1988.
- [4] A. Sihvola, *Electromagnetic mixing formulas and applications*, The Institution of Electrical Engineers, London, UK, 1999.
- [5] H. Wallén, H. Kettunen, and A. Sihvola, "Singularities or emergent losses in radially uniaxial spheres," *Proceedings of the 2013 International Symposium on Electromagnetic Theory*, 2013.
- [6] C. Guclu, S. Campione, and F. Capolino, "Hyperbolic metamaterial as super absorber for scattered fields generated at its surface," *Phys. Rev. B*, vol. 86, 205130, 7 pp., 2012.

REweighted, STandardized, Recursively Iterated Cerebral Tomography Algorithm (RESTRICTA).

M. Muzi⁽¹⁾

⁽¹⁾Institute of Advanced Biomedical Imaging, University "G. d'Annunzio"
Chieti-Pescara, via dei Vestini 31, 66100 Chieti (CH), Italy
marco.muzi@unich.it

Abstract

One of the biggest challenges in neuroimaging is to localize as accurately and precisely as possible the brain activity of subjects in vivo during the execution of specific tasks. In fact, the better the localization of areas involved in the task, the better the chances for neurologists / psychologists to understand the correct physiology of the brain. In this paper we proposed a new algorithm of resolution of the inverse problem of MagnetoEncephalography (MEG): RESTRICTA. It is based on the application of a recursive minimum norm solver, properly standardized, regularized in $\ell_{2,1}$ norm. It is shown how it is able to provide more accurate estimates in terms both of localization and of extension of the activation area compared to other algorithms of common use as eLORETA.

Index Terms – Inverse problem, MagnetoEncephalography (MEG), Minimum norm estimation methods.

I. INTRODUCTION

The MEG is a noninvasive technique for brain activity mapping based on recording the induction magnetic field (in order 10 fT – 100 fT) produced by electrical currents naturally occurring in the brain. Brain activity has very low frequency components ($f < 1$ kHz range).

From the measurements obtained by the MEG it is possible to try to localize the areas involved in the signal generation. Actually there exist different kinds of algorithms designed for the resolution of the MEG inverse problem, among which those belonging to the minimum norm algorithm family. The algorithm proposed here is linked to this family.

II. METHODS

The brain volume is sampled on a 3D grid and in every knot is defined an electric current dipole with free polarization. The set of the polarization components is collected in the vector \mathbf{Q} . The estimation of the vector elements is the goal of a MEG inverse problem algorithm.

The relation between the magnitude of the measured magnetic field B by a sensor positioned in \mathbf{r}'_i with the electric dipole \mathbf{Q} positioned in \mathbf{r}_k can be resumed by the following:

$$\begin{bmatrix} B(\mathbf{r}'_1) \\ B(\mathbf{r}'_i) \\ B(\mathbf{r}'_m) \end{bmatrix} = \begin{pmatrix} \left(\frac{(\mathbf{r}_1 - \mathbf{r}'_1) \times \hat{\mathbf{s}}_1}{\|\mathbf{r}_1 - \mathbf{r}'_1\|^3} \right)^T & \left(\frac{(\mathbf{r}_k - \mathbf{r}'_1) \times \hat{\mathbf{s}}_1}{\|\mathbf{r}_k - \mathbf{r}'_1\|^3} \right)^T & \left(\frac{(\mathbf{r}_n - \mathbf{r}'_1) \times \hat{\mathbf{s}}_1}{\|\mathbf{r}_n - \mathbf{r}'_1\|^3} \right)^T \\ \left(\frac{(\mathbf{r}_1 - \mathbf{r}'_i) \times \hat{\mathbf{s}}_i}{\|\mathbf{r}_1 - \mathbf{r}'_i\|^3} \right)^T & \left(\frac{(\mathbf{r}_k - \mathbf{r}'_i) \times \hat{\mathbf{s}}_i}{\|\mathbf{r}_k - \mathbf{r}'_i\|^3} \right)^T & \left(\frac{(\mathbf{r}_n - \mathbf{r}'_i) \times \hat{\mathbf{s}}_i}{\|\mathbf{r}_n - \mathbf{r}'_i\|^3} \right)^T \\ \left(\frac{(\mathbf{r}_1 - \mathbf{r}'_m) \times \hat{\mathbf{s}}_m}{\|\mathbf{r}_1 - \mathbf{r}'_m\|^3} \right)^T & \left(\frac{(\mathbf{r}_k - \mathbf{r}'_m) \times \hat{\mathbf{s}}_m}{\|\mathbf{r}_k - \mathbf{r}'_m\|^3} \right)^T & \left(\frac{(\mathbf{r}_n - \mathbf{r}'_m) \times \hat{\mathbf{s}}_m}{\|\mathbf{r}_n - \mathbf{r}'_m\|^3} \right)^T \end{pmatrix} \cdot \begin{bmatrix} Q(\mathbf{r}_1) \\ Q(\mathbf{r}_k) \\ Q(\mathbf{r}_n) \end{bmatrix} \\ = L \cdot Q \quad (1)$$

where $\hat{\mathbf{s}}_i$ is the orientation of the i -th sensor. Once the positions of the dipoles and sensors are defined, L becomes a linear operator. Effects of the volume currents are treated as described in [1].

Due to the ill-posedness of the linear system defined by Eq. (1) (in real cases $n \gg m$) and to the presence of measurement noise, the solution of the inverse problem must be reformulated with the following minimization problem:

$$\hat{Q} = \min_Q \|B - LVQ\|_2^2 + \tau \|Q\|_{2,1} \quad (2)$$

Where V is the standardization matrix, here defined according to [6] and $\|Q\|_{2,1}$ is the $\ell_{2,1}$ norm defined as:

$$\|Q\|_{2,1} = \sum_{i=1}^n \|Q^i\|_2 = \sum_{i=1}^n \sqrt{q_1^{i2} + q_2^{i2} + q_3^{i2}} \quad (3)$$

where (q_1^i, q_2^i, q_3^i) are the polarization components of the i -th dipole. The adoption of the $\ell_{2,1}$ norm ensures both the sparsity and the rotational invariance [2].

RESTRICTA is the specialization of the general scheme proposed in [3] for the resolution of MEG inverse problem. The weight matrix is initialized so as to perform the standardization of L as described in [5] in order to mitigate the bias on the estimation of the depth of the activation areas. The weight matrix is updated in every iteration in order to refine the standardization and to correct false positive activation in presence of noisy data.

RESTRICTA can be resumed by the following pseudocode:

```

Inizialization:  $V_i^O = \left( \sqrt{L_{i(1,2,3)}^T (L_{i(1,2,3)} L_{i(1,2,3)}^T + \alpha H_{i(1,2,3)})^+ L_{i(1,2,3)}} \right), \forall i \in [1, n];$ 
 $t \in \mathbb{R};$ 
WHILE (ctrl)
     $\hat{Q} = \min_Q \|B - LVQ\|_2^2 + \tau \|Q\|_{2,1}$      with  $V = \text{diag}(V_i^O);$ 
     $V_i^N = \frac{1}{\hat{Q}_{i(1,2,3)} + \epsilon};$ 
    ctrl =  $(\|\hat{Q}\|_1 < t);$ 
     $V_i^O = V_i^O * V_i^N, \forall i \in [1, n];$ 
END
```

The algorithm ends when the desired grade of sparsity is reached

III. RESULTS

The simulations were carried out considering a standard anatomical model of the head as phantom, consisting of a sampling of the scalp and one of the volume of the brain (the latter is executed on a regular grid of 5 mm of step). The configuration of the field sensors is considered the same as the 153-channel MEG system currently operating at the ITAB.

The components of the polarization of the dipoles $\mathbf{Q}(\mathbf{r}_k)$ used for the definition of the matrix \mathbf{L} are oriented in such a way to present a radial component and two components orthogonal to it. This choice is dictated by the need to isolate the magnetically silent component of the elementary dipoles during the simulations, and it is justified by the rotational invariance of the resolution method adopted.

Vectors \mathbf{B} are obtained by solving the direct problem of MEG using sources whose intensity was distributed spatially according to a Gaussian ball ($\sigma = 1.5 \text{ cm}$) centered at 3000 different locations within the brain volume.

As useful parameters to quantify the quality of the estimated solution, we use the following ones: Dipole Localization Error (DLE), Spatial Dispersion (SD) [6] and Area Under the Curve (AUC) [7]. DLE, SD and AUC were calculated for the reconstructions performed with RESTRICTA and compared with those obtained with eLORETA [5] applied to the same data, in order to compare the performance of the algorithm proposed here with those of an algorithm already known in the literature.

The matrix used for the standardization for RESTRICTA and for eLORETA are identical, and the control parameter of the matrix of standardization has been set to: $\alpha = 450$.

In table 1, are reported the mean values and variances of the parameters to vary in the number of iterations (only the first three) of the RESTRICTA and regularization parameter τ , which is taken as the threshold for the step of thresholding the FISTA [8].

Table I - Expected value and variance of: DLE, SD, and AUC for eLORETA and RESTRICTA (1, 2, and 3 iterations; $\tau = 0.01$ and $\tau = 0.75$).

Algorithm	DLE [cm]	SD [cm]	AUC
<i>No noise</i>			
eLORETA	0.94±0.92	2.60±0.09	0.96±0.02
RESTRICTA (1 iter., $\tau = 0.01$)	0.92±0.92	2.60±0.09	0.96±0.02
RESTRICTA (2 iter., $\tau = 0.01$)	0.98±0.70	2.08±0.13	0.97±0.03
RESTRICTA (3 iter., $\tau = 0.01$)	0.98±0.70	1.48±0.18	0.96±0.05
RESTRICTA (1 iter., $\tau = 0.75$)	0.94±0.92	1.82±0.15	0.96±0.03
RESTRICTA (2 iter., $\tau = 0.75$)	0.96±0.72	1.31±0.17	0.86±0.12
RESTRICTA (3 iter., $\tau = 0.75$)	0.96±0.72	1.04±0.18	0.78±0.08
<i>3dB SNR</i>			
eLORETA	3.13±2.98	2.63±0.13	0.94±0.05
RESTRICTA (1 iter., $\tau = 0.01$)	3.26±3.01	2.62±0.13	0.93±0.05
RESTRICTA (2 iter., $\tau = 0.01$)	2.34±2.35	2.16±0.18	0.95±0.05
RESTRICTA (3 iter., $\tau = 0.01$)	2.26±2.32	1.60±0.26	0.93±0.09

RESTRICTA (2 iter., $\tau = 0.75$)	2.22±2.27	1.45±0.32	0.78±0.15
RESTRICTA (3 iter., $\tau = 0.75$)	2.17±2.23	1.10±0.30	0.62±0.09

IV. CONCLUSIONS

The adoption of RESTRICTA ensures that the SD of the estimated activation decreases with increasing the number of iterations, irrespective of the presence or absence of noise. If you use a high value of the regularization parameter (as in the case reported here of $\tau = 0.75$) there is also a decrease in AUC. This is mainly due to the fact that with the progress of iterations it can run in an underestimation of the activation which leads to a deterioration in the overlap with the test activation.

In the absence of noise the mean value of the DLE of RESTRICTA is slightly worse (maximum 0.4 mm) but from the second iteration its variance is about the 30% less than eLORETA. Such behavior does not seem to depend on the value of the regularization parameter.

In the presence of noise there is still the lowering of the variance of the DLE, to which is added a lowering of the average value of the order of 30% compared to eLORETA. Setting a higher regularization factor seems to get a better result.

Ultimately RESTRICTA, through the adoption of a simple decisive scheme, allows to obtain a better estimate of the brain activity, both in terms of spatial localization and of dimension definition.

REFERENCES

- [1] G. Nolte, "The magnetic lead field theorem in the quasi-static approximation and its use for magnetoencephalography forward calculation in realistic volume conductors," *Physics in medicine and biology*, vol. 58, no. 22, pp. 3637-3652, 2003.
- [2] S. Haufe, et al., "Combining sparsity and rotational invariance in EEG/MEG source reconstruction," *NeuroImage*, vol. 52, no. 2, pp. 726-738, 2008.
- [3] E. Candes, M. Wakin, and S. Boyd, "Enhancing sparsity by reweighted ℓ_1 minimization," *Journal of Fourier analysis and applications*, vol. 15, no. 5-6, pp. 877-905, 2008.
- [4] M. Muzi, "Resolution of MEG inverse problem via reweighted ℓ_1 minimization algorithm," *Proceedings of the XIX RiNEm*, pp. 651-655, 2012.
- [5] R. D. Pascual-Marqui et al., "Assessing interactions in the brain with exact low-resolution electromagnetic tomography," *Philosophical Transactions of the Royal Society A: Mathematical, Physical and Engineering Sciences*, vol. 369, no. 1952, pp. 3768-3785, 2011.
- [6] O. Hauk, D. Wakeman, and R. Henson, "Comparison of noise-normalized minimum norm estimates for MEG analysis using multiple resolution metrics," *Neuroimage*, vol. 55, no. 3, pp. 1966-1975, 2011.
- [7] T. Fawcett, "An introduction to ROC analysis," *Pattern recognition letters*, vol. 27, no. 8, pp. 861-875, 2006.
- [8] A. Beck and M. Teboulle, "A fast iterative shrinkage-thresholding algorithm for linear inverse problems," *SIAM Journal on Imaging Sciences*, vol. 2, no. 1, pp. 183-202, 2009.

CYLINDRICAL-WAVE REFLECTION BY PLANE INTERFACES AS A SOLUTION OF THE INHOMOGENEOUS BESSEL EQUATION

Nicola Tedeschi⁽¹⁾

- ⁽¹⁾ Department of Information Engineering, Electronics and Telecommunications, "La Sapienza" University of Rome, via Eudossiana 18, 00184 Roma, Italy
nicola.tedeschi@uniroma1.it

Abstract

In this paper, we present an analytical solution for the spectral integral representing the reflected cylindrical wave at a plane interface. The analytical solution involves the Bessel and Anger-Weber functions, that are solution of the inhomogeneous Bessel differential equation. We compare the analytical expression with the results obtained with a quadrature method previously proposed in the literature, finding very good agreement. Moreover, we find that the quadrature method is affected by some numerical errors in the near field, due to the highly oscillating integral's kernel. We try a physical interpretation of the result obtained connecting it to the well known Image Principle.

Index Terms – Cylindrical waves, electromagnetic scattering, image principle, special functions

I. INTRODUCTION

The reflection of cylindrical waves at planar interfaces is an important topic, in both electromagnetic and acoustic research. The typical application of this problem is to the scattering by cylindrical objects placed near plane interfaces. The Reflected cylindrical Wave (RW) is expressed as a plane-wave spectrum [1]. In the literature, an adaptive quadrature method has been proposed for the numerical evaluation of this integral [2]. Another method, proposed for the integral evaluation, is based on the Fourier expansion of the reflection coefficient in the kernel [3]. This technique allows to compute the homogeneous part of the integral analytically. However, the inhomogeneous part has still to be computed numerically.

In a recent paper, the analytic solution of the spectral integral has been presented, involving the Anger-Weber functions, solutions of the inhomogeneous Bessel differential equation [4]. The solution has been validated by comparison with the adaptive quadrature method and it shows very good behavior especially in the near field where the numerical solution is affected by strong errors.

II. THE GENERALIZED IMAGE PRINCIPLE

The Reflected cylindrical Wave (RW) has been introduced in the scattering by a circular cylinder placed near a plane interface. We consider a reference frame (x, z) and a plane interface, parallel to the z -axis, between a medium 1, with relative permittivity and permeability ϵ_1 and μ_1 , respectively, and a medium 2, with relative permittivity and permeability ϵ_2 and μ_2 , respectively. We normalize the coordinates with respect to the wave number of medium 1: $\xi = k_1 x$ and $\zeta = k_1 z$. If we consider a cylindrical wave of order m propagating in medium 1, the RW can be expressed by the following spectral integral [1]:

$$RW_m(\xi, \zeta) = \frac{1}{2\pi} \int_{-\infty}^{+\infty} R_{E/H}(n_{\parallel}) \widehat{CW}_m(\xi, n_{\parallel}) \exp(i\zeta n_{\parallel}) dn_{\parallel} \quad (1)$$

where: n_{\parallel} is the component parallel to the interface of the wave vector normalized with respect to the wave number of the medium, $R_{E/H}$ is the Fresnel reflection coefficient, for either E or H polarization, respectively, and \widehat{CW}_m is the plane-wave spectrum of a cylindrical function presented in the literature in both the lossless and the lossy case [1]. In [4], an analytical evaluation of the integral (1) has been presented. To obtain the solution, it is needed to expand the reflection coefficient $R_{E/H}$ in series. Unfortunately, the reflection coefficients, in either E or H polarization, cannot be expanded in Laurent series in the whole complex plane because of a polar singularity away from the real axis. On the other hand, we are interested in the values of the function only on the real axis, where the function does not have singularities. The idea is to perform a conformal mapping of the function to transform the real axis into a circumference away from the singularities. In [4], a suitable conformal mapping has been proposed, and the following expression for the RW has been obtained:

$$RW_m(\rho, \theta) = \sum_{k=0}^{\infty} R_{2k}^{E/H} [F_{m-2k}(\rho, \theta) + (-1)^m F_{-m-2k}(\rho, -\theta)] \quad (2)$$

where ρ and θ are the normalized radius and angle of a polar reference frame on the plane (ξ, ζ) . The function $F_n(\rho, \theta)$ is defined as follows:

$$F_n(\rho, \theta) = \exp(in\theta) \sum_{k=-\infty}^{+\infty} [a_{n,k}(\theta) J_k(\rho)] - iA_{-n}(\rho) \quad (3)$$

where $J_k(\rho)$ is the Bessel function of the first kind and order k , and $A_n(\rho)$ is the Anger-Weber function of order n [5]. Moreover, the coefficients of the series are the following:

$$a_{n,k}(\theta) = \frac{2}{\pi} i^{k-n} \exp \left[i(k+n) \left(\frac{\pi}{4} - \frac{\theta}{2} \right) \right] \left(\frac{\pi}{4} + \frac{\theta}{2} \right) \operatorname{sinc} \left[(k+n) \left(\frac{\pi}{4} + \frac{\theta}{2} \right) \right] \quad (4)$$

The analytical expression (5) is of great importance. In fact, up to now, the only way to evaluate the function (1) was by a quadrature

method. Moreover, the expression (6), allows us to physically interpret the analytical solution. In fact, the RW is represented as a superposition of solutions of the homogeneous and inhomogeneous Bessel differential equation. If we consider a cylindrical wave, generated at distance χ above the interface, we can see that the reflected wave is centered at distance χ below the interface. In fact, each elementary wave of the spectrum propagates for a distance χ towards the interface, it is multiplied by the reflection coefficient and it propagates again towards the origin of the reference frame and, after it, continues to propagate in the positive ξ direction. The solution suggests that the interface can be substituted by a cylindrical source placed symmetrically at the origin of the incident cylindrical wave, with respect to the interface, in the same way we proceed in the presence of an electric charge in front of a perfectly conducting plane in the well known Image Principle. In this sense, we call this solution a Generalized Image Principle for cylindrical waves.

III. NUMERICAL RESULTS

In this section, we present some comparisons between the RW calculated with the analytical formula (5) and with the adaptive quadrature method presented in the literature [2]. In Fig. 1a, the amplitude of the RW of order 0 is shown as a function of the angle θ , for a radius $\rho = 0.6$. We see that the solution obtained with the quadrature method strongly oscillates around the analytical solution. This result means that the numerical errors made with the quadrature method in the near field are not negligible. Moreover, up to now, it was not possible to demonstrate these numerical errors, because it was not possible to evaluate the RW with other techniques. In Fig. 1b, the same amplitude of Fig. 1a is shown, but with a radius $\rho = 0.3$. Here we see that the oscillations increase when the radius decreases. Furthermore, for angles near to $\pm\pi/2$, the oscillations become so large that we have been obliged to cancel the extreme values of the function in the graphic because they go out of the scale.

IV. CONCLUSIONS

In this paper, we considered the Generalized Image Principle recently proposed in the literature, to evaluate analytically the reflection of a cylindrical wave by a plane interface between two dielectrics. We provided some comparisons between the reflected cylindrical wave evaluated with the analytic formula and with a quadrature method previously presented in the literature. We found a good agreement

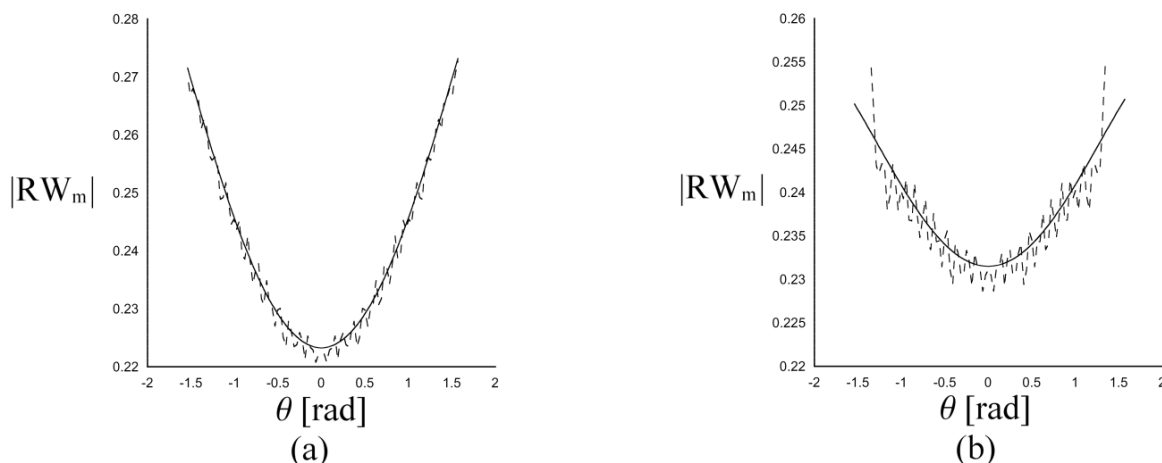


FIG. 1 – Amplitude of the RW of order 0, when medium 1 is a vacuum and medium 2 has $\varepsilon_2 = 10$. The RW is computed in $\rho = 0.6$ (a), and in $\rho = 0.3$ (b). We applied the analytic formula (5) (solid line) and the quadrature method proposed in the literature [2] (dashed line).

between the two methods, but we noted that the quadrature method shows some numerical errors for high and low values of the radius.

We consider that the analytical solution of the RW spectral integral is important from the point of view of both electromagnetic theory and applications. Moreover, the possibility to recognize a physical interpretation of the RW as a wave generated by cylindrical sources below the interface is of interest in itself.

REFERENCES

- [1] R. Borghi, F. Gori, M. Santarsiero, F. Frezza, and G. Schettini, "Plane-wave scattering by a perfectly conducting circular cylinder near a plane surface: cylindrical-wave approach," *Journal of the Optical Society of America A*, 13(3), 483-493, Mar. 1996.
- [2] R. Borghi, F. Frezza, M. Santarsiero, C. Santini, and G. Schettini, "A quadrature algorithm for the evaluation of a 2D radiation integral with highly oscillating kernel," *Journal of Electromagnetic Waves and Applications*, 14(10), 1353-1370, Oct. 2000.
- [3] P. Pawliuk and M. Yedlin, "Scattering from cylinders near a dielectric half-space using a general method of images," *IEEE Transactions on Antennas and Propagation*, 60(11), 5296-5304, Nov. 2012.
- [4] F. Frezza and N. Tedeschi, "A generalized image principle for cylindrical waves," *Optics Letters*, accepted paper.
- [5] F.W. Olver, D.W. Lozier, R.F. Boisvert, and C.W. Clark, *NIST handbook of mathematical functions*, New York, Cambridge University Press, 2010, pp. 295-298.

LEAKY WAVE INTERACTIONS WITH A PLANAR INTERFACE BETWEEN DISSIPATIVE MEDIA

N. Tedeschi⁽¹⁾

⁽¹⁾ Department of Information Engineering, Electronics and Telecommunications, “La Sapienza” University of Rome, Via Eudossiana 18, 00184 Rome, Italy
nicola.tedeschi@uniroma1.it

Abstract

We present the analysis of the interaction of inhomogeneous plane waves with planar interfaces between dissipative media. We consider a leaky-wave antenna proposed in the literature, based on a stub-loaded rectangular waveguide. We simulate the antenna on a FEM software, validating the results with the measurements presented in the literature. Moreover, we consider the incidence of the leaky wave generated by the antenna on a dielectric-conductor interface and we compute the transmission angles of both the phase and attenuation vectors with the theoretical analysis and with the simulations, finding a very good agreement.

Index Terms – Inhomogeneous waves, Leaky waves, Lossy media, Plane interfaces,

I. INTRODUCTION

The interaction of inhomogeneous plane waves with planar interfaces is a classical topic in the electromagnetic research [1,2]. In particular, the canonical problem is the incidence of a uniform plane wave at a dielectric-conductor interface, where in the conducting medium an inhomogeneous plane wave is transmitted. However, the case of inhomogeneous plane wave incidence on an interface between lossy media has been studied in more recent works [3,4]. In [4], an analytical expression for the transmitted angles of the phase and attenuation vectors has been presented. In [5], a careful study of the power transmitted in a lossy medium has been performed. Moreover, in [6], the analytical expressions of the critical angles for which the transmitted either phase or attenuation vectors are purely parallel to the interface have been obtained. Unfortunately, to the best of my knowledge, all the results presented in the literature on this topic are obtained in the theoretic hypothesis of the incidence of an inhomogeneous plane wave with an infinite wave front. Now, as it is well known, the inhomogeneous waves are improper solutions of the Maxwell equations, due to the growing real exponential in their expressions. Therefore, the results presented may be invalid in realistic scenarios.

In the present paper, we want to validate the theoretical results obtained in [4-6] by considering realistic scenarios involving inhomogeneous waves. We consider the leaky-wave antenna proposed in [8]. This antenna has been designed by the analytical study of the structure and the results have been validated by experimental measurements. We reproduce this antenna on a Finite Element Method (FEM) based software, and we make a comparisons between the results of the simulation and the measurements presented in the literature. Afterwards, we consider a dielectric-conducting interface above this antenna and we consider the transmitted wave in the lossy medium. We compare the transmitted angles of both the phase and attenuation vectors with the theoretical predictions.

In Section II, we present the simulations of the leaky-wave antenna proposed in [8], and we compare the transmitted angles of the inhomogeneous wave with the theoretical results. In Section III, the conclusions are drawn.

II. THE LEAKY-WAVE ANTENNA

Let us consider the leaky-wave antenna proposed in [8]. The antenna is a stub-loaded rectangular waveguide. The dimensions of the wave guide are $a = 23.00$ mm, $b = 11.95$ mm. The stub guide length is $c = 15.65$ mm. The stub guide is terminated with very wide flanges (essentially an infinite ground plane). The antenna works in a band between 8 GHz and 12 GHz. We reproduced the leaky-wave antenna on the FEM based software and simulated it in free space. In Fig. 1a, a comparison between the components parallel to the antenna of the phase vectors obtained from the simulations and from both the measures and the theoretical prediction presented in [8] is shown. Similarly, in Fig 1b, a comparison between the components parallel to the antenna of the attenuation vectors is shown. We can see that the simulation is in a very good agreement with the measurements, better than the theoretical prediction. The small difference between the simulations and the measures is because of some reflections of the inhomogeneous wave on the Perfectly Matched Layer on the edge of the computational domain. These reflections affect mainly the attenuation because of its small absolute value. At this point, we placed an interface 2λ above the leaky-wave antenna with a medium with relative permittivity $\varepsilon = 3 - j0.5$. As it is well known, the leaky-wave antenna is able to scan different angles of radiation simply by changing the operating frequency. Therefore, we considered different angles of incidence of the inhomogeneous wave by varying the frequency from 8 GHz to 12 GHz. The problem of the incidence of an inhomogeneous wave at a dielectric-conducting interface can be solved again with the results of [4]. We computed the transmitted angles of the phase and attenuation vectors and compared them with the results of the FEM

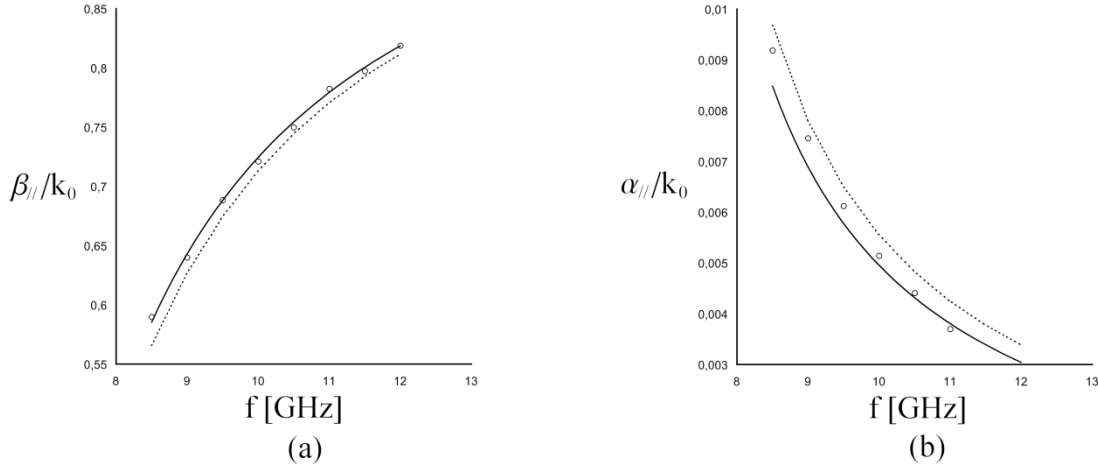


FIG. 1 – Comparison between the components parallel to the antenna of the phase (a) and attenuation (b) vectors, obtained with the FEM code (solid line), with the theory (dashed line), and by the measures in [8] (circles).

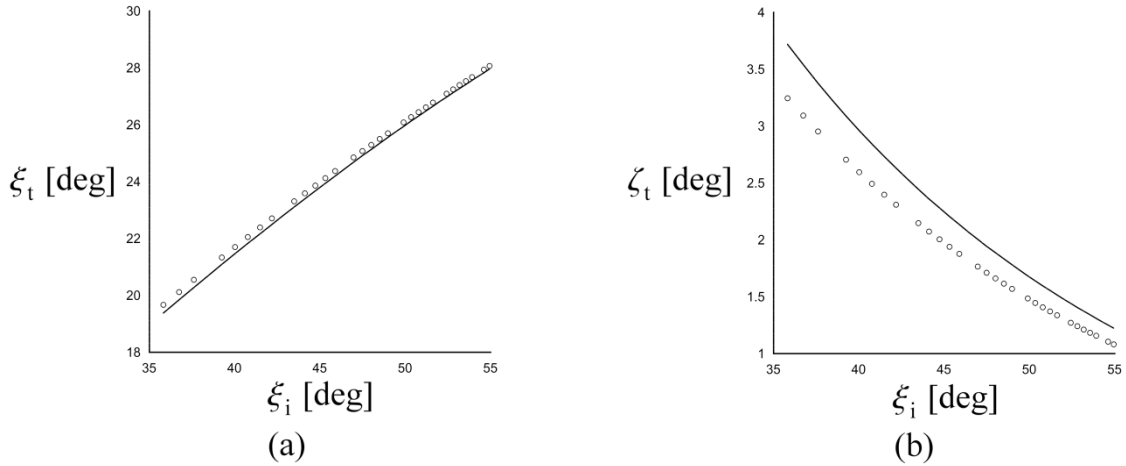


FIG. 2 – Comparison between the transmitted angles of the phase (a) and attenuation (b) vectors, as a function of the leaky-wave incident angle, obtained with the theoretical analysis (circles) and by the simulations with the FEM code (solid line).

simulation. In Figs. 2, the comparisons between these transmitted angles are shown. We can see again a very good agreement between the simulation and the theory. This result is important because, in our knowledge, this is the first demonstration of the validity of the results presented in [4-6] in a realistic scenario.

III. CONCLUSIONS

In this paper, we consider a realistic scenario of inhomogeneous-wave interaction at the planar interface with a dissipative medium. We considered a leaky-wave antenna proposed in the literature and we simulated it with a FEM code. After the validation of the simulation, we considered the incidence of the leaky wave, generated by the antenna, at the interface with a dissipative medium. We compared the theoretical

prediction for the transmitted angle of the phase and the attenuation vectors with the results of the simulations, obtaining a good agreement. The results found validate the theoretical analysis carried out in [4-6], so they validate many of the considerations done in such papers on the power transmission in lossy media and on the possibility of deeply penetrating into a conducting medium.

ACKNOWLEDGEMENT

This paper is devoted to the Memory of Prof. Arthur A. Oliner.

REFERENCES

- [1] J.A. Stratton, *Electromagnetic theory*, New York, McGraw-Hill, 1941, pp. 500-511.
- [2] R.B. Adler, L.J. Chu, and R.M. Fano, *Electromagnetic energy transmission and radiation*, New York, Wiley, 1960, pp. 402-449.
- [3] R.D. Radcliff and C.A. Balanis, "Modified Propagation Constants for Nonuniform Plane Wave Transmission Through Conducting Media," *IEEE Transactions on Geoscience and Remote Sensing*, 20(7), pp. 408-411, Jul. 1982.
- [4] J.E. Roy, "New Results for the Effective Propagation Constants of Nonuniform Plane Wave at the Planar Interface of Two Lossy Media," *IEEE Transactions on Antennas and Propagation*, 51(6), pp. 1206-1215, Jun. 2003.
- [5] F. Frezza and N. Tedeschi, "On the Electromagnetic Power Transmission Between Two Lossy Media: Discussion," *Journal of the Optical Society of America A*, 29(11), pp. 2281-2288, Nov. 2012.
- [6] F. Frezza and N. Tedeschi, "Deeply Penetrating Waves in Lossy Media," *Optics Letters*, 37(7), pp. 2616-2618, Jul. 2012.
- [7] T. Tamir, "Inhomogeneous waves types at planar interfaces: III—Leaky waves," *OPTIK*, 38 (3), pp. 269-297, Mar. 1973.
- [8] M. Tsuji, H. Shigesawa, F. Frezza, P. Lampariello, and A.A. Oliner, "A versatile leaky-wave antenna based on stub-loaded rectangular waveguide: part III-comparisons with measurements," *IEEE Transactions on Antennas and Propagation*, 46(7), pp. 1047-1055, Jul. 1998.

FAST TUNABLE FIBER OPTICAL FREQUENCY COMB BASED ON CASCADED FOUR-WAVE MIXING

F. Chiarello

Department of Information Engineering, University of Padova
Via Gradenigo 6/b, 35131 Padova, Italy

fabrizio.chiarello@dei.unipd.it

Abstract

We present a fiber optical frequency comb realized exploiting cascaded four-wave mixing with fast tunable teeth spacing achieved by means of the time-dispersion technique.

Index Terms – optical frequency comb, nonlinear fiber optics, tunable infrared optical source

I. INTRODUCTION

Recently, optical frequency combs (OFCs) have been gathering conspicuous attention because they are key components in several applications in communication, signal processing, metrology and spectroscopy. The key characteristics of an OFC include frequency separation, power equalization, spectral purity, phase locking orthogonality (needed for some coherent applications like OFDM), tunability across a given spectral region, long term stability and, in some cases, locking to an absolute frequency reference. Currently, no OFC provides all these characteristics simultaneously.

The most straightforward OFCs are bulk mode-locked lasers [1] which are extremely accurate devices, though large and cumbersome. More compact solutions that have appeared are monolithic semiconductor mode-locked lasers [2], or optical parametric oscillators based on high Q-factor monolithic resonators [3,4] like microtoroids, silica microspheres, silicon or silicon nitride microrings. In monolithic cavities high spectral purity can be achieved but the main drawback is that the comb frequency spacing is often fixed by the cavity properties. But even when tunability is achieved, like in parametric oscillators based on high Q-factor monolithic microresonators [3], the tuning speed is small and often realized through thermal effects [5].

Tunable OFCs can be also achieved in optical fibers, by means of cascaded four-wave mixing (CFWM) [6] in single pass, doubly CW pumped fiber amplifier [7], or through a two-stage amplifier exploiting phase-sensitive amplification [8,9]. Those setups are very simple, but OFC spectral purity is strongly influenced by the frequency and phase stability of the pumps [10] that should be realized through a feedback stabilization. In Fabry-Perot resonators [11] Brillouin scattering limits the spectral purity. The use of doubly pumped ring cavities prevents the growth of Brillouin oscillations, but still presents limitations in

[12] has very recently been realized, but exploiting intracavity tunable filters, thus limiting the comb reconfiguration time.

Here, we present an OFC obtained in a singly pumped fiber CFWM resonator [13]. By using the time-dispersion tuning (TDT) technique, we can achieve fast tuning of the frequency spacing (0.4 nm/ μ s).

II. EXPERIMENTAL SETUP

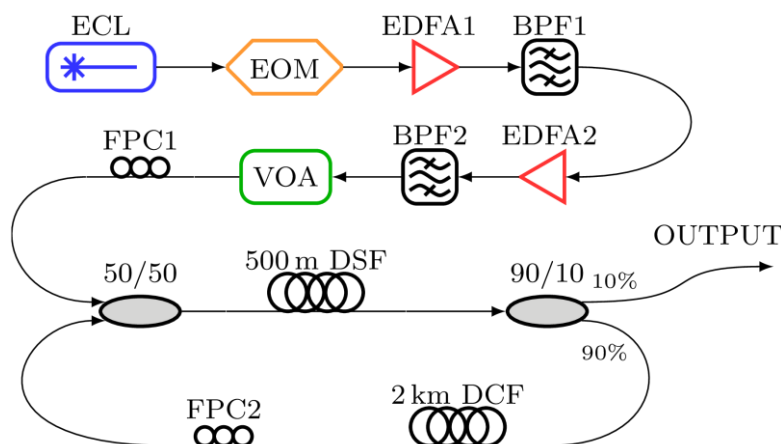


FIG. 1 – Experimental setup.

The experimental setup is shown in Fig. 1. A train of optical pulses with a duration of 1 ns and a repetition rate f_p of about 2.31 MHz is carved from the beam emitted by the external cavity laser (ECL) through an electro-optic modulator (EOM), driven by an electrical pulse generator. Optical pulses are then amplified by erbium-doped fiber amplifiers (EDFAs) operating in strong saturation, so that the output pulse peak power can be up to a few tens of Watts. The band pass filters (BPFs) have a 3 dB bandwidth of 3.5 nm and are centered at the pump wavelength to reduce the amplified spontaneous emission (ASE) noise. Finally, the variable optical attenuator (VOA) controls the pump power level while the fiber polarization controller (FPC1) fixes the pump state of polarization (SOP) entering the loop through a 50/50 power coupler. The nonlinear fiber is a spool of 500 m of dispersion-shifted fiber (DSF), with the average zero-dispersion wavelength (ZDW) around 1548 nm. The pump wavelength is set above the ZDW to achieve parametric amplification in a large band around the pump wavelength. The measured nonlinear coefficient is $\gamma \approx 2 \text{ W}^{-1}\text{km}^{-1}$. Beyond the parametric amplification stage, 10% of power is directed to the output, while the remaining 90% is fed back into the loop through a 2 km long dispersion-compensating fiber (DCF), with a dispersion coefficient of $\beta_2 \approx 131 \text{ ps}^2/\text{km}$. FPC2 controls the alignment of the SOP of the circulating signal with respect to that of the input pump.

III. RESULTS

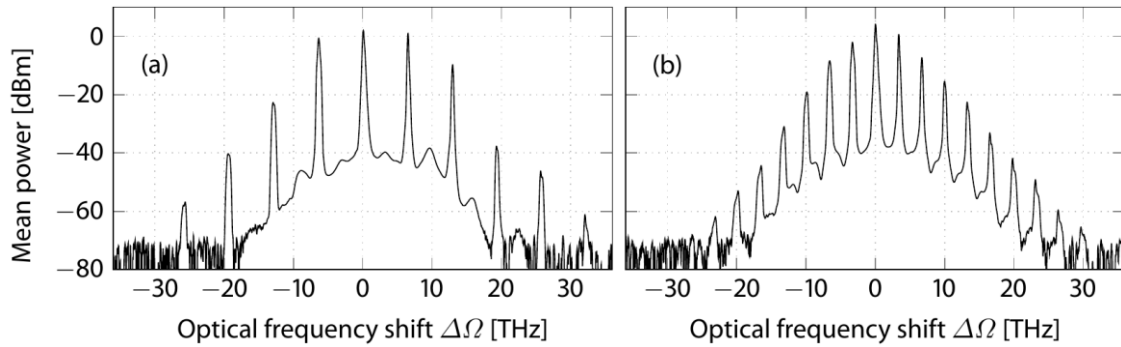


FIG. 2 – Spectra of the OFC for two synchronously pumped wavelengths.

Fig. 2 shows the spectra obtained by pumping slightly above the ZDW and through the TDT technique. TDT exploits the wavelength dependence of the group velocity in the ring to synchronize only a narrow band of the feedback signal with a new incoming pump pulse. The synchronously pumped wavelength is selected to be very close to the pump wavelength. In this case efficient CFWM occurs and an OFC is obtained. In Fig. 2 two examples of different frequency spacing $\Delta\Omega$ and different numbers of Stokes waves are shown [(a) $\Delta\Omega$ 6.4 THz and four Stokes waves; (b) $\Delta\Omega$ 3.3 THz and seven Stokes waves]. The frequency spacing is controlled by the shift Δf of the repetition rate of the pump through

$$\Delta\Omega \simeq \frac{\Delta f}{\beta_2 f_p v_g}, \quad (1)$$

where v_g is the group velocity. For the DSF used in the experiments, parametric gain drops significantly for a pump-signal frequency detuning smaller than 2.3 THz, so no OFC formation has been observed below such value.

Differently from [7], coherence between comb teeth is assured by the CFWM process and the fact that a single pump is injected. The first remarkable property of the obtained OFC is the possibility of very fast tuning, the speed depending on the sweep rate with which Δf is changed. The second is that the obtained high frequency modulation $\Delta\Omega$ is set by a low frequency electrical signal Δf ; therefore it can be locked to microwave frequency standards.

IV. CONCLUSIONS

We presented an OFC based on CFWM extending over 80nm. Exploiting the TDT technique, the frequency spacing of the comb may be quickly tuned without modifying the teeth bandwidth (a useful property in applications such as OFDM). Moreover, an oscillation at very high frequency can be locked directly to a microwave frequency standard.

ACKNOWLEDGEMENTS

This research was supported by the University of Padova (project “Nan

University (project ROAD-NGN, PRIN 20102KAZKN_005) and of Foreign Affairs (Direzione Generale per la Promozione del Sistema Paese) and was held within the agreement with ISCTI.

REFERENCES

- [1] T. Udem, R. Holzwarth, and T. W. Hänsch, “Optical frequency metrology”, *Nature*, vol. 416, no. 6877, pp. 233–237, Mar. 2002.
- [2] E. U. Rafailov, M. A. Cataluna, and W. Sibbett, “Mode-locked quantum-dot lasers”, *Nat Photon*, vol. 1, no. 7, pp. 395–401, Jul. 2007.
- [3] P. Del’Haye, A. Schliesser, O. Arcizet, T. Wilken, R. Holzwarth, and T. J. Kippenberg, “Optical frequency comb generation from a monolithic microresonator”, *Nature*, vol. 450, no. 7173, pp. 1214–1217, Dec. 2007.
- [4] J. S. Levy, A. Gondarenko, M. A. Foster, A. C. Turner-Foster, A. L. Gaeta, and M. Lipson, “CMOS-compatible multiple-wavelength oscillator for on-chip optical interconnects”, *Nat Photon*, vol. 4, no. 1, pp. 37–40, Jan. 2010.
- [5] P. Del’Haye, T. Herr, E. Gavartin, M. L. Gorodetsky, R. Holzwarth, and T. J. Kippenberg, “Octave Spanning Tunable Frequency Comb from a Microresonator”, *Phys. Rev. Lett.*, vol. 107, no. 6, p. 063901, Aug. 2011.
- [6] C. J. McKinstrie and M. G. Raymer, “Four-wave-mixing cascades near the zero-dispersion frequency”, *Opt. Express*, vol. 14, no. 21, pp. 9600–9610, Oct. 2006.
- [7] A. Cerqueira Sodre, J. M. Chavez Boggio, A. A. Rieznik, H. E. Hernandez-Figueroa, H. L. Fragnito, and J. C. Knight, “Highly efficient generation of broadband cascaded four-wave mixing products”, *Opt. Express*, vol. 16, no. 4, pp. 2816–2828, Feb. 2008.
- [8] R. Tang, J. Lasri, P. S. Devgan, V. Grigoryan, P. Kumar, and M. Vasilyev, “Gain characteristics of a frequency nondegenerate phase-sensitive fiber-optic parametric amplifier with phase self-stabilized input”, *Opt. Express*, vol. 13, no. 26, pp. 10483–10493, Dec. 2005.
- [9] A. Gershikov and G. Eisenstein, “Narrowband phase sensitive fiber parametric amplifier”, *Opt. Lett.*, vol. 37, no. 15, pp. 3204–3206, Aug. 2012.
- [10] F. C. Cruz, “Optical frequency combs generated by four-wave mixing in optical fibers for astrophysical spectrometer calibration and metrology”, *Opt. Express*, vol. 16, no. 17, pp. 13267–13275, Aug. 2008.
- [11] D. Braje, L. Hollberg, and S. Diddams, “Brillouin-Enhanced Hyperparametric Generation of an Optical Frequency Comb in a Monolithic Highly Nonlinear Fiber Cavity Pumped by a cw Laser”, *Phys. Rev. Lett.*, vol. 102, no. 19, p. 193902, May 2009.
- [12] N. A. Cholan, M. H. Al-Mansoori, A. S. M. Noor, A. Ismail, and M. A. Mahdi, “Multi-wavelength generation by self-seeded four-wave mixing”, *Opt. Express*, vol. 21, no. 5, pp. 6131–6138, Mar. 2013.
- [13] F. Chiarello, L. Palmieri, A. Galtarossa, and M. Santagiustina, “Widely time-dispersion-tuned fiber optical oscillator and frequency comb based on multiple nonlinear processes”, *Opt. Lett.*, vol. 38, no. 22, pp. 4621–4624, Nov. 2013.

PHASELESS MICROWAVE IMAGING OF DIELECTRIC TARGETS: A COMBINED TWO-PROBES/INEXACT-NEWTON METHOD

S. Costanzo⁽¹⁾, A. Borgia⁽¹⁾, G. Di Massa⁽¹⁾, M. Pastorino⁽²⁾, A. Randazzo⁽²⁾

⁽¹⁾Department of Informatics, Modeling, Electronics and System
Engineering (DIMES), University of Calabria
Via P. Bucci cubo 42C, 87036 Rende (CS), Italy
{costanzo; dimassa}@deis.unical.it

⁽²⁾Department of Electrical, Electronic, Telecommunications
Engineering, and Naval Architecture (DITEN), University of Genoa
Via Opera Pia 11A, 16145, Genova, Italy
{matteo.pastorino; andrea.randazzo}@unige.it

Abstract

A combined strategy for the reconstruction of dielectric targets at microwave frequencies is proposed. It is based on the hybridization of a two-probes measurement approach, which includes a phase-retrieval technique, with an inverse scattering method based on an inexact-Newton algorithm. The proposed strategy is aimed at taking advantages of the good regularization capabilities of the considered inverse scattering method with the effectiveness of the two-probes approach toward the idea of developing a simple and low-cost imaging setup. The formulation of the proposed combined method is reported together with some experimental validations.

Index Terms – Microwave imaging, dielectric targets, phaseless measurements, inverse scattering.

I. INTRODUCTION

This paper deals with microwave imaging, where two research directions can be essentially highlighted, namely the development of theoretical/numerical methods for data inversion and image construction, and the design and realization of apparatuses for illuminating the unknown target and measuring the scattered electric field. With reference to the second aspect, some proposed prototypes can be rather complex and expensive, and the relative usage can be reasonable only for certain applications (e.g., in medical imaging). In other industrial applications there is the need for simple and chip apparatuses. The exploitation of the two-probes measurement approach proposed in [1]-[2] can provide an interesting solution at this regards. Toward this idea, the present paper discusses a hybrid approach, which combines the above mentioned technique with a recently developed inversion procedure based on an inexact-Newton method [3]. The

preliminary idea of this approach has been formulated in [4]. In the present paper, the method is described and results concerning its experimental validation are reported.

II. OUTLINE OF MATHEMATICAL FORMULATION

Let us consider the configuration in Fig. 1. An investigation area D_{inv} is illuminated by a known transverse magnetic (TM) electromagnetic field (a $e^{j\omega t}$ time dependence is assumed). The field scattered by the target is collected by two identical probes (separated by a distance $d = i\lambda_0/2, i \geq 1$) simultaneously moving along the observation domain D_{obs} .

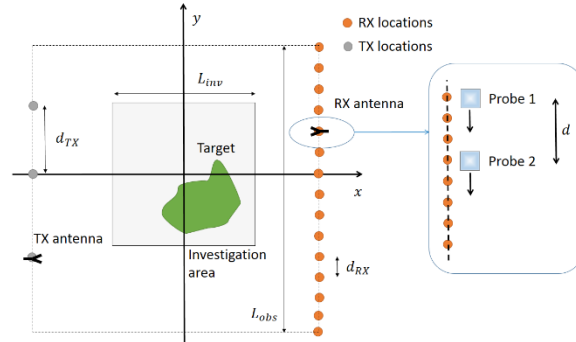


FIG. 1 – Schematic representation of the imaging configuration.

Phaseless near-field data are measured with the simple microstrip circuit described in [1], and subsequently processed for obtaining the phase shifts between the probes, i.e., [1]-[2]:

$$\Delta\varphi = \text{tg}^{-1} \left[\frac{|V_1 + jV_2|^2 - |V_1|^2 - |V_2|^2}{|V_1 + V_2|^2 - |V_1|^2 - |V_2|^2} \right] \quad (1)$$

where $V_1 = |V_1|e^{j\varphi_1}$, $V_2 = |V_2|e^{j\varphi_2}$ are the complex signals at the output of probes and $\Delta\varphi = \varphi_1 - \varphi_2$. By using eq. (1), a set of complex field values, determined apart from a set of unknown phase shifts, is computed. Such phase shifts are retrieved by adopting a nonredundant field representation and applying a suitable minimization algorithm [1]-[2]. The obtained complex values of the scattered electric field, \tilde{e}_{scatt} , are used as input data for the IN-based inversion procedure. Such approach solves in a regularized sense the following equation:

$$\tilde{e}_{scatt}(\mathbf{r}) = G_d c(\mathbf{r}) (I - G_s c)^{-1} E_{inc}(\mathbf{r}) \quad (2)$$

where $c(\mathbf{r}) = \epsilon_r(\mathbf{r}) - 1$, being ϵ_r the relative complex dielectric permittivity, $G_{d/s} f(\mathbf{r}) = -k_0^2 \int_{D_{inv}} f(\mathbf{r}') g_0(\mathbf{r}, \mathbf{r}') d\mathbf{r}'$, $\mathbf{r} \in D_{obs/inv}$, being $k_0^2 = \omega^2 \epsilon_0 \mu_0$, and g_0 is the free-space Green's function. As detailed in [3], the INM is based on an inner-outer solving scheme. In the outer steps, eq. (2) is iteratively linearized; in the inner ones, the obtained linear problems are solved, in a regularized sense, by means of a truncated Landweber algorithm in order to find an update to the current solution.

III. EXPERIMENTAL RESULTS

The two-probes measurement strategy described in [1]-[2] is applied to realize an imaging setup with two receiving antennas collecting the scattered field on three sides of a square investigation domain (excluding the side containing the transmitting antenna) having length equal to 39 cm. A number $M = 53$ measurement points $\lambda/4$ spaced at a frequency $f = 10\text{ GHz}$ is considered, with $S = 9$ different positions of the source antenna spaced by a distance equal to 9.75 cm. Standard X-band horn are assumed as both transmitting and receiving antennas, and a wood cylinder with length approximately equal to 60 cm ($\sim 20\lambda$ @ 10 GHz) and square section of side equal to 4 cm is considered as test target.

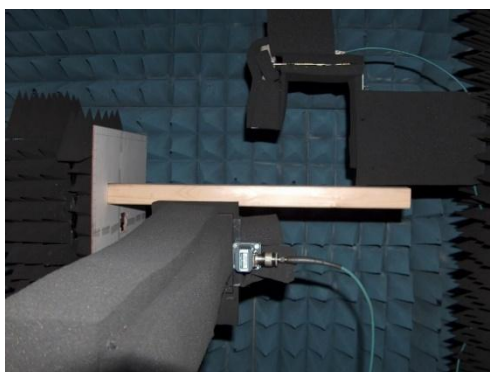


FIG. 2 – Measurement setup at University of Calabria.

Phaseless measurements are performed into the Microwave Laboratory at the University of Calabria, as illustrated in Fig. 2, with an example of measured data reported in Fig. 3, where the field amplitude (Fig. 3(a)) and the comparison between exact and retrieved field phase (Fig. 3(b)) are shown. The application of the proposed hybrid method gives the dielectric permittivity reconstruction illustrated in Fig. 4, where quite similar results can be observed from both complex and phaseless input data.

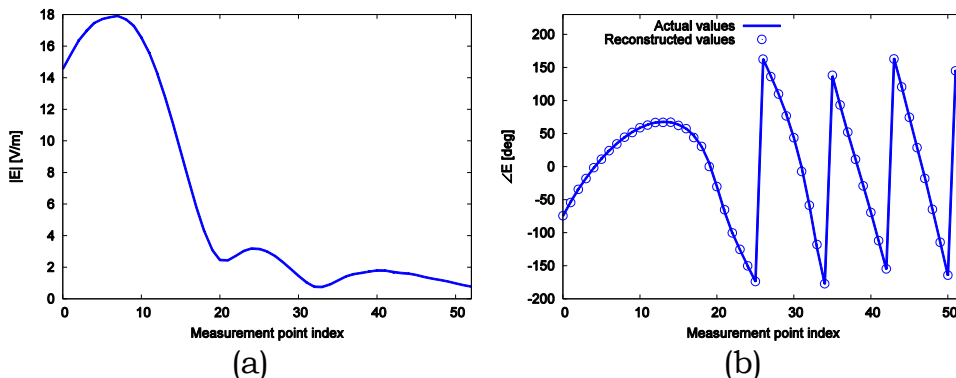


FIG. 3 – (a) Measured amplitude and (b) comparison between measured and retrieved phase (second source position).

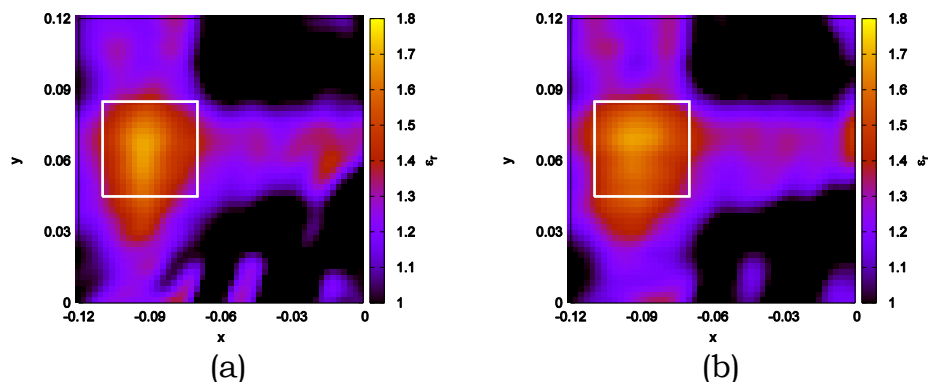


FIG. 4 – Reconstructed dielectric profile inside the investigation domain: (a) phaseless input data and (b) complex input data.

IV. CONCLUSIONS

The inverse scattering problem for the dielectric reconstruction of two-dimensional dielectric targets has been proposed. It is based on a combined strategy in which a two-probes measurement approach including a phase-retrieval technique is used together with a regularization algorithm based on an inexact-Newton algorithm. In this way, the good regularization properties of the inversion method can be exploited without the need of measuring the complex values of the field scattered by the target, resulting in a simple and inexpensive imaging setup. The formulation of the approach has been described and some validations, based on a preliminary experiment with real data, have been provided. Further evaluations will be devoted to further assess the effectiveness and the limitations of the method, by using more complex scenarios.

V. REFERENCES

- [1] S. Costanzo, G. Di Massa, and D. Migliore, "A Novel Hybrid Approach for Far-Field Characterization from Near-Field Amplitude-Only Measurements on Arbitrary Scanning Surfaces," *IEEE Trans. Antennas Propag.*, vol. 53(6), pp. 1866–1874, June 2005.
- [2] S. Costanzo and G. Di Massa, "Wideband Phase Retrieval Technique from Amplitude-Only Near-Field Data," *Radioengineering*, vol. 17(4), pp. 8–12, Dec. 2008.
- [3] G. Oliveri, A. Randazzo, M. Pastorino, and A. Massa, "Electromagnetic Imaging Within the Contrast-Source Formulation by Means of the Multiscaling Inexact Newton Method," *J. Opt. Soc. Am. A*, vol. 29(6), pp. 945–958, May 2012.
- [4] S. Costanzo, G. Di Massa, M. Pastorino, A. Randazzo, A. Borgia, "Non-invasive microwave characterization of inhomogeneous dielectric scatterers," in: S. Costanzo, Ed., *Microwave Materials Characterization*, InTech, 2012, pp. 37–50.

RADAR ACTIVITY AT UNIVERSITY OF CALABRIA

S. Costanzo, G. Di Massa, F. Spadafora, A. Raffo, A. Borgia, A. Costanzo, L. Morrone

DIMES, Università della Calabria
Via P. Bucci, cubo 41D, 87036 Rende (CS), Italy
costanzo@deis.unical.it

Abstract

Radar activity performed at University of Calabria in the framework of a national project on “Landslides Early Warning” is described in this contribution. Two compact and low-cost radar configurations, the first one based on the adoption of a software radio platform, the second one using a compact Vector Network Analyzer as SFCW scatterometer module, are described. Experimental results are discussed as validation tests to demonstrate the radars range detection capabilities.

Index Terms – Radar, Software Defined Radar, FMCW radar, SFCW radar.

I. INTRODUCTION

Current challenges in the framework of radar researches are mainly devoted to the development of low-cost, compact radar systems, able to provide high resolution capabilities and flexible signal processing techniques with multipurpose features. Recently, a research activity at University of Calabria has been started to address the above requirements in the framework of a national project (PON 01_01503 National Italian Project “Landslides Early Warning”) focused on the monitoring, early warning and mitigation of landslide risk, where the accurate detection of displacements from large areas is of primary importance. When considering standard real aperture radars, limited resolution capabilities, typically of the order of tens meters at high microwave frequencies, can be achieved. To further improve the resolution, synthetic aperture radar techniques and/or interferometric methods are usually adopted, but at the expense of increased signal processing complexity. On the other hand, to achieve penetrating capabilities, high wavelengths should be adopted, at the expense of an increasing size of the required antennas. To face the above difficulties, radar activity at University of Calabria has been addressed to the design of simple and low-cost solutions, by identifying two specific radar configurations: a versatile radar based on an innovative software platform, and a C-band SFCW scatterometer radar adopting a compact structure based on Vector Network Analyzer.

II. SOFTWARE DEFINED RADAR

Software Defined Radar (SDRadar [1]- [3]) represents a new challenge in radar technology, due to the possibility of performing most of the basic operations (i.e. mixing, filtering, modulation) by employing simple software modules, thus providing a strong versatility in terms of signal generation and processing. A software defined FMCW radar architecture, as described in Fig. 1(a), has been developed at University of Calabria to provide a low-cost and compact solution for target detection.

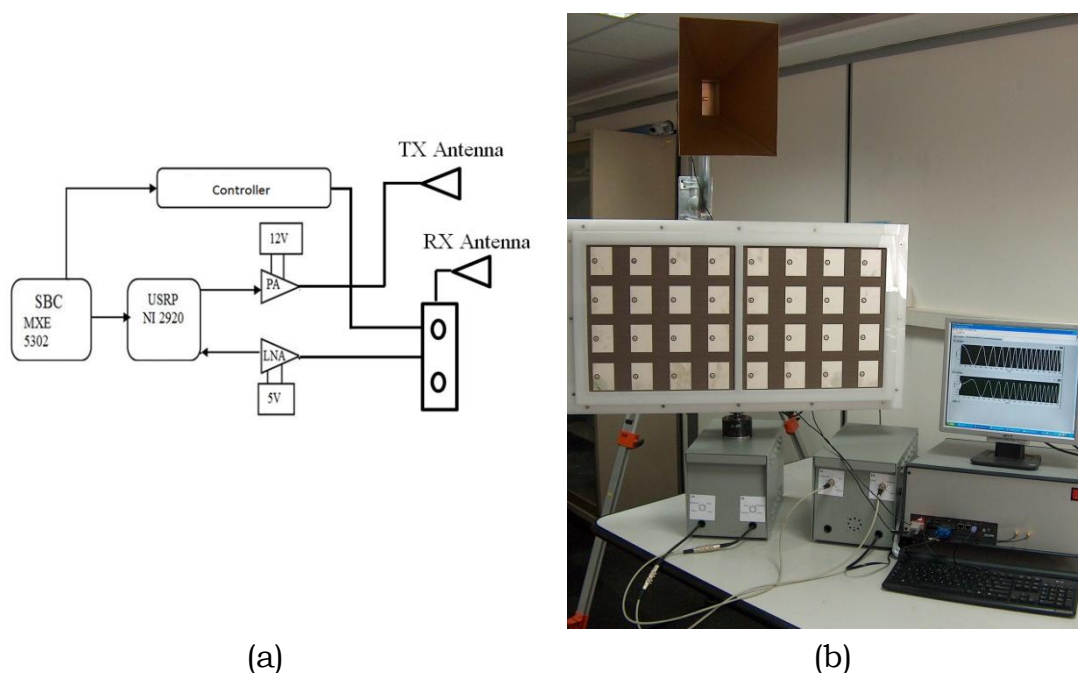


FIG. 1 – Software Defined Radar: (a) block diagram and (b) realized configuration.

The basic idea is to adopt a Universal Software Radio Peripheral (USRP) transceiver, leading to implement by software all required radar modules, namely signal generation, modulation/demodulation, mixer, A/D and D/A conversion and signal processing. A LabView code controlling the USRP operation is implemented on a compact PC (MXE 5302) to give the final configuration illustrated in Fig. 1(b).

Various experimental test have been performed to validate the range detection capabilities of the developed SDRadar, actually able to provide a range resolution equal to 6 m (due to the available bandwidth of 25 MHz), which however can be easily improved by the introduction of higher bandwidth interface modules. An example of accurate target detection is reported in Fig. 2, where a test metal plate positioned 54 m away from the SDRadar system, and covered by vegetation, is properly identified.

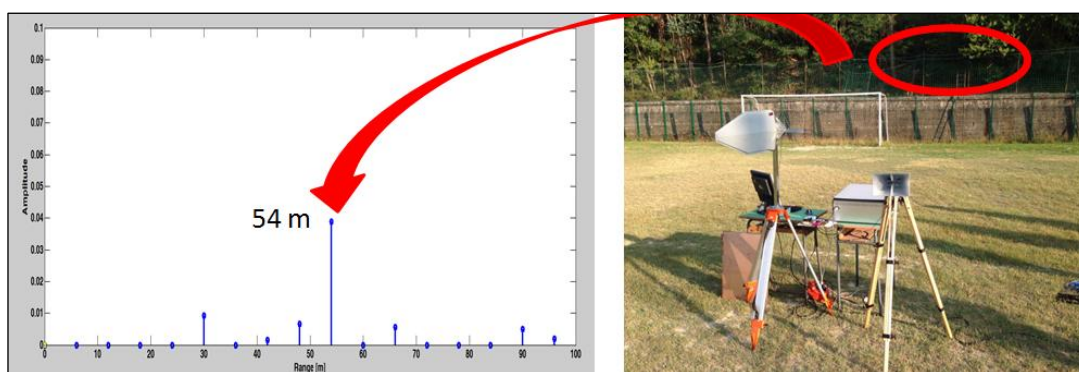
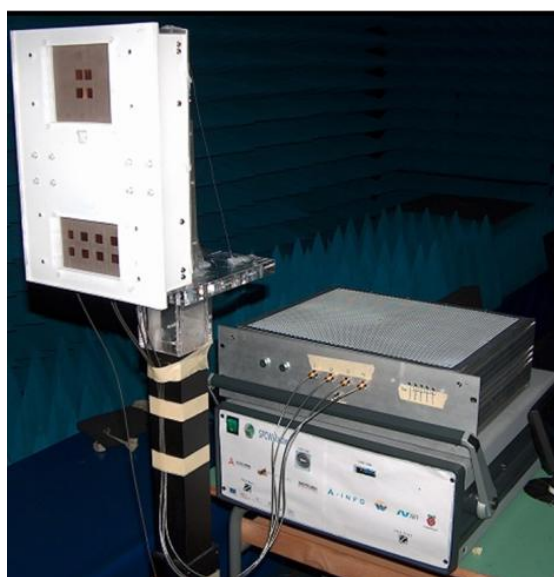


FIG. 2 – Example of accurate target detection with SDRadar.

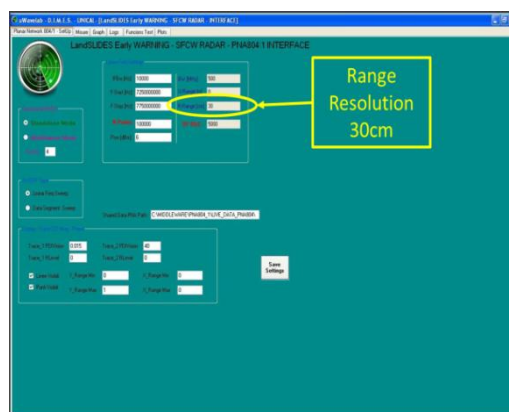
III. C-BAND SFCW RADAR

A C-band SFCW radar has been realized by adopting a compact Vector Network Analyzer, controlled by a Visual Basic interface, and connected through a switch module and a Butler matrix to transmitting and receiving microstrip array antennas, in order to realize an azimuthal scanning capability able to select a specific investigation area. A photograph of the C-band radar system is illustrated in Fig. 3(a), while the software interface is reported in Fig. 3(b).

Experimental tests have been performed to validate the radar range resolution, equal to 30 cm for a bandwidth operation of 500 MHz (Fig. 3(b)). An example of accurate position identification in the presence of two test targets given by two metal plates (Fig. 4(a)) is reported in Fig. 4(b).



(a)



(b)

FIG. 3 – (a) Photograph of C-band SFCW radar and (b) software interface.

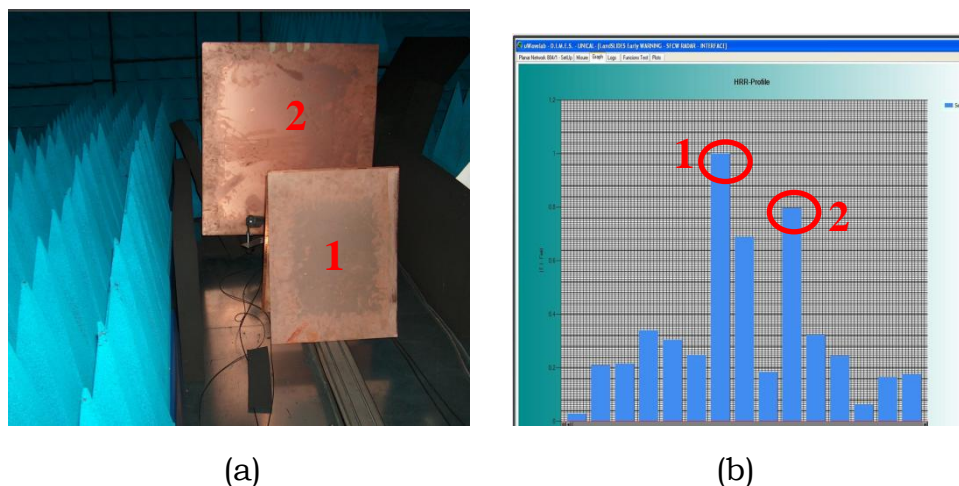


FIG. 4 – (a) Two test targets and (b) proper targets identification by C-band SFCW radar.

IV. CONCLUSION

The research activity performed at University of Calabria for the development of compact and low-cost radars able to work in the framework of landslides monitoring, has been described in this work. The first proposed radar configuration is based on an innovative software radio platform, while the second radar system is based in the adoption of a compact Vector Network Analyzer. Experimental validations properly demonstrating the range detection capabilities have been discussed for both radar structures.

REFERENCES

- [1] S. Costanzo, F. Spadafora, A. Borgia, O. H. Moreno, A. Costanzo and G. Di Massa, "High resolution software defined radar system for target detection," *Journal of Electrical and Computer Engineering*, vol. 2013, Article ID 573217, 2013.
- [2] S. Costanzo, F. Spadafora, G. Di Massa, A. Borgia, A. Costanzo, G. Aloï, P. Pace, V. Loscri and H. O. Moreno, "Potentialities of USRP-based software defined radar systems," *Progress In Electromagnetics Research B*, vol. 53, pp. 417-435, 2013.
- [3] S. Costanzo, F. Spadafora, O. H. Moreno, F. Scarcella and G. Di Massa, "Multiband software defined radar for soil discontinuities detection," *Journal of Electrical and Computer Engineering*, vol. 2013, Article ID 379832, 2013.

MEASUREMENT AND SIMULATION OF STIRRING EFFECTS OF FIELD PROBES IN A REVERBERATION CHAMBER

Luca Bastianelli, Valter Mariani Primiani, Franco Moglie

Università Politecnica delle Marche, DII
Via Brecce Bianche 12, 60131 Ancona.

Abstract

The residual stirring action of two commercially available electric field probes is experimentally and numerically analyzed. The capability to stir the reverberation chamber field is not negligible, and it alters the independent positions of mechanical rotating paddles when the spatial correlation matrix method is applied to evaluate them. The numerical code adopted for the simulations reveals its reliability and it can be employed to check probes during the design stage.

Index Terms – Field correlation, field probes, reverberation chambers, statistical independent positions.

I. INTRODUCTION

Field probes are widely employed to check reverberation chamber (RC) electric field amplitude and uniformity in EMC measurements [1]. Three-axes probes are important to correlate field levels to the antenna received power [3], [4]. Also, the statistical analysis of RC fields takes benefit from the use of three-axes probes, especially when the behavior in the proximity of RC walls or device boundary is sought [4], [5]. Recently, a spatial field probing has been introduced to determine stirrer performance in terms of statistical independent positions [6]-[8]. To that purpose, electric fields probes are moved within a volume and the field values in each point are recorded. Due to their physical dimensions and manufacturing materials, probes can produce themselves a stirring action of the chamber fields, that could affect the determination of the paddle independent position number.

In the present paper, we numerically and experimentally analyze the residual stirring effect of two commercially available field probes having a size commonly encountered in RC measurements.

II. MEASUREMENT SETUP

Our RC has dimensions of $6 \times 4 \times 2.5$ m³. The resonant frequency of the fundamental mode is about 45 MHz. Two log-periodic antennas and a vector network analyzer (VNA) are used. A PC controls all measurement

instruments and motors. We removed all the paddles from a stirrer and we mounted the probe under test at a fixed distance (80 cm) from the rotation axis, Fig. 1. The two considered probes are shown in Fig. 2. The first (A) is characterized by a resistive line that connects the sensor diodes to the electric-optic converter, having a total length of about 50 cm. The second (B) is very compact because of the three sensors are directly mounted on a smaller electric-optic converter. Independent positions are evaluated following the procedure as described in IEC standard [1].



FIG. 1 – RC interior showing a probe mounted on a plastic support at 80 cm from the rotation axis.



FIG. 2 – Detailed view of the two probes.

III. SIMULATION DETAILS

The numerical analysis of the RC consists of multiple runs of the overall structure with the stirrer being sequentially rotated of a uniform angle. The simulation were performed using a home made Finite-Difference Time-Domain (FDTD) code, optimized for parallel computing [9]. The simulated band is 200 MHz to 2 GHz. The reverberation chamber was subdivided into $400 \times 266 \times 166$ cubic cells with side of 15 mm. RC walls, stirrers, and antennas are simulated as perfect electric conductors (PEC). The conductivity of the air is $\sigma = 10^{-5}$ S/m to reproduce a realistic quality factor value. Transmitting and receiving antennas were simulated accounting for their actual reflections.

IV. RESULTS

All the measurements operate in tuned mode. The measurement frequency step was 250 kHz, in the band from 200 MHz to 8.4 GHz. The horizontal stirrer axis was rotated in 72 positions, while the vertical stirrer remained in the same place. Fig. 3 shows the independent positions measured for the probe (A) and (B) for the empty chamber.

Three orientations of probe (A), with the respect to its rotation plane, were considered: 0 deg. (#1), 45 deg. (#2) and 90 deg. (#3). Due to the small dimensions and to its shape, only one orientation was chosen for probe (B) (#4). The same Figure also shows results obtained without moving anything inside the RC, switching off the stirrer motor (#0). The independent positions yielded in that case are due to the thermal drift and mechanical vibrations [10]. The number of position reduces at higher frequencies because of the chamber quality factor reduction, due to imperfections of joints that are not negligible for the empty chamber at higher frequencies. Even though very small, also probe (B) can affect the parameter evaluation, especially for stirrer with a low independent position number. Fig. 4 reports a comparison between the numerical and the experimental evaluation in the case of probe (A). It can be noted that the code is able to well predict the probe residual stirring effect, within the measurement and simulation uncertainty.

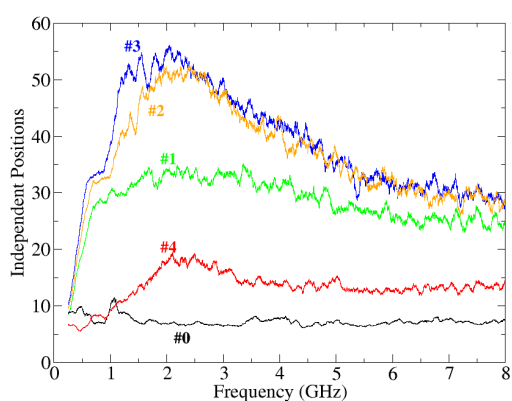


FIG. 3 – Independent positions measured for the two probes and when nothing is moved inside the chamber.

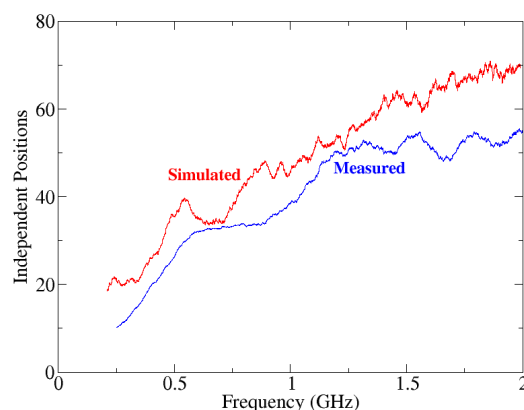


FIG. 4 – Comparison between simulated and measured independent positions for probe (A) and the case (#3).

V. CONCLUSION

The residual stirring action of field probes cannot be neglected. In particular, some commercially available electric field probes exhibit dimensions comparable or greater than the wavelength within their operating frequency band. When such probes are moved in the RC to analyzed field correlation, their stirring action combines to that of mechanical paddles, leading to an overestimation of the stirrer efficiency.

REFERENCES

- [1] *Electromagnetic compatibility (EMC) - Part 4-21: Testing and measurement techniques - Reverberation chamber test methods*, 2nd ed., International Standards - IEC 61000-4-21, Geneva, Switzerland, Apr. 2011.
- [2] J. M. Ladbury and G. H. Koepke, "Reverberation chamber relationships: corrections and improvements or three wrongs can (almost) make a right," in *1999 IEEE International Symposium on Electromagnetic Compatibility*, vol. 1, Seattle, WA, USA, Aug. 1999, 6pp.
- [3] A. Sorrentino, G. Ferrara, A. Gifuni, M. Migliaccio, "Antenna pattern in a multipath environment emulated in a reverberating chamber," *7th European Conference on Antennas and Propagation (EuCAP) 2013*, pp. 3561-3565, 8-12 April 2013.
- [4] D. A. Hill, "Boundary fields in reverberation chambers," *IEEE Trans. Electromagn. Compat.*, vol. 47(2), pp. 281-290, May 2005.
- [5] G. Gradoni and L. R. Arnaut, "Generalized extreme-value distributions of power near a boundary inside electromagnetic reverberation chambers," *IEEE Trans. Electromagn. Compat.*, vol. 52(3), pp. 506-515, Aug. 2010.
- [6] G. Gradoni, V. Mariani Primiani, and F. Moglie, "Reverberation chamber as a multivariate process: FDTD evaluation of correlation matrix and independent positions," *Progress In Electromagnetics Research*, vol. 133, pp. 217-234, 2013.
- [7] R. J. Pirkel, K. A. Remley, and C. S. L. Patané, "Reverberation chamber measurement correlation," *IEEE Trans. Electromagn. Compat.*, vol. 54, (3), pp. 533-545, Jun. 2012.
- [8] S. Pfennig and H. Krauthüser, "Comparison of methods for determining the number of independent stirrer positions in reverberation chambers," *2013 International Symposium on Electromagnetic Compatibility (EMC EUROPE)*, Sept 2013, pp. 431-436.
- [9] F. Moglie and V. Mariani Primiani, "Numerical analysis of a new location for the working volume inside a reverberation chamber," vol. 54(2), pp. 238-245, Apr. 2012.
- [10] G. Esposito, G. Gradoni, F. Moglie, V. Mariani Primiani, "Stirrer performance of reverberation chambers evaluated by time domain fidelity," *2013 IEEE International Symposium on Electromagnetic Compatibility (EMC)*, pp. 207-212, 5-9 Aug. 2013.

SIGe BiCMOS TECHNOLOGY FOR KA-BAND SATCOM ON THE MOVE USER TERMINALS

Luigi Boccia¹, Alireza Shamsafar¹, Emilio Arnieri¹, Ali Imran Sandhu¹, Giandomenico Amendola¹, Tatyana Purtova², Filipe Tarabani³, Václav Valenta³, Hermann Schumacher³, Erika Meniconi⁴, Mehmet Kaynak⁵, Bernd Tillack⁵, Q.Luo⁶, S.Gao⁶, Volker Ziegler⁴

¹ Università della Calabria, DIMES, Rende, Italy, luigi.boccia@unical.it

² now with TriQuint Semiconductor GmbH, Germany

³Universität Ulm, Albert-Einstein-Allee 41, 89081 Ulm, Germany

⁴ EADS Innovation Works, Willy-Messerschmitt-Str., 85521 Ottobrunn, Germany

⁵ IHP - Innovations for High Performance Microelectronics, Im Technologie park 25 15236 Frankfurt (Oder), Germany

⁶ School of Engineering and Digital Arts, University of Kent, Canterbury, Ukff

luigi.boccia@unical.it

Abstract

This work describes the potential of SiGe BiCMOS technology for the development of SatCom user terminal antennas for wideband global SatCom satellite services operating in Ka-band. This application is attracting a strong attention both from military and civil users. In particular, analysts predict a very positive outlook for Ka-band on the move applications which will provide interesting opportunities for industrial providers. In this work it will be briefly introduced the of SiGe BiCMOS technology for the implementation of low-cost user terminal antennas for Ka-band mobile applications. The results introduced in this work have been obtained within the framework of the EU FP7 project FLEXWIN.

Index Terms – Sat-Com, Ka-band, SiGe.

I. INTRODUCTION

In the last few years, with the introduction of more Ka-band capacity and INMARSAT's Global Express service there has been an increasing interest for Sat-Com on the move user terminal antennas [1]. In this context, one of the most critical aspect is related to the development of the phased-array antenna system [2], [3]. Indeed, antenna requirements for Sat-Com user terminal are usually very challenging [4]. Typically, it is required beam scanning over very wide angles, low interactions with the environment, dual band (Tx and Rx) operation, low-cost and low-profile.

In the most typical approach, these requirements are satisfied by employing two separated radiation apertures for the Rx and Tx channel

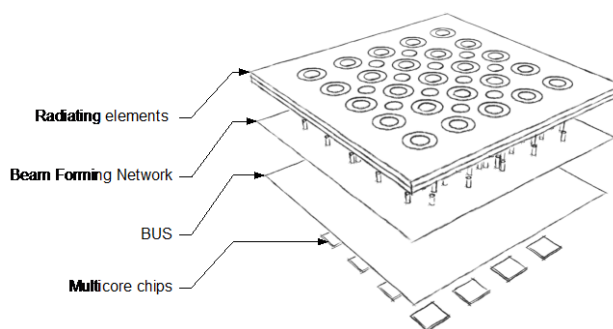


Fig. 1 Conceptual layout of the Ka-band SatCom on-the-move user terminal antenna demonstrator with "intelligent pixels": exploded view.

[5]. Pointing of the two dual-polarized antennas is usually mechanical in azimuth and electronically steered in elevation [6]. This approach results in a complex antenna architecture which can be hardly mounted on vehicles or airplanes without affecting their aerodynamic and aesthetic profile. Furthermore, the cost of this solution remains high even for mass production. Arrays with full electronic beam scanning were proposed using customized GaAs MMICs [7], [8]. Although this is a step in the right direction, it is still not enough to greatly reduce the cost of the user terminals. Indeed, independent silicon chips will be required to control Tx and Rx modules and it is not possible to integrate multiples cores in the same MMIC with high yield.

This paper will illustrate the potential of SiGe BiCMOS technology for the development of Ka-band SatCom on the move user terminal antennas. The results to be presented in the final paper have been achieved within the framework of the FP7 EU project FLEXWIN [9]. In this project, a phased array demonstrator is being developed using multicore SiGe BiCMOS MMICs combined with a quasi-planar antenna array.

II. ARRAY CONFIGURATION

The proposed configuration is based on highly reconfigurable RFIC components referred to as "intelligent pixels" combined with a highly integrated antenna array. Each element of the array is integrated with a SiGe BiCMOS multicore chip which contains 2Rx and 4Tx front ends reconfigurable both in amplitude and phase. Each chip can thus serve different array elements which are controlled individually through a I²C bus implemented in the same chip. In the same chip are present also environmental sensors. In terms of reconfigurability, this approach proposes to achieve a significant advance towards smart RF micro-systems enabling the realization of highly reconfigurable and multifunctional millimetre-wave building blocks.

Even if the availability of multifunctional chips reduces the complexity of the phased array, the design of the passive components is also critical mainly because a single radiating aperture is employed for dual band operation. To solve this issue, an interleaved array configuration based on dual-band printed annular slots is implemented.

In the final demonstrator, the chips are embedded into cavities inside a multilayer PCB [10]. The MMICs are then wire-bonded to the distribution network which feeds the antenna elements through vertical transitions.

ACKNOWLEDGEMENT

This work is funded by the European Union under the project FP7-ICT-2009-5 (FLEXWIN, www.flexwin.eu).

REFERENCES

- [1] J. Farserotu e R. Prasad, «A survey of future broadband multimedia satellite systems, issues and trends», *IEEE Commun. Mag.*, vol. 38, n. 6, pagg. 128 –133, giu. 2000.
- [2] G. Rebeiz e K. Koh, «Silicon RFICs for phased arrays», *IEEE Microw. Mag.*, vol. 10, n. 3, pagg. 96 –103, mag. 2009.
- [3] D. Parker e D. C. Zimmermann, «Phased arrays-part II: implementations, applications, and future trends», *IEEE Trans. Microw. Theory Tech.*, vol. 50, n. 3, pagg. 688 –698, mar. 2002.
- [4] S. Vaccaro, F. Tiezzi, D. Llorens, M. F. Rua, e C. D. G. de Oro, «Ku-Band Low Profile Antennas for Mobile Satcom», in *Advanced Satellite Mobile Systems, 2008. ASMS 2008. 4th*, 2008, pagg. 24 – 28.
- [5] M. Lisi, «Antenna technologies for multimedia mobile satellite communications», in *Antennas and Propagation, 2001. Eleventh International Conference on (IEE Conf. Publ. No. 480)*, 2001, vol. 1, pagg. 241 –245 vol.1.
- [6] R. Baggen, S. Vaccaro, e D. L. del Rio, «Design Considerations for Compact Mobile Ku-Band Satellite Terminals», in *The Second European Conference on Antennas and Propagation, 2007. EuCAP 2007*, 2007, pagg. 1 –5.
- [7] L. Baggen, S. Vaccaro, D. Llorens del Rio, e G. Langgartner, «Compact phased arrays for mobile terminals», in *Semiconductor Conference (CAS), 2010 International*, 2010, vol. 01, pagg. 3 –9.
- [8] S. H. Son, U. H. Park, S. I. Jeon, e C. J. Kim, «Mobile antenna system for Ku-band satellite Internet service», in *Vehicular Technology Conference, 2005. VTC 2005-Spring. 2005 IEEE 61st*, 2005, vol. 1, pagg. 234 – 237 Vol. 1.
- [9] Flexwin Consortium, «www.flexwin.eu». [In linea]. Available at: www.flexwin.eu/.

- [10] E. Meniconi, V. Ziegler, R. Sorrentino, e T. Chaloun, «3D integration technologies for a planar dual band active array in Ka-band», in *Microwave Conference (EuMC), 2013 European*, 2013, pagg. 215–218.

DESIGN OF MAGNETIC-RESONANT WIRELESS POWER TRANSFER LINKS REALIZED WITH CLASS E AMPLIFIERS

M. Dionigi⁽¹⁾, G. Leuzzi⁽²⁾, F. M. Lombardi⁽¹⁾, M. Mongiardo⁽¹⁾, V. Stornelli⁽²⁾

⁽¹⁾ Dipartimento di Ingegneria, Università di Perugia

⁽²⁾ DIIIIE, Università dell'Aquila

mauro.mongiardo@unipg.it

Abstract

A simple approach is proposed for realizing wireless power transfer links by using high efficiency class E amplifiers. We start from the standard design of a class E amplifier operating at a desired frequency; the design provides the value of the reactive elements as well as the value of the load impedance. Next we design an efficient magnetic resonant wireless power transfer link, which presents, as input impedance, the same load impedance of the class E amplifier. The class E amplifier can now be directly connected to the wireless link. As an example of application we present a structure capable of transferring energy from one side to the other of a wood table. The proposed network has been realized and measured with excellent results.

Index Terms – Class E amplifiers, Efficient energy transfer, Wireless power transfer.

I. INTRODUCTION

Magnetic resonant wireless power transfer (WPT) is currently receiving considerable attention [1] – [7]. In fact, there are many applications that can take advantage from this technology [8].

In order to develop a WPT system one needs also a suitable source and class E amplifiers are good candidates for this task [9]. Class E amplifiers have been introduced in [10] and well investigated in subsequent works, e.g. in [11], [12]. However, so far there have been only few applications of Class E amplifiers to wireless power links. In [13] a Colpitts oscillator for low power wireless applications has been proposed; in [9] the design and optimization for a loosely coupled wireless power system has been considered; application to biomedical implants has been dealt with in [14].

In this work we show how it is possible to combine in a simple way the design of a Class E amplifier with the design of the wireless network obtaining fairly good results for the practical case of power transmission through a wood table.

II. CLASS E AMPLIFIER DESIGN

Class E tuned power amplifiers have gained widespread acceptance since their introduction [10] due to their simplicity, high efficiency, excellent design ability, and relatively high tolerance to circuit variations. Moreover, the class E power amplifier ranging its reliability from few KHz to tens of GHz with output power level up to several KW. The basic circuit of the class E amplifier with a shunt inductor is shown in Fig. 1. It consists of a single transistor and a load network. The transistor operates cyclically as a switch at the desired carrier frequency of the output signal.

Concerning the design steps, the project starts with the analytical calculation, at the input signal frequency $f=13.56\text{MHz}$, and applying the well-known basic formulas of the class E Amplifier [10]; this must be done after the choice of the transistor and of the power supply voltage. Generally in its class E amplifiers use, the inductance L_x has to be a choke for the RF fundamental tone. In our design the transistor used is a 2N2219, from Philips, with a 12 V power supply value while the remaining elements have been calculated as follows: $C_0 = 27\text{pF}$, $C_x = 130\text{pF}$, $L_0 = 2200\text{nH}$. The load resistance R_L is also obtained from the amplifier design.

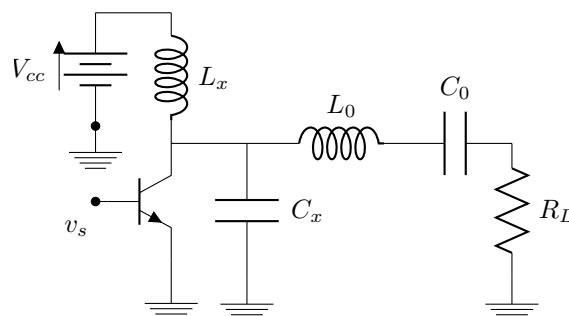


FIG. 1 - Class E amplifier schematic.

III. WIRELESS LINK DESIGN

Our goal is to obtain a portion of a table surface capable to deliver energy to devices placed above it. This can be realized by using a couple of resonators, one positioned above the table and one positioned under the table, coupled via their magnetic fields.

We have developed an integrated planar substrate resonator, shown in Fig. 2, which presents several advantages such as very limited space occupation, ease of manufacture, low cost and a relatively high Q. The structure has been realized to operate at the frequency of 13.56 MHz. The measured Q factor for the single resonator is $Q = 300$.

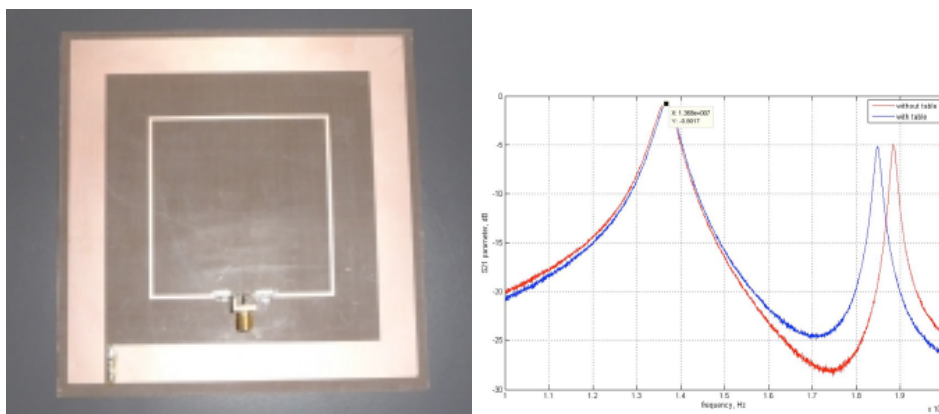


FIG. 2 – Substrate integrated coils used for realize WPT and comparison between measurements and full-wave analysis for transmission through a wood table of thickness 3.2 cm; the comparison shows an excellent agreement at the operating frequency of 13.56 MHz.

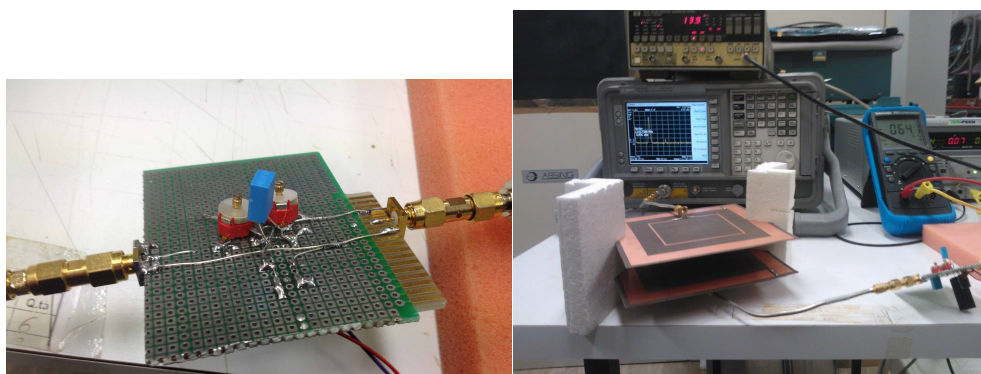


FIG. 3 – Photographs of the Class E amplifier circuit (left side) and of the entire system; for illustration purposes the power transmission has been realized in air, but minor changes occur when applied to a wood table.

IV. ENTIRE SYSTEM MEASUREMENT

The class E amplifier has been connected to the wireless link of the previous section as shown in Fig. 10. We have designed the class E amplifier for operating with 1w output power and a voltage of 12V. The Q factor of the resonant LC network (LOC0) has been set to 3. The measured efficiency of the entire system has been around 75%. This value is very close to that obtained by multiplying the efficiency of the amplifier times the measured efficiency of the wireless link.

V. CONCLUSION

We have proposed a simple approach to realize wireless power transfer links using class E amplifiers. As an example of application we have realized a structure usable to send energy from one side to the other of

a wood table. The proposed network has been realized and measured with fairly good results.

REFERENCES

- [1] A. Kurs, A. Karalis, R. Moffatt, J. D. Joannopoulos, P. Fisher, and M. Soljacic, "Wireless power transfer via strongly coupled magnetic resonances," *Science*, vol. 317, no. 5834, pp. 83–86, 2007.
- [2] Z. N. Low, R. A. Chinga, R. Tseng, and J. Lin, "Design and Test of a High-Power High-Efficiency Loosely Coupled Planar Wireless Power Transfer System," *Industrial Electronics, IEEE Transactions on*, vol. 56, no. 5, pp. 1801–1812, Oct. 2009.
- [3] B. L. Cannon, J. F. Hoburg, D. D. Stancil, and S. C. Goldstein, "Magnetic Resonant Coupling As a Potential Means for Wireless Power Transfer to Multiple Small Receivers," *IEEE Transactions on Power Electronics*, vol. 24, no. 7, pp. 1819–1825, Oct. 2009.
- [4] A. P. Sample, D. A. Meyer, and J. R. Smith, "Analysis, Experimental Results, and Range Adaptation of Magnetically Coupled Resonators for Wireless Power Transfer," *Industrial Electronics, IEEE Transactions on*, vol. 58, no. 2, Oct. 2011.
- [5] M. Dionigi, A. Costanzo, F. Matri, and M. Mongiardo, "Magnetic Resonant Wireless Power Transfer," Chapter of the book "Wireless Power Transfer", p. 159, 2012.
- [6] M. Dionigi and M. Mongiardo, "CAD of wireless resonant energy links (WREL) realized by coils," in *IEEE MTT-S International Microwave Symposium digest*, IEEE, 2010, pp. 1760–1763.
- [7] —, "CAD of efficient wireless power transmission systems," *Microwave Symposium Digest (MTT)*, 2011 IEEE MTT-S International, pp. 1–4, 2011.
- [8] H. Shoki, "Issues and initiatives for practical use of wireless power transmission technologies in Japan," *Microwave Workshop Series on Innovative Wireless Power Transmission: Technologies, Systems, and Applications (IMWS)*, 2011 IEEE MTT-S International, pp. 87–90, 2011.
- [9] J. J. Casanova, Z. N. Low, and J. Lin, "Design and Optimization of a Class-E Amplifier for a Loosely Coupled Planar Wireless Power System," *IEEE Transactions on Circuits and Systems II: Express Briefs*, vol. 56, no. 11, pp. 830–834, Feb. 2009.
- [10] N. O. Sokal and A. D. Sokal, "Class E-A new class of high-efficiency tuned single-ended switching power amplifiers," *Solid-State Circuits, IEEE Journal of*, vol. 10, no. 3, pp. 168–176, 1975.
- [11] F. Raab, "Idealized operation of the class E tuned power amplifier," *Circuits and Systems, IEEE Transactions on*, vol. 24, no. 12, pp. 725–735, 1977.
- [12] F. H. Raab, "Class-E, class-C, and class-F power amplifiers based upon a finite number of harmonics," *Microwave Theory and Techniques, IEEE Transactions on*, vol. 49, no. 8, pp. 1462–1468, 2001.
- [13] R. Devine and M. R. Tofighi, "Class E Colpitts oscillator for low power wireless applications," *Electronics Letters*, vol. 44, no. 21, p. 1257, 2008.
- [14] A. N. Laskovski, M. R. A. S. i. B. Yuce, and C. T. I. . 3rd International Symposium on, "Class-E oscillators as wireless power transmitters for biomedical implants," *Applied Sciences in Biomedical and Communication Technologies (ISABEL)*, 2010 3rd International Symposium on, Feb. 2010.

NEURAL NETWORK APPROACHES TO POLARIMETRIC SAR DATA PROCESSING

Ruggero G. Avezzano⁽¹⁾, Fabio Del Frate⁽¹⁾, Giovanni Schiavon⁽¹⁾

⁽¹⁾ Department of Civil Engineering and Computer Science Engineering, University of Rome Tor Vergata
Via del Politecnico, 1 00133 - Roma
avezzano@disp.uniroma2.it

Abstract

The use of AutoAssociative Neural Network (AANN) has been tested for polarimetric data dimensionality reduction, demonstrating its compression capabilities and performances. The use of textural information has been added as a valuable source of information, highlighting how the use of this solution allows an immediate and interesting interpretation of results. Finally a multifrequency comparison of information compression has been assessed, demonstrating the improved performances of AANNs in a classification task.

Index Terms – Compression, Multifrequency Classification, Neural Networks, PolSAR.

I. INTRODUCTION

The forthcoming generation of spaceborne Synthetic Aperture Radar (SAR) systems will provide high resolution full-polarimetric operational products (COSMO-SkyMed Seconda Generazione, ALOS-2, Radarsat Constellation Mission, SAOCOM), while ESA Sentinel-1 will supply coherent dual-pol images.

The amount of data to be processed is rapidly increasing, demanding high computational capabilities for near-real time processing.

Neural Networks approach is often used for specific statistical analysis, such as repetitive curve fitting problems, real-time applications and high volumes of data processing.

An interesting application of Neural Network algorithms consists in their implementation for data dimensionality reduction.

II. AUTOASSOCIATIVE NEURAL NETWORKS

A widely employed dimensionality reduction technique is the classical Principal Component Analysis (PCA): it aims at representing the high-dimensional set into a lower dimensionality set that describes as much of the variance in the data as possible. A number of nonlinear dimensionality reduction techniques have been developed [1], in various cases better suited for real-world data description, and some of them have been tested on polarimetric SAR datasets [2-4].

Autoassociative Neural Networks (AANN), also known as Autoencoders, are MultiLayer Perceptron (MLP) feedforward neural networks with an odd number of hidden layers. Sigmoid functions, or other non-linear functions, are used as nodes' activation functions to perform the NonLinear Principal Component Analysis (NLPCA) [5].

The network is trained to describe the identity mapping function, i.e. the input and the output vectors are equal. Using a reduced number of nodes in the central layer (bottleneck) with respect to inputs/outputs forces the network to compress the information during the training process. This allows, at its ending, to extract a feature vector from the bottleneck layer which has a reduced number of components, called Non-Linear Principal Components.

III. DATA COMPRESSION

The first step was to assess the capability of AANN and NLPCA to compress polarimetric information. To this end, a PolSAR image acquired from Radarsat-2 (Fine Quad, 5.405 GHz, incidence angle 29°) was employed.

The network input vector was composed of a set of common polarimetric observables derived from scattering matrix and coherency matrix: total power (or span) of scattering matrix, normalized radar cross sections (NRCS) of HH, HV and VV channels, amplitudes and phase variances of complex coherence evaluated over HH and VV channels and RR and LL channels, the co-pol and cross-pol ratios.

The feature vector was compressed in 5, 4 and 3 components, using the classical PCA and NLPCA approaches. A classification exercise has been set up in order to compare the performances of the two techniques: a visual selection of ground truth pixels over 6 classes (Dense and Sparse Urban, Rough and Smooth Sea, Dense and Sparse Vegetation) was made over the image and the compressed vectors were considered. Results are shown in Table I, showing a more robust performance of the NLPCA compared with the significant reduction of accuracy in PCA when the number of components becomes too small.

In the second step the textural information compression was investigated. It is generally defined as the information contained in neighboring pixels with respect to a pixel under test. The information contained in those pixels is most likely correlated to the central one [6]. This kind of information is found in intensity and amplitude images. Polarimetry allows to consider different textures per sample, at different polarization intensities.

The input vector to be compressed in this second experiment was represented by all values contained in the analysed area, taken at the three different available intensities (HH,HV,VV). The total number of inputs depends on the dimension of the window; here a 5x5 window was considered for each of the three polarizations.

The suitable topology was chosen using a grid search algorithm (75-30-3-30-75), and the network was trained in 30k epochs using backpropagation and training set of 9800 samples.

The compressed components are shown in Fig. 1. From a visual comparison with a classical target decomposition technique [7], it is possible to highlight how the compression performed using AANN retrieved non-linear correlation among pixels [8-9] and emphasized

three different areas where three different scattering mechanisms apply, as shown in Fig. 2.

TABLE I - CLASSIFICATION PERFORMANCES

Input Set	Original Features	5 NLPC	5 PC	4 NLPC	4 PC	3 NLPC	3 PC
OA %	88.68	85.99	86.41	85.58	86	85.39	83.69
K-coeff	0.86	0.83	0.836	0.82	0.83	0.82	0.80



FIG. 1 – NonLinear Principal Components extracted using Textural Information contained in Polarimetric Images.

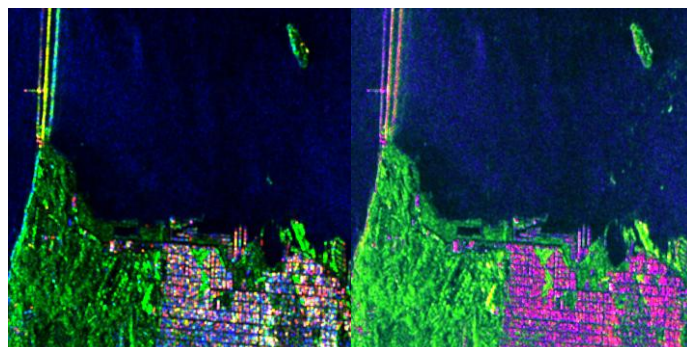


FIG. 2 – Comparison between the Freeman-Durden and AANN decomposition.

IV. MULTIFREQUENCY ASSESSMENT

A further analysis was carried out to test AANNs processing over products acquired at different frequency bands (L-, C-, X-band). The overall compression and classification over 4 classes (Water, Buildings, Low Vegetation and Trees) was compared to 3 classical feature extraction techniques based on polarimetric data, namely the Entropy/alpha/Anisotropy, Freeman-Durden and Pauli Decompositions [10]. Images of San Francisco bay were processed and each set was classified using a Support Vector Machine algorithm.

Regarding AANNs, L- and C- band images were compressed into 5 components, while for X-band 4 components were found as the best trade-off between training errors and epochs.

The classifications showed the improved manifold description capabilities of the Neural Network approach, due to nonlinear correlations detection. The overall accuracies are showed in Table 2.

TABLE 2 - MULTIFREQUENCY CLASSIFICATIONS OVERALL ACCURACIES

Band	H/ α /A	Freeman-Durden	Pauli	AANN
L	73.92 %	80.23 %	73.36 %	86.98 %
C	84.92 %	76.11 %	76.24 %	86.82 %
X	82.27 %	80.86 %	63.09 %	91.67 %

V. CONCLUSION

A compression of polarimetric information by means of AutoAssociative Neural Networks has been explored. Textural descriptors have been added as a valuable source of information data interpretation and analysis.

AANNs have been demonstrated to be an important tool for efficient description of polarimetric manifolds, comparing their compression performances with respect to PCA and classification accuracies with respect to classical polarimetric information extraction techniques.

REFERENCES

- [1] L. J. P. van der Maaten, E. O. P. and van den Herik, H. J., "Dimensionality reduction: A comparative review".
- [2] Ainsworth, T. L., and J. S. Lee. "Optimal image classification employing" optimal" polarimetric variables." *Geoscience and Remote Sensing Symposium, 2003. IGARSS'03. Proceedings. 2003 IEEE International*. Vol. 2. IEEE, 2003.
- [3] Tu, Shang Tan, et al. "Laplacian eigenmaps-based polarimetric dimensionality reduction for SAR image classification." *Geoscience and Remote Sensing, IEEE Transactions on* 50.1 (2012): 170-179.
- [4] Shi, Lei, et al. "Supervised graph embedding for polarimetric sar image classification." *Geoscience and Remote Sensing Letters, IEEE* 10.2 (2013).
- [5] Kramer, M. A., "Nonlinear principal component analysis using autoassociative neural networks," *AICHE J.* 37(2), 233{243 (1991).
- [6] Haralick, R., Shanmugam, K., and Dinstein, I., "Textural features for image classification," *Systems, Man and Cybernetics, IEEE Transactions on* SMC-3(6), 610{621 (1973).
- [7] A. Freeman and S.L. Durden, "A three-component scattering model for polarimetric sar data," *Geoscience and Remote Sensing, IEEE Transactions on*, vol. 36, no. 3, pp. 963–973, 1998.
- [8] Del Frate, Fabio, G. Licciardi, and Riccardo Duca. "Autoassociative neural networks for features reduction of hyperspectral data." *Hyperspectral Image and Signal Processing: Evolution in Remote Sensing, 2009. WHISPERS'09. First Workshop on*. IEEE, 2009.
- [9] Picchiani, M., Del Frate, F., Schiavon, G., & Stramondo, S. (2013). Compression of SAR interferograms for parameter retrieval using neural networks. - *IGARSS 2013*.
- [10] Jong-Sen Lee and Eric Pottier, "Polarimetric Radar Imaging: From Basics to Applications", *Optical Science and Engineering*, CRC Press, 2009.

GRATING LOBES IN SYNTHETIC ARRAYS: EFFECTS AND COMPENSATION

Gerardo Di Martino, Antonio Iodice, Daniele Riccio, Giuseppe Ruello

Department of Electric Engineering and Information Technology,
Università degli Studi di Napoli Federico II, Naples, Italy
{gerardo.dimartino; iodice; daniele.riccio; ruello}@unina.it

Abstract

In this paper we propose a method for the mitigation of azimuth ambiguities in stripmap SAR images based on the compensation of the grating lobes of the synthetic array antenna pattern. Our framework is based on a two-step procedure. In the first step, two asymmetric filters are used to suppress ambiguities due to the first grating lobe on each side of the main lobe; the ratios between the original and filtered images are used to produce two maps of the ambiguity-affected areas. In the second step, these maps are used to produce a final image in which only the areas affected by the ambiguities are replaced by their filtered versions. The proposed method can be employed in situations in which similar approaches fail and it has a smaller computational burden.

Index Terms – Azimuth ambiguity, grating lobes, Synthetic Aperture Radar.

I. INTRODUCTION

Usually, Synthetic Aperture Radar (SAR) azimuth ambiguity is set in the framework of Doppler signal sampling. From this viewpoint it is caused by the use of a finite pulse repetition frequency (PRF) combined with the fact that the azimuth antenna pattern (AAP), in practice, cannot be abruptly limited to the specified azimuth illumination beamwidth [1]. By using the language of signal sampling theory, the AAP acts as a non-ideal anti-aliasing filter and the azimuth ambiguity can be seen as an aliasing effect. Alternatively, by using the language of antenna array design, the AAP acts as the individual radiating element pattern, which should ideally suppress “grating lobes” of the (synthetic) array pattern. Azimuth ambiguity can be then seen as the effect of non-ideal suppression of grating lobes. Due to this effect, replicas (or “ghosts”) of brilliant points appear on SAR images: they are shifted both in azimuth and (in a smaller extent) in range with respect to their original position. The replicas are strongly attenuated due to AAP-sidelobe weighting. However, if these ghosts are located in a low-scattering area, e.g. the sea surface, they emerge with respect to the background. In fact, these ghosts are one of the main reasons of false alarm in ship detection [2].

In the literature, different ways are known for the suppression of azimuth ambiguities due to point targets, based on in-phase cancellation [3] or on the evaluation of shifts in position of the ghosts [2], [4]. However, these methods are not adequate for ocean scenes in

high-resolution images, where many ambiguities due to distributed targets are present. In this case, the use of techniques based on the concept of selective filtering has been advocated [1], [5]. These techniques use a band-pass filter to select from the whole azimuth spectrum those areas that are less affected by ambiguities.

In the present paper, a two-step procedure is presented. As in [5], the first step is aimed at identifying areas actually affected by azimuth ambiguities. However, while the method in [5] may fail to identify ambiguities for some configurations of AAP and PRF actually encountered in current high resolution spaceborne SAR systems, our approach does not suffer from this problem. Once the ambiguity maps have been generated, they are used to produce a final image in which only the areas affected by the ambiguities are replaced by their filtered versions.

II. AZIMUTH AMBIGUITIES IN SAR IMAGES

The phenomenon of SAR azimuth ambiguity can be effectively described in the framework of antenna array theory. In particular, using this formulation it is very easy to evaluate the azimuth, Δx_n , and range, Δr_n , displacements of the ambiguity contributions on the final focused image. The SAR system is designed to synthesize a broadside array in the azimuth direction: in this case, the array factor is responsible for the appearance of grating lobes, which cause the azimuth ambiguity phenomenon. The array factor is a periodic function that presents maxima for angles ψ (between observation and broadside directions)

$$2kd \sin \psi = 2n\pi \Rightarrow \sin \psi = \frac{n\text{PRF} \lambda}{2v} \Rightarrow \Delta x_n = \frac{n\text{PRF} \lambda r_0}{2v} \quad (1)$$

where λ is the electromagnetic wavelength, $k = 2\pi/\lambda$ is the free-space electromagnetic wavenumber, v is the uniform sensor velocity, r_0 is the closest range between the sensor and the center of the footprint, $d = v/\text{PRF}$ is the distance between the elements of the array, and $\Delta x_n = r_0 \sin \psi$. Similarly, via simple geometric considerations, we have

$$r_0 + \Delta r_n = \sqrt{r_0^2 + \Delta x_n^2} \approx r_0 \left(1 + \Delta x_n^2 / 2r_0^2\right) \Rightarrow \Delta r_n = \Delta x_n^2 / 2r_0 \quad (2)$$

It must be now noted that the observed scene is not in the far field zone of the synthetic array: however, it can be shown that, around the points of maximum of the array factor, the far-field formulas can still be used if one replaces the individual radiating element pattern (i.e., the AAP of the physical antenna) with its smoothed version, obtained by averaging it over an angular interval equal to the physical antenna effective beamwidth [6]. The obtained expression of the focused intensity SAR image I in the wavenumber domain is

$$I(\xi) = \Gamma_0(\xi)W_0(\xi) + \Gamma_+(\xi)W_+(\xi) + \Gamma_-(\xi)W_-(\xi) \quad (3)$$

where ξ is the Fourier mate of the azimuth coordinate x , Γ_0 , Γ_+ , and Γ_- are $\Gamma(\xi - 2\pi i \text{PRF}/v)$ for $i=0,+1,-1$ respectively (i.e. the reflectivities of the unambiguous and ambiguous targets, respectively), and

$$W_0(\xi) = W\left(\frac{\xi - \xi_{DC}}{2a_0r_0}\right) \text{rect}\left(\frac{\xi - \xi_{DC}}{2a_0X}\right) \quad (4)$$

$$W_{\pm}(\xi) = W\left(\frac{\left(\xi \pm \frac{2\pi \text{PRF}}{v}\right) - \xi_{DC}}{2a_0r_0}\right) \text{rect}\left(\frac{\xi - \xi_{DC}}{2a_0X}\right) \quad (5)$$

with $W(\psi)$ being the AAP of the physical antenna, $\xi_{DC} = 2\pi f_{DC}/v$, f_{DC} the Doppler centroid frequency, $a_0 = 2\pi/\lambda r_0$, and $X = \lambda r_0/L$ the effective azimuth footprint, with L the azimuth length of the physical antenna. Note that we consider here a one-dimensional problem.

III. COMPENSATION PROCEDURE

Computing the power spectral densities of the terms in Eq. (3), where the first term represents the ambiguous signal and the last two the ambiguity contributions due to the first (left and right) grating lobes, and assuming that ambiguities due to the two sidelobes are present only one at a time, we get the following expressions for Wiener filters:

$$H_{\pm}(\xi) = \frac{\sigma_0}{\sigma_{\pm}} \left(\frac{|W_{\pm}(\xi)|^2}{|W_0(\xi)|^2} + \frac{\sigma_t}{\sigma_{\pm}} \frac{1}{|W_0(\xi)|^2} + \frac{\sigma_0}{\sigma_{\pm}} \right)^{-1} \quad (6)$$

where σ_0 , σ_{\pm} , and σ_t are the power spectral densities of reflectivity, ambiguous targets and white thermal noise, respectively. The ratio between the original and the obtained filtered images is used to obtain two ghost maps. Finally, these maps are used to produce a final image in which only the areas affected by the ambiguities are replaced by their filtered versions, according to the proper one of the two filters.

IV. EXPERIMENTAL RESULTS

As an example of application of our method, we consider a TerraSAR-X image of the coast of Algeria shown in Fig. 1 (a). In Fig. 1 (b) the image obtained applying the proposed compensation is reported. It can be noted that the ambiguities in the red boxes are strongly mitigated. As a comparison, in Fig. 1 (c) the result obtained applying the technique of [5] on the same image is presented: the ghosts in the boxes result to be almost unchanged. This is due to the particular combination of AAP and PRF value of TerraSAR-X in the considered acquisition geometry.

V. CONCLUSION

A technique for the compensation of azimuth ambiguities due to grating lobes in synthetic apertures has been presented. Obtained results show that it can be employed in situations in which similar approaches fail.

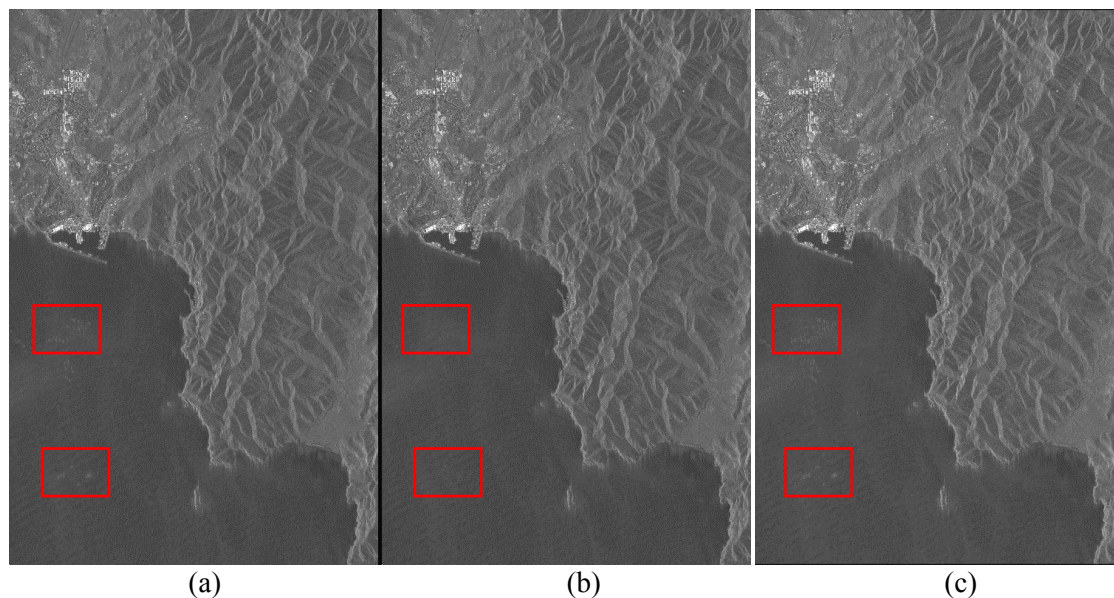


FIG. 1 – Original image (a), proposed compensation (b), technique of [5] (c).

ACKNOWLEDGEMENT

This work was supported by the EU-FP7 project "Development of Pre-Operational Services for Highly Innovative Maritime Surveillance Capabilities" (DOLPHIN).

REFERENCES

- [1] F. K. Li and W. T. K. Johnson, "Ambiguities in Spaceborne Synthetic Aperture Radar Systems," *IEEE Trans. Aerosp. Electron. Syst.*, vol. 19, no. 3, pp. 389–397, May 1983.
- [2] S. Brusch, S. Lehner, T. Fritz, M. Soccorsi, A. Soloviev, and B. van Schie, "Ship Surveillance with TerraSAR-X," *IEEE Trans. Geosci. Remote Sens.*, vol. 49, no. 3, pp. 1092–1103, Mar. 2011.
- [3] A. Moreira, "Suppressing the azimuth ambiguities in synthetic aperture radar images," *IEEE Trans. Geosci. Remote Sens.*, vol. 31, no. 4, pp. 885–895, July 1993.
- [4] R. K. Raney and G. J. Prinz, "Reconsideration of Azimuth Ambiguities in SAR," *IEEE Trans. Geosci. Remote Sens.*, vol. 25, no. 6, pp. 783–787, Nov. 1987.
- [5] A. Monti Guarnieri, "Adaptive Removal of Azimuth Ambiguities in SAR Images," *IEEE Trans. Geosci. Remote Sens.*, vol. 43, no. 3, pp. 625–633, Mar. 2005.
- [6] R. C. Heimiller, "Theory and Evaluation of Gain Patterns of Synthetic Arrays," *IRE Trans. Mil. Electron.*, vol. MIL-6, no. 2, pp. 122–129, Apr. 1962.

ANALITICAL OPTIMIZATION METHODS TO DESIGN COILS FOR MAGNETIC FIELD GRADIENTS

M. Tannino⁽¹⁾, F. Mangini⁽¹⁾

⁽¹⁾ Dept. of Information Engineering, Electronics and Telecommunications, "La Sapienza" University, Rome, Italy
marco.tannino@diet.uniroma1.it fabio.mangini@diet.uniroma1.it

Abstract

The purpose of this work is to compare two general methods of analytical optimization to design coils capable of generating a gradient of magnetic field with different degree of linearity and to simulate the field generated. The approach we have chosen is based on finding the geometrical conditions to null the unnecessary terms of the Taylor expansion of the analytical description of the field to generate. One of the methods is based on a paper written by Prof. Sir Peter Mansfield the second one use the Target Field Method devised by Professor Robert Turner and can be useful even to design coils with active scree.

Index Terms – Analytical optimization, coil design, magnetic field gradients, numerical simulation.

I. INTRODUCTION

With this work we show the results of a basic optimization approach to design coils to generate magnetic fields with a desired spatial distributions, in particular for the gradient $G_y = dB_z/dy$. This approach is useful at working frequencies from DC up to few kHz, so in quasi-static regime. Like many other approaches in coil designing [1], our procedure starts from the mathematical function that describes the magnetic field related to a specific current distribution. Then we look for the geometrical conditions to null the unnecessary terms of the Taylor series of this mathematical function. Because one could not need a high homogeneity of the field nor a high linearity of the gradient generated, we write a MATLAB script to simulate the field and compare the results.

II. METHOD

We compare the analytical derivations proposed by Mansfield and Caparelli [2], [3] for the gradient G_y . The former is a direct method, the latter an inverse method in Fourier k-space. For a magnetic induction field in the transverse plane, the optimization procedure consists in the search of geometrical parameters of the coils, by zeroing the coefficients in the field expansion of the magnetic field factoring powers of the coordinates x and y greater than one. The simplest geometries we consider are the BM3 and CAP3 models. Four straight segments of current are displaced along the x direction, placed at coordinates $z = \pm d_1$, $y = \pm y_1$. For higher degree of linearity, we analyze models CAP5 and CAP7, with eight parallel wires. Results are in Fig. 5 Table I.

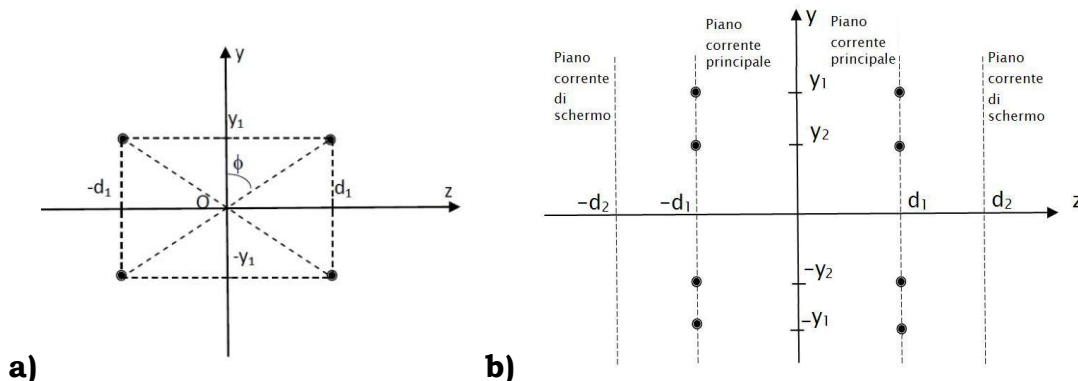


FIG. 1 – a) Geometry for BM3 and CAP3 models: 4 current segments parallel to the x axis; b) For CAP5 and CAP7: 8 current segments parallel to the x axis.

For BM3 model, the component B_z of the field generated by a single wire with the DC current I , in polar coordinates, is:

$$B_z(y, z) = \frac{\mu_0 I}{2\pi} \operatorname{Re}(\underline{\rho} - \underline{\varepsilon})^{-1}$$

$\underline{\varepsilon} = y + iz$ is the observation point, $\underline{\rho} = y_1 + id_1 = \rho^{i\phi}$ is the wire position (see Fig. 5.a). Then the Fourier series for four current segments is:

$$B_z(y, z) = \frac{\mu_0 I}{2\pi\rho} \left[\frac{y}{\rho} \cos(2\phi) + \operatorname{Re}\left(\frac{\underline{\varepsilon}}{\underline{\rho}}\right)^3 \cos(4\phi) + \operatorname{Re}\left(\frac{\underline{\varepsilon}}{\underline{\rho}}\right)^5 \cos(6\phi) + \dots \right]; \quad (|\underline{\varepsilon}| < |\underline{\rho}|)$$

The optimization consists in finding ϕ to obtain $\cos(4\phi) = 0$.

For the inverse method [3], the unknown current density is searched in the k -space. Then, using the Fourier Transform, the real current density can be estimated. The general use of this method is for shielded coils but imposing the outer secondary current distribution at an infinite distance we design coils without active shielding. We consider two independent current density distributions to obtain the desired field into the Region Of Interest (ROI), and a zero field outside the coil. For a G_y gradient coil, the goal is to obtain:

$$B_z(x, y, z) = B_z^1(x, y, z) + B_z^2(x, y, z) = (0, 0, G_y y) \quad (z \leq d_1)$$

$$B_z(x, y, z) = B_z^1(x, y, z) + B_z^2(x, y, z) = 0 \quad (z \geq d_1)$$

In the region with $|z| < d_1$, the Taylor series expansion for B_z , is:

$$B_z^-(\underline{r}) = Q_1 \left(\frac{d_2}{d_1}, \frac{y_1}{d_1} \right) y + \sum_{n=3}^{\infty} Q_n \left(\frac{d_2}{d_1}, \frac{y_1}{d_1} \right) f(y^l z^m) = (0, 0, G_y y) ; \quad l + m = n; n \text{ odd}$$

where

$$Q_n \left(\frac{d_2}{d_1}, \frac{y_1}{d_1} \right) = \int_0^{\infty} \frac{\sinh \left[\left(\frac{d_2}{d_1} - 1 \right) y \right]}{\cosh \left(\frac{d_2}{d_1} k_y \right)} \cos \left(k_y \frac{y_1}{d_1} \right) k_y^n dk_y$$

In order to solve the integral equations we use the numerical solver of MAPLE. CAP3 optimization consists in finding the solutions for the integral $Q_3(y_1/d_1; d_2/d_1) = 0$. For CAP5, we fix $\eta=I_2/I_1$, then we solve:

$$\begin{cases} Q_3\left(\frac{y_1}{d_1}\right) + \eta Q_3\left(\frac{y_2}{d_1}\right) = 0 \\ Q_5\left(\frac{y_1}{d_1}\right) + \eta Q_5\left(\frac{y_2}{d_1}\right) = 0 \end{cases}$$

For CAP7 model, the set is:

$$\begin{cases} Q_3\left(\frac{y_1}{d_1}\right) + \eta Q_3\left(\frac{y_2}{d_1}\right) = 0 \\ Q_5\left(\frac{y_1}{d_1}\right) + \eta Q_5\left(\frac{y_2}{d_1}\right) = 0 \\ Q_7\left(\frac{y_1}{d_1}\right) + \eta Q_7\left(\frac{y_2}{d_1}\right) = 0 \end{cases}$$

III. RESULTS

The results for the optimizations are shown in Fig. 1. Table I reports some of these and Fig. 2 shows the simulated field.

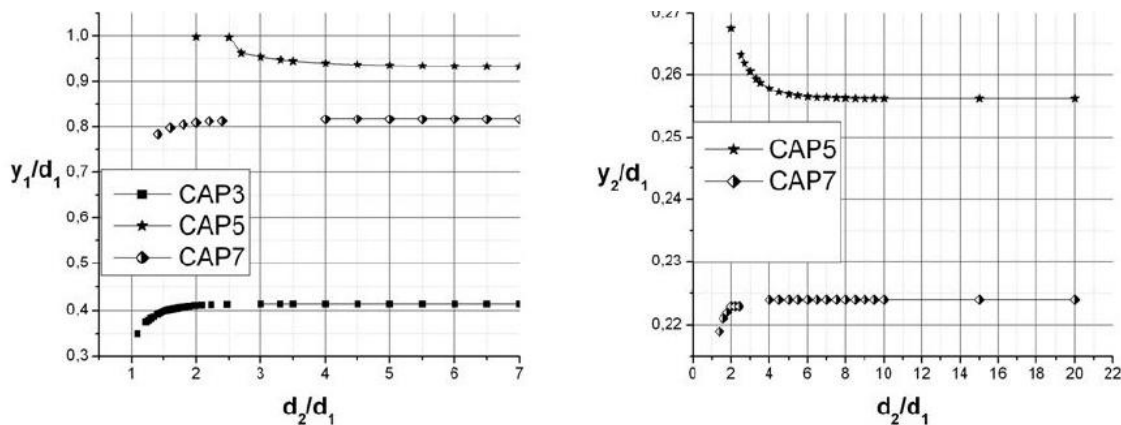


FIG. 2 – Optimization results for the model CAP3, CAP5 and CAP7. We use the asymptotic values of y_2/d_1 useful for coils without active screen.

Table 1 – STABLE SOLUTIONS CHOSEN FOR UNSHIELDED COILS

Model Name	I_2/I_1	Parameters			Optimization: zeroed terms	Notes
		Y_1/D_1	Y_2/D_1	L/D_1		
BM3	-	2.414	-	4	y^3	Direct Method
CAP3	-	0.421	-	4	yz^2-y^3	Target Field Method
CAP5	6:10	0.931	0.256	4	(yz^2-y^3) and $(yz^4-y^3z^2+ y^5)$	Target Field Method
CAP7	0.574	0.817	0.224	4	(yz^2-y^3) and $(yz^4-y^3z^2+ y^5)$ and $(yz^6-y^3z^4+ y^5z^2+ y^7)$	Target Field Method

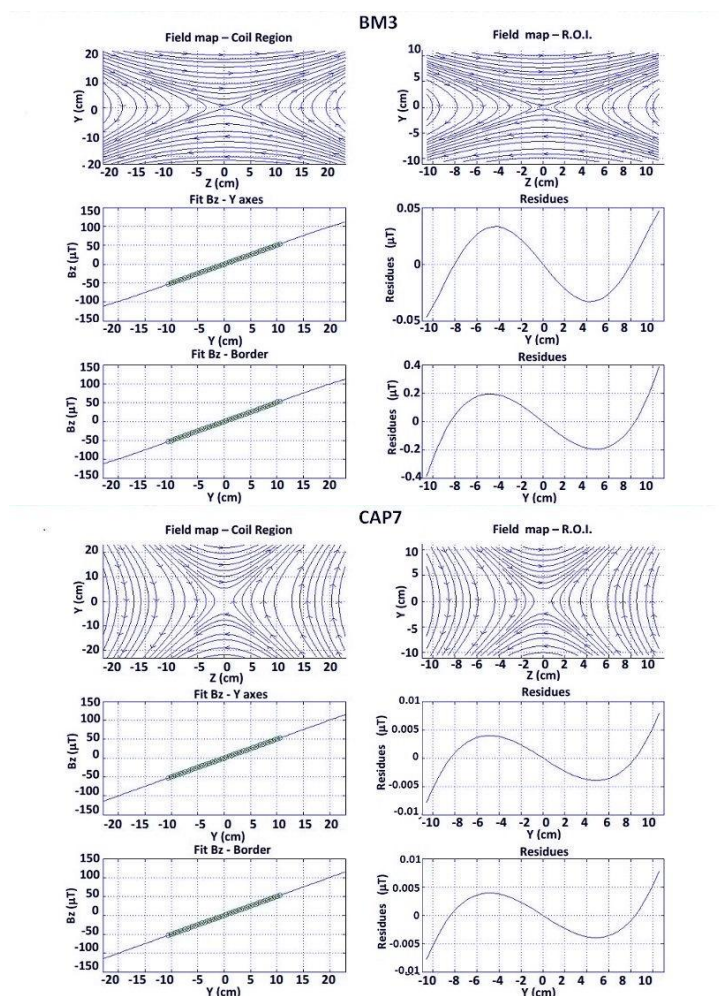


FIG. 3 – Simulation results for BM3 and CAP7 models for $G_y = 500 \mu\text{T}/\text{m}$.

IV. CONCLUSION

We have shown a simple procedure to optimize current distributions to design coils to generate magnetic fields with a specific spatial distribution with a degree of accuracy suitable for specific applications.

ACKNOWLEDGEMENT

This work is based on Marco Tannino's master-degree thesis supervised by Prof. Bruno Maraviglia and Dr. Antonino Mario Cassarà.

REFERENCES

- [1] R. Turner, "A target field approach to optimal coil design," *Journal of Physics D: Applied Physics*, vol. 19, 1986, pp. L147-L151.
- [2] V. Bangert and P. Mansfield, "Magnetic field gradient coils for NMR imaging," *J. Phys. E Sci. Instrum.*, vol. 15(2), 1982, pp. 235-239.
- [3] E.C. Caparelli, D. Tomasi, and H. Panepucci, "Shielded biplanar gradient coil design," *J. Magn. Reson. Imaging*, vol. 9, 1999, pp. 725-731.

HYDROMETEOR EXTINCTION MODELING FOR FREE-SPACE OPTICAL CHANNEL CHARACTERIZATION: RAIN AND SNOW EFFECTS

S. Mori⁽¹⁾, F. S. Marzano⁽¹⁾, G. M. Tosi Beleffi⁽²⁾, S. di Bartolo⁽³⁾

⁽¹⁾ D.I.E.T., Sapienza University of Rome & CETEMPS
Via Eudossiana 18, 00184 Rome, Italy
 {mori,marzano}@diet.uniroma1.it

⁽²⁾ Min. of Economic Development

⁽³⁾ I.S.C.O.M., Min. of Economic Development
Viale America 201, 00144 Rome, Italy
 {giorgio.tosibeleffi,silvia.bartolo}@mise.gov.it

Abstract

Wireless communications through free space using optical carrier (Free Space Optics, FSO) technology ensure high data rates, low error rates and power consumption and inherent security. However, FSO channel availability can be limited by path attenuation due to atmospheric hydrometeors, especially fog but also snowflakes and raindrops. In this work a parametric model to simulate droplets scattering effects on FSO links is proposed. Extinction and scattering effects versus precipitation rate will be analyzed for snow and rain particles. Multiple scattering effects will be briefly discussed.

Index Terms – Free space optics, hydrometeor effects modeling, rain rate, equivalent snow rate

I. INTRODUCTION

Optical carriers represent a promising possibility in realizing peer-to-peer links and wide area networks (WANs) [1]. This technology, often indicated as Optical Wireless Communications (OWC) or in outdoor connections Free Space Optics (FSO), relies on the transmission of modulated near-infrared (NIR) beams of collimated light through the channel focused by lens on detectors at the receiver [2]. Optical carriers allow high data rates with relatively low error rates. Moreover the narrow beam ensures privacy protection, channel spatial density and potential spatial diversity. However an acceptable Quality of Service (QoS) can be achieved only for short ranges (up to 1 km about). FSO systems development is also limited by the sensitivity to turbulence and atmospheric particles. In particular hydrometeors present in any meaningful way within the communication channel can introduce severe attenuations to the transmitted beam, reducing the channel availability up to the complete interruption in the most intense events. The most severe contribution to path attenuation is due to fog particles, but also snowflakes and raindrops can contribute significantly. This work will show a model for the analysis of extinction due to path hydrometeors. In particular in this work will be analyzed raindrops (for

light, moderate and heavy rain) and snowflakes (dry and wet) contributions as function of their precipitation rate. Effects of multiple scattering will be also briefly discussed. Analysis will be performed for a carrier wavelength of 1550 [nm] commonly used in FSO applications.

II. HYDROMETEOR SCATTERING MODELING

Hydrometeors single scattering properties can be derived through Mie theory determining the extinction σ_e , scattering σ_s and absorption σ_a cross sections and the asymmetry factor g of the particle [3]. So the extinction coefficient k_e is:

$$k_e = \int_{r_m}^{r_M} \sigma_e(r) N_p(r) dr = \int_{r_m}^{r_M} [\sigma_a(r) + \sigma_s(r)] N_p(r) dr \quad (1)$$

where r_m and r_M are minimum and maximum of the radius r , and $N_p(r)$ the Particle Size Distribution (PSD) of particle class p .

Mie theory applies to spherical particles while hydrometeors shapes depend on their microphysics and thermodynamical development. In this work, non-spherical particles have been modeled as equi-volume spherical particles. Regarding PSD, in the developed framework we have adopted the Scaled Gamma (SG) PSD as a general model for all hydrometeor class. As independent variables we have considered the shape parameter μ_e , effective radius r_e [mm], water content W [g·m⁻³], all varying with a given range, and specific density ρ_p [g·cm⁻³]. Regarding complex refractive index we have considered liquid water and ice, and applied the Maxwell-Garnett approximation for snow particles. Altogether we have defined 8 hydrometeor classes (advection and radiation fog, light, medium and heavy rain, dry and wet snow, graupel). Precipitation rate R_p [mm/h] can be estimated through:

$$R_p = \int_{r_m}^{r_M} v_p(r) \frac{m_p(r)}{\rho_p} N_p(r) dr \quad (2)$$

with v_p the terminal velocity, m_p the mass and ρ_p the density. While (2) applies to raindrops, snowfall rate is usually expressed in millimeters of equivalent liquid water per hour, respect liquid water density ρ_w . In this work we have determinate particle terminal velocity and snow mass by literature models.

Fig. 1 shows the extinction and scattering coefficients [dB/km] versus precipitation rate [mm/h] for rain and snow particles. Regression curves are given. We can observe how snowflakes extinction is much intense than raindrops ones. Finally extinction curves of rain and snow are respectively compared with [4] and [5] empirical laws.

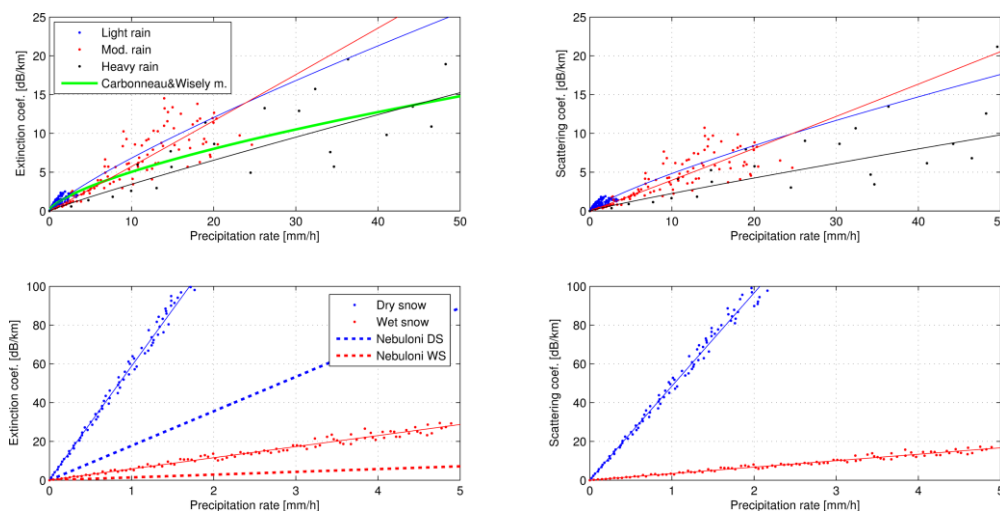


FIG. 1 – Extinction (left) and scattering (right) coefficients [dB/km] versus precipitation rate [mm/h] for raindrops (top) and snowflakes (bottom). Plots show also regression curves and extinction comparison with [9]-[10] models.

III. MULTIPLE SCATTERING MODELING

In presence of a medium characterized by both absorbing and scattering properties, its extinction law has to be expressed by complex models such as the Radiative Transfer Equation (RTE). Its full solution requires the use of computationally-cost numerical techniques, but quite accurate results can be achieved also using fast approximated analytical approaches. An example is the hybrid Eddington method within the two-stream hypothesis [6], adopted in this work.

Multiple scattering effects can be evaluated in terms of transmittance T [adim.] as derived by the Beer-Lambert law:

$$I(z, \theta, \varphi) = I(0, \theta, \varphi) e^{-\tau} = I_0 e^{-k_e z} = I_0 T \quad (3)$$

being z [km] the range, (θ, φ) the incidence angles, I_0 the incident intensity [$\text{W} \cdot \text{sr}^{-1} \cdot \text{m}^{-2}$], τ the optical thickness [adim.] and k_e [km^{-1}] the extinction coefficient. In RTE context T , τ and k_e have to be considered apparent properties due to both single and multiple scattering.

Fig. 2 shows the single and multiple scattering transmittances of raindrops and snowflakes versus the single scattering optical thickness. Multiple scattering reduces the apparent attenuation of the channel by increasing the incoherent component redirected towards the receiver.

IV. CONCLUSION

A parametric model of atmospheric hydrometeors scattering effects on FSO links has been illustrated. Extinction and scattering effects due to rain and snow precipitation rate have been analyzed. Multiple scattering effects have been discussed. The developed model and hydrometeors characterization will be verified and refined by mean of in-situ measurements collected by the experimental set-up realized in Rome. Other measurements campaigns have been established within COST

IC1101 group WG1. Objective of this work is realizing a generalized parametric model of extinction, scattering asymmetry and volumetric albedo respect of water content, fall rate or visibility.

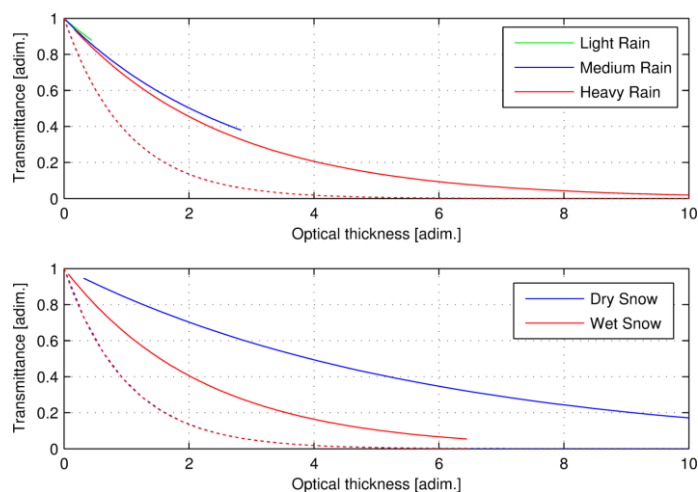


FIG. 2 – Transmittance T [adim.] versus single scattering optical thickness τ [adim.] for raindrops and snowflakes. Dotted lines refer to single scattering transmittance, continuous lines to multiple scattering one.

ACKNOWLEDGEMENT

This work has been carried out within a joint project through ISCOM (Department of Communications – Ministry of Economic Development) and University La Sapienza. F. Consalvi of Fondazione Ugo Bordoni is acknowledged for his support on technical activities. COST IC1101 group WG1 and Special Interest Group TESEO are also acknowledged.

REFERENCES

- [1] COST Action IC1101, “Optical wireless communications - an Emerging technology”, Memorandum of Understanding official document, http://www.cost.esf.org/domains_actions/ict/Actions/IC1101, 2011.
- [2] A.K. Majumdar and J.C. Ricklin “Free-Space Laser Communications, Principles and Advantages”, Springer Science LLC, 233 Spring Street, New York, NY 10013, U.S.A., 2008.
- [3] C.F. Bohren and D.R Huffman, “Absorption and Scattering of Light by Small Particles”, *Wiley*, 1983
- [4] T. H. Carbonneau and D. R. Wisley, “Opportunities and challenges for optical wireless; the competitive advantage of free space telecommunications links in today’s crowded market place,” *SPIE Conference on Optical Wireless Communications, Massachusetts*, pp. 119-128, 1998.
- [5] R. Nebuloni and C. Capsoni, “Laser Attenuation by Falling Snow”. *Proc. of 6th International Symposium on Communication Systems, Networks and Digital Signal Processing (CNSDSP)*, Graz, 23 – 25, 2008
- [6] W.E. Meador and W.R. Weaver, “Two-stream approximations to radiative transfer in planetary atmospheres - A unified description of existing methods and a new improvement”, *J. Atmos. Sci.*, vol. 37(3), pp. 630-643, 1980

ALL-SOLID PHOTONIC BANDGAP FIBERS WITH MICROSTRUCTURED CLADDING

E. Coscelli⁽¹⁾, F. Poli⁽¹⁾, A. Cucinotta⁽¹⁾, S. Selleri⁽¹⁾

⁽¹⁾ Information Engineering Department, University of Parma
Parco Area delle Scienze 181/a, 43124 Parma, Italy
enrico.coscelli@unipr.it

Abstract

Double cladding all-solid photonic bandgap fibers can provide several advantages over index-guiding PCFs for amplifier and laser applications, being able to filter out unwanted transmission bands by properly tuning the bandgap position. Such properties can be exploited to obtain amplification at wavelengths not normally accessible with Yb-doped fibers, such as those above 1100 nm. In order to obtain single-mode propagation in this kind of fibers, advanced cladding designs are required, to allow effective delocalization of the high-order modes. Single-mode properties of so called heterostructured bandgap fibers are here discussed, and the better performances are numerically demonstrated.

Index Terms – Fiber lasers and amplifiers, photonic crystal fibers, photonic bandgap.

I. INTRODUCTION

A huge interest is currently devoted to power scaling of fiber lasers and amplifiers, fueled by the demand of many applications in the industry, medical, defense and science fields [1]. A fundamental limit to this power scaling is given by the tradeoff between the need to increase the core area to avoid the onset of nonlinearities and the requirement of Single-Mode (SM) propagation. Index guiding PCFs are designed to solve this problem by decreasing the core NA, but technological issues thwart the practical control of this parameter with accuracy higher than $\pm 10^{-4}$, limiting the possibility of mass-production of SM LMA step-index fibers with core diameter larger than about 10 μm . All-Solid Photonic BandGap Fibers (AS-PBGFs) have been appointed as a promising technology to be employed in the development of high power fiber lasers and amplifiers [2-4]. This particular kind of optical fiber is characterized by the presence of an array of high refractive index inclusions in a glass matrix, which provides confinement to the guided modes through the photonic bandgap effect. This guiding mechanism can be exploited to realize fibers with very large mode area, selective spectral filtering of the transmitted light, allowing amplification at wavelengths not normally accessible with Yb-doped fibers, such as those above 1100 nm [5], and low sensitivity to bending. Unfortunately, the latter property has one major drawback, that is that differential bending loss between the Fundamental Mode (FM) and the High-Order Modes (HOMs) cannot be exploited to suppress the HOMs. As a consequence, smarter designs are required to effectively delocalize the HOMs from the core, so that they

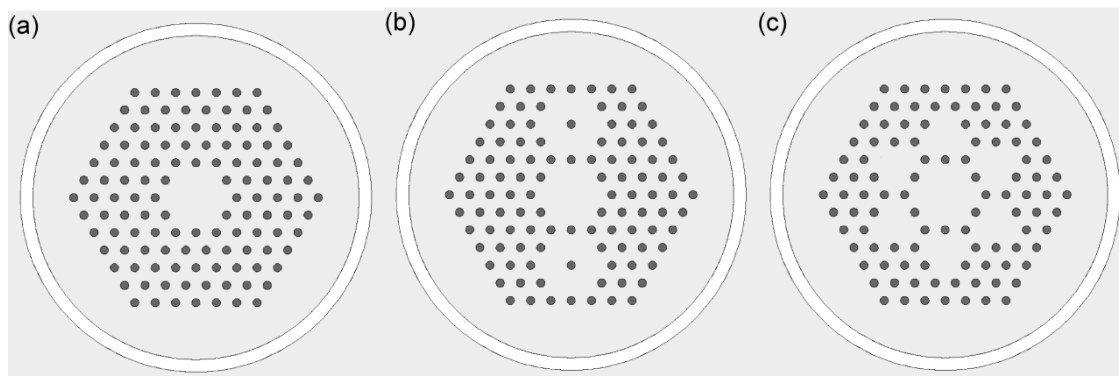


Fig. 1 - Cross-section of the three AS-PBGFs considered: (a) fiber A (with conventional cladding), (b) fiber B and (c) fiber C.

are not amplified.

In this paper, the single-mode properties of two AS-PBGFs with the so called heterostructured-cladding [6] have been numerically analyzed by means of a full-vector modal solver based on the finite-element method [7]. For comparison purposes, an AS-PBGFs with a conventional cladding, that is with a triangular lattice of high-index inclusions, has been considered. Simulation results have demonstrated the capability of heterostructured-cladding fibers to effectively suppress the HOMs while maintaining all their good properties.

II. RESULTS AND DISCUSSION

The cross-section of the three double-cladding AS-PBGFs numerically analyzed are shown in Fig. 1(a)-(c). All of them are 7-cell PCFs whose cladding is made of resonators with spacing $\Lambda = 11.8 \mu\text{m}$, diameter of $7.1 \mu\text{m}$ and parabolic graded-index profile with $\text{NA} = 0.29$. A $7 \mu\text{m}$ -wide air-cladding with inner diameter of $200 \mu\text{m}$ encloses the structure, which is built over a silica matrix with refractive index 1.45. The first fiber, fiber A, shown in Fig. 1(a), is a normal AS-PBGF with a complete triangular lattice of resonators. Two different heterostructured-cladding AS-PBGFs have been considered, that is fiber B, shown in Fig. 1(b), where two sets of six elements around a central one, placed on the axis orthogonal to the bending plane have been removed, and fiber C, shown in Fig. 1(c), where six groups of 3 elements around the core have been removed. In order to simulate fiber bending with a diameter of 30 cm, as in practical high-power applications, conformal mapping has been applied. The overlap integral Γ over the doped core of the FM and of the first HOMs, that is the LP_{11} -like HOM_{11} and HOM_{12} , which has been calculated to assess the guided-mode confinement [8], is shown in Fig. 2(a)-(c) in the wavelength range between 900 and 1150 nm for the three AS-PBGs considered in the analysis.

Notice that for fiber A the overlap integral of both FM and HOM_{11} , shown in Fig. 2(a), is higher than 0.8 in the wavelength range between 960 nm and the red-edge of the PBG. As a consequence, the HOM suppression is possible only near the blue edge of the FM transmission

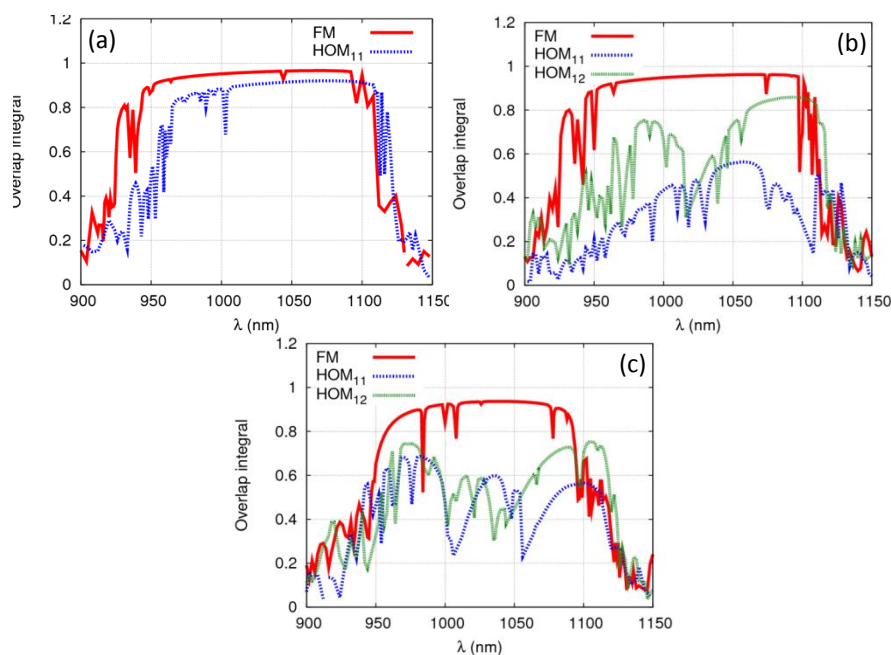


Fig. 2 - Overlap integral of the FM and most detrimental HOMs of (a) fiber A, (b) fiber B and (c) fiber C.

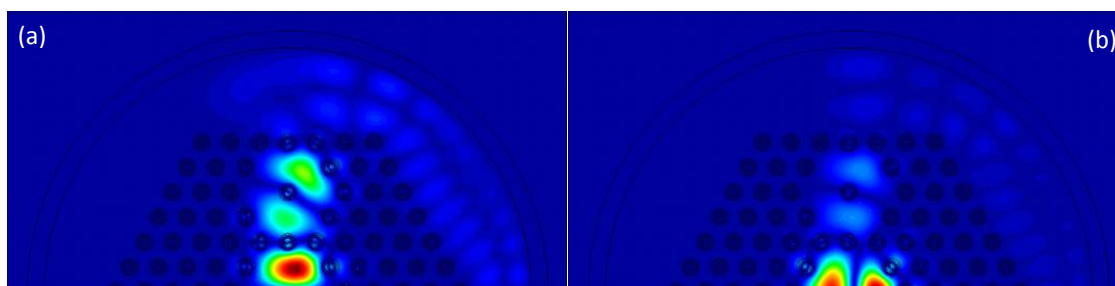


Fig. 3 - Magnetic field modulus distribution of (a) HOM_{11} and (b) HOM_{12} of fiber A, calculated at 1064 nm with a bending diameter of 30 cm.

window, roughly between 940 nm and 960 nm. Unfortunately, in this region several spikes appear, which are caused by the bending-induced coupling of the core modes with cladding ones, located either between consecutive rings of high-index elements or between them and the air-cladding.

Fig. 2(b) and 2(c) show that the heterostructured cladding provides a significant reduction of the Γ value of the two HOMs, especially around the PBG central wavelength, by favoring their coupling with the modes existing inside the cladding defects. Notice that, with a bending diameter of 30 cm, the transmission band for the FM is almost immune to this effect, being its overlap integral higher than 0.9 in a wavelength range spanning from about 950 nm to 1100 nm, and from about 950 nm to 1080 nm for fiber B and C, respectively. As reported in Fig. 2(c), an overlap difference between FM and both HOM_{11} and HOM_{12} larger than 0.3 is obtained for fiber C between 1000 nm and 1060 nm, greatly improving the SM properties with respect to fiber A. On the contrary, for

fiber B the suppression is more effective for HOM_{11} , whose field distribution has the zero aligned with the bending plane. In fact, as demonstrated by the magnetic field modulus distribution reported in Fig. 3(a), it is poorly confined at almost any wavelength, with overlap integral lower than 0.6. On the contrary, HOM_{12} , whose field distribution has the zero direction orthogonal to the bending plane, is more confined, as shown in Fig. 3(b), with Γ generally higher than 0.7. This different behavior is due to the fact that the cladding defects are aligned with the lobes of HOM_{11} , thus causing a stronger coupling. As a consequence, by taking into account HOM_{12} , a differential overlap higher than 0.3 is achieved only over a 20 nm range around 1030 nm.

III. CONCLUSION

In this paper the single-mode properties of two innovative designs of AS-PBGFs with heterostructured cladding have been numerically analyzed by means of a full-vector modal solver based on the finite-element method. Results have shown that a better HOM suppression, and a consequent wider SM range, can be obtained by adding proper cladding defects in the conventional triangular lattice of high-index inclusions.

REFERENCES

- [1] D.J. Richardson, J. Nilsson, W.A. Clarkson, "High power fiber lasers: current status and future perspectives," *J. Optics Soc. Am. B*, vol. 27, pp. B63-B92, Nov. 2010.
- [2] F. Luan, A.K. George, T.D. Hedley, G.J. Pearce, D.M. Bird, J.C. Knight, P. St. J. Russell, "All-solid photonic bandgap fiber," *Optics Lett.*, vol. 29, pp. 2369-2371, Oct. 2004.
- [3] O.N. Egorova, S.L. Semjonov, A.F. Kosolapov, A.N. Denisov, A.D. Pryamikov, D.A. Gaponov, A.S. Biriukov, E.M. Dianov, M.Y. Salganskii, V.F. Khopin, M.V. Yashkov, A.N. Gurianov, D.V. Kuksenkov, "Single-mode all-silica photonic bandgap fiber with 20- μm mode-field diameter," *Opt. Express*, vol. 16, pp. 11735-11740, Aug 2008.
- [4] F. Kong, K. Saitoh, D. McClane, T. Hawkins, P. Foy, G. Gu, L. Dong, "Mode area scaling with all-solid photonic bandgap fibers," *Opt. Express*, vol. 20, 26363-26372, Nov 2012.
- [5] C.B. Olausson, A. Shirakawa, M. Chen, J.K. Lyngsø, J. Broeng, K.P. Hansen, A. Bjarklev, K. Ueda, "167 W, power scalable ytterbium-doped photonic bandgap fiber amplifier at 1178 nm," *Opt. Express*, vol. 18, pp. 16345-16352, Aug. 2010.
- [6] A. Baz, L. Bigot, G. Bouwmans, Y. Quiquempois, "Single-mode, large mode area, solid-core photonic bandgap fiber with hetero-structured cladding," *J. of Lightwave Technology*, vol. 31 no. 5, pp. 830-835, 2013.
- [7] F. Poli, A. Cucinotta, S. Selleri, "Photonic Crystal Fibers. Properties and Applications," *Springer Series in Material Science*, Dordrecht (2007).
- [8] E. Coscelli, F. Poli, T.T. Alkeskjold, F. Salin, L. Leick, J. Broeng, A. Cucinotta, S. Selleri, "Single-mode design guidelines for 19-cell double-cladding photonic crystal fibers," *J. of Lightwave Technology*, vol. 30, pp. 1909-1914, June 2012.

ARC CURVATURE EFFECT ON CONFINEMENT LOSS IN HYPOCYCLOID HOLLOW CORE KAGOME FIBERS

M. Masruri⁽¹⁾, L. Vincetti⁽²⁾, B. Debord⁽³⁾, M. Alharbi^(3,4), T. Bradley^(3,4), C. Fourcade-Dutin⁽³⁾, Y.Y. Wang⁽³⁾, F. G er ome⁽³⁾ and F. Benabid⁽³⁾

⁽¹⁾ Department of Information Engineering, University of Parma
Viale G.P: Usberti 181/A, 43124 Parma, Italy

⁽²⁾ Department of Engineering “Enzo Ferrari”, University of Modena and Reggio Emilia
Via Vignolese 905b, 41125 Modena, Italy
luca.vincetti@unimore.it

⁽³⁾ GPPMM group, Xlim Research Institute, UMR 7252 CNRS, Universit  de Limoges, Limoges, France

⁽⁴⁾ Department of Physics, University of Bath, Claverton Down, BA2 7AY, UK

Abstract

Numerical and experimental results about the influence of the arc curvature on the confinement loss in hypocycloid hollow core Kagome fibers are reported. The results show that by increasing arc curvature, confinement loss strongly decreases.

Index Terms – Photonic crystal fibers; Fiber design and fabrication.

I. INTRODUCTION

Hollow-core photonic crystal fiber (HC-PCF) consists of an optical-guiding central air-core surrounded by a microstructured cladding composed by an arrangement of air holes running along its length. So far two main types of HC-PCF have been established and their guidance mechanisms characterized. The first HC-PCF family guides via photonic bandgap (PBG). They hold the potential for guiding light with attenuation significantly lower than the fundamental limit of ~0.16 dB/km in conventional optical fibers even though the lowest loss obtained with this type of fiber is 1.2 dB/km, due to the roughness of the air/glass interface and the presence of silica residing interface modes that couple with the core modes [1]. Moreover HC-PCF suffers of a limited transmission bandwidth (typically less than ~70 THz), which has hindered its use in applications where a large optical spectral band is required [2].

The second type of HC-PCF is distinguished by its broadband optical guidance and the relatively higher transmission loss-levels compared to the PBG guiding HC-PC. This HC-PCF family guides via inhibited coupling (IC) between the cladding modes and the guided core modes [3]. Unlike in PBG guiding HC-PCF, the cladding of the IC guiding HC-PCF doesn't exhibit any photonic bandgap but relies on a strong transverse mismatch between the continuum of cladding modes and those of the core. Despite the effort in optimizing the cladding structure, loss has been remain relatively high (>0.5 dB/m).

Recently, a new route in enhancing IC in Kagome HC-PCF has been proposed and demonstrated a dramatic reduction of loss. This consists in core-shaping the HC-PCF to a hypocycloid-like contour so as to minimize the core and cladding mode coupling [4]. These new developments call for a further understanding on the relevant physical parameters behind the confinement loss. This is of interest in the fundamental physics underlying this novel optical guidance mechanism, and to assess IC guiding HC-PCF as a potential long-haul optical fiber.

In this work the effect of arcs curvature of the hypocycloid core is experimentally and numerically investigated. Results show that by increasing the curvature of the cups a reduction of several order of magnitude in propagation loss can be obtained.

II. LOSS DEPENDENCE ON ARC CURVATURE

Fig. 1(a) shows a typical example of hypocycloid-like core HC-PCF with a Kagome lattice cladding. In the case considered here, the hypocycloid core contour results from seven missing cells of a triangular arrangement of circular tubes. Consequently, the core contour is formed by two alternating arcs, which result in a small circle with radius R_{in} that is tangent with the six most inward arcs, and a larger circle with radius R_{out} which is tangent with the six most outward arcs. The curvature of the hypocycloid-like core is quantified through the parameter b (see Fig. 1(b)) defined as $b=d/r$, where d is the distance between the top of the arcs and the chord joining the nodes connecting the inward cusp to its two neighboring ones and r is half the chord-length.

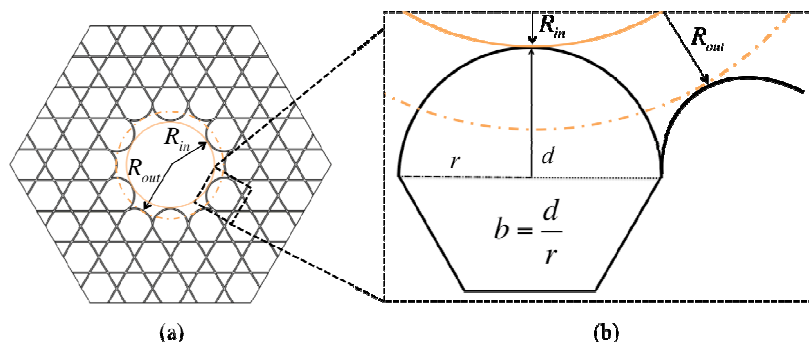


FIG. 1 – (a) Structure of a hypocycloid-like core HC-PCF. (b) Definition of the parameters quantifying the curvature of the core arcs.

With this definition, the “classical” Kagome fiber with a “quasi” circular core corresponds to $b=0$, whilst $b=1$ corresponds to a core contour with circular shaped arcs. For $b>1$, the inward arcs have an elliptical shape whilst the outward ones are set to have a circular shape. Fig. 2(a) shows the calculated loss spectra of the HE_{11} core mode for a hypocycloid-like core Kagome-lattice HC-PCF with different arcs curvatures. In the simulations, all the HC-PCFs have a 7-cell core defect and a Kagome-latticed cladding of 3 rings. The strut thickness t is equal to 350 nm . The HC-PCF structure has been studied for core arcs varying from $b=0$ to $b=1.5$ by keeping constant the core inner radius. For all the fibers, the loss spectrum exhibits a high loss spectral-region near 700 nm ; corresponding to the resonance of the fundamental core mode with the cladding modes with low spatial dependence [1, 3]. The calculated spectra clearly show the strong influence of the arcs curvature on the loss confinement. The loss level drops from $\sim 1000\text{ dB/km}$ in the case of a “quasi” circular core (i.e. $b=0$) to lower than the 1 dB/km for hypocycloid core with $b\geq 1$. Fig. 2(c) illustrates this trend for one wavelength in the first transmission band ($\lambda_j=1000\text{ nm}$), and one wavelength at the second order transmission window ($\lambda_j=500\text{ nm}$).

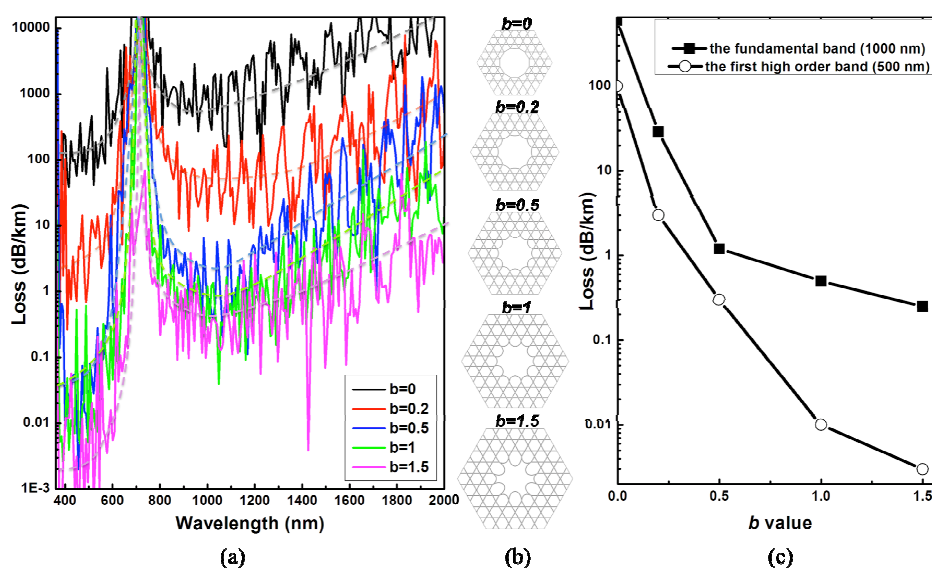


FIG. 2 – (a) Kagome-latticed HC-PCF computed loss evolution with the arcs curvature ($b=0, 0.2, 0.5, 1$ and 1.5). The dashed lines are added for eye-guidance. (b) The fiber structure transverse profile for the different b values. (c) Evolution with b of the transmission loss figures for 1000 nm (joined solid squares) and for 500 nm (joined open circles) wavelengths.

This evolution has been experimentally confirmed with the fabrication of four Kagome-latticed fibers with different b . Fig. 3(a) shows scanning electronic microscope (SEM) images of the fibers around the fiber core.

Care was taken in the fiber design and fabrication so as to have all the fibers with the same strut thickness of 350 nm , core diameter of $60\text{ }\mu\text{m}$ and the pitch of $21\text{ }\mu\text{m}$ within a measured relative uncertainty of less than 10%.

Fig. 3(b) shows the loss spectra in the fundamental band obtained by a cut back measurement using a supercontinuum source and the fiber length were in range fo 50-70 m. The loss level was found to be $\sim 1300\text{ dB/km}$ for $b=0$, 400 dB/km for $b=0.39$, 200 dB/km for $b=0.68$, and 40 dB/km for $b=0.75$, which is in very good qualitative agreement with the theoretical calculations.

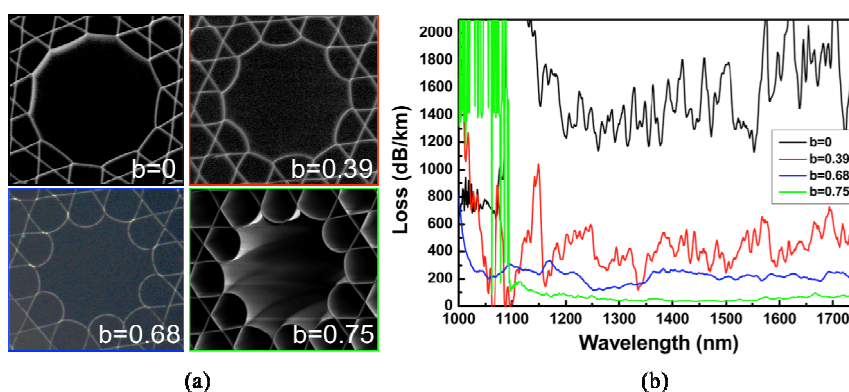


FIG. 3 – SEM images (a) and measured loss spectra (b) of fabricated hypocycloid-core Kagome-latticed HC-PCFs with different b .

III. CONCLUSION

In conclusion, a systematic numerical and experimental study on the effect of the hypocycloid-core Kagome HC-PCF arc curvature on the fiber transmission loss have been reported. The results show that the enhancement of the curvature allows a significant reduction of the fundamental mode confinement loss.

REFERENCES

- [1] P. J. Roberts, F. Couny, H. Sabert, B. J. Mangan, D. P. Williams, L. Farr, M. W. Mason, A. Tomlinson, T. A. Birks, J. C. Knight, and P. St. J. Russell, "Ultimate low loss of hollow-core photonic crystal fibres," *Opt. Express* vol. 13, pp. 236–244, 2005.
- [2] F. Benabid and J. P. Roberts, "Linear and nonlinear optical properties of hollow core photonic crystal fiber," *J. Mod. Opt.* vol. 58, pp. 87–124, 2011.
- [3] L. Vincetti and V. Setti, "Waveguiding mechanism in tube lattice fibers," *Opt. Expr.* vol. 18, pp. 23133–23146, 2010.
- [4] Y. Y. Wang, N. V. Wheeler, F. Couny, P. J. Roberts, and F. Benabid, "Low loss broadband transmission in hypocycloid-core Kagome hollow-core photonic crystal fiber," *Opt. Lett.* vol. 36, pp. 669–671, 2011.

PROCESSING OF THIN FILM MATERIALS BY MEANS OF NS AND PS LASER RADIATION

M. Sozzi⁽¹⁾, A. Lutey⁽²⁾, S. Selleri⁽¹⁾, A. Cucinotta⁽¹⁾

⁽¹⁾ Dept. of Information Engineering, University of Parma, Area Parco delle Scienze 181/A, Parma, Italy

⁽²⁾ Dept. of Industrial Engineering, University of Bologna, Viale Risogimento 2, Bologna, Italy
sozzi@tlc.unipr.it

Abstract

Thin-film materials such as aluminum, polyethylene, and polypropylene have been exposed to different laser radiation. A wide number of samples have been processed with 10 - 12.5 ns IR and Green, and 500 - 800 ps IR laser radiation at different translating speeds ranging from 50 mm/s to 1 m/s. High quality incisions have been obtained for all tested materials within the experimental conditions. The presented results provide the necessary parameters for an efficient cut and processing of the tested materials, for the employment of pulsed laser sources in the packaging industry, allowing the laser to prevail in lieu of more costly and energy intensive methods.

Index Terms – Aluminum, laser ablation, material processing, thin films.

I. INTRODUCTION

Although laser technology is quite a mature technology [1], only recently have lasers been used in the industrial processing of product wrapping materials. The understanding of the mechanisms that govern the ablation process of thin-film metal and plastics foils is very important.

Several experimental works are present in the literature dealing with the ablation of aluminum. Colina et al., and Porneala et al. [2] [3], in their respective works, used nanosecond, infrared and green lasers. Despite similar experimental conditions, the results are rather variable, with differences in ablation threshold of even two orders of magnitude. A large amount of records dealing with the ablation of PMMA [4] are present in literature, while a limited number of works deal with polypropylene and polyethylene [5] [6].

In this work, ablation depth in relation to the applied fluence, is determined experimentally for thin aluminum (AL), polypropylene (PP) and polyethylene (PE) films subject to 500 ps and 800 ps pulses of wavelength 1064 nm, and 10 ns and 12.5 ns pulses of wavelength 515 nm and 1030 nm. In each case, the ablation threshold is first determined, the ablation rates subsequently presented as functions of the incident fluence.

II. EXPERIMENTAL

A large number of samples of aluminum (AL), polyethylene (PE), polypropylene (PP) were exposed to pulsed infrared (IR) and green laser radiation.

Two laser systems were utilised for the tests. The IR laser was a Helios IR (Coherent Inc.) emitting a beam of wavelength 1064 nm and diameter 2.5 mm with a pulse duration ranging from 500 ps at a repetition rate (RR) of 30 kHz to 800 ps at a RR of 70 kHz. The beam was attenuated externally by a half-wave plate and polariser. The green laser was a BOREAS G15 (Eolite Systems) emitting a beam of wavelength 515 nm, and 1030 nm, and diameter 2 mm with a pulse duration ranging from 10 ns at a RR of 20 kHz to 16 ns at a RR of 150 kHz. Control of beam intensity in this case was undertaken by using the internal attenuator provided by the manufacturer. The lasers were installed in separate machines equipped with X-Y translation stages on which the samples were mounted.

Ablation tests were performed by translating samples at a speed of 50 mm/s under the focused beams. The experiments were carried out at RRs of 30 kHz and 70 kHz for the IR laser, corresponding to pulse durations of 500 ps and 800 ps, and 30 kHz and 100 kHz for the green laser, corresponding to pulse durations of 10 ns and 12.5 ns. The respective maximum fluences were 20 J/cm² and 10 J/cm² for the IR laser and 37 J/cm² and 17 J/cm² for the green laser.

III. RESULTS

High quality incisions were obtained for all materials of interest under certain conditions. The ablation threshold of each single-layer material was calculated by averaging the minimum tested fluence at which interaction was observed and that immediately below. Table 1 presents the measured values for each set of tests where ablation was possible within the maximum pulse energy of the laser.

The measured ablation threshold of aluminium with the picosecond laser was found to be approximately 10% of that with the nanosecond laser. Such a reduction was the result of lower thermal energy transport. The ablation threshold of PP and PE were found to be similar for picosecond pulses, while onset of ablation was not observed for nanosecond pulses. In all cases, little variation in ablation threshold was observed with pulse duration within the tested range of each laser. The measurement of ablation depth was undertaken with a mechanical profiler. Due to the sharp onset of ablation in some samples it was not possible to obtain a measured value before complete penetration of the material took place.

TABLE I – ABLATION THRESHOLDS AT 50 MM/S

Laser beam	Material	Thresholds fluence (J/cm ²)
IR 500 ps	AL	0.5
IR 800 ps	AL	0.5
IR 10 ns	AL	4.4
Green 10 ns	AL	6
Green 12.5 ns	AL	5.2
IR 500 ps	PP	6.6
IR 800 ps	PP	6.2
IR 500 ps	PE	6.6
IR 800 ps	PE	7.2

Measured ablation depths of AL for all tested laser sources are presented in Fig. 1. A considerable drop in ablation efficiency is observed for picosecond pulses. Measured ablation depths of PE and PP are presented for the 500 ps IR laser in Fig. 2, for both the tested conditions and single pulses.

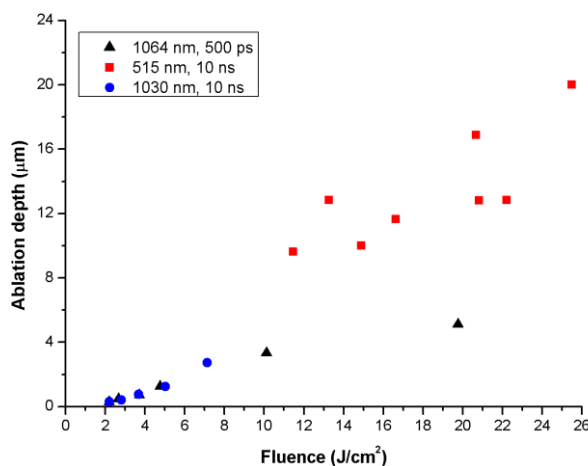


FIG. 1 – Measured ablation depth for AL foils, at a translating speed of 50 mm/s.

IV. CONCLUSION

The presented results provide useful data for the application of laser-based systems to the packaging industry. High quality laser scribes of packaging materials may be performed; however, it has been found that ps pulsed IR laser radiation of relatively low fluence can be used to efficiently scribe single-layer PP and PE at 50 mm/s, with a full cut of PP. By using such a laser, a one order of magnitude reduction in the ablation threshold of AL with respect to longer pulses is possible. On the other hand, the material removal efficiency for fluences above 7

J/cm² was found to be far superior for nanosecond pulsed laser radiation.

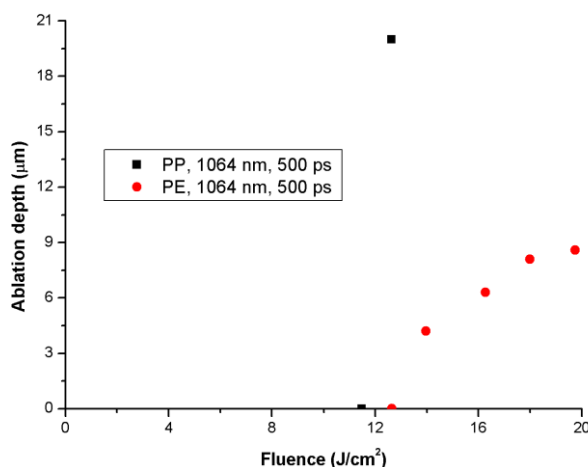


FIG. 2 – Measured ablation depth for PP and PE, at a translating speed of 50 mm/s.

REFERENCES

- [1] E. Kannatey-Asibu, “Principles of Laser Materials Processing,” *John Wiley & Sons, Inc.*, United states of America, April 2009.
- [2] M. Colina, C. Molpeceres, M. Morales, F. Allens-Perkins, G. Guadano and J. Ocana, “Laser ablation modelling of aluminium, silver and crystalline silicon for applications in photovoltaic technologies,” *Surface Engineering*, vol. 27, pp. 414-423, 2011.
- [3] C. Porneala and D. A. Willis, “Time-Resolved Dynamics of Nanosecond Laser-Induced Phase Explosion,” *Journal of Physics D: Applied Physics*, vol. 42, pp. 155503, 2009.
- [4] T. Lippert and J. T. Dickinson, “Chemical and Spectroscopic Aspects of Polymer Ablation: Special Features and Novel Directions,” *Chemical Reviews*, vol. 103, pp. 453-485, 2003.
- [5] I. B. Sohn, Y. C. Noh, Y. S. Kim, D. K. Ko and J. Lee, “Laser Ablation of Polypropylene Films using Nanosecond, Picosecond, and Femtosecond Laser,” *Journal of the Optical Society of Korea*, vol. 12, pp. 38-41, 2008.
- [6] F. O. Leme, Q. Godoi, P. H. M. Kiyataka, D. Santos, J. A. M. Agnelli and F. J. Krug, “Effect of Pulse Repetition Rate and Number of Pulses in the Analysis of Polypropylene and High Density Polyethylene by Nanosecond Infrared Laser Induced Breakdown Spectroscopy,” *Applied Surface Science*, vol. 258, pp. 3598-3603, 2012.

SYNTHETIC APERTURE INTERFEROMETRIC RADIOMETER: DESIGN, TRADE-OFF AND TECHNOLOGY

S. Pompili^(1,2,3), F. S. Marzano^(3,4), S. Varchetta⁽²⁾

⁽¹⁾ Department of Industrial and Information Engineering and Economics, University of L'Aquila, 67100 L'Aquila, Italy

⁽²⁾ Thales Alenia Space, 00131 Rome, Italy

⁽³⁾ CETEMPS –University of L'Aquila, 67010 L'Aquila, Italy

⁽⁴⁾ Department of Information Engineering, 'La Sapienza' University of Rome, 00184 Rome, Italy

Abstract

The research activity has been focused on the preliminary sizing of a Synthetic Aperture Interferometric Radiometer (SAIR). This activity has involved the definition of the SAIR sizing parameters and relationships between them. The sizing trade-offs have been identified, allowing to identify the optimum choices of design, among the possible ones, that could be applied to any SAIR design.

Index Terms – Aperture synthesis, interferometry, radiometry, Visibility.

I. INTRODUCTION

SAIRs instruments allow to overcome the technological limitations in the realization of large aperture antennas presented by high resolution real aperture radiometers for high frequencies space missions. This is done by taking advantage of the interferometric technique with the benefit of a lighter antenna system and no need of scanning mechanism [1], [2]. Section II of this paper reports the parameters summarizing the main system characteristics. In Section III, the recent achievements in SAIR design are illustrated. In Section IV, the conclusions are drawn.

II. TRADE-OFF IN SAIR DESIGN

The interferometric technique exploited by a SAIR is based on the measurement of the cross-correlations between the signals received from each pair of antennas in an interferometric array at many different spacing or baselines. At each correlation corresponds a measurement of the Visibility function V in the baseline, or (u,v) , domain [1], [2].

A. Main Sizing Parameters:

In the ideal case of identical receivers, unitary radiation patterns and no decorrelation effects, the brightness temperature distribution, T_B , is obtained as inverse Fourier transform of the Visibility function computed on a discrete and finite number of sample points (u,v) . Consequently, the Visibility sampling has a periodical behavior, within (u,v) domain, that can be described according to a specific periodicity matrix. Thus, Visibility is sampled on a discrete and finite number of sample points, whose number and position depend on the array configuration, giving to the Visibility spectrum a specific coverage shape in (u,v) domain. Accordingly to the selected array configuration, V is

computed adopting an opportune sampling grid [1], [2]. In order to have a correct sampling to recover Visibility from its samples, the distance between adjacent antennas in the array has to satisfy the sampling Nyquist criterion. In addition, it has to minimize the aliasing generation due to the overlap among Visibility spectrum and its replicas. So, the condition to satisfy for having a correct V sampling depends on different factors: dimension and geometry of the array and, also, resulting shape of sampling grid in (u,v) domain. In Fig.1(a) it is shown the block scheme that illustrates the relationships between these parameters. The sizing of the antenna spacing is a trade-off between the required Field Of View (FOV), or the Alias Free-FOV, and the needed array thinning.

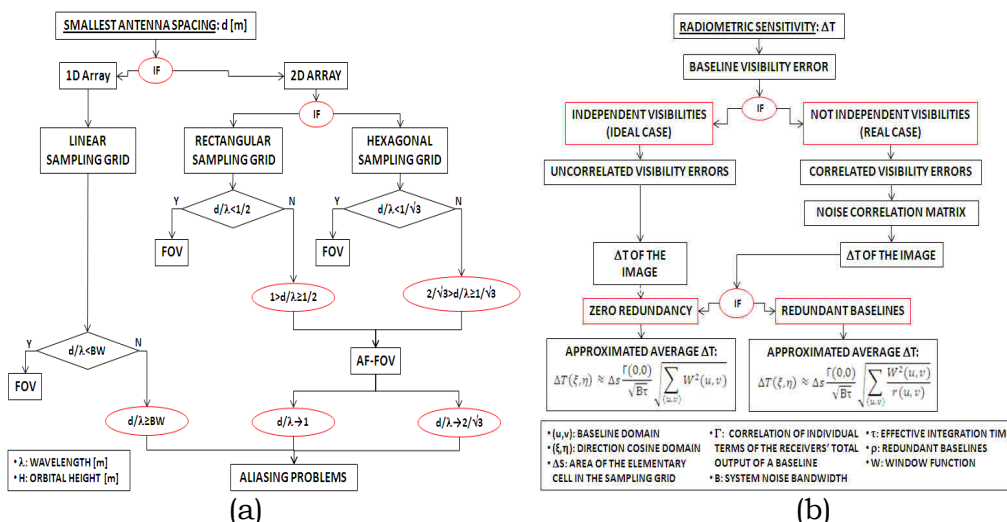


FIG. 1 – (a) Block scheme characterizing the smallest antenna spacing in a SAIR. (b) Block scheme characterizing the radiometric sensitivity in a SAIR.

In the case in which the Visibilities are assumed independent, the sensitivity ΔT of a SAIR is obtained as the transformation of errors of individual Visibilities into the image; while, considering not independent Visibilities (i.e. real case [3]), the sensitivity of the image will be affected by the correlation of Visibility errors. In this case, in order to give a general description of the sensitivity of a SAIR, it has to be taken into account not only the power contribution from the target and receiver noise, but also the total correlation of a pair of receivers; the sensitivity of the image is then obtained as the transformation of all the Visibility error correlations. If small Visibility error correlations are ignored, the average ΔT of all pixels is determined by the Visibility error correlations of single baselines [3]. The sensitivity of the image is the average error in each T_B map obtained after an integration time of τ seconds and it is valid if the image is retrieved under the assumption of zero redundancy array. In practice, only a few cases satisfy the zero redundancy requirement, so it is needed to consider the effect of redundancy by the variance of the average value of $r(u,v)$ redundant baselines [3]. In Fig.1(b) it is illustrated the block scheme characterizing the sensitivity in a SAIR. The choice of ΔT is function of array size and decreases with

the number of redundant baselines. Furthermore, smoother weighting windows reduce the side lobes level of the instrument impulse response at the expense of spatial resolution, allowing to achieve better ΔT [1], [2].

B. Numerical Simulations:

In 2012 it was presented an ASI study on a multi-frequency microwave passive payload, named LIRAS (Lunar Interferometric Radiometer by Aperture Synthesis) and addressed to the high-resolution mapping and vertical sounding of the Moon sub-surface (see [8]). This study is still going on relating to the optimization of the instrument and of the “LIRAS End-to-end Performance Simulator” (LEPS), modeled on the existing software SEPS. Fig.2(a) and (b) show the simulated impulse response and the Visibility coverage of a Y-array. Fig.2(c) reports the LIRAS orbital coverage computed using LEPS [8].

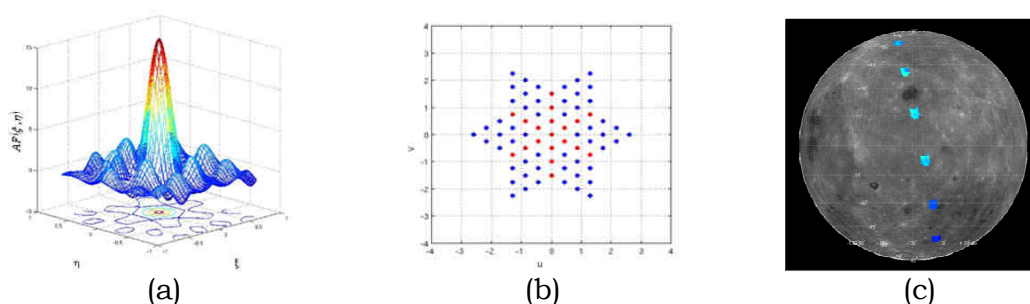


FIG. 2 –(a) Simulated impulse response using rectangular weighting function and (b) Visibility coverage for a Y-shaped array. (c) LEPS orbital coverage.

III. ARCHITECTURES AND TECHNOLOGIES FOR THE FUTURE

In this Section, different SAIR mission concepts are analyzed in order to highlight their different implementation approach (see Fig.3).

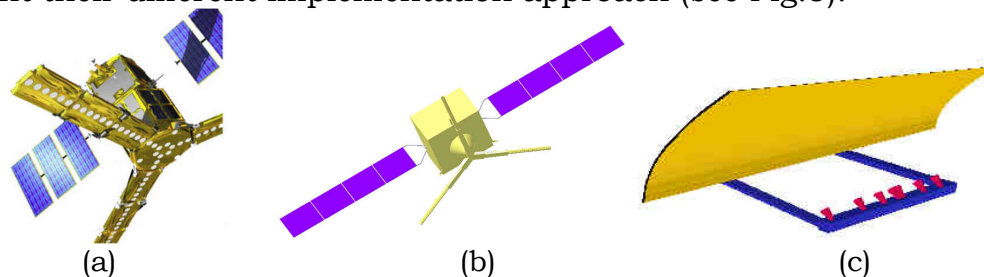


FIG. 3 – (a) Image of SMOS and (b) GAS in deployed configuration. (c) Image of the parabolic cylinder reflector of MeoSTAR.

SMOS (Soil Moisture and Ocean Salinity) is the first ESA’s mission using a SAIR, MIRAS (Microwave Imaging Radiometer using Aperture Synthesis). For the future it is possible to use a different shape for the interferometric array. For example, the hexagon-shaped array, on the place of the Y-shaped one, could provide low side lobes in the instrument impulse response, an improved Visibility coverage and, also, a better RFI rejection. On that concept is based the ESA study on Super-MIRAS, formed by a large number of miniaturized receivers [4].

During the ESA’s Geosounder activity, carried out in 2010, it was presented GAS (Geostationary Atmospheric Sounder), a rotating

interferometer that allows to reduce the number of receivers with respect to the static array configuration. The implementation in one MMIC per polarization is used for LNAs, harmonic LO generation, down conversion and IF amplification. The transport of the signals from the front-end receivers to a central cross correlator is performed by means of an IF system. A 45 nm CMOS technology would grant the needed density to accommodate a complete cross correlator on single chip [5].

A microwave atmospheric temperature sounder radiometer, working in a Middle Earth Orbit (MEO), has been studied by JPL for the NOAA, NESDIS. The proposed concept is MeoSTAR (MEO Synthetic Thinned Array Radiometer); it uses a 1D thinned SAIR for each spectral working band in order to provide a pushbroom antenna pattern. The main antenna of MeoSTAR is a stationary linear parabolic reflector. The electrical complexity and resource requirements for this instrument are significantly lower than those for 2D SAIR instruments [6], [7].

IV. CONCLUSION

The SAIR sizing parameters, their relationships and some simulation results have been presented. The main trade-offs among the sizing parameters have been organized in block schemes applicable in general to any SAIR design; the capability to choose among all the possible SAIR realizations is considered a main issue to find the opportune sizing for the required application. Finally, future mission architectures are illustrated to give an overview on the possible sizing options in addition to the already existing ones, also looking toward their optimization.

REFERENCES

- [1] J.A. Camps Carmona, "Application of Interferometric Radiometry to Earth Observation", *PhD thesis*, Barcelona, Nov. 1996.
- [2] N. D. Skou, D. M. Le Vine, "Microwave Radiometer Systems: design and analysis", 2nd ed., *Artech House remote sensing library*, Norwood (MA), 2006.
- [3] J. Yan, J. Wu, M. Martín-Neira, "Study on Sensitivity of Interferometric Radiometer", 2007 IEEE.
- [4] M. Martín-Neira, I. Corbella, F. Torres, J. Kainulainen, R. Oliva, G. Buenadicha, S. Nieto, R. Castro, A. Gutierrez, J. Barbosa, F. Cabot, J. Tenerelli, N. Reul, P. Spurgeon, J. Gourrion, J. Boutin, J. Closa, A. Camps, E. Anterrieu, Martín-Porqueras, E. Daganzo, "Overview: MIRAS Instrument Performance and Status of RFI", *SMOS Science Workshop*, Arles (France), 2011.
- [5] J. Christensen, A. Carlström, H. Ekström, A. Emrich, J. Embretsén, P. de Maagt, A. Colliander, "GAS: the Geostationary Atmospheric Sounder", 2007 IEEE.
- [6] W. J. Wilson, A. B. Tanner, B. H. Lambrigtsen, T. A. Doiron, J. R. Piepmeier, C. S. Ruf, "STAR Concept for Passive Microwave Temperature Sounding from Middle Earth Orbit (MeoSTAR)", 2004 IEEE.
- [7] T. A. Doiron and J. R. Piepmeier, "Hybrid Synthetic/Real Aperture Antenna for High Resolution Microwave Imaging", 2003 IEEE.
- [8] S. Pompili, A. Di Carlofelice, P. Romano, C. Sciannella, "Spaceborne Microwave Interferometric Radiometers: Lunar Sub-Surface Remote Sensing, Inverse Problems and Electromagnetic Diagnostics", *XIX RiNEm*, Italy, 2012.

IMAGING AND INVERSE SCATTERING @ ELEDIA RESEARCH CENTER

M. Donelli, N. Anselmi, G. Oliveri, L. Poli, P. Rocca, L. Tenuti,
M. Salucci, and A. Massa

ELEDIA Research Center@DISI, University of Trento
Via Sommarive 9, 38123 Trento, Italy
andrea.massa@ing.unitn.it

Abstract

An overview of a set of innovative inverse scattering methodologies recently developed at the ELEDIA Research Center is presented. The application of the proposed methodologies to the solution of classical monitoring problems as well as innovative applicative problems (such as the passive detection and tracking of non-cooperative targets) is addressed. A selected set of examples are presented and discussed to remark the innovative contribution of each presented algorithm.

Index Terms – Evolutionary Algorithms, inverse scattering, microwave imaging, localization and tracking, optimization techniques, wireless sensor networks, Compressive Sensing.

I. INTRODUCTION

Microwave imaging and inverse scattering techniques have been widely developed in the last few years because of the growing interest in the application of such methods to various scenarios including industrial, military and civil engineering monitoring, biomedical diagnosis, and geophysical inspections.

From a general viewpoint, the objective of standard imaging is to determine the distribution of the dielectric characteristics of the whole investigation domain starting from the knowledge of the electromagnetic field scattered from an inaccessible area. Unfortunately, the associated inverse scattering problems are known to be ill-posed and nonlinear. Accordingly, suitable strategies aimed at overcoming such theoretical difficulties are mandatory.

In such a context, the ELEDIA Research Center has recently developed and successfully applied a set of innovative imaging methodologies to solve complex electromagnetic problems. The objective of this contribution is thus to provide a review of the most innovative inversion techniques developed at the ELEDIA Research Center, and to present a selected set of practical applications. More in detail, a set of methodological approaches developed in the framework of Compressive Sensing, Evolutionary Algorithms, Multi-Resolution Strategies, and Learning-by-Example methodologies will be reviewed along with the associated reference applicative scenarios.

II. MICROWAVE IMAGING AND INVERSE SCATTERING METHODOLOGIES

In the last years, the ELEDIA research center developed different innovative methodologies able to handle inversion problems in the field of Compressive Sensing [1]. More in detail, an innovative technique based on the contrast source (CS) formulation of the microwave imaging problem that exploits the Bayesian compressive sampling (BCS) paradigm has been proposed for the reconstruction of sparse distributions either when dealing with transverse magnetic [2] or transverse electric [3] illuminations. Such a methodological approach has been then extended [4] to handle contrast field (CF) versions of the inverse scattering problem, also taking into account Born Approximated formulations.

The main drawback of standard CS methodologies is indeed related to their capability to handle only real-valued problems. To overcome this problem, the proposed Compressive Sensing methodology has been enhanced by considering a three steps strategy [5] able to manage real as well as imaginary linear problem. More in detail, the inversion technique has been extended to take into account the relationships among the real and imaginary part of the “contrast currents” at the different probing views considering a multi-step procedure comprising a minimum-norm current expansion [5]. The arising methodology is able to retrieve the dielectric characteristics of complex scenarios characterized by various scatterers, under different noise conditions and to provide results well above with respect to the state of the art inversion techniques when dealing with sparse targets.

The ELEDIA Research Center also proposed a set of multi-resolution methodologies integrated with state-of-the-art imaging techniques. As an example, a new imaging strategy that integrates the inexact Newton method into a multi-focusing scheme within the contrast-source formulation of the inverse scattering problem has been proposed in [6] and validated with synthetic as well as experimental scattering data.

Since the imaging problem can be reformulated as an optimization one by defining and then minimizing (with a suitable minimization algorithm) a cost function, the development of suitable optimization techniques able to reach a solution in a fast and efficient way has been considered by members of the ELEDIA Research Center. In such research area, different innovative optimization techniques based on evolutionary algorithms have been developed and validated recently, as it is discussed in [7][8], where a detailed set of examples, practical applications and guidelines for a proper calibration of such algorithms are reported and illustrated.

III. SELECTED APPLICATIVE EXAMPLES

The application of microwave and inverse scattering methodologies in biomedical diagnosis and civil engineering has raised a growing interest

during the last years because of its potential advantages with respect to alternative technological solutions in terms of costs, risks, effectiveness, and speed. In more detail, one of the most interesting areas of application of microwave imaging concerns the early breast cancer detection [9]. For instance, an imaging methodology based on a powerful evolutionary algorithm for early breast cancer detection has been proposed in [10]. Such an approach is able to detect and localize a malignant tissue belonging to human breast, and it has been assessed considering realistic breast structures derived from magnetic nuclear resonance (MNR) data [10].

Moreover, concerning civil engineering monitoring applications, Ground Penetrating Radar (GPR) technologies have been widely and successfully used [11]. The development and validation of GPR algorithms and methodologies represent one of the most active research areas within the ELEDIA Research Center. More in detail, great efforts have been devoted towards the development of inversion techniques based on the integration of deterministic and stochastic search algorithms with multi-focusing strategies [11]. In this research area, some examples of recent advancements reached at the ELEDIA research have been reported in [11].

Furthermore, the availability of low power and pervasive devices that integrate on-board sensing, processing, and radio frequency circuitry for information transmission has enabled a rapid diffusion of distributed monitoring devices which can be applied also for imaging purposes [12][13]. In this scenario, the ELEDIA Research Center has recently worked on the exploitation of such technologies for localization and tracking purposes [12][13]. The main efforts have been devoted to develop opportunistic approaches exploiting existing systems and architectures for localizing targets not equipped with a transmitting device [12][13]. Indeed, inversion procedures based on “contrast source” formulations have been successfully used to solve the problem of localization and tracking of passive objects starting from the measurements of the RSS indexes available at the nodes of a WSN [12][13]. The measurements of the perturbation effects at the sensor nodes of moving targets have been employed as an input for an inversion strategy to determine the equivalent source modeling the presence of the target/scatterer generating the perturbation itself. More in detail, innovative strategies for the localization and tracking of passive targets in real time by using a learning by example technique have been developed [12][13].

IV. CONCLUSION

In this contribution, a brief review of a selected set of the most innovative inverse scattering algorithms, methodologies, and applications recently developed at the ELEDIA Research Center has been reported and briefly discussed. The applications of such

methodologies in different application areas ranging from civil and industrial monitoring, biomedical diagnosis, buried objects inspection up to the detection and tracking of passive targets with distributed monitoring methodologies has been discussed.

REFERENCES

- [1] A. Massa, P. Rocca, and G. Oliveri, "Compressive sensing in electromagnetics - A review," *IEEE Antennas Propag. Mag.*, 2014, in press.
- [2] G. Oliveri, P. Rocca, and A. Massa, "A bayesian compressive sampling-based inversion for imaging sparse scatterers," *IEEE Trans. Geosci. Remote Sensing*, vol. 49, no. 10, pp. 3993-4006, Oct. 2011.
- [3] L. Poli, G. Oliveri, P. Rocca, and A. Massa, "Bayesian compressive sensing approaches for the reconstruction of two-dimensional sparse scatterers under TE illuminations," *IEEE Trans. Geosci. Remote Sens.*, vol. 51, no. 5, pp. 2920-2936, May 2013.
- [4] L. Poli, G. Oliveri, and A. Massa, "Microwave imaging within the first-order Born approximation by means of the contrast-field Bayesian compressive sensing," *IEEE Trans. Antennas Propag.*, vol. 60, no. 6, pp. 2865-2879, June 2012.
- [5] L. Poli, G. Oliveri, F. Viani, and A. Massa, "MT-BCS-based microwave imaging approach through minimum-norm current expansion," *IEEE Trans. Antennas Propag.*, vol. 61, no. 9, pp. 4722-4732, September 2013.
- [6] G. Oliveri, A. Randazzo, M. Pastorino, and A. Massa, "Electromagnetic imaging within the contrast source formulation by means of the multiscaling inexact Newton method," *J. Optical Soc. America A*, vol. 29, no. 6, pp. 945-958, 2012.
- [7] P. Rocca, M. Benedetti, M. Donelli, D. Franceschini, and A. Massa, "Evolutionary optimization as applied to inverse problems," *Inverse Problems*, vol. 25, 123003, pp. 1-41, Dec. 2009.
- [8] P. Rocca, G. Oliveri, and A. Massa, "Differential Evolution as applied to electromagnetics," *IEEE Antennas Propag. Mag.*, vol. 53, no. 1, pp. 38-49, Feb. 2011.
- [9] S. C. Hagness, E. C. Fear, and A. Massa, "Guest Editorial: Special Cluster on Microwave Medical Imaging," *IEEE Antennas Wireless Propag. Lett.*, vol. 11, pp. 1592-1597, 2012.
- [10] M. Donelli, I. J. Craddock, D. Gibbins, and M. Sarafianou, "A three-dimensional time domain microwave imaging method for breast cancer detection based on an evolutionary algorithm," *Progress In Electromagnetics Research M*, vol. 18, pp. 179-195, 2011.
- [11] M. Salucci, L. Tenuti, C. Nardin, G. Oliveri, F. Viani, P. Rocca, and A. Massa, "Civil engineering applications of ground penetrating radars -Recent advances @ the ELEDIA Research Center," 2014 European Geoscience Union General Assembly (EGU-GA 2014), Vienna, Austria, 27 April - 02 May 2014
- [12] F. Viani, P. Rocca, G. Oliveri, D. Trincherro, and A. Massa, "Localization, tracking, and imaging of targets in wireless sensor networks: An invited review," *Radio Science*, vol. 46, RS5002, 2011.
- [13] F. Viani, P. Rocca, M. Benedetti, G. Oliveri, and A. Massa, "Electromagnetic passive localization and tracking of moving targets in a WSN-infrastructure environment," *Inverse Problems*, vol. 26, pp. 1-15, March 2010.

ELECTROMAGNETIC INTERACTION WITH THE STAINED GLASS WINDOWS OF THE MAGDALENE CHAPEL IN THE BASILICA IN ASSISI

L. Rivaroli⁽¹⁾, E. Stoja⁽²⁾, and F. Mangini⁽³⁾

⁽¹⁾ Private restorer, laura_rivaroli@yahoo.it

⁽²⁾ Engineering Department, Lancaster University, Bailrigg,
Lancaster LA1 4YR, United Kingdom

⁽³⁾ Department of Information Engineering, Electronics and
Telecommunications, “La Sapienza” University of Rome, Via
Eudossiana 18, 00184 Roma, Italy

Abstract

The electromagnetic scattered field by the stained glass window of the Magdalene Chapel of the Lower Basilica in Assisi is calculated by means of frequency domain numerical simulations and by making use of the scattered-field formulation. Two different polarizations to determine the most useful in terms of scattered field sensibility are considered. In this preliminary study a panel of a light is considered, knowing that the study is extendible for all panels. In particular the transmitted and the reflected power before and after the restoration are studied as function of the frequency, the amount of radiation passing through the window is analyzed: in fact, during the different phases of the restoration, several kilograms of leads were removed.

Index Terms – Electromagnetic scattering, stained glass, Fresnel coefficients, restoration, numerical techniques.

I. INTRODUCTION

In this paper we present a numerical study of the electromagnetic scattering on the stained glass windows of the Magdalene Chapel of the Lower Basilica in Assisi. These stained glass were made in the late XIV century. The stained glass of the Chapel is situated in four north-facing windows; each light is composed of six glass panels (Fig. 1). The panels illustrate the scenes of Magdalene’s life and were made during the first two decades of the fourteenth century.

In the course of time the windows underwent numerous interventions, in particular in the past, to repair the glass cracks, the restorer used the addition of mending leads on the fractures [1], [2]. Today the methodologies have changed much, in particular they consist in consolidating the cracked parts with epoxy resin, therefore in this case the restorers had to remove the mending leads and glued the glass with the transparent resin, characterized by electromagnetic properties as similar as possible to the glass to be repaired [3], [4]. For this reason, we wanted to investigate the amount of electromagnetic radiation that can be transmitted and reflected before and after restoration, in particular we studied the trend of the transmitted and reflected power as function of the frequency, showing the differences between these quantities before and after the restoration:

$$T = \frac{|\underline{\Pi}_T|}{|\underline{\Pi}_I|} \quad R = \frac{|\underline{\Pi}_R|}{|\underline{\Pi}_I|}$$

having indicated with $\underline{\Pi}_T$, $\underline{\Pi}_R$ and $\underline{\Pi}_I$ the Poynting vector of the transmitted, reflected and incident field, respectively.

The restoration was directed by D. Radeaglia, R. Bollati, and E. Huber, and performed by the conservators L. Rivaroli, M. Massera, and M. G. Chilosì.

In the second Section a numerical study of the electromagnetic scattering on the stained glass is presented, in particular a study of the Fresnel coefficient as function of the frequency is shown. At last, in Section 3 the conclusions are given.

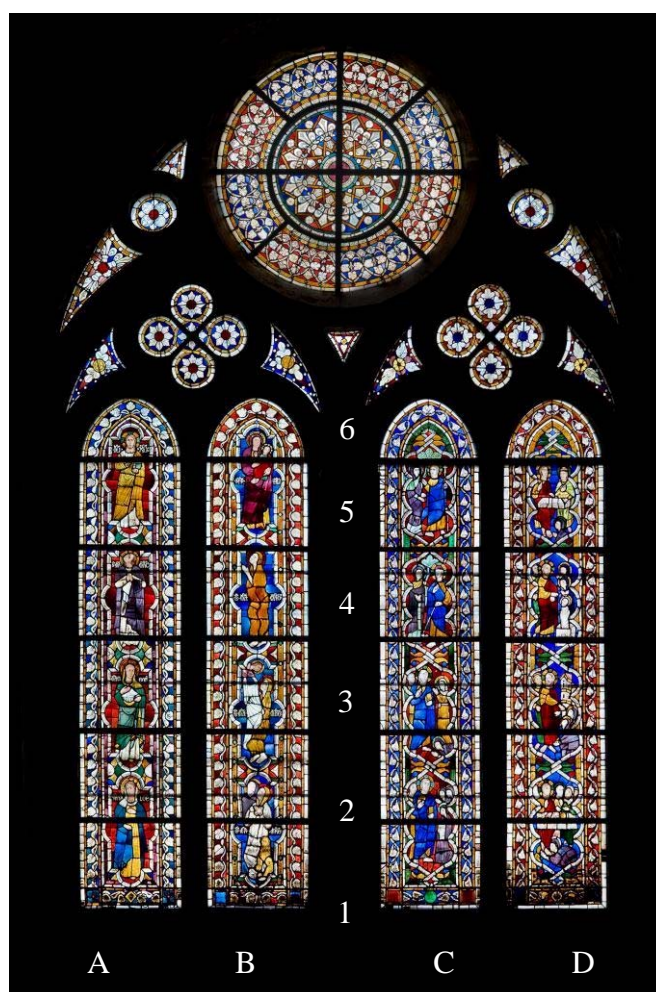


FIG. 1 – Stained-glass windows of the Magdalene Chapel of the Lower Basilica of San Francesco in Assisi, Italy.

II. NUMERICAL STUDY

The numerical study was carried out with a commercial software (Comsol Multiphysics) based on the Finite Element Method (FEM), in

particular for our study we have taken into account a panel (B1) of the second light of the chapel of the Magdalene, lower Basilica of San Francesco in Assisi (Fig. 2).



FIG. 2 – B1 Panel of the second light (Fig. 1) of the Magdalene Chapel of the Lower Basilica of San Francesco in Assisi: a) before and b) after the restoration completed by L. Rivaroli, M. Massera, C.B.C., and I.S.C.R. .

The study consists in several phases: the first was the realization of the tridimensional CAD starting by the high-resolution photographs of the stained glass, the second step consists in the import of the CAD in the simulator and the creation of the simulation domain, the third one consists in the choice of the external field, in particular to excite the model, a circular-polarized plane wave impinging normally on the above-mentioned interface. Finally the mesh (Fig. 3) and the simulation in the range of frequencies between 1 MHz and 600 MHz is performed.

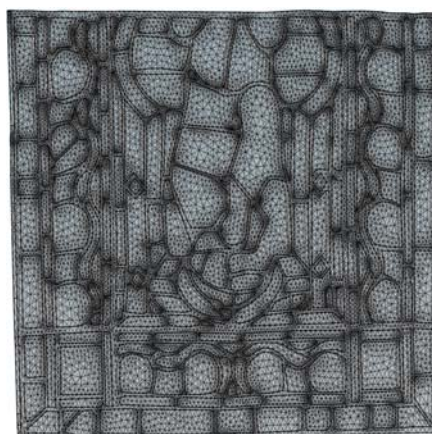


FIG. 3 – Mesh of the B1 panel

In Fig. 4, the trends of the transmission and reflection power ratio before and after the new restoration are shown, we can note how the removal of the lead strips has increased and decreased the transmission

and reflection coefficients for all frequencies, respectively, just as expected.

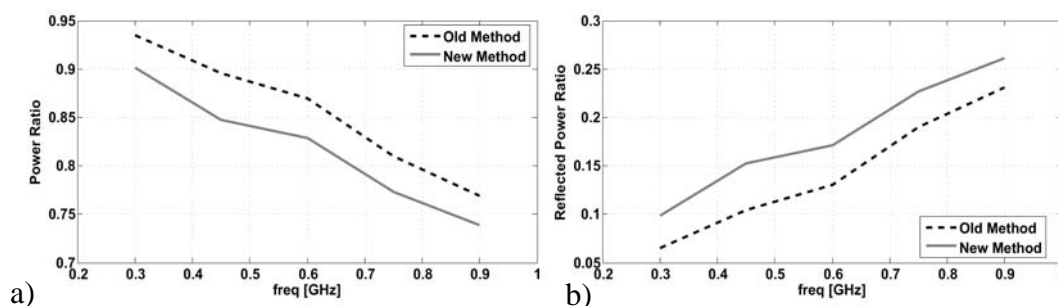


FIG. 4 – a) Transmitted power ratio and b) reflected power ratio as function of the frequencies. Old restoration method (dashed black line), new method (solid grey line).

III. CONCLUSION

In this paper, we presented a numerical study for the analysis of the transmitted and reflected power ratio as function of the frequencies, in particular with highlighted the difference of these quantities before and after the restoration, i.e. in presence and in absence of the mending lead added in the previous restorations. We demonstrated how the new methodology of restoration, which consists in repairing the stained glasses with epoxy resins, allows a larger passage of electromagnetic radiation through the stained-glass window. The future work aims at studying the electromagnetic interactions with the stained glass in the range of frequencies of the visible light using the different electromagnetic properties of the glass in those frequencies, and at extending the study to all the lights in the chapel.

REFERENCES

- [1] R. Bollati, E. Huber, M. E. Prunas, P. Santopadre, and M. Verità, "The Conservation of a Fourteenth-Century Stained Glass Window from Assisi, Italy," *The Art of Collaboration Stained glass conservation in the Twenty-First Century, Acts Forum of the International Committee of the Corpus Vitrearum for the Conservation of Stained Glass*, pp. 161-168, 2010.
- [2] R. Bollati, E. Huber, and M. E. Prunas, "Il restauro della vetrata della Cappella della Maddalena," *Bollettino ICR*, no. 20-21, pp. 46-63, 2010.
- [3] D. Radeaglia, "Sintesi delle vicende conservative," *Bollettino ICR*, no. 20-21, pp. 17-45, 2010.
- [4] R. Bollati, C. Cacace, G. Guida, M. G. Chilosi, E. Huber, M. Massera, G. F. Priori, M. E. Prunas, D. Radeaglia, L. Rivaroli, A. Rubino, P. Santopadre, D. Ventura, and M. Verità, "Le vetrate della cappella della Maddalena, Assisi," from <http://www.icr.beniculturali.it/pagina.cfm?usz=5&uid=73&rid=49>.

ANTENNA SYNTHESIS AND ANALYSIS @ ELEDIA RESEARCH CENTER

M. Donelli, N. Anselmi, E. Bekele, M. Carlin, L. Manica, G. Oliveri,
L. Poli, P. Rocca, M. Salucci, L. Tenuti, L. Zambiasi, and A. Massa

ELEDIA Research Center@DISI, University of Trento
Via Sommarive 9, 38123 Trento, Italy
andrea.massa@unitn.it

Abstract

An overview of some innovative methodologies developed at ELEDIA Research Center at the University of Trento in the context of Antenna Synthesis, Analysis and development is presented. Selected examples of the application of such techniques for the design, diagnosis and control of complex radiating structures are presented and briefly discussed.

Index Terms – antenna arrays, antenna design, optimization techniques, reconfigurable antennas.

I. INTRODUCTION

The development of design, control, and diagnosis methodologies for antenna systems to be used in modern telecommunication, remote sensing, and radar systems is an extremely active research area because of the challenging constraints that such antennas need to satisfy in terms of size, radiation performance, reconfigurability, and costs.

Accordingly, several architectures and design methodologies have been proposed recently for the synthesis of the antenna layout and radiation pattern, the diagnosis of the failures of radiating elements, and eventually the reconfiguration of the beam pattern in order to guarantee satisfactory performance in all operative conditions.

In such a framework, the ELEDIA Research Center has recently proposed several innovative antenna architectures, design paradigms, and methodologies for the control and diagnosis of complex radiating structures such as large antenna arrays. These methodologies, which include techniques based on Compressive Sensing, Evolutionary Algorithms, Interval Analysis, and Learning-by-Example methods, have been widely validated in several applicative context including, but not limited to, communications, radars, power transmission, and remote sensing.

The aim of this contribution is therefore to present a brief review of the most innovative methodologies recently developed at the ELEDIA Research Center, also demonstrating their efficacy and advantages with respect to state-of-the-art methods.

II. INNOVATIVE ANTENNA SYNTHESIS AND DIAGNOSIS METHODOLOGIES

The synthesis of large planar arrays is a classical problem in applied electromagnetics which has received a lot of attention in the last few years because of the increasing complexity of applications that require a high resolution in both elevation and azimuth. Nevertheless, the development of numerically efficient and robust methods, in particular for the design of maximally sparse arrays, is still an open research area. To effectively address such a challenging problem, the design of sparse arrays has been recently solved through a set of innovative and efficient pattern matching algorithms within the *Bayesian Compressive Sensing* (BCS) framework [1]-[4]. Towards this end, the sparse synthesis problem has been formulated in a probabilistic fashion and the single-task (ST) and the multi-task (MT) BCS solutions have been derived [1]-[4].

The problem of handling the design of antenna arrays considering the practical realization of the antenna, that implies unavoidable inaccuracies, tolerances and errors due to the manufacturing processes, has been recently considered as well. More in detail, the problem of analyzing the variations of the field radiated by the real array with respect to the expected one because of the control point tolerances has been addressed. Indeed, state-of-the-art methodologies that handle such a problem turn out time-consuming and complex, especially if large arrangements are of interest. To overcome such issues, an innovative synthesis method based on interval analysis (IA) has been presented [5]. In particular, the proposed method computes the bounds of all possible patterns generated by an array, within given tolerances by means of analytical rules [5]. As a matter of fact, the arithmetic of intervals, available in IA, allows one to analytically address arithmetic problems where the variables at hand are not characterized by single points but intervals. The amplitude excitations have been defined in terms of intervals of width corresponding to the maximum manufacturing tolerance around the nominal values. These latter are successively optimized by means of a stochastic global optimizer to yield, at the convergence, the bounds of the arising power patterns laying within user-defined masks [5].

The methodologies based on the BCS and the IA previously reported as synthesis techniques can be efficiently adopted for the diagnosis of radiating structures as well. In [6], an analytical method based on IA has been proposed to predict the impact of the manufacturing tolerances of the excitation amplitudes on the radiated array pattern of linear arrays. The proposed method considers the array factor according the rules of the Interval Arithmetic, and the radiation features of the linear array are described in terms of intervals whose bounds are analytically determined as functions of the nominal value and the tolerances of the array amplitudes, providing a robust and fast analysis tool [6]. Moreover, a method for an efficient and reliable diagnosis of large linear arrays based on a BCS strategy is presented in [7]. The

proposed methodology allows the determination of the array elements which have been damaged also providing an estimation of the degree of reliability of the solution [7]. The far-field data are processed by means of an efficient algorithm based on a relevance vector machine (RVM).

Processing techniques aimed at estimating the direction of arrival of signals (DoAs) have been recently developed at the ELEDIA Research Center [8]. More specifically, the estimation of DoAs of narrowband signals impinging on linear arrays has been addressed in [8] within the Bayesian compressive sensing (BCS) framework. Unlike several state-of-the-art approaches, the voltages at the output of the receiving sensors are directly used to determine the DoAs of the signals thus avoiding the computation of the correlation matrix, and providing a fast and accurate strategy for the direction of arrival estimation.

III. INNOVATIVE ANTENNA ARCHITECTURES

Innovative antenna architectures based on Time-Modulated-Arrays (TMAs) have attracted a great interest recently. Such an interest is motivated by the fact that radiation performance of TMAs can be controlled by a set of radio-frequency (RF) switches that modulate the static amplitude and phase array weights. Thanks to the use of the time as additional degree of freedom, TMAs have demonstrated to be a suitable solution to the synthesis of fully reconfigurable arrays with ultra-low sidelobe levels. In this framework, pulse-shaping strategies for TMAs have been recently proposed by members of the ELEDIA Research Center in order to overcome the performance of standard TMA architectures [9].

In the framework of reconfigurable systems, the ELEDIA Research Center has also recently proposed an innovative mono-pulse array able to reconfigure the radiation pattern from the sum mode to the difference one by electronically switching a set of parasitic dipoles placed in front of a driven array of radiating dipoles [10]. The antenna architecture has been synthesized by optimizing the geometric parameters of the passive elements, namely their positions and lengths, by acting on suitable electronic switches [10].

IV. INNOVATIVE APPLICATIONS

The antenna synthesis methodologies have been recently proposed for the synthesis of radiating planar arrays for wireless power transmission (WPT) [11]. More specifically, an analytical methodology aimed at the maximization of the ratio between the power radiated on a target area and the total transmitted power has been proposed in [12]. The problem has been solved finding the solution of a generalized eigenvalue problem whose descriptive matrices are either computed in closed-form or obtained through numerical integration depending on the problem geometry [12].

V. CONCLUSION

A review of the most innovative methodologies for the design, diagnosis and control of radiating systems recently developed at the ELEDIA Research Center has been reported and discussed. The effectiveness of the proposed synthesis and diagnosis techniques, and the advantages of the proposed innovative antenna typologies have been illustrated by considering different applicative scenarios.

REFERENCES

- [1] G. Oliveri and A. Massa, "Bayesian compressive sampling for pattern synthesis with maximally sparse non-uniform linear arrays," *IEEE Trans. Antennas Propag.*, vol. 59, no. 2, pp. 467-481, Feb. 2011.
- [2] G. Oliveri, M. Carlin, and A. Massa, "Complex-weight sparse linear array synthesis by Bayesian Compressive Sampling," *IEEE Trans. Antennas Propag.*, vol. 60, no. 5, pp. 2309-2326, May 2012.
- [3] F. Viani, G. Oliveri, and A. Massa, "Compressive sensing pattern matching techniques for synthesizing planar sparse arrays," *IEEE Trans. Antennas Propag.*, vol. 61, no. 9, pp. 4577-4587, Sept. 2013.
- [4] G. Oliveri, E. T. Bekele, F. Robol, and A. Massa, "Sparsening conformal arrays through a versatile BCS-based method," *IEEE Trans. Antennas Propag.*, vol. 62, no. 4, pp. 1681-1689, Apr. 2014.
- [5] L. Manica, N. Anselmi, P. Rocca, and A. Massa, "Robust mask-constrained linear array synthesis through an interval-based particle swarm," *IET Microwaves, Antennas & Propagation*, vol. 7, no. 12, pp. 976-984, 2013.
- [6] N. Anselmi, L. Manica, P. Rocca, and A. Massa, "Tolerance analysis of antenna arrays through interval arithmetic," *IEEE Trans. Antennas Propag.*, vol. 61, no. 11, pp. 5496-5507, November 2013.
- [7] G. Oliveri, P. Rocca, and A. Massa, "Reliable diagnosis of large linear Arrays - A bayesian compressive sensing approach," *IEEE Transactions on Antennas and Propagation*, vol. 60, no. 10, pp. 4627-4636, October 2012.
- [8] M. Carlin, P. Rocca, G. Oliveri, F. Viani, and A. Massa, "Directions-of-arrival estimation through Bayesian Compressive Sensing strategies," *IEEE Trans. Antennas Propag.*, vol. 61, no. 7, pp. 3828-3838, July 2013.
- [9] E. Bekele, L. Poli, P. Rocca, M. D'Urso, and A. Massa, "Pulse-shaping strategy for time modulated arrays - Analysis and design," *IEEE Trans. Antennas Propag.*, vol. 61, no. 7, pp. 3525-3537, July 2013.
- [10] P. Rocca, M. Donelli, G. Oliveri, F. Viani, and A. Massa, "Reconfigurable sum-difference pattern by means of parasitic elements for forward-looking monopulse radar," *IET Radar, Sonar & Navigation*, vol. 7, no. 7, pp. 747-754, 2013.
- [11] A. Massa, G. Oliveri, F. Viani, and P. Rocca, "Array designs for long-distance wireless power transmission - State-of-the-art and innovative solutions," *Proc. IEEE*, vol. 101, no. 6, pp. 1464-1481, June 2013.
- [12] G. Oliveri, L. Poli, and A. Massa, "Maximum efficiency synthesis of planar arrays for wireless power transmission," *IEEE Trans. Antennas Propag.*, vol. 61, no. 5, pp. 2490-2499, May 2013.

STATISTICAL PREDICTION OF RECEIVED FRAMES ALONG EARTH-SATELLITE KA-BAND LINKS IN DEEP SPACE MISSIONS

M. Biscarini^{1,3}, F.S. Marzano^{1,3,5}, M. Montopoli,^{1,4} K. De Sanctis^{4,5}, L. Iess^{2,3}, M. Gregnanin^{2,6}, M. Parisi^{2,6}, M. Montagna⁷, M. Lanucara⁷

⁽¹⁾ DIET, Sapienza University of Rome, Italy

biscarini@diet.uniroma1.it , marzano@diet.uniroma1.it

⁽²⁾ DIMA, Sapienza University of Rome, Italy

⁽³⁾ CRAS, Sapienza University of Rome, Italy

⁽⁴⁾ CETEMPS, University of L'Aquila, Italy

⁽⁵⁾ HIMET, L'Aquila, Italy

⁽⁶⁾ ARPSOFT, Rome, Italy

⁽⁷⁾ ESOC, European Space Agency, Germany

Abstract

Deep space exploration is aimed at acquiring information about the solar system, ka-band channels can provide a significant communication capacity for such very large distances. Statistical methods to predict received data-frames during the link transmissions (by using weather forecast predictions and climatological statistics data) are here presented. Numerical results, in terms of received frame data are discussed taking the fully-adaptive bit-rate test case as a benchmark.

Index Terms — Antenna, propagation, measurement.

I. INTRODUCTION

Deep space (DS) exploration of the solar system and its composition can be achieved only if a significant communication capacity can be provided to spacecrafts at very large distances [1]-[2]. The Ka-band (at 32-34 GHz) and higher frequency band channels can provide this capacity if compared to the current X-band (around 8.4 GHz). Ka-band can offer a striking performance advantage over X-band because of the squared-frequency law increase of directivity of the downlink beam for the same physical antenna size. This opens up a possible and useful trade space for Ka-band missions with the same antenna size (and spacecraft constraints) and radio frequency power, since a Ka-band mission can return four times more data than a comparable X-band mission. The first European deep-space mission adopting such frequency operationally will be BepiColombo (BC), the European Space Agency (ESA) cornerstone mission to Mercury due to launch in August 2016 [3].

The optimal allocation of channel resources above Ku band is limited by the significant impact of radio-meteorological factors which can irretrievably degrade the quality of service for fairly high percentage of time [4]. The major cause of outages at Ka band and above is not only

convective rainfall, as for lower frequencies, but even non-precipitating clouds and moderate precipitation produced by stratiform clouds [5]. For small carrier-to-noise ratio (CNR), the system equivalent noise temperature decreases and the impact of atmospheric noise temperature can become non-negligible. With the transition towards shorter wavelengths, the atmospheric effects become more and more relevant by inducing significant path attenuation on the Space-to-Earth link. At Ka band, for instance, attenuation due to cloudy and rainy troposphere can be even one order of magnitude larger than at X-band. This means that large link margins should be allocated in order to mitigate these atmospheric impairments and to reduce the target outage probability .

In order to achieve the optimum data return at Ka-band, a different approach with respect to the link budget computation at lower frequencies (e.g., S or X band) is necessary. Such link analysis is based on the statistical computation of the expected data return in a probabilistic framework rather than on a specified link statistical availability. Recent methods uses monthly statistics collected at the receiving site with the aim of defining average values of expected received data volume. Both data rate and minimum elevation angle can be optimized for acquisition at the same time within each deep-space satellite pass.

A further step in the optimization of science data return at frequency band higher than X band is to exploit the forecast capability of numerical weather prediction (NWP) models which, coupled with proper radio-propagation microphysical parameterization, can provide the Ka-band average received frames within a deep-space satellite pass (or sub-pass). The advantage of this approach is to cope with the most probable radio-meteorological situation during the foreseen data transfer instead of relying on a long-term (monthly or yearly) statistics which can strongly penalize the available link margin. On the other hand, as any NWP models, forecast errors should be taken into account especially for what concerns the convective atmosphere space-time prediction [5].

This paper describes statistical techniques to compute predicted received frames in an Earth-satellite Ka-band link

Numerical results, in terms of received frames data for constrained and unconstrained systems using monthly statistics, are also described using specifications from the BepiColombo mission (for which the referring ground station is Cebreros).

II. RESULTS AND CONCLUSIONS

Results in terms of average received and percentage of lost frames are briefly discussed here, using monthly statistical data derived from the rain gauge measurements in Cebreros during the whole 2012, NWP forecast data at 24-h lead time for the same year 2012 using combined

with the radiative transfer model (RTM) and monthly statistical data derived from 24-hours forecasts. Both benchmark and frame estimation methodologies are applied to a simulated BC spacecraft elevation profile for the year 2021, derived from BC ephemeris data, which is attributed to the year in 2012 where meteorological measurements are available in Cebreros.

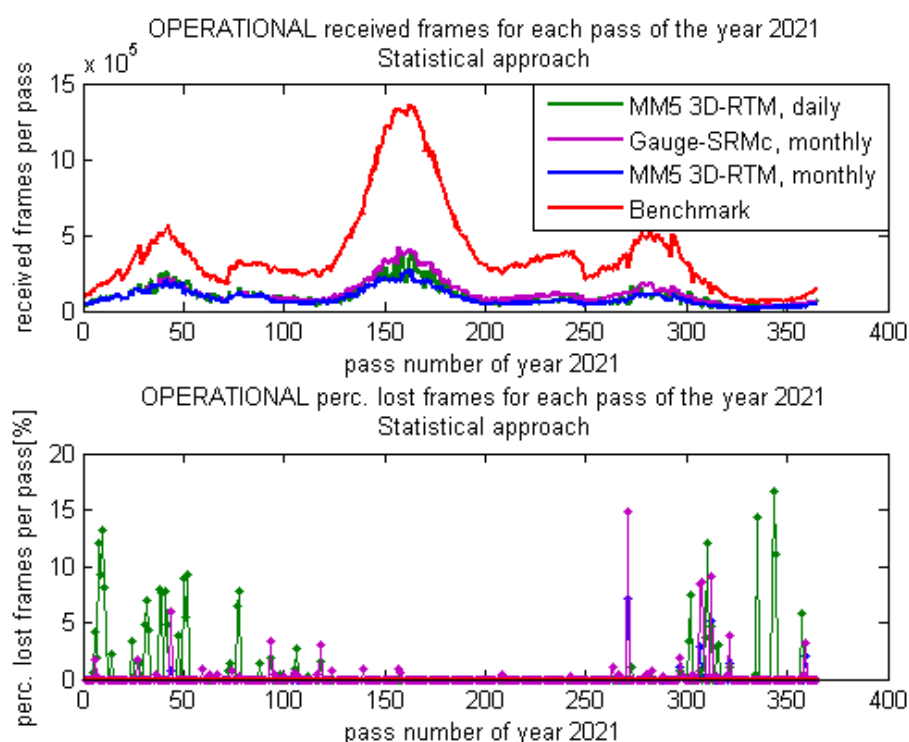


Fig.2 - Prediction of received and percentage of lost frames per pass for the year 2021 using the statistical approach and BC mission specifications

Fig. 2 shows the prediction of received and lost frames per pass using the statistical prediction methods for each pass of the whole year 2021, trained by radio-gauge monthly data, radio-forecast monthly and daily data. Benchmark fully-adaptive results are also shown.

The use of Cebreros meteo-gauge data combined with corrected simplified radiative model (SRMc) allows to define a reference time series for the atmospheric channel behavior. In this respect, we can define the operational received frames as the effective received frames at the DS ground station. Of course, the assumption is that SRMc is correctly reproducing the radiometeorological effects of the atmosphere which should, indeed, be provided by the Ka-band channel measurements or, to certain extent, by ground microwave radiometric measurements (which are usually operated only in clear and cloudy conditions).

The previous figure points out that results obtained with forecast data (blue and green curve) are in agreement with the one obtained with measured gauge data (magenta curve). Moreover the use of daily forecast provides better results (more received frames) than the use of monthly statistics. As expected, the benchmark case (red curve) always gives the biggest number of received frames with no losses at all.

These results confirm that radio-forecast models can be successfully used for predicting the received frames on a yearly basis using monthly and daily statistics. At the same time, it opens the possibility to exploit the hourly forecast (but also 5-days forecast) as a tool for planning satellite data return capacity.

Better results in term of data volume can be obtained by investigating the maximization approach that maximizes received frames with the constraint of a threshold on the percentage of lost frames for each pass.

ACKNOWLEDGMENT

This work has been partially funded by the Sapienza University of Rome and by the European Space Agency (ESA) under the contract ESOC-2013 “Study of Ka-band downlink operation concept for BepiColombo based on the use of weather forecasts”.

REFERENCES

- [1] E. Matricciani, “An optimum design of deep-space downlinks affected by tropospheric attenuation”, *Int. J. Satell. Commun. Network*, DOI: 10.1002/sat, 2009.
- [2] F.S. Marzano, V. Mattioli, C. Capsoni, E. Matricciani, C. Riva, M. Luccini, N. Pierdicca, L. Pulvirenti, M. Montopoli, A. Puiatti, G. Corti, P. Basili, A. Martellucci “Sky-Noise Temperature Modeling and Prediction for Deep Space Applications From X Band to W Band”, *Proc. of TTC Conference, Noordwijk (NL)*, 21-23 Sept. 2010.
- [3] M. Montagna, M. Mercolino, M. Arza, M. Lanucara, E. Montagnon, E. Vassallo, “Maximisation of Data Return at Ka-Band for Interplanetary Missions,” 18th Ka and Broadband Communications, Navigation and Earth Observation Conference, Ottawa, 24-27 September 2012.
- [4] F.S. Marzano, M. Biscarini, L. Iess, M. Gregnanin, M. Parisi, M. Montopoli, K. De Sanctis, S. Di Fabio, L. Bernardini, M. Montagna, E. Montagnon, M. Arza, M. Mercolino, M. Lanucara, “Investigating ka-band science data transfer for BepiColombo mission by using radiometeorological numerical models”, *TTC 2013 6th ESA International Workshop on Tracking, Telemetry and Command Systems for Space Applications*, Sept. 8-11, 2013.
- [5] F.S. Marzano, “Predicting antenna noise temperature due to rain clouds at microwave and millimeter-wave frequencies,” *IEEE Trans. Antennas and Propagat.*, vol. 55, n. 7, pp. 2022-2031, 2007.

RADIATION LOSSES IN SUBSTRATE INTEGRATED WAVEGUIDES: A FORMULA FOR A QUANTITATIVE DETERMINATION

M. Pasian, M. Bozzi, L. Perregrini

Dept. of Electrical, Computer and Biomedical Eng, University of Pavia
Via Adolfo Ferrata, 5, 27100 Pavia, Italy
marco.pasian@unipv.it

Abstract

Substrate Integrated Waveguide, a manufacturing technology suitable for microwave and mm-wave circuits, is affected by three loss mechanisms: Ohmic and dielectric, as standard waveguides, and radiation. While for Ohmic and dielectric losses equations to determine the expected deterioration are available, for radiation loss no quantitative relationship was derived.

This paper presents a quantitative approach to predict the attenuation constant due to radiation loss in Substrate Integrated Waveguides.

Index Terms – Substrate Integrated Waveguide, Radiation Losses, Attenuation Constant, Electromagnetic Modeling.

I. INTRODUCTION

Substrate Integrated Waveguide (SIW) technology offers a promising approach to realize microwave and mm-wave circuits [1]. A typical SIW transmission line, shown in Fig. 1, is based on a dielectric slab where the electromagnetic field is confined using a top and a bottom metal plate and two rows of metalized vias. The propagation of the electromagnetic field can be studied according to the classic waveguide theory. In particular, related to Ohmic and dielectric losses can be described according to well known formulas derived for classic waveguides [2]. On the other side, radiation loss is a typical aspect of SIW circuits [3-6]. Previous works indicated that radiation loss can be minimized with the proper ratio between the via spacing s and the via diameter d [7]. However, no explicit formula to calculate the attenuation constant is available. This paper describes the mathematical approach used to derive a formula suitable to calculate the attenuation constant due to radiation losses in SIW transmission lines.

II. MODEL AND VALIDATION

The principle of the model was presented in [8, 9], and it is summarized here for completeness. Assuming that the power of the fundamental quasi TE_{10} mode of the SIW decreases exponentially along the z axis due to radiation loss, the attenuation constant α_r due to radiation losses can be expressed as [2]:

$$\alpha_r = \frac{W(z)}{2P(z)} \quad (1)$$

where $W(z)$ is the power lost by radiation per unit length at a given section z and $P(z)$ is the power flowing along the propagation axis at section z . To

determine $W(z)$ and $P(z)$ the TE_{10} mode is de-composed into two plane waves traveling along a direction indicated by an angle $\pm\theta$ with respect to the waveguide axis z , calculated according to the classic theory for waveguide simulators [2]:

$$\theta = \arcsin\left(\frac{\lambda}{2a}\right) \quad (2)$$

where λ is the operation wavelength and a is the SIW equivalent waveguide width, calculated for the most practical cases with [10]. The power density $S(z)$ associated to each plane wave can be expressed as:

$$S(z) = S_0 e^{-2\alpha_r z} \quad (3)$$

where S_0 is the power density for $z = 0$. For each plane wave, the flux of the Poynting vector through the cross section of the SIW yields half of the power $P(z)$ associated to the fundamental SIW mode:

$$P(z) = 2 S(z) w t \cos(\theta) = 2 S_0 e^{-2\alpha_r z} w t \cos(\theta) \quad (4)$$

where w and t are the SIW width and thickness, respectively. Similarly, the flux of the Poynting vector through a surface $dz \cdot t$ along the side wall of the waveguide yields half of the power P_{side} lost by radiation, which directly returns $W(z)$:

$$W(z) = \frac{P_{side}(z)}{dz} = 2 t S_0 e^{-2\alpha_r z} \sin(\theta) |T|^2 \quad (5)$$

where T is the transmission coefficient of the plane wave incident on an infinite grid of metal vias. The attenuation constant α_r is calculated substituting (5) and (4) into (1):

$$\alpha_r = \frac{W(z)}{2P(z)} = \frac{2 S_0 t |T|^2 \sin(\theta) e^{-2\alpha_r z}}{4 S_0 t w \cos(\theta) e^{-2\alpha_r z}} = \tan(\theta) \frac{|T|^2}{2w} \quad (6)$$

The value of T for an infinite grid of metal cylinders can be calculated with an analytical variational model of the grid, but this can be done under the approximation $d \ll s$ [11], which exclude the normal region of interest for SIW interconnects, i.e. $s/d < 2.5$ [1]. For this reason, the calculation of T is done on a numerical basis, exploiting the Floquet theorem for a TE-polarized plane wave impinging on an infinite grid of metal cylinders [12].

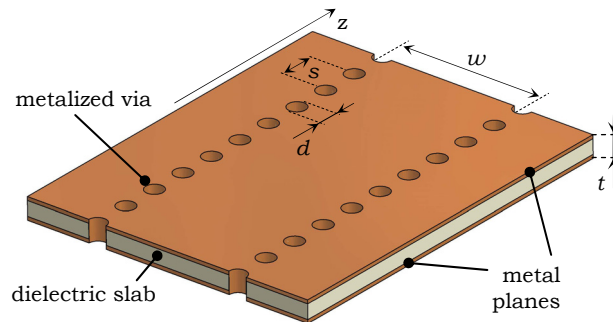


FIG. 1 – Substrate Integrated Waveguide schematic.

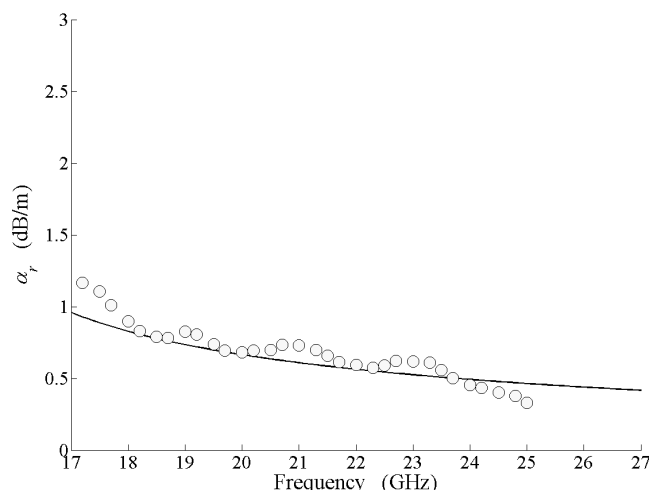


FIG. 2 – Attenuation constant α_r vs. frequency calculated using (9), black curve, and measured (data from [7], white dots).

In particular, the magnitude of the transmission coefficient T can be conveniently represented by the following expression:

$$|T| = \xi \left(\frac{d}{w} \right)^\gamma \left(\frac{s}{d} - 1 \right)^\tau \quad (7)$$

where ξ , γ and τ are scalar parameters used to interpolate the response of the transmission coefficients T . Eq. (7) is a good compromise between accuracy and complexity, and the scalar parameters are calculated with the least square method, minimizing the difference between the attenuation constant calculated when (7) is substituted into (6), and the attenuation constant calculated with a full-wave method [13]. The least square method is applied for the single-mode band of the fundamental quasi-TE₁₀ mode (defined from $1.25 f_0$ to $1.90 f_0$, being f_0 the cut-off frequency of the fundamental mode), and for the normal region of interest for SIW interconnects, defined by:

$$\frac{s}{d} > 1.6 \quad \frac{s}{d} < 3 \quad s < \frac{\lambda_c}{4} \quad s < \frac{\lambda_c}{4} \quad (8)$$

where $\lambda_c = 2a$ is the cut-off wavelength of the fundamental quasi TE₁₀ mode, and the top limit ($s/d < 3$) is extended above $s/d < 2.5$ to include some practical cases where the normal limit cannot be met for manufacturing reasons. After calculating with the least square method the scalar parameters of (7), (6) can be written as:

$$\alpha_r = \frac{\frac{1}{w} \left(\frac{d}{w} \right)^{2.84} \left(\frac{s}{d} - 1 \right)^{6.28}}{4.85 \sqrt{\left(\frac{2w}{\lambda} \right)^2 - 1}} \left[\frac{\text{dB}}{\text{m}} \right] \quad (9)$$

where w is expressed in meters. Eq. (8) represents the geometrical limit of validity of (9), while no intrinsic limit holds in terms of dielectric constant and operation frequency, because of the H-plane nature of SIW circuits. To

demonstrate the accuracy of (9), Fig. 2 shows the comparison between the attenuation constant measured in [7] ($w = 7.2$ mm, $d = 0.8$ mm, $s = 2$ mm, $\epsilon_r = 2.33$) and calculated using (9).

III. CONCLUSION

This paper presented a model used to derive an explicit formula to calculate the attenuation constant due to radiation loss in Substrate Integrated Waveguides (SIW) given the SIW geometrical parameters.

ACKNOWLEDGEMENT

This work was partially supported by the Italian Ministry of Education, University and Scientific Research under the project PRIN “GreTa” 2010WHY5PR.

REFERENCES

- [1] R. Garg, I. Bahl, and M. Bozzi, *Microstrip Lines and Slotlines*, Third Edition, Artech House, 2013.
- [2] R. E. Collin, *Foundations for Microwave Engineering*, McGraw-Hill, 1966.
- [3] M. Bozzi, A. Georgiadis, and K. Wu, “Review of Substrate Integrated Waveguide (SIW) circuits and antennas,” *IET Microwave Antennas and Propagation*, Vol. 5, No. 8, pp. 909–920, June 2011.
- [4] M. Bozzi, L. Perregrini and K. Wu, “Modeling of conductor, dielectric and radiation losses in Substrate Integrated Waveguide by the Boundary Integral-Resonant Mode Expansion Method,” *IEEE Transactions on Microwave Theory and Techniques*, Vol. 56, No. 12, pp. 3153–3161, December 2008.
- [5] M. Bozzi, M. Pasian, L. Perregrini, and K. Wu, “On the losses in Substrate Integrated Waveguides and cavities,” *International Journal of Microwave and Wireless Technologies*, Vol. 1, No. 5, pp. 395-401, October 2009.
- [6] M. Bozzi, M. Pasian, L. Perregrini, and K. Wu, "On the Losses in Substrate Integrated Waveguides," *37th European Microwave Conference 2007 (EuMC 2007)*, Munich, Germany, October 8-12, 2007.
- [7] F. Xu, and K. Wu, “Guided-wave and leakage characteristics of Substrate Integrated Waveguide,” *IEEE Transactions on Microwave Theory and Techniques*, Vol. 53, No. 1, pp. 66–73, January 2005.
- [8] M. Pasian, M. Bozzi, and L. Perregrini, “Radiation losses in Substrate Integrated Waveguides: a semi-analytical approach for a quantitative determination,” *2013 IEEE MTT-S International Microwave Symposium (IMS2013)*, Seattle, WA, U.S.A., June 2-7, 2013.
- [9] M. Pasian, M. Bozzi, and L. Perregrini, “A Formula for Radiation Loss in Substrate Integrated Waveguide,” *IEEE Transactions on Microwave Theory and Techniques*, submitted for publication.
- [10] Y. Cassivi, *et al.*, “Dispersion characteristics of Substrate Integrated rectangular Waveguide,” *IEEE Microwave and Wireless Components Letters*, Vol. 12, No. 9, pp. 333–335, 2002.
- [11] N. Marcuvitz, *Waveguide Handbook*, McGraw-Hill, 1951.
- [12] B. A. Munk, *Frequency Selective Surfaces – Theory and Design*, John Wiley & Sons, 2000.
- [13] Ansys official website: www.ansys.com, accessed April 2014.

SOME RECENT ADVANCEMENTS IN OPTIMAL CONSTRAINED POWER FOCUSING FOR MICROWAVE HYPERTHERMIA

L. Crocco⁽¹⁾, L. Di Donato⁽²⁾, D. A.M. Iero⁽³⁾, T. Isernia^(1,3), R. Scapatucci⁽¹⁾

⁽¹⁾ IREA-CNR, Institute for Electromagnetic Sensing of the Environment - National Research Council of Italy
Via Diocleziano 328, 80124 Napoli, Italy
{crocco.l, scapatucci.r}@irea.cnr.it

⁽²⁾ Department of Electrical, Electronics and Computer Engineering, University of Catania, Catania, Italy,
Viale Andrea Doria n. 6, 95100 Catania, Italy
loreto.didonato@unict.it

⁽³⁾ Mediterranea University of Reggio Calabria,
Via Graziella, Loc. Feo di Vito, 96100 Reggio Calabria, Italy
{domenica.iero; tommaso.isernia}@unirc.it

Abstract

In this communication, we review some of our recent results concerned with the problem of focusing the power of an electromagnetic field radiated by a fixed geometry array at a given location. Such a problem is relevant to microwave hyperthermia treatments, wherein the aim is to ensure the deposition of power at the tumor location, while keeping the field level low in healthy tissues to avoid side effects. In particular, we present a method to achieve the values of the optimal array excitations by means of the solution of one or more constrained convex programming optimization problems, address its robustness against uncertainties on the scenario and describe an integrated adaptive sensing/synthesis strategy that makes it possible the adoption of such a method in unknown or partially known scenarios.

Index Terms – Array synthesis, Convex Optimization, Microwave Hyperthermia.

I. INTRODUCTION

Microwave hyperthermia is a medical treatment in which the selective heating of tumor tissues above the therapeutic temperature of 43° is exploited to improve the effectiveness of chemo- and radio-therapy drugs or even to induce cellular death (apoptosis). In particular, noninvasive hyperthermia entails the adoption of fixed geometry arrays, whose shape is determined by the anatomy of the specific area to be treated.

From the point of view of the electromagnetic engineer, the problem to be faced consists in the synthesis of the array excitations in such a way to ensure that the maximum amount of power is deposited in the

tumor, while minimal power is dissipated in the surrounding healthy tissues, in order to avoid possible damages to the patient.

Remarkably, such a synthesis problem is also crucial from a medical point of view, as it allows to devise the patient-specific and optimized tools needed to plan an effective and safe treatment. However, the development of such tools is not at all straightforward, due to the complex relationship existing between the array excitations and the resulting temperature distribution.

With respect to such a framework, in this communication, we review our recent and ongoing efforts, concerned with the development of methods capable to solve the underlying electromagnetic focusing problem in actual treatment conditions, that is taking into account the vectorial nature of the fields, and the possible lack (or inaccuracy) of patient specific information.

II. TREATMENT PLANNING IN KNOWN SCENARIOS: THE OPTIMAL CONSTRAINED POWER FOCUSING STRATEGY

When the hyperthermia treatment planning is carried out with respect to an exactly known scenario, the strategy we exploit takes advantage of the analogy between the focusing problem at hand and antennas synthesis of pencil beams, and indeed relies on established results in this framework, which allow to obtain the *optimal* configuration of the array excitations, for a given geometry of the array and for given constraints on the field's power distribution [1].

In particular, as long as scalar fields are concerned, the extension of the approach in [1], which is based on the formulation of the synthesis problem in terms of a constrained convex optimization, is almost straightforward, but for the adoption of suitable numerical tools to model the interaction among the fields radiated by the array elements and the biological structure at hand [2].

Remarkably, an extended analysis, has shown that the proposed method, by using only monochromatic excitations, is capable to outperform widely exploited methods based on the time-reversal principle [3,4]. Moreover, the optimal constrained power focusing method (OPCF) is robust against inaccuracies on the parameters assumed on the unknown scenario, both in terms of electromagnetic properties and morphology [5].

The extension of the OCPF to the case of vectorial fields, which is indeed the one actually dealt with in most hyperthermia applications, is not straightforward, as indeed the vectorial nature of the field yields to a non deterministic polynomial time (NP)-hard optimization problem. However, results from multi-objective optimization theory can be exploited to turn the problem into a computationally feasible one [6]. In particular, within a multi-objective framework, the problem can be recast as the solution of an intrinsically parallel collection of single objective optimization problems (whose complexity is comparable to the

scalar OCPF). Such a generalization opens the way to the actual adoption of the method in actual therapeutic applications. The details of this generalization and its assessment against uncertainties will be presented at the conference.

III. TREATMENT PLANNING IN PARTIALLY KNOWN OR UNKNOWN SCENARIOS: AN IMPLICIT ADAPTIVE SYNTHESIS STRATEGY

As mentioned above, OCPF is quite robust against uncertainties on the assumed scenario. However, in some situations, the uncertainty level may exceed the allowed limits. Moreover, it would be obviously desirable to devise procedures capable to adaptively acquire the needed patient specific information and thus avoid an “a priori” modeling of the scenario. Notably, this is a technologically feasible goal, thanks to the dual, *theranostic*, nature of microwaves, which indeed provide both the means to deploy the (thermal) treatment and a means to image (diagnose) the region of interest. However, as well known, the diagnostic task entails the solution of an inverse scattering problem and it is thus prone to the occurrence of false solutions. Hence, suitable, smart, strategies have to be defined to overcome this issue.

As a contribution in this direction, for the case of scalar fields, we have proposed an adaptive strategy in which the diagnostic stage is meant to directly provide an approximated expression of the internal fields [7,8], rather than estimating the electromagnetic and morphological features of the scenario. Such a strategy is made possible thanks to new effective approximations (largely exceeding the Born approximation) for the internal fields that we have recently introduced [9], which rely on suitably determined incident fields. Notably, these latter are determined by means of the solution of a linear ill-posed problem corresponding to the one tackled in qualitative imaging methods [7,9]. Accordingly, false solutions are completely avoided (as they do not occur in linear inverse problems). Such a remarkable outcome is “paid” by the fact that no explicit knowledge on the electromagnetic parameters is gained in the diagnostic stage. However, this is not an issue in the considered application framework, wherein the internal field’s distributions are the information actually required by the synthesis task.

Therefore, by relying on such a set of incident and approximated total fields, which are implicitly and adaptively devised in an actual patient-specific fashion, it is then possible to apply the OCPF methodologies described in the previous paragraph, thus preserving their advantages also in the challenging case of a “partially blind” focusing [8].

At the conference, details on how this adaptive theranostic strategy can be exploited in the case of vectorial fields will be discussed.

REFERENCES

- [1] T. Isernia and G. Panariello, "Optimal focusing of scalar fields subject to arbitrary upper bounds", *Electronics Letters*, Vol. 34, 162-164, 1998.
- [2] D. Iero, T. Isernia, A. F. Morabito, I. Catapano, and L. Crocco, "Optimal Constrained Field Focusing for Hyperthermia Cancer Therapy: a Feasibility Assessment on Realistic Phantoms", *Prog. in Electromag. Res., PIER*, vol. 102, pp. 125-141, 2010.
- [3] D. A. M. Iero, T. Isernia and L. Crocco, "Power Focusing of Vectorial Fields: an Innovative Optimal Constrained Strategy", *submitted*, 2014
- [4] D. A. M. Iero, T. Isernia, L. Crocco, "Focusing Time Harmonic Scalar Fields in Complex Scenarios: A Comparison", *IEEE Antennas Wireless Propag. Lett.*, vol.12, pp.1029-1032, 2013.
- [5] D. A. M. Iero, T. Isernia, L. Crocco, "Focusing Time Harmonic Scalar Fields in Non-Homogenous Lossy Media: Inverse Filter vs. Constrained Power Focusing Optimization", *Appl. Phys. Lett.*, vol.103, no.9, pp.093702-4, August 2013.
- [6] D.A.M. Iero, L. Crocco, T. Isernia, "Thermal and Microwave Constrained Focusing for Patient-Specific Breast Cancer Hyperthermia: A Robustness Assessment," *IEEE Trans. Antennas Propag.*, vol.62, no.2, pp.814-821, Feb. 2014.
- [7] L. Crocco, L. Di Donato, D. A. M. Iero and T. Isernia, " An Adaptive Method to Focusing in an Unknown Scenario", *Progress In Electromagnetics Research, PIER* 130, 5pp. 63-579, 2012.
- [8] L. Crocco, L. Di Donato, D. A. M. Iero and T. Isernia, "A New Strategy for Constrained Focusing in Unknown Scenarios", *IEEE Antennas Wireless Propag. Lett.*, vol. 11, pp. 1450-1453, 2012.
- [9] L. Crocco, I. Catapano, L. Di Donato, and T. Isernia, "The linear sampling method as a way for quantitative inverse scattering", *IEEE Trans. Antennas Propag.*, vol. 60, no. 4, pp. 1844-1853, Apr. 2012.

A PROCEDURE FOR ESTIMATION ON THE ELECTROMAGNETIC FIELD EXPOSURE LEVELS

M. Strappini⁽¹⁾, M. Angelucci⁽¹⁾, M. Vecchiocattivi⁽¹⁾, P. Gianola⁽²⁾,
R. Scotti⁽²⁾, V. Villani⁽²⁾, D. Migagheli^(1,3)

- 1) Arpa Umbria, via Pievaiola 207/B-3 06132, Perugia, Italy
m.strappini@arpa.umbria.it
- 2) Telecom Italia TILab, Wireless Innovation Via Reiss Romoli 274
10148 Torino, Italy - paolo.gianola@telecomitalia.it
- 3) University of Perugia, via G. Duranti, 06132 Perugia, Italy

Abstract

The development of the new radio mobile technologies such as 4G/LTE is a crucial issue for the achievement of the Digital Agenda in Europe. However, the roll-out of the mobile networks is subject to some regulatory constraints. In particular, the regulatory framework on Electromagnetic Field (EMF) human exposure is a critical task which the mobile operators and authorities have to face. The EMF exposure limits have been regulated in Europe on the base of the International Commission on Non-Ionising Radiation Protection (ICNIRP) Guidelines. Nevertheless, in some countries more restrictive limits have been adopted. Italy is one of them where recently new concepts have been imposed by the regulator about the compliance procedure assessments that have to take care of the average EMF levels instead of the peak values as usually assumed in a conservative approach worldwide accepted. In this paper a procedure for the estimation on the EMF exposure levels averaged on an interval of time is shown based on a list of in field measurements and a set of traffic data extracted by the network counters.

Index Terms–. Estimation on EMF exposure levels, LTE, correlation functions

I. INTRODUCTION

In a conservative approach, the compliance assessments on the EMF exposure limits is usually based assuming the Radio Base Station (RBS) is transmitting constantly the maximum power. The EMF values are usually estimated through computation models implemented in dedicated tools. However it is well known that, for people skilled in the art, the power transmitted by an RBS in a mobile network varies in time depending on the amount of communication traffic, on the radio propagation conditions and on some specific functionalities such as the *power control*. The result is that, in general, the average EMF levels are in the reality much lower than those estimated by considering the maximum power. As a consequence, the compliance assessment based on maximum power leads to an overestimation of the existing exposure conditions. In the Italian regulatory framework, an exposure limit of about 6V/m is imposed in long term exposure conditions (at least 4 h/day) in living spaces and in outdoor intensely frequented places. The

regulation in force since December 17th 2012 (Law 179/2012) revised the DPCM July 8th 2003 by varying the EMF evaluation methods and the scope-of-application of exposure limits. In particular, it prescribed that the 6V/m limit must be evaluated as average value over 24 hours. It is evident that, in the compliance daily assessment on the EMF limits, it is impracticable to monitor the EMF levels by means of in-field measurement over such a long period of time. In this paper, a procedure for the estimation on the EMF exposure levels averaged over a generic interval of time is showed by considering the 4G/LTE technology provided by Nokia and implemented in the Telecom Italia mobile network. The method is based on a list of in field measurements made both in spectral and code domain and on a set of traffic data extracted by the proprietary Telecom Italia network counters.

II. THE PROJECT

During summer 2013 an LTE signal transmitted by a urban RBS, located in the neighborhood of the ARPA building, has been monitored by using a narrowband measuring bench.

A measurement set-up was defined in order to investigate some issues such as: in-field spectral analysis of the LTE signal, implementation of the procedures described in CEI 211/7 Appendix E [2], analysis of the correlation functions between in-field power measurements and transmitted power estimated via network counters. Observation intervals of 4-6 hours have been generally adopted and the carrier at 806 MHz was explored. The R&S spectrum analyzer model FSH 8, implementing time domain analysis for LTE, and the biconical CLAMPCO AP2000 antenna have been employed.

The cell traffic, in some cases, has been randomly forced by the operator.

III. ANALYSIS OF THE IN-FIELD AND NETWORK COUNTED MEASUREMENTS

The transmitted power has been estimated by means of a combination of a specific subset of network counters: this was performed thanks to the *Simtel Measurements Open Platform* (SMOP) implemented in the Telecom Italia network. SMOP is a data base based on a client-server platform able to elaborate different data sets coming from different network elements. The SMOP system provides network performance counters averaged over 15-minute intervals.

The sets of measured power values with respect to the SMOP transmitted power have been time-aligned and then analyzed in terms of:

- Comparison between time behaviors
- Statistical analysis by means of correlation functions.
- Linear regression between data sets: an attenuation factor useful for long time in-field predictions was determined by mean of the angular coefficient of the regression line

- Signal prediction: extrapolation models, for both the electric field and the received power
- Comparison between received power to maximum-nominal-power ratio. The maximum nominal power has been obtained by applying the extrapolation method described in [2]

IV. RESULTS

In the following, some results according to the above listed analyses will be represented:

- *Linear regression:* in Fig. 1 an example of scatter plot and linear regression obtained by forcing the intercept to 0 is shown.

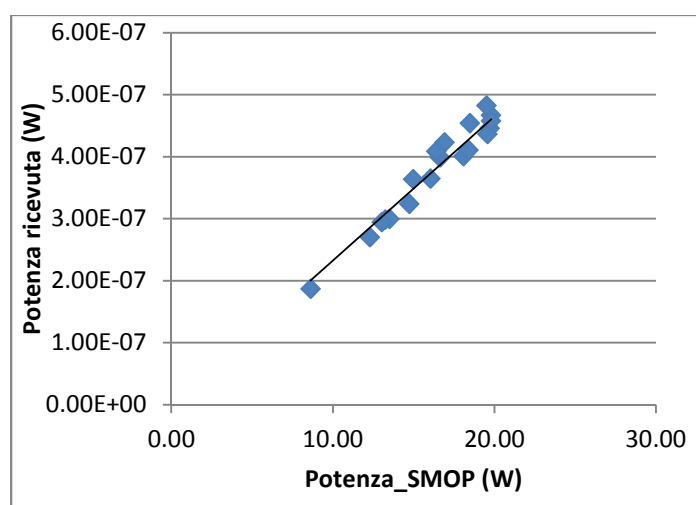


FIG. 1 – Scatter plot and linear regression between SMOP detected power and in field measured power. The linear regression coefficient is $\alpha = 2,32 \cdot 10^{-8}$. The scatter plot shows the dynamic range for the RBS power.

- *Signal prediction:* in Fig. 2 the comparison between the measured power and the in-field predicted power obtained by applying the linear regression coefficient α to the SMOP estimated power is shown.

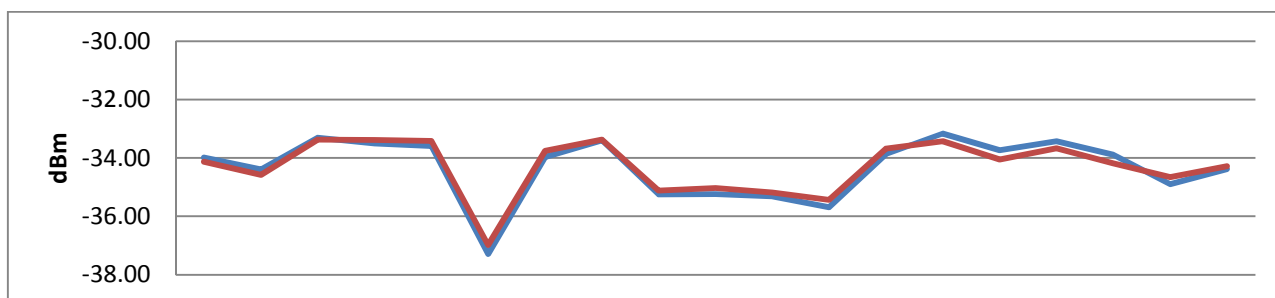


FIG. 2 – Comparison between in field predicted (red) and measured (blue) power, both averaged on 15 minutes. The example shows a good agreement between data sets and demonstrates the reliability of the proposed procedure

The tested good agreement between predicted and measured in field values establishes the reliability of the proposed procedure. In Fig. 3 a comparison between results for different prediction techniques, using also the regression coefficients procedure obtained for lower sample sets, is performed.

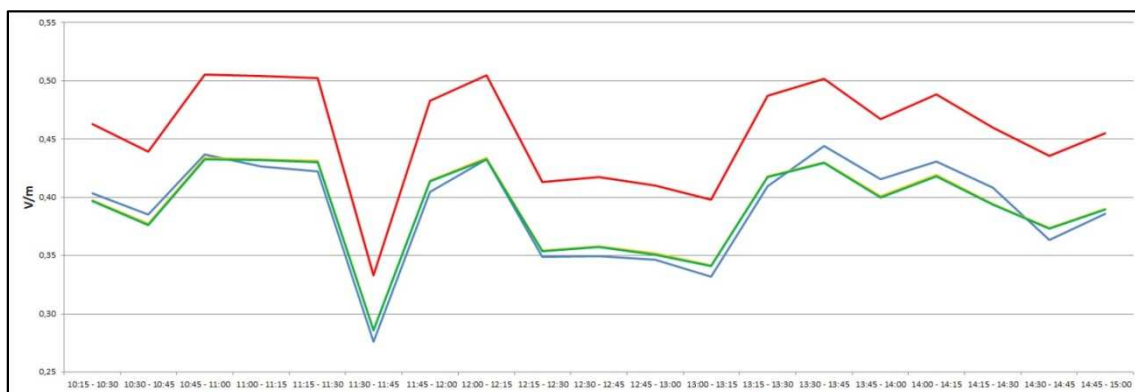


FIG. 3 – Comparison between in field and predicted electric field values (V/m):
 i) Free space loss prediction (red), ii) measured (blue), iii) predicted over 19 samples (yellow), iv) predicted over 6 samples (green)

V. CONCLUSION

The EMF levels entered by a RBS for mobile network are varying in time due to traffic and propagation conditions. As a matter of that, the Italian regulation imposed that compliance assessment of an RBS on the EMF exposure limit of 6 V/m has to consider the average value over a period of 24 hours. With this work it has been demonstrated that it will be possible to estimate the EMF average level over a certain period of time by properly correlating the EMF levels measured in field in shorter period with the power transmitted by the RBS achievable by means of a proper set of network counters available every 15 minutes. The authors found that that the correlation factor between in field measurement and data counters is close to 1 such as to make the proposed compliance assessment well reliable.

REFERENCES

- [1] Legge n. 221 del 17 dicembre 2012, “*Ulteriori misure urgenti per la crescita del paese*”, Supplemento ordinario n. 208 della gazzetta ufficiale n. 294 del 18 dicembre 2012.
- [2] Norma italiana CEI 211-7 “*Guida per la misura e per la valutazione dei campi elettromagnetici nell’intervallo di frequenza 10kHz – 300GHz, con riferimento all’esposizione umana*” Fascicolo 5909, Edizione Prima, Pubblicazione Gennaio 2001.
- [3] Norma italiana CEI 211-7 Appendice E: *Misura del campo elettromagnetico da stazioni radio base per sistemi di comunicazione mobile (2G, 3G, 4G)*, Fascicolo 13105, Pubblicazione Settembre 2013.

IN SOIL DISTRIBUTED TEMPERATURE MEASUREMENTS FOR SMALL SCALE PHYSICAL MODELS

S. Bersan⁽¹⁾, L. Schenato^(2,*), A. Rajendran⁽³⁾, L. Palmieri⁽³⁾, S. Cola⁽¹⁾, A. Pasuto⁽²⁾, A. Galtarossa^(3,4), P. Simonini⁽¹⁾

(1) Civil, Architectural and Environmental Engineering, Padova University, Via Marzolo 9 – 35131 Padova, Italy

(2) Research Institute for Geo-Hydrological Protection, National Research Council, Corso Stati Uniti 4, 35137 Padova, Italy

(3) Department of Information Engineering, Padova University Via Gradenigo 6/b, 35131 Padova, Italy

(4) IIUSE, Southeast University, Nanjing, China

(*) luca.schenato@cnr.it

Abstract

A distributed temperature optical fibre sensors system with a sub-centimetre spatial resolution has been incorporated in a sand-box model. The aim is to monitor the temperature field induced in the sand by a horizontal water flow with inflowing water maintained at a constant temperature higher than the room temperature. It is shown that by distributed fibre optic sensors accurate temperature mapping in a soil sample can be obtained. The measurements has such a richness of detail which is not comparable with that achievable with any other system of point-wise sensors.

Index Terms – Fibre optic Sensor, Optical Backscattered Reflectometer. Distributed Temperature Sensing, Soil temperature.

I. INTRODUCTION

Over the last three decades fibre optic sensor (FOS) technology has become an established sensing tool in many fields of application; it is indeed true that the proposal of using fibre optics as sensing media is almost as old as their use as transmission media [1]. Several review papers ([2] and therein references) have celebrated the many advantages offered by FOSs with respect to traditional electronic/mechanical sensors. In particular, for those applications with high demanding requirements, i.e. large number of sensing points, harsh environments and large areas to cover, features as immunity to electromagnetic interference, cheapness of the sensing element, low operating cost, flexibility, easiness of multiplexing and reliability make that technology a very competitive and appropriate (sometimes the only one viable) sensing solution [3], [4]. Geoenvironmental applications are among the most representative cases of those demanding sectors and this partially explains the massive initial penetration of FOS into oil and gas industry. Nowadays, fibre optic sensors are available, also

commercially, as viable replacement of many standard legacy sensors used in geotechnical and environmental engineering.

Among the others, the class of distributed FOSs (DFOSs), is the most promising class of sensors for geoenvironmental monitoring, because of their unique feature, i.e. the ability of distributedly mapping the field of the measured physical quantity along the entire fibre [2,5]. Furthermore, with a terrific spatial resolution at centimetre scale or even less and few tens of seconds of sampling time, they are a revolutionary tool for small and medium scale physical modelling. Here, we apply DFOSs to measure the spatio-temporal evolution of temperature within a sand box model. Such a sensing technique is usually referred to as Distributed Temperature Sensing (DTS) and some examples of DTS for geoenvironmental applications can be found in the literature ([6] and therein references).

Sand box models are tools used to observe phenomena as they actually occur in porous media. A typical application is the modelling of groundwater flow at small or medium scale [7]. A sand box consists of a rigid, watertight container filled with a porous matrix, one or more fluids, measuring devices and a supply system that reproduces the boundary conditions of the natural reservoir. The sand box described in this work reproduces in small scale the foundation layer of a water retaining structure and the ultimate aim is studying the viability of DTS to detect internal erosion under water retaining structures, and in particular in river embankments. The highly localized nature of the process in its initial phase makes its detection cumbersome if traditional monitoring techniques, based on point-wise sensors, are employed. On the other side, DTS-based approaches are based on the fact that, if an initial temperature difference exists between the inflowing water and the soil, the increase of flow velocity in the erosion channel and its surroundings generates variations in the temperature field of the embankment [8].

II. MODEL DESCRIPTION AND PRELIMINARY RESULTS

The sand box model reproduces in detail the model designed by van Beek et al. [9] for improving and validating the piping law adopted by the Dutch code.

We present here preliminary results obtained inducing a horizontal flow in a homogeneous sample where no internal erosion occurred. The sample was 30 cm wide, 15 cm tall and 35 cm long in the direction of the flow (Fig. 1). It was built by wet deposition of uniform medium sand ($d_{50} = 0.3$ mm, $C_u = 1.5$) and compacted by shock waves to a relative density of around 90%. The optical fibre (0.9mm tight-buffered) was embedded in the sand so that 15 measuring lines orthogonal to the flow direction have been arranged in three layers of five lines each. An Optical Backscatter Reflectometer (OBR) from Luna™ has been used for measuring the Rayleigh shift along the fiber. Four resistive platinum

sensors (PT-100) measured the temperature of the inflowing and outflowing water as well as the temperature in the sand at two positions close to a couple of fibre lines, thus providing an absolute temperature reference.

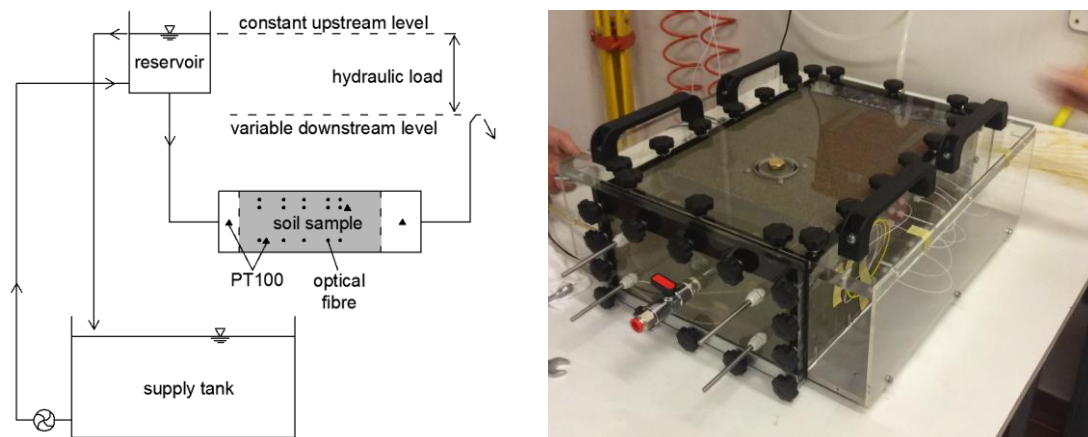


FIG. 1 – On the left: setup of the experiment; on the right: the sand-box with the fibre visible on the side.

The test was performed by flushing the sample with water at a temperature constantly kept 10 °C higher than the room temperature. The flow was forced by maintaining a fix head difference between inlet and outlet. Five piezometer tubes inserted into one of the lateral walls allowed to verify the effective hydraulic load applied to the sample and the trend of the hydraulic head inside the sample. The average Darcy velocity during the experiment was 9.5×10^{-5} m/s.

Figure 2 shows the normalized frequency shift measured by the fibre after 4 hours from the beginning of the test. Here, the frequency shift is normalized by the maximum shift registered during the test; indeed, the temperature coefficient of the fibre will be measured soon in a climatic chamber and this will ultimately allow the calculation of the actual temperature variation. Data show a strong asymmetry along the y axis; this may be partially explained by the different materials of the box, with its base made of aluminium, which transfers heat differently than Plexiglass. An additional contribution may come from strain experienced by the fibers in the upper levels, due to the different thermal expansion of Plexiglass and aluminium; ongoing investigations with a strain-free fibre deployment will provide better insight.

III. CONCLUSIONS

Results show the potentialities of the sensing platform. High-density measurements highlighted details of the transfer of heat occurring in the sample, which would not have been observed even with numerous point-wise sensors. Further investigation is ongoing to determine the

temperature coefficient of the fibre and to avoid any strain experienced by the fibre during the tests.

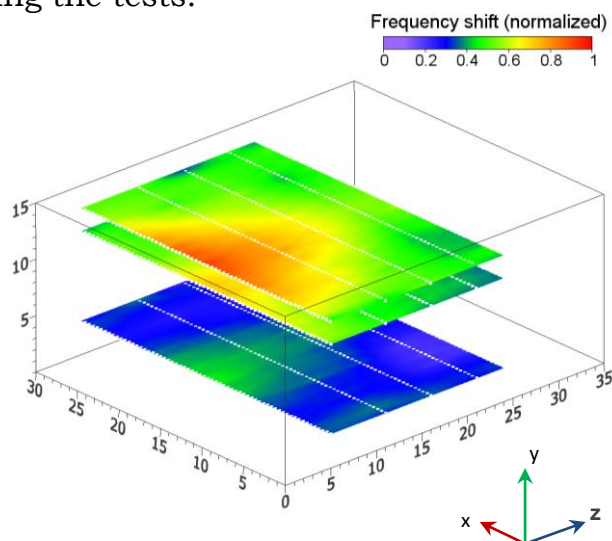


FIG. 2 – Normalized frequency shift measured by the fibre (dotted lines in figure) after 4 hours from the beginning of the test.

ACKNOWLEDGEMENT

Partial financial support from Fondazione Cassa di Risparmio di Padova e Rovigo is acknowledge.

REFERENCES

- [1] B. Culshaw, A. Kersey, "Fiber-optic sensing: a historical perspective," *IEEE J. Lightwave Technol.*, vol.26, No.9, 2008, pp.1064-1078.
- [2] A.D. Kersey, A. Dandridge, "Distributed and multiplexed fibre-optic sensor systems," *Journal of the Institution of Electronic and Radio Engineers*, vol.58, No.5, 1988, S99-S111.
- [3] J.M. López-Higuera, "Handbook of optical fibre sensing technology," 1 st ed. Wiley, 2002.
- [4] L. Schenato, L. Palmieri, G. Gruca, D. Iannuzzi, G. Marcato, A. Pasuto, A. Galtarossa, "Fiber optic sensors for precursory acoustic signals detection in rockfall events," *Journal of the European Optical Society – Rapid Publications*, vol.7, 2012.
- [5] L. Palmieri, L. Schenato, "Distributed optical fiber sensing based on Rayleigh scattering," *The Open Optics Journal*, vol.7 (Suppl-1, M7), 2013, pp.104–127.
- [6] J. Selker, L. Thévenaz, H. Huwald, A. Mallet, W. Luxemburg, N. van de Giesen, M. Stejskal, J. Zeman, M. Westhoff, M. Parlange, "Distributed Fiber Optic Temperature Sensing for Hydrologic System," *Water Resources Research*, vol. 42, No. 12, 2006.
- [7] J. Bear, "Dynamics of fluids in porous media," Elsevier, New York, 1972.
- [8] S. Bersan, A.R. Koelewijn, "Temperature monitoring in piping-prone hydraulic structures," *IEAG XII Congress*, Torino, 2014 [in press].
- [9] V.M. van Beek, J.G. Knoeff, J.B. Sellmeijer, "Observations on the process of piping by underseepage in cohesionless soils in small-, medium- and full-scale experiments," *European Journal of Environmental and Civil Engineering*, vol.15, No.8, 2011, pp. 1115-1138.

Notes

Notes

Notes

Notes

List Of Authors

- Aceves A.B.: S4.5
 Addamo G.: S3.2, S8.1, P.06
 Agneessens S.: S3.7
 Alharbi M.: P.39
 Allegretti M.: S10.1
 Amabile C.: S11.1
 Amendola G.: P.32
 Amicucci L.: S6.7
 Amitrano D.: S10.2
 Angeloni G.: S5.8
 Angelucci M.: P.48
 Angiulli G.: S7.5
 Anniballe R.: S1.5
 Annoni A.: P.22, S4.4
 Anselmi N.: P.42, P.44
 Arcioni P.: S11.3
 Arcuti P.: P.08
 Argyros A.: S2.3
 Arnieri E.: P.32
 Assanto G.: S4.3
 Avezzano R.G.: P.34
 Baccarelli P.: S7.3
 Barbiroli M.: S6.2
 Barbuto M.: S7.6
 Baroni A.: P.07, S3.3
 Baronio F.: S4.1
 Barthélémy A.: S4.5
 Bassi P.: S4.4, S2.3
 Bastianelli L.: P.31
 Bekele E.: P.44
 Bellanca G.: P.22, S4.4,
 S2.3, S4.8
 Bellizzi G.: S11.5
 Benabid F.: P.39
 Berardino P.: S10.4
 Bersan S.: P.49
 Bertoldo S.: S10.1
 Bevacqua M.: S12.5, S11.6
 Bianchi G.: P.21
 Bianco G.V.: S9.2
 Bilotti F.: S7.6
 Biscarini M.: P.45
 Bjarklev A.O.: PL.1
 Boccia L.: P.32
 Bolli P.: P.06, P.21
 Bonafoni S.: S1.5
 Borgia A.: S5.3, P.29, P.30
 Boscolo S.: S9.1
 Bozzetti M.: S5.8
 Bozzi M.: S11.3, P.46, S3.6,
 S3.7
 Bradley T.: P.39
 Braglia A.: S2.5
 Bressan M.: S3.6
 Bruno G.: S9.2
 Bucci O.M.: S11.5, S5.5
 Buffi A.: P.07, S3.5
 Burghignoli P.: S7.3
 Busacca A.C.: P.18, S4.3
 Buttazzoni G.: P.05
 Calò G.: S4.6
 Candiani A.: S2.4
 Capobianco A.D.: S9.1
 Cardinali A.: S6.7
 Carlin M.: P.44
 Carminati M.: S4.2
 Carta P.: S5.8
 Caso R.: P.07, S3.5
 Cassarino S.: S11.1
 Castaldo C.: S6.7
 Castellano T.: S5.8
 Castorina G.: S1.4
 Castro G.: S8.3
 Casula G.A.: S3.1, P.01
 Catapano I.: S12.2
 Cavagnaro M.: S11.1, S11.4
 Ceccuzzi S.: P.12
 Celona L.: S8.3
 Cerri G.: S8.2
 Cesario R.: S6.7
 Chiapperino M.: S5.8
 Chiarello F.: P.28
 Cino A.C.: P.18, S4.3
 Ciotola A.: S6.8
 Cola S.: P.49
 Comite D.: S12.2
 Conforti M.: S4.1, S4.8
 Congedo F.: P.08
 Coscelli E.: S2.1, P.38
 Costa F.: S5.7, S7.7
 Costanzo A.: P.02, P.03, P.30
 Costanzo S.: S5.2, S5.3,
 P.10, P.29, P.30
 Couderc V.: S4.5
 Crocco L.: S12.5, P.47
 Cuccaro A.: P.14
 Cucinotta A.: S2.1, S2.2,
 S2.4, P.38, P.40
 Curcio L.: S4.3
 D'Agostino F.: S5.1, P.04
 D'Alessandro A.: P.07
 D'Orazio A.: S9.2
 De Angelis C.: S9.1
 De Carlo D.: S7.5
 De Ceglia D.: S9.2
 De Leo A.: S8.2
 De Palma L.: S4.7
 De Sanctis K.: P.45
 De Vittorio M.: S9.2
 Debord B.: P.39
 Degasperis A.: S4.1
 Degli-Esposti V.: S6.2
 Del Frate F.: P.34
 Di Bartolo S.: P.37
 Di Donato A.: S11.2
 Di Donato L.: S8.3, S1.4,
 S12.5, P.47
 Di Filippo M.: S5.4
 Di Martino G.: P.09, S10.2,
 S10.3, P.35, S6.8
 Di Massa G.: S5.2, S5.3,
 P.29, P.30
 Di Mattia V.: P.20
 Di Ruscio D.: S7.3
 Di Simone A.: S10.3
 Dionigi M.: S1.1, P.33
 Donelli M.: P.42, P.44
 Esposito C.: S10.4
 Ettore M.: S6.6
 Falciasecca G.: S6.2
 Fanti A.: S8.5
 Fantuzzi M.: P.03
 Farina L.: S11.1
 Farina M.: S11.2, S5.8
 Ferrara F.: S5.1, P.04
 Ferrari G.: S4.2
 Ferrari M.: S4.7
 Fornaro G.: S10.4
 Fourcade-Dutin C.: P.39
 Franceschetti G.: S1.2
 Francia P.: P.02
 Frezza F.: S11.4
 Fuscaldo W.: S6.6
 Fuschini F.: S6.2
 Galli A.: S7.3, S6.6, S3.4,
 S12.2, S6.7
 Galli P.: S9.5
 Galtarossa A.: S2.6, P.49
 Gammino S.: S8.3
 Gao S.: P.32
 Gauthier-Lafaye O.: S4.6
 Gennarelli C.: S5.1, P.04
 Genovesi S.: S5.7, S7.7
 Giannini A.: S3.6
 Gianola P.: P.48
 Giarola E.: P.13
 Gifuni A.: S10.4
 Giorcelli M.: S9.4
 Goldberg S.N.: S11.1
 Gradoni G.: S6.1, P.19
 Grande M.: S4.6, S9.2
 Gregnanin M.: P.45
 Grillanda S.: S4.2, S4.4
 Guerriero R.: S5.1, P.04
 Gérôme F.: P.39

Hajj Yahya M.: S9.4
 Iero D.A.M.: P.47
 Iess L.: P.45
 Iodice A.: P.09, S1.2, S10.2,
 S10.3, P.35, S6.8
 Iovine R.: P.15
 Isernia T.: S8.3, S12.5, P.47
 Jackson G.: S10.4
 Kaynak M.: P.32
 Khalid M.: S7.4
 Kimerling L.C.: S9.5
 Kishi T.: S4.7
 Krupa K.: S4.5
 La Spada L.: S7.1, S7.2
 Labruyère A.: S4.5
 Lanari R.: S10.4
 Lanucara M.: P.45
 Laurita R.: S11.4
 Lemme M.: PL.2
 Leon-Saval S.G.: S2.3
 Leuzzi G.: P.33
 Lingua A.: P.21
 Liu Y.: S2.5
 Locatelli A.: S9.1
 Lombardi F.M.: P.33
 Lopresto V.: S11.1
 Losito O.: S5.8
 Love J.D.: S2.3
 Lozes-Dupuy F.: S4.6
 Lucci L.: S5.4
 Lucianaz C.: S10.1
 Lumia M.: S3.2
 Luo Q.: P.32
 Lutey A.: P.40
 Lwin R.: S2.3
 Magenes G.: S11.3
 Magno G.: S4.6, S9.2
 Maisto M.A.: S12.1
 Malaguti S.: S4.4, S4.8
 Manara G.: S5.7, S7.7
 Mangini F.: P.23, P.24, S1.3,
 S6.4, S6.5, P.36, P.43
 Manica L.: P.44
 Marchesi S.: P.13
 Mari E.: P.16
 Mariani Primiani V.: S8.2,
 P.31
 Marzano F.S.: P.37, P.41,
 P.45, S10.6
 Mascali D.: S8.3
 Masotti D.: P.02, P.03
 Masruri M.: S2.2, P.39
 Massa A.: P.13, P.42, P.44
 Matri F.: P.02
 Matrone G.: S11.3
 Mauro G.S.: S1.4
 Maxia P.: P.01
 Mazzanti A.: S11.3
 Mazzarella G.: P.01, S8.5
 Mazzocchi S.: S3.4
 Melloni A.: S4.2, P.22, S4.4
 Mencarelli D.: S11.2, S5.8
 Meniconi E.: P.32
 Michel A.: P.07, S3.5
 Michel J.: S9.5
 Midrio M.: S9.1, S9.5
 Migagheli D.: P.48
 Migliorati M.: S8.6
 Migliore M. D.: S5.3
 Migliozi M.: S5.1, P.04
 Minoni U.: S4.5
 Mioc F.: P.11
 Miscuglio M.: S9.4
 Modotto D.: S4.5
 Moglie F.: P.31
 Molardi C.: S2.1
 Monari J.: P.21
 Mongiardo M.: S1.1, P.33
 Monmayrant A.: S4.6
 Monorchio A.: S5.7, S7.7
 Montagna M.: P.45
 Monti A.: S7.6
 Monti G.: P.08
 Montisci G.: P.01
 Montopoli M.: P.45
 Morabito A.F.: S1.4
 Morandotti R.: P.18
 Moreno H.O.: S5.2
 Mori S.: P.37, S10.6
 Morichetti F.: S4.2, P.22,
 S4.4
 Morini A.: S5.8
 Moro R.: S3.7
 Morrone L.: P.30
 Moréac A.: S4.7
 Moscato S.: S11.3
 Murgía M.: P.21
 Muzi M.: S1.3, P.25
 Napoli F.: S6.7
 Nazabal V.: S4.7
 Nepa P.: P.07, S3.3
 Neri L.: S8.3
 Nissenbaum Y.: S11.1
 Notarpietro R.: S10.5
 Ntibarikure L.: S8.4
 Oliveri G.: S9.3, P.42, P.44
 Onorato M.: S4.1
 Orlandi P.: S4.4
 Orta R.: S3.2, P.06
 Pajewski L.: P.12
 Palma G.: S4.7
 Palmieri L.: S2.6, P.49
 Paonessa F.: P.06
 Parini A.: P.22, S4.4, S2.3
 Parisi G.: P.16
 Parisi M.: P.45
 Pasian M.: S11.3, P.46, S3.6
 Pastorino M.: P.29, S12.4
 Pasuto A.: P.49
 Pauciullo A.: S10.4
 Peccianti M.: P.18
 Pei Y.: S10.5
 Pelosi G.: S8.4, S5.4
 Perini F.: P.21
 Perna S.: S5.5, S10.4
 Perona G.: S10.1
 Perregrini L.: S11.3, P.46,
 S3.6
 Perrone G.: S2.5
 Persichelli S.: S8.6
 Peruzzi G.: PL.3
 Petruzzelli V.: S4.6, S9.2
 Peverini O.A.: S3.2, P.06
 Pierdicca N.: S1.5, S10.6
 Pierri R.: S12.1, P.14
 Pietrangelo T.: S11.2
 Pinchera D.: S5.3, S5.5
 Pinto R.: S11.1
 Poli F.: S2.1, P.38
 Poli L.: P.42, P.44
 Polo A.: P.13
 Polverari F.: S10.6
 Pompili S.: P.41
 Ponti C.: P.12, S6.3
 Prudenzeno F.: S5.8, S4.7
 Pulvirenti L.: S10.6
 Pupillo G.: P.21
 Purtova T.: P.32
 Raffetto M.: S12.4
 Raffo A.: P.30
 Rajendran A.: P.49
 Ramaccia D.: S7.6
 Randazzo A.: P.29, S12.4
 Renghini C.: S5.8
 Riccio D.: P.09, S1.2, S10.2,
 S10.3, P.35, S6.8
 Riesen N.: S2.3
 Rivaroli L.: P.43
 Rizzoli V.: P.02, P.03
 Robol F.: P.13
 Rocca P.: P.42, S5.6, P.44
 Rogier H.: S3.7
 Romagnoli M.: S9.5
 Romanato F.: P.16
 Rorato O.: S10.1
 Rossi F.: P.11
 Ruello G.: P.09, S1.2, S10.2,
 S10.3, P.35, S6.8

Russo P.: S8.2
 Sabbadini M.: P.11
 Salucci M.: P.42, P.44
 Sampietro M.: S4.2
 Sandhu A.I.: P.32
 Santagiustina M.: S2.6
 Santini C.: S6.5
 Sassaroli D.: S3.4
 Sauleau R.: S6.6
 Savi P.: S10.5, S9.4
 Scalora M.: S9.2
 Scapatucci R.: P.47, S11.6
 Schenato L.: P.49
 Schettini G.: P.12, S6.7
 Schiavon G.: P.34
 Schillirò F.: P.21
 Schumacher H.: P.32
 Scotti R.: P.48
 Selleri S.: S2.1, S8.4, S5.4,
 S2.2, S2.4, P.38, P.40
 Sgrò A.: S7.5
 Shalaby B.M.: S4.5
 Shamsafar A.: P.32
 Simonini P.: P.49
 Soldovieri F.: S12.2
 Solimene R.: S12.1, P.14
 Someda C.G.: P.16
 Sorbello G.: S8.3, S1.4
 Sorel M.: S4.4
 Sozzi M.: P.40
 Spadafora F.: P.30
 Spinello F.: P.16
 Stivala S.: P.18, S4.3
 Stoja E.: S1.3, P.43
 Stomeo T.: S9.2
 Stornelli V.: P.33
 Strain M.J.: S4.4
 Strappini M.: P.48
 Summers P.: S11.3
 Svelto F.: S11.3
 Tagliaferro A.: S9.4
 Tamburini F.: P.16
 Tannino M.: P.36, S11.4
 Tarabani F.: P.32
 Tarparelli R.: P.15
 Tarricone L.: P.08
 Tartarini G.: P.21
 Tascone R.: S3.2, P.06
 Tedeschi N.: P.24, P.26, P.27,
 S6.4, S6.5
 Tenuti L.: P.42, P.44
 Tian L.: S6.2
 Tibaldi A.: S8.1
 Tillack B.: P.32
 Tomasino A.: P.18, S4.3
 Tonello A.: S4.5
 Torrisi G.: S8.3
 Toscano A.: S7.6
 Tosi Beleffi G.M.: P.37
 Tosoratti N.: S11.1
 Trillo S.: S4.8
 Tuccillo A.A.: S6.7
 Valenta V.: P.32
 Valerio G.: S6.6
 Varchetta S.: P.41
 Vecchiocattivi M.: P.48
 Vegni L.: S7.1, S7.2, P.15
 Venanzoni G.: S5.8
 Venneri F.: P.10
 Vescovo R.: P.05
 Viani F.: P.13, S12.3
 Villani V.: P.48
 Vincenti M.A.: S9.2
 Vincetti L.: S2.2, P.39
 Virone G.: S3.2, P.06, P.21
 Vitucci E.M.: S6.2
 Wabnitz S.: S4.1, S4.5
 Wang Y.Y.: P.39
 Weiss N.: S11.1
 Yano T.: S4.7
 Zambiasi L.: P.44
 Zappelli L.: P.17
 Zappini L.: P.13
 Ziegler V.: P.32
 Zorer A.: P.13
 Zucca M.: S3.4